UNIVERSITÀ DEGLI STUDI DI NAPOLI FEDERICO II

CHEMISTRY SCIENCE DOCTORATE

XXX CYCLE

Novel polyolefin based elastomers with tailored stiffness from metallorganic catalysis: the crystalline elastomers

TUTORS:
Prof. Claudio De Rosa
Prof. Finizia Auriemma

CANDIDATE:
Miriam Scoti

UNIVERSITÀ DEGLI STUDI DI NAPOLI FEDERICO II

DOTTORATO DI RICERCA IN SCIENZE CHIMICHE

XXX CICLO

Nuovi elastomeri a base di poliolefine a rigidità controllata da catalisi organometallica: gli elastomeri cristallini

TUTORI:
Prof. Claudio De Rosa
Prof. Finizia Auriemma

CANDIDATA:
Miriam Scoti

Index

Summary of PhD research activities

Novel polyolefin based elastomers with tailored stiffness from metallorganic catalysis: the crystalline elastomers.

Elastomers are generally amorphous polymers made by long and highly flexible chains with high molecular mass and glass-transition temperature much below room temperature.[1] The flexible segments of the random coil conformation in the unstretched state, assume extended conformation upon stretching and the entropy-driven recoiling upon releasing the stress is responsible for the elastic recovery of size and shape of the whole material in the undeformed state.[1,2] The existence of chemical or physical cross-links acting as network knots prevents the material from flowing during application of the tensile stress. These amorphous rubbers may partially crystallize under stretching.[1] The small number of small crystals acts as knots of the elastomeric network. When the applied tensile stress is removed, the crystals melt, providing a positive enthalpic contribution to the Gibbs free energy change involved during the elastic recovery of the material; therefore, the elasticity in these materials is merely of entropic nature, due to the conformational changes experienced by the amorphous "tie-chains"[1] (Figure 1).

In general, high level of crystallinity may strongly reduce the elastic performances of these materials. However, many semicrystalline polymers show elastic properties in spite they present high crystallinity and high mechanical strength.[3-19] Phase transitions may play a key role in the elasticity of these systems, resulting in materials where elasticity is not merely entropic as in conventional elastomers but similar to super-elasticity of shape memory alloys that undergo martensitic phase transitions.[6-19] An example of this type of rubbers is the class of "*crystalline elastomers*" based on syndiotactic polypropylene (sPP) and its copolymers.[13-16] The unusual elastic behavior of sPP is associated with a reversible crystal-crystal martensitic-like phase transition between the metastable form III with chains in trans-planar conformation, which develops upon stretching, and the more stable form II, with chains in helical conformation, that develops upon releasing the tension[6-9,13-16] (Figure 2).

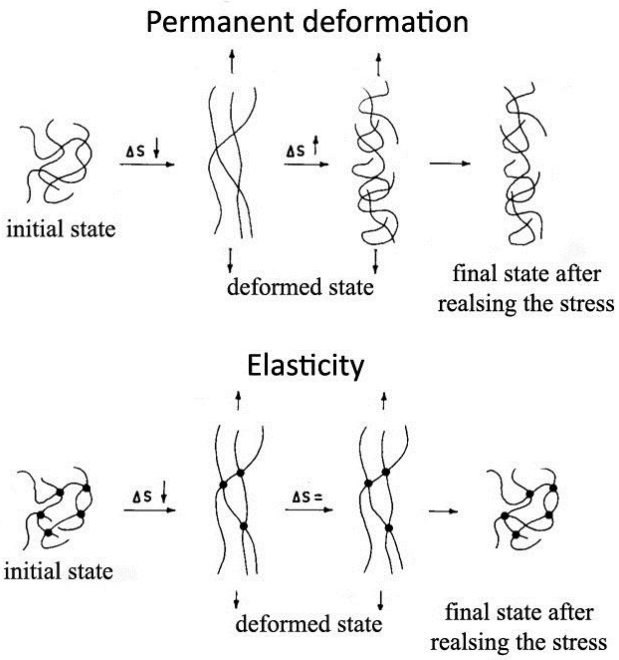

Figure 1. *In absence of network knots the viscous flow of the chain during stretching is not prevented and the result is a permanent deformation. In presence of network knots the transformation between the random-coil conformation of lower entropy stable in the undeformed state and the extended conformation of higher entropy assumed during deformation by the tie-chains is reversible. Therefore, after the tensile stress is removed, the transformation from the extended conformation and the more stable random-coil conformation is still possible (resulting in the recovery of the original shape of the sample).*

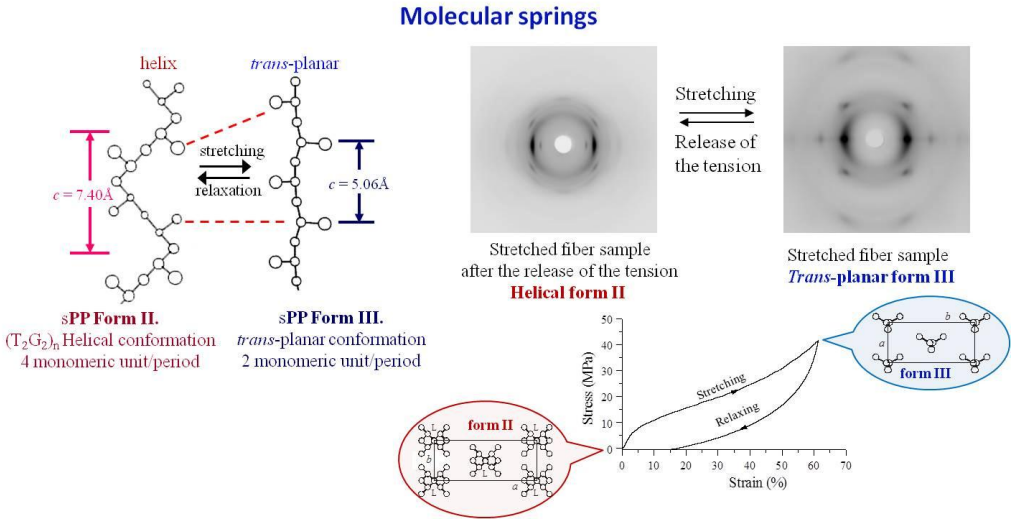

Figure 2. *The reversible crystal-crystal martensitic-like phase transition between the metastable form III of syndiotactic polypropylene (sPP) with chains in trans-planar conformation, which develops upon stretching, and the more stable form II of sPP, with chains in helical conformation is partially responsible for the elastic behavior of sPP.*

The study of these materials has introduced new concepts in thermoplastic elastomers and a definition of unconventional elastomers with high crystallinity and large modulus,[8,13,14] with strength, modulus and elasticity that can be tailored through a balance of enthalpic and entropic contributions to the elastic recovery by modification of the chemical structure and degree of crystallinity.[13,14,16-19]

This project is aimed at studying the new class of materials defined "*crystalline elastomers*", which are innovative polyolefin-based elastomers that present increased and tailored stiffness, with respect to conventional elastomers, thanks to the presence of non-negligible level of crystallinity. These materials are characterized by a combination of mechanical properties typical of crystalline polymers (high mechanical strength and stiffness) and of elastomers (ease of deformability, ductility and perfect elasticity).

Starting from syndiotactic polypropylene (sPP), new elastomeric materials of different molecular architecture and topology, such as random copolymers of sPP, showing elastic properties despite of the presence of non-negligible level of crystallinity have been developed.

Depending on the molecular architecture and copolymer composition, different types of structural and morphological transformations may occur during deformation, such as mechanical melting, re-crystallization, first order crystal-crystal phase transitions, distortions of lattice parameters, orientation of the crystals etc. These transformations may possibly be related to the mechanical behavior.

In this project the structure and the crystals morphology of these materials and the nature of these transformations have been studied with the aim of building correlations between structure and structural evolution during deformation and mechanical and viscoelastic behavior.

Most of the polymers and copolymers studied in this project have been synthesized with novel different organometallic catalysts that are able to produce polyolefins and copolymers of olefins with molecular structure (stereoregularity, regioregularity, molecular mass, distribution of defects and molecular architecture) that depends strictly on the structure of the catalysts, in particular the ligand framework and type of metal of the organometallic complex.[20-23]

The key point of the project is the study of the relationships between the structures of the metallorganic catalysts and the synthetic strategy used for the

preparation of the polymers, the molecular and the crystalline structure of the obtained materials and the final end-use material properties. Particular attention is paid to the links between molecular and crystalline structure, solid-state mechanical and viscoelastic properties, crystallization ability, chain dynamic, as a function of the molecular architecture fixed in the polymerization step.[24]

In details the project involves the study of the role played by crystals in the elastic recovery of these crystalline polymers. Elasticity in these materials can develop only if crystals play an active role in the elastic recovery through various mechanisms. In particular, two different mechanisms of action of crystals have been studied:

1) the occurrence of reversible conformational transformations during deformation and relaxation that defines the concept of molecular spring, as in the case of syndiotactic polypropylene (sPP) and random copolymers of sPP with other 1-olefins (Figure 2). The morphology of crystals of sPP samples of different stereoregularity and of copolymers of sPP with different comonomeric units has been studied and correlated to the mechanical behavior and elastic properties;

2) the birth of crystalline knots through stress-induced crystallization in commercial rubbers based on ethylene-propene random copolymers (EPM).

1. Study of crystal morphology of sPP and random copolymers of sPP.

In samples of sPP, crystallinity, mechanical properties and the nature of elastic behavior (enthalpic or entropic) depend on the molecular structure, in particular the presence stereodefects and of constitutional defects, for example comonomeric units. In stereoirregular sPP samples, the presence of steric defects affects the degree of crystallinity and in turn the occurrence of the polymorphic transitions during deformation and relaxation. For high concentrations of stereodefects very low crystallinity is achieved and formation of the trans-planar form III at high deformation is prevented. Therefore, the elastic behavior observed in poorly syndiotactic samples is mainly entropic.[11,14,25-27]

In random copolymers of sPP, the presence of constitutional defects affects the conformational transition since high concentration of ethylene stabilizes the *trans*-planar conformation, while high concentration of long and branched comonomers stabilizes the helical conformation. In any case, high concentration of comonomeric units prevents occurrence of the polymorphic transitions between trans-planar form III and the helical form II during

deformation and relaxation. Therefore, in these materials the enthalpic contribution to the elasticity becomes negligible with increasing comonomer concentration.

In poorly crystalline samples, where all polymorphic transformations are prevented because of the high concentration of defects, the small crystalline domains in the amorphous matrix act as physical knots of the elastomeric lattice, preventing the viscous flow of the amorphous chains. Since the molecular weights of the samples are very high, the amorphous chains, in turn, are highly entangled and connect as *tie-chains* the small crystalline domains. They act as spring between the crystals being well-oriented and in extended conformation in the stretched state, and return in the disordered coil conformation when the tension is removed. The result is a complex network made of rigid knots (crystals) and flexible tie-chains that accounts for the elastic behavior of these samples even at high defect concentration. According to this structural model, these materials necessarily show mechanical properties of more or less flexibility, elasticity and strength that depend on the size and stability of knots (crystals) and length and entanglement density of tie-chains. This in turn depend on the degree of crystallinity and on the properties of the amorphous phase in term of packing length.[28] With increasing concentration of molecular defects (streodefects or constitutional defects) and decreasing crystallinity, size and stability of crystals decreases and the length of tie-chains increases. If in these materials the space-filled spherulites, typical of high crystalline polymers, are replaced by thin and elongated crystals, and if the amorphous tie-chains connecting these crystals are highly entangled, it is expected that the resulting network acts as an elastomeric network with development of elastic properties.

The study of the morphology performed by using Polarized Optical Microscopy reported in this work was, indeed, aimed at verifying the existence of such elastomeric network in sPP and copolymers of sPP and at finding evidences of the presence of small and thin crystals organized in an interwoven morphology acting as knots of the network. In addition, the study of the rheology of these materials could provide information about the entanglement density of the amorphous phase to support the hypothesis of a classic entropic contribution to the elasticity.

We have found that in sPPs and in copolymers of sPP with low defect concentrations (stereodefects or constitutional defects) crystals are organized in relatively big aggregates, such as bundles of rod lamellae, bow-tie and small

open multi-faceted aggregates, along with smaller needle crystals (Figures 3A,A' and 3B,B'), but very big space-filled spherulitic superstructures are never observed. This morphology is in agreement with the ductility and flexibility of these materials notwithstanding the high degrees of crystallinity, and the relatively high mechanical strength. These crystalline aggregates are not able to fill the space as in the case of completely impinged spherulites of highly crystalline polymers (as isotactic polypropylene), probably due to the properties of the amorphous chains connecting the crystals that fill and occupy the available space between the crystals. This morphology, in particular the presence of irregular open aggregates (Figures 3A,B) and of the interwoven structure made by needle-type crystals (Figures 3A',B'), is also in agreement with the idea that the crystalline aggregates actively participate to the elasticity of sPP and its copolymers, locally acting as microscopic engines through the activation of reversible phase transformations during deformation and elastic recovery providing an enthalpic contribution to the elasticity, and with presence of an entropic contribution to the elasticity provided by the elastomeric network formed even in the presence of relatively big crystalline aggregates.

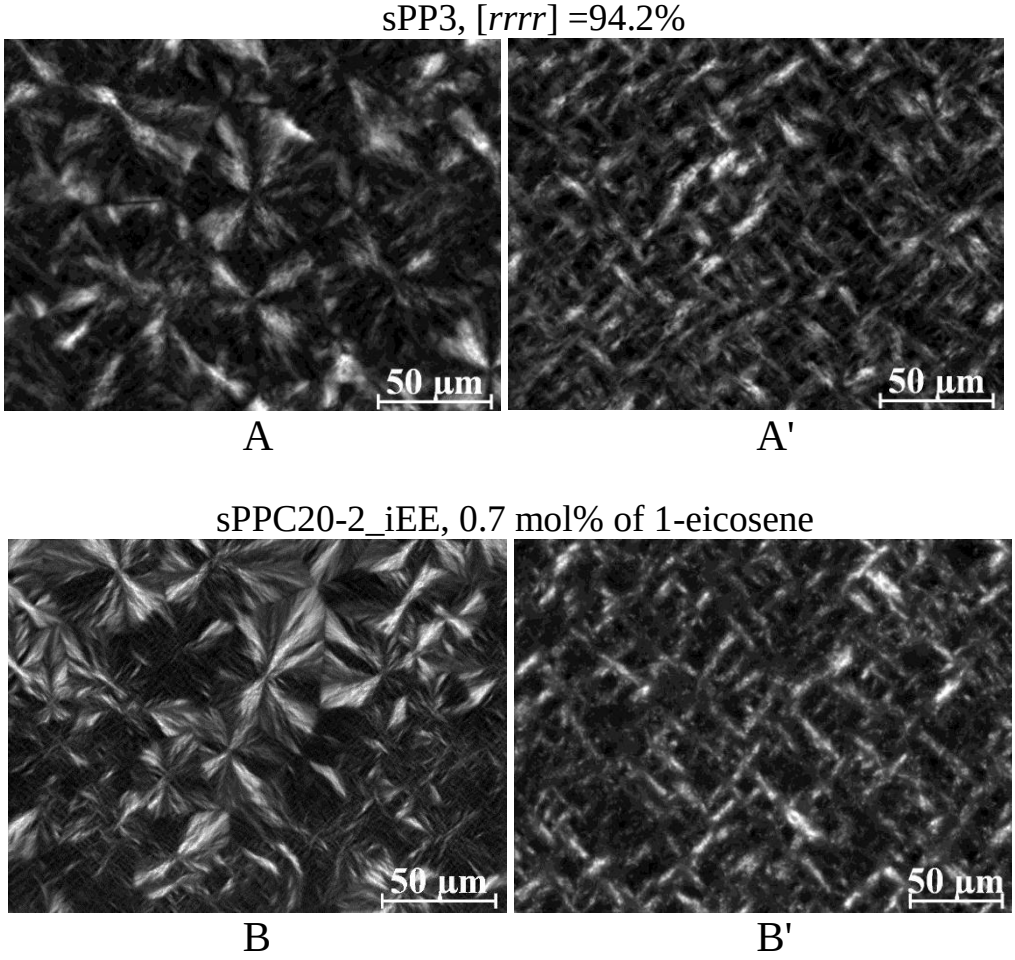

Figure 3. Comparison of POM images of samples of homopolymer sPP3 with [rrrr] =94.2% (A,A') and random copolymer of sPP with 1-eicosene sPPC20-2_iEE with 0.7 mol% of 1-eicosene (B,B') recorded in thinner (A,B) and thicker (A',B') zones of the samples. Thinner zones display bow-tie and aggregates bigger than those observed in thicker zones where the interwoven network prevails.

With increasing defect concentration in sPP and its copolymers (stereodefects or constitutional defects) we have found that the open crystalline aggregates (bundles of rod lamellae, bow-tie and open multi-faceted aggregates) are replaced by small and elongated needle-type crystals organized in an interwoven structure where thin and elongated crystals are connected by long amorphous tie-chains. This structure resembles a dense elastomeric network where small and thin crystals act as efficient knots of the network. This morphology accounts for the elastomeric properties shown by sPP and its copolymers when the concentration of defects is very high and crystallinity is very low.

2. Structure, stress-induced crystallization and morphology of ethylene-propene random copolymers (EPM).

In the second part of this work the role played by crystals in the mechanical behavior of several commercial ethylene-propylene copolymers (EPM) and ethylene-propylene-diene terpolymers (EPDM) grades has been analyzed. Three sets of samples of copolymers and terpolymers having different concentrations of ethylene have been analyzed: the first set of EPM and EPDM samples is characterized by high ethylene content in the range 78-70 wt%; a second set with ethylene content in the range 67-64 wt%; a third set with low ethylene concentration in the range 52-44 wt%.

EP(D)M terpolymers with high ethylene contents (higher than 78-80 wt%) are generally crystalline, with crystallinity arising from crystallization of ethylene sequences in the polymorphic forms of polyethylene (PE). EP(D)M samples with ethylene concentration in the range 60-70 wt% appear instead amorphous in the undeformed state,[31-33] if analyzed by classic wide-angle X-ray diffraction (WAXS). However, the possible presence of crystallinity in the underformed state in these copolymers even when not visible through WAXS (***faint or crypto crystallinity***) has been analyzed in detail with different techniques of structural analysis in different length scales. In particular, analysis by small-angle X-ray diffraction scattering (SAXS) has surprisingly revealed the presence of a correlation peaks in samples with low ethylene concentration (67-64 wt%) that appear amorphous from the WAXS profiles. For these samples the presence of crystallinity has also been revealed by the presence of endothermic and exothermic peaks in the DSC heating and cooling curves. Therefore, SAXS and DSC data indicate the presence of a ***cryptocrystallinity*** in the undeformed state of these samples, surprisingly not detected by WAXS but revealed by SAXS. This result also indicate that, depending on the catalyst used for the synthesis, these samples are characterized by ethylene sequences long enough to crystallize even in the presence of a so high concentration of propylene units.

In this work it has also been demonstrated that crystallization of ethylene sequences may further occur during deformation. The Stress-Induced Crystallization (SIC) in EPM copolymers and EPDM terpolymers of different ethylene concentrations has been studied in detail and correlated with the ethylene concentrations and the presence of initial crystallinity in the undeformed state.

It is well-known that SIC influences mechanical properties of materials such as tensile strength, ductility, ability to relax when stress is applied and then removed (elastic recovery) or in experiments of stress-relaxation or creep. Small crystals formed upon stretching act as physical knots in the elastomeric network, resulting in increase of tensile strength of the rubber.

Figure 4 shows a comparison between stress-strain curves of the crystalline sample EPM (78 wt% of ethylene) and one of the three copolymers belonging to the first set (K5470NT, 70 wt% of ethylene) and the corresponding X-ray diffraction patterns recorded during deformation. The sample EPM is already crystalline in the undeformed state and stretching produce only orientation of these crystals of pseudohexagonal form of PE. The sample K5470NT, instead, is initially amorphous or shows faint crystallinity, but further crystallization occurs during stretching via SIC. The two samples show great differences in modulus and stress at yield, the crystalline sample EPM having higher modulus and yield stress, but they display similar stress at break and ductility thanks to occurrence of SIC in the sample K5470NT. As a matter of fact, the sample K5470NT shows stress at break even slightly higher than the crystalline sample EPM, even though it is initially nearly amorphous.

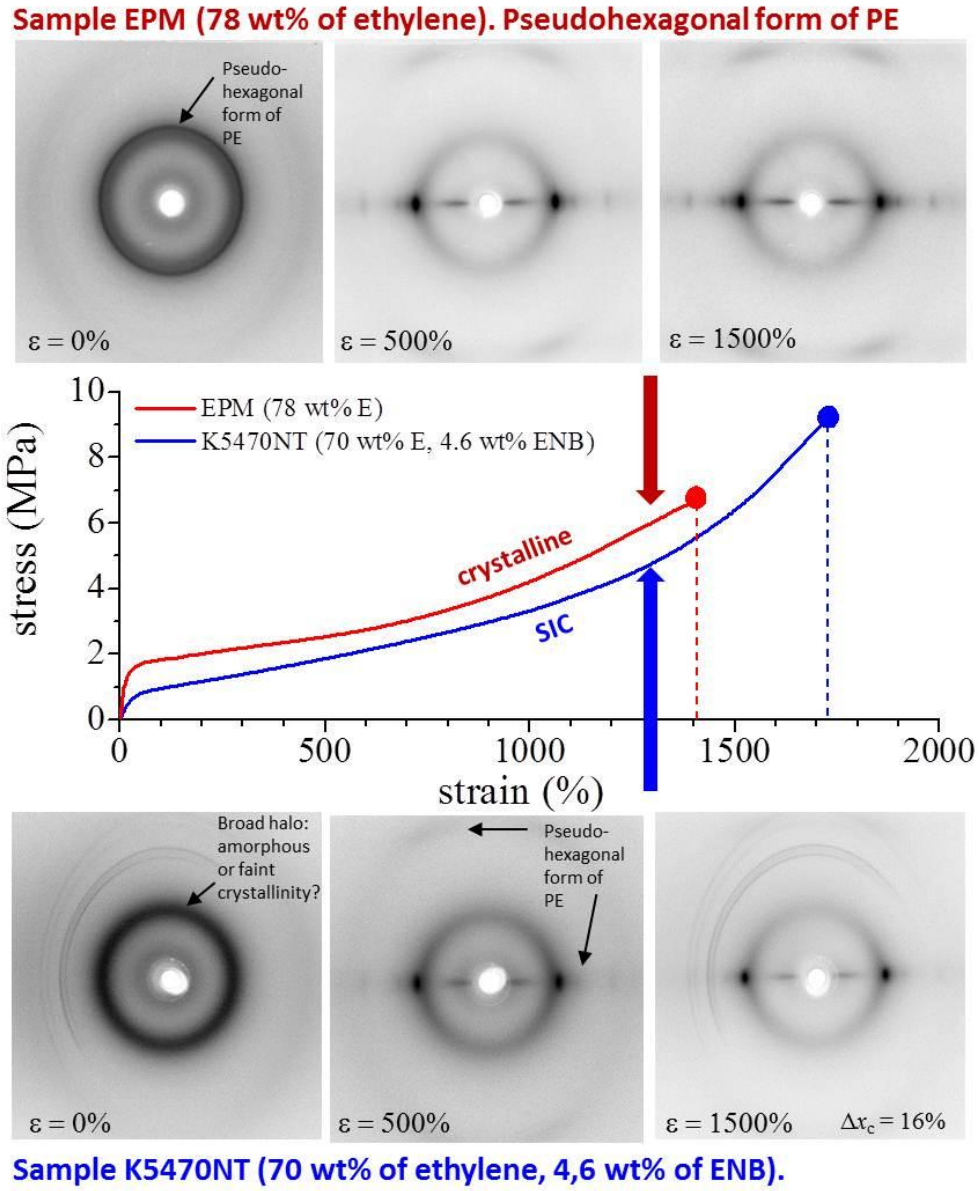

Figure 4 *Comparison of stress-strain curves and corresponding X-ray diffraction patterns recorded during stretching of the copolymer EPM (78 wt% of ethylene, red curve) and the terpolymer K5470NT (70 wt% of ethylene, blue curve).*

Figure 5 shows a comparison between stress-strain curves and corresponding X-ray diffraction patterns recorded during deformation of samples K5470NT (with 70 wt% of ethylene) and K6160D (with 64 wt% of ethylene). Both samples initially appear amorphous or contain the discussed cryptocrystallinity. Crystallization occurs upon stretching but the entity of SIC is higher in the sample K5470NT (belonging to the first set of samples) than in sample K6160D

(belonging to the second set of samples), as demonstrated by X-ray diffraction patterns. The difference in the amount of SIC has been explained in terms of difference of ethylene content and, hence, difference in the lengths of ethylene sequences, between samples belonging to the first set (having ethylene content in the range 78-70 wt%) and samples belonging to the second set (with 67-64 wt% of ethylene). The two samples show big differences in ductility and tensile strength due to different amounts of SIC. Without (or with small) SIC the mechanical properties do not improve during deformation.

For samples of EPDM, when the tension is removed after deformation at a maximum strain elastic recovery is observed and, correspondingly, a partial melting of crystals formed upon stretching and a partial loss of crystal orientation have also been observed. SIC is therefore a reversible phenomenon. Nevertheless, we have observed that a residual crystallinity remains in stress-relaxed fibers, which is related to the ethylene concentration. Since crystals act as physical knots in the elastomeric network, the residual crystallinity also influence the elastic recovery and the mechanical properties of stress-relaxed fibers. It has been demonstrated that the degree of elastic recovery increases with decreasing ethylene concentration. In the sample EPM with 78 wt% of ethylene the residual crystallinity, similar to the initial crystallinity, is relatively high, so that the elastic recovery is low. A fast increase of elastic recovery is observed already for small decrease of ethylene concentration and all samples with ethylene content in the range 73-64% show similar high values of elastic recovery. Therefore, in this range of ethylene concentration, the presence of initial crystallinity, the occurrence of strain-hardening and the low values of tension set give the best elastic properties associated with remarkable strength.

In conclusion, the relationships among composition, initial crystallinity, stress induced crystallization, residual crystallinity after relaxation and physical properties of EPM copolymers and EPDM terpolymers have been analyzed. Crystallinity and SIC are influenced by the ethylene concentration and distribution of comonomers along the chains and, in particular, by the length of ethylene sequences, which, in turn, is defined by the used catalyst. Hence, different microstructures induced by different catalysts produce different degrees of crystallinity and SIC, and consequent different mechanical properties and elastic behavior. This study is an exemplary case of how the properties of targeted materials can be retro-designed by tailoring the microstructure by controlling the polymerization through the rational choice of catalysts and condition of polymerization.

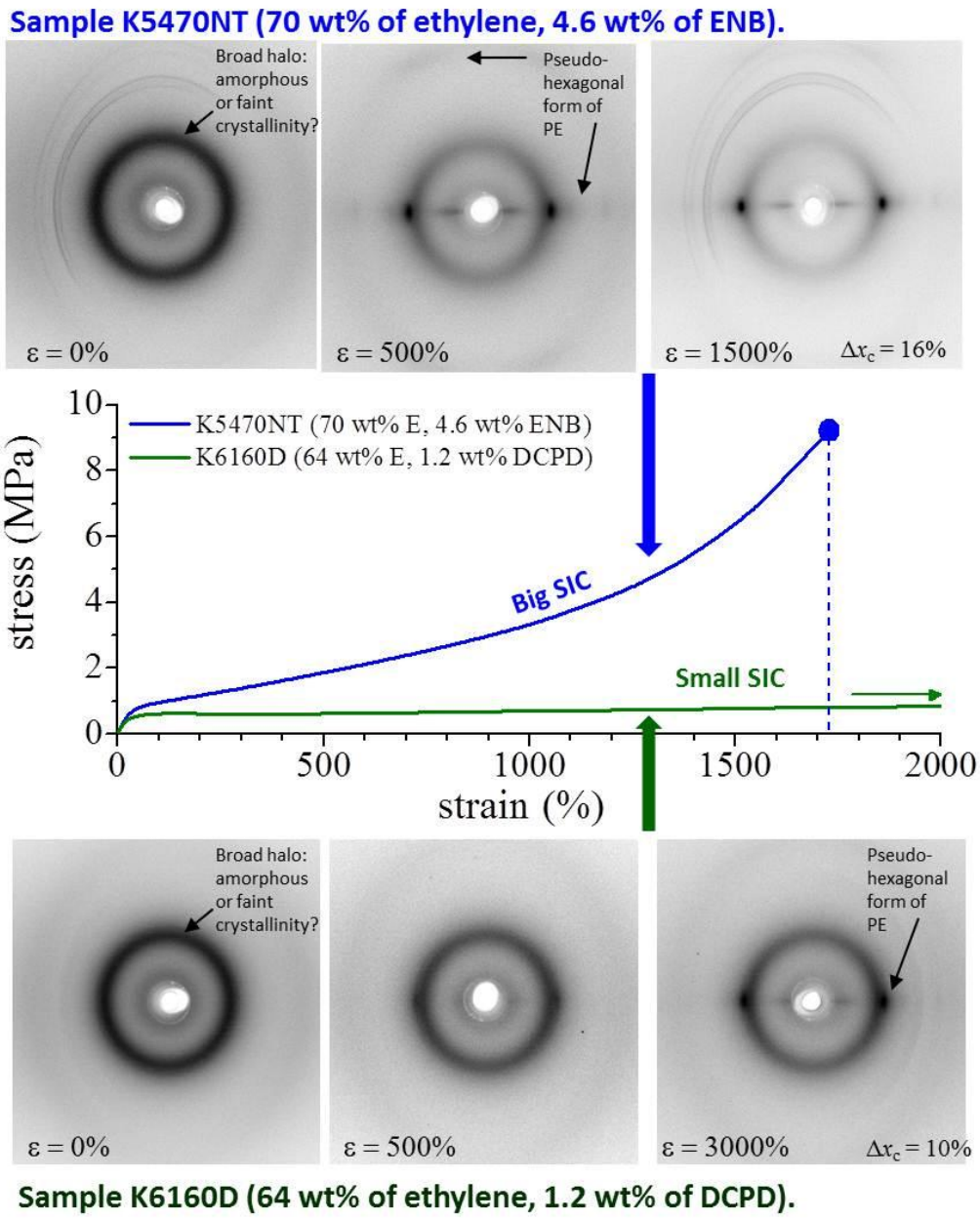

Figure 5 *Comparison of stress-strain curves and corresponding X-ray diffraction patterns recorded during stretching of the terpolymer K5470NT (70 wt% of ethylene, blue curve) and the terpolymer K6160D (64 wt% of ethylene, green curve).*

References.

1) L. R. G. Treolar, *The Physics of Rubber Elasticity*, Claderon Press, Oxford, **1975**.

2) J. E. Mark,. *Prog. Polym. Sci*. **2003**, 28, 1205.

3) A. Ciferri, *Trans. Faraday Soc.* **1963**, *59*, 562.

4) A. Ciferri, K. J. Smith, Jr., *J. Pol. Sci., Part A* **1964**, *2*, 731.

5) K. Tashiro, Y. Nakai, Y. M. Kobayashi, H. Tadokoro, *Macromolecules* **1980**, *13*, 137.

6) F. Auriemma, O. Ruiz de Ballesteros, C. De Rosa, *Macromolecules* **2001**, 34, 4485.

7) C. De Rosa, M. C. Gargiulo, F. Auriemma, O. Ruiz de Ballesteros, A. Razavi, *Macromolecules* **2002**, *35*, 9083.

8) F. Auriemma, C. De Rosa, *J. Am. Chem. Soc.* **2003**, *125*, 13143.

9) F. Auriemma, C. De Rosa, *Macromolecules* **2003**, *36*, 9396.

10) C. De Rosa, F. Auriemma, O. Ballesteros, L. Resconi, A. Fait, E. Ciaccia, I. Camurati, *J. Am. Chem. Soc*. **2003**, *125*, 10913.

11) C. De Rosa, F. Auriemma, O. Ruiz de Ballesteros, *Macromolecules* **2003**, *36*, 7607.

12) C. De Rosa, O. Ruiz de Ballesteros, F. Auriemma, *Macromolecules* **2004**, *37*, 7724.

13) C. De Rosa, F. Auriemma, *Prog. Polym. Sci*. **2006**, 31, 145.

14) C. De Rosa, F. Auriemma, O. Ruiz de Ballesteros, *Chem. Mater.* **2006**, *18*, 3523.

15) F. Auriemma, C. De Rosa, S. Esposito, G. R. Mitchell, *Angew. Chem. Int. Ed.* **2007**, 46, 4325.

16) C. De Rosa, F. Auriemma, *Polym. Chem*. **2011**, *2*, 2155.

17) C. De Rosa, F. Auriemma, *Adv. Mat.* **2005**, *17*, 1503.

18) C. De Rosa, F. Auriemma, *Macromolecules* **2006**, *39*, 249.

19) C. De Rosa, F. Auriemma, M. Corradi, L. Caliano, O. Ruiz de Ballesteros, R. Di Girolamo, *Macromolecules* **2009**, *42*, 4728.

20) L. Resconi, L. Cavallo, A. Fait, F. Piemontesi, *Chem. Rev.* **2000**, *100*, 1253.

21) H. H. Brintzinger, D. Fischer, R. Mülhaupt, B. Rieger, R. M. Waymouth, *Angew Chem. Int. Ed* **1995**, *34*, 1143.

22) G. W. Coates, *Chem. Rev.* **2000,** *100,* 1223.

23) G. W. Coates, P. D. Hustad, S. Reinartz, *Angew. Chem., Int. Ed.***2002**, *41*, 2236.

24) C. De Rosa, F. Auriemma, *Crystals and Crystallinity in Polymers*, Wiley, 2014.

25) De Rosa, F. Auriemma, O. Ruiz de Ballesteros, *Phys. Rev. Lett.* **2006**, *96 (16)*, 167801.

26) C. De Rosa, F. Auriemma, O. Ruiz de Ballesteros, L. Resconi, A. Fait, E. Ciaccia, I. Camurati, *J. Am. Chem. Soc.* **2003**, *125*, 10913.

27) C. De Rosa, F. Auriemma, O. Ruiz de Ballesteros, *Macromolecules* **2004**, *37*, 1422.

28) N. Ahmad, R. Di Girolamo, F. Auriemma, C. De Rosa, N. Grizzuti, *Macromolecules* **2013**, *46*, 7940.

29) I. W. Bassi, P. Corradini, G. Fagherazzi, A. Valvassori, *Eur. Polym. J.* **1970**, *6*, 709.

30) F. P. Baldwin, G. Ver Strate, *Rubber Chem. Tecnol.* **1972**, *45*, 709.

31) G. Ver Strate, Z. W. Wilchinsky, *J. Polym. Sci*. Part A2 **1971**, *9*, 127.

32) B. J. R. Scholtens, E. Riande, J. E. Mark, *J. Polym. Sci. Polym. Phys. Edn*. **1984**, *22*, 1223.

33) G. Guerra, M. Ilavský, J. Biroš, K. Dušek, *Colloid Polym Sci.* **1981**, *259*, 1190.

Introduction

Elastomers are generally amorphous polymers made by long and highly flexible chains with high molecular mass and glass-transition temperature much below room temperature.[1] The flexible segments of the random coil conformation in the unstretched state, assume extended conformation upon stretching and the entropy-driven recoiling upon releasing the stress is responsible for the elastic recovery of size and shape of the whole material in the undeformed state.[1,2] The existence of chemical or physical cross-links acting as network knots prevents the material from flowing during application of the tensile stress. These amorphous rubbers may partially crystallize under stretching.[1] The small number of small crystals acts as knots of the elastomeric network. When the applied tensile stress is removed, the crystals melt, providing a positive enthalpic contribution to the Gibbs free energy change involved during the elastic recovery of the material; therefore, the elasticity in these materials is merely of entropic nature, due to the conformational changes experienced by the amorphous "tie-chains" (Figures 1 and 2).[1]

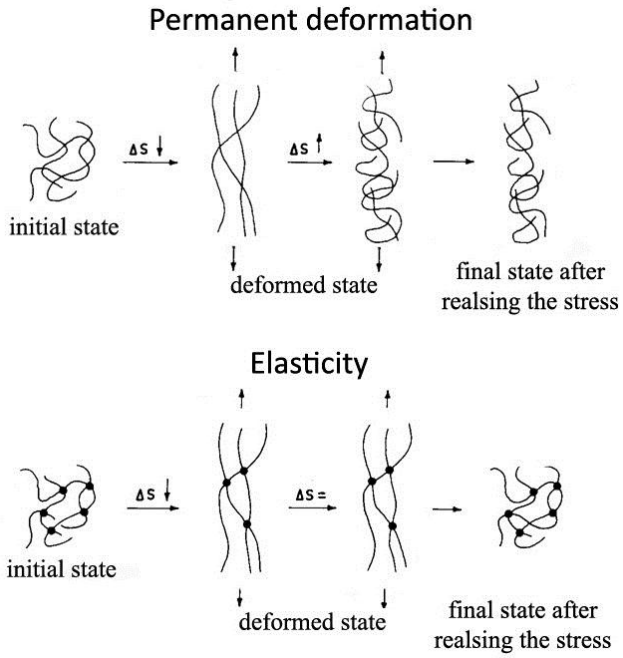

Figure 1. In absence of network knots the viscous flow of the chain during stretching is not prevented and the result is a permanent deformation. In presence of network knots the transformation between the random-coil conformation of lower entropy stable in the undeformed state and the extended conformation of higher entropy assumed during deformation by the tie-chains is reversible. Therefore, after the tensile stress is removed, the transformation from the extended conformation and the more stable random-coil conformation is still possible (resulting in the recovery of the original shape of the sample).

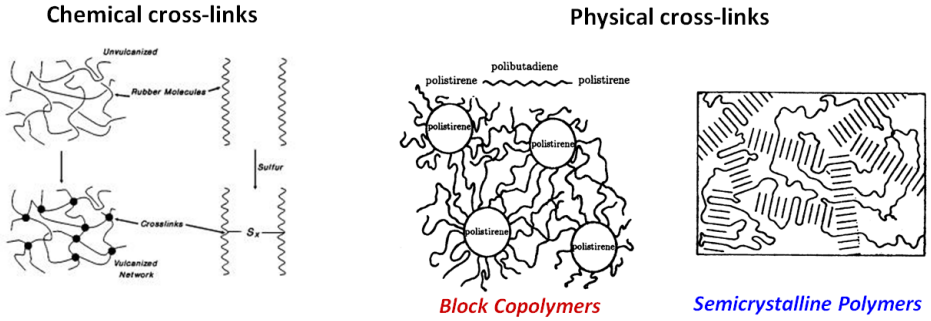

Figure 2. Chemical or physical cross-links can act as network knots. The most important example of chemical cross-links are the S-S bonds formed upon vulcanization in many types of commercial rubber. The rigid domains formed by an amorphous rigid block in a diblock copolymer like the styrene-butadiene block copolymer and the small crystals present in a semicrystalline polymer (or eventually formed upon stretching) can be considered two examples of physical cross-links.

In general, high level of crystallinity may strongly reduce the elastic performances of these materials. However, many semicrystalline polymers show elastic properties in spite they present high crystallinity and high mechanical strength.[3-19] Phase transitions may play a key role in the elasticity of these systems, resulting in materials where elasticity is not merely entropic as in conventional elastomers but similar to super-elasticity of shape memory alloys that undergo martensitic phase transitions.[6-19] An example of this type of rubbers is the class of "*crystalline elastomers*" based on syndiotactic polypropylene (sPP) and its copolymers.[13-16] The unusual elastic behavior of sPP is associated with a reversible crystal-crystal martensitic-like phase transition between the metastable form III with chains in trans-planar conformation, which develops upon stretching, and the more stable form II, with chains in helical conformation, that develops upon releasing the tension[6-9,13-16] (Figure 3).

The study of these materials has introduced new concepts in thermoplastic elastomers and a definition of unconventional elastomers with high crystallinity and large modulus,[8,13,14] with strength, modulus and elasticity that can be tailored through a balance of enthalpic and entropic contributions to the elastic recovery by modification of the chemical structure and degree of crystallinity.[13,14,16-19]

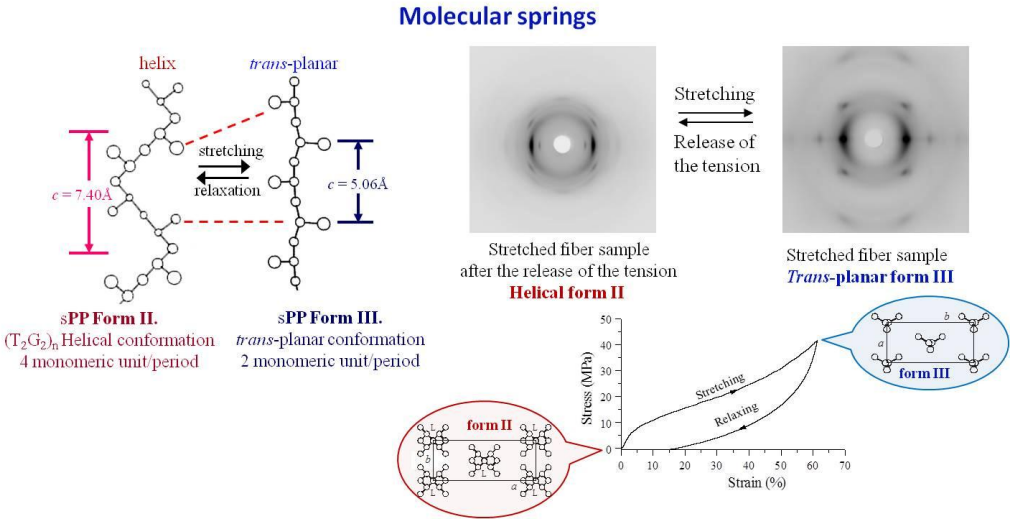

Figure 3. The reversible crystal-crystal martensitic-like phase transition between the metastable form III of syndiotactic polypropylene (sPP) with chains in trans-planar conformation, which develops upon stretching, and the more stable form II of sPP, with chains in helical conformation is partially responsible for the elastic behavior of sPP. This transformation will be investigated in more details in the chapter 1.

Aim of the project

This project is aimed at studying the new class of materials defined "*crystalline elastomers*", which are innovative polyolefin-based elastomers that present increased and tailored stiffness, with respect to conventional elastomers, thanks to the presence of non-negligible level of crystallinity. These materials are characterized by a combination of mechanical properties typical of crystalline polymers (high mechanical strength and stiffness) and of elastomers (ease of deformability, ductility and perfect elasticity).

Starting from syndiotactic polypropylene (sPP), new elastomeric materials of different molecular architecture and topology, such as random copolymers of sPP and block copolymers, showing elastic properties despite of the presence of non-negligible level of crystallinity have been developed.

Depending on the molecular architecture and copolymer composition, different types of structural and morphological transformations may occur during deformation, such as mechanical melting, re-crystallization, first order crystal-crystal phase transitions, distortions of lattice parameters, orientation of the crystals etc. These transformations may possibly be related to the mechanical behavior.

In this project the structure and the crystals morphology of these materials and the nature of these transformations have been studied with the aim of

building correlations between structure and structural evolution during deformation and mechanical and viscoelastic behavior.

The structure and the morphology of these materials have been studied using different techniques, as X-ray diffraction, calorimetry, solution NMR, optical microscopy and atomic force microscopy (AFM). The mechanical and viscoelastic properties, and the structural and morphological transformations occurring during tensile deformation have also been studied in detail by recording stress-strain curves during stretching and relaxation and performing dynamic mechanical thermal analysis in bending and stretching mode to study the segmental relaxation as a function of the chain architecture.

Most of the polymers and copolymers studied in this project have been synthesized with novel different organometallic catalysts that are able to produce polyolefins and copolymers of olefins with molecular structure (stereoregularity, regioregularity, molecular mass, distribution of defects and molecular architecture) that depends strictly on the structure of the catalysts, in particular the ligand framework and type of metal of the organometallic complex.[20-23]

The key point of the project is the study of the relationships between the structures of the metallorganic catalysts and the synthetic strategy used for the preparation of the polymers, the molecular and the crystalline structure of the obtained materials and the final end-use material properties. Particular attention is paid to the links between molecular and crystalline structure, solid-state mechanical and viscoelastic properties, crystallization ability, chain dynamic, as a function of the molecular architecture fixed in the polymerization step.[24] The research activities are based on the attempt to establish the rules of synthetic retro-design (Figure 4), that is the rules that for any given set of desired properties and final applications allow identifying the best molecular architecture and the most suitable synthetic approach (including catalysts, synthetic method, and polymerization conditions) for preparation of the targeted polymeric material (Figure 4). As shown in Figure 4, with organometallic catalysts our ability to control the molecular structure of the chains of poly(α-olefins) is increased because we can control type and concentration of incorporated defects, in particular, defects of stereoregularity and regioregularity, or constitutional defects like comonomeric units, and the distribution of defects along the chains (random or blocky), by changing the structure of the catalyst and tailoring its stereoselectivity and ability to incorporate comonomers of any size. This affords a unique opportunity for

controlling the final physical properties of the materials because the molecular structure influences the crystallization behaviour, which, in turn, affects the physical and mechanical properties.[24] Therefore, the physical properties can be retro-designed through catalyst design (Figure 4).

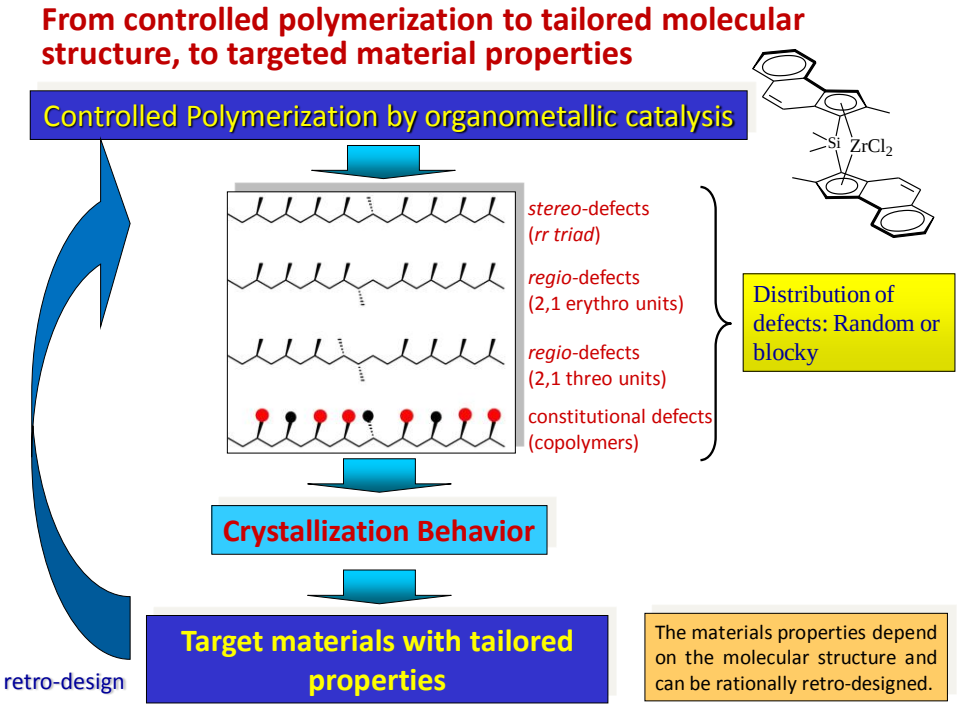

Figure 4. *From design of the catalyst structure to targeted material properties of polyolefins. The physical properties of polyolefins depend on the molecular structure which can be controlled by organometallic catalysts.*

In details the project involves the study of the role played by crystals in the elastic recovery of these crystalline polymers. Elasticity in these materials can develop only if crystals play an active role in the elastic recovery through various mechanisms. In particular, two different mechanisms of action of crystals have been studied:

1) the occurrence of reversible conformational transformations during deformation and relaxation that defines the concept of molecular spring, as in the case of syndiotactic polypropylene (sPP) and random copolymers of sPP with other 1-olefins (Figure 3);

2) the birth of crystalline knots through stress-induced crystallization in commercial rubbers based on ethylene-propene random copolymers (EPM).

References.

1) L. R. G. Treolar, *The Physics of Rubber Elasticity*, Claderon Press, Oxford, 1975

2) J. E. Mark,. *Prog. Polym. Sci*. **2003**, 28, 1205.

3) A. Ciferri, *Trans. Faraday Soc.* **1963**, *59*, 562.

4) A. Ciferri, K. J. Smith, Jr., *J. Pol. Sci., Part A* **1964**, *2*, 731.

5) K. Tashiro, Y. Nakai, Y. M. Kobayashi, H. Tadokoro, *Macromolecules* **1980**, *13*, 137.

6) F. Auriemma, O. Ruiz de Ballesteros, C. De Rosa, *Macromolecules* **2001**, 34, 4485.

7) C. De Rosa, M. C. Gargiulo, F. Auriemma, O. Ruiz de Ballesteros, A. Razavi, *Macromolecules* **2002**, *35*, 9083.

8) F. Auriemma, C. De Rosa, *J. Am. Chem. Soc.* **2003**, *125*, 13143.

9) F. Auriemma, C. De Rosa, *Macromolecules* **2003**, *36*, 9396.

10) C. De Rosa, F. Auriemma, O. Ballesteros, L. Resconi, A. Fait, E. Ciaccia, I. Camurati, *J. Am. Chem. Soc*. **2003**, *125*, 10913.

11) C. De Rosa, F. Auriemma, O. Ruiz de Ballesteros, *Macromolecules* **2003**, *36*, 7607.

12) C. De Rosa, O. Ruiz de Ballesteros, F. Auriemma, *Macromolecules* **2004**, *37*, 7724.

13) C. De Rosa, F. Auriemma, *Prog. Polym. Sci*. **2006**, 31, 145.

14) C. De Rosa, F. Auriemma, O. Ruiz de Ballesteros, *Chem. Mater.* **2006**, *18*, 3523.

15) F. Auriemma, C. De Rosa, S. Esposito, G. R. Mitchell, *Angew. Chem. Int. Ed.* **2007**, 46, 4325.

16) C. De Rosa, F. Auriemma, *Polym. Chem*. **2011**, *2*, 2155.

17) C. De Rosa, F. Auriemma, *Adv. Mat.* **2005**, *17*, 1503.

18) C. De Rosa, F. Auriemma, *Macromolecules* **2006**, *39*, 249.

19) C. De Rosa, F. Auriemma, M. Corradi, L. Caliano, O. Ruiz de Ballesteros, R. Di Girolamo, *Macromolecules* **2009**, *42*, 4728.

20) L. Resconi, L. Cavallo, A. Fait, F. Piemontesi, *Chem. Rev.* **2000**, *100*, 1253.

21) H. H. Brintzinger, D. Fischer, R. Mülhaupt, B. Rieger, R. M. Waymouth, *Angew Chem. Int. Ed* **1995**, *34*, 1143.

22) G. W. Coates, *Chem. Rev.* **2000,** *100*, 1223.

23) G. W. Coates, P. D. Hustad, S. Reinartz, *Angew. Chem., Int. Ed.***2002**, *41*, 2236.

24) C. De Rosa, F. Auriemma, *Crystals and Crystallinity in Polymers*, Wiley, 2014.

CHAPTER I

Syndiotactic Polypropylene and Copolymers

Since the discovery of stereoselective olefin polymerization in 1954, syndiotactic polypropylene (sPP) has been considered only a scientific curiosity because it showed scarcely interesting physico-chemical properties due to the low stereo- and regioregularities of the macromolecules synthesized with the Ziegler–Natta based catalysts, and low crystallinity and melting temperature of the produced materials. For these reasons sPP has never had industrial fortune and commercial diffusion and the term 'polypropylene' has been used for over thirty years only to indicate the isotactic polymer of propylene, industrially produced with heterogeneous Ziegler–Natta catalysts.

A re-birth of sPP has been observed in the mid 1980s, after the discovery of new single-center metallorganic catalysts. Some of these novel catalysts were able to produce highly stereoregular and regioregular sPP and completely new sPP samples, having high crystallinity and melting temperature, was obtained. The new sPP has shown outstanding physical properties, completely different from those of the commercial isotactic polypropylene, some of them absolutely unexpected. This has refocused the scientific and industrial interest for sPP. The most important and unique property relies on the fact that sPP is a high modulus thermoplastic elastomer, notwithstanding the high crystallinity and the relatively high glass transition temperature.

The physical properties of sPP basically depend on the crystallization behavior, which in turn is strongly related to the chemical structure of the single macromolecules. For vinyl polymers the term microstructure of macromolecules may be used to describe the sequence distribution of monomeric units and the stereochemical relationships between consecutive units, therefore indicates stereoregularity and regioregularity of the chains, types and concentration of defects in the regular constitutional and configurational enchainment of monomeric units (stereo- and regio-defects) and distribution of defects along the polymer chains. Different catalysts produce different microstructures through different polymerization mechanisms, and, as a consequence, sPPs produced with different catalysts display different crystallization behavior and physical properties.[1]

1.1. Synthesis of sPP and of random copolymers of sPP

Syndiotactic polypropylene (sPP) was first obtained by Natta as a minor product of the synthesis of isotactic polypropylene (iPP) with heterogeneous Ziegler-Natta catalysts based on $TiCl_3$-$Al(C_2H_5)_2Cl$.[1,2] These catalysts are, indeed, multi-sites and simultaneously produce isotactic, syndiotactic and stereoirregular macromolecules, although isotactic polypropylene is the main reaction product.[3]

Later, syndiotactic polypropylene was selectively produced by Zambelli and Natta using homogeneous single-site vanadium-based catalysts.[4] This catalytic system comprises a variety of vanadium compounds, as VCl_4 or V(III)-β-diketonates (V(acetylacetonate)$_3$),[4,5] an alkyl aluminum halide (typically $Al(C_2H_5)_2Cl$), and a Lewis base (e.g. anisole).[6,7] Since this catalytic system is thermolabile, the polymerization temperature has to be performed much below room temperature (-78 °C). The soluble active species also promote copolymerization of ethylene with propylene.

The precursors vanadium compounds are soluble in hydrocarbons and the oxidation state of vanadium is at least 3.[7] The catalytic systems are thermolabile and quickly decompose at room temperature producing poorly characterized precipitates containing Al, V(II) and Cl,[1,7] unable to promote polymerization. Therefore the polymerization has to be performed either at low temperature, or in the presence of a component able to continuously re-oxidate V(II) to a higher oxidation state during polymerization (for instance a chlorinated ester). This expedient is used, for example, for the commercial production of ethylene-propylene and ethylene-propylene-diene rubbers.[1]

Values of the content of *r* diads up to 90% are obtained for sPP samples produced at -78 °C but the syndiotacticity decrease with increasing temperature and atactic polypropylene is obtained above 0 °C.[8]

The ^{13}C NMR spectroscopy analysis of sPP samples produced with these vanadium-based catalysts has allowed clarifying the microstructure of chains and the mechanism of stereocontrol of the insertion reaction on the metal-carbon bond.[9-22] The analysis of the saturated chain-ends generated by initiation at V-(^{13}C-enriched-alkyl) species, have indicated that the initiation step involves primary 1,2 insertion of propylene followed by other non-stereospecific primary insertion steps. Therefore, propene insertion into V-CH_2R bond is prevailingly 1,2 and is not enantioselective. However, the presence in the ^{13}C NMR spectra (Figure 1.1) of resonances in the ranges 12-16 ppm and 27-43 ppm, diagnostic of methyl groups of head-to-head units (–

$CH_2CH(CH_3)CH(CH_3)CH_2$–) and of methylene carbon atoms of tail-to-tail units (–$CH(CH_3)CH_2CH_2CH(CH_3)$–), indicates that the regiospecificity of the monomer insertion is not high.[12-15] Once a secondary 2,1 insertion occurs and a V-$CH(CH_3)$-CH_2R bond is occasionally formed, the 2,1 insertion tends to be maintained and sequences of secondary insertion much longer than the sequences of primary insertion are obtained. The sequences of secondary insertion lead to monomer sequences with a prevailingly syndiotactic arrangement. The presence of ^{13}C NMR signals of methyl carbon atoms corresponding to *rrrm* and *rrmr* pentads (besides the fully syndiotactic pentad *rrrr*, Figure 1.1B) indicate that stereodefects are basically isolated *m* diads. This indicates that the stereochemistry of the syndiotactic chain propagation is controlled by the chiral last unit of the growing chain (*chain-end control*).[3,11,12]

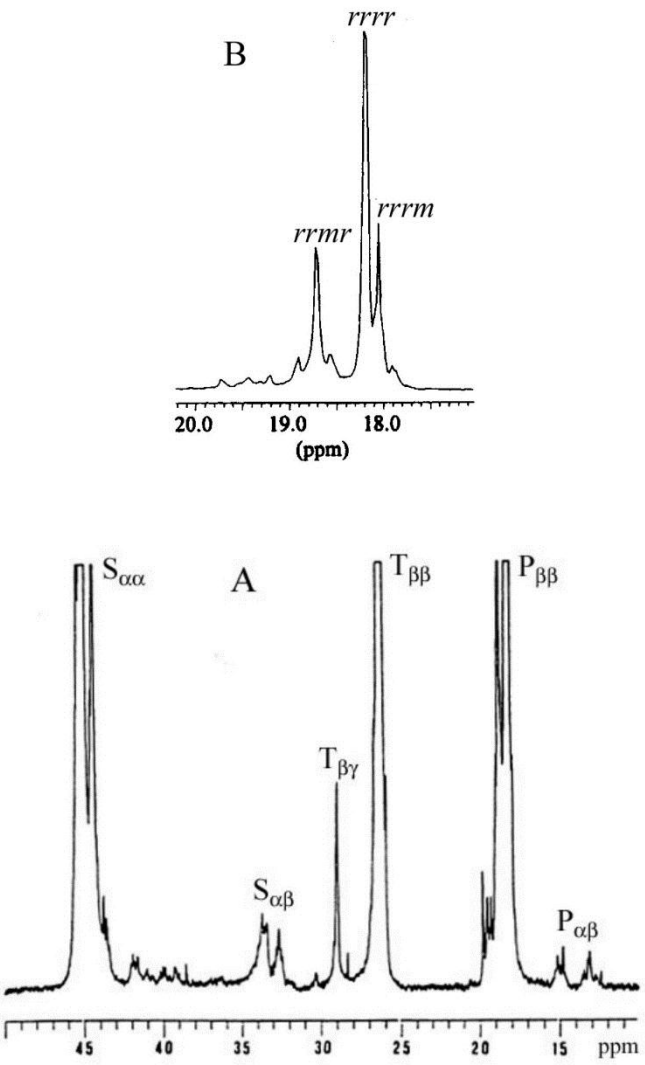

Figure 1.1. *(A) Solution ^{13}C NMR spectrum of a sample of sPP prepared with the catalytic system $VCl_4/Al(C_2H_5)_2Cl$ at -78 °C. The chemical shift scale is in ppm downfield of hexamethyl-disiloxane. The resonances of methyl, methine and methylene carbon atoms in regiodefective sequences, $P_{\alpha\beta}$, $T_{\beta\gamma}$ and $S_{\alpha\beta}$, respectively, are shown.[1,21b] (B) Region of the spectrum of the methyl carbon atoms resonance. The assignment of methyl signals to pentads stereo-sequences is also indicated.[1,22]*

These features result in a block structure of sPP macromolecules consisting in syndiotactic stereoblocks spanned by shorter atactic blocks with reversals of monomer enchainment at the junctions of blocks (Figure 1.2). The syndiotactic blocks are made of tail-to-head (2,1) sequences (–$CH(CH_3)CH_2CH(CH_3)CH_2$–), whereas the shorter atactic blocks are made of head-to-tail (1,2) sequences (–

$CH_2CH(CH_3)CH_2CH(CH_3)$–). Head-to-head and tail-to-tail units bridge the different blocks.[21]

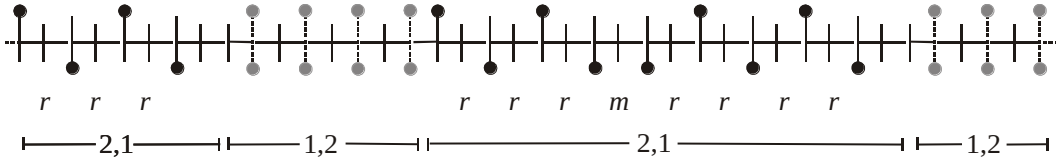

Figure 1.2. *Typical microstructure of a regioirregular chain of sPP produced with vanadium-based catalysts. The chain is shown in an adapted Fisher projection, which assumes a hypothetical zig-zag conformation of the chain backbone, whose plane is perpendicular to that of the figure. Consecutive couples of asymmetric tertiary carbon atoms in R or S relative configurations define steric diads meso (m) or racemo (r).*[1]

Samples of sPP obtained with homogeneous vanadium-based catalysts are able to crystallize, but low degrees of crystallinity are generally achieved with melting temperatures never exceeding 120-130 °C. The same soluble catalysts also promote copolymerization of ethylene with propylene and of higher α-olefins, such as 1-butene, with either ethylene or propylene.

However, homopolymerization of higher α-olefins only affords low molecular mass materials.[23] Because of the low stereoregularity and crystallinity, syndiotactic polypropylene prepared with these catalysts showed scarcely interesting physico-chemical properties and has received in the past only a very little attention. The homogeneous vanadium-based catalysts are, however, of great importance and used commercially for the production of ethylene-propylene-diene (EPDM) rubber.[24,25]

1.1.1. Metallocene catalysts

In the mid 1980s it was discovered that metallorganic complexes of transition metals catalyze in homogeneous phases the polymerization of olefins.[26,27] Stereorigid zirconocenes and titanocenes with C_2 symmetry, such as *rac*-ethane(indenyl)$_2$$MCl_2$ (with M = Zr or Ti), in combination with methylaluminoxane (MAO),[28] produce isotactic polypropylene.[26,27] Some years later in 1988 it was found that *ansa*-zirconocenes with C_s symmetry are able to produce highly stereoregular and almost completely regioregular syndiotactic polypropylene.[29] The prototype of this class of *ansa*-metallocene is isopropylidene(cyclopentadienyl)(Fluorenyl) zirconium dichloride ($Me_2C(Cp)(9\text{-}Flu)ZrCl_2$, Me = Methyl Cp = Cyclopentadienyl, Flu = Fluorenyl)

shown in the chart 1.[29] These catalysts do not require subambient reaction temperature in order to promote stereospecific polymerization.

1.1.1.1 C_s-symmetric metallocenes

As for the Ziegler-Natta heterogeneous catalysts, also for the homogeneous metallocene complex, the polymerization reactions are generally agreed to proceed by coordination of the olefin to a metal, followed by *migratory insertion* of the coordinated olefin into the growing polymer chain (*chain migratory insertion* mechanism). The C_s-symmetric metallocene of Chart 1, $Me_2C(Cp)(9\text{-}Flu)ZrCl_2$, after alkylation and cationization by MAO provide a racemic mixture of chiral metallocenium cations (Figure 1.3).[30,31] The two available coordination positions are enantiotopic,[32] that is, they have a preference for opposite propene enantiofaces. The steric arrangement of ligands and the non-bonded interactions with the alkyl ligand (that after the first insertion step becomes the growing chain) cause, indeed, enatioface selective π coordination of the incoming monomer (Figure 1.3). Molecular models for C_s-symmetric syndiospecific systems are substantially identical to those for C_2-symmetric isospecific systems and have been proposed by various authors.[33-37]

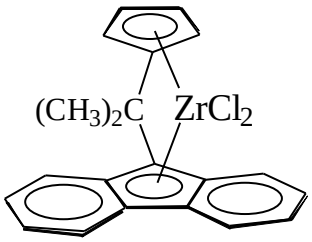

1

Chart 1

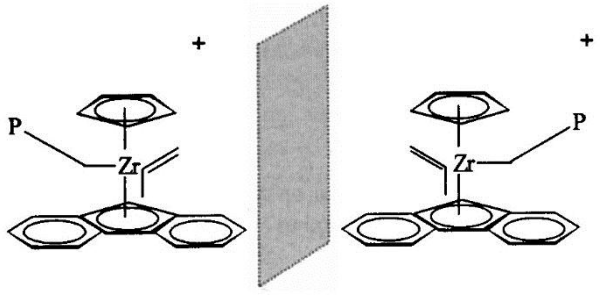

Figure 1.3. *Enantiomorphous interconverting active species produced from C_s-symmetric metallocene after cationization. The chain orientation and monomer coordination mode are shown.*[1,22]

As an example, the energetically favored structures for the R and S chirality at the metal atom of the model system $[Me_2C(Cp)(9\text{-}Flu)Zr(isobutyl)(propene)]^+$, which can be thought to correspond to two successive insertion steps, are shown in Figure 1.4a and b, respectively. The chirality of the catalytic system pushes the growing chain into an open sector, i.e., it imposes a chiral orientation to the growing chain. Again, the favored propene enantioface is the one which places the propene methyl group *anti* to the growing chain, thereby minimizing repulsive interactions with the growing chain itself. In particular, the *re* and *si* propene enantiofaces are favored for the *R* and *S* chirality at the metal atom, respectively.[33] Each enantiomer, independently, would produce isotactic chains, but they interconvert after each monomer insertion through the chain migratory insertion mechanism.[38-40]

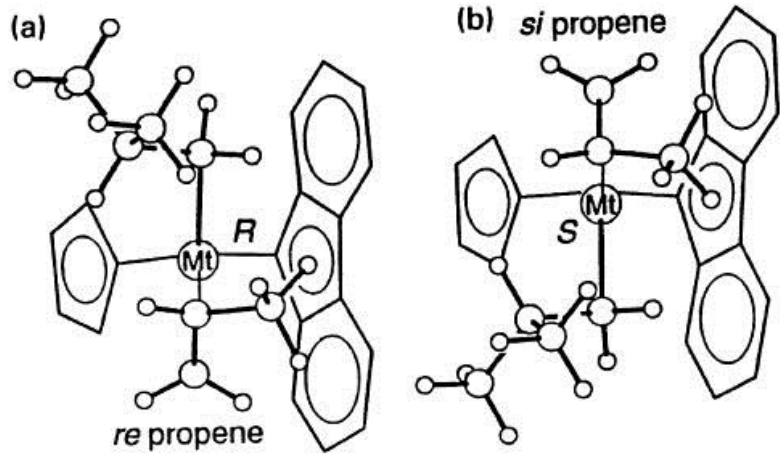

Figure 1.4. *Model of catalytic complexes $[Me_2C(Cp)(9\text{-}Flu)Mt(isobutyl)]^+$ cation with coordinate propene molecule and the isobutyl group that simulates a growing primary polypropylene chain. The coordinated bridged π-ligands presents a local C_s-symmetry and the two coordination positions which are availble for monomer and growing chain are enantiotopic. The carbon atoms of the methyl groups of the isopropyl bridge are omitted for the sake of clarity. According to the chain migratory polymerization mechanism, situations (a) and (b), with R and S chirality at the metal atom, respectively, alternate regularly during chain propagation, which explain the syndiotactic selectivity of the catalyst.*[40]

According to this mechanism after each insertion step the growing chain will reside at the coordination site previously occupied by the monomer (Figure 1.5). Chain migratory causes an inversion of the configuration of the zirconium cation (Figures 1.3 and 1.4) and consequently of the enantioface selectivity, at any insertion steps. Therefore, in two successive insertion steps opposite

propene enantiofaces are inserted, resulting in a syndiotactic chain propagation.[30,31,38,40]

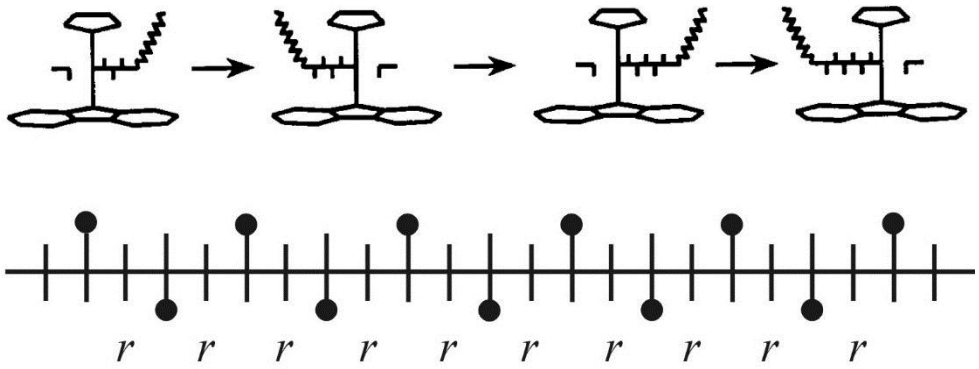

Figure 1.5. *Schematic representation of the chain migratory insertion polymerization mechanism promoted by C_s-symmetric metallocene catalyst $Me_2C(Cp)(9\text{-}Flu)MtCl_2$ and resulting regular sequence of r diads in a syndiotactic chain.*[1]

The preferred mode of propene insertion is primary (1,2)[41] and the ^{13}C NMR analysis of sPP produced with C_s-symmetric zirconocene of Chart 1 gives no evidence of regioerrors, indicating that these catalysts are in general highly regiospecific. A typical ^{13}C NMR spectrum of highly regioregular and stereoregular sPP sample is shown in Figure 1.6. The presence of resonances corresponding to methyl carbon atoms belonging to the pentads stereosequences *rrrm*, *rrmm*, *rmmr* and *rrmr*, besides the fully syndiotactic *rrrr* pentad, and the corresponding relative intensities, indicate that the chains contain isolated *mm* stereodefects (A in Figure 1.7) and isolated *m* defects (B in Figure 1.7).

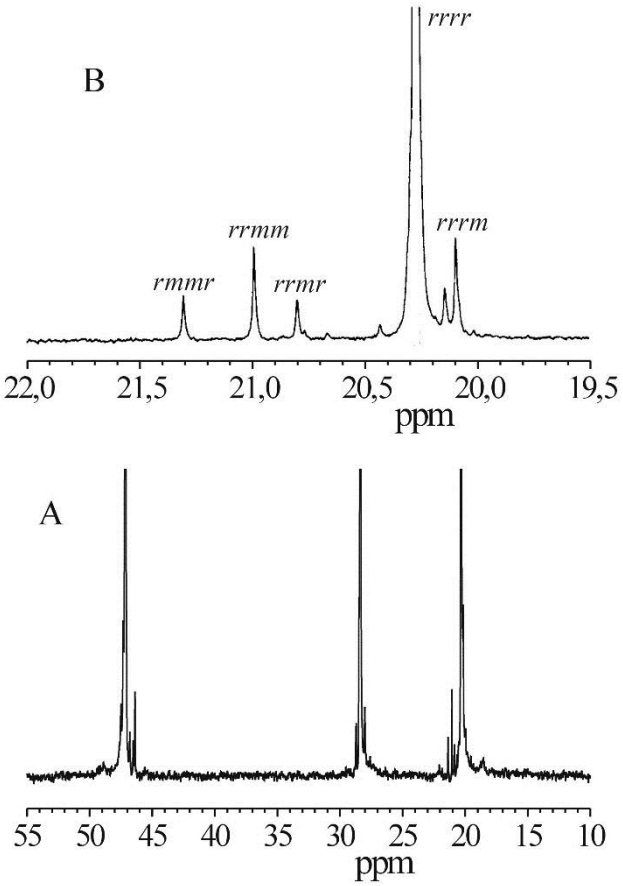

Figure 1.6. *Solution ^{13}C NMR spectrum of a sample of sPP prepared with the catalyst **1** of Chart 1 and MAO (A) and region of the spectrum of the methyl carbon atoms resonance (B). The assignment of methyl signals to pentads stereo-sequences are also shown.*[1]

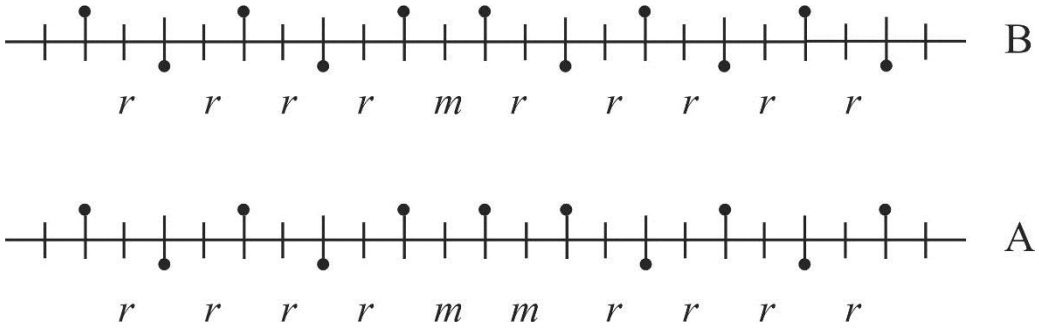

Figure 1.7. *Schematic representation of the chain microstructure containing isolated mm triad (A) and isolated m diad (B) of sPP produced with C_s-symmetric zirconocene of Chart 1.*

The *mm* defects come from monomer insertion with the "wrong" enantioface and are consistent with the fact that the stereochemistry of the syndiotactic chain propagation is controlled by the chirality of the catalytic site (enantiomorphic site control). The *m* defects are instead due to occasional back-skipping of the chain after the migratory insertion, that is, the chain flips back to the original coordination site in between two consecutive insertions. This occurs if the rate of interconversion of the two enantiomorphic sites is faster than the actual rate of monomer insertion, and sites epimerize before the next insertion. This increases the chance of two consecutive insertions taking place at the same enantiomorphic coordination position, adding two monomers with the same prochiral face with the corresponding formation of a *m* diad [ref 30,38]. This event has been also described as *chain back-skip*, *skipped insertion* or *site epimerization*.

The concentration of *m* defects increases with decreasing monomer concentration, and consequently the chain propagation rate, whereas the amount of *mm* defects only depends on the polymerization temperature.[29-31,42,43] To decrease the concentration of *m* defects and increase the overall stereoregularity of the sPP samples, the site epimerization rate should be reduced to greatest possible extent. This can be accomplished performing the polymerization in liquid propylene at lowest possible temperature. However, even by solution polymerizations highly syndiotactic polypropylene samples with low contents of *mm* defects and concentration of *rrrr* pentad higher than 90%, with melting temperatures as high as 150 °C, can be obtained with the catalyst **1** of Chart 1 at polymerization temperatures between 0 °C and ambient temperature.[43]

Changes in the structure of the metallocene complex produce differences in catalytic behavior.[38,44] Several modifications of the structure of the original zirconocene 1 of Chart 1, preserving the C_s symmetry, have been reported in the literature. The most significant examples have recently been reviewed[38] and some are reported in the Charts 2 and 3. The change of interannular bridge may produce interesting effects. In particular, changing the bridge from -Me_2C- to -Ph_2C- (**2** in Chart 2) results in sPP samples with much higher molecular mass.[31c,45,46,] However, a bridge made of a single carbon atom gives the best performance and the molecular mass decreases in the order Ph_2C > PhP > C_2H_4 > Me_2C ~ Me_2Si > Ph2Si, whereas syndiotacticity decreases in the order Me_2C > Ph_2C > PhP ~ C_2H_4 > Ph_2Si > Me_2Si.[38]

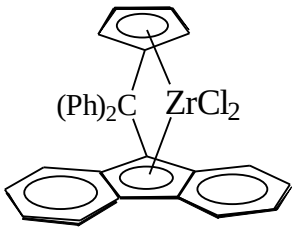

2

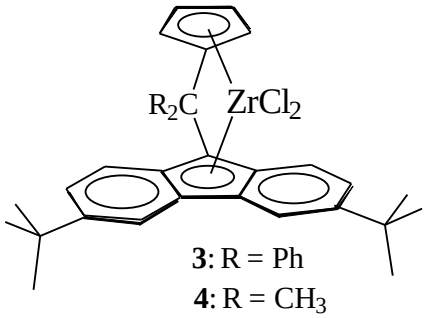

3: R = Ph
4: R = CH_3

Chart 2

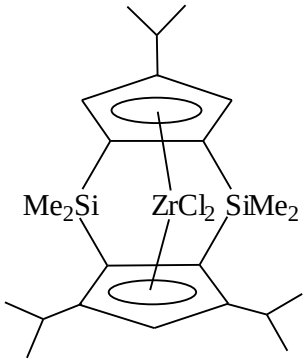

5

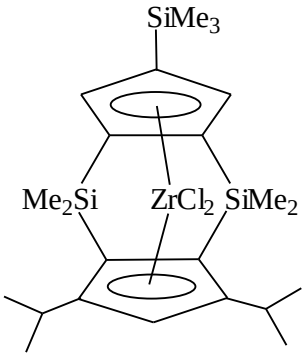

6

Chart 3

Expansion of the fluorenyl moiety generally produces increasing of syndiotacticity.[47,48] Modification of the catalyst structure by introducing substituents on the aromatic ligands may, indeed, induce lowering of frequency of *m* defects and may also enhance the enantioselectivity of the catalysts, lowering the concentration of mm defects.[31c,h] For instance the substitution in positions 3 and 6 of the fluorenyl moiety of the ligand in zirconocenes 1 and 2 of Charts 1 and 2 with t-butyl groups (3, 4 of Chart 2) causes substantial improvement in stereoselectivity of the catalyst with a decrease of concentration of both *m* and *mm* defects.[49] This has been reasonably explained by the enhanced substituents effect in directing the orientation of the growing polymer chain, providing a more effective guidance for the enatioface selective π coordination of the incoming monomer (Figure 1.4), and a lowering of the site epimerization rate due to steric interactions between t-butyl group and the MAO counter ion.[49]

It is worth noting that the same C_s-symmetric zirconocene precursors reported in Charts 1 and 2 that, once activated with MAO, promote prevailingly syndiotactic-specific polymerization of propylene, are able to produce highly syndiotactic polymers of other 1-olefins, as poly(1-butene) and poly(4-methyl-1-pentene).[50] Quite surprisingly, they instead promote isotactic-specific polymerization of 3 branched 1-olefins such as 3-methyl-1-butene and 3-methyl-1-pentene.[51,52]

It is worth mentioning that the condition of the C_s-symmetry of the precatalyst is not sufficient in order to promote syndiotactic-specific polymerization of propylene. Actually, C_s-symmetric precursors such as $Me_2Si(Cp)(4\text{-}MeCp)ZrCl_2$, $Ph_2C(Cp)(H8\text{-}Flu)ZrCl_2$, $Me_2Si(Cp)(3,4\text{-}(Me_3Si)_2Cp)ZrCl_2$ and the analogous Ti complex 5 in Chart 3, produce atactic poly(propylene) after activation with MAO.[51,31a,53a] The additional requirements for highly syndiotactic polymerization are a slow chain back-skip rate in comparison with the chain propagation rate, and a particularly delicate balancing of the non-bonded interactions between the growing chain, the spectator ligands and the incoming monomer.[31a,33,35]

1.1.1.2. Half-metallocenes, "constrained geometry" catalysts

Different catalysts that promote polymerization of propene are based on amido complexes of group IV transition metals, the so-called *constrained geometry* catalysts of general formula $Me_2Si(Me_4Cp)(NR)MtX_2$ (Chart 4), with Mt = Ti or Zr, R = alkyl, X = alogen or alkyl.[54,55] Atactic polypropylene is generally obtained with molecular masses and activities that depend on the substitution of the cyclopentadienyl ring.[56-58] In several cases, very high molecular masses have been obtained.[59]

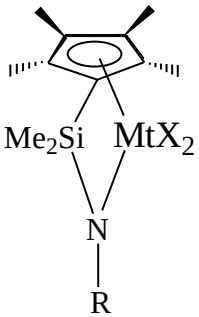

Chart 4

Some attempts have been made in order to introduce a stereoselecting ability by means of ligand substitution. The substitution of the Cp ring with fluorenyl moiety produces a catalyst that promote the syndiotactic polymerization of propene. In particular, it has been reported that a fluorenyl *tert*-butylamido zirconium complex (Chart 5, Mt = Zr)[60,61] and the analogous Ti complex[62] produce moderately syndiotactic polypropylene. The stereodifferentiation arises from enantiomorphic site control, quite to be expected in a complex having the C_s-symmetry required for syndiospecificity, and the mechanism of stereocontrol is strictly analogous to that for the C_s-symmetric ansa-metallocenes (Charts 1 and 2). However, only poorly syndiotactic polypropylene samples have been obtained with these catalysts.

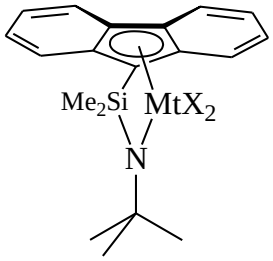

Mt = Ti, Zr; X = Cl, Me

Chart 5

More syndiospecific catalysts have been obtained with slight changes of the structure of the complex of Chart 5, using di-*tert*-butyl-substituted fluorenyl ligands (Chart 6).[63,64] These Ti complexes, [Me_2Si(2,7-*t*-Bu_2Flu)(*t*-BuN)]$TiCl_2$[63] and, better, [Me_2Si(3,6-*t*-Bu_2Flu)(*t*-BuN)]$TiCl_2$[64] give, after activation with MAO, high molecular weight syndiotactic polypropylene with high activity. Although the polymers show only very limited crystallinity, *rrrr* pentad contents reach values in the range 60-80%, with melting temperatures in the range 80-120 °C.[49] The stereoselectivity is higher than that expected from catalytic precursors with such flexible and low stereorigid structure. Under more favorable conditions, in liquid propylene and low temperatures (< 30 °C), these catalysts are even more stereoselective. According to the enantiomorphic-site controlled chain migratory insertion mechanism, the stereoregularity suffers with decreasing monomer concentration and/or increasing polymerization temperature, mainly as a result of increased probability of skipped insertion and the corresponding increase of *m* defects concentration.[49,65,66] The

stereoselectivity decreases much faster compared to the original Ewen's catalyst (**1** in Chart 1) with increasing polymerization temperature due to a much sharper increase of *m* defects content.

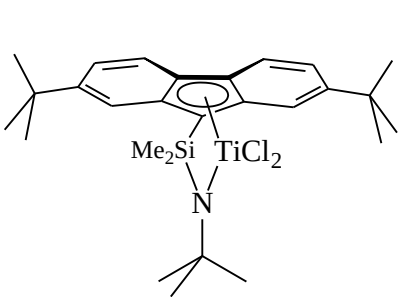

1

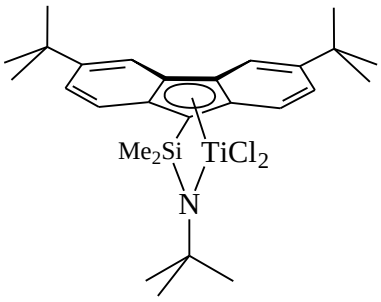

2

Chart 6

More recently Resconi has described silyl-bridged indenyl-*tert*-butylamido complexes of Ti in which the indenyl ligand has a heterocycle condensed onto the cyclopentadienyl moiety[67,68] (Chart 7). These complexes, after activation with MAO, show a high activity in propylene polymerization and produce poorly syndiotactic polypropylenes, with concentrations of *rrrr* pentad of 40-55%. The methyl region of the ^{13}C NMR spectrum of a typical sample prepared with catalyst **2** of Chart 7 is presented in Figure 1.8. Soft and non-sticky polypropylenes of very high molecular masses (higher than 10^6) with prevailingly syndiotactic microstructure and no measurable regioerrors are obtained with these catalytic systems. These properties, most remarkably the high molecular masses, are maintained even at the relatively high polymerization temperature of 80 °C. In addition, syndiotacticity is not affected by polymerization temperature.[67]

The samples are mainly amorphous but are able to crystallize and only a low level of crystallinity (16-20%) is achieved with melting temperatures of 45-60 °C.[86] However, the very high molecular mass and the presence of small crystallinity give very interesting mechanical properties.[1]

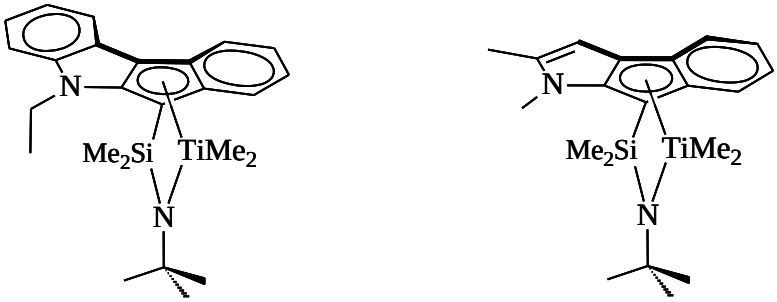

1 **2**

Chart 7

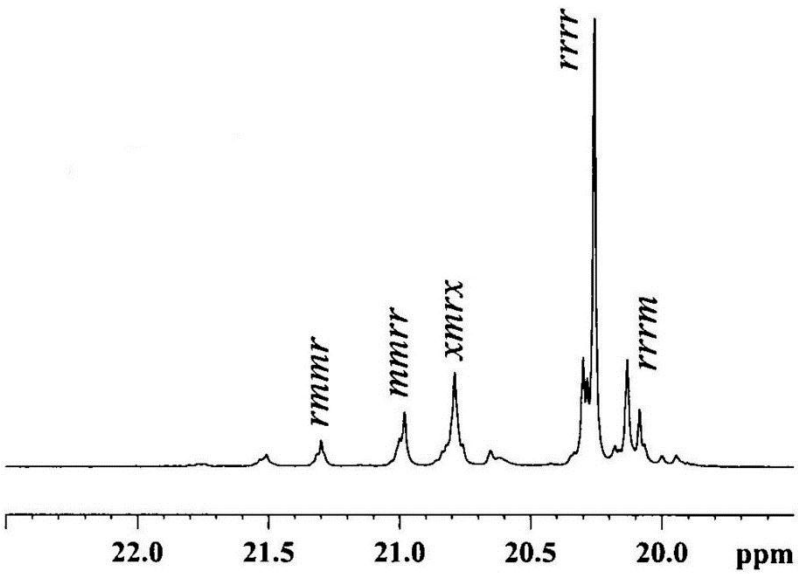

Figure 1.8. *Methyl region of the solution ^{13}C NMR spectrum ($C_2D_2Cl_4$, 120°C) of a poorly stereoregular sPP sample (sam-PP) prepared with catalyst **2** of Chart 7 and MAO in liquid monomer at 80 °C. The assignment of most intense resonances to pentads stereosequences is indicated.*[1]

1.1.2. Late transition metal-based catalysts

In 1995 Brookhart and coworkers[69-71] reported very efficient single-center catalysts for the polymerization of ethylene and 1-olefins based on Ni(II) or Pd(II) α-diimine compounds and MAO or other cationizing reagents (Chart 8). The used ligands contrast the high tendency of late transition metals to promote β-hydrogen elimination, which prevent polymerization of 1-alkenes, by

hindering the space around the metal needed for the agostic back-biting of the growing chain and the monomer-assisted chain transfer. When these square-planar diimine complexes of Ni(II) and Pd(II) are used as catalysts for promoting the polymerization of propylene only atactic polypropylene of low molecular mass is obtained at room temperature. However, at lower temperatures (e. g. –78 °C) the resulting polymer is prevailingly syndiotactic,[72,73] due to the onset of the chain-end control of the stereochemistry.

As a matter of fact, the ^{13}C NMR spectrum of polypropylene obtained at –78 °C in the presence of [1,2-bis(2,6-diisopropylphenyl)ethylenediimine]nickel dibromide – MAO, presented in Figure 1.9, looks quite similar to that of sPP obtained in the presence of homogeneous vanadium catalysts (Figure 1.1). In particular, the presence and the similar intensities of the ^{13}C resonances corresponding to *rrrm* and *rrmr* pentads and the negligible intensity of the signal corresponding to the *rmmr* pentad, indicate that the stereodefects are mainly isolated *m* diads, and the stereochemistry of the insertion is controlled by the chain end.

The analysis of the ^{13}C-enriched end groups proved that with these catalysts the stereospecific propagation occurs through primary (1,2) insertion of the monomer on the nickel carbon bond of the active species.[74,75] However, the NMR data of Figure 1.9 in the regions of methyl and methylene resonances, show the presence of a considerable amount of tail-to-tail and head-to-head monomer units, indicating that the regioregularity is not high. The polymer may, indeed, contain up to 10% of 2,1 and/or 3,1 units.

It is worth noting that pentacoordinate Fe(II) catalysts bearing tridentate pyridine-bis(imine) ligands, activated with MAO produce at low temperatures highly regioregular predominantly isotactic polypropylene (with *mmmm* pentad concentration up to 67%) with prevalent secondary (2,1) monomer insertion and chain-end control.[76-79]

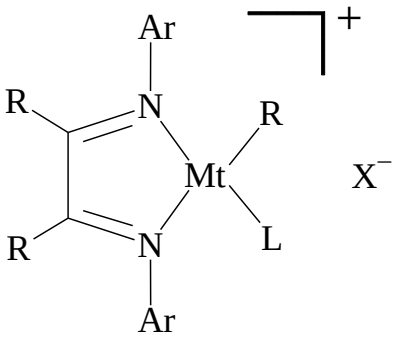

Chart 8

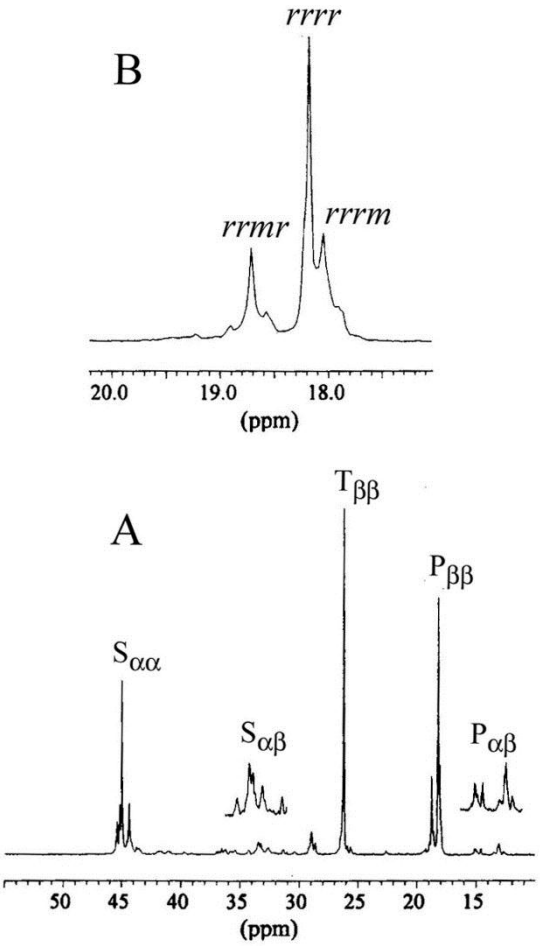

***Figure 1.9**. Solution [13]C NMR spectrum of a sample of sPP prepared with the catalytic system [1,2-bis(2,6-diisopropylphenyl)ethylenediimine]nickel dibromide/MAO at -78 °C (A), and region of the spectrum of the methyl carbon atoms resonance (B). The resonances of methyl and methylene carbon atoms in regiodefective sequences, $P_{\alpha,\beta}$ and $S_{\alpha,\beta}$, respectively, and the assignment of methyl signals to pentads stereo-sequences are shown.[1,22]*

1.1.3. Non-metallocene catalysts

A new family of single-center catalysts based on non-metallocene complexes, which promote polymerization of ethylene and propylene, have recently been discovered.[80-90] These compounds are titanium chlorides bearing phenoxyimine (PHI) ligands and have octahedral coordination geometry and C_2 symmetry (Chart 9). These catalysts are based on a class of compounds extensively studied by Mitsui for ethylene polymerization.[83-90] Because of the C_2 symmetry they were initially targeted as catalysts for the isospecific site controlled polymerization of propylene, as it occurs with the chiral C_2-symmetric metallocenes. Surprisingly these catalysts produced highly syndiotactic polypropylenes.[80-90] The reasons by which these chiral C_2-symmetric catalysts perform a syndiospecific polymerization instead of producing isotactic polymers like the symmetrically related *ansa*-metallocenes is related to the different mechanism. Coates et al.[83-90] have proposed that the selectivity derives from chain-end control of stereochemistry enhanced by a secondary mechanism of enchainment. Fujita and co-workers have recently reported evidences of the presence of end groups of polypropylene consistent with elimination following 2,1-insertion of propylene.[90] Moreover, end-group analysis revealed that insertion of propylene into the initiating titanium hydride occurs with high 1,2-regiochemistry. Subsequent insertions into primary titanium alkyls are regiorandom, while insertions into secondary titanium alkyls proceed with high 2,1-regioselectivity.[82] This mechanism is in agreement with the observed unusual high activity for ethylene polymerization, modest activity for propylene polymerization, and inactivity for 1-hexene polymerization.

Besides the unusual ability of producing highly syndiotactic polypropylene through exclusive chain-end control of stereoregularity and secondary (2,1) monomer insertion mechanism, these catalysts present the very important feature of promoting living polymerizations with control of the molecular mass. This is the most important improvement with respect to metallocene catalysts for which control of molecular weight has been met with limited success as most metallocene catalysts are plagued by chain termination and transfer reactions that prohibit the synthesis of block copolymers by sequential monomer addition.[38] The importance of living olefin polymerization catalysts is largely proportional to their ability to form block copolymers with blocks having high melting or glass transition temperatures from common commercial monomers, such as ethylene and propylene. The non-metallocene catalysts of

Chart 9 have achieved this goal since they are able to promote living polymerization of propylene and ethylene producing polymers having narrow polydispersities.[80-90] Syndiotactic polypropylene with very high molecular mass and ethylene and propylene-based block copolymers have been obtained with these catalytic systems.[81,82]

The ^{13}C NMR spectrum of a sPP sample prepared with the bis(phenoxyimine)titanium-based catalyst **2** of Chart 9, is reported in Figure 1.10. The presence of resonances in the region of methyl carbon atoms, corresponding to *rrrr*, *rrmr* and *rrrm* pentad stereosequences and the similar intensities of *rrrm* and *rrmr* signals (Figure 1.10B), indicates that isolated *m*-diads are the lone source of stereoerrors, consistent with a chain-end control mechanism. However, such an extremely high level of chain-end control was unprecedented in a propylene polymerization; when activated by MAO, the pentafluoro catalyst **2** of Chart 9 produces sPP with a *rrrr*-pentad content of 96% at 0 °C.[81]

Moreover, the spectrum of Figure 1.10A also presents less intense and broad resonances in the range 14.6-15.8 ppm and 16.6-17.4 ppm, corresponding to vicinal threo and erythro methyl carbon atoms, respectively, in the range 34-36.4 ppm, corresponding to vicinal methylene carbon atoms and vicinal threo and erythro methine carbon atoms, and in the range 41.5-44.6 ppm, corresponding to methylene carbon atoms close to vicinal methine or methylene groups.[91] This indicates the presence of defects of regioregularity, due to primary (1,2) insertions in a prevailingly secondary (2,1) enchainment.[80,81]

Because of the chain-end stereocontrol and the secondary (2,1) insertion, s-PP prepared with phenoxyimine-based titanium catalysts of Chart 9, presents a microstructure different from that of sPP prepared with C_s-symmetric metallocene catalysts of Charts 1 and 2. Chains of sPP prepared with non-metallocene catalysts of Chart 9 are, indeed, characterized by defects of stereoregularity represented basically by isolated *m* diads (..*rrrmrrr*..), consistent with chain-end control, and ethylene sequences as a result of occurrence of defects in the secondary (2,1)-regiospecificity.

The development of single centers metallocene and nonmetallocene catalysts for the syndiospecific polymerization of propylene has allowed production of syndiotactic polypropylene having virtually any degree of stereoregularity. Depending on the structure of the catalytic precursors, different chain microstructures, with different types and concentration of stereodefects and regiodefects are produced. Highly syndiotactic polypropylene with high

crystallinity and melting temperatures can be obtained with the classic C_s-symmetric metallocene catalysts (Chart 1 and 2), or with non-metallocene catalysts of Chart 9. Depending on the polymerization conditions (polymerization temperature and monomer concentration) samples with *rrrr* pentad contents from nearly 75% up to values as high as 96%, can be obtained. Lower syndiotactic and crystalline samples, with values of concentration of *rrrr* pentads in the range 60-80%, can be obtained with the constrained geometry catalysts of Chart 6 having the preserved C_s symmetry. Finally nearly amorphous, poorly syndiotactic polypropylene with high molecular mass and *rrrr* contents of 40-55% can be produced with constrained geometry catalysts of Chart 7. The availability of highly crystalline and stereoregular sPP has allowed clarifying the complex polymorphic behavior, the determination of crystal structures of the various polymorphic forms and finding unexpected interesting physical properties.[1] Moreover, the availability of sPP samples covering the whole range of stereoregularity compatible with maintenance of crystallinity (from [*rrrr*] = 40% up to [*rrrr*] > 96%), has allowed finding relationships between the chain microstructure (i.e type and concentration of defects of stereo- and regioregularity) generated by the catalysts through different polymerization mechanisms, and the crystal structure, the crystallization behavior and the physical-mechanical properties of sPP.[1]

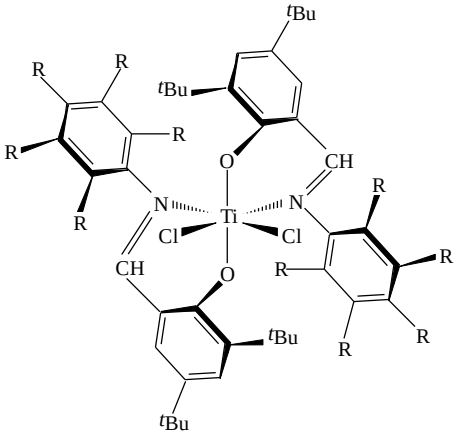

1. R = H
2. R = F

Chart 9

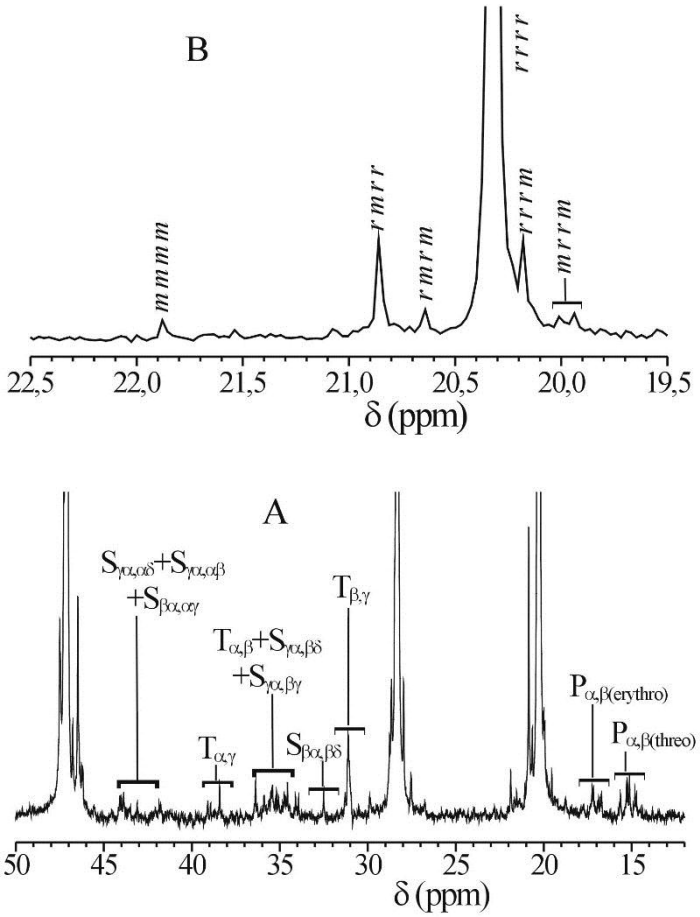

Figure 1.10. *Solution ^{13}C NMR spectrum of a sample of sPP prepared with the catalyst **2** of Chart 9 (A) and regions of the spectrum of the methyl carbon atoms resonance (B). The resonances of methyl, methine and methylene carbon atoms in regiodefective sequences, and the assignment of methyl signals to pentads stereo-sequences are also shown.*[1]

1.2. Crystal structure and polymorphic behavior

Syndiotactic polypropylene presents a very complex polymorphic behavior. The studies performed in the early 1960s on regioirregular and poorly syndiotactic polypropylene samples prepared with the vanadium-based Ziegler-Natta catalysts have already shows the presence of polymorphism.[2,92-95] Two different crystalline forms, characterized by macromolecular chains having different conformations, were described at that time. In the most stable form the chains presents a two-fold helical conformation, with **s**(2/1)2 symmetry[95,96] (the sequence of torsion angles along the backbone is $(TTGG)_n$, where T and G indicates bonds in trans and gauche conformation, respectively).[2,92,93,95] The less stable form[94] is characterized by chains in *trans*-planar conformation and

t*cm* symmetry,[96a] with a sequence of torsion angles of the kind $(TTTT)_n$. The two-fold helical and *trans*-planar conformations of sPP chains are shown in the Figure 1.11.

Only the more recent structural studies, performed on the highly regioregular and stereoregular sPP,[97-132] prepared with metallocene catalysts,[29] have shown that the polymorphic behavior of sPP is more complex[109] for the presence of new crystalline forms and for the presence of different types and amounts of disorder in the crystalline phases, depending on the degree of stereoregularity and the mechanical and thermal histories of the samples.[109-122]

It has also been found that sPP chains may assume in the crystalline phase a third different conformation, shown in Figure 1.11C, characterized by a sequence of torsion angle $T_6G_2T_2G_2$[108] and **t**2 symmetry.[119] This conformation contains both features of helical and *trans*-planar conformations (Figures 1.11A,B) since it is constituted by rather long sequences in *trans*-planar conformation (T_6) and portions in the two-fold helical TTGG conformation.

Four different polymorphic crystalline forms (shown in Figure 1.12) and a disordered mesomorphic form have been found so far. They have been called forms I, II, III and IV regardless of the chronology of their discovery but only considering that form I is the most stable and common form (even though it has been discovered much later than form II),[97] whereas forms III and IV are the less stable forms observed only in oriented fibers.[94,107,108] This nomenclature has been proposed by De Rosa, Auriemma and Corradini[110] and is nowadays widely accepted. Form I and form II are characterized by chains in **s**(2/1)2 helical conformation packed in different orthorhombic crystalline lattices (Figure 1.12 A and B, respectively), form III presents polymer chains in the *trans*-planar conformation with **t***cm* symmetry (Figure 1.12C) and, finally, form IV is characterized by chains in $T_6G_2T_2G_2$ conformation (Figure 1.12D).

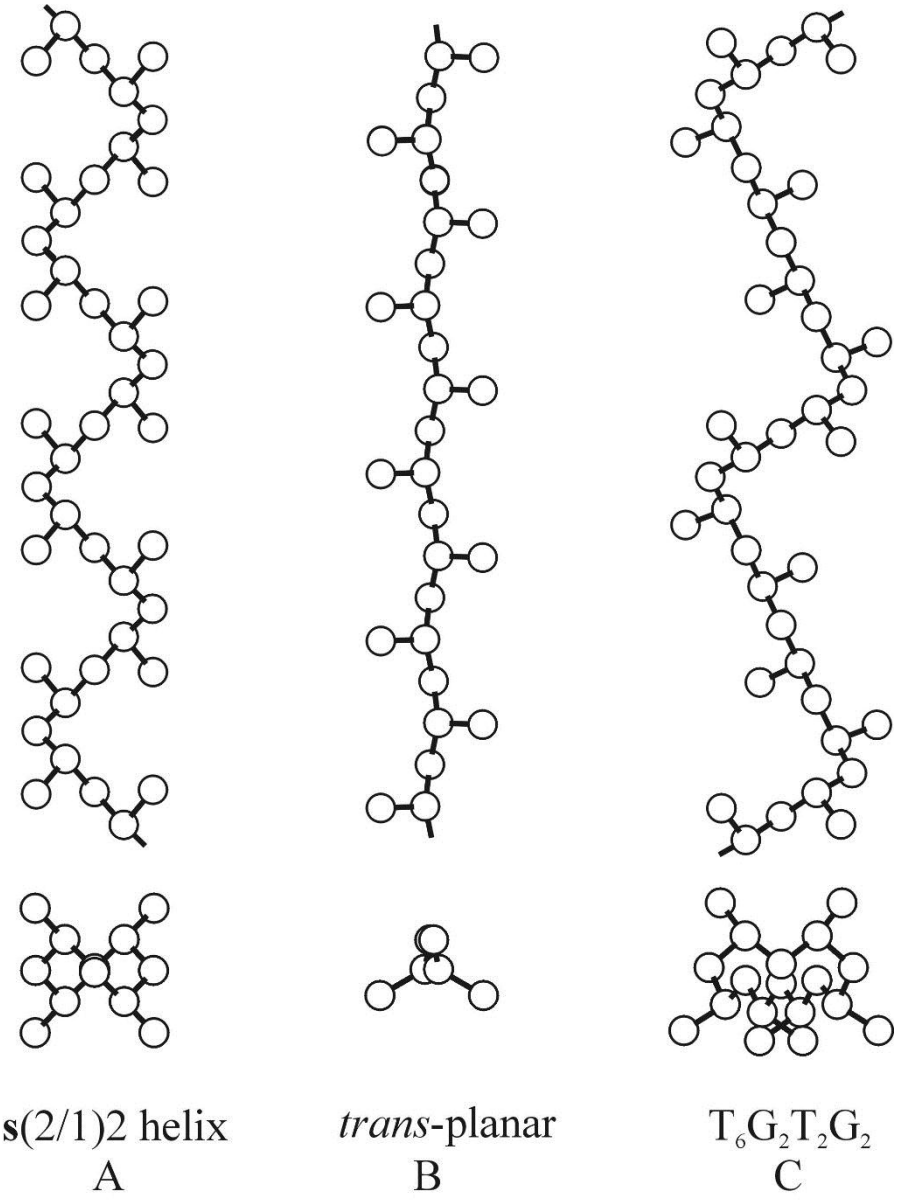

Figure 1.11. *Conformations of chains of sPP in the different crystalline polymorphic forms. Helical $(TTGG)_n$ conformation with* ***s****(2/1)2 symmetry (A), trans-planar conformation with* ***t****cm symmetry (B) and $T_6G_2T_2G_2$ conformation with* ***t****2 symmetry (C).*[1]

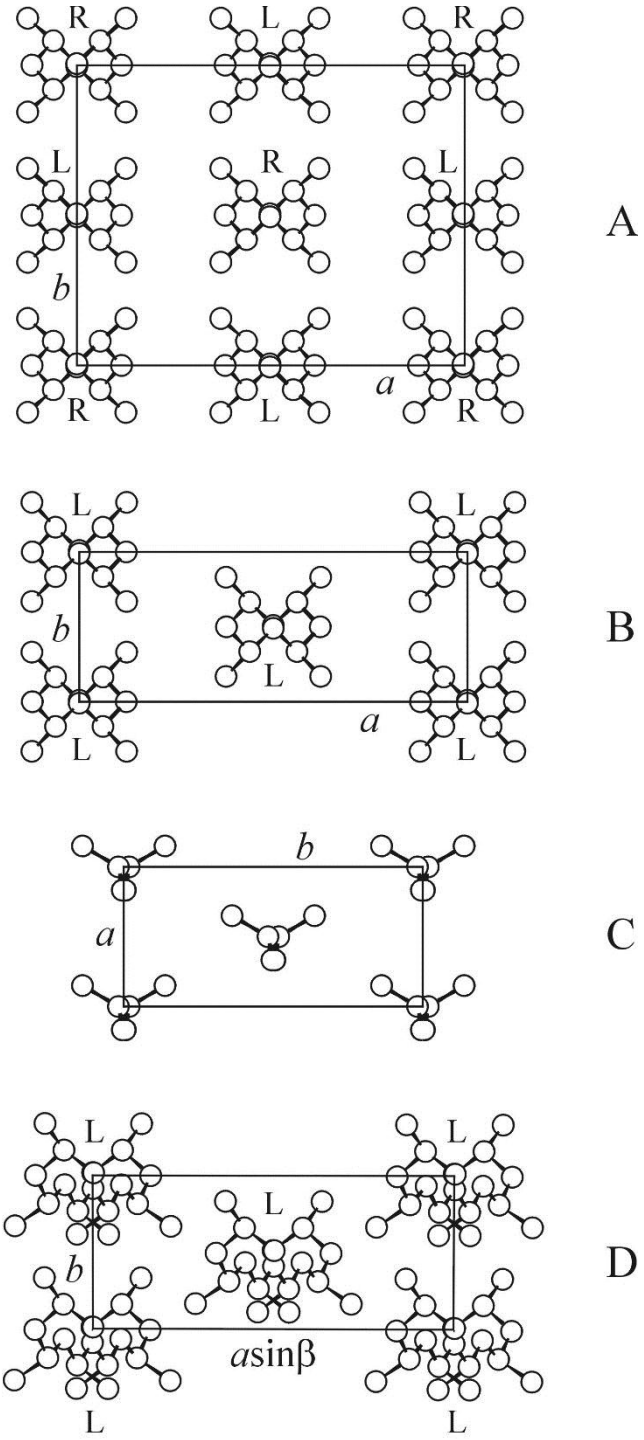

***Figure 1.12**. Limit ordered models of packing of form I (A), form II (B), form III (C) and form IV (D) of sPP. R = right-handed helix, L = left-handed helix.*[1]

1.2.1. Form I

Form I was found by Lotz, Lovinger et al.;[97-100] it is the stable form of sPP obtained under the most common conditions of crystallization, by melt and solution crystallizations in powder samples and single crystals of sPP. Lotz and Lovinger succeeded in growing highly regular single crystals of sPP and performed the first electron diffraction analysis on single crystals of this polymer.[97-100] They found the same molecular conformation and basic unit cell dimensions as reported by Corradini in the 1960s,[2,95] but they obtained a different polymorphic form with a different packing of the two-fold helical chains.[97] It is now well known that this new polymorphic form (form I) is the most stable form of sPP, much more stable than the polymorphic form found by Corradini in the 1960 (form II).

Form I is characterized by chains in **s**(2/1)2 helical conformation packed in the orthorhombic unit cell having axes a = 14.5 Å, b = 11.2 Å, c = 7.4 Å (Figure 1.12A). As proposed by Lotz and Lovinger.[97-100] the axes of the helical chains are in the positions (0,0,z) and (1/2,0,z) of the orthorhombic unit cell and, in the ideal limit ordered structure, helical chains with opposite chirality, right-handed and left-handed, alternate along a and b axes of the unit cell (Figure 1.12A), according to the space group *Ibca*.

More detailed studies performed with X-ray and electron diffraction and solid state ^{13}C NMR CPMAS techniques have shown that the lattice has a symmetry lower than *Ibca*.[110] A lower symmetry can be obtained by removing the crystallographic twofold axes, so that the chains may rotate around their axes and translate along the chain axis.[110] If the chains are slightly rotated around their axes, the local two-fold rotation axes of the chains, perpendicular to the chain axis, are lost in the lattice and the symmetry is broken. The space group is monoclinic $P2_1/a$ and two of the four chains included in the unit cell are independent, that is, not related by any element of symmetry (Figure 1.13B).[110]

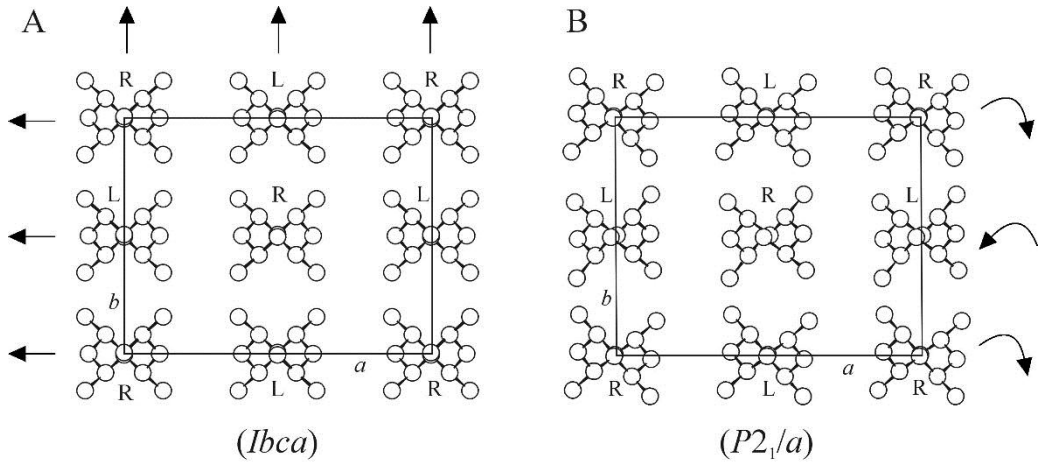

***Figure 1.13**. Models of packing of chains in the form I of sPP according to the space groups Ibc[97-100] (A) and P2$_1$/a[110] (B). The arrows indicate the crystallographic twofold axes, present in A and lost in B. In the model B the chains are rotated by nearly 5° around the chain axes, according to the direction indicated by the arrows.*[133]

1.2.2. Form II

Form II is the metastable polymorphic form of sPP with chains in helical conformation (Figure 1.12B). It corresponds to the structure deduced by Corradini et al.[2,95] from the analysis of the X-ray fiber diffraction pattern of oriented fibers of the low stereoregular and regioregular sPP samples available in the 1960s, prepared with Ziegler-Natta catalysts.[2,4] This form is characterized by chains in **s**(2/1)2 helical conformation packed in the *C*-centered orthorhombic unit cell with axes a = 14.5 Å, b = 5.60 Å, c = 7.4 Å, according to the space group $C222_1$ (Figure 1.12B).[2,95] Helical chains having the same chirality are included in the unit cell. Since the resolution of the crystal structure of form II by Corradini, dating back to 1960,[2] this helical form has been considered for long time, till to 1988, the most stable polymorph of sPP.

Form II has been obtained only in oriented fibers, by stretching low stereo- and regioregular sPP samples prepared with vanadium-based Ziegler-Natta catalysts[2,95,112] or by removing the tension in fibers initially in the *trans*-planar form III stretched from highly stereoregular sPP samples.[112] In fact, when highly syndiotactic samples, prepared with homogeneous metallocene catalysts, are stretched at room temperature fibers in the *trans*-planar form III (Figure 1.12C) are generally obtained.[107,109,112] Form III is stable only in the stretched state and transforms into the more stable isochiral helical form II (Figure 1.12B) by releasing the tension.[112,125-128] The X-ray diffraction patterns of a fiber of highly stereoregular sPP sample, having *rrrr* pentad content of 96%,

stretched at 600% deformation and after removing the tension are reported in Figure 1.14 A and B, respectively. The presence of the equatorial $(020)_t$ and $(110)_t$ reflections at $2\theta = 15.9$ and 18.8°, respectively, and of reflections on the first layer line corresponding to a *trans*-planar chain axis periodicity of 5.1 Å ($(021)_t$ and $(111)_t$ reflections),[107] indicate that the fiber in Figure 1.14A is in the *trans*-planar form III.[109,111,125] The diffraction pattern obtained upon removing the tension (Figure 1.14B) shows the typical 200 and 110 reflections at 2θ = 12.2 and 17° of the isochiral form II, and reflections on the first layer line (201 and 111 reflections at 2θ = 17.1 and 20.7°, respectively) corresponding to the helical chain axis periodicity of 7.4 Å,[112,125] indicating transformation of form III into form II upon releasing the tension.

Form II also develops, still in oriented fibers, by annealing at high temperatures (100-120 °C) fibers in the *trans*-planar form III keeping the fiber specimens under tension.[109,112]

Recently, form II has also been observed in powder samples by crystallization from the melt at elevated pressure.[129]

Finally, form II has also been obtained by epitaxial crystallization from the melt of single crystals in ultrathin films on the surface of crystals of a low molecular weight substance (2-quinoxalinol).[106]

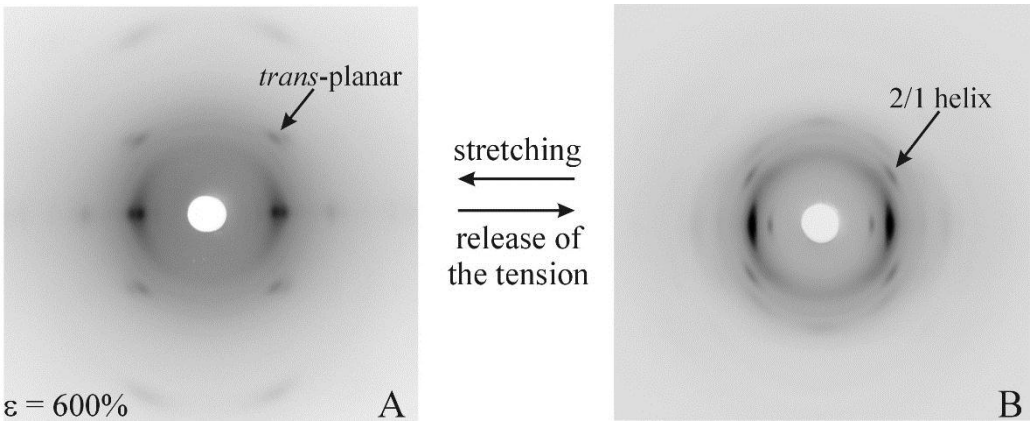

***Figure 1.14**. X-ray fiber diffraction patterns of oriented fibers of a highly stereoregular sPP sample, having concentration of rrrr pentad of 93%, obtained by stretched compression-molded films up to 600% deformation, kept in tension (A), and after the release of the tension (B). The arrows indicate reflections on the first layer line arising from the diffraction of crystals in the trans-planar form III with a periodicity of 5.1 Å and in the helical form II with a periodicity of 7.4 Å. The fiber in A is in the pure trans-planar form III, whereas the fiber in B is basically in the helical form II.*[1,125]

1.2.3. Form III

Form III is characterized by chains in *trans* planar conformation packed in an orthorhombic unit cell with axes a = 5.22 Å, b = 11.17 Å, c = 5.06 Å, according to the space group $P2_1cn$ (Figure 1.12C).[107] It is obtained by stretching at room temperature and at high deformations films of highly stereoregular samples of sPP prepared with metallocene catalysts.[107,109,112] Crystals of the most stable antichiral helical form I, present in the film prepared, for instance by compression-molding, transform by stretching into the *trans*-planar form III.[109] The degree of this transformation basically depends on the stereoregularity of the sample [112,125,128]. For highly syndiotactic samples, with *rrrr* pentad contents higher than 90%, the transition of the helical form into the *trans*-planar form III is complete already at nearly 300-400% deformation, whereas higher values of deformations are necessary to obtain the pure form III in samples of lower stereoregularity ([*rrrr*] = 75-80%).[125,126]

The polymorphic form of sPP with chains in *trans*-planar conformation was first obtained in the 1964 by cold-drawing specimens quenched from the melt of regioirregular and low stereoregular sPP samples prepared with Ziegler-Natta catalysts.[94] Because of the low stereo- and regioregularity of the samples, highly disordered form with low crystallinity was obtained, so that only the *trans*-planar conformation was determined from the value of the chain axis periodicity of 5.1 Å.[94] The complete crystal structure of form III has been determined only recently by Chatani et al.[126] by using the X-ray fiber diffraction data obtained from fibers of highly syndiotactic and fully regioregular samples prepared with metallocene catalysts.

Form III transforms into the most stable helical forms by annealing the stretched fibers at temperatures above 100 °C and keeping the fibers under tension.[109,112]; as shown in Figure 1.15, fibers in mixtures of crystals of the helical form I and form II are generally obtained by annealing.[109,112,126] Moreover, as discussed above form III is stable only in the stretched state and transforms into the helical form II by releasing the tension (Figure 1.14).[99,112-115]

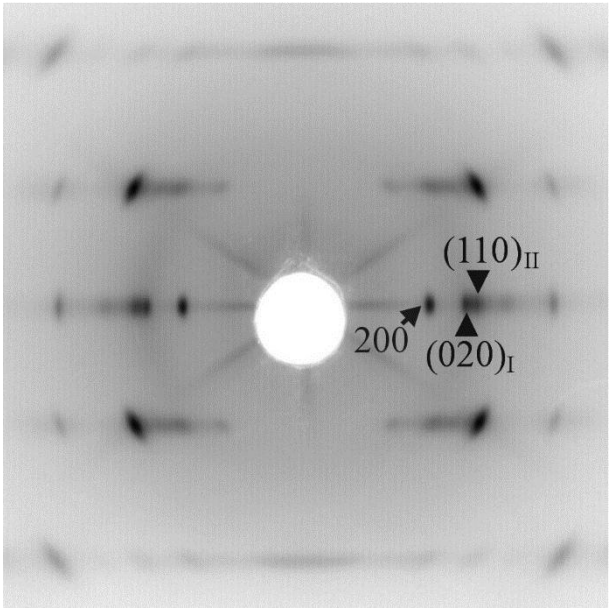

***Figure 1.15**. X-ray fiber diffraction pattern of a fiber of trans-planar form III annealed at 130 °C for 20 minutes. The annealed fiber is in a mixture of crystals of the helical forms I and II. The 020 reflection of form I at 2θ = 16° and the 110 reflection of form II at 2θ = 17° are indicated.*[1,112]

1.2.4. Form IV

Form IV was obtained by Chatani et al.[108] by exposing stretched fiber of s-PP originally in the *trans*-planar form III to organic solvents (e.g. benzene at temperature below 50 °C). The crystal structure of form IV, as reported by Chatani,[108] is characterized by chains in the $(T_6G_2T_2G_2)_n$ helical conformation having **t**2 symmetry (Figure 1.11C), packed in a triclinic unit cell with axes a = 5.72 Å, b = 7.64 Å, c = 11.60 Å, α = 73.1°, β = 88.8° and γ = 112.0°, according to the space group $P1$ (Figure 1.16A).[108]

It has recently been found that the crystal structure of form IV could be described by an analogous model having higher symmetry.[119] In this alternative model the unit cell is monoclinic with parameters a_m = 14.17 Å, b_m =5.72 Å, c_m = 11.60 Å and β_m = 108.8° and the space group is $C2$ with two chains included in the unit cell (Figures 1.12D and 1.16B).[119] The monoclinic model can be easily obtained from the triclinic structure by small changes of the atomic coordinates and packing arrangement.[119] A comparison between the triclinic and monoclinic models is shown in Figure 1.16.

Form IV has been found only in oriented fibers and never in powder samples. It is metastable and readily transforms into the two-fold helical forms by annealing above 50 °C.[108]

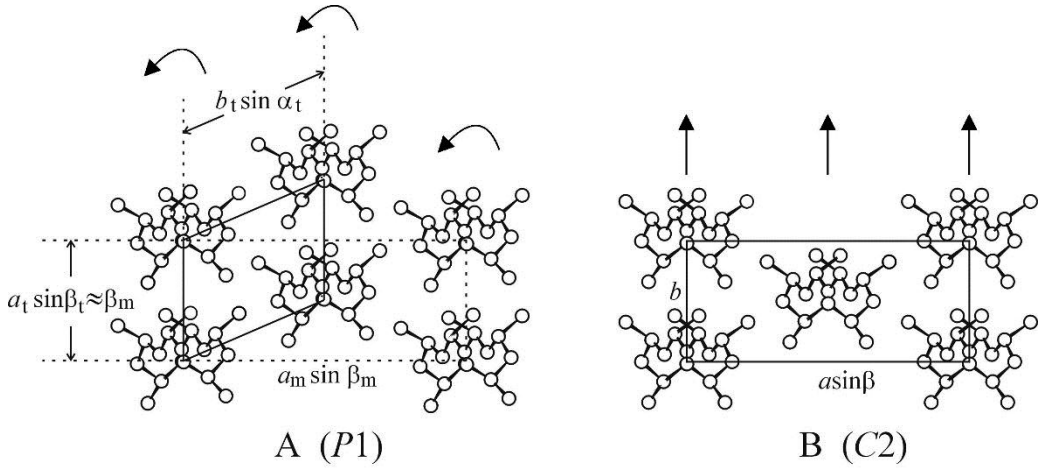

Figure 1.16. *Models of packing of form IV of sPP, according to the triclinic space group P1*[108] *(A) and monoclinic space group C2*[119] *(B). The arrows indicate the crystallographic two fold axes, present in B and lost in A. In the model A the chains are rotated by 6.5° according to the direction of the arrows and the continuous and dashed lines show the triclinic and monoclinic unit cells, respectively.*[133]

1.2.5. The mesomorphic form

Nakaoki et al.[130] reported that the crystallization of the *trans*-planar form III may be spontaneously induced by quenching the melt to 0 °C without any mechanical stress, keeping the sample at 0 °C for long time (at least 20 h).

If the samples are immediately taken out from the bath at 0 °C and heated to room temperature, they rapidly crystallize at room temperature in the more stable helical forms.[130] Longer residence times at 0 °C of the sample increase the number of long chain stretches in the *trans*-planar conformation, which inhibit the crystallization of the sample into the more stable helical form I at room temperature.[130-132]

Accurate analyses of the X-ray powder and fiber diffraction patterns (Figures 1.17 and 1.18A, respectively) and solid-state ^{13}C NMR spectra (Figure 1.18B) have shown that this crystalline form of sPP, obtained by quenching the melt to 0 °C, cannot be identified as the known crystalline form III, but it should be considered as a new phase characterized by disorder in the packing of chains in the ordered *trans*-planar conformation.[131] This phase is more properly defined as a mesomorphic form of sPP,[131] characterized by lateral disorder in the packing of *trans*-planar chains, probably associated to a rotational disorder of chains around the chain axes and to translational disorder along the chain axes. The X-ray powder and fiber diffraction patterns of the mesomorphic form,

shown in Figure 1.17 and 1.18A, respectively, are, indeed, characterized by broad reflections on the equator at 2θ = 17° and on the first layer line at 2θ = 24°, indicating disorder in the structure. The layering of the reflection in the X-ray fiber diffraction pattern corresponds to a chain periodicity of 5.1 Å (Figure 1.18A).

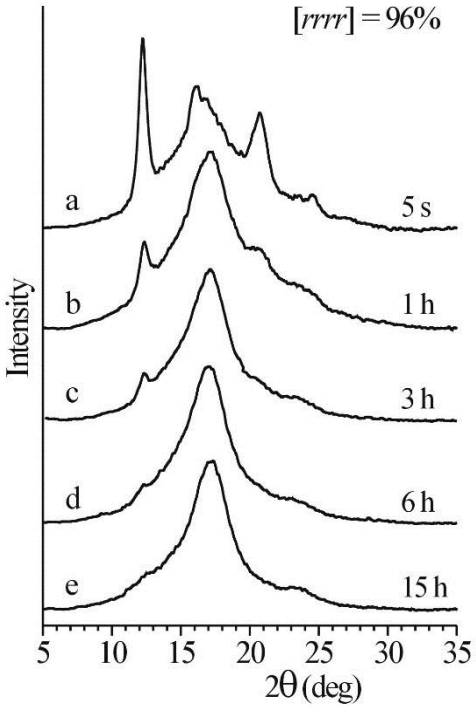

Figure 1.17. *X-ray powder diffraction profiles of samples of a highly stereoregular sPP sample, having concentration of rrrr pentad of 96%, quenched from the melt at 0 °C and kept at 0 °C for 5 seconds (a), 1 hour (b), 3 hours (c), 6 hours (d) and 15 hours (e).*[121]

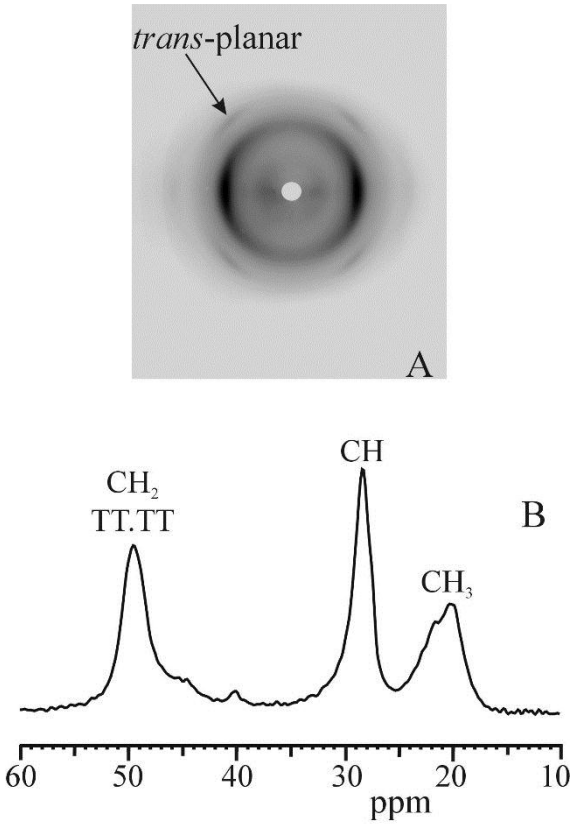

***Figure 1.18**. A) X-ray fiber diffraction pattern of an oriented fiber of a highly stereoregular sPP sample, having concentration of rrrr pentad of 91%, in the trans-planar mesomorphic form. The arrow indicates reflection on the first layer line corresponding to the chain periodicity of 5.1 Å of the trans-planar conformation.[123] B) Solid-state ^{13}C NMR CP-MAS spectrum of a powder sample of sPP in the mesomorphic form. The assignment of resonances to methyl, methine and methylene carbon atoms are indicated.[131]*

1.2.6. Transitions between polymorphic forms

The presence of many different types of disorder in the crystals of the polymorphic forms and the structural transitions between the various crystalline forms occurring in different conditions, for instance by annealing or stretching, result in a very complex pattern of the polymorphic behavior of sPP. A scheme of the condition of crystallization of the different polymorphic forms and of the structural transitions is reported in Figure 1.19.[1] The polymorphic transitions are strongly affected by the chain microstructure, in particular the stereoregularity of the sample and are the basis for understanding some outstanding physical properties of sPP.[1,134,135]

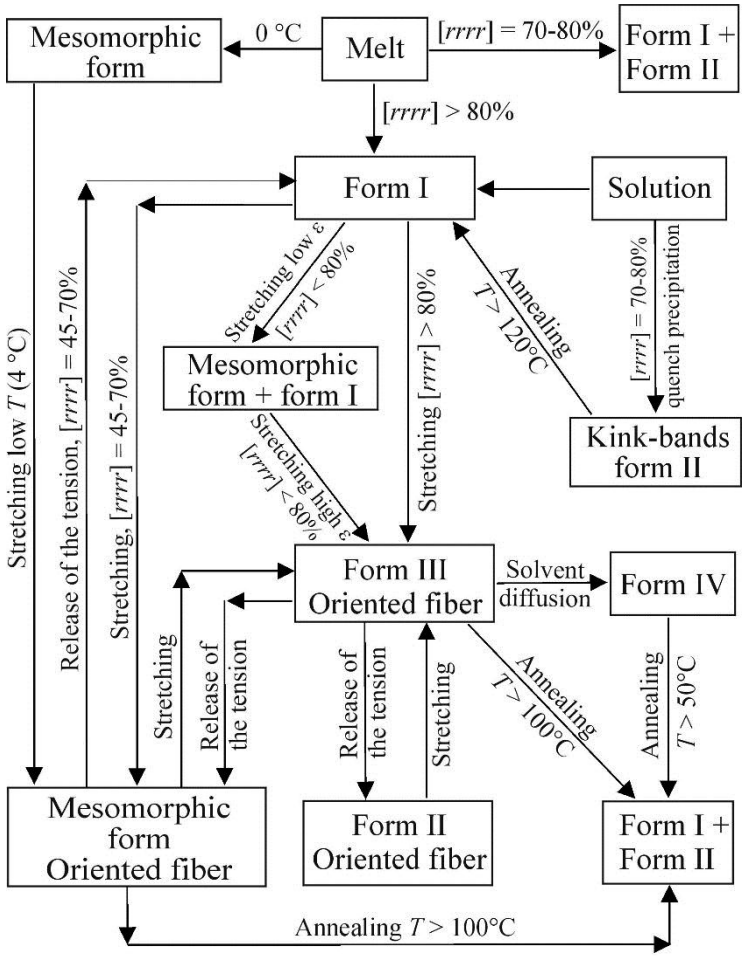

Figure 1.19*. Schematic representation of the polymorphism of sPP. The conditions of crystallization of the different polymorphic forms in powder and fiber samples and of interconversion between the forms are shown.*[1]

1.2.7. Effect of stretching and relaxation

In this section a short overview of the main polymorphic transitions induced by stretching is reported.

In the case of highly stereoregular sPP samples, the stretching at high deformation of an unoriented film initially crystallized in any crystalline forms (helical form I or *trans*-planar mesomorphic form, obtained, for instance, by compression-molding and cooling to room temperature or quenched at 0 °C, respectively), produces transformation into the crystalline *trans*-planar form III.[107,109,112,123-128,134,135] Both the helical form I and the mesomorphic form transform by stretching into the form III. In the first case the structural transformation involves a conformational transition, whereas in the latter case

the transformation basically corresponds to an increase of order in the packing of the chains in *trans*-planar conformation.[123,134,135]

sPP samples of low stereoregularity (for instance the samples prepared with constrained geometry catalyst),[67,68] generally crystallized in the disordered helical form I,[136-138] do not transform by stretching into the crystalline form III but only the *trans*-planar mesomorphic form is obtained even at high deformations.[134-138] The conformational transition from helical chains into *trans*-planar chains occurs by stretching, but the high concentration of defects of stereoregularity prevents formation of the ordered form III.[138]

The phase transition and the associated irreversible morphological changes occurring while stretching unoriented samples in the helical form have been followed in real time by in situ X-ray diffraction using a syncrotron radiation.[128] The X-ray diffraction patterns, and the corresponding integrated diffraction profiles along 2θ, collected while stretching an unoriented compression molded film up to obtain a uniaxially oriented fiber are reported in Figure 1.20. The unoriented film shows initially a powder pattern with typical Debye-Scherrer rings and is initially crystallized in the form I, as indicated by the presence of the $(200)_{hI}$, $(020)_{hI}$, $(211)_{hI}$ and $(121)_{hI}$ reflections of form I in the diffraction profile of Figure 1.20B (curve at ε=0). With increasing deformation, the crystallites tend to orient with chain axes parallel to the stretching direction. At a critical deformation around 90-100% the $(200)_{hI}$ and $(020)_{hI}$ reflections result strongly polarized on the equatorial layer line (Figure 1.20A) and appear also rather broad due to the fact that the size of the crystallites in the direction normal to the chain axis decreases during deformation. Along with this morphological transformation, small crystals of form I simultaneously transform into the *trans*-planar form III, as indicated by appearance of the reflection on the first layer line, corresponding to the periodicity c = 5.1Å, and the $(020)_t$ and $(110)_t$ equatorial reflections, characteristic of form III of sPP, at 2θ = 7.55 and 8.44° (λ = 0.718 Å) in the patterns of Figure 1.20A for deformations higher than 106%.[128] For ε = 136% (last frame in Figure 1.20A) the fiber is mainly in the *trans*-planar form III of sPP. The index of crystallinity, initially equal to 60% for the unoriented sample, does not change during elongation. This indicates that during the stretching, the crystallites in the helical form I transform directly into the *trans*-planar form III in correspondence to a critical strain. No evidences of temporary melting of crystals of the helical form followed by rapid re-crystallization into the *trans*-planar form III have been observed.[128]

All these data indicate that during stretching, when the critical value of the strain is achieved, the sample undergoes abrupt structural and morphological transformations. The morphological changes from powder into fiber specimens are accompanied by two simultaneous phenomena: the breaking of the crystallites in direction normal to the chain axes[139] and the sudden transformation of portion of crystals previously in the helical form I into the *trans*-planar form III.[128]

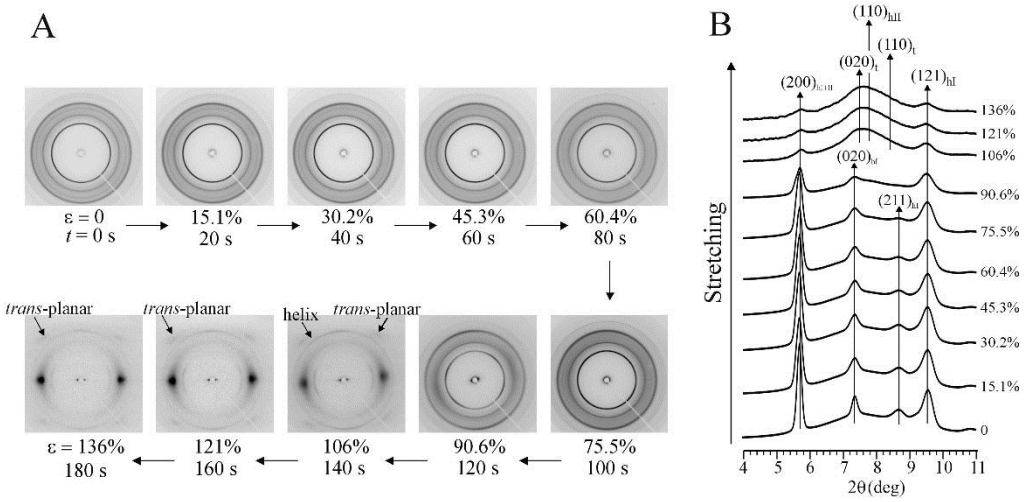

Figure 1.20. *(A) X-ray fiber diffraction patterns of an unoriented compression molded film of a highly stereoregular sample of sPP with [rrrr] = 93% recorded in situ while stretching the sample at rate of 5mm/min, using monochromatic X-ray syncrotron radiation. The deformation ε and the time t are indicated. The characteristic reflections on the first layer line of the helical form I and of the trans-planar form III of sPP are also indicated with arrows. (B) X-ray diffraction intensity profiles integrated from the two dimensional diffraction patterns reported in A, as a function of 2θ. The positions of $(200)_{hI}$, $(020)_{hI}$, $(211)_{hI}$ and $(121)_{hI}$ reflections of the helical form I, of the $(110)_{hII}$ reflection of form II and of $(020)_t$ and $(110)_t$ reflections of the trans-planar form III are also indicated.*[128]

The *trans*-planar form III obtained by stretching transforms into the isochiral helical form II when the tensile stress is removed.[112,125-128] This indicates that the transition from the stable helical form I into the *trans*-planar form III occurring by stretching unoriented samples is irreversible and is associated to the plastic deformation of the crystalline lamellae.[125] Figure 1.21 illustrates the transformation occurring for fibers cyclically stretched and immediately relaxed at controlled rate, followed by X-ray diffraction with syncrotron radiation.[127,128] The index of crystallinity of the sample over consecutive cyclic stress-relaxation runs remains constant at nearly 60%, as in the original unoriented film.[127,128] In the unstrained state, the fiber is basically in the isochiral helical

form II, as shown by the presence of strong $(111)_{hII}$ reflection at *d*=4.29Å, and by strong $(200)_{hII}$ and $(110)_{hII}$ reflections of form II at *d* = 7.20 and 5.26Å (2θ = 5.72 and 7.83°, respectively, λ = 0.718 Å) in the patterns of Figure 1.21A,A' for ε = 0%.[127,128]

The stretching of the fiber in form II induces transformation into the *trans*-planar form III (Figure 1.21A). For strain lower than a characteristic value, $\varepsilon_c \approx 10\%$, no significant changes in the X-ray diffraction patterns are observed.[127,128] For higher deformations, $\varepsilon > \varepsilon_c$ the intensity of the $(200)_{hII}$ reflection gradually decreases with increasing ε, while the intensities of $(020)_t$ and $(110)_t$ reflections of form III increase (Figure 1.21A,A'). This indicates that with increasing deformation, the relative amount of crystals of form II decreases and the content of crystals of form III increases. Since the index of crystallinity does not change, this indicates that a stress-induced phase transition from form II into form III occurs when the sample is stretched above a characteristic deformation value.[127,128]

The structural and morphological changes occurring during stretching are reversible. The crystals of the *trans*-planar form III gradually transform back into the helical form II as the tensile stress is released (Figures 1.21B,B').[127,128] The $(020)_t$ and $(110)_t$ reflections of the *trans*-planar form III, indeed, gradually disappear and the intensities of the $(200)_{hII}$ and $(110)_{hII}$ reflections of helical form II increase, while releasing the tension (Figure 1.21B). Below a critical strain, the sample is almost fully in the helical form II.

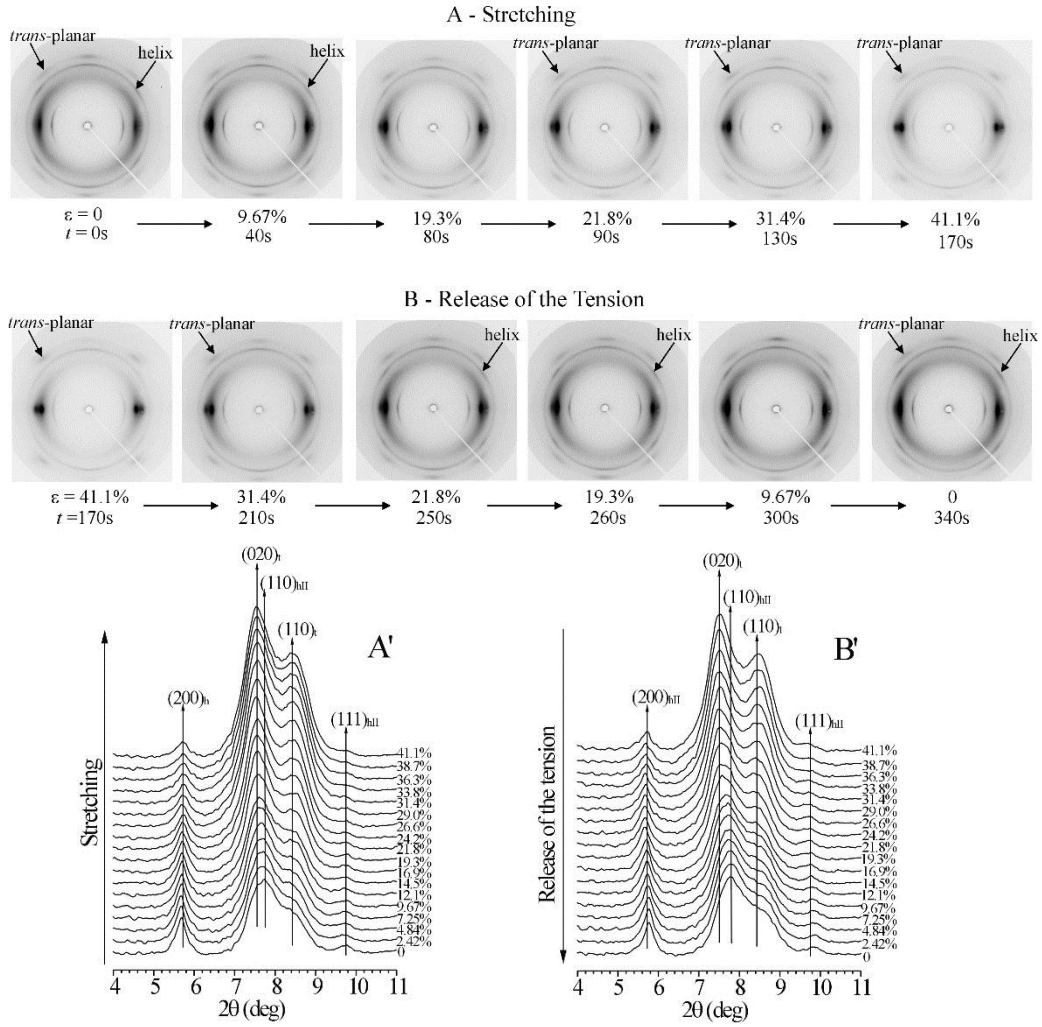

Figure 1.21. *X-ray fiber diffraction patterns (A,B) and corresponding diffraction profiles read along the equatorial layer line (A', B'), of an uniaxially drawn fiber of a highly stereoregular sample of sPP with [rrrr] = 93%, recorded in situ during cyclic elongation and recovery using monochromatic X-ray syncrotron radiation. The patterns in A,A' were recorded while stretching the sample, whereas the patterns in B,B' were recorded while releasing the tension. The deformation ε and the time t are indicated. The characteristic reflections of helical form II and trans-planar form III of sPP on the first layer line are also indicated with arrows. The positions of the $(200)_{hII}$, $(110)_{hII}$ and $(111)_{hII}$ reflections of the helical form II and of the $(020)_t$ and $(110)_t$ reflection of the trans-planar form III are also indicated.*[128]

The reversible phase transition between form II and form III occurs instantaneously and directly, without involving a third disordered, intermediate phase.[125-128] It has been suggested that this crystal-crystal transition is a cooperative process, involving conformational and structural rearrangements of bundles of close neighboring chains in short time and may be considered as a martensitic transition, with associated characteristic values of stress-strain

parameters.[127,128] As in the case of martensitic transitions occurring in alloys and steels, also for sPP, the critical values of the stress-strain parameters depend on the temperature. For instance, for temperatures higher than 60 °C the helical form does not transform into form III upon stretching.[126]

Only when the *trans*-planar form of sPP is obtained by stretching, can the chiral form II of sPP be formed by releasing the tension, through the spontaneous solid-state transition. When the *trans* planar form III of sPP does not form by stretching, like for instance at high stretching temperature,[126] or in low stereoregular sPP samples[134-138] or in copolymers of sPP with butene comonomeric units,[140] the chiral form II does not form anymore by releasing the tension and the most stable antichiral helical form I is obtained.

It has been suggested that the evolution of form III into form II, instead that into the most stable antichiral form I, is imposed by conformational and steric constraints and the isochirality of the resulting helical phase was taken as an indication that the transformation is a cooperative process that occurs through instantaneous and simultaneous conformational and structural rearrangements of close neighboring chains, involving the whole ordered domains.[120,128]

During the crystal-crystal phase transition from form III to form II, the generation of a helix structure requires the introduction of G^+ or G^- bonds in an all-*trans* chain.

...TTTTTTTTTT... → ...TTTGGTTTTT... → ...TTGGTTGGTT...

This implies a modification in chain direction and, ultimately, generation of a helix with a larger cross section than that of the initial conformation. Such process also involves very major molecular readjustments which, to take place, must be direct and cooperative. A possible mechanism for the crystal-crystal phase transition from form III into form II of s-PP is shown in Figure 1.22 [ref.120,128]. Upon releasing the tension form III (Figure 1.22A) is unstable and transforms into the more stable isochiral form II (Figure 1.22C). This transition implies the generation of ...$TTG^+G^+TTG^+G^+$... (right-handed) or ...$G^-G^-TTG^-G^-TT$... (left-handed) conformational sequences starting from a fully extended chain. Since this transformation is direct and occurs in a very short time, it necessarily requires that, in a given ordered aggregate of sPP chains initially in form III, *gauche* bonds having the same sign are formed cooperatively, for steric reasons, as sketched in Figure 1.22B. The parallelism of the chains may be, indeed, preserved only if the helical stretches, which form from the extended chains, are isochiral, i.e. *gauche* bonds have all the same sign (G^+ or G^-). In fact, formation of right- and left-handed helical stretches (as in

the stable form I) appears sterically forbidden, because it would result in two local stem orientations, which would diverge on opposite sides of the initial *trans*-planar chain (Figure 1.22B') producing steric interactions with the neighboring chains. The two enantiomorphic helical stretches would be oriented at right angle each other. As a consequence, during the transformation, helical sequences generated in neighboring chains have the same chirality in order to avoid steric interactions, and the isochiral form II is obtained, even though the antichiral form I is more stable. The cooperativity imposed by steric constraints control the generation of *gauche* bonds and applies traveling in unison along the extended chains in the whole ordered domain, in a very short time, inducing the formation of the chiral helical form II, even though the antichiral form I is more stable.[120,128]

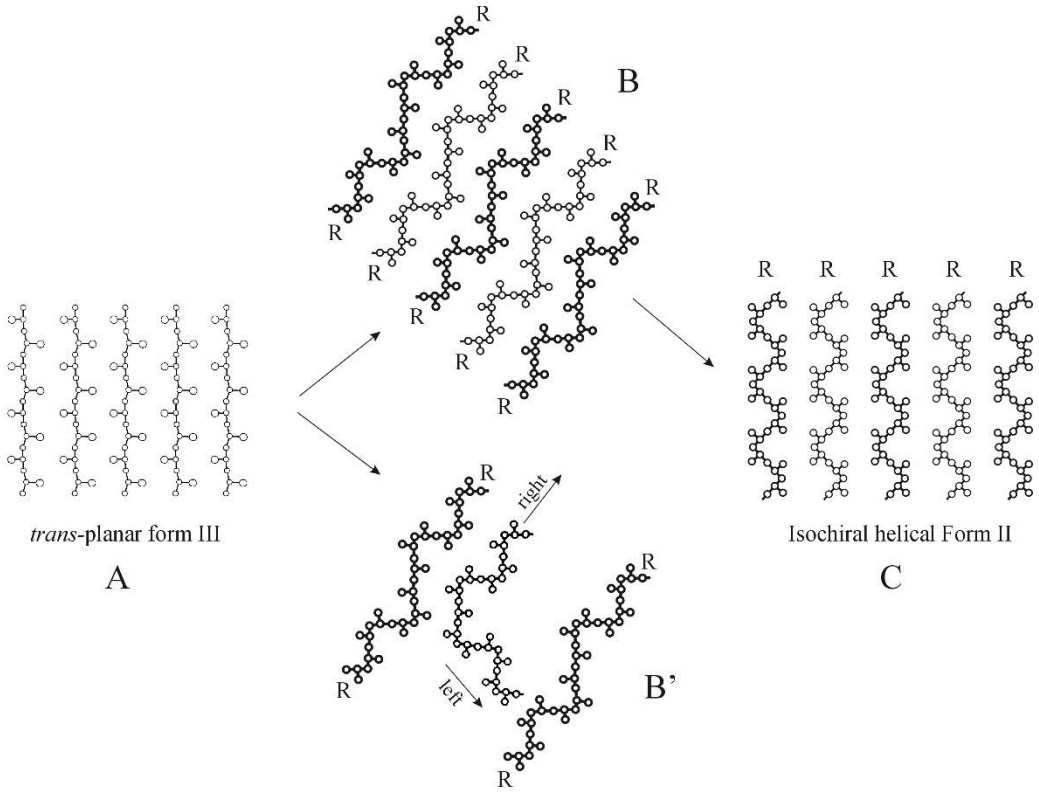

Figure 1.22. *A possible cooperative mechanism of the phase transition from the trans-planar form III (A) into the isochiral helical form II (C) of sPP. The transition occurs through formation of a transient state (B) of the crystalline aggregates of chains originally in form III, characterized by right handed (R) helical portions of chains formed in unison, connected by portions of chains in trans-planar conformation forming king-bands. The formation of helical portions of chains having opposite chirality within the same ordered domain is forbidden because two antichiral stems would be oriented at right angle each other, producing steric interactions with neighboring chains (B').*[128]

The structural evolution of the *trans*-planar form III upon removing the tension depends instead on the crystalline forms present in the starting unoriented material.[123] In particular, when sPP samples containing mixtures of crystals of the *trans*-planar mesomorphic form and of the helical form I are stretched at 25 °C, orientation of both crystals occurs at low deformations, whereas the transition into the crystalline *trans*-planar form III occurs at higher deformation. The *trans*-planar form III transforms into the mixture of crystals in the helical and mesomorphic forms present initially in the unoriented sample upon releasing the tension.[123]

These results indicate that the structural evolution of the *trans*-planar form III upon removing the tension in stretched fibers strongly depends on the memory of the crystalline forms present in the starting unoriented material.[123]

1.2.8. Influence of constitutional defects on the crystallization behavior of sPP

Large changes of the polymorphism and physical properties of sPP have also been observed by introducing constitutional defects as comonomeric units. The effect of the presence of comonomeric units on the polymorphic behavior of sPP has been extensively investigated in syndiotactic copolymers of propene with ethylene,[141,142] butene,[140,141,142a,143], pentene,[141] hexene,[141,144-146] 4-methyl-1-pentene,[141,144] octene,[144-146] decene,[144] dodecene,[150] and octadecene,[145] prepared with C_s-symmetric metallocene catalysts. In particular, the effect of the presence of ethylene,[141,142] butene,[140,141,142a,143] hexene[141,144-146] and octene[144-149] comonomeric units on the structure and polymorphic behavior of sPP has been investigated in as-prepared, melt-crystallized samples and oriented fibers of copolymers.

Propylene-ethylene copolymers are crystalline up to an ethylene content of 20-22 mol %, with melting temperatures decreasing with increasing ethylene content from 150 °C, typical of sPP homopolymer, to nearly 50 °C.[142c] Ethylene units are partially included in the crystals of both as-prepared and melt-crystallized samples.[142] As-prepared samples crystallize in conformationally disordered modifications of form II of sPP of the kind of Figure 1.22B, containing kink bands,[142a-c] that is, with chains in prevailingly 2/1 helical conformation but containing short sequences in trans-planar conformation, which form kink bands defects,[142] as in the intermediate model of Figure 1.22B. These structures are metastable and transform by crystallization from the melt into the most stable antichiral helical form I or in the conformationally ordered

isochiral helical form II, depending on the ethylene concentration.[142c] Samples having low ethylene contents (up to 6-7 mol %) crystallize from the melt into the stable helical form I of sPP, but disordered modifications of form I, with disorder in the alternation of right and left-handed helical chains along the axes of the unit cell, are always obtained.[142c] For higher ethylene content, mixtures of crystals of forms I and II are obtained by crystallization from the melt.[142c] The fraction of form II increases with increasing crystallization temperature and ethylene content.

The presence of ethylene also influences the polymorphic behavior of oriented fibers.[142d-f] For low ethylene contents the stretching produces transformation of the helical form I into the *trans*-planar form III,[142d-f] which transforms into the isochiral helical form II upon releasing the tension,[142d-f] as in the case of sPP. For copolymers with ethylene content in the range 13–18 mol% the helical form transforms into the *trans*-planar mesomorphic form by stretching.[142d-e] Even though high concentrations of ethylene units stabilize the *trans*-planar conformation of the chains, the high content of defects prevents the ordered packing of conformationally ordered *trans*-planar chains and, hence, prevents the formation of the ordered crystalline *trans*-planar form III by stretching. As a consequence the trans-planar mesophase crystallizes at high deformations.[142e]

The presence of high concentration of ethylene comonomeric units, partially included in the crystals of sPP, increases the relative stability of the polymorphic forms of sPP with chains in *trans*-planar conformation, that is, the form III in fibers of copolymers with ethylene contents in the range 2–10 mol%, and of the mesomorphic form for ethylene concentrations in the range 10–18 mol%.[142d-e] For ethylene concentrations higher than 8-10 mol%, indeed, the *trans*-planar forms (form III or mesomorphic form) obtained by stretching do not transform into the helical forms upon removing the tension.[142d-e]

Syndiotactic propene-butene copolymers are crystalline in the whole range of comonomer composition.[143] The values of *a* and *b* axes of the unit cell increase from the values typical of crystals of sPP to those of crystals of sPB,[151-152] with increasing concentration of 1-butene (Figure 1.23A).[143a,b,e] This indicates cocrystallization of comonomeric units and that propene and 1-butene are included in the unit cells of both homopolymers.[143] The melting temperature decreases from the value of nearly 150 °C of sPP to the value of 50 °C of syndiotactic poly(1-butene) (sPB) (Figure 1.23B).[151-154]

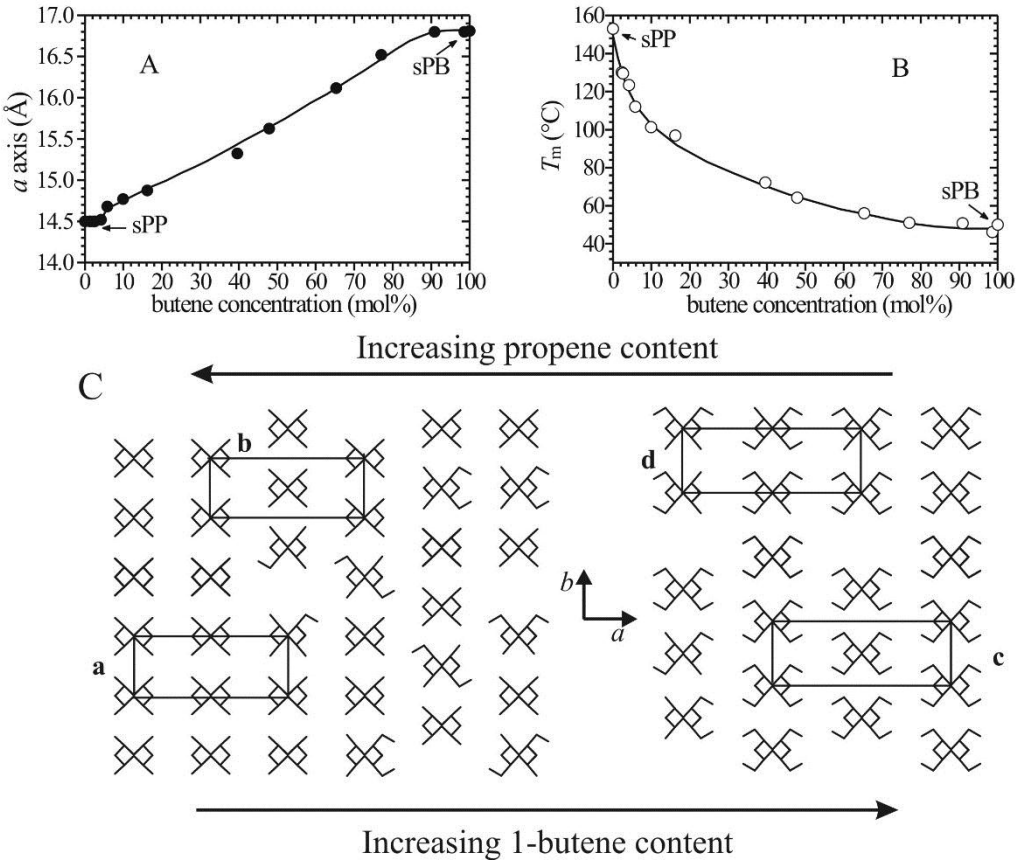

***Figure 1.23**. Values of the a axis of the unit cell (A) and melting temperature (B) of syndiotactic propene–butene copolymers as a function of the butene concentration.[143a] (C) Models of packing of s(2/1)2 helical chains of syndiotactic propene–butene copolymers as a function of butene concentration.[143e] The unit cells of the B-centered form I of sPP (**a**,**d**), the C-centered isochiral form II of sPP (**b**) and the C-centered isochiral form I of sPB (**c**) are indicated. For propene-rich copolymers, local arrangements of chains as in the C-centered form II of sPP (**b**) or form I sPB (**c**) are present in a prevailing mode of packing of the B-centered form I of sPP (**a**). At high butene content, local arrangements of chains as in the B-centered form I of sPP (**a**,**d**) are present in a prevailing mode of packing of the C-centered form I of sPB (**c**).[133b]*

The cocrystallization of propene and 1-butene in syndiotactic copolymers is due to the very similar crystal structures of sPP[1,95,97-101,109] and sPB.[151,152] The crystal structure of the stable form I of sPB (Figure 1.24B) is characterized by chains in **s**(2/1)2 helical conformation packed in an orthorhombic unit cell according to the space group $C222_1$,[151,152] producing an isochiral structure similar to that of form II of sPP (Figures 1.24A an 1.12B).[95] The copolymers crystallize in modifications having structures intermediate between those of form I of sPP and form I of sPB (Figure 1.23C).[143e] As-prepared samples having small contents of 1-butene crystallize in disordered modifications of

form I, characterized by statistical disorder in the alternation of right and left handed helices along both axes of the unit cell. At higher 1-butene content *b*/4 shift disorder develops and increases with increasing 1-butene content, and disordered modifications having structures intermediate between those of form I of sPP and form I of sPB, are obtained.[143] Samples with contents of 1-butene higher than 70 mol% crystallize in a structure similar to that of the isochiral form I of sPB, as well as of form II of sPP (Figure 1.23C).[143e]

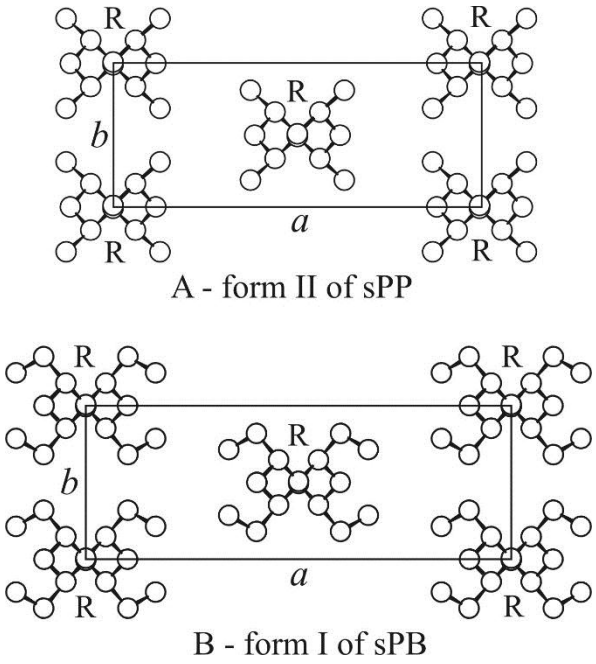

***Figure 1.24**. Models of crystal structures of form II sPP[95,109] (A) and form I of sPB[152] (B). In both cases, chains in s(2/1)2 helical conformation are packed in an orthorhombic unit cell according to the space group $C222_1$, resulting in an isochiral packing of helices. R indicates right-handed helix.*

Samples of propene-butene copolymers crystallize from the melt in the form I of sPP up to a content of 1-butene of 60-70 mol%, although disorder in the alternation of right and left handed helical chains along both axes of the unit cell is present.[140] More ordered modifications, close to the limit ordered, fully antichiral, form I of sPP are obtained by crystallization at high temperatures only for samples containing small contents of 1-butene (1-2 mol%).[140] The presence of 1-butene prevents development of the order in the alternation of right- and left-handed helical chains at high crystallization temperatures.[140]

Fiber samples of propene-butene copolymers with small content of 1-butene (1-2 mol%) present the same behavior as sPP. Stretched fibers are in the *trans*-

planar form III of sPP, which transforms into the isochiral helical form II of sPP upon releasing the tension.[140,143e] High concentration of butene units stabilizes the helical conformation and the presence of 1-butene units, for contents higher than 4 mol%, prevents the formation of the *trans*-planar form III of sPP by stretching.[140,143e] In these samples only the antichiral helical form I of sPP is observed in the stretched fibers of the copolymers, as well as upon releasing the tension.[143e] The formation of the antichiral form I of sPP, instead of the isochiral form II, either in the stretched fibers or upon releasing the tension, is a further evidence that the isochiral helical form II of sPP can be obtained only from fibers initially in the *trans* planar form III, through the cooperative conformational transformation of Figure 1.22, which induces the formation of helical chains having the same chirality.[120,125-128,133] Therefore, anytime the formation of the *trans*-planar form III of sPP is prevented, like in the presence of butene comonomeric units,[140,143] or by stretching at high temperatures,[126] or for low stereoregular samples,[134-138] the isochiral helical form II is not observed.

In copolymers of sPP with higher 1-olefins, as hexene, octene, dodecene, or octadecene, the presence of these long branched comonomers destabilize the *trans*-planar conformation of sPP chains and, at relatively high concentrations (higher than 4-5 mol%) prevents the crystallization of both the *trans*-planar form III and the *trans*-planar mesophase.[145,146] Only at very low concentrations (around 1-2 mol%) the behavior of these copolymers is similar to that of sPP, that is, the stable helical form I of the melt-crystallized samples transforms into the *trans*-planar form III by stretching at high deformations.[146] For hexene or octene concentrations in the range 2-5 mol% the stretching produces transformation of the helical form I into the *trans*-planar mesophase. For hexene and octene concentrations higher than 4-5 mol% the helical form I transforms by stretching at high deformation into a different mesomorphic form, characterized by chains in the ordered 2/1 helical conformation, and disorder in the lateral packing of the chains.[146] In these samples the *trans*-planar mesomorphic form has not been obtained.

1.3. Physical and mechanical properties of sPP and copolymers of sPP

Depending on the catalyst and condition of polymerization samples of sPP having different stereoregularities, from only slightly syndiotactic fully amorphous to highly syndiotactic and crystalline samples, showing different physical and mechanical properties can be prepared.[1,154] In particular the use of metallocene catalyst has made it possible to tailor tacticity and melting

temperature of polypropylene. The nearly linear relationship between melting temperature and syndiotacticity, expressed as concentration of *rrrr* pentad, is shown in Figure 1.25.[1,134,155] The C_s-symmetric metallocene catalysts of Charts 1 and 2 produce highly syndiotactic polypropylene with *rrrr* pentad contents in the range 75-96%and melting temperatures in the range 120-153 °C.[1,134,155] Half-metallocene "constrained geometry" catalysts (Chart 6) produce lower syndiotactic s-PP samples, with *rrrr* pentad contents in the range 60-80% and melting temperatures in the range 80-120 °C.[1,134,155] Poorly syndiotactic polypropylenes with concentration of the *rrrr* pentad of 40-55% and melting temperatures of 45-60 °C have been obtained with similar constrained geometry catalysts containing a heterocycle condensed onto the cyclopentadienyl moiety (Chart 7).[1,134,155] Finally, totally amorphous, moderately syndiotactic polypropylene, with *rrrr* contents of about 20-25% are prepared with the complexes precursors of the class of constrained geometry catalysts (Charts 4 and 5).[1,134,155] Therefore, stereoregularity and the melting temperature can be finely tuned in a wide range by changing catalyst structure, while keeping high values of the molecular mass. As a consequence, interesting mechanical properties are maintained even when stereoregularity, crystallinity and melting temperatures are very low.[1,134,155]

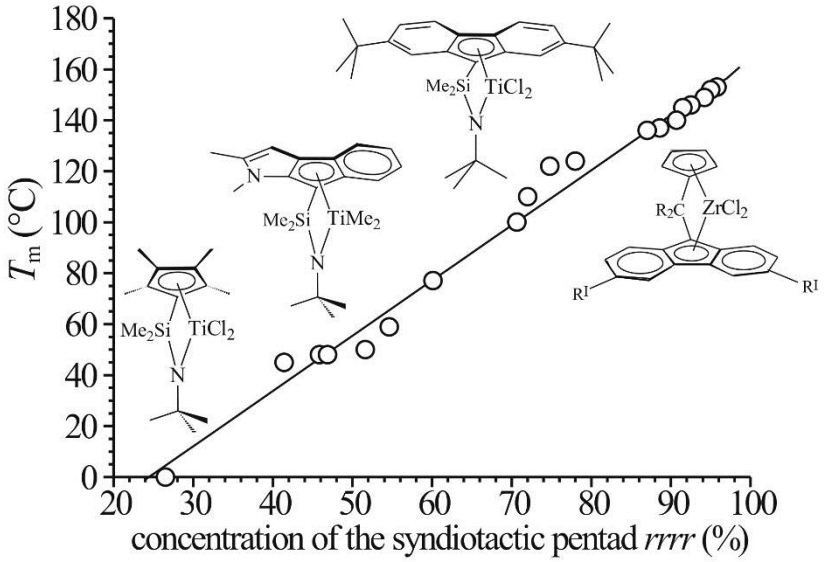

Figure 1.25*. Values of melting temperature of samples of sPP of different stereoregularity produced with different organometallic catalysts as a function of the concentration of the fully syndiotactic pentad rrrr.*

The mechanical properties of sPP strongly depend on the stereoregularity and initial morphology of the sample.[1,134,155] Unoriented samples of high stereoregular and crystalline sPP behave as a typical crystalline thermoplastic material showing plastic deformation via necking during stretching, with high values of the Young's modulus.[1,124-128,134,155] The samples experience a partial elastic recovery after breaking or upon releasing the tension after a given deformation.[124-128] Oriented fibers of sPP show instead a perfect elastic behavior upon successive stretching and relaxation cycles.[124-128] This is the most important characteristic and unusual physical property of sPP. It is a thermoplastic elastomer notwithstanding the high values of crystallinity and melting temperature (nearly 50-60% and 150 °C, respectively, for highly syndiotactic samples) and the relatively high glass transition temperature (around -6 and 0 °C).[1,155]

The stress-strain curves of compression-molded films of s-PP samples having different stereoregularity and melting temperatures, prepared with different catalysts of Charts 1, 2, 6 and 7 (see Figure 1.25), are reported in Figure 1.26A,B[124-128,134,136,137] in comparison with the nearly atactic, totally amorphous samples prepared with the catalyst of Chart 4 (Figure 1.26C).[136,137] These data show that even highly stereoregular and crystalline sPP samples present high ductility and toughness at room temperature. The values of the Young's modulus and of the residual deformation (tension set) after breaking, reported in Figure 1.27 as a function of stereoregularity (concentration of *rrrr* pentad) and crystallinity, decrease with decreasing syndiotacticity.[124-128,134,136,137] The decrease of the values of tension set up to nearly 10% with decreasing stereoregularity and crystallinity indicates that poorly stereoregular sPP samples show elastic behavior even in the form of unoriented compression-molded films.[136,137]

The origin of elasticity in s-PP and the mechanism of plastic deformation have been extensively studied.[1,124-128,134-138,155] For more stereoregular samples the plastic deformation is associated with the polymorphic transition from the stable helical form I, generally present in the unoriented compression-molded films, into the *trans*-planar form III (Figure 1.28) obtained in the stretched oriented fibers (see section 1.2.7, Figure 1.20).[109,112] For less stereoregular samples with *rrrr* content lower than 80% the helical from I first transforms into the mesomorphic form at strains higher than the critical value, and then into the *trans*-planar form III at higher values of deformation.[134,135] For poorly syndiotactic samples having *rrrr* pentad contents in the range 45-70%, the

ordered *trans*-planar form III does not form by stretching even at very high deformation. The helical form I transforms at high deformation into the *trans*-planar mesomorphic form and the crystalline form III never forms.[136-138]

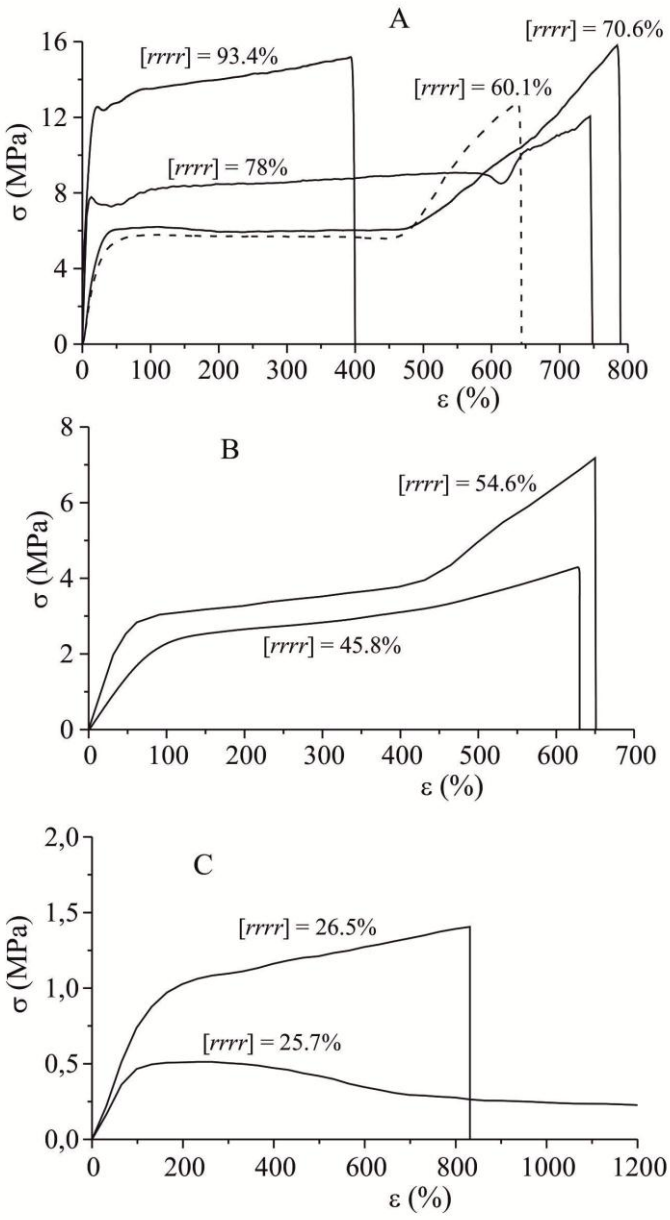

***Figure 1.26**. Stress–strain curves of unoriented compression molded films of samples of sPP having different stereoregularity.*[1,124-128,134,136,137,155]

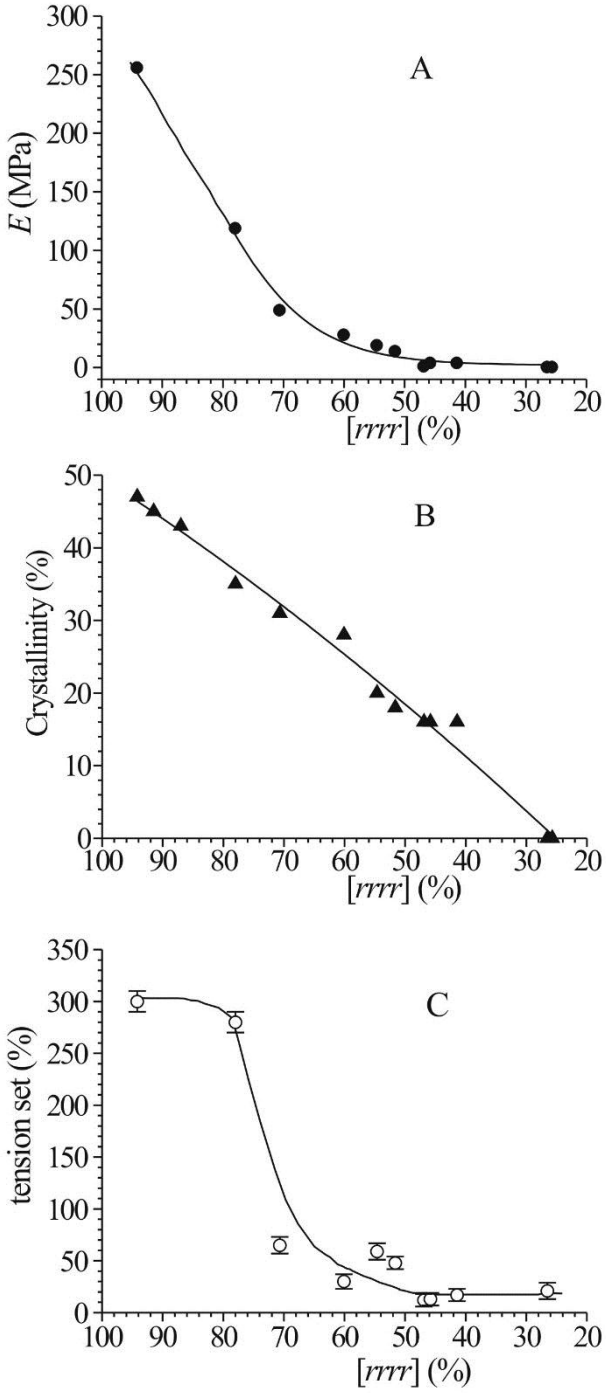

***Figure 1.27**. Values of the Young's modulus (A), X-ray crystallinity (B) and tension set after breaking (C) of unoriented compression-moulded films of samples of sPP of different stereoregularity, as a function of the concentration of rrrr pentad.*

The *trans*-planar form III obtained by stretching is stable only in the stretched fibers and transforms into the helical form II (Figure 1.28) upon releasing the tension or after breaking (Figure 1.21).[112,124-128] Due to the irreversible plastic deformation only a partial elastic recovery is observed.

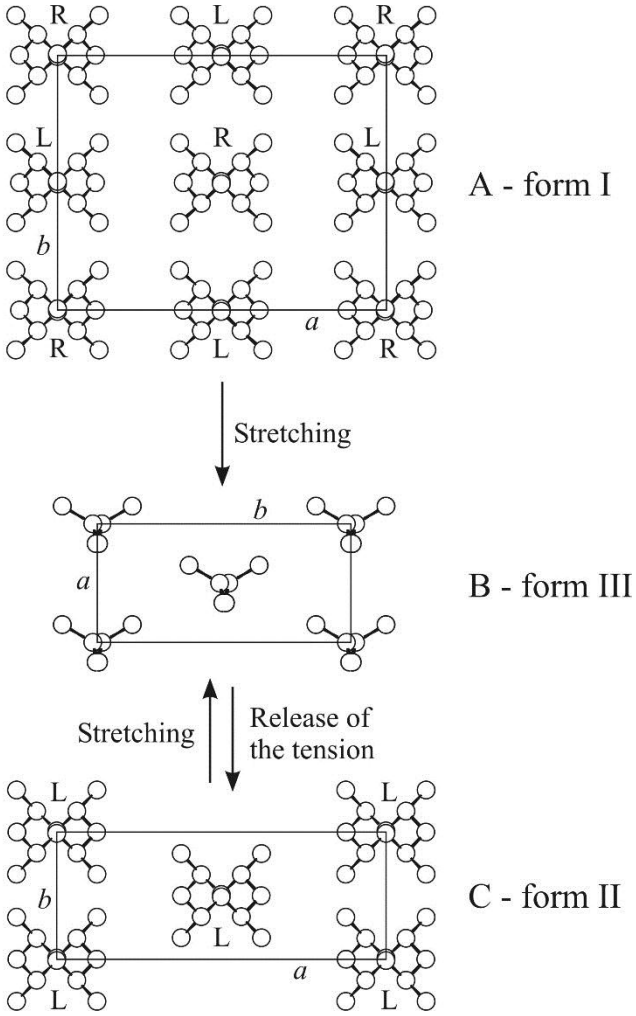

Figure 1.28. *Polymorphic transformations occurring during stretching and relaxation of sPP. The helical form I (A) transforms by stretching into the trans-planar form III (B) which transforms into the helical form II (C) by releasing the tension of the stretched fibers.*

During the transition from the two-fold helical form into the *trans*-planar form III by stretching (Figure 1.28), an increase of the periodicity per structural unit *h* (which comprises two monomeric units) from $h = c/2 = 3.7$ Å of the two-fold helical form to $h = c = 5.1$ Å of the *trans*-planar form III, is involved. The crystal dimensions increase about 38% along *c*. This increase is completely recovered upon the releasing the tension due to the transition of the *trans*-planar

form into the helical form, and, correspondingly, a reduction of the length of the specimen occurs. As a result, for a not previously oriented material, a partial recovery of the macroscopic dimensions of the sample is attained.[124-128]

It has been suggested that the polymorphic transition of the metastable *trans*-planar form III into the helical form II is in part responsible for the elasticity of s-PP due to the enthapy gain achieved when the fibers are relaxed.[124-128] A model of "elasticity assisted" by the crystal-crystal phase transition has been suggested for the elastic behavior of sPP.[124-128] In this idea, both the crystalline and amorphous chains play key roles. The small crystalline aggregates actively participate to the elasticity of sPP, locally acting as microscopic engines. The chains in the amorphous regions are possibly well oriented and in extended conformation in the stretched state, and experience a reversible conformational transition between disordered random-coil and extended conformations when the samples are repeatedly stretched and relaxed. These chains are also highly entangled and connect, as *tie-chains*, different crystals, which undergo the structural transition during the mechanical cycles. During elongation, the chains in the amorphous regions assume extended conformations and tend to orient parallel to the stretching direction. The crystalline aggregates also tend to assume a preferred orientation with the chain axes parallel to the stretching direction; at the same time, when a given crystal experiences a stress higher than a critical value a crystal-crystal phase transition from the helical form II into the *trans*-planar form III occurs and the size of the crystal increases by 38% along the chain axis direction. During the relaxation step, when a given crystal experiences a stress below a critical value, the *trans*-planar form III becomes unstable and transforms instantaneously into the more stable form II; correspondingly, the crystal shrinks by 38% along the chain axis direction. Since the enthalpy change in this transition is negative, it, in turn, induces an abrupt conformational transition in the chains of the amorphous phase close to the crystals. These amorphous springs assume suddenly less extended conformations generating a sort of chain reaction, which rapidly extends to the whole material. The return into entropically favored disordered conformations of amorphous chains produces the entropic factor also involved in the recovery process. Therefore, while the driving force leading the conventional elastomers to recover the initial dimensions is merely entropic, in the case of s-PP elasticity is also assisted by the enthalpic gain achieved when the sample is relaxed. When the tension is removed, both the enthalpic factor, due to the structural transition in the crystalline regions, and an entropic factor, due to the

conformational transition of the chains in the entangled amorphous phase, contemporarily contributes to the elastic recovery of the s-PP fibers.[1,124-128,134,155]

In poorly syndiotactic samples with lower crystallinity the trans-planar form III does not form any more by stretching, therefore the enthalpic contribution to the elasticity decreases or disappears. These samples, however, present good elastic properties for both unoriented compression-molded films and oriented fibers,[134,136,137] associated with low tensile strength and Young's modulus (Figures 1.26-1.27) and high values of strains at break. Because of the very low crystallinity these materials experience a negligible plastic deformation and show a typical thermoplastic elastomeric behavior (Figure 1.26B). The small crystalline domains in the amorphous matrix act as physical knots of the elastomeric lattice, preventing the viscous flow of the amorphous chains. The entropic effect of the conformational transition of the amorphous chains is mainly responsible for the elasticity. Since the molecular weights of the samples are very high, these amorphous chains are highly entangled and connect as *tie-chains* the small crystalline domains. They act as spring between the crystals being well-oriented and in extended conformation in the stretched state, and return in the disordered coil conformation when the tension is removed.[136,137]

Very poorly syndiotactic nearly atactic samples are unable to crystallize and present lower strength and experience rapid viscous flow of the chains at high deformations (Figure 1.26C). In these samples only when the molecular weight is very high the viscous flow is prevented giving interesting elastic properties but, however, with very low strength.[136,137]

These data indicate that s-PP shows different elastic behaviors depending on the steoregularity, which can be controlled through the choice of the catalysts and conditions of polymerization. Thermoplastic elastomeric materials based on sPP with finely controlled physical and mechanical properties can be produced. As shown in Figure 1.29, for the more crystalline samples having high melting temperatures, the elasticity has a mainly enthalpic character, due to the metastability of the *trans*-planar form III that transforms into the more stable helical form II. For less crystalline samples, with low melting temperatures, the elastic recovery is not associated to any polymorphic transitions and has a pure entropic origin, as in conventional elastomers. Depending on melting temperature, elastomers showing conventional entropic or unconventional enthalpic elasticity, can be obtained. The development of enthalpic elasticity

allows maintenance of elastic properties even when the crystallinity, the melting temperature and the mechanical strength of the samples are very high.

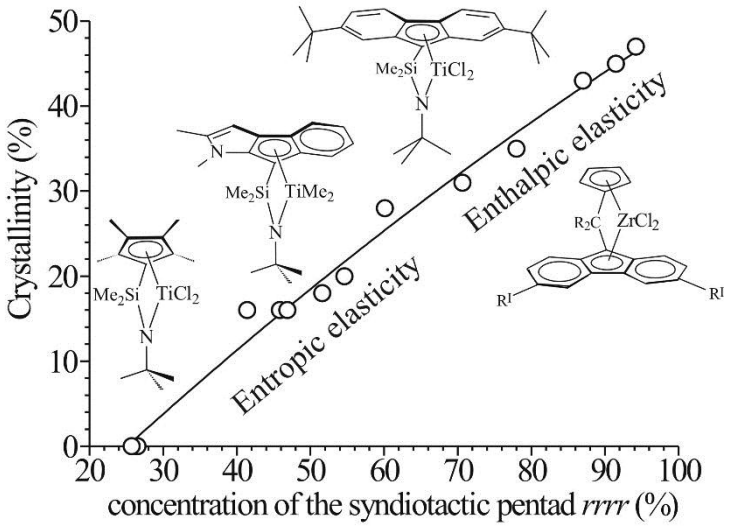

Figure 1.29. *Different elastic behaviors of s-PP samples having different melting temperatures and crystallinity prepared with different catalysts. Highly syndiotactic samples with high melting temperatures and crystallinity show enthalpic elasticity, whereas samples with low stereoregularity, melting temperatures and crystallinity exhibit conventional entropic elasticity.*[1]

A similar effect on elasticity is produced in random copolymers of sPP with other 1-olefins, such as ethylene, butene, hexene, octene, 1-dodecene, 1-octadecene, 1-eicosene by the presence of constitutional defects instead of steric defects. Samples of copolymers with concentrations of comonomeric units variable in a wide range have been synthesized with the C_s symmetric syndiospecific catalyst used for the preparation of highly stereoregular samples of sPP (Chart 1). In these copolymers the presence of constitutional defects affects the conformational transition since high concentrations of ethylene stabilizes the *trans*-planar conformation, while high concentration of branched comonomers stabilizes the helical conformation. In any case, high concentration of comonomeric units prevents occurrence of this transformation during deformation and relaxation.

Samples of copolymers of sPP with ethylene (sPPET) with concentration of ethylene lower than 18-20 mol % are crystalline and show interesting mechanical properties, whereas samples with ethylene content higher than 20% are amorphous and experience rapid viscous flow even for low deformation and/or by application of stress for long time.[142]

Unoriented films of the crystalline sPPET samples with ethylene content lower than 18 mol% present high ductility with remarkable values of deformation at break higher than 1000%, and high values of the tensile strength. The elastic modulus and the stress at any strain decrease with increasing ethylene content, consistent with the decrease of crystallinity, whereas the tensile strength remain nearly constant up to ethylene contents of 14-15% because of the strong strain hardening which occurs at high deformations. The most crystalline samples, with low ethylene content, show poor elastic properties because of the irreversible plastic deformation occurring during stretching of unoriented films. The elastic properties are greatly improved for the lowest crystalline samples with ethylene contents in the range 16-18 mol%.[142d,f]

Oriented films of all sPPET samples show good elastic properties regardless of the ethylene concentration. The presence of crystalline domains ensures values of modulus and tensile strength higher than those of conventional elastomers. The elastic behavior of most crystalline sPPET copolymer samples with low ethylene contents (lower than 6-7 mol%) is associated to a reversible polymorphic transition between the *trans*-planar form III and the helical form II occurring during stretching and relaxation cycles. In these samples elasticity has a mainly enthalpic character, due to the metastability of the *trans*-planar form III that transforms into the more stable helical form II upon releasing the tension. Lower crystalline sPPET samples with higher ethylene concentrations (higher than 10 mol%) show similar elastic properties, which are not associated to any polymorphic transitions. In these samples the *trans*-planar forms are stable and do not transform into helical forms during elastic recovery, and elasticity has a pure entropic origin as in conventional elastomers.[142d,f]

These studies have demonstrated that sPPET copolymers prepared with C_s-symmetric metallocene catalysts represent new materials with improved and unprecedented mechanical properties of thermoplastic elastomers, whose physical properties and values of mechanical parameters can be finely tuned through the simple introduction of the proper amount of ethylene comonomer units.[142]

Copolymers of sPP with butene show good elastic properties with remarkable rigidity and mechanical strength due to the cocrystallization of the comonomers that produces non-negligible level of crystallinity at any comonomer concentration. The elastic properties are improved in oriented fibers.[143]

For the more crystalline samples with low butene concentration the elastic properties are associated with the reversible polymorphic transformations between form III and form II that occur during the processes of stretching and elastic recovery of fibers. The occurrence of these reversible phase transitions assists the elasticity of sPPBu copolymers with butene content lower than 20 mol%, through a non-negligible free energy contribution.[143]

In the case sPPBu samples with butene content higher that 20mol%, no stress induced phase transitions occur, and the defective crystals of form I of sPP merely act as physical knots of the elastomeric network, preventing the viscous flow of the chains, as in the case of conventional thermoplastic elastomers. Also for these copolymers the crystallization properties are responsible for the development of the outstanding mechanical properties, providing a variety of elastomeric materials characterized by values of stiffness and mechanical strength that may be tuned by simply changing the comonomer concentration.[143]

As discussed in the section 1.2.8, the effect of the presence of higher α-olefin comonomers and branched comonomers on the crystallization behavior of sPP has also been investigated. In particular, studies on the polymorphic behavior and the thermal properties of copolymers of sPP with pentene,[141] hexene,[141,144-146] 4-methyl-1-pentene,[141,144] octene,[144-146] decene,[144] dodecene,[150] and octadecene,[145] prepared with C_s-symmetric metallocene catalysts, have been reported. The values of the melting and glass transition temperatures of these copolymers are reported in in Figure 1.30 as a function of comonomer concentration. The melting temperature and the glass transition temperatures decrease with increasing comonomer concentration with a different rate depending on the size of the commoner. The slower decrease is observed for sPPBu copolymers thanks to the compatibility of propene and butene in the crystals and their cocrystallization in the whole composition range All these copolymers show outstanding mechanical properties of high flexibility and ductility and show elastic behaviour either at low or at high comonomer concentration regardless of the comonomer content. However, in these copolymers high concentration of comonomeric units prevents occurrence of the form II - form III transformation during deformation and relaxation because the *trans*-planar form III is destabilized and does not form by stretching. Therefore, in these materials the enthalpic contribution to the elasticity becomes negligible with increasing comonomer concentration, and the entropic contribution becomes prevalent, as illustrated in Figure 1.30.

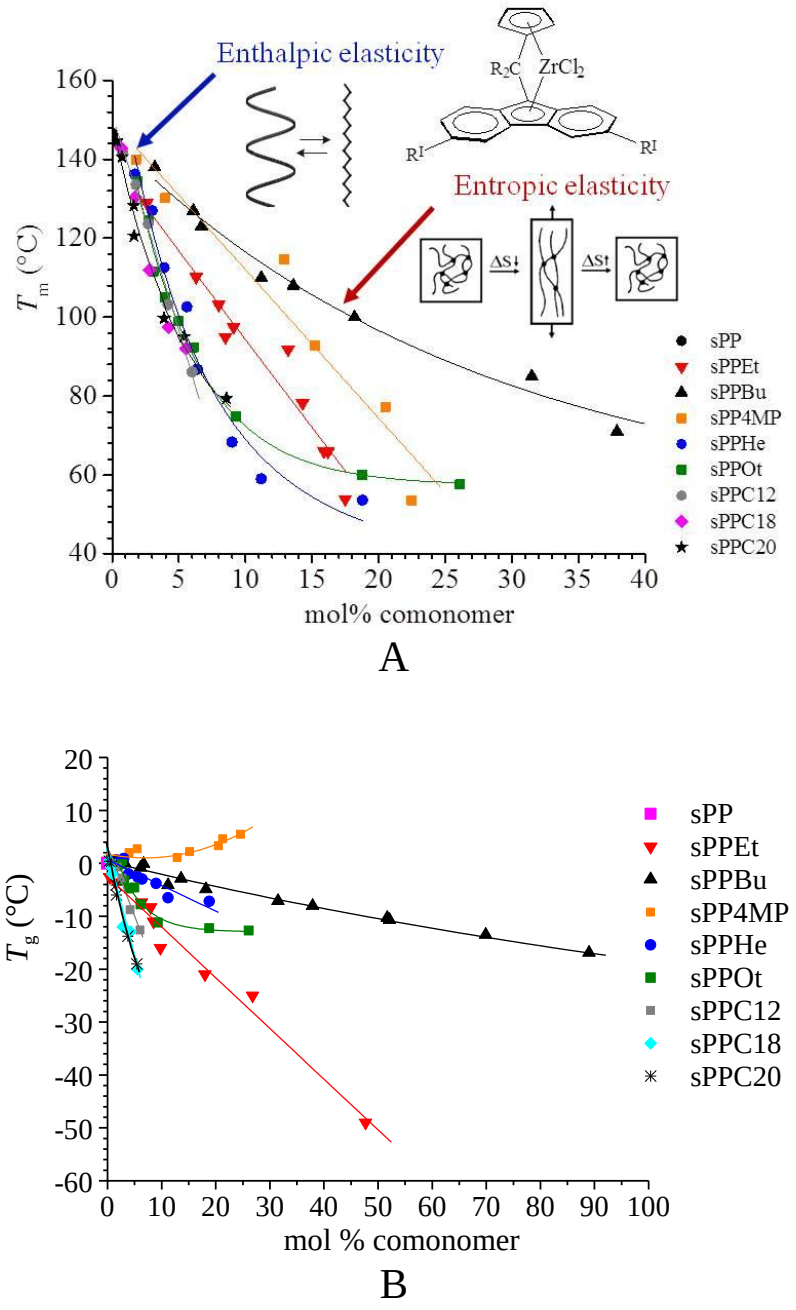

Figure 1.30. *Values of melting temperature (A) and glass transition temperature (B) of random copolymers of sPP with different comonomers produced with the indicated Cs metallocene catalyst as a function of the comonomer concentration.*

1.4. Aim of the study of the morphology of sPP and copolymers of sPP

It is well known that mechanical properties of semicrystalline polymers depend not only on the crystal structure but also by on the organization of crystals on nanometric scale, size and form of crystals and on the relationships between chains belonging to the two amorphous and crystalline phases that form an interpenetrating network.

The case of sPP is particularly complex because it is a highly crystalline polymers with elastic properties. It has been suggested that both crystalline and amorphous phases play key roles in the development of elasticity.[1,124-128,134,136-138,155] The crystalline aggregates actively participate to the elasticity of sPP, locally acting as microscopic engines through the activation of reversible phase transformation during deformation and elastic recovery. The chains in the amorphous regions are possibly well oriented and in extended conformation in the stretched state, and experience a reversible conformational transition between disordered random-coil and extended conformations when the samples are repeatedly stretched and relaxed. These chains are also highly entangled and connect, as *tie-chains*, different crystals, which undergo the structural transition during the mechanical cycles.[1] The relative weights of the roles played by crystals and amorphous chains depends on the degree of crystallinity, which, in turn, depends on the molecular structure of sPP (stereoregularity and presence of constitutional defects). The same molecular parameters influence not only the degree of crystallinity but also the morphology of crystals (size and form of crystals and relationships with amorphous chains), that can be different even at the same degree of crystallinity.

In this work the morphology of crystals of samples of sPP of different stereoregularity and samples of random copolymers of sPP with different comonomers has been studied and the relationships between crystal morphology and elastic properties have been analyzed. The morphology has been analyzed in different length scales by using polarized optical microscopy (POM), atomic force microspcopy (AFM) and small angle X-ray scattering (SAXS).

1.5. Materials and methods

The morphological analysis has been performed on samples of sPP of different stereoregularity and on samples of random copolymers of sPP with ethylene, butene, 4-methyl-pentene, hexene, octene, 1-dodecene, 1-octadecene, 1-eicosene.

Samples of sPP of different stereoregularity have been prepared with the catalysts of Charts 1, 2, 4, 6 and 7.[134] All the analyzed samples of are listed in Table 1.1. Highly stereoregular samples, having concentrations of fully syndiotactic pentad *rrrr* in the range 75-95%, have been prepared using the single center C_s-symmetric metallocene catalyst **1** of Chart 1, isopropylidene-(cyclopentadienyl)(9-fluorenyl)zirconium dichloride ($Me_2C(Cp)(9\text{-}Flu)ZrCl_2$, Me = Methyl, Cp = Cyclopentadienyl, Flu = Fluorenyl), activated with methylaluminoxane (MAO).[29] Samples of different stereoregularity have been obtained with catalyst **1**/MAO performing the polymerization at different temperatures (samples sPP1-sPP4, sPP6, sPP7, sPP9 and sPP10 of Table 1.1). Highly stereoregular samples with high molecular mass (samples sPP5 and sPP8) have been prepared with the catalyst **3** of Chart 2 ($Ph_2C(Cp)(3,6\text{-}t\text{-}Bu_2Flu)ZrCl_2$, Ph = Phenyl, *t*-Bu = *t*-Butyl), activated with MAO, at polymerization temperatures of 40 and 60 °C, respectively.[49] These two samples have been provided by Dr. A. Razavi of Atofina. Samples of sPP of medium stereoregularity have been prepared with the constrained geometry catalysts **1** and **2** of chart 6, described by Razavi et al.[49a,64] These Ti complexes, $[Me_2Si(2,7\text{-}t\text{-}Bu_2Flu)(t\text{-}BuN)]TiCl_2$ (**1** of Chart 6)[49] and $[Me_2Si(3,6\text{-}t\text{-}Bu_2Flu)(t\text{-}BuN)]TiCl_2$ (**2** of chart 6),[64] give sPP samples characterized by high molecular weight, concentrations of *rrrr* pentad in the range 60-80%, and melting temperatures in the range 80-120 °C. Samples sPP11 and sPP12 with *rrrr* contents of 70.6% and 60.1%, prepared with **1** and **2** of chart 6, respectively, activated with MAO, have been provided by Dr. A. Razavi of Atofina. Finally, poorly syndiotactic samples with concentration of *rrrr* pentad in the range 40-55% (samples sPP13-sPP17), have been prepared with the catalysts **1** and **2** of chart 7, composed of silyl-bridged indenyl-*tert*-butylamido complexes of titanium, in which the indenyl ligand has a heterocycle condensed onto the cyclopentadienyl moiety.[67] A fully amorphous polypropylene sample (sPP18) having the lowest syndiotacticity ([*rrrr*] = 26%), but very high molecular mass, have been prepared with the Dow catalyst dimethylsilyl (tetramethylcyclopentadienyl)(*tert*-butylamido)$TiCl_2$ (catalyst of chart 4).[54]

These samples have been provided by Dr. Luigi Resconi of Basell Polyolefins. All catalysts have been activated with MAO.

The melting temperature, the concentration of the fully syndiotactic *rrrr* pentad and the average molecular mass of all analyzed samples are reported in Table 1.1. The melting temperatures were obtained with a differential scanning calorimeter Perkin Elmer DSC-7 performing scans in a flowing N_2 atmosphere and heating rate of 10 °C/min. The stereoregularity has been determined by analysis of the ^{13}C NMR spectra.

Samples of random copolymers of sPP with ethylene (sPPET) having concentration of ethylene in the range 0.4 - 59 mol% have been prepared using the *C*s symmetric metallocene catalyst (phenyl)$_2$methylen(cyclopentadienyl)(9-fluorenyl)$ZrCl_2$ ($Ph_2C(Cp)(Flu)ZrCl_2$) (**1** of chart 1) activated with methylaluminoxane (MAO), according to the method described in ref. 142b. All samples and conditions of polymerization are listed in Tables 1.2 and 1.3.

Tables 1.4 - 1.10 reports the lists of samples and the conditions of polymerization of random copolymers of sPP with butene (sPPBu), 4-methyl-pentene (sPP4MP), 1-hexene (sPPHe), 1-octene (sPPOt), 1-dodecene (sPPC12), 1-octadecene (sPPC18), 1-eicosene (sPPC20) prepared with the same catalyst **1** of Chart 1 activated with MAO, according to the method described in ref. 142b.

Table 1.1. *Concentration of rrrr pentad, m diad, mm triad and total concentration of stereodefects, melting temperature T_m and weight average molecular mass M_w of sPP samples prepared with the indicated different catalysts.*

Sample	Catalyst	[*rrrr*] %	[*m*] %	[*mm*] %	[total defects] %	T_m (°C)	M_w (g/mol)
sRDG-2-1	1 of Chart 1	95.5	0	0.7	0.7	152	-
sPP2	1 of Chart 1	95.0	0	0.8	0.8	152	228000
sPP3	1 of Chart 1	94.2	1.48	1.1	2.6	149	213000
sPP4	1 of Chart 1	92.5	1.7	1.7	3.4	146	164000
sPP5	3 of Chart 2	91.5	2	1.5	3.5	145	766000
sPP6	1 of Chart 1	90.7	2.3	1.5	3.8	140	77000
sPP7	1 of Chart 1	88.6	3.5	1.6	5.1	137	115000
sPP8	3 of Chart 2	87.0	4	1.7	5.7	136	509000
sPP9	1 of Chart 1	78.0	6.5	1.8	8.3	124	193000
sPP10	1 of Chart 1	74.8	8.5	1.9	10.4	122	52000
sPP11	1 of Chart 6	70.6	9.8	2.5	12.3	100	297000
sPP12	2 of Chart 6	60.1	12.5	4.3	16.8	77	241000
sPP13	1 of Chart 7	54.6	13	4.9	17.9	59	1308600
sPP14	2 of Chart 7	51.6	13.6	5.2	18.8	50	672700
sPP15	2 of Chart 7	46.9				48	885700
sPP16	2 of Chart 7	45.8				48	1153200
sPP17	2 of Chart 7	41.4				45	589200
sPP18	Chart 4 with Mt=Ti, X=Cl, R = *t*-butil	26.5				-	1190800

Table 1.2. *Composition, melting temperatures (T_m), intrinsic viscosities ([η]), and viscosity average molecular mass (M_v) of sPPET copolymer samples prepared with the catalytic systems $Ph_2C(Cp)(Flu)ZrCl_2$/MAO (**1** of Chart 1).*[a]

Samples	Feed composition (mol % ethylene)	Copolymer composition (mol % ethylene)[b]	T_m (°C)[c]	[η] (dL/g)[d]	M_v (g/mol)[e]
sPPET(1)	0.9	0.4	141.3	0.66	0.84×10^5
sPPET(2)	2.4	1.5	136.3	0.69	0.88×10^5
sPPET(3)	4.9	2.6	129.0	0.89	1.14×10^5
sPPET(4)	7.6	6.3	110.2	1.78	2.37×10^5
sPPET(5)	10.3	8.0	103.2	2.26	3.03×10^5
sPPET(6)	12.1	8.5	95.0	1.94	2.59×10^5
sPPET(7)	12.6	9.1	97.5	2.12	2.84×10^5
sPPET(8)	15.4	9.8	93.7	2.10	2.80×10^5
sPPET(9)	17.3	13.2	91.8	2.02	2.69×10^5
sPPET(10)	21.4	14.3	78.2	1.13	1.45×10^5
sPPET(11)	24.9	15.9	66.0	1.47	1.94×10^5
sPPET(12)	27.1	16.2	65.9	1.47	1.94×10^5
sPPET(13)	34.4	17.5	53.9	1.14	1.48×10^5
sPPET(14)	45.5	26.8	/	1.17	1.53×10^5
sPPET(15)	71.2	47.7	/	0.89	1.14×10^5
sPPET(16)	82.5	59.1	/	1.01	1.31×10^5

[a]) Polymerization temperature = 10 °C; pressure = 1 atm; solvent = toluene (100 mL); molar ratio Al/Zr = 1000; catalyst amount = 2-3 mg; reactor volume = 250 mL; polymerizzation time = 2 h; flow rate = 5mL/s; yeld 2-5g. [b]) Determined from ^{13}CNMR spectra, recorded with a Varian XL-200 spectrometer operating at 50.3 MHz, of 10% w/v polymer solutions in deuterated tetrachloroethane (also used as internal standard) at 120 °C. [c]) Determined from maximum of melting endotherm recorded using a Perkin-Elmer DSC 7 apparatus in N_2 atmosphere at 10°C/min heating rate. [d]) Measured in 1,2,3,4-tetrahydronaphtalene solutions at 135 °C. [e]) Molecular masses evaluated from values of intrinsic viscosity, using the parameters of Mark-Houwink equation reported for atactic polypropylene $\alpha = 0.96$, $k = 1.24\times10^{-5}$ dL/g.[156]

Table 1.3. *Composition and melting temperatures (T_m), of sPPET copolymer samples prepared with the catalytic systems $Ph_2C(Cp)(Flu)ZrCl_2$/MAO (**1** of Chart 1).*[a]

Samples	Feed composition (mol % ethylene)	Copolymer composition (mol % ethylene)[b]	T_m (°C)[c]
RDG-2-41	0.85	0.4	145.5
RDG-2-40	2.8	1.7	136.3
AK-sPPEt-2	4	1.9	133.2
RDG-2-42	5.8	2.4	132.5
AK-sPPEt-10	16	8.3	95.4
AK-sPPEt-15	23	11.9	70.2
AK-sPPEt-25	43	27.5	-

[a]) Polymerization temperature = 10 °C; pressure = 1 atm; solvent = toluene (100 mL); molar ratio Al/Zr = 1000; catalyst amount = 2-3 mg; reactor volume = 250 mL; polymerizzation time = 2 h; flow rate = 5mL/s; yeld 2-5g. [b]) Determined from ^{13}CNMR spectra. [c]) Determined from maximum of melting endotherm recorded at 10°C/min heating rate.

Table 1.4. *Composition, melting temperatures (T_m), intrinsic viscosities ([η]), and viscosity average molecular mass (M_v) of sPPBu copolymers prepared with the catalytic systems $Ph_2C(Cp)(Flu)ZrCl_2$/MAO (**1** of Chart 1).*[a]

Samples	Feed composition (mol% of 1-butene)	Copolymer Composition (mol% of 1-butene)[b]	T_m (°C)[c]	[η] (dL/g)[d]	M_v (g/mol)[e]
sPPBu-1	1.1	3.2	138	2.60	349000
sPPBu-2	2.6	6.1	126	2.00	266000
sPPBu-3	4.8	6.7	123	2.50	335000
sPPBu-4	6.6	11.2	110	2.30	307500
sPPBu-5	7.6	13.6	108	3.00	405500
sPPBu-6	11.0	18.2	100	2.10	279600
sPPBu-7	16.5	31.5	85	2.00	266000
sPPBu-8	22.6	37.9	71	1.50	197000
sPPBu-9	34.6	51.7	70	1.46	191500
sPPBu-10	45.2	52.1	64	1.35	176500
sPPBu-11	65.1	69.9	57	1.10	142600
sPPBu-12	84.7	89.0	54	1.65	217500

[a]) Polymerization temperature = 10 °C; pressure = 1 atm; solvent = toluene (100 mL); molar ratio Al/Zr = 1000; catalyst amount = 2-3 mg; reactor volume = 250 mL; polymerization time = 2 h; flow rate = 0.3 L/min; yield = 2-5 g. [b]) Determined from ^{13}C NMR spectra. [c]) Determined from DSC curves of as-prepared samples recorded at heating rate 10 °C/min. [d]Measured in 1,2,3,4-tetrahydronaphthalene solutions at 135 °C. [e]) Molecular masses evaluated from values of intrinsic viscosity.

Table 1.5. *Composition, melting temperatures (T_m), intrinsic viscosities ([η]), and viscosity average molecular mass (M_v) of sPP4MP copolymers prepared with the catalytic systems $Ph_2C(Cp)(Flu)ZrCl_2$/MAO (**1** of Chart 1).*[a]

Samples	Feed composition (mL of 4-methyl-1-pentene)	Copolymer Composition (mol% of 4-methyl-1-pentene)[b]	T_m (°C)[c]	[η] (dL/g)[d]	M_v (g/mol)[e]
sPP4MP-1	1	1.8	140.0	2.8	377406
sPP4MP-2	2	4	130.2	2.4	321420
sPP4MP-3	2.8	5.5	125.0	n.a[f]	n.a[f]
sPP4MP-4	4	12.9	114.7	2.2	293568
sPP4MP-5	8	15.2	92.8	2.0	265823
sPP4MP-6	11.1	20.5	55.9, 77.2[g]	1.8	238192
sPP4MP-7	16	21.3	53.5	1.7	224424
sPP4MP-8	20	24.6	/	1.2	156135
sPP4MP-9	16	32	57.3	1.3	169711

[a]) Polymerization temperature = 10 °C; pressure = 1 atm; solvent = toluene (100 mL); molar ratio Al/Zr = 1000; catalyst amount = 2-3 mg; reactor volume = 250 mL; polymerization time = 2 h; flow rate = 0.3 L/min; yield = 2-5 g. [b]) Determined from ^{13}C NMR spectra. [c]) Determined from DSC curves of as-prepared samples recorded at heating rate 10 °C/min. [d]) Measured in 1,2,3,4-tetrahydronaphthalene solutions at 135 °C. [e]) Molecular masses evaluated from values of intrinsic viscosity; [f]) not available data. [g]) Multiple melting peaks have been observed.

Table 1.6. *Composition, melting temperatures (T_m), intrinsic viscosities ([η]), and viscosity average molecular mass (M_v) of sPPHe copolymers prepared with the catalytic systems $Ph_2C(Cp)(Flu)ZrCl_2$/MAO (**1** of Chart 1).*[a]

Samples	Feed composition (mL of 1-hexene)	Copolymer Composition (mol% of hexene)[b]	T_m (°C)[c]	[η] (dL/g)[d]	M_v (g/mol)[e]
sPPHe-1	1.0	1.7	135.8	3.0	4.1×10^5
sPPHe-2	2.0	3.0	125.2	3.75	5.1×10^5
sPPHe-3	3.0	3.9	111.3	2.3	3.1×10^5
sPPHe-4	4.0	5.6	99.8	3.0	4.1×10^5
sPPHe-5	6.0	6.4	83.2	2.7	3.6×10^5
sPPHe-6	7.8	9.0	68.3	2.4	3.2×10^5
sPPHe-7	9.8	11.2	59.0	2.3	3.1×10^5
sPPHe-8	12.0	18.8	53.6	2.6	3.5×10^5

[a]) Polymerization temperature = 10 °C; pressure = 1 atm; solvent = toluene (100 mL); molar ratio Al/Zr = 1000; catalyst amount = 2-3 mg; reactor volume = 250 mL; polymerization time = 2 h; flow rate = 0.3 L/min; yield = 2-5 g. [b]) Determined from ^{13}C NMR spectra. [c]) Determined from DSC curves of as-prepared samples recorded at heating rate 10 °C/min. [d]) Measured in 1,2,3,4-tetrahydronaphthalene solutions at 135 °C. [e]) Molecular masses evaluated from values of intrinsic viscosity.

Table 1.7. *Composition, Composition, melting temperatures (T_m), intrinsic viscosities ([η]), and viscosity average molecular mass (M_v) of sPPOt copolymers prepared with the catalytic systems $Ph_2C(Cp)(Flu)ZrCl_2$/MAO (**1** of Chart 1).*[a]

Samples	Feed composition (mL of 1-octene)	Copolymer Composition (mol% of octene)[b]	T_m (°C)[c]	[η] (dL/g)[d]	M_v (g/mol)[e]
sPPOt-1	1.25	1.9	134.4	2.4	3.2×10^5
sPPOt-2	2.5	2.7	124.6	2.4	3.2×10^5
sPPOt-3	3.75	3.1	111.6	2.0	2.5×10^5
sPPOt-4	5	4	104.9	2.1	2.6×10^5
sPPOt-5	6.25	5	99.0	2.4	3.2×10^5
sPPOt-6	7.5	6.1	92.3	2.4	3.2×10^5
sPPOt-7	10	9.3	61.1	1.2	1.6×10^5
sPPOt-8	12.5	18.8	60.0	2.2	2.7×10^5
sPPOt-9	15	26.1	57.5	2.1	2.6×10^5

[a]) Polymerization temperature = 10 °C; pressure = 1 atm; solvent = toluene (100 mL); molar ratio Al/Zr = 1000; catalyst amount = 2-3 mg; reactor volume = 250 mL; polymerization time = 2 h; flow rate = 0.3 L/min; yield = 2-5 g. [b]) Determined from ^{13}C NMR spectra. [c]) Determined from DSC curves of as-prepared samples recorded at heating rate 10 °C/min. [d]) Measured in 1,2,3,4-tetrahydronaphthalene solutions at 135 °C. [e]) Molecular masses evaluated from values of intrinsic viscosity.

Table 1.8. *Composition, melting temperatures (T_m), intrinsic viscosities ([η]), and viscosity average molecular mass (M_v) of sPPC12 copolymers prepared with the catalytic systems $Ph_2C(Cp)(Flu)ZrCl_2$/MAO (**1** of Chart 1).*[a]

Samples	Feed composition (mL of 1-dodecene)	Copolymer Composition (mol% of 1-dodecene)[b]	T_m (°C)[c]	[η] (dL/g)[d]	M_v (g/mol)[e]
sPPC12-1	1.0	0.8	141.4	2.8	3.7×10^5
sPPC12-2	2.5	1.8	133.6	2.8	3.8×10^5
sPPC12-3	4.0	2.7	123.7	2.5	3.3×10^5
sPPC12-4	8.0	4.2	103.2	2.4	3.2×10^5
sPPC12-5	12.0	6.0	86.1	1.3	1.7×10^5

[a]) Polymerization temperature = 10 °C; pressure = 1 atm; solvent = toluene (100 mL); molar ratio Al/Zr = 1000; catalyst amount = 2-3 mg; reactor volume = 250 mL; polymerization time = 2 h; flow rate = 0.3 L/min; yield = 2-5 g. [b]) Determined from ^{13}C NMR spectra. [c]) Determined from DSC curves of as-prepared samples recorded at heating rate 10 °C/min. [d]) Measured in 1,2,3,4-tetrahydronaphthalene solutions at 135 °C. [e]) Molecular masses evaluated from values of intrinsic viscosity.

Table 1.9. *Composition, melting temperatures (T_m), intrinsic viscosities ([η]), and weight average molecular mass (M_w) of sPPC18 copolymers prepared with the catalytic systems $Ph_2C(Cp)(Flu)ZrCl_2$/MAO (**1** of Chart 1).*[a]

Samples	Feed composition (mL of 1-octadecene)	Copolymer Composition (mol% of 1-octadecene)[b]	T_m (°C)[c]	[η] (dL/g)[d]	M_w (g/mol)[e]
sPPC18-1_iAc	1	0.3	144.7	0.65	83259
sPPC18a_iAc	2	0.7	142.8	0.40	51308
CA-sPPC18-4_iAc	4	0.9	131.9	2.39	338209
sPPC18-2_iAc	8	2.8	55.6, 111.9[f]	0.54	78394
CA-sPPC18-12_iAc	12	4.2	51.6, 97.4[f]	2.24	258896
sPPC18c_iAc	16	5.53	55.3, 92.1[f]	0.92	144658

[a]) Polymerization temperature = 10 °C; pressure = 1 atm; solvent = toluene (100 mL); molar ratio Al/Zr = 1000; catalyst amount = 2-3 mg; reactor volume = 250 mL; polymerization time = 2 h; flow rate = 0.3 L/min; yield = 2-5 g. [b]) Determined from ^{13}C NMR spectra. [c]) Determined from DSC curves of as-prepared samples recorded at heating rate 10 °C/min. [d]) Measured in o-dichlorobenzene solutions at 145 °C. [e]) Molecular masses evaluated from GPC. [f]) Multiple melting peaks have been observed.

Table 1.10. *Composition, melting temperatures (T_m), intrinsic viscosities ([η]), and weight average molecular mass (M_w of sPPC20 copolymers prepared with the catalytic systems $Ph_2C(Cp)(Flu)ZrCl_2$/MAO (**1** of Chart 1).*[a]

Samples	Feed composition (mL of 1-eicosene)	Copolymer Composition (mol% of 1-eicosene)[b]	T_m (°C)[c]	[η] (dL/g)[d]	M_w (g/mol)[e]
sPPC20-1_iEE	1.1	0.3	144.6	2.66	283422
sPPC20-2_iEE	2.2	0.7	140.6	2.78	304852
sPPC20-3_iEE	4.4	1.6	128.3	2.50	256778
sPPC20-4_iEE	8.8	1.6	120.6	1.73	214386
sPPC20-5_iEE	13.2	3.9	99.7	1.24	173742
sPPC20-6_iEE	17.6	5.4	95	2.00	268381
sPPC20-7_iAc	25.0	8.6	-0.4, 50.3, 79.4 [f]	1.85	282259

[a]) Polymerization temperature = 10 °C; pressure = 1 atm; solvent = toluene (100 mL); molar ratio Al/Zr = 1000; catalyst amount = 2-3 mg; reactor volume = 250 mL; polymerization time = 2 h; flow rate = 0.3 L/min; yield = 2-5 g. [b]) Determined from ^{13}C NMR spectra. [c]) Determined from DSC curves of as-prepared samples recorded at heating rate 10 °C/min. [d]) Measured in o-dichlorobenzene solutions at 145 °C. [e]) Molecular masses evaluated from GPC. [f]) Multiple melting peaks have been observed.

Thin films (20-50 μm thick) of the samples have been prepared for polarized optical microscopy (POM) experiments. Small amounts of the powder samples have been sandwiched between glass coverslips, heated at temperature 20-30°C higher than the melting temperature T_m of the sample at 40°C/min kept at that temperature for 2-5 minutes, and then slowly cooled to room temperature at 2.5 °C/min. Optical microphotographs of the samples have been recorded at room temperature in polarized light using a Zeiss Axioskop 40 microscope provided with a Mettler FP82 and/or a Linkam hot stage.

Calorimetric measurements were performed with a differential scanning calorimeter (DSC-822) by Mettler Toledo in a flowing N_2 atmosphere. In all experiments, small amount of the sample has been heated from room temperature up to a temperature 20-30°C higher than the melting temperature of the sample at 40°C/min. The sample has been kept at that temperature for several minutes (2-5 minutes) and then cooled to room temperature at 2.5°C/min. X-ray powder diffraction profiles have been obtained with Ni-filtered CuKα radiation using automatic powder diffractometers X'Pert (for thick samples) and Empyrean Multipurpose (for thin films), both by PANalytical.

AFM and SAXS experiments have been performed in the group of Professor Thomas Thurn-Albrecht at Martin Luther Universität of Halle-Wittenberg. Thin films of the samples have been prepared for AFM measurements. Small amounts of the powder samples have been sandwiched between a glass coverslip and a kapton foil, then heated at temperature 20-30 °C higher than the melting temperature T_m of the sample at 30 °C/min and cooled at 2.5 °C/min to room temperature in a Linkam hotstage provided with a THMS600 Temperature Controller. The kapton foil has been removed before the AFM measurement. Measurements in Tapping mode have been performed on a Bruker MultiMode 8 AFM at room temperature.

Small Angle X-ray scattering measurements on compression molded films with 2 mm of thickness of random copolymers of sPP with ethylene (sPPEt) and 1-butene (sPPBu) have been collected using a Kratky compact camera in the slit collimation configuration, attached to a conventional X-ray source (CuKα, wavelength λ =1.5418 Å). The scattered radiation was recorded on with Position Sensitive Detector (PSD). The measurements have been performed at room temperature, after heating up to a temperature 20-30°C higher than the melting temperature of the sample and cooling to room temperature. Heating and cooling rates were not controlled. Small Angle X-ray scattering

measurements on two samples of random copolymers of sPP with 1-butene have been collected on powder of compression-molded samples using a SAXSLAB's GANESHA Instrument provided with Microfocus Rotating Anode source (CuKα, wavelength λ =1.5418 Å) and Pilatus detector. Powder of as prepared samples have been heated up to a temperature 20-30 °C higher than the melting temperature of the sample and then cooled to room temperature at 10 °C/min in a Linkam stage provided with a TMS94 controller and a Liquid Nitrogen Pump.

1.6. Study of the crystal morphology by polarized optical microscopy

In this section a study of the crystal morphology of samples of sPP of different stereoregularity and samples of random copolymers of sPP with ethylene, 1-butene, 4-methyl-pentene, 1-hexene, 1-octene, 1-dodecene, 1-octadecene, 1-eicosene by using polarized optical microscopy will be discussed.

1.6.1. Crystal morphology of sPP of different stereoregularity

The X-ray powder diffraction profiles of the analyzed as-prepared samples of sPP of different stereoregularity of Table 1.1 (rapidly crystallized from the polymerization solution) are reported in Figure 1.31A,B. Almost all samples are crystallized in the helical form I of sPP (Figure 1.12A), as indicated by the presence of the 200 and 010 reflections at 2θ = 12 and 16°, respectively, in most of the diffraction profiles of figure 1.31A,B. The absence of the 211 reflection at 2θ = 18.8° indicate that the sample are crystallized in disordered modifications of form I, characterized by disorder in the regular alternation of left and right handed helices along the axes of the unit cell. Samples sPP6 and sPP7 with relatively low stereoregularity ([*rrrr*] = 88-90%) quench precipitated from polymerization solution are crystallized in disordered modifications of form II of sPP (Figure 1.12B), as indicated by the presence of the 110 reflection at 2θ = 17° in the diffraction profiles f-g of Figure 1.31A. The disorder corresponds to the presence of conformational kink-bands defects in the prevailingly two-fold helical conformation (Figure 1.22).

Figure 1.31C shows X-ray powder diffraction profiles of thin films of samples of sPP crystallized from the melt by cooling at 2.5 °C/min, prepared for polarized optical microscopy (POM) experiments. The quality of the diffraction patterns is low because of the very low thickness of the film and the use of the glass coverslip used as a support for the measurements. Therefore, the background and the amorphous halo of the glass often cover the crystalline

reflections of the samples. In any case the profiles of Figure 1.31C are sufficient to demonstrate that all samples observed by POM are crystallized from the melt in form I of sPP. Samples sPP13-sPP17 do not crystallize from the melt but crystallize in form I by aging at room temperature.

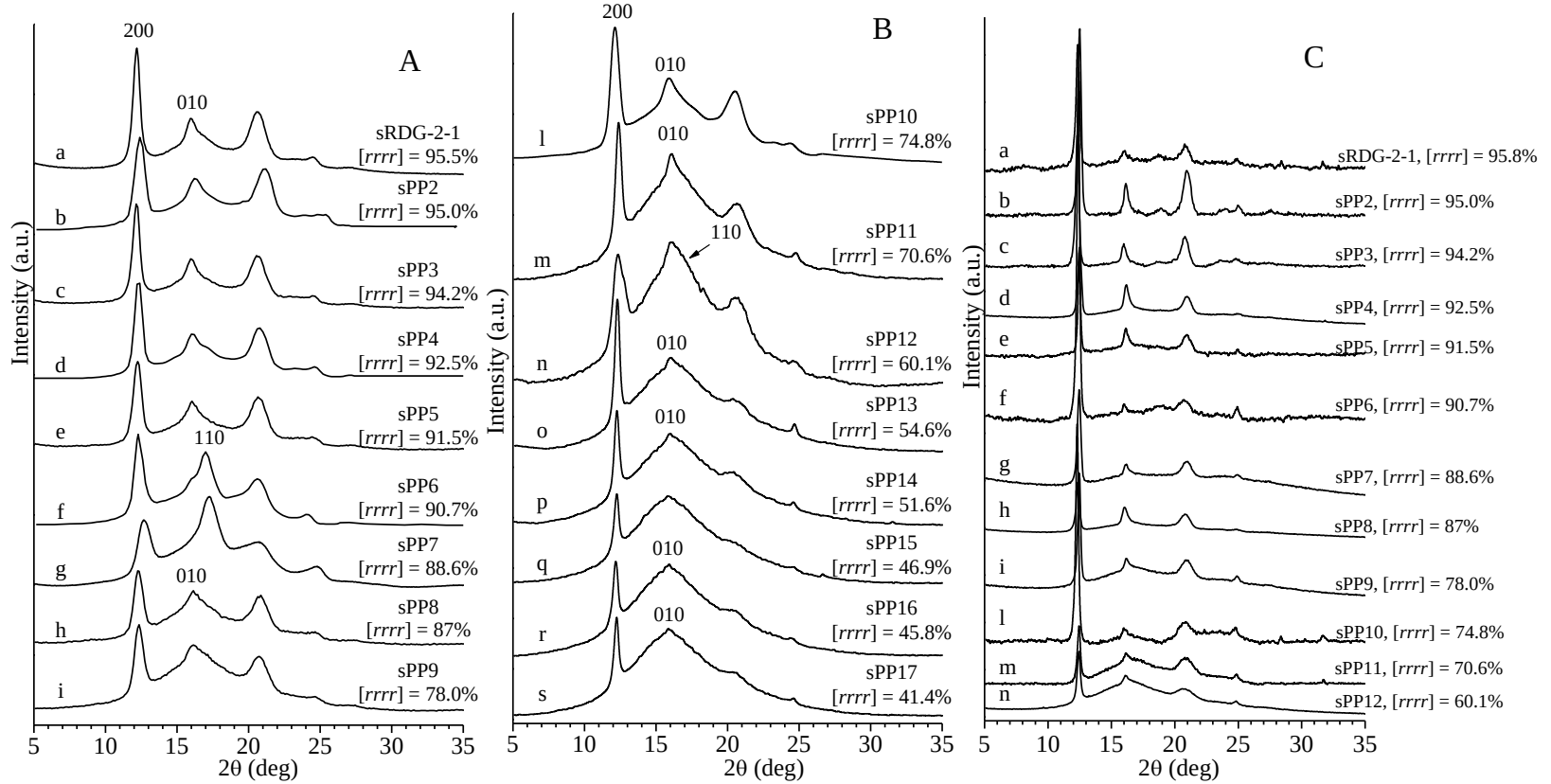

Figure 1.31. *X-ray powder diffraction profiles of as-prepared samples (A,B) and selected samples crystallized from the melt at cooling rate of 2.5 °C/min (C) of samples of sPP of different stereoregularity of Table 1.1. The 200 and 010 reflections at 2θ = 12 and 16°, respectively, of the helical form I, and the 110 reflection at 2θ = 17° of the helical form II of sPP are indicated.*

Polarized optical microscopy (POM) images of samples of sPP of different stereoregularity of Figure 1.31 crystallized from the melt at cooling rate of 2.5 °C/min are reported in Figures 1.32-1.35 at two different magnifications 20X (Figures 1.32A-E - 1.35A-E) and 40X (Figures 1.32A'-E' - 1.35A'-E'). Samples sPP13-sPP18 do not crystallize from the melt, therefore POM images of these samples have been collected after melting, slow cooling to room temperature and aging at room temperature for at least one month. Moreover, only samples sPP13 and sPP14 have showed birefringence after aging and no POM images have been collected for samples sPP15-sPP18.

Different kind of crystalline superstructures have been observed depending on stereoregularity. Typical bundles of rod-like lamellae, bow-tie and open multi-faceted aggregates have been observed in samples with *rrrr* content in the range 96-91% (Figure 1.32), indicating occurrence of space filling crystallization. While the growth of the needles is one-dimensional, rodlike and bow-tie aggregates have a clear lateral structure with branches commonly perpendicular to the growth direction.[157] Rare structures also form during the crystallization of some stereoregular samples. Figures 1.32D,D' depicts spherulites with a star structure, which are not regularly branched. It seems that this structures have one main growth direction and the branching that would give a three dimensional spherulites is hindered, so that the typical Maltese cross cannot be observed.

sRDG-2-1, [*rrrr*] = 95.5%

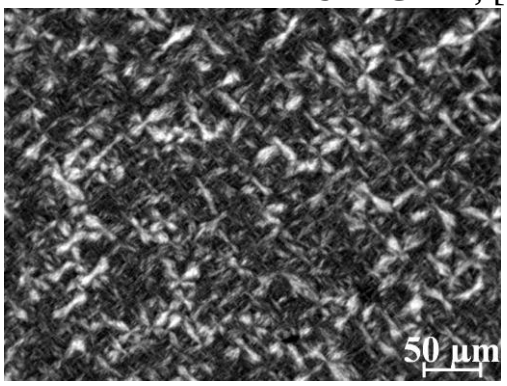

A

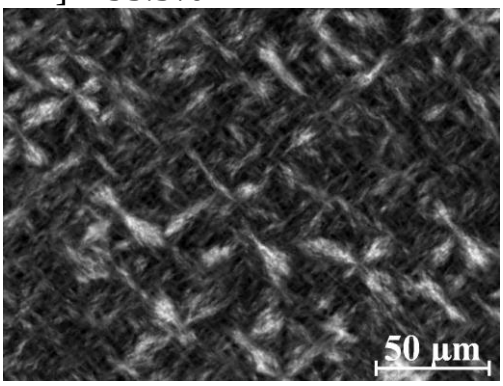

A'

sPP2, [*rrrr*] =95%

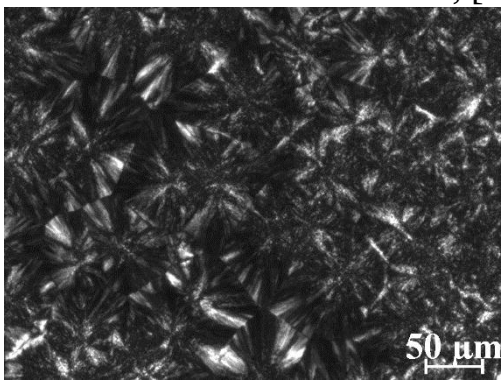

B

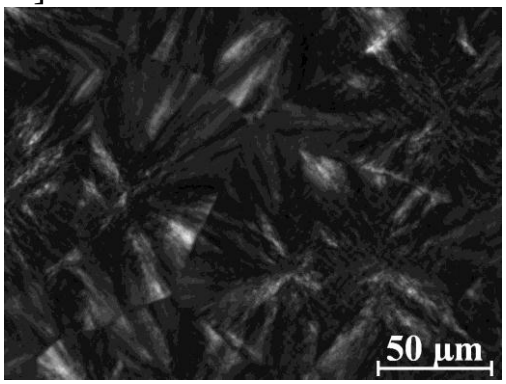

B'

sPP3, [*rrrr*] =94.2%

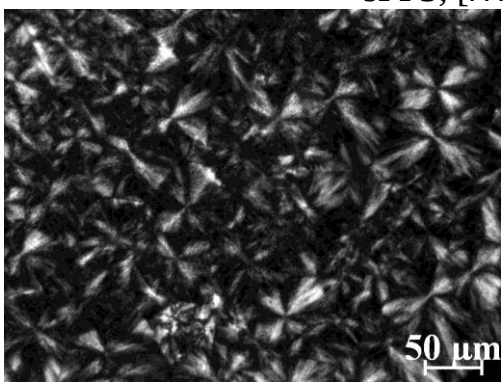

C

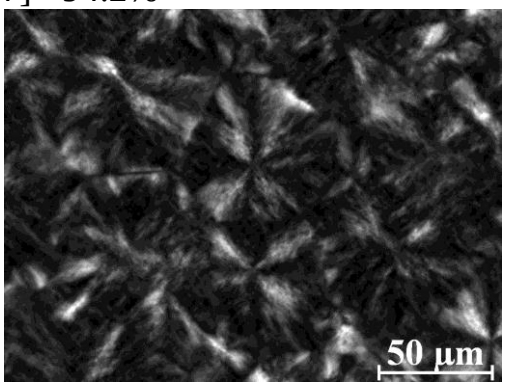

C'

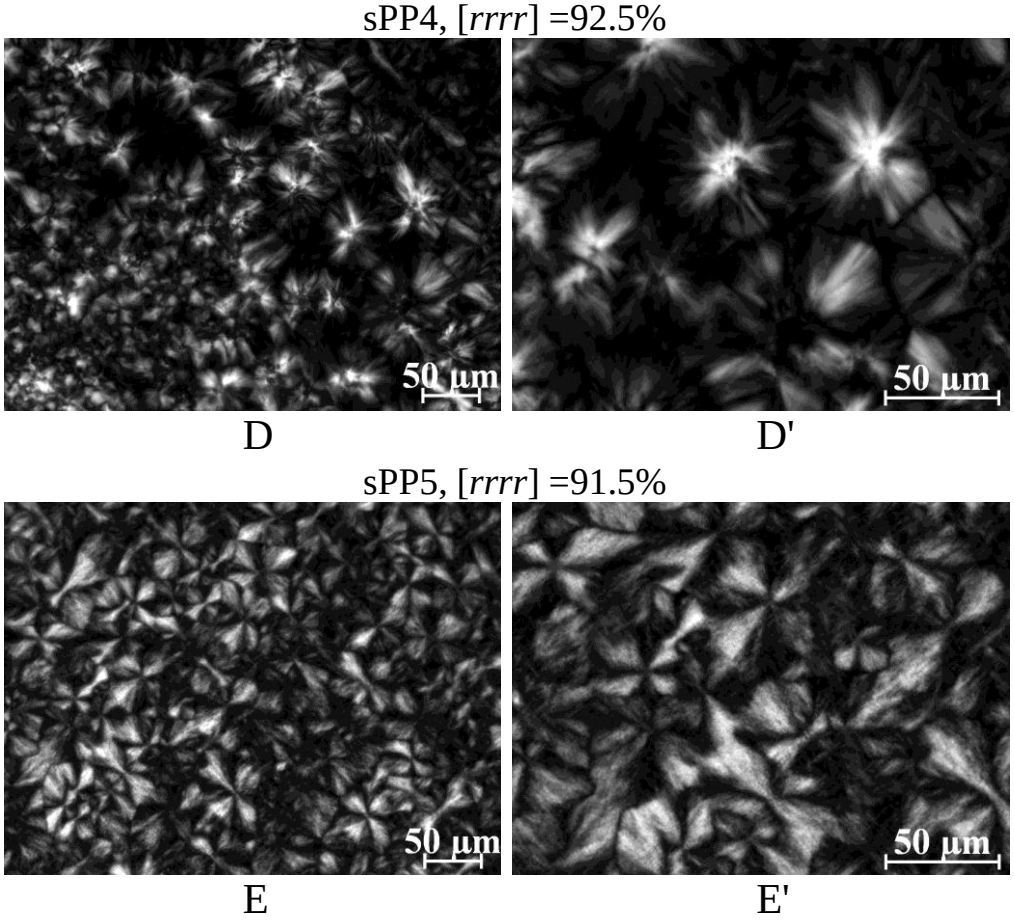

Figure 1.32. *POM images of samples sRDG-2-1 with [rrrr] = 95.5% (A,A'), sPP2 with [rrrr] = 95% (B,B') sPP3 with [rrrr] = 94.2% (C,C',) sPP4 with [rrrr] = 92.5% (D,D') and sPP5 with [rrrr] = 91.5% (E,E').*

Samples of sPP with *rrrr* content in the range of 90-87% exhibit the typical bundle-like elongated crystalline entities and needle-like crystals with few small bow-tie aggregates (Figure 1.33). The higher amount of stereodefects avoid crystallization of bigger crystalline aggregates except in the sample sPP7 with *rrrr* concentration of 88.6 mol% where star structures, open multi-faceted and other irregular aggregates are visible (Figure 1.33B,B').

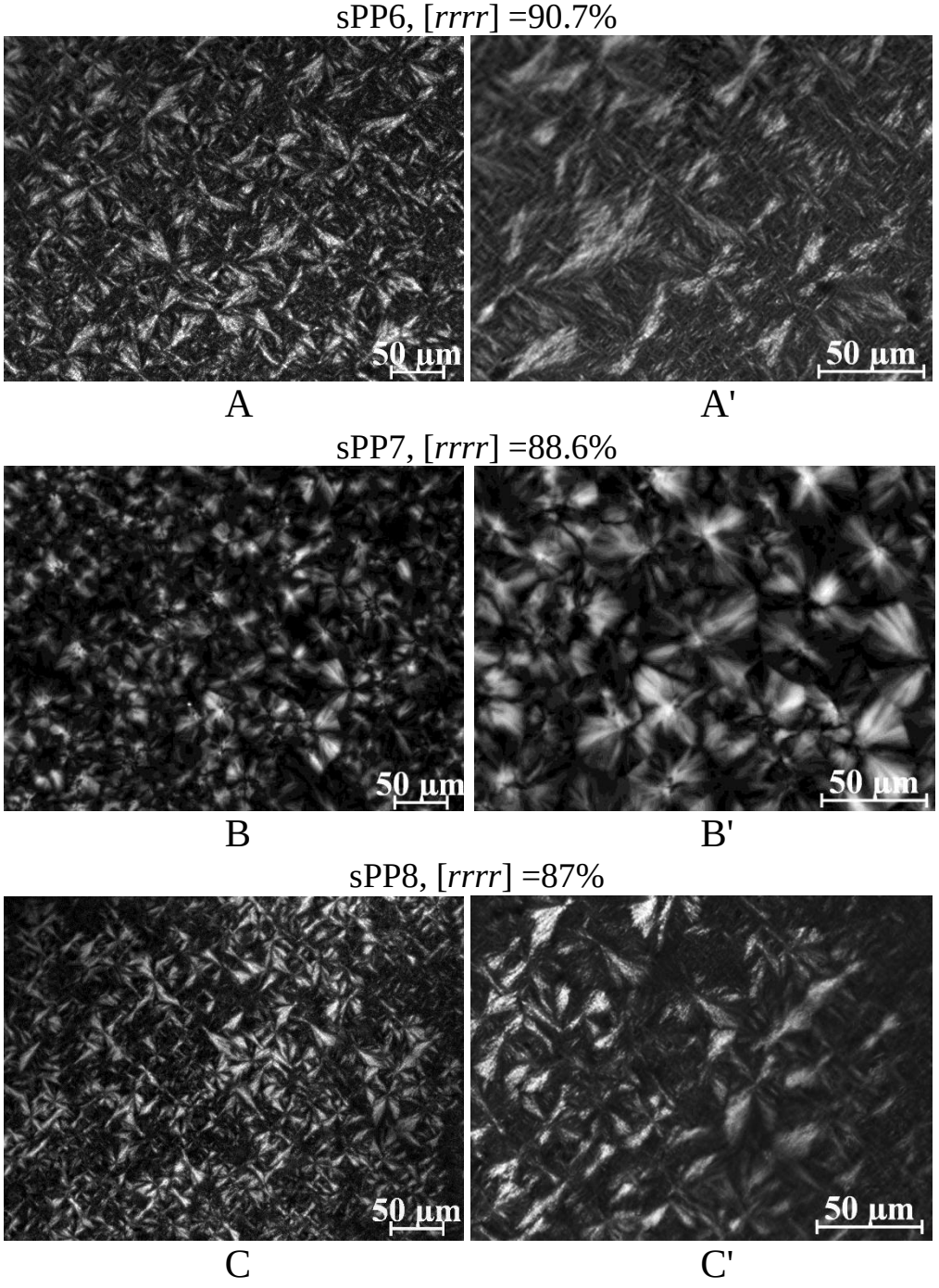

***Figure 1.33**. POM images of samples sPP6 with [rrrr] = 90.7% (A,A'), sPP7 with [rrrr] = 88.6% (B,B') and sPP8 with [rrrr] = 87% (C,C').*

Samples with *rrrr* content in the range of 78-60% exhibit the typical bundle like elongated crystalline entities and needle-like crystals (Figure 1.34) with only few small bow-tie aggregates appearing in more stereoregular samples sPP9 and sPP10 (Figure 1.34 A,A'-B,B').

sPP9, [*rrrr*] = 78%

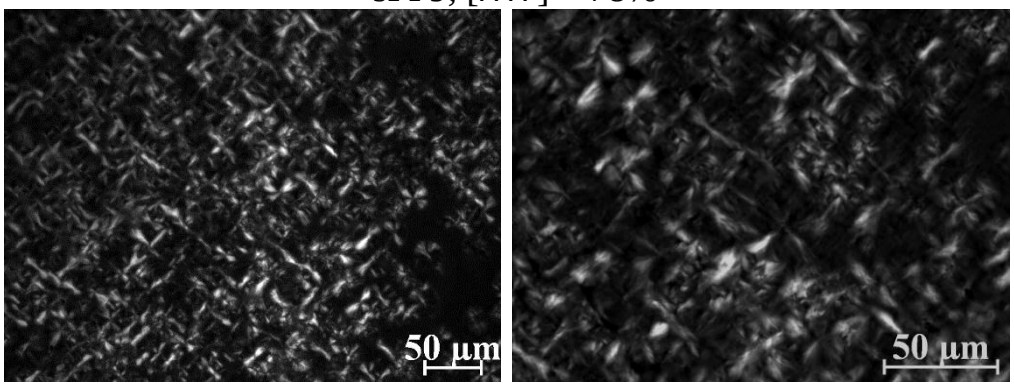

A A'

sPP10, [*rrrr*] = 74.8%

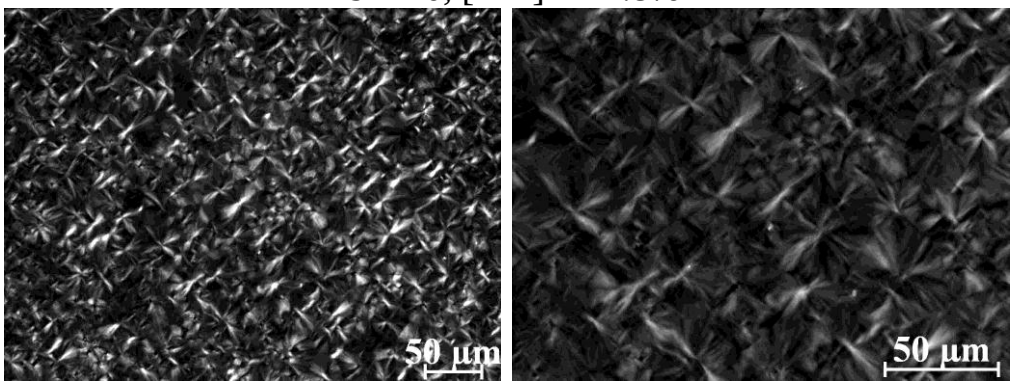

B B'

sPP11, [*rrrr*] = 70.6%

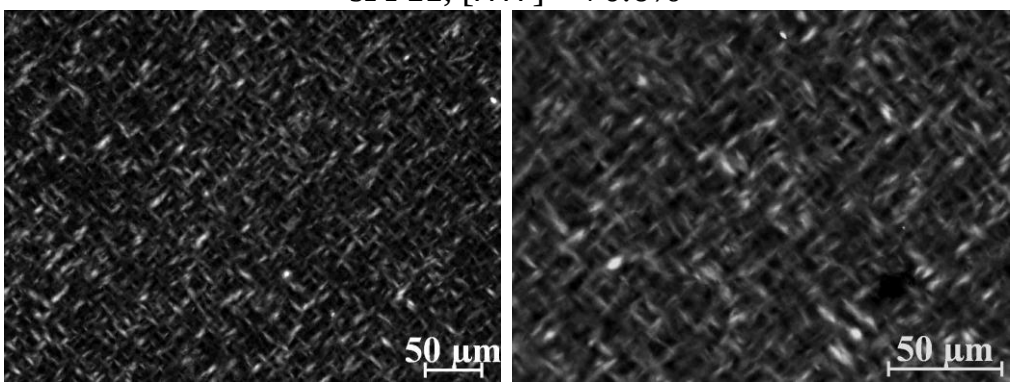

C C'

sPP12, [*rrrr*] = 60.1%

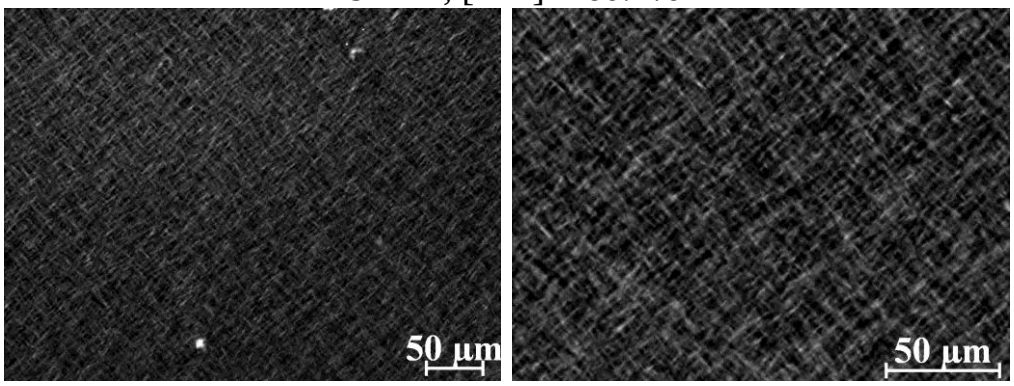

D D'

Figure 1.34. *POM images of samples sPP9 with [rrrr] = 78% (A,A'), sPP10 with [rrrr] = 74.8% (B,B'), sPP11 with [rrrr] = 70.6% (C,C'), sPP12 with [rrrr] = 60.1% (D,D').*

Poorly syndiotactic samples with *rrrr* lower than 60% do not crystallize from the melt and POM images, reported in Figure 1.35, have been recorded after crystallization by aging at room temperature for one month. Only needle crystals are observed because the low stereoregularity avoids the formation of additional bigger aggregates.

The data of Figures 1.32-1.35 indicate that the morphology of crystals of form I of sPP depends on the stereoregularity. For high stereoregularity and concentrations of *rrrr* pentad in the range 96-91%, bigger crystalline aggregates, such as open multi-faceted aggregates, spherulites with a star structure, bundles of rod-like lamellae and bow-tie aggregates, are observed (Figure 1.32). For lower stereoregularity and concentrations of *rrrr* pentad in the range 90-87% only bundle-like elongated entities and needle-like crystals with few small bow-tie aggregates are observed (Figure 1.33), whereas for concentrations of *rrrr* pentad in the range 78-60% bundle like elongated entities and needle-like crystals are observed (Figure 1.34), and finally for poorly syndiotactic samples with concentrations of *rrrr* pentad lower than 60% only needle-like crystals are observed (Figure 1.35).

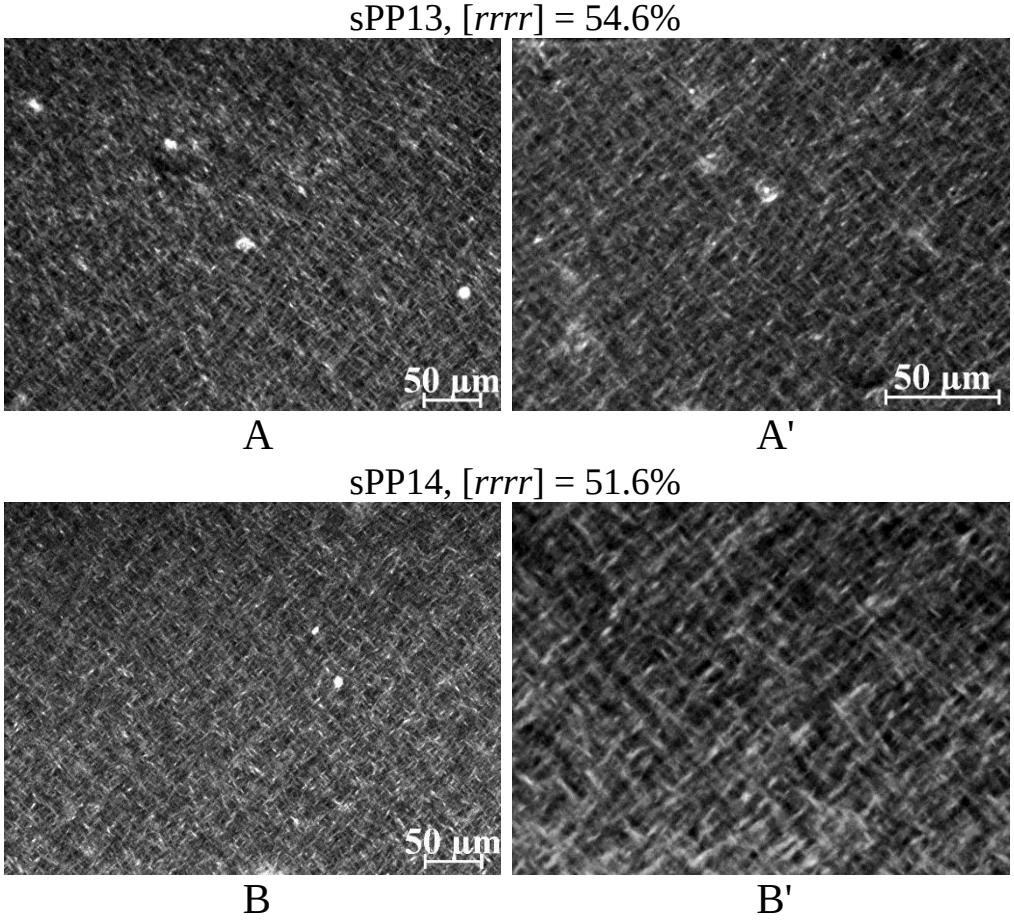

Figure 1.35. *POM images of samples sPP13 with [rrrr] =54.6% (A,A') and sPP14 with [rrrr] = 51.6% (B,B').*

This analysis has also shown that, in addition to the superstructures observed in the Figures 1.32-1.35, that is, open multi-faceted aggregates, spherulites with a star structure, bundles of rod-like lamellae and bow-tie aggregates, which are observed in thinner regions of the films, also needle-like birefringent entities are always present in thicker regions of the films of all samples, regardless of stereoregularity. This is shown in Figure 1.36, where POM images recorded in thick regions of the films of all samples are reported. For poorly syndiotactic samples with *rrrr* in the range 70-50% (samples sPP11-sPP14), both thin and thick regions of the films always depicts only the needle and bundle-like morphology observed in Figure 1.34 C,C' and D,D' and in Figure 1.35 because the high concentration of stereodefects avoids the formation of bigger aggregates. Therefore, further POM images of these samples in thick regions are not reported in Figure 1.36.

sRDG-2-1, [*rrrr*] = 95.5%

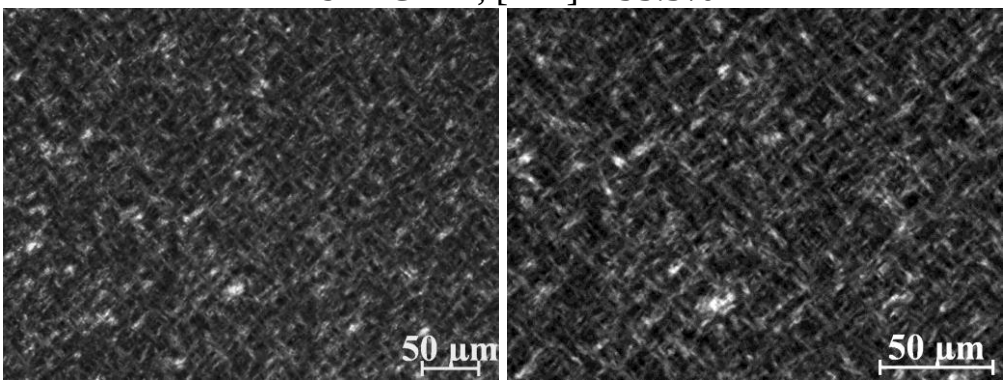

A A'

sPP2, [*rrrr*] =95%

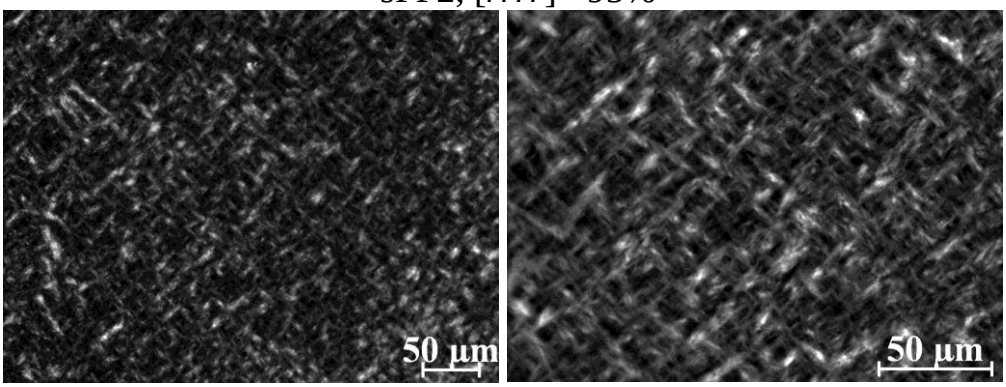

B B'

sPP3, [*rrrr*] =94.2%

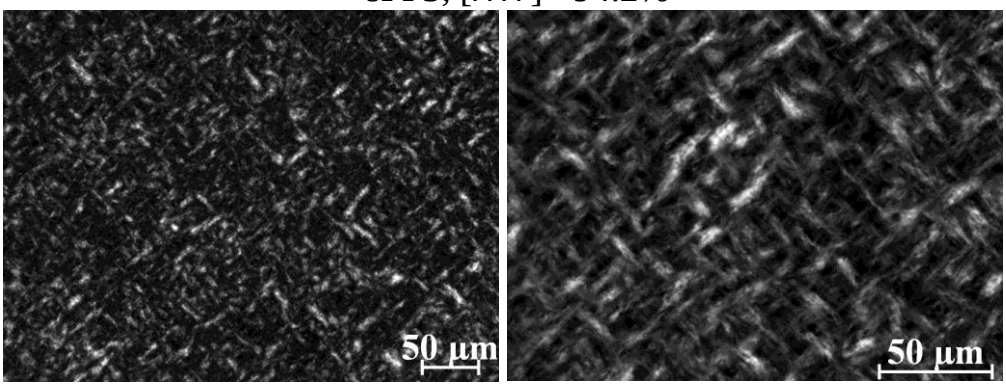

C C'

sPP4, [*rrrr*] =92.5%

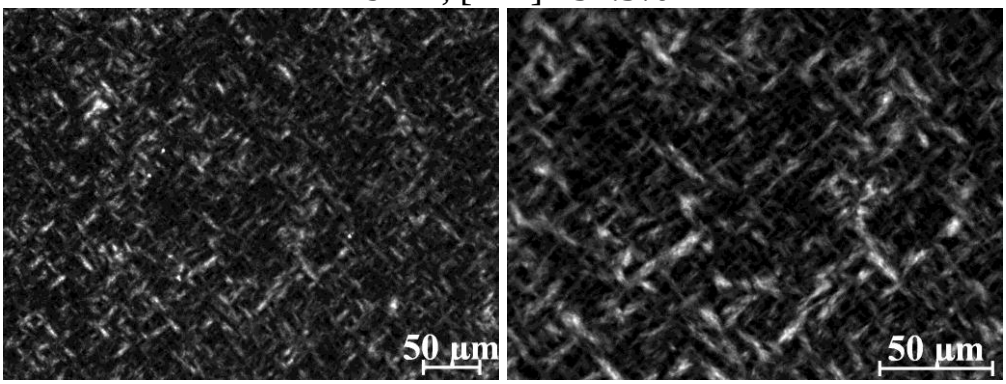

D D'

sPP5, [*rrrr*] =91.5%

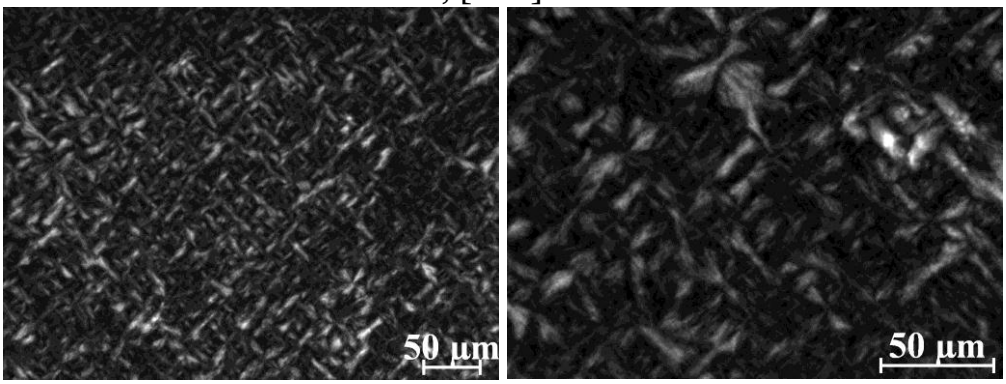

E E'

sPP6, [*rrrr*] =90.7%

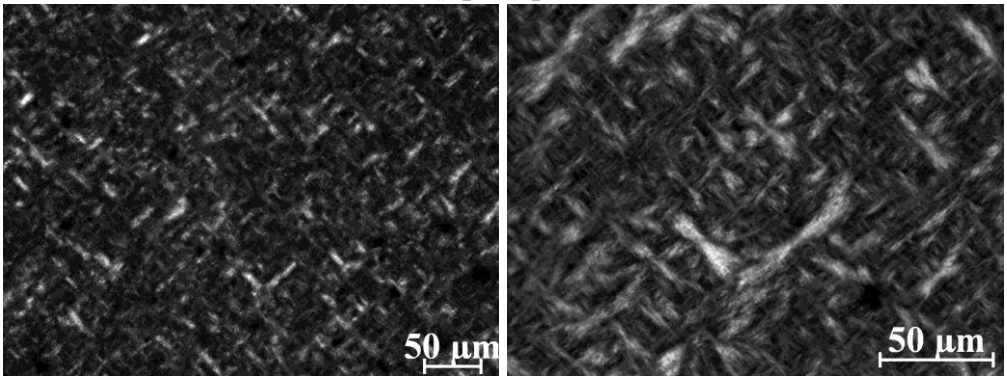

F F'

sPP7, [*rrrr*] =88.6%

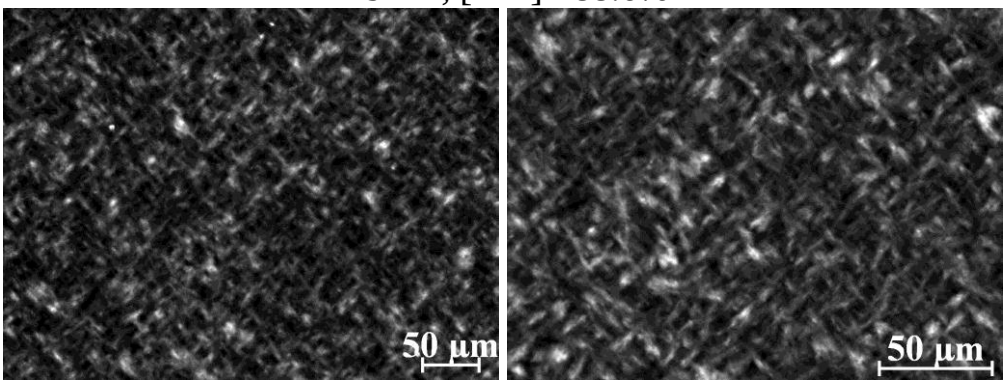

G G'

sPP8, [*rrrr*] =87%

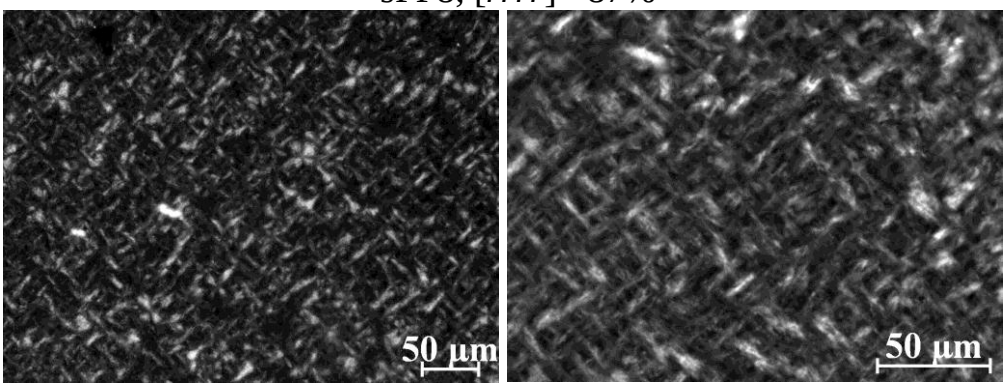

H H'

sPP9, [*rrrr*] = 78%

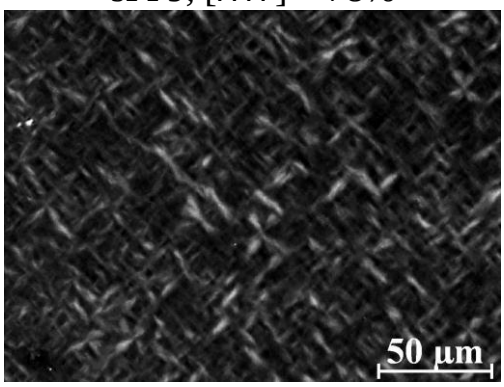

I

sPP10, [*rrrr*] = 74.8%

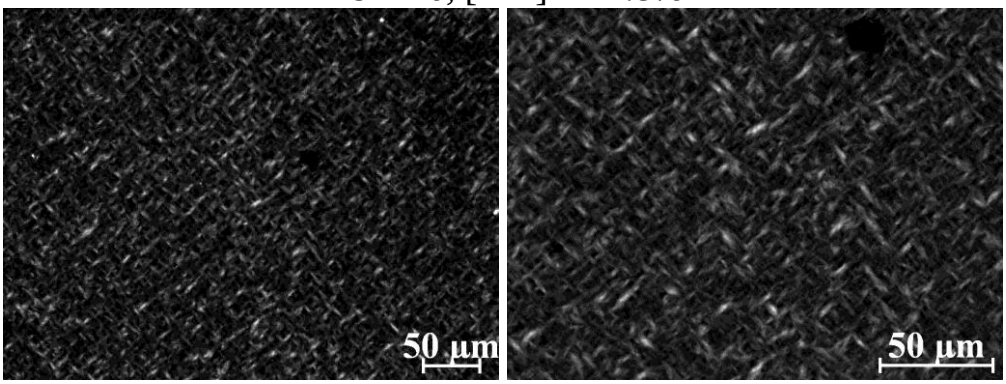

L L'

Figure 1.36. *POM images of samples sRDG-2-1 with [rrrr] = 95.5% (A,A'), sPP2 with [rrrr] = 95% (B,B') sPP3 with [rrrr] = 94.2% (C,C',) sPP4 with [rrrr] = 92.5% (D,D'), sPP5 with [rrrr] = 91.5% (E,E'), sPP6 with [rrrr] = 90.7% (F,F'), sPP7 with [rrrr] = 88.6% (G,G'), sPP8 with [rrrr] = 87% (H,H'), sPP9 with [rrrr] = 78% (I,I') and sPP10 with [rrrr] = 74.8% (L,L')*

This morphology, in addition to the structural transformations typical of sPP occurring during deformation and relaxation, is in part responsible of the mechanical properties of high ductility and flexibility and the elastic behavior of the sPP samples, in particular in the case of samples of low stereoregularity. Small and elongated needle-like crystals organized in the interwoven morphology of Figures 1.36 act as physical cross-links in the amorphous matrix, producing the elastomeric network. In the case of samples of high stereoregularity showing bigger crystalline aggregates of Figure 1.32-1.34, the elastic behavior is mainly due to the enthalpic contribution of the reversible polymorphic transformation between the trans-planar form III and the helical form II. However, since very big and well-formed spherical spherulites are never observed, the contribution to the elastic properties of long and densely entangled amorphous tie-chains[158] is not negligible.

1.6.2. Crystal morphology of copolymers of sPP with ethylene

Samples syndiotactic propylene-ethylene copolymers (sPPET) are crystalline up to an ethylene concentration of 18-20 mol%. Ethylene units are partially included in the crystals of both as-prepared and melt crystallized samples.[142] As-prepared sPPET samples basically crystallize in conformationally disordered modifications of form II of sPP containing kink bands (Figure 1.22B),[142b,c] as demonstrated by the X-ray diffraction profiles of Figure 1.37A,B that present for all samples the typical 110 reflection at $2\theta = 17°$ of form II of sPP. The amount of kink bands defects, represented mainly by T_6G_2 sequences, increases with the ethylene content. These modifications are metastable and transform by crystallization from the melt into the most stable form I or form II, depending on the ethylene concentration. As shown by X-ray powder profiles of thin films crystallized from the melt at 2.5 °C/min of Figure 1.37C, sPPET samples having low ethylene content (up to 6-7 mol%) crystallize from the melt into the antichiral form I, even though disordered modifications of form I are always obtained.[142c] For higher ethylene contents, mixtures of crystals of forms I and II are obtained by crystallization from the melt. The fraction of form II increases with increasing the ethylene content.[142c] The form II obtained by melt-crystallizations does not present kink-band disorder, all chains being in the more stable $(T_2G_2)_n$ helical conformation.[142c] Samples with ethylene content higher than 8 mol% do not crystallize from the melt but they crystallize upon aging at room temperature.[142]

As discussed in the section 1.3, all the crystalline samples show elastic properties.[142f] The most crystalline samples, with ethylene contents lower than 6-7 mol%, show poor elastic properties as in the case of sPP, but higher ductility. In these samples the elastic behavior is associated to a reversible polymorphic transition between the *trans*-planar form III and the helical form II that provides an enthalpic contribution to the elasticity.[142f] The elastic properties are improved with increasing ethylene concentration. For less crystalline samples, with higher ethylene concentration, the elastic recovery is not associated to any polymorphic transitions and has a pure entropic origin, as in conventional elastomers.[142d,f]

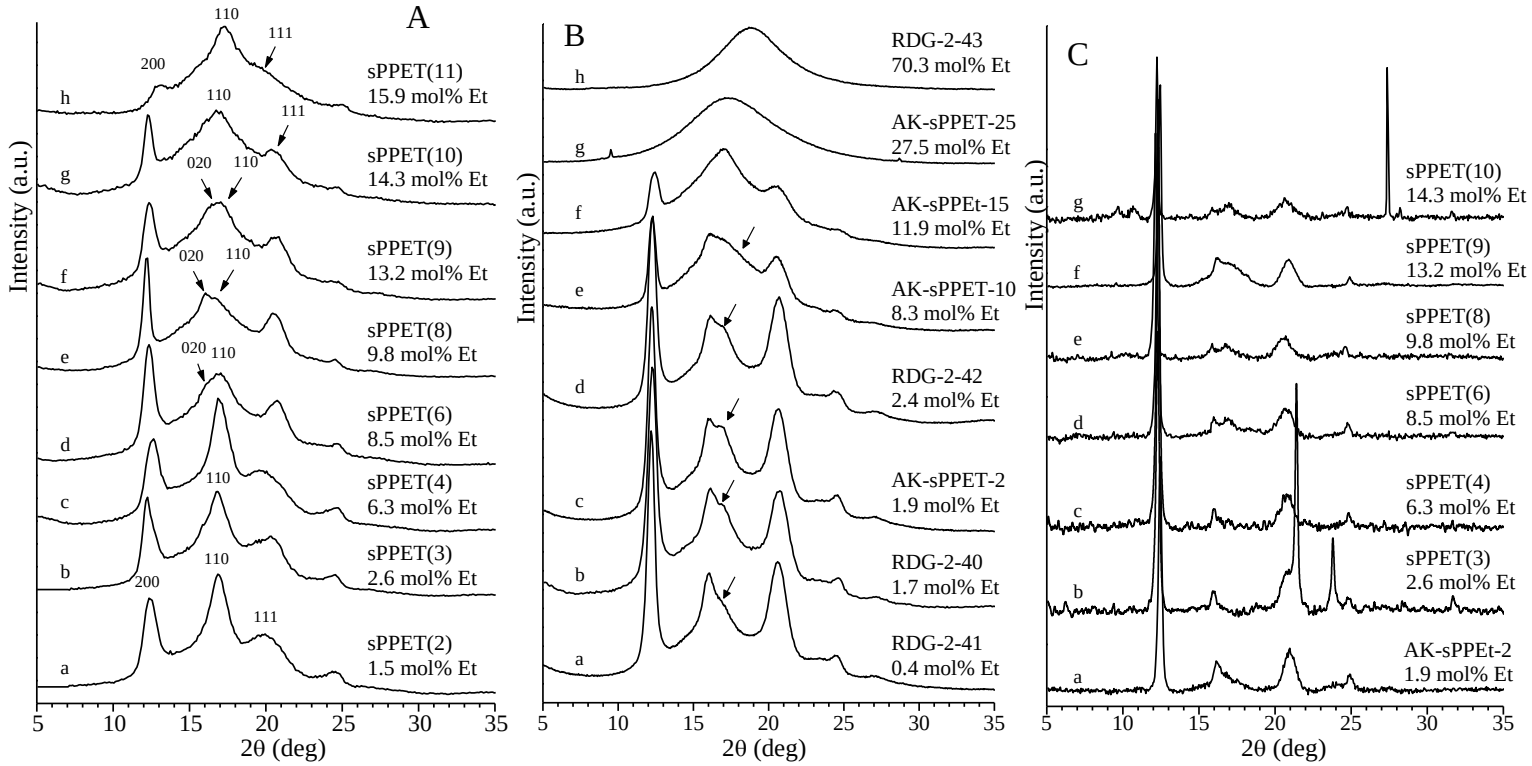

Figure 1.37. *X-ray powder diffraction profiles of as-prepared samples (A,B) and samples crystallized from the melt at cooling rate of 2.5 °C/min (C) of sPPET copolymers of Table 1.2 (A) and Table 1.3 (B) prepared with the catalyst 1 of Chart 1. The 200 and 010 reflections at 2θ = 12 and 16°, respectively, of the helical form I, and the 110 reflection at 2θ = 17° of the helical form II of sPP are indicated.*

The POM images of thin films of the samples of copolymers sPPET selected from samples reported in Tables 1.2 and 1.3 (AK-sPPEt-2) crystallized from the melt by cooling at 2.5 °C/min are shown in Figure 1.38-1.40 at two magnification. The morphology of samples with low ethylene concentration, up to ≈ 6 mol%, that crystallize mainly in the form I, is characterized by the presence of bundles of rod-like lamellae, bow-tie and open multi-faceted aggregates (Figure 1.38).

POM images of samples with ethylene content in the range 7-10 mol%, still crystallizing mainly in form I of sPP, show prevailingly needle-like and bundle-like morphology with only small bow-tie aggregates (Figure 1.39).

For ethylene concentrations higher than 10 mol%, the samples crystallize upon aging in form II with low degrees of crystallinity and only needle-like morphology has been observed (Figure 1.40). When the ethylene content is higher than 15 mol% no birefringence is observed even after aging at room temperature for long time.

sPPET(2), 1.5 mol% of ethylene

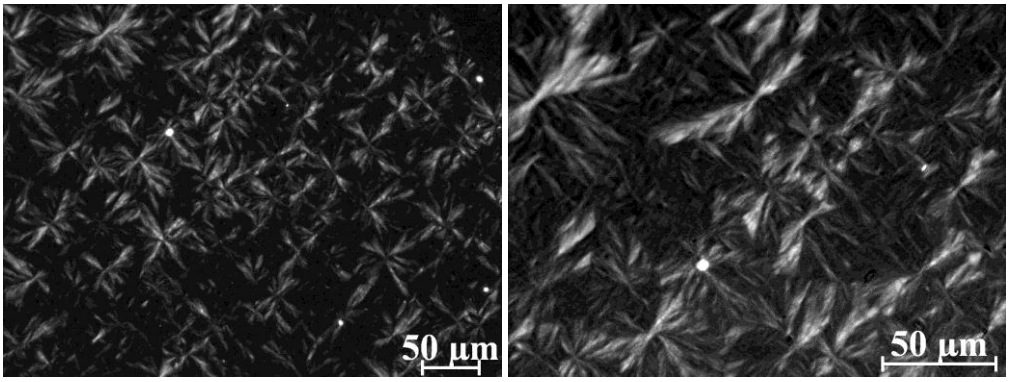

A A'

AKsPPEt-2, 1.9 mol% of ethylene

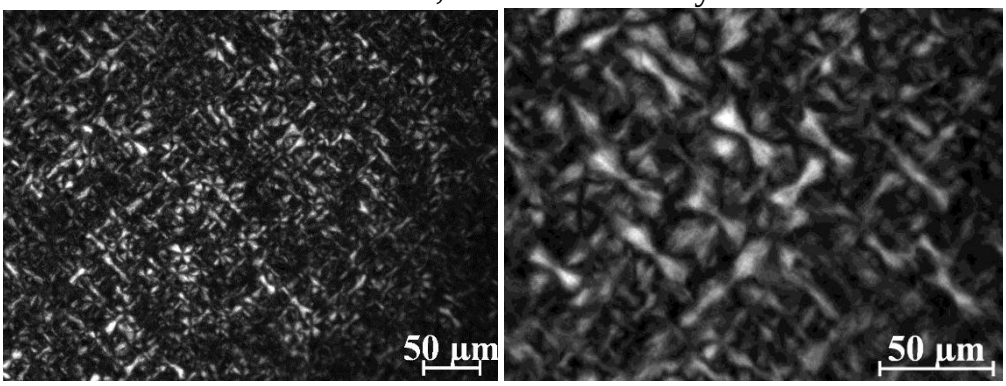

B B'

sPPET(3), 2.6 mol% of ethylene

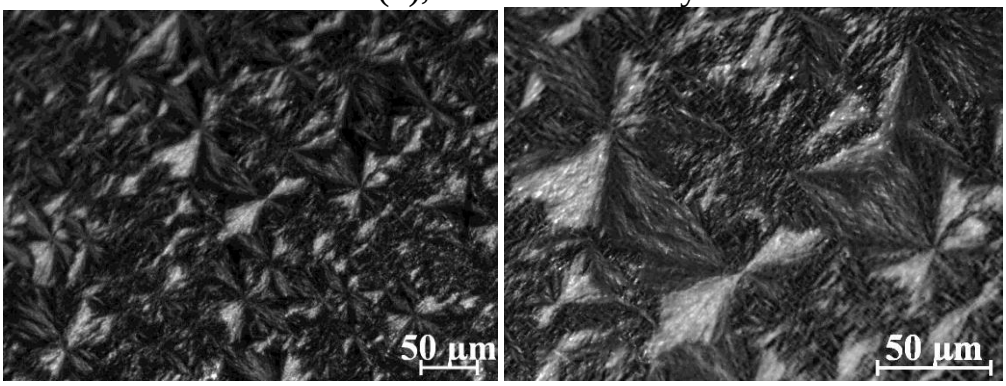

C C'

Figure 1.38. *POM images of samples sPPET(2) with 1.5 mol% of ethylene (A,A'), AKsPPEt2 with 1.9 mol% of ethylene (B,B'), sPPET(3) with 2.6 mol% of ethylene (C,C').*

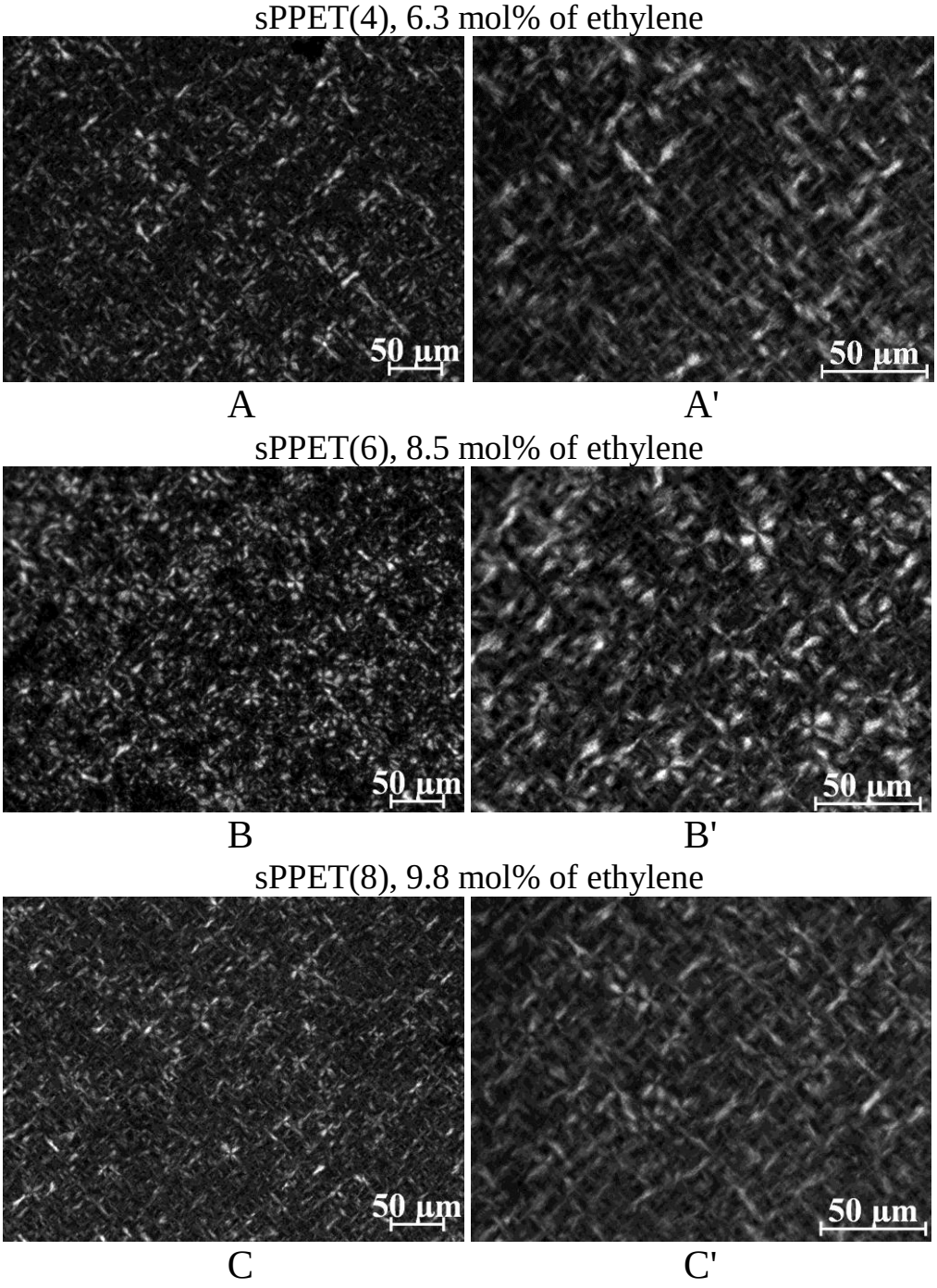

Figure 1.39. *POM images of samples sPPET(4) with 6.3 mol% of ethylene (A,A'), sPPET(6) with 8.5 mol% of ethylene (B,B') and sPPET(8) with 9.8 mol% of ethylene (C,C').*

sPPET(9), 13.2 mol% of ethylene

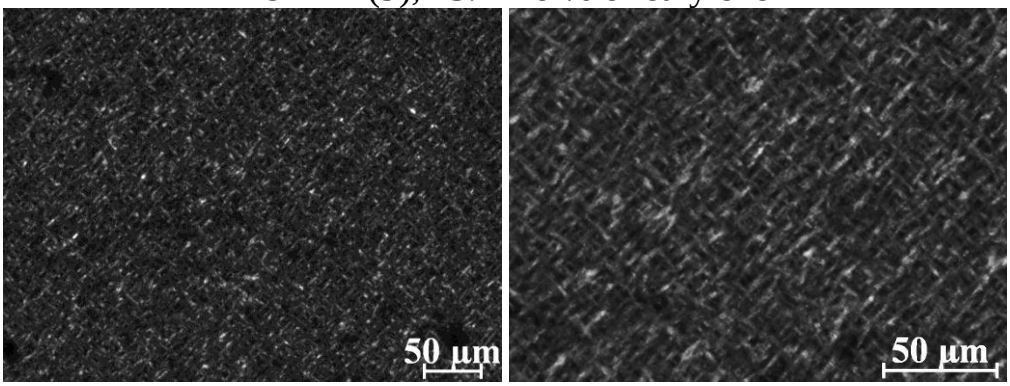

A A'

sPPET(10), 14.3 mol% of ethylene

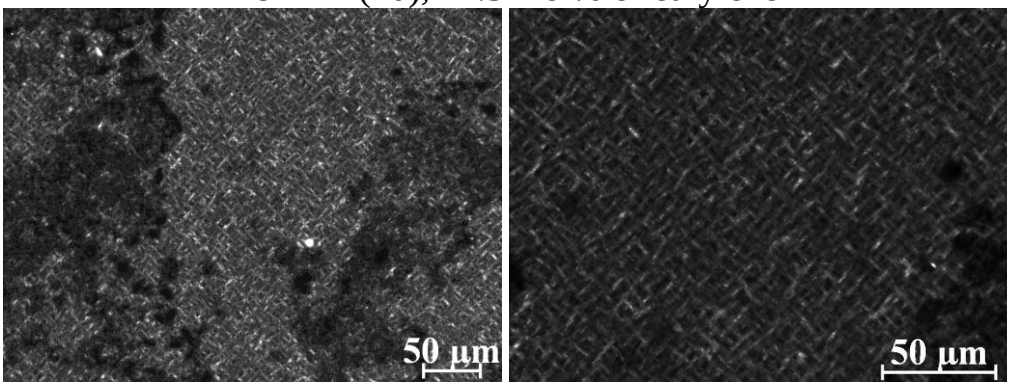

B B'

Figure 1.40. *POM images of samples sPPET(9) with 13.2 mol% of ethylene (A,A') and sPPET(10) with 14.3 mol% of ethylene (B,B').*

1.6.3. Crystal morphology of copolymers of sPP with butene

Syndiotactic propylene-butene copolymers (sPPBu) are crystalline in the whole range of comonomer composition due to the complete cocrystallization of butene and propylene in the crystalline lattices of sPP and sPB.[140,143] The X-ray powder diffraction patterns of as-prepared samples of sPPBu copolymers are reported in Figure 1.41A. It is apparent that the samples are crystalline in the whole range of comonomer composition. Samples with the highest content of 1-butene (>80 mol %) behave like syndiotactic poly(1-butene) (sPB); they are amorphous just after the polymerization but crystallize if kept at room temperature for several days. The X-ray diffraction profiles of all copolymers present strong analogies with the X-ray patterns of the corresponding homopolymers, i.e., they present three strong reflections in the 2θ angular ranges 10.5-12.2°, 15-16°, and 19-21° and indicate that samples with low butene concentrations are crystallized in the form I of sPP, whereas samples with butene content higher than 60-70 mol% are crystallized in form I of sPB.[140,143] The same crystallization behavior has been observed in thin films crystallized from the melt by cooling at 2.5 °C/min, as shown by the diffraction profiles of Figure 1.41B. Samples are crystallized in the form I of sPP up to a content of 1-butene of 60-70 mol %, as indicated by the indexing of the reflection at 2θ = 15-16° as a 010 reflection of sPP,[140,143] although disorder in the alternation of right- and left-handed helical chains along both axes of the unit cell is present as indicated by the absence of the 211 reflection of sPP.[1,97,109] Samples with contents of 1-butene higher than 70 mol % crystallize in structures similar to that of form I of sPB,[140] as indicated by the indexing of the reflection at 2θ = 15-16° as a 110 reflection of sPB.[152] However, samples with butene content higher than 30 mol% are amorphous just after cooling the melt but crystallize by aging at room temperature for several days.[143g]

Melt-crystallized unoriented films of sPPBu copolymers show good elastic properties even though the samples present non-negligible level of crystallinity at any comonomer composition. Compared to the sPPET copolymers, sPPBu samples show higher crystallinity and melting temperature (Figure 1.30) thanks to the cocrystallization of the comonomers at any composition. Therefore, sPPBu copolymers behave as thermoplastic elastomers with remarkable high rigidity and mechanical strength that can also be tuned by changing the comonomer composition. In samples with low butene concentration the elastic properties are associated with the reversible transformation between the *trans*-planar form III of sPP, obtained by stretching, and the helical form II, formed

by releasing the tension. The occurrence of reversible phase transitions assists the elasticity of these materials through a non negligible free energy contribution that is added to the conventional entropic contribution.[143g]

The POM images of the samples of sPPBu copolymers crystallized from the melt at cooling rate of 2.5 °C/min of Figure 1.41B are shown in Figure 1.42, for samples up to 18 mol% of butene and in Figure 1.43 for higher butene concentration. For low butene content bow-tie crystals and bigger fan-type crystals have been observed along with thin needle crystals (Figure 1.42A,A'). As butene content increases, needle-like morphology prevails with crystals that become thinner and smaller with increasing butene content (Figure 1.42B,B' and D,D'). In some case, a granular morphology instead of needle-like morphology has been observed (Figure 1.42C,C').

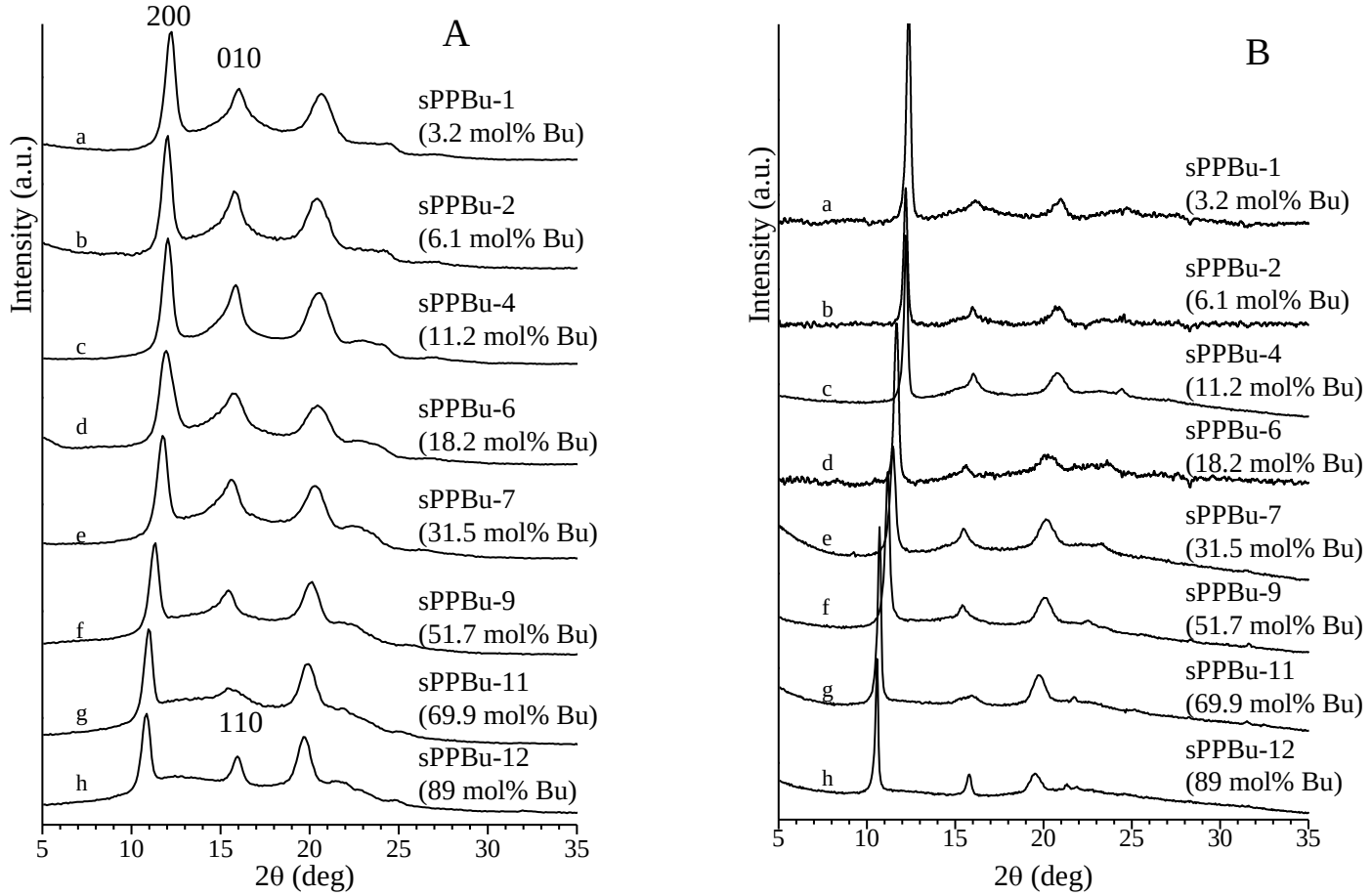

Figure 1.41. *X-ray powder diffraction profiles of as-prepared samples (A) and selected samples crystallized from the melt at cooling rate of 2.5 °C/min (B) of sPPBu copolymers of Table 1.4 prepared with the catalyst* ***1*** *of Chart 1. The 200 and 010 reflections at 2θ = 12 and 16°, respectively, of form I of sPP, and the 110 reflection at 2θ = 17° of form I of sPB are indicated.*

sPPBu-1, 3.2 mol% of 1-butene

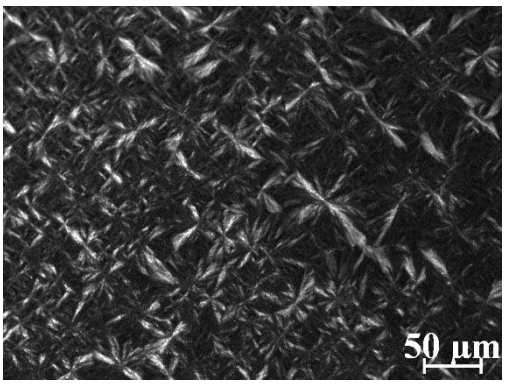

A

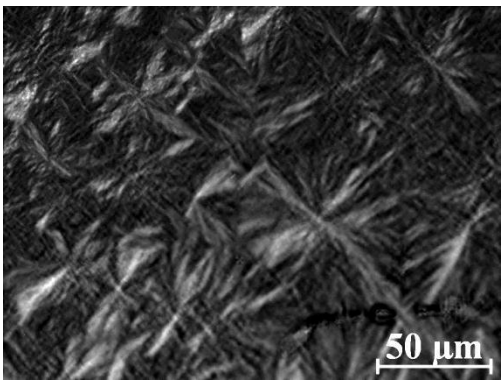

A'

sPPBu-2, 6.1 mol% of 1-butene

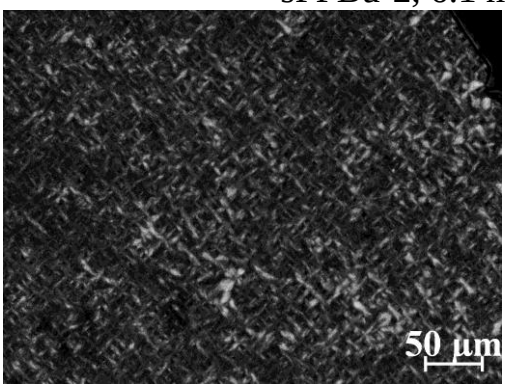

B

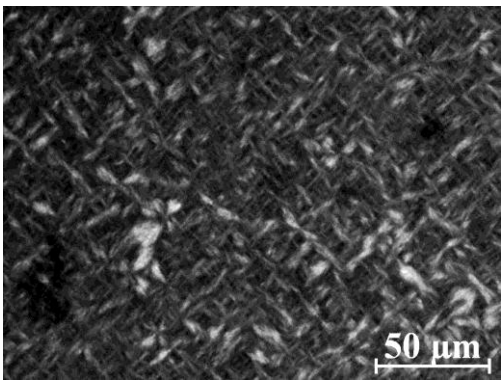

B'

sPPBu-4, 11.2 mol% of 1-butene

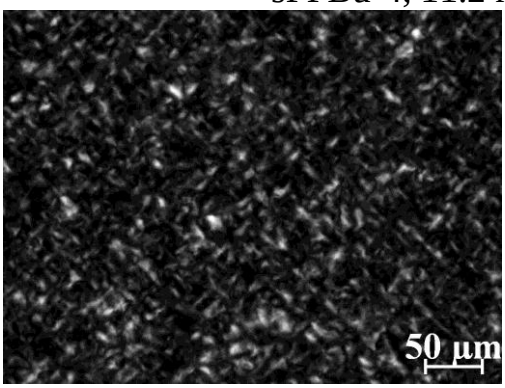

C

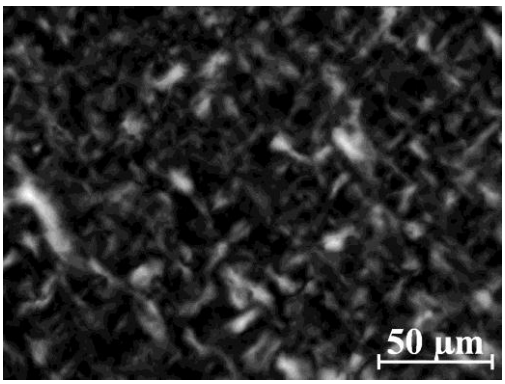

C'

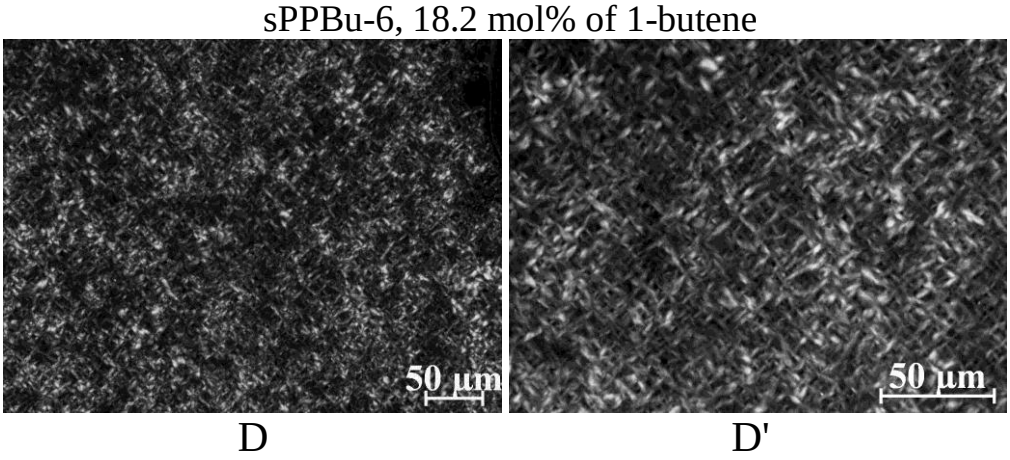

Figure 1.42. *POM images of samples sPPBu-1 with 3.2 mol% of 1-butene (A,A'), sPPBu-2 with 6.1 mol% of 1-butene (B,B'), sPPBu-4 with 11.2 mol% of 1-butene (C,C') and sPPBu-6 with 18.2 mol% of 1-butene (D,D').*

Samples with higher butene content do not crystallize from the melt. Samples sPPBu7 (31.5 mol% of 1-butene) and sPPBu9 (51.7 mol% of 1-butene) crystallize upon cooling at 2.5°C/min to room temperature and aging at room temperature for 90 and 22 days, respectively, in the form I of sPP (Figura 1.41B). These samples show prevalently a "salt and pepper" granular morphology with some needle-crystals visible only at high magnification (Figure 1.43 A,A' and B,B'). Further increase in butene concentration leads to a small increase of crystallinity. Samples sPPBu11 (69.9 mol% of 1-butene) and sPPBu12 (89 mol% of 1-butene) crystallize upon cooling at 2.5°C/min to room temperature and aging at room temperature for 22 days in form I of sPB (Figure 1.41B). This small increase in crystallinity leads to a small increase in birefringence. Therefore, the needle-like and granular morphology displayed by the samples sPPBu11 and sPPBu12 (Figure 1.43C,C' and D,D') is characterized by crystals slightly bigger than the samples sPPBu7 and sPPBu9.

sPPBu-7, 31.5 mol% of 1-butene

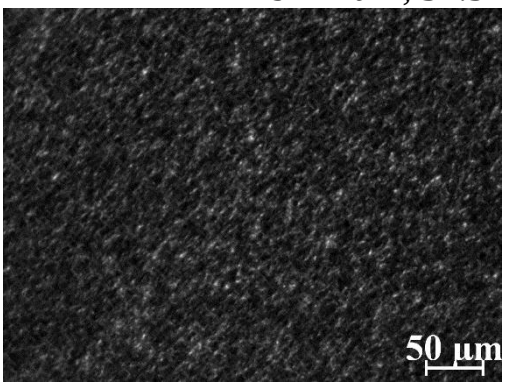

A

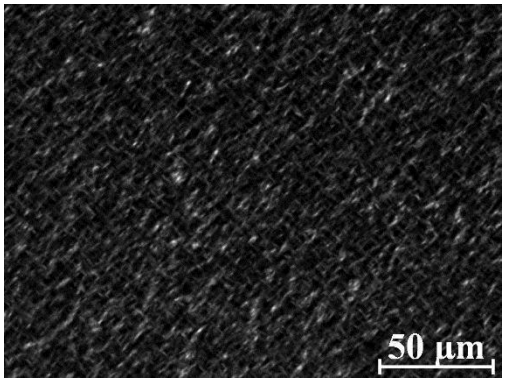

A'

sPPBu-9, 51.7 mol% of 1-butene

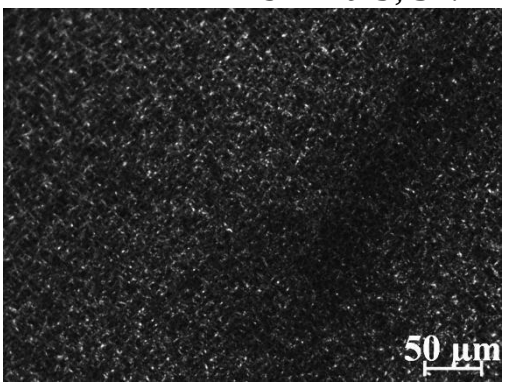

B

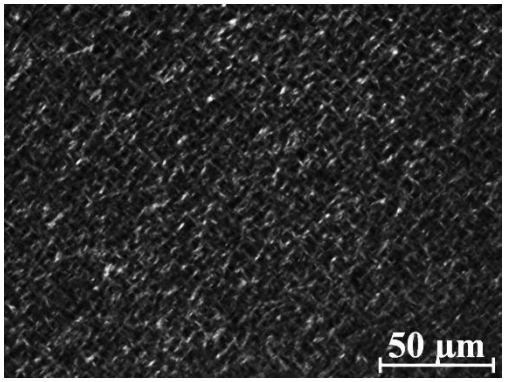

B'

sPPBu-11, 69.9 mol% of 1-butene

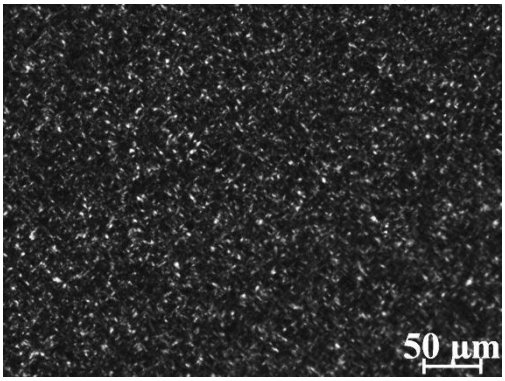

C

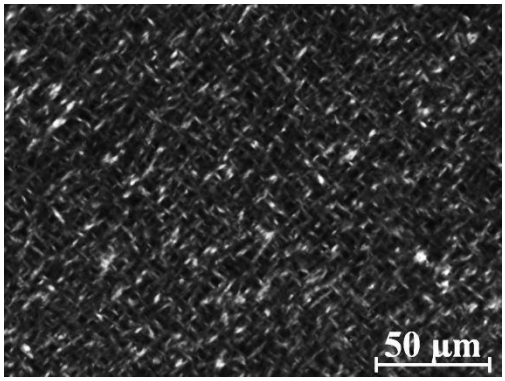

C'

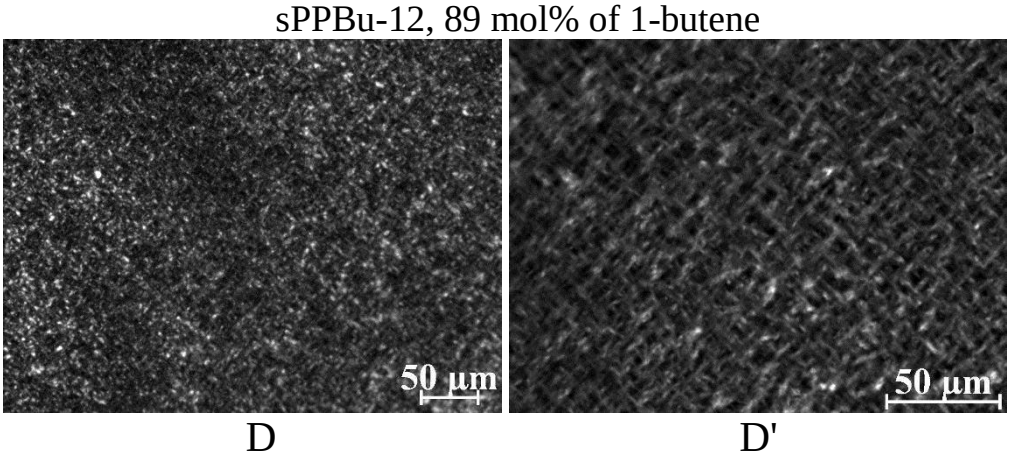

Figure 1.43. *POM images of samples sPPBu-7 with 31.5 mol% of 1-butene (A,A'), sPPBu-9 with 51.7 mol% of 1-butene (B,B'), sPPBu-11 with 69.9 mol% of 1-butene (C,C') and sPPBu-12 with 89 mol% of 1-butene (D,D').*

1.6.4. Crystal morphology of copolymers of sPP with 4-methyl-1-pentene

Syndiotactic propylene-(4-methyl-1-pentene) copolymer (sPP4M1P) samples are crystalline up to a 4-methyl-1-pentene concentration of 20 mol%. The X-ray powder diffraction profiles of as-prepared samples of sPP4M1P copolymers, reported in Figure 1.44A, show that all samples crystallize in the form I of sPP, as indicated by the presence of the 010 reflection of form I of sPP at $2\theta = 16°$ in the diffraction profiles of all samples. Thin films of samples crystallized from the melt at 2.5 °C/min of sPP4M1P copolymers are also crystallized in the form I of sPP (Figure 1.44B). Samples with 4-methyl-1-pentene content higher than 15 mol% do not crystallize from the melt but crystallize upon aging at room temperature. Contrary to sPPBu copolymers, the 200 and 010 reflections of the diffraction profiles of Figure 1.44A and B are at the constant values of $2\theta = 12$ and 16°, respectively. This indicates that the 4-methyl-1-pentene units are mainly excluded by the crystals of form I of sPP.

All copolymer samples show good elastic properties (data not shown). X-ray fiber diffraction patterns recorded during deformation (data not shown) indicate that in samples with 4-methyl-1-pentene concentration lower than 15 mol% the elastic properties are associated with the reversible transformation between the *trans*-planar form III of sPP, obtained by stretching, and the helical form II, formed by releasing the tension. For less crystalline samples, with higher 4-methyl-1-pentene concentration, the elastic recovery is not associated to any polymorphic transitions and has a pure entropic origin, as in conventional elastomers.

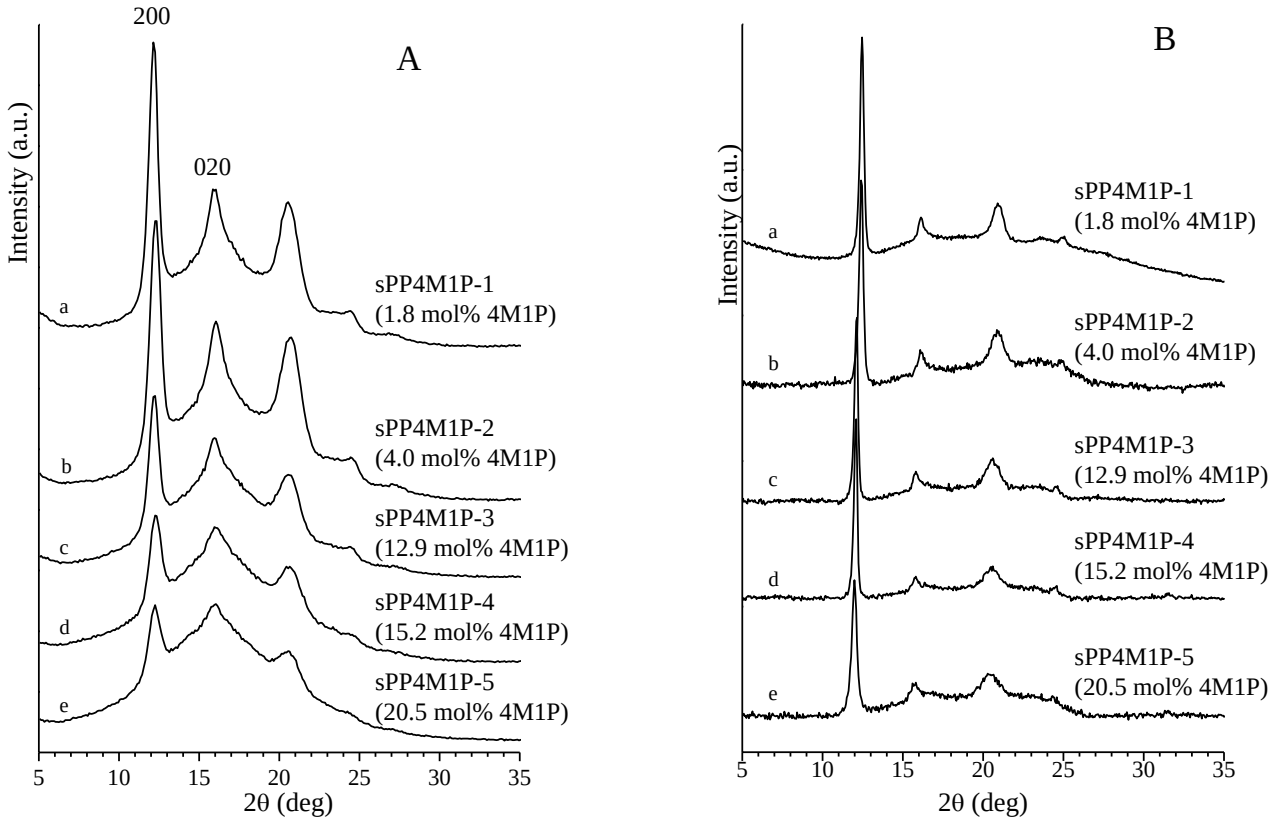

Figure 1.44. *X-ray powder diffraction profiles of as-prepared samples (A) and samples crystallized from the melt at cooling rate of 2.5 °C/min (B) of sPP4M1P copolymers of Table 1.5 prepared with the catalyst* ***1*** *of Chart 1. The 200 and 020 reflections at 2θ = 12 and 16°, respectively, of form I of sPP are indicated.*

The POM images of the samples of sPP4M1P copolymers crystallized from the melt at cooling rate of 2.5 °C/min of Figure 1.44B, aged at room temperature for one week in order to achieve the complete crystallization and improve the birefringence, are shown in Figure 1.45. For low comonomer content very small open-multifaceted aggregates together with bow-tie and granular crystals appear (Figure 1.45A,A'). As the comonomer content increases, the morphology is characterized by the presence of granular crystals and also by small bow-tie and needle crystals, more visible at higher magnification (Figure 1.45B,B'-C,C'). Only the sample sPP4MP1P-4 shows mainly a "salt and pepper" granular morphology because of the higher comonomer content (15.4 mol% of 4-methyl-1-pentene). Sample sPP4MP1P-5 with 20.5 mol% of 4-methyl-1-pentene (not shown) do not show birefringence even after long aging time probably because of the too low crystallinity achieved after aging (profile e of Figure 1.44B).

sPP4M1P-1, 1.9 mol% of 4MP

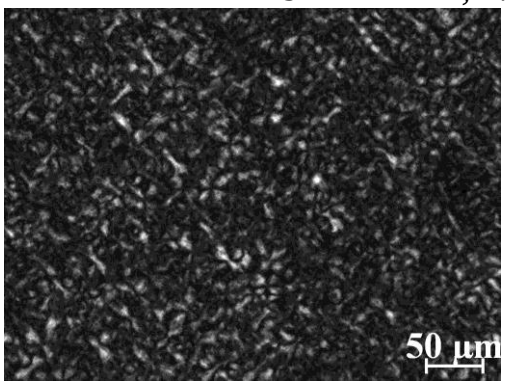

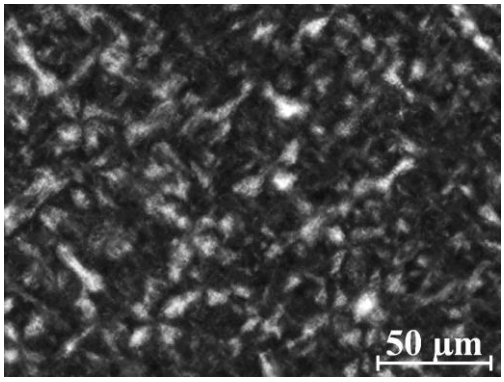

A A'

sPP4M1P-2, 4 mol% of 4MP

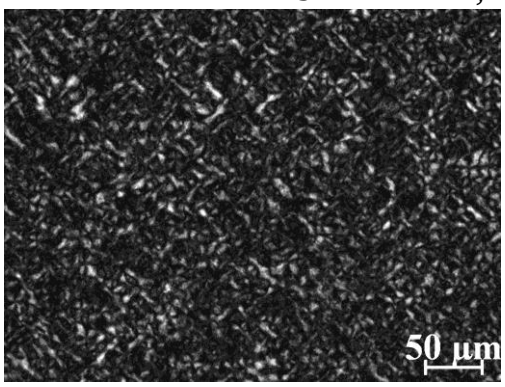

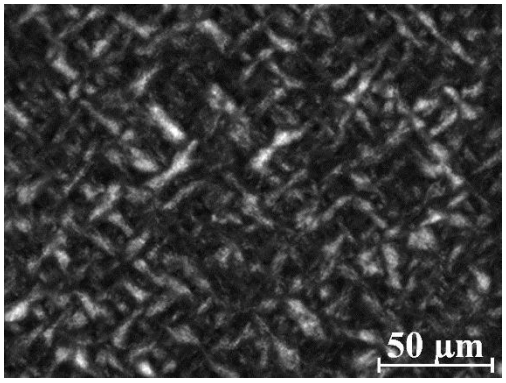

B B'

sPP4M1P-3, 12.9 mol% of 4MP

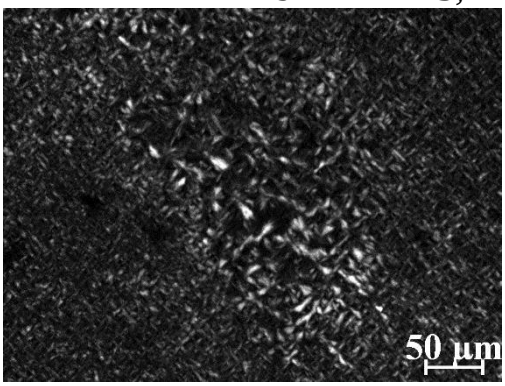

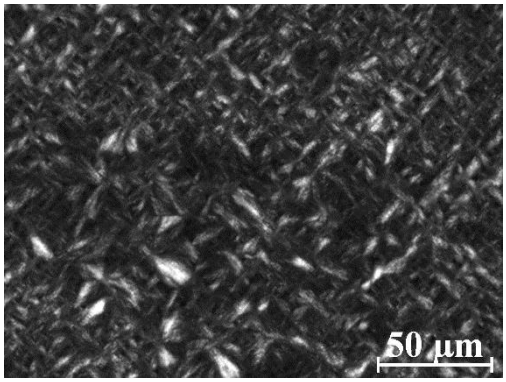

C C'

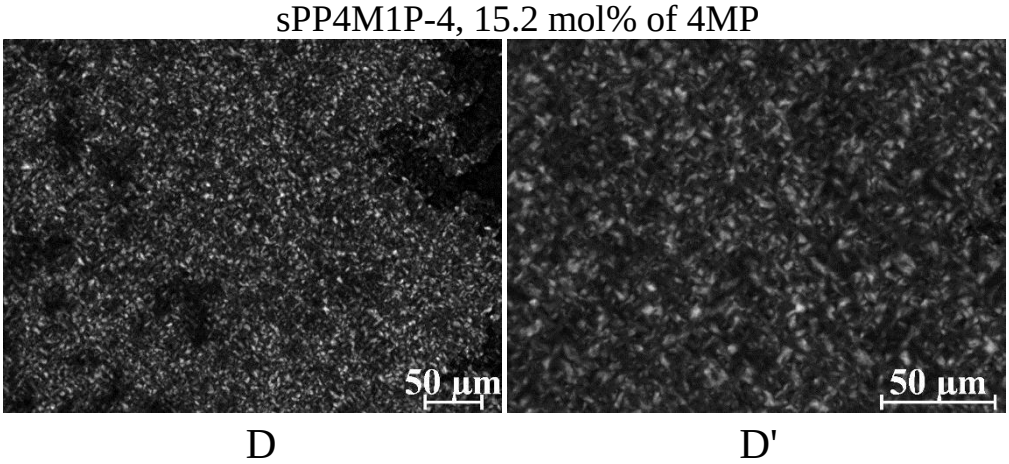

Figure 1.45. *POM images of samples sPP4M1P-1 with 1.9 mol% of 4-methyl-1-pentene (A,A'), sPP4M1P-2 with 4 mol% of 4-methyl-1-pentene (B,B'), sPP4M1P-3 with 12.9 mol% of 4-methyl-1-pentene (C,C') and sPP4M1P-4 with 15.2 mol% of 4-methyl-1-pentene (D,D').*

1.6.5. Crystal morphology of copolymers of sPP with 1-hexene and 1-octene

The X-ray powder diffraction profiles of as-prepared samples of syndiotactic propylene-1-hexene (sPPHe) and syndiotactic propylene-1-octene copolymer samples (sPPOt) are reported in Figure 1.46A and Figure 1.47A, respectively. The X-ray powder diffraction profiles of samples crystallized from the melt at 2.5 °C/min of sPPHe and sPPOt copolymers are shown in parts B of Figures 1.46 and 1.47, respectively.[146] These data indicate that both as-prepared and melt-crystallized samples are all crystallized in the helical form I of sPP,[146] as indicated by the presence of the 200 and 010 reflections at 2θ = 12° and 16°, respectively, of form I.[1,109] The absence in all the diffraction profiles of the 211 reflection at 2θ = 18.8°, typical of the ordered fully antichiral form I of sPP with perfect alternation of right- and left handed helical chains along both axes of the orthorhombic unit cells,[97-101] indicates that all samples are crystallized in modifications close to the fully disordered form I with disorder in the positioning of right- and left-handed helical chains in the orthorhombic lattice.[1,97,109] The presence of a weak reflection at 2θ = 17° in the diffraction profiles a of Figure 1.46A and 1.47A of as-prepared samples indicates that a small amount of crystals of form II of sPP is also present in samples with low comonomer contents. The Bragg distances of 200 and 010 reflections of form I are basically constant at the values of form I of the sPP homopolymer in all copolymer samples regardless of the comonomer concentration, indicating that hexene and octene units are mainly excluded from crystals of sPP.[146]

The crystallinity decreases with increasing comonomer concentrations, and for hexene or octene contents higher than 18-20 mol% both as-prepared and melt-crystallized samples are basically amorphous with traces of crystals of form I.[146] The samples sPPHe6-sPPHe8 with hexene concentration higher than 9 mol % and the samples sPPOt4-sPPOt9 with octene content higher than 4 mol% are amorphous soon after the cooling from the melt of the compression-molded samples and slowly crystallize in several days by aging at room temperature.[146] Traces of crystallinty of form I of sPP is still present up to a concentration of comonomers of 20-26 mol%.[146]

The presence of the branched comonomers, however, influences the polymorphic behavior when the samples are stretched at high deformations.[146] They destabilize the *trans*-planar conformation of sPP chains and at relatively high concentrations (higher than 5-6 mol%) prevents the crystallization of both the trans-planar form III and the *trans*-planar mesophase.[146] At low concentrations of hexene or octene (in the range 1-2 mol%) the behavior of these copolymers is similar to that of sPP; that is, the stable helical form I of the melt-crystallized samples transforms into the *trans*-planar form III by stretching at high deformations.[146] For hexene or octene concentrations in the range 3-5 mol% the stretching produces transformation of the helical form I into the *trans*-planar mesophase.[146] Finally, for hexene and octene concentrations higher than 5-6 and 3 mol%, respectively, the helical form I transforms by stretching at high deformation into a different mesomorphic form, characterized by chains in the ordered 2/1 helical conformation and disorder in the lateral packing of the chains.[146] Therefore, high concentrations of hexene or octene units stabilize the helical conformation of the chains, but the high content of constitutional defects prevents the formation of the ordered crystalline form I by stretching and the helical mesophase crystallize at high deformations.[146]

All samples exhibit good elastic properties (data not shown). For hexene or octene concentrations lower than 2 mol% the elastic properties are associated with the reversible transformation between the *trans*-planar form III of sPP, obtained by stretching, and the helical form II, formed by releasing the tension (data not shown). For less crystalline samples with hexene and octene concentrations higher than 5-6 mol% and 3 mol%, respectively, that crystallize only in helical forms in fibers stretched at high deformations,[146] no phase transformations occur during deformation and relaxation (data not shown) and the elastic recovery has a pure entropic origin, as in conventional elastomers.

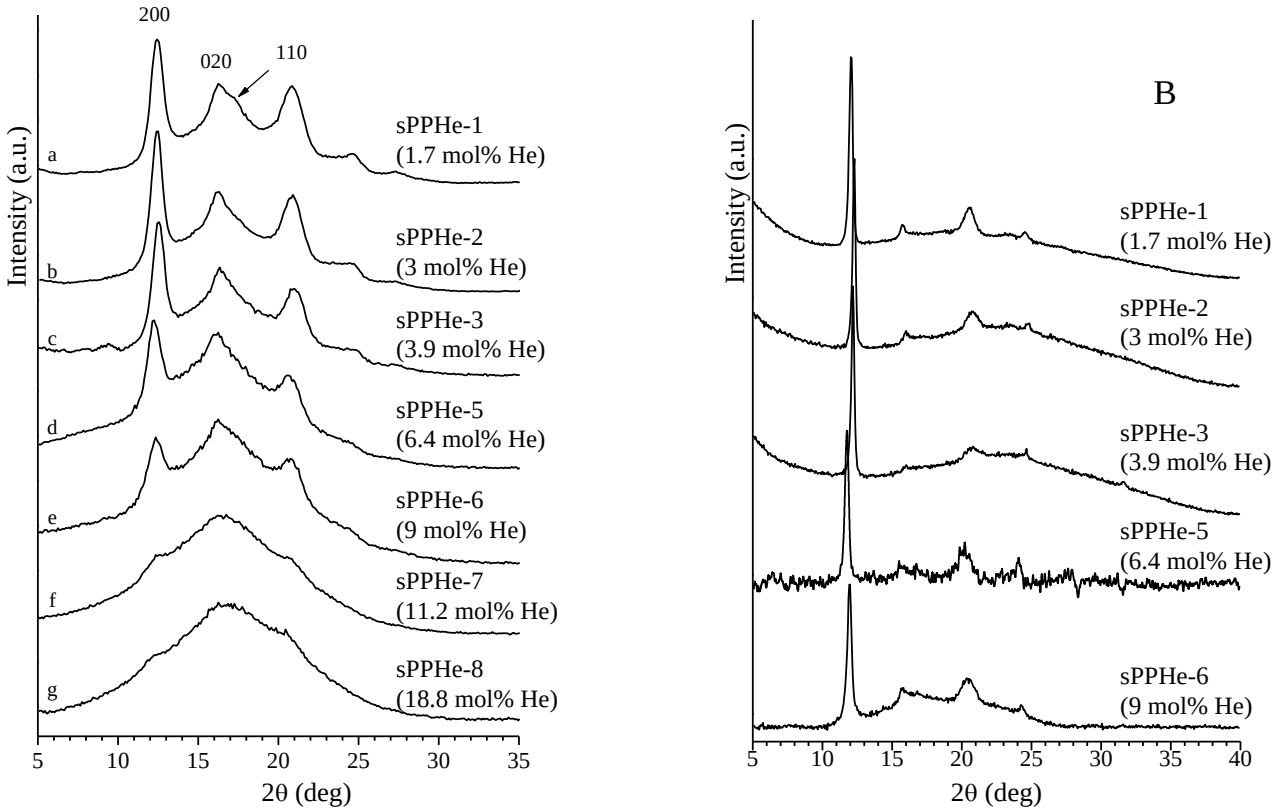

Figure 1.46. *X-ray powder diffraction profiles of as-prepared (A) and selected samples crystallized from the melt at cooling rate of 2.5 °C/min (B) of sPPHe copolymers of Table 1.6 prepared with the catalyst* ***1*** *of Chart 1. The 200 and 010 reflections at $2\theta = 12$ and 16°, respectively, of the helical form I, and the 110 reflection at $2\theta = 17°$ of the helical form II of sPP are indicated.*

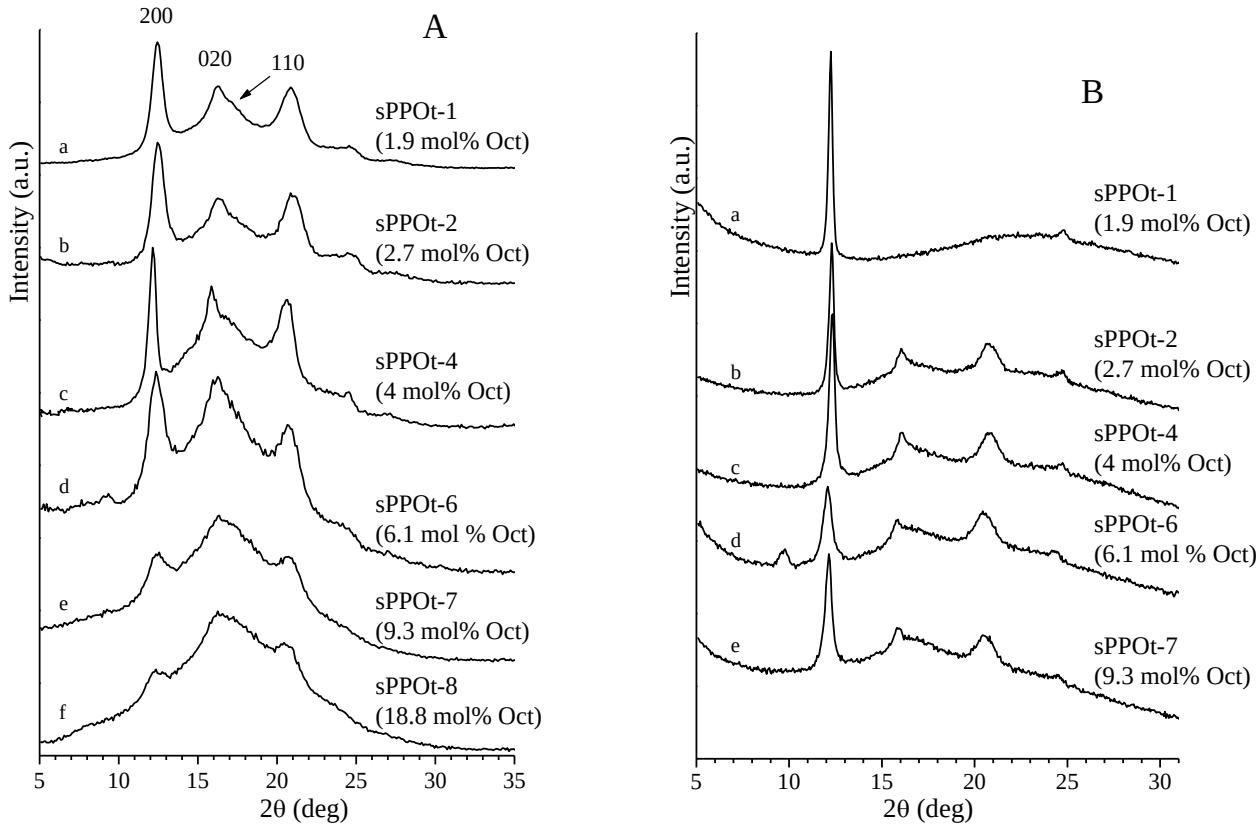

Figure 1.47. *X-ray powder diffraction profiles of as-prepared (A) and selected samples crystallized from the melt at cooling rate of 2.5 °C/min (B) of sPPOt copolymers of Table 1.7 prepared with the catalyst* ***1*** *of Chart 1. The 200 and 010 reflections at 2θ = 12 and 16°, respectively, of the helical form I, and the 110 reflection at 2θ = 17° of the helical form II of sPP are indicated.*

The POM images of the samples of sPPHe and sPPOc copolymers crystallized from the melt at cooling rate of 2.5 °C/min of Figures 1.46B and 1.47B, aged at room temperature in order to achieve the complete crystallization and improve the birefringence, are shown in Figures 1.48 and 1.49, respectively. For very low hexene concentration, a complex morphology characterized by the presence of a mixture of few small open multi-faceted aggregates, bundles of rod-like lamellae, bow-tie and needle-like crystals, has been observed (Figure 1.48A,A'). As hexene content increases, open multi-faceted aggregates disappear ,while bow-tie crystals become thinner and thinner until they disappear completely in samples with the highest 1-hexene content (Figure 1.48A,A'-E,E'). In fact, POM images of samples sPPHe-5 and sPPHe-6 (Figure 1.48D,D' and Figure 1.48E,E', respectively) show mainly needle-like morphology. Samples sPPHe-7 and sPPHe8 do not show birefringence even after long aging time probably because too low crystallinity is achieved after aging.

In the case of sPPOt copolymers, needle-like morphology seems to prevail regardless of octene concentration (Figure 1.49). Only the sample sPPOt-1 with 1.9 mol% of octene shows few bigger bow-tie crystals (Figure 1.49A,A'), while in POM images at high magnification of the sample sPPOt-2 with 2.7 mol% of octene some bigger bundles of rod-like lamellae can be observed (Figure 1.49B,B'). POM images of samples sPPOt-4, sPPOt-6 and sPPOt-7 (Figures 1.49C,C', D,D' E,E', respectively) cooled from the melt at 2.5°C/min and aged at room temperature for 20-60 days in order to achieve the complete crystallization show only needle-like morphology. In all samples the needle crystals become thinner and smaller as octene content increases (Figure 1.49 B,B'-E,E'). Sample sPPOt-8 with 18.8 mol% of octene does not show birefringence even after long aging time probably because a too low crystallinity is achieved after aging. In sPPOc copolymers the bigger octene units prevent formation of the big aggregates that have been observed in sPPHe copolymers at the same comonomer concentration (Figure 1.48).

sPPHe-1, 1.7 mol% of 1-hexene

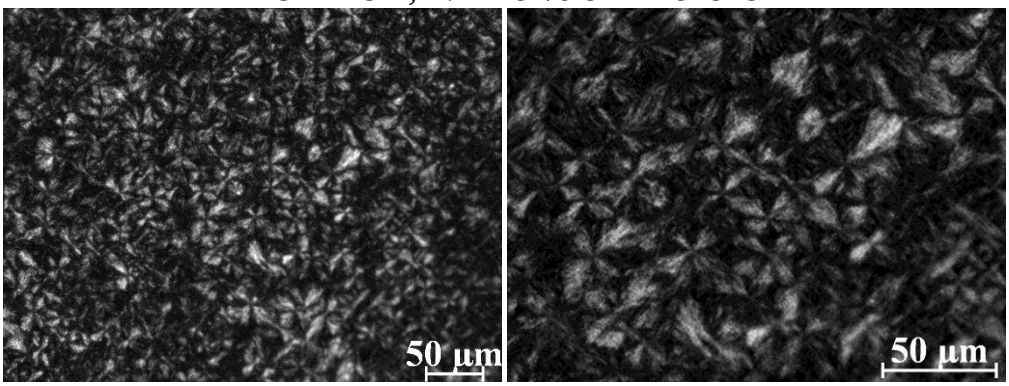

A A'

sPPHe-2, 3 mol% of 1-hexene

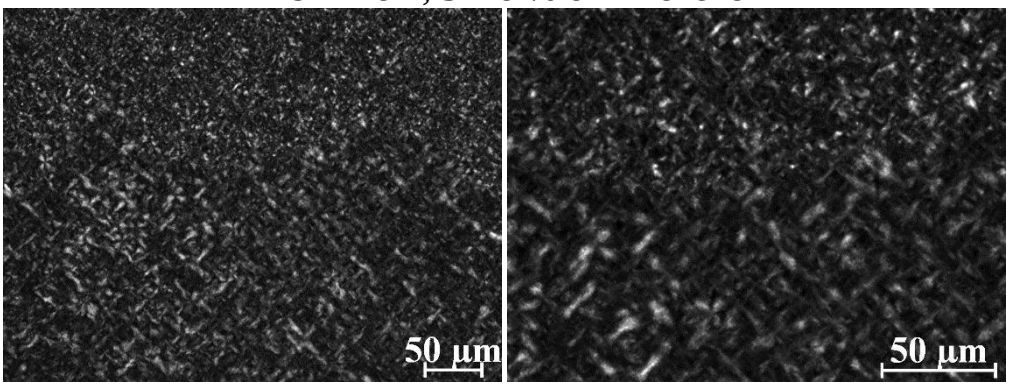

B B'

sPPHe-3, 3.9 mol% of 1-hexene

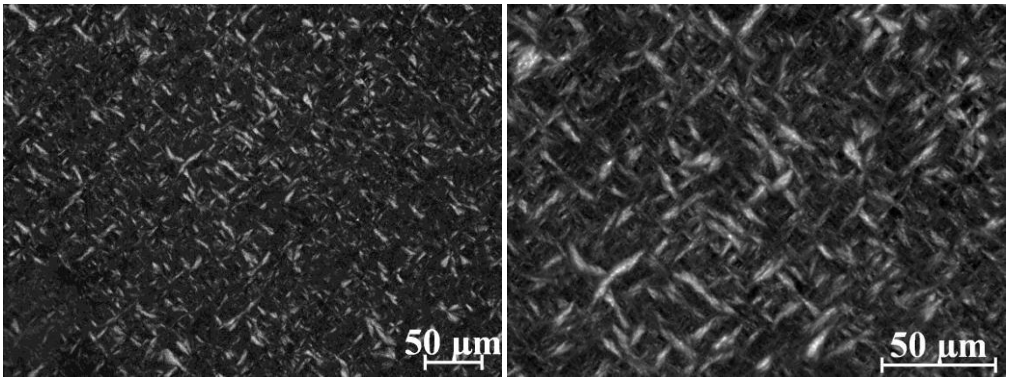

C C'

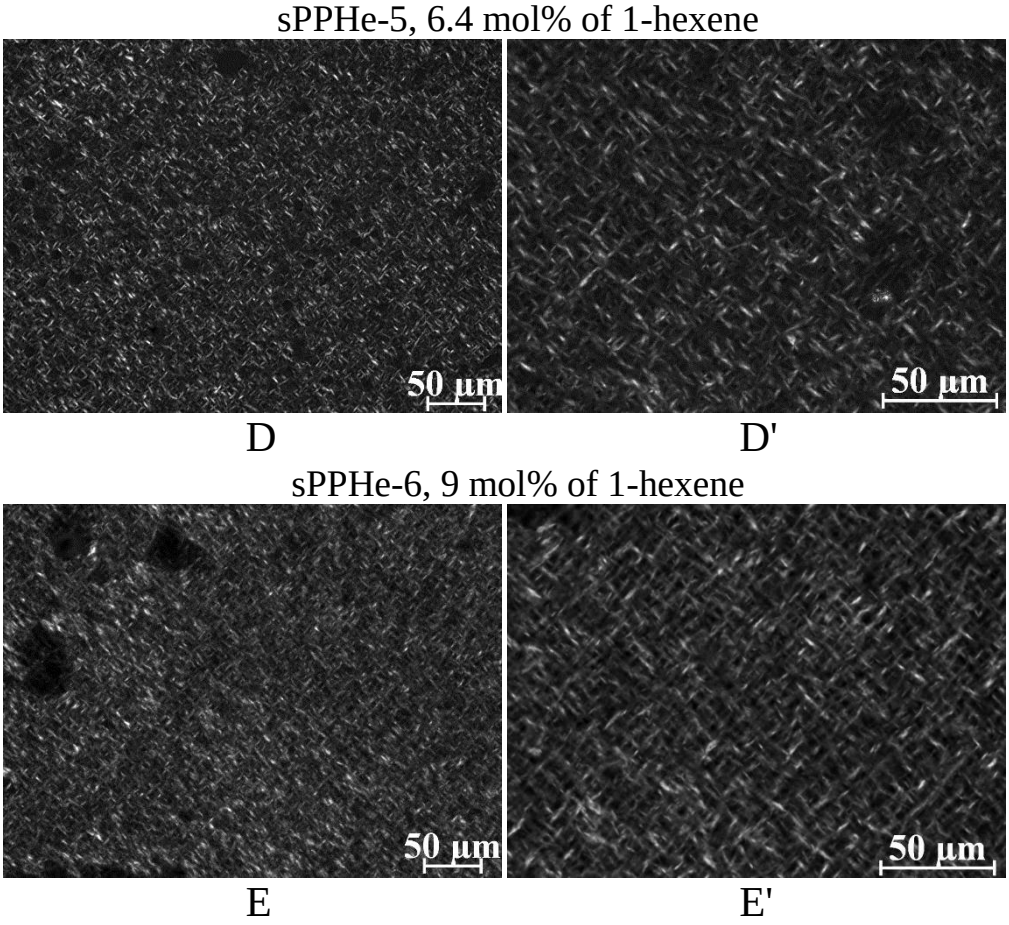

Figure 1.48. *POM images of samples sPPHe-1 with 1.7 mol% of 1-hexene (A,A'), sPPHe-2 with 3 mol% of 1-hexene (B,B'), sPPHe-3 with 3.9 mol% of 1-hexene (C,C') sPPHe-5 with 6.4 mol% of 1-hexene (D,D') and sPPHe-6 with 9 mol% of 1-hexene (E,E').*

sPPOt-1, 1.9 mol% of 1-octene

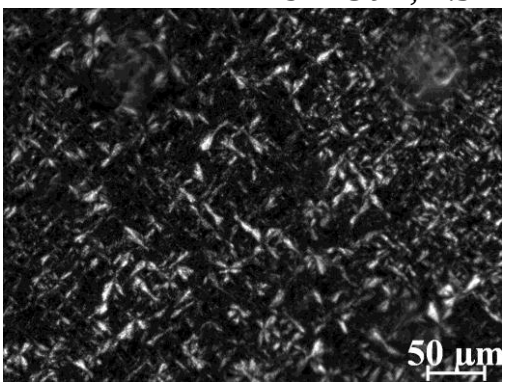

A

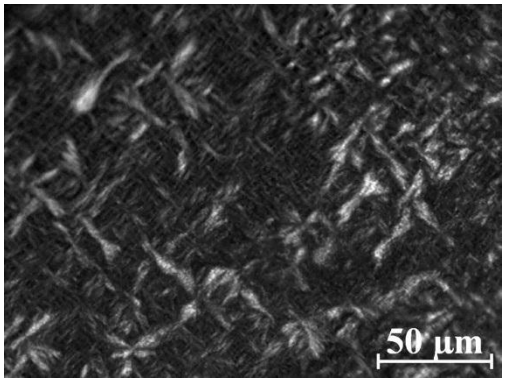

A'

sPPOt-2, 2.7 mol% of 1-octene

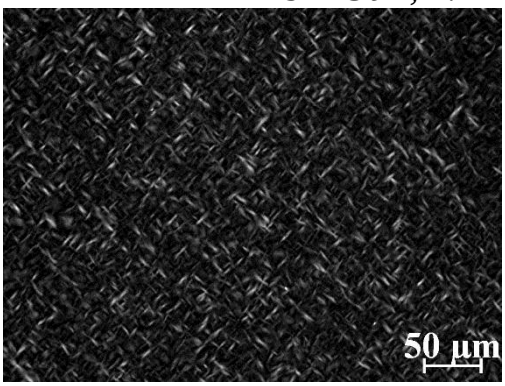

B

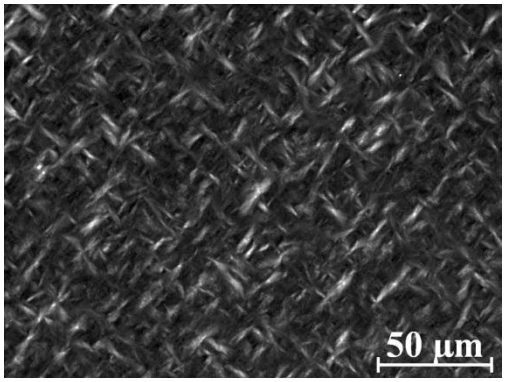

B'

sPPOt-4, 4 mol% of 1-octene

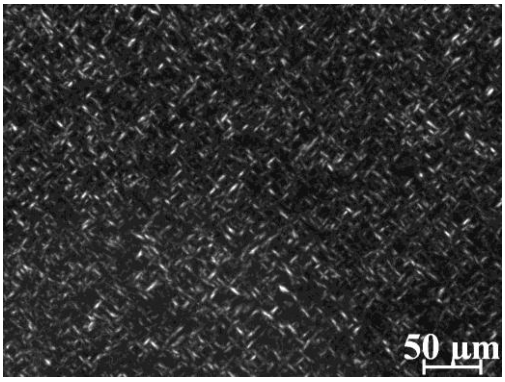

C

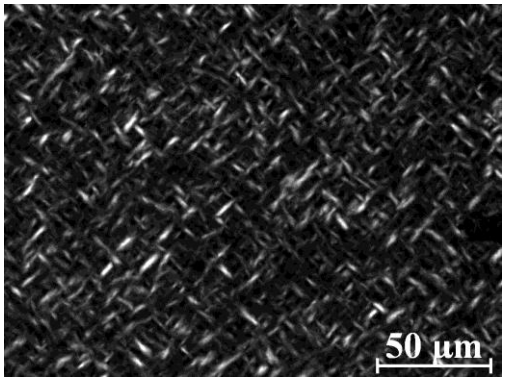

C'

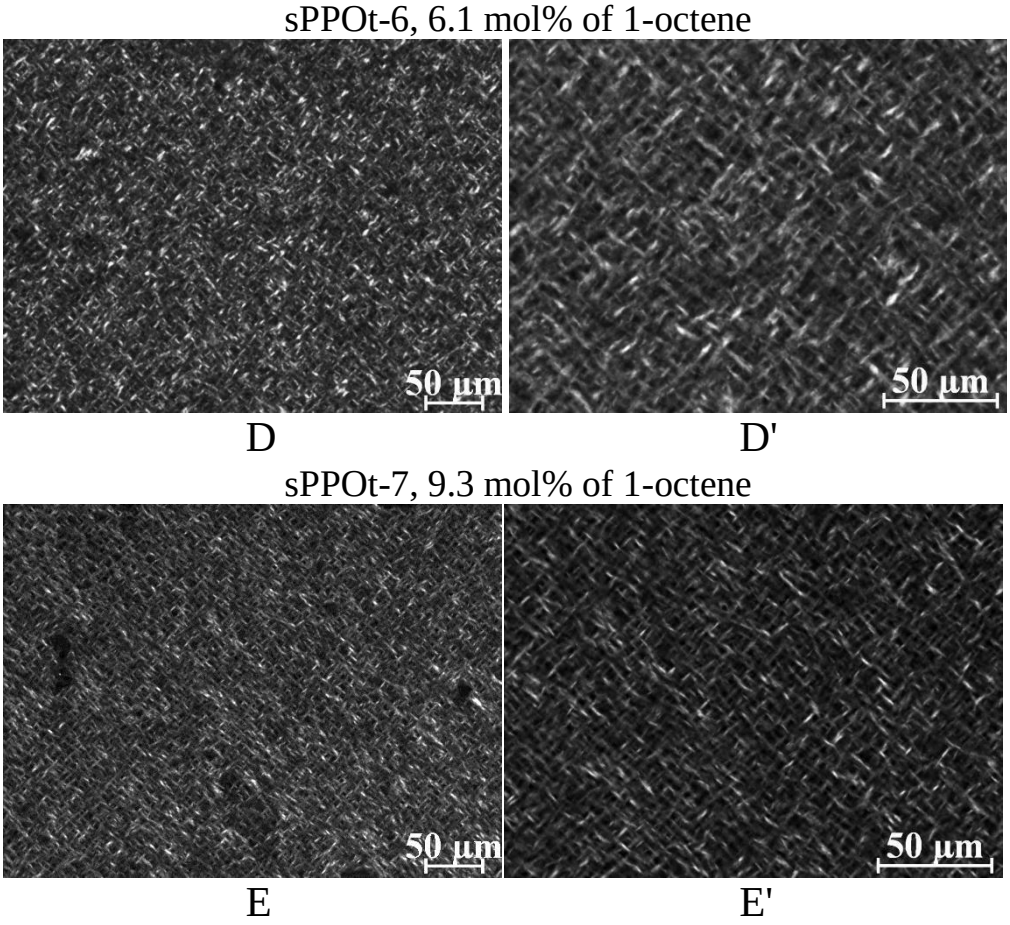

Figure 1.49. *POM images of samples sPPOt-1 with 1.9 mol% of 1-octene (A,A'), sPPOt-2 with 2.7 mol% of 1-octene (B,B'), sPPOt-4 with 4 mol% of 1-octene (C,C') sPPOt-6 with 6.1 mol% of 1-octene (D,D') and sPPOt-7 with 9.3 mol% of 1-octene (E,E').*

1.6.6. Crystal morphology of copolymers of sPP with 1-dodecene, 1-octadecene and 1-eicosene

Copolymers of sPP with branched comonomers as 1-dodecene (C12), 1-octadecene (C18) and 1-eicosene (C20) are still able to crystallize in form I of sPP as indicated by the presence of 200 and 020 reflections at $2\theta = 12$ and 16°, respectively, in the diffraction profiles of Figures 1.50A, 1.51A and 1.52A, respectively. The weak reflection at $2\theta = 17°$ in the diffraction profiles of the as-prepared samples indicates the presence of small amount of crystals of form II of sPP.

These copolymers show a similar crystallization behavior from the melt and similar morphology of crystals. All samples crystallize from the melt in the form I of sPP, as demonstrated by the diffraction profiles of Figures 1.50B, 1.51B and 1.52B. All samples show good elastic properties (data not shown). For 1-dodecene, 1-octadecene and 1-eicosene concentrations lower than 5, 5 and 3 mol% respectively the elastic properties are associated with the reversible transformation between the polymorphic forms of sPP with chains in *trans*-planar conformation, obtained by stretching, and the helical forms, formed by releasing the tension. (data not shown). For less crystalline samples, with higher comonomer concentrations no phase transformations occur during deformation and relaxation (data not shown) and the elastic recovery has a pure entropic origin, as in conventional elastomers.

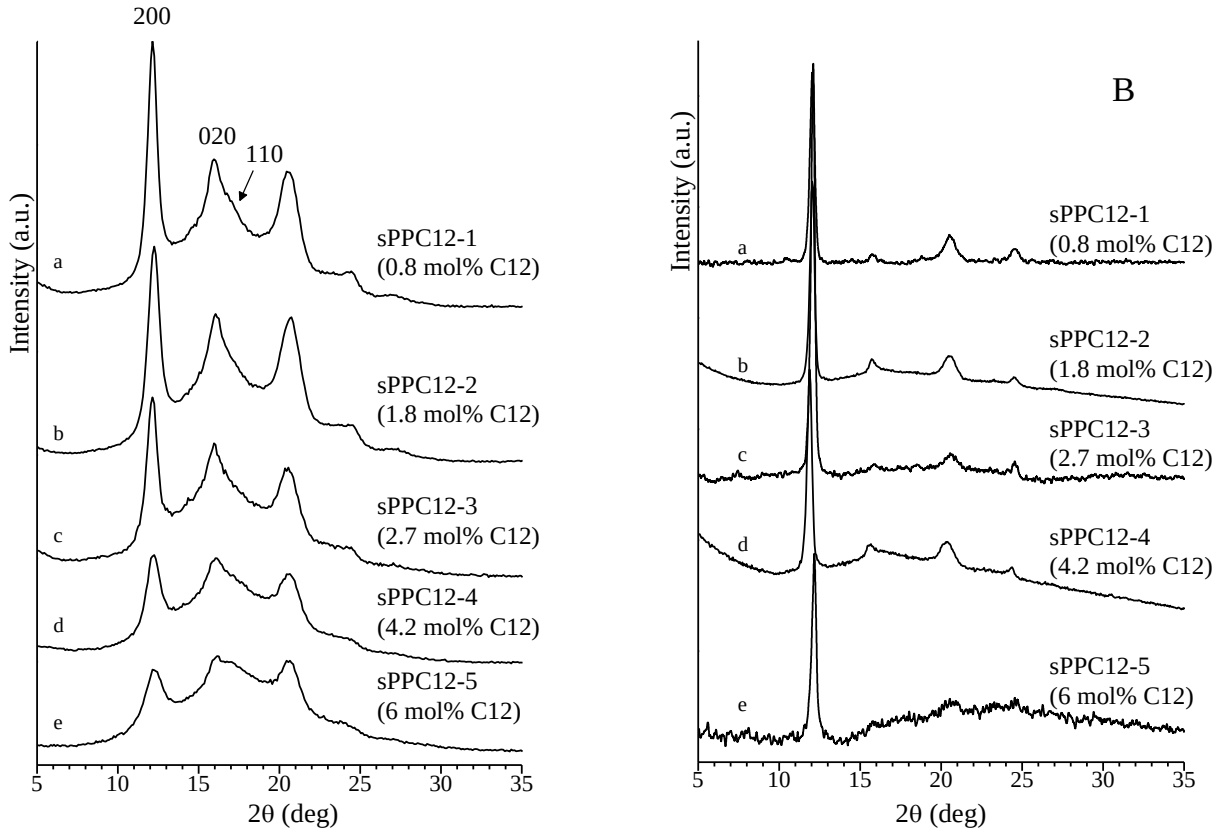

Figure 1.50. *X-ray powder diffraction profiles of as-prepared (A) and selected samples crystallized from the melt at cooling rate of 2.5 °C/min (B) of sPPC12 copolymers of Table 1.8 prepared with the catalyst* ***1*** *of Chart 1. The 200 and 010 reflections at 2θ = 12 and 16°, respectively, of the helical form I, and the 110 reflection at 2θ = 17° of the helical form II of sPP are indicated.*

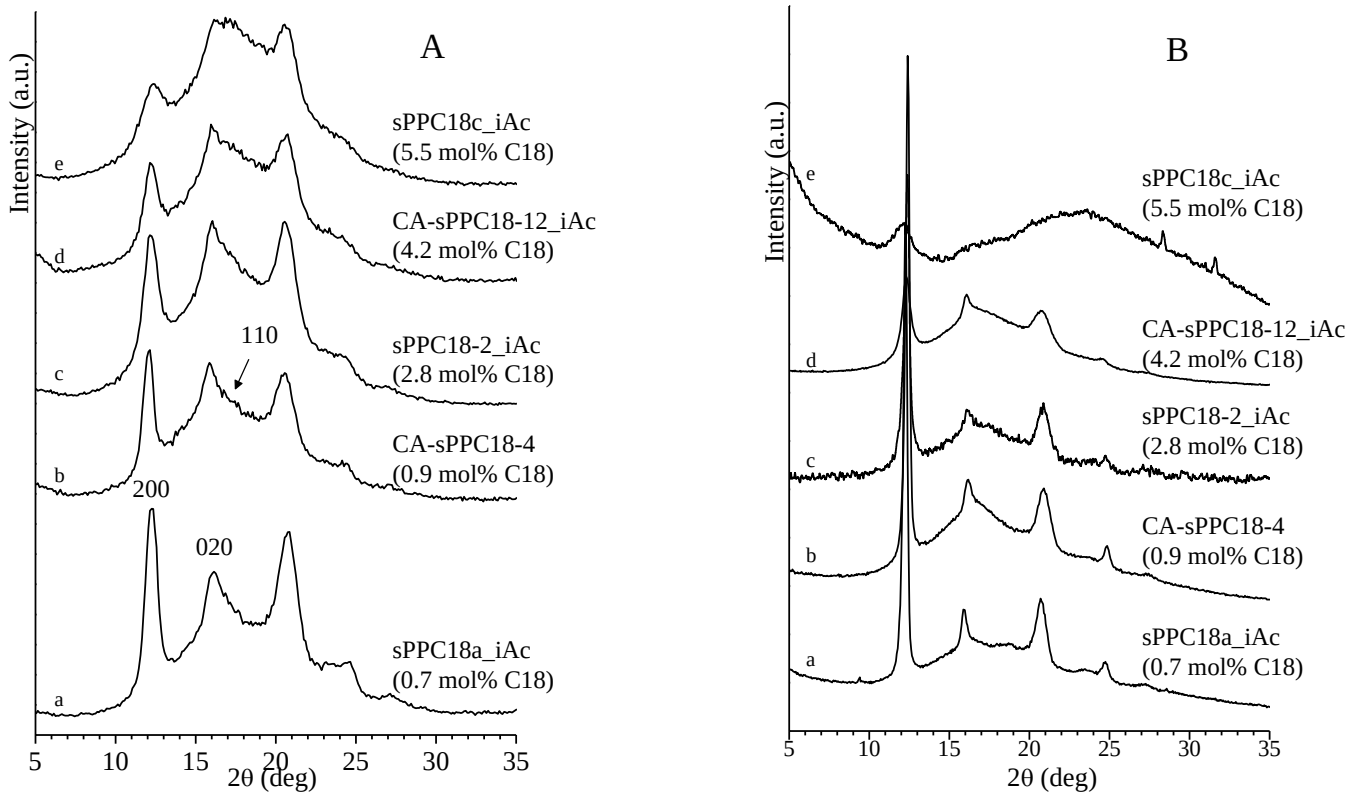

Figure 1.51. *X-ray powder diffraction profiles of as-prepared (A) and selected samples crystallized from the melt at cooling rate of 2.5 °C/min (B) of sPPC18 copolymers of Table 1.9 prepared with the catalyst* ***1*** *of Chart 1. The 200 and 010 reflections at 2θ = 12 and 16°, respectively, of the helical form I, and the 110 reflection at 2θ = 17° of the helical form II of sPP are indicated.*

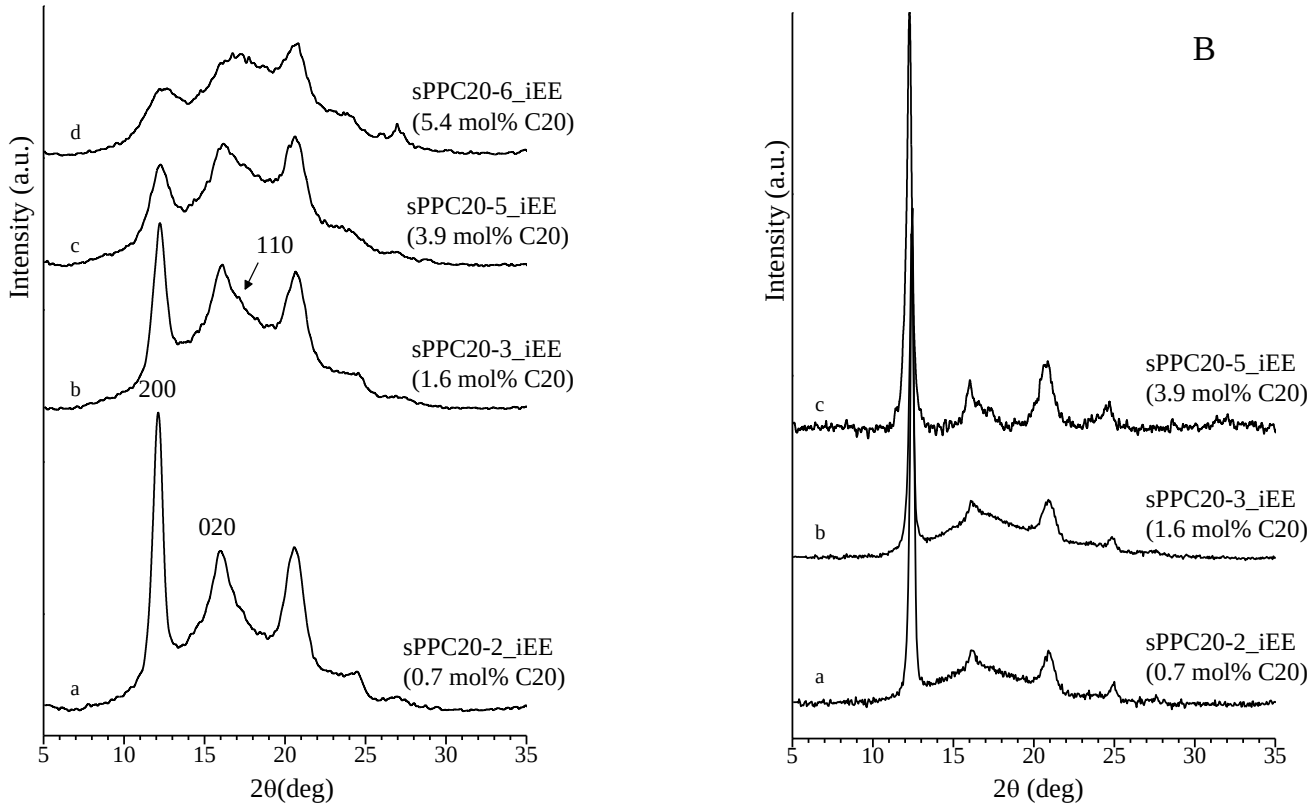

Figure 1.52. *X-ray powder diffraction profiles of as-prepared (A) and selected samples crystallized from the melt at cooling rate of 2.5 °C/min (B) of sPPC20 copolymers of Table 1.10 prepared with the catalyst* ***1*** *of Chart 1. The 200 and 010 reflections at 2θ = 12 and 16°, respectively, of the helical form I, and the 110 reflection at 2θ = 17° of the helical form II of sPP are indicated.*

The POM images of the samples of sPPC12, sPPC18 and sPPC20 copolymers crystallized from the melt at cooling rate of 2.5 °C/min of Figures 1.50B, 1.51B and 1.52B, in some cases aged at room temperature in order to achieve the complete crystallization and improve the birefringence, are shown in Figures 1.53, 1.54 and 1.55, respectively. For very low dodecene concentrations, morphology characterized by the presence of few small open multi-faceted aggregates, bow-tie aggregates, bundles of rod-like lamellae over the less evident needle crystals network has been observed (Figure 1.53A,A'). As dodecene content increases, open multi-faceted aggregates disappear while bow-tie crystals become thinner and thinner (Figures 1.53B,B'-C,C') until they disappear completely in samples with the highest dodecene content (Figures 1.53D,D'-E,E').

sPPC12-1, 0.8 mol% of 1-dodecene

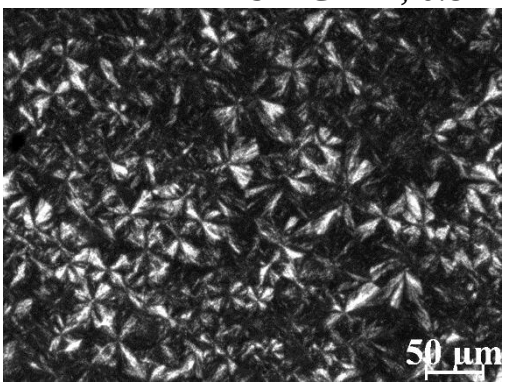

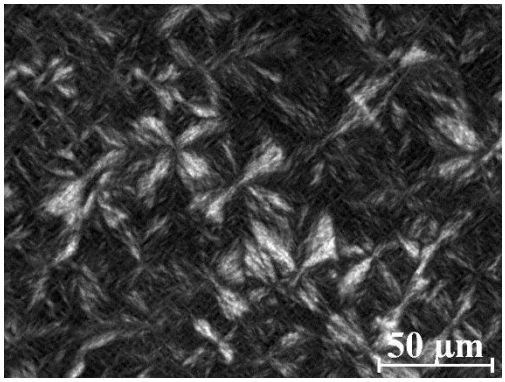

A A'

sPPC12-2, 1.8 mol% of 1-dodecene

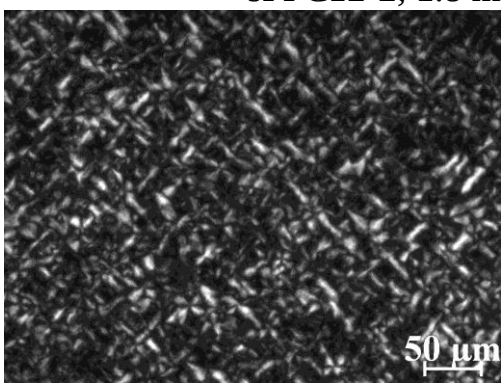

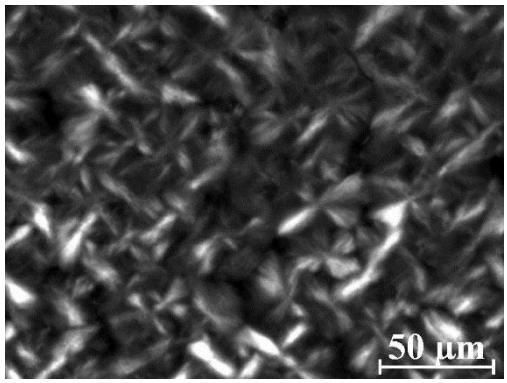

B B'

sPPC12-3, 2.7 mol% of 1-dodecene

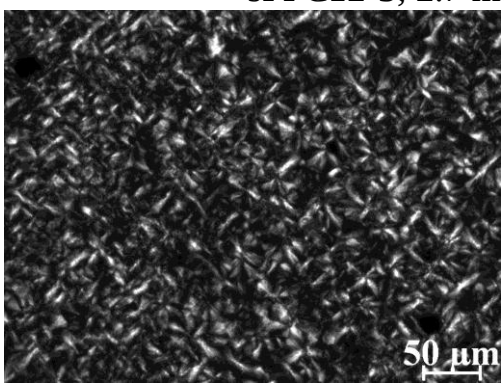

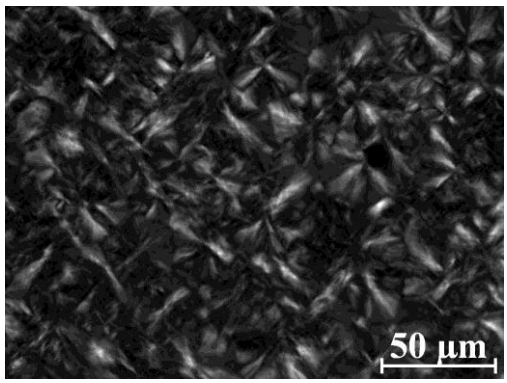

C C'

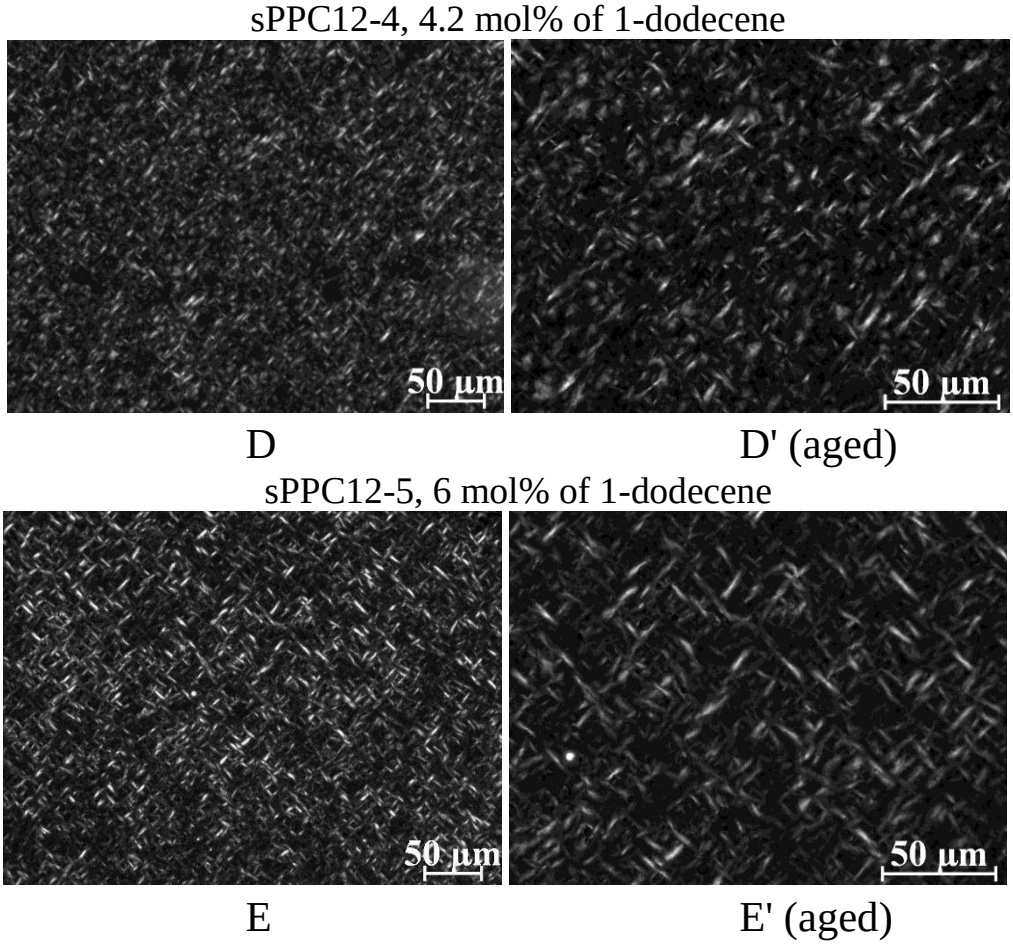

Figure 1.53. *POM images of samples sPPC12-1 with 0.8 mol% of 1-dodecene (A,A'), sPPC12-2 with 1.8 mol% of 1-dodecene (B,B'), sPPC12-3 with 2.7 mol% of 1-dodecene (C,C') sPPC12-4 with 4.2 mol% of 1-dodecene (D,D') and sPPC12-5 with 6 mol% of 1-dodecene (E,E').*

Similar morphologies have been observed in sPPC18 copolymers. In this case the correlation with the composition is less clear than in sPPC12 copolymers. When the 1-octadecene content is lower than 1 mol% open multi-faceted aggregates, bow-tie aggregates, bundles of rod-like lamellae over the less evident needle crystals network are clearly visible (Figures 1.54A,A'-B,B'). As octadecene increases a "salt and pepper" morphology with few small and thin needle crystals more visible at high magnification has been observed (Figures 1.54C,C'). Further decrease of octadecene content leads to the appearance of a clear thick needle crystals network (Figures 1.54D,D').

Sample sPPC18C_iAc does not crystallize from the melt and no birefringence has been observed even after long aging time.

sPPC18-a_iAc, 0.7 mol% of 1-octadecene

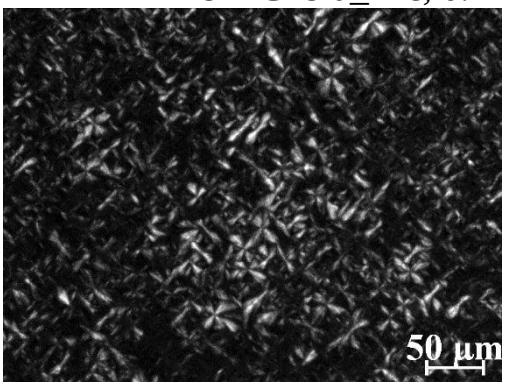

A

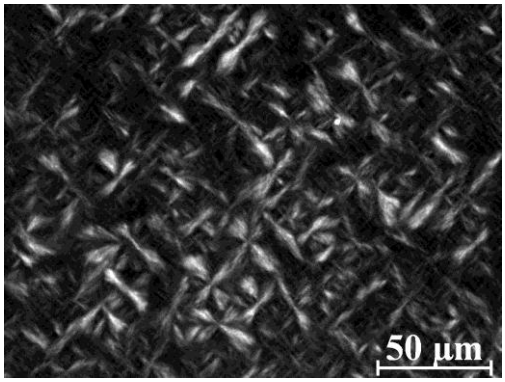

A'

CA-sPPC18-4_iAc, 0.9 mol% of 1-octadecene

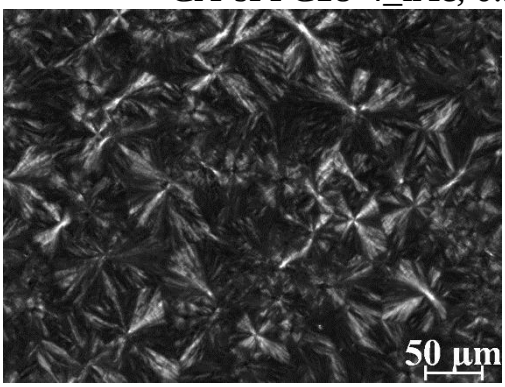

B

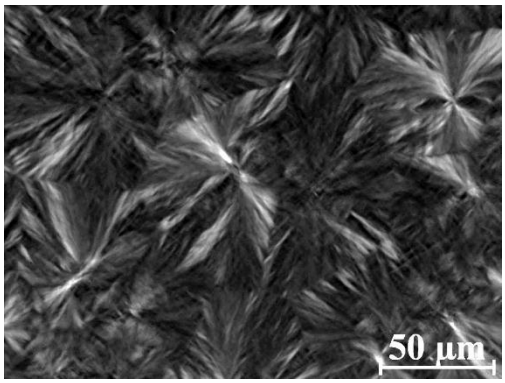

B'

sPPC18-2_iAc, 2.8 mol% of 1-octadecene

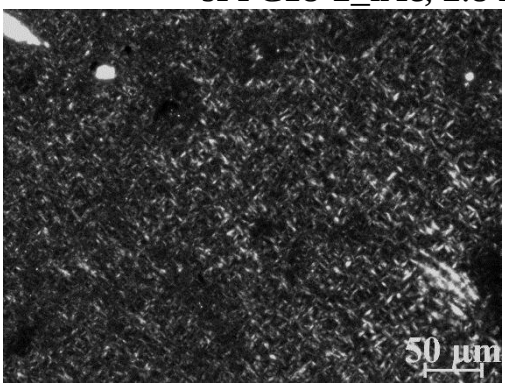

C

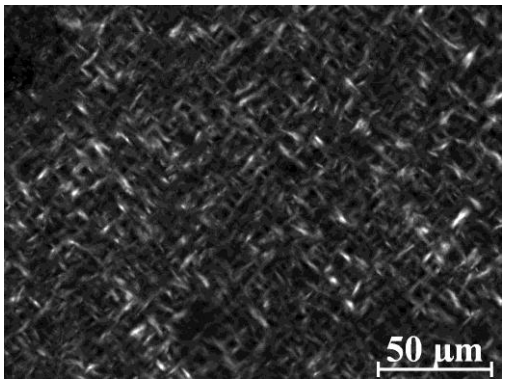

C'

CA-sPPC18-12_iAc, 4.2 mol% of 1-octadecene

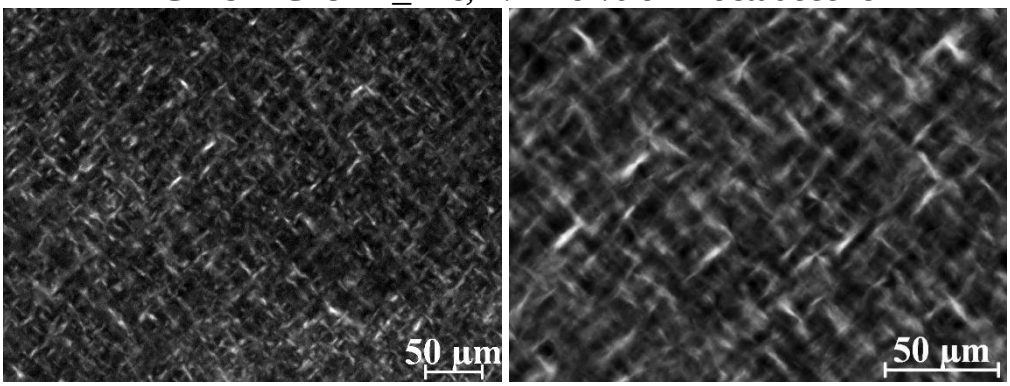

D D'

Figure 1.54. *POM images of samples sPPC18-a_iAc with 0.7 mol% of 1-octadecene (A,A'), CA-sPPC18-4_iAc with 0.9 mol% of 1-octadecene (B,B'), sPPC18-2_iAc with 2.8 mol% of 1-octadecene (C,C') and CA-sPPC18-12_iAc with 4.2 mol% of 1-octadecene (D,D').*

Samples of copolymers of sPP with 1-eicosene are an exemplary case of the general effect of comonomer content on morphology of sPP and its copolymers observed in all samples discussed above. When comonomer concentration is lower than 1 mol%, bundles of rod lamellae, bow-tie and open multi-faceted aggregates are clearly visible over the less evident needle crystals network (Figures 1.55A,A'-B,B'). These space filled superstructures completely disappear for comonomer content around 4 mol% and only needle-like morphology remains (Figure 1.55C,C'). In particular, in the sample sPPC20-5_iEE with 3.9 mol% of 1-eicosene the needle-like crystals form a dense network (Figure 1.55C,C'). Finally, sample sPPC20-6_iEE does not crystallize from the melt and no birefringence has been observed even after long aging time.

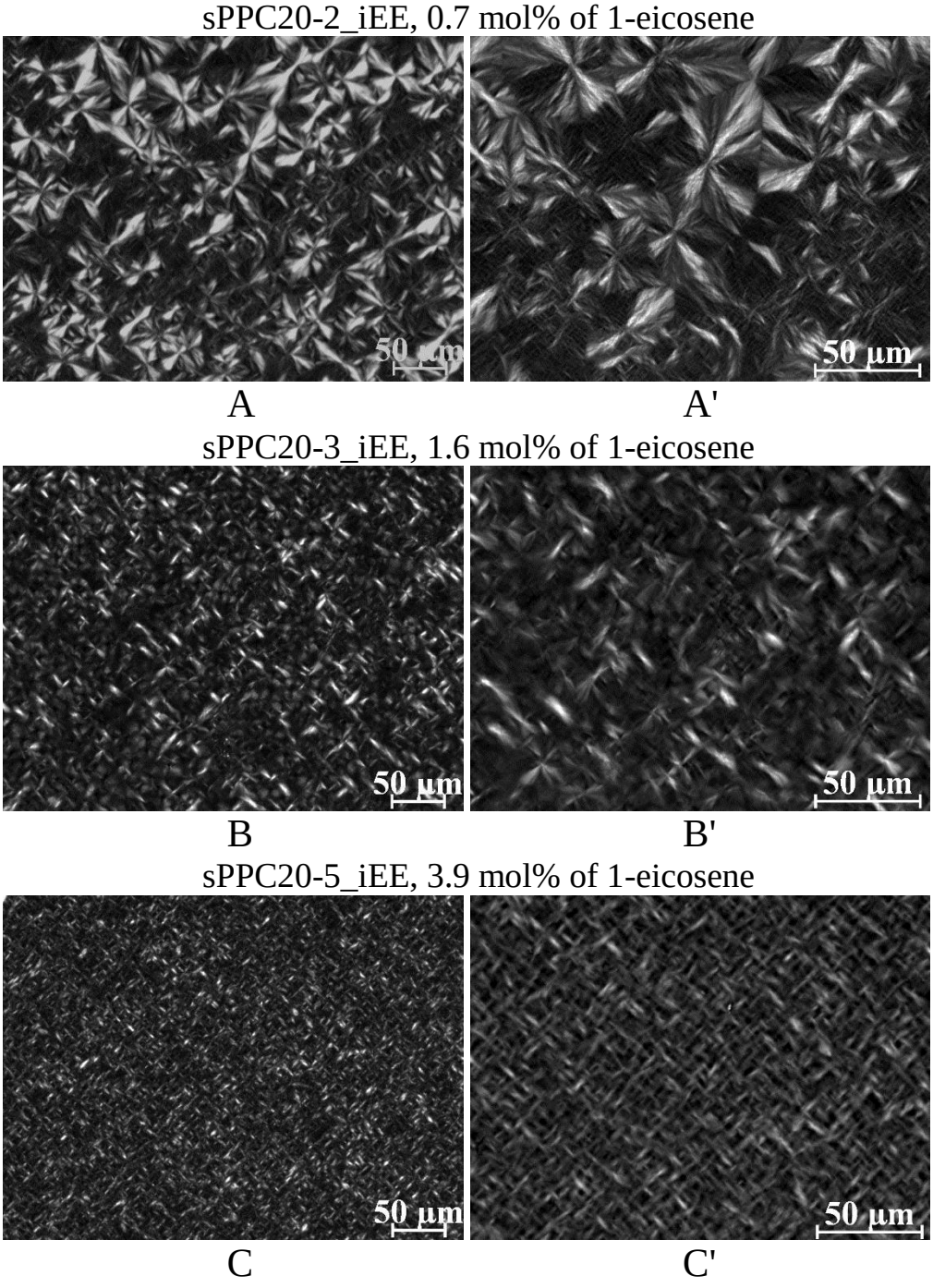

Figure 1.55. *POM images of samples sPPC20-2_iEE with 0.74 mol% of 1-eicosene (A,A'), sPPC20-3_iEE with 1.61 mol% of 1-eicosene (B,B'), sPPC20-5_iEE with 3.9 mol% of 1-eicosene (C,C').*

As in sPPs samples of different stereoregularity, also in for copolymers of sPP, this analysis has shown that, in addition to the superstructures observed for low comonomer content, that is, bundles of rod-like lamellae and bow-tie aggregates, which are observed in thinner regions of the films, also needle-like birefringent entities are always present in thicker regions of the films of all samples, regardless of stereoregularity. This is shown in Figure 1.56, where POM images recorded in thick regions of the films of all samples with a comonomer content in the range 0.7-3.2 mol% are reported. For all copolymers, from ethylene to 1-eicosene comonomers, at any comonomer concentration the morphology reveals an interwoven crystalline structure embedded in the amorphous matrix. This morphology is in agreement with the observed elastomeric behavior of all copolymers of sPP.

sPPET(3), 2.6 mol% of ethylene

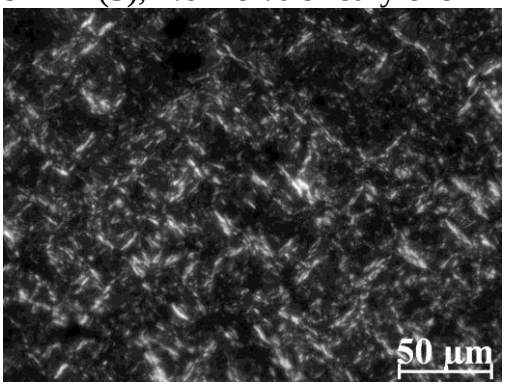

A

sPPBu-1, 3.2 mol% of 1-butene

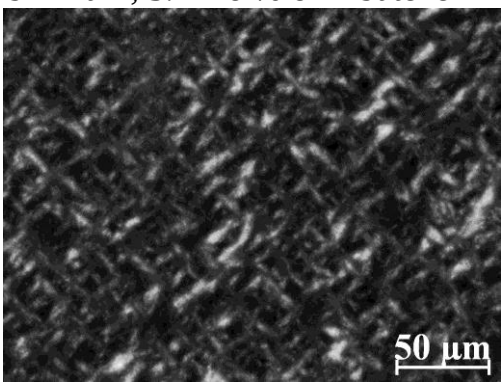

B

sPP4M1P-1, 1.8 mol% of 4MP

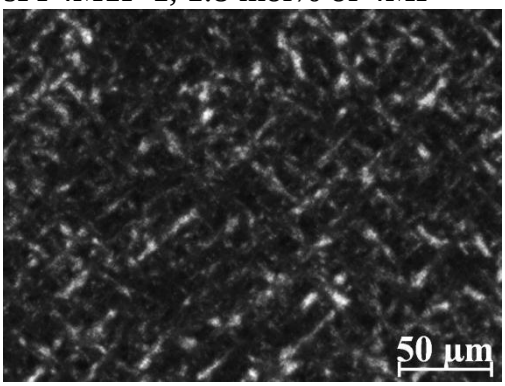

C

sPPHe-1, 1.7 mol% of 1-hexene

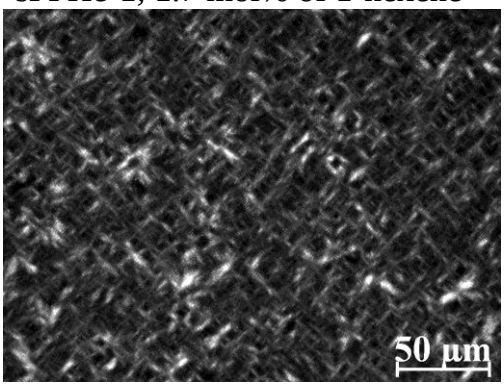

D

sPPOt-1, 1.9 mol% of 1-octene

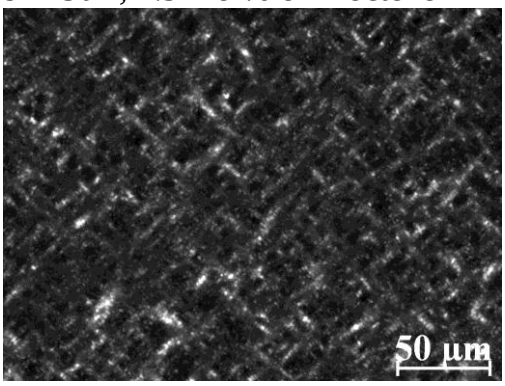

E

sPPC12-1, 0.8 mol% of 1-dodecene

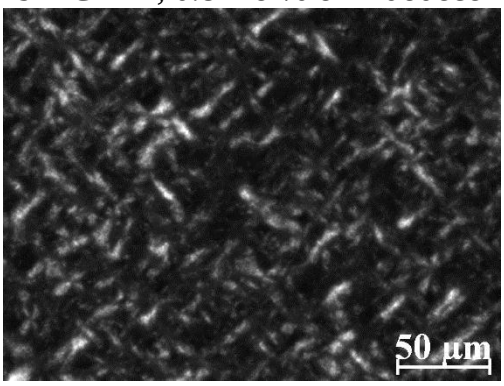

F

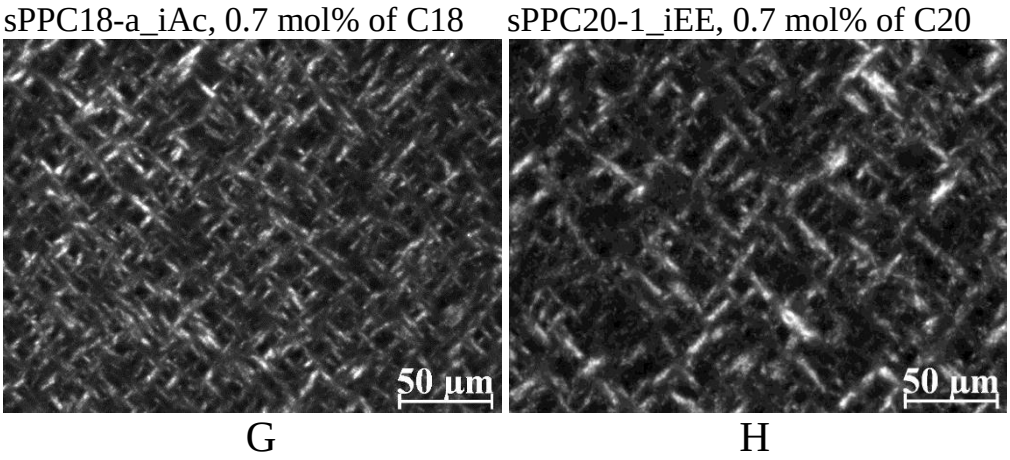

Figure 1.56. *Comparison of POM images of samples sPPEt(3) with 2.6 mol% of ethylene (A), sPPBu-1 with 3.2 mol% of 1-butene (B), sPP4M1P-1 with 1.8 mol% of 4-methyl-1-pentene (C), sPPHe-1 with 1.7 mol% of 1-hexene (D), sPPOt-1 with 1.9 mol% of 1-octene (E), sPPC12-1 with 0.8 mol% of 1-dodecene (F), sPPC18-a_iAc with 0.7 mol% of 1-octadecene (G), sPPC20-1_iEE with 0.7 mol% of 1-eicosene (N).*

1.6.7. Comparison between effects of stereodefects and constitutional defects on morphology of sPP

In the previous sections the influence of the presence of comonomers and their concentration on the crystal morphologies observed in random copolymers of sPP has been discussed. For low comonomer contents superstructures such as open multi-faceted aggregates and bow-tie crystals have been observed, together with the interwoven morphology formed by bundle-like and needle-like crystals. For high comonomer contents the space filled superstructures completely disappear and only the needle-like interwoven morphology remains. The comonomer concentration at which the bigger aggregates, such as the bundles of rod lamellae and bow-tie crystals, are still visible and at which they disappear leaving only needle-like crystals, depends on the size of the comonomeric units and on their possible inclusion or exclusion into crystals of form I or form II of sPP. In general, the comonomer concentration at which bigger aggregates disappear decreases with increasing size of comonomer unit.

In this section the role played by the type of comonomer (short or branched comonomer), and then by the type of defect (stereodefect or constitutional defect) on the morphology will be discussed. A comparison of POM images at the same magnification of samples of sPP homopolymer of different stereoregularity with the total concentration of stereodefects in the range 2.6-3.8% and samples of different sPP copolymers with comonomer concentration in the similar range of 2.6-4 mol%, is shown in Figure 1.57. Excluding the sample sPP4 with concentrations of *rrrr* pentad of 92.5% and total steric defects of 3.4% showing rare star structures, in copolymers with short comonomers, such as ethylene and butene, the presence of the ethylene or butene constitutional defects exerts the same influence of stereodefects on the morphology of sPP. In fact similar structures such as bow-tie and bundle crystals, in addition to the interwoven needle-like morphology, have been observed in samples of homopolymers sPP3, sPP5 and sPP6 with total concentration of defects of 2.6, 3.5 and 3.8%, respectively (Table 1.1), and copolymers sPPEt(3) and sPPBu-1 with 2.6 mol% of ethylene and 3.1 mol% of butene, respectively (Figure 1.57A,C,D,E,F).

sPP3, [*total defects*] = 2.6 mol%

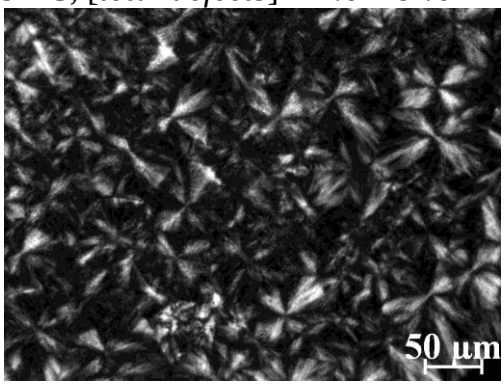

A

sPP4, [*total defects*] = 3.4 mol%

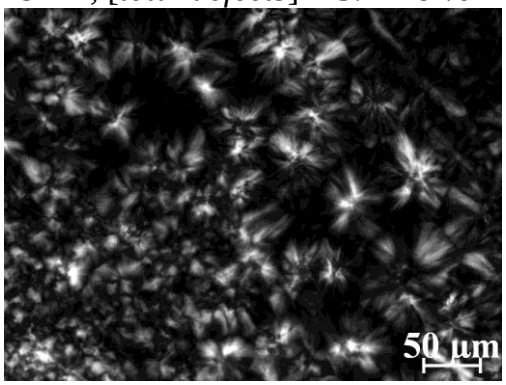

B

sPP5, [*total defects*] = 3.5 mol%

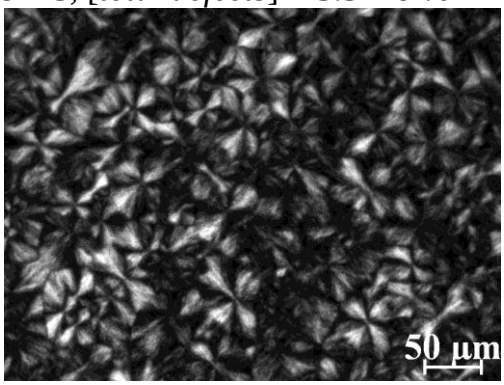

C

sPP6, [*total defects*] = 3.8 mol%

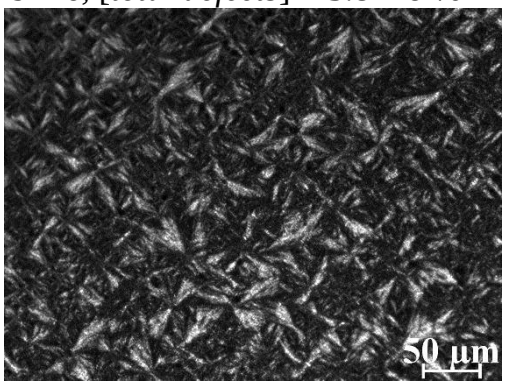

D

sPPEt(3), 2.6 mol% of ethylene

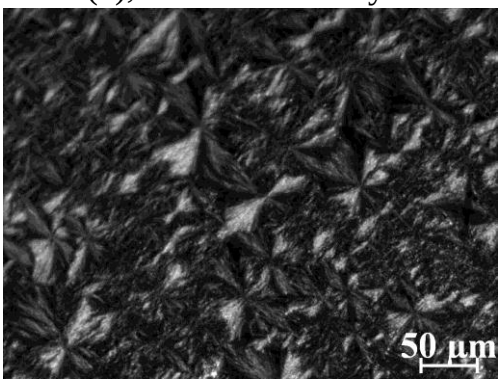

E

sPPBu-1, 3.2 mol% of 1-butene

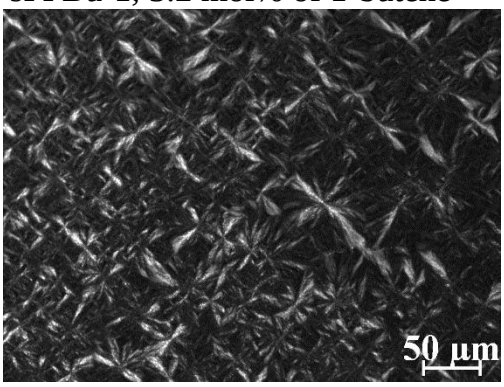

F

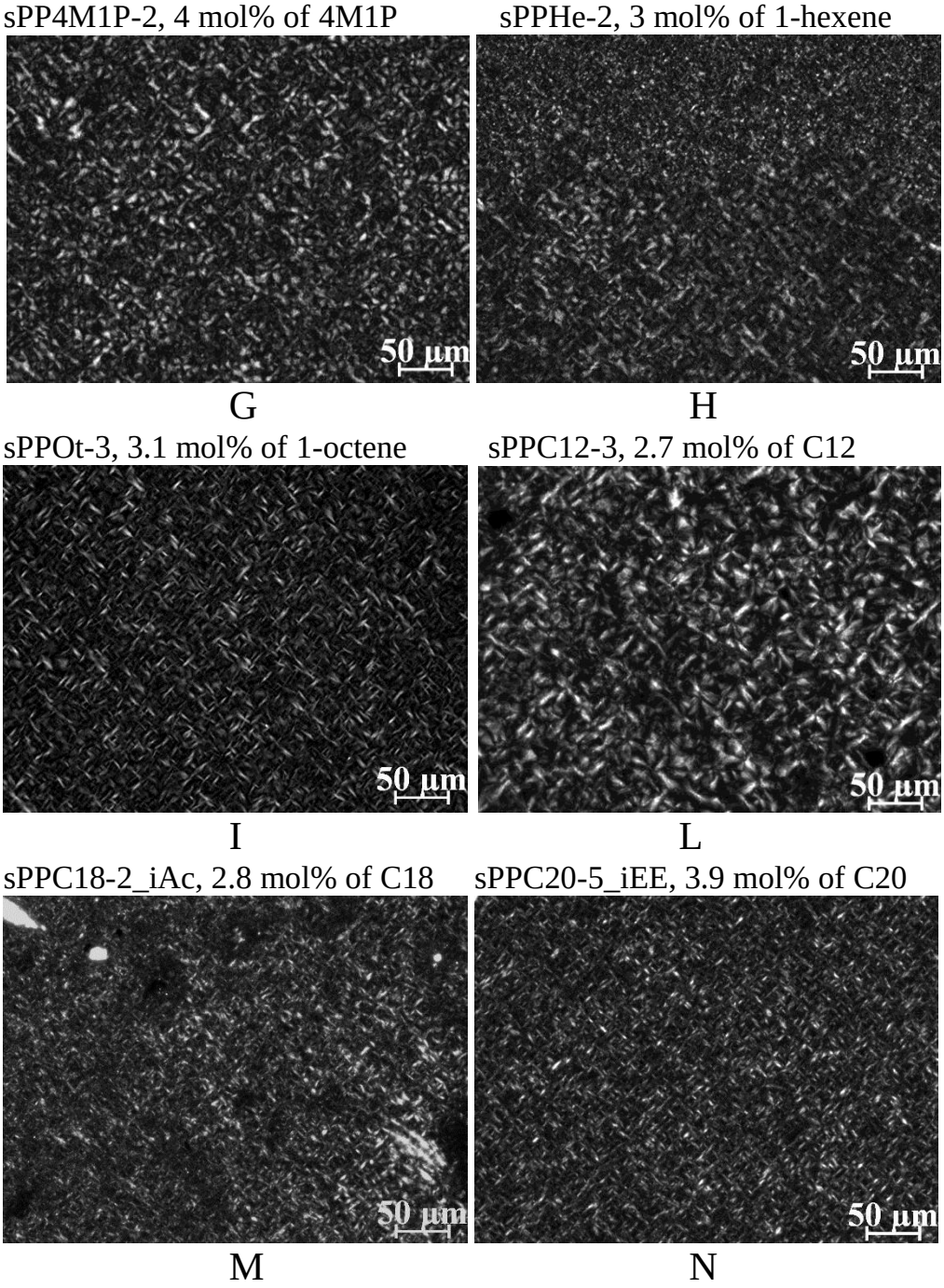

Figure 1.57. *Comparison of POM images of samples sPP3 with [total defects] =2.6% (A), sPP4 with [total defects] =3.4 mol% (B), sPP5 with [total defects] =3.5 mol% (C), sPP6 with [total defects] =3.8 mol% (D), sPPEt(3) with 2.6 mol% of ethylene (E), sPPBu-1 with 3.2 mol% of 1-butene (F), sPP4M1P-2 with 4 mol% of 4-methyl-1-pentene (G), sPPHe-2 with 3 mol% of 1-hexene (H), sPPOt-2 with 3.1 mol% of 1-octene (I), sPPC12-3 with 2.7 mol% of 1-dodecene (L), sPPC18-2_iAc with 2.8 mol% of 1-octadecene (M), sPPC20-5_iEE with 3.9 mol% of 1-eicosene (N).*

In copolymers with comonomers longer than 1-butene, such as 4-methyl-1-pentene, 1-hexene, 1-octene and 1-dodecene, with the same comonomer concentration in the range 2.6-4 mol% only needle crystals and some slightly bigger bundle-like crystals, have been observed (Figure 1.57G-N). This is due to the presence of longer comonomers that are always excluded from crystals of form I and form II and that slow down the crystallization kinetics avoiding the formation of bigger structures. This is also proved by the fact that in copolymers with the longest comonomers, that is 1-octadecene and 1-eicosene, "salt and pepper" and needle-like morphologies without bundles or bigger structures have been observed already at relatively low comonomer concentrations.

1.6.8. Concluding remarks on the analysis of crystal morphology

The influence of steric and constitutional defects on structure and mechanical properties of sPP and random copolymers based on sPP has been already discussed in literature and in previous sections.[1,109-128,134-138,140,142,143,146,155] The crystallinity, the mechanical properties and the nature of elastic behavior (enthalpic or entropic) depend on the concentration of stereodefects (*m* diad and *mm* triad) in sPP with different stereoregularity or on the type and concentration of constitutional defects (comonomeric units) in sPP random copolymers. The presence of steric defects affects the degree of crystallinity and in turn the occurrence of the polymorphic transitions during deformation and relaxation. For high concentrations of stereodefects very low crystallinity is achieved and formation of the trans-planar form III at high deformation is prevented. Therefore, the elastic behavior observed in poorly syndiotactic samples is mainly entropic.[134-138]

In random copolymers of sPP, the presence of constitutional defects affects the conformational transition since high concentration of ethylene stabilizes the *trans*-planar conformation, while high concentration of long and branched comonomers stabilizes the helical conformation. In any case, high concentration of comonomeric units prevents occurrence of the polymorphic transitions between trans-planar form III and the helical form II during deformation and relaxation. Therefore, in these materials the enthalpic contribution to the elasticity becomes negligible with increasing comonomer concentration.

In poorly crystalline samples, where all polymorphic transformations are prevented because of the high concentration of defects, the small crystalline

domains in the amorphous matrix act as physical knots of the elastomeric lattice, preventing the viscous flow of the amorphous chains. Since the molecular weights of the samples are very high, the amorphous chains, in turn, are highly entangled and connect as *tie-chains* the small crystalline domains. They act as spring between the crystals being well-oriented and in extended conformation in the stretched state, and return in the disordered coil conformation when the tension is removed. The result is a complex network made of rigid knots (crystals) and flexible tie-chains that accounts for the elastic behavior of these samples even at high defect concentration. According to this structural model, these materials necessarily show mechanical properties of more or less flexibility, elasticity and strength that depend on the size and stability of knots (crystals) and length and entanglement density of tie-chains. This in turn depend on the degree of crystallinity and on the properties of the amorphous phase in term of packing length.[158] With increasing concentration of molecular defects (streodefects or constitutional defects) and decreasing crystallinity, size and stability of crystals decreases and the length of tie-chains increases. If in these materials the space-filled spherulites, typical of high crystalline polymers, are replaced by thin and elongated crystals, and if the amorphous tie-chains connecting these crystals are highly entangled, it is expected that the resulting network acts as an elastomeric network with development of elastic properties.

The study of the morphology reported in this chapter was, indeed, aimed at verifying the existence of such elastomeric network in sPP and copolymers of sPP and at finding evidences of the presence of small and thin crystals organized in an interwoven morphology acting as knots of the network. In addition, the study of the rheology of these materials could provide information about the entanglement density of the amorphous phase to support the hypothesis of a classic entropic contribution to the elasticity.

We have found that in sPPs and in copolymers of sPP with low defect concentrations (stereodefects or constitutional defects) crystals are organized in relatively big aggregates, such as bundles of rod lamellae, bow-tie and open multi-faceted aggregates, along with smaller needle crystals, but very big space-filled spherulitic superstructures are never observed. This morphology is in agreement with the ductility and flexibility of these materials notwithstanding the high degrees of crystallinity, and the relatively high mechanical strength. These crystalline aggregates are not able to fill the space as in the case of completely impinged spherulites of highly crystalline polymers (as isotactic

polypropylene), probably due to the properties of the amorphous chains connecting the crystals that fill and occupy the available space between the crystals. This morphology, in particular the presence of irregular open aggregates and of the interwoven structure made by needle-type crystals, is also in agreement with the idea that the crystalline aggregates actively participate to the elasticity of sPP and its copolymers, locally acting as microscopic engines through the activation of reversible phase transformations during deformation and elastic recovery providing an enthalpic contribution to the elasticity, and with presence of an entropic contribution to the elasticity provided by the elastomeric network formed even in the presence of relatively big crystalline aggregates.

With increasing defect concentration in sPP and its copolymers (stereodefects or constitutional defects) we have found that the open crystalline aggregates (bundles of rod lamellae, bow-tie and open multi-faceted aggregates) are replaced by small and elongated needle-type crystals organized in an interwoven structure where thin and elongated crystals are connected by long amorphous tie-chains. This structure resembles a dense elastomeric network where small and thin crystals act as efficient knots of the network. This morphology accounts for the elastomeric properties shown by sPP and its copolymers when the concentration of defects is very high and crystallinity is very low.

1.7. Crystallization kinetics of sPP and copolymers

The different morphologies observed in sPPs of different stereoregularity and in copolymers of sPP with different comonomers may also be a result of different kinetics of crystallization and growth mechanisms induced by the presence of different types and concentration of defects. To verify this hypothesis a study of the crystallization kinetics in non-isothermal conditions, similar to the conditions used for the crystallization of the thin films prepared for the observation of the crystal morphology by POM, has been carried out by DSC measurements. The aim is to correlate the observed crystal morphology with the crystallization kinetics. All samples have been crystallized from the melt in DSC by cooling to room temperature at low cooling rate of 2.5 °C/min and the kinetics of the crystallization has been determined by evaluating the rate of crystallinity increase during crystallization time and treated with the Avrami model.

Samples of sPP homopolymers and copolymers have been heated at heating rate of 40 °C/min up to a temperature 20-30°C higher than the melting temperature T_m of the sample, kept at that temperature for 2-3 minutes, and then slowly cooled to room temperature at 2.5 °C/min. From the exothermic peaks observed in the cooling scans the evolution of the degree of crystallinity with time $x'(t\text{-}t_0)$ normalized for the total crystallinity achieved at the time t_{end} corresponding to the end of crystallization has been evaluated as:

$$x'(t-t_0)=\frac{\Delta H(t-t_0)}{\Delta H_{tot}}=\frac{\int_{t_0}^{t}\frac{dQ}{dt}dt}{\int_{t_0}^{t_{end}}\frac{dQ}{dt}dt} \qquad (1.1)$$

where

- t_0 is the time corresponding to the onset of crystallization (incipient crystallization), that is, the incubation time necessary to form stable nuclei;
- t_{end} is the time at the end of crystallization;
- dQ/dt is the heat flow released during the cooling scans;
- $\Delta H(t\text{-}t_0)$ is the crystallization enthalpy evaluated from t_0 up to a time t;
- ΔH_{tot} is the total crystallization enthalpy, evaluated from t_0 up to t_{end}.

We define the degree of crystallinity $x'(t\text{-}t_0)$ normalized for the total crystallinity achieved at the end of crystallization as *apparent crystallinity* whose values are comprised between 0 and 100%.

When crystallinity is plotted as a function of time a S-shaped curve is obtained. At the beginning the apparent crystallinity is zero, then it start increasing at the incubation time t_0 and rapidly increase up to the value of 100% is reached at t_{end}. The kinetics curves have been fitted by using the Avrami approach.

It is well known that the Avrami equation in the original formulation:

$x(t) = 1 - \exp(-K\, t^{n})$

gives the fraction of material crystallized after a the time t at a given crystallization temperature T_c. This equation was derived for isothermal

crystallization kinetics following the assumptions that: nucleation rate is either zero (i.e. crystallization occurs due to the growth of pre-existing nuclei) or constant; isotropical growth rate is proportional to either time t or to semi-crystallization time $t_{1/2}$ (depending whether the devitrification is interface or diffusion controlled).[159,160] Nevertheless, since many processes involving nucleation and growth occur in non-isothermal conditions, many attempts to fit the Avrami equation to non-isothermal experiments are reported in literature.[161]

In the application of the Avrami equation in non-isothermal crystallizations, the evaluated Avrami constants K and n could deviate from the real values. Under non-isothermal conditions, indeed, both the growth rate and the nucleation rate are no longer constant during the transformation. In general they are rapidly varying functions of temperature and in principle their functional dependence on temperature is quite different.[162]

However, the kinetics curves have been described using the following modified Avrami equation:

$$x'(t-t_0) = x'_0 + (1-x'_0)[1-\exp(-\ln(2)\,k^n\,(t-t_0)^n)] \qquad (1.2)$$

where:

- x'_0 is the crystallinity at the incipient crystallization time t_0,
- $x'(t\text{-}t_0)$ is the crystallinity developed at time t after the incubation time t_0
- k is the Avrami constant;
- n is the Avrami exponent.

The reciprocal of k is the semi-crystallization time $t_{1/2}$:

$$t_{1/2} = \frac{1}{k} \qquad (1.3)$$

If crystallinity develops from a complete amorphous or melted sample at t_0, then $x'_0 = 0$. This equation has been used for a rough evaluation of the Avrami constants. The value of the Avrami exponent n reflects the nucleation rate and/or the growth morphology. Generally, values of the Avrami exponent equal to 1, 2, 3 in case of heterogeneous nucleation, or equal to 2, 3, 4 in case of homogeneous nucleation, correspond to growth in 1, 2, 3 dimensions respectively. This means to assume nucleation rate equal to 0 in the first case,

constant in the second case. Values of Avrami exponents equal to 4 correspond to heterogeneous nucleation and growth in 3 dimensions. Not integer values of the Avrami exponent or values lower than 1 are attributable, for example, to the factors discussed above due to non-isothermal conditions: different mechanisms controlling the crystallisation process, a time dependent nucleation rate, possibility of simultaneous grain growth of the crystallized region during crystallization, impingement effect, which is important especially at the final stage of crystallization, if the anisotropy of the crystals is sufftciently high.[160b]

1.7.1. Crystallization kinetics of sPP of different stereoregularity

The DSC curves recorded during cooling from the melt at cooling rate of 2.5 °C/min of samples of sPP of different stereoregularity, with *rrrr* pentad concentration in the range 96-60%, that crystallize from the melt (see Figure 1.31), are reported in Figures 1.58A-1.69A. The corresponding crystallization kinetics curves, evaluated from the crystallization exotherms with the equation 1.1, and the fitting of these curves with the equation 1.2 are reported in Figures 1.58B-1.69B. The melt is achieved by heating at fast heating rate of 40 °C/min and the corresponding heating curves are also shown in Figures 1.58A-1.69A. Sample sPP12 does not crystallize from the melt and only the DSC curves are reported in Figure 1.69. The X-ray diffraction profiles of the samples crystallized in DSC after the cooling scans from the melt of Figures 1.58A-1.69A are reported in Figure 1.70. The diffraction profiles of thin films of the same samples of sPP crystallized from the melt in the same conditions by cooling at 2.5 °C/min, prepared for POM experiments of Figure 1.32-1.35, have already been shown in Figure 1.31C. Both data of Figure 1.70 and 1.31C show that that all samples cooled from the melt at 2.5 °C/min, used for the study of the crystallization kinetics or observed by POM, are crystallized in form I of sPP. Samples sPP12-sPP17 with *rrrr* pentad concentration lower than 60% do not crystallize from the melt, but they crystallize in form I by aging at room temperature.[134-138] The kinetics of crystallization form the amorphous phase of these stereoirregular samples have been reported in the literature,[137,138] therefore, these samples were not considered for the study of the kinetics of melt-crystallization with the Avrami model.

The melting (T_m) and crystallization (T_c) temperatures, and the melting (ΔH_m) and crystallization (ΔH_c) enthalpies for all samples are reported in the Table 1.11. Since the heating is performed at 40 °C/min the values of melting temperature and enthalpy are not significant. Figures 1.71A,B reports the

crystallization temperature (T_c) and enthalpy (ΔH_c) as a function of *rrrr* pentad concentration. As expected, both crystallization temperature and crystallization enthalpy decrease with decreasing stereoregulrity.

From the interpolation of the experimental data of Figures 1.58B-1.62B with the Avrami equation 1.2, the kinetic parameters, as the Avrami exponent *n*, the incipient crystallization time t_0, the semi-crystallization time $t_{1/2}$, defined as the time required for the crystallization of 50% of the crystallizable materials once crystallization has begun (starting from the incipient crystallization time $t_0 = 0$), and the total time ($t_{1/2} + t_0$) required to achieve 50% of the apparent crystallinity, have been evaluated. All the kinetic parameters are reported in Table 1.11. The values of the semi-crystallization time are also reported in Figure 1.71C as a function of the stereoregularity.

The values of Avrami exponent *n* are always included in the range 2-4. Higher values, in the range 3-4, have been observed in the most stereoregular samples (sRDG-2-1, sPP2 and sPP3) and, quite surprisingly, in the most defective samples (sPP9 and sPP10). These values are consistent with growth of crystals in 3 dimensions with homogeneous nucleation ($n = 4$), and crystals growth in 2 dimensions with homogeneous nucleation or in 3 dimensions with heterogeneous nucleation ($n = 3$). Lower values of *n* in the range 2-2.5 have been observed for all other samples and indicate crystals growth in 2 dimensions with heterogeneous nucleation or in 1 dimension with homogeneous nucleation.

Finally, the data of Table 1.11 and Figure 1.71C indicate that the values of semi-crystallization time $t_{1/2}$ are relatively low (≈ 100-200 s) in more stereoregular samples with [*rrrr*] higher than 85%, and much higher (≈ 300-500 s) in samples with *rrrr* content lower than 80%.

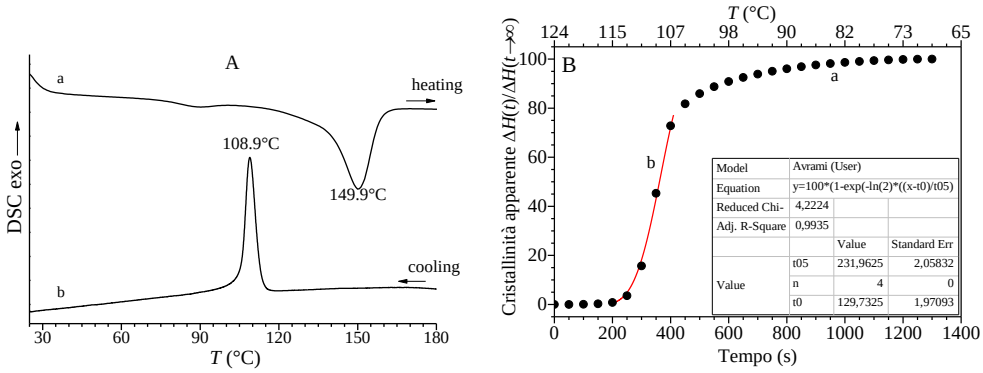

Figure 1.58. *DSC curves recorded during heating at 40°C/min from room temperature up to 190°C (a) and successive cooling to room temperature at 2.5°C/min (b) of the sample sRDG-2-1 ([rrrr]=95.5%) (A). Degree of apparent crystallinity as a function of time and temperature evaluated from DSC curves using equation 1.1 and interpolation with Avrami equation 1.2 (B).*

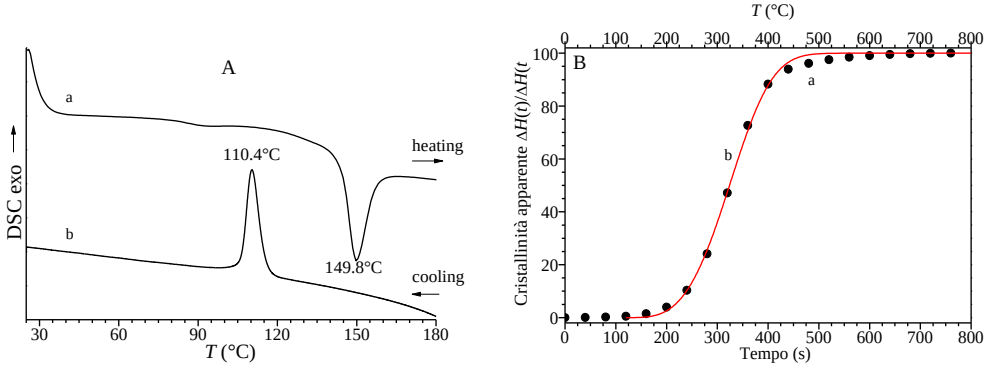

Figure 1.59. *DSC curves recorded during heating at 40°C/min from room temperature up to 190°C (a) and successive cooling to room temperature at 2.5°C/min (b) of the sample sPP2 ([rrrr]=95%) (A). Degree of apparent crystallinity as a function of time and temperature evaluated from DSC curves using equation 1.1 and interpolation with Avrami equation 1.2 (B).*

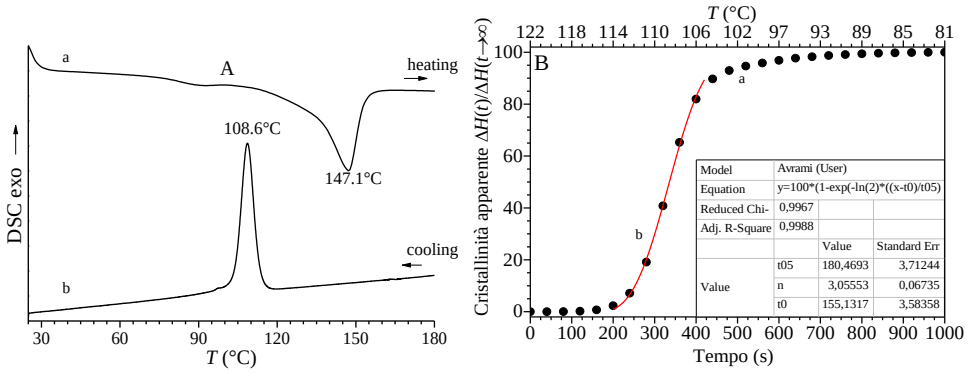

Figure 1.60. *DSC curves recorded during heating at 40°C/min from room temperature up to 190°C (a) and successive cooling to room temperature at 2.5°C/min (b) of the sample sPP3 ([rrrr]=94.2%) (A). Degree of apparent crystallinity as a function of time and temperature evaluated from DSC curves using equation 1.1 and interpolation with Avrami equation 1.2 (B).*

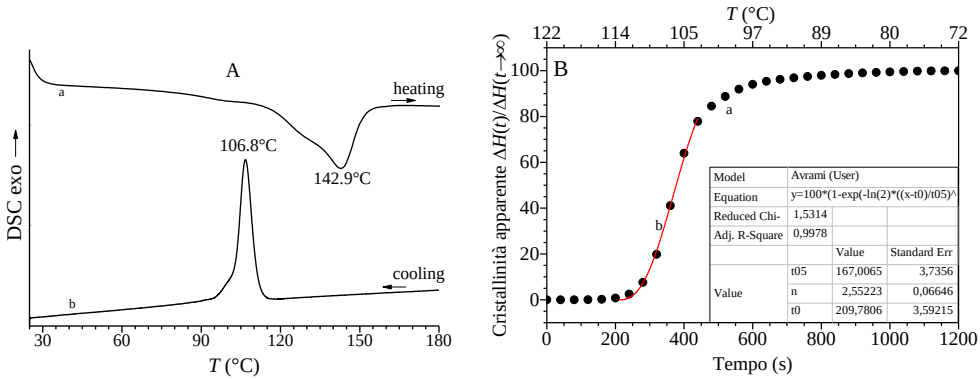

Figure 1.61. *DSC curves recorded during heating at 40°C/min from room temperature up to 190°C (a) and successive cooling to room temperature at 2.5°C/min (b) of the sample sPP4 ([rrrr]=92.5%) (A). Degree of apparent crystallinity as a function of time and temperature evaluated from DSC curves using equation 1.1 and interpolation with Avrami equation 1.2 (B).*

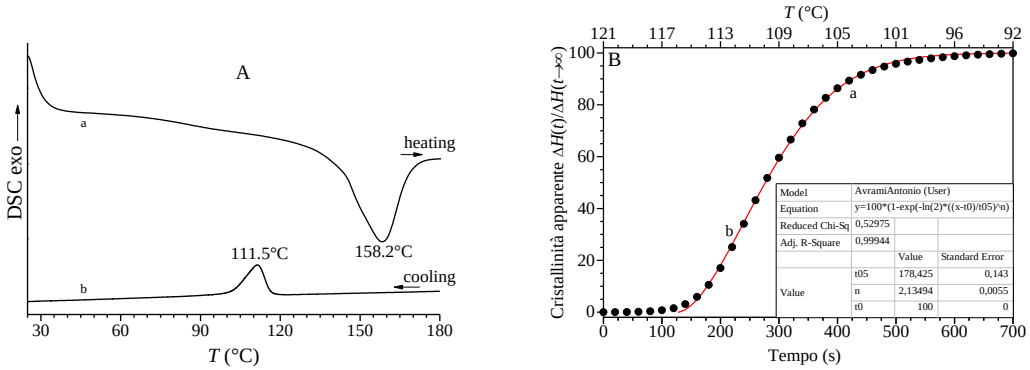

Figure 1.62. *DSC curves recorded during heating at 40°C/min from room temperature up to 190°C (a) and successive cooling to room temperature at 2.5°C/min (b) of the sample sPP5 ([rrrr]=91.5%) (A). Degree of apparent crystallinity as a function of time and temperature evaluated from DSC curves using equation 1.1 and interpolation with Avrami equation 1.2 (B).*

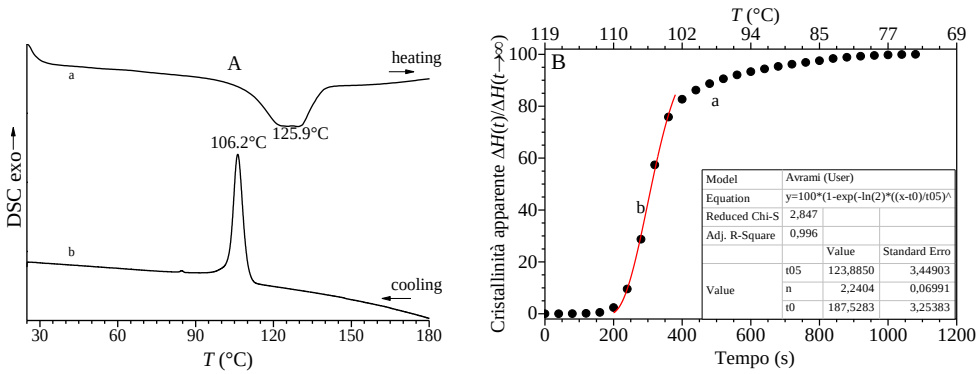

Figure 1.63. *DSC curves recorded during heating at 40°C/min from room temperature up to 190°C (a) and successive cooling to room temperature at 2.5°C/min (b) of the sample sPP6 ([rrrr]=90.7%) (A). Degree of apparent crystallinity as a function of time and temperature evaluated from DSC curves using equation 1.1 and interpolation with Avrami equation 1.2 (B).*

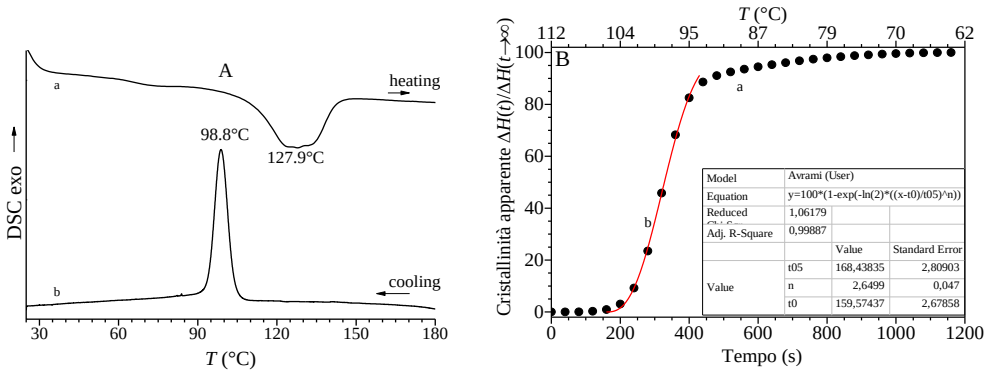

Figure 1.64. *DSC curves recorded during heating at 40°C/min from room temperature up to 190°C (a) and successive cooling to room temperature at 2.5°C/min (b) of the sample sPP7 ([rrrr]=88.6%) (A). Degree of apparent crystallinity as a function of time and temperature evaluated from DSC curves using equation 1.1 and interpolation with Avrami equation 1.2 (B).*

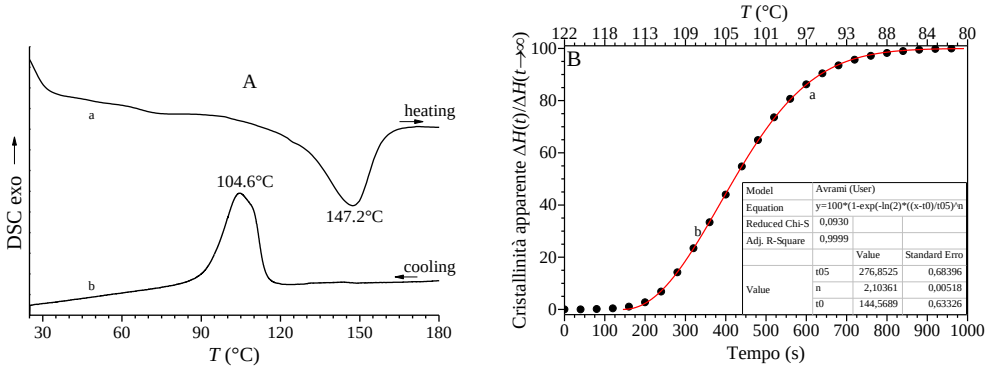

Figure 1.65. *DSC curves recorded during heating at 40°C/min from room temperature up to 190°C (a) and successive cooling to room temperature at 2.5°C/min (b) of the sample sPP8 ([rrrr]=87%) (A). Degree of apparent crystallinity as a function of time and temperature evaluated from DSC curves using equation 1.1 and interpolation with Avrami equation 1.2 (B).*

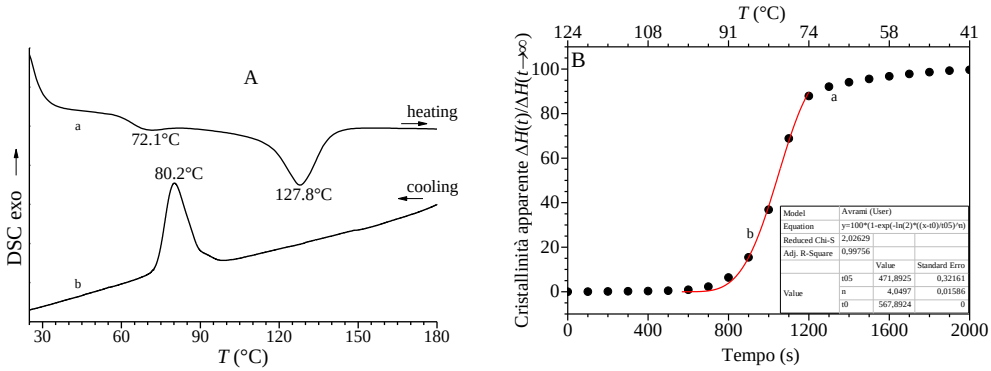

Figure 1.66. *DSC curves recorded during heating at 40°C/min from room temperature up to 190°C (a) and successive cooling to room temperature at 2.5°C/min (b) of the sample sPP9 ([rrrr]=78%) (A). Degree of apparent crystallinity as a function of time and temperature evaluated from DSC curves using equation 1.1 and interpolation with Avrami equation 1.2 (B).*

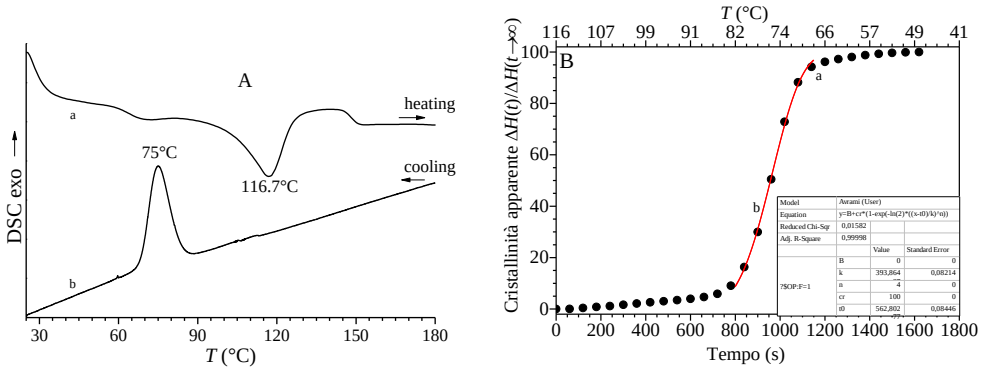

Figure 1.67. *DSC curves recorded during heating at 40°C/min from room temperature up to 190°C (a) and successive cooling to room temperature at 2.5°C/min (b) of the sample sPP10 ([rrrr]=74.8%) (A). Degree of apparent crystallinity as a function of time and temperature evaluated from DSC curves using equation 1.1 and interpolation with Avrami equation 1.2 (B).*

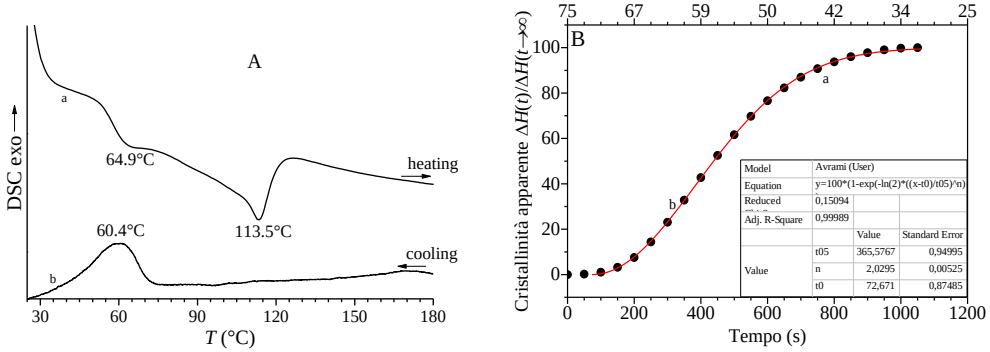

Figure 1.68. *DSC curves recorded during heating at 40°C/min from room temperature up to 190°C (a) and successive cooling to room temperature at 2.5°C/min (b) of the sample sPP11 ([rrrr]=70.6%) (A). Degree of apparent crystallinity as a function of time and temperature evaluated from DSC curves using equation 1.1 and interpolation with Avrami equation 1.2 (B).*

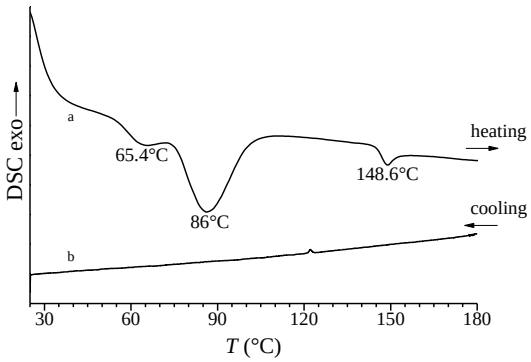

Figure 1.69. *DSC curves recorded during heating at 40°C/min from room temperature up to 190°C (a) and successive cooling to room temperature at 2.5°C/min (b) of the sample sPP12 ([rrrr]=60.1%).*

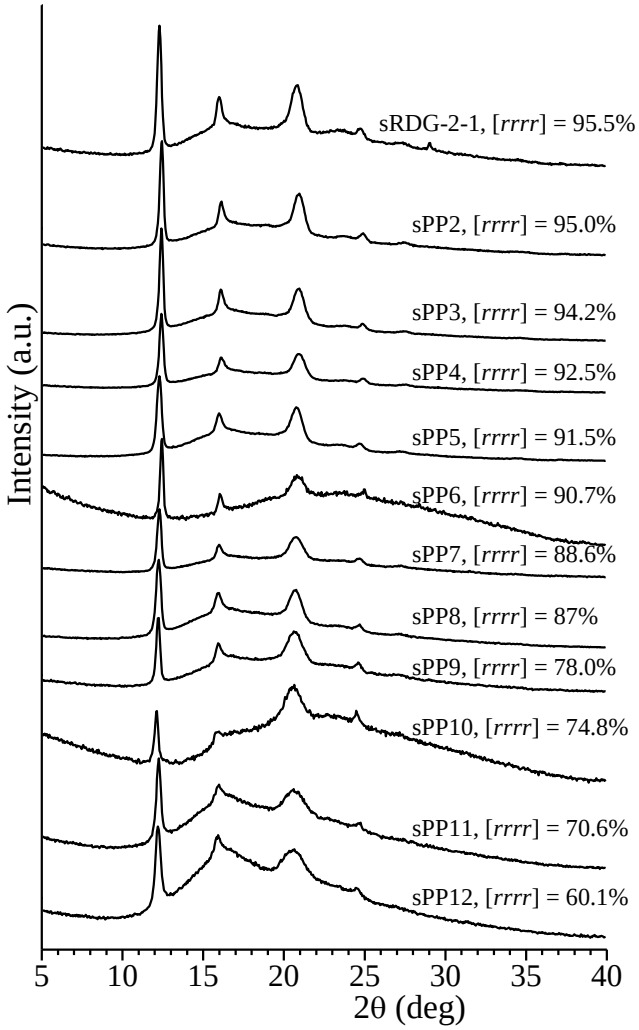

Figure 1.70. *X-ray powder diffraction profiles of samples of sPP of different stereoregularity crystallized from the melt in DSC by cooling at 2.5 °C/min cooling rate (curves b of Figures 1.58A-1.68A and 1.69).*

Table 1.11. *Melting temperature (T_m) and enthalpy (ΔH_m), crystallization temperature (T_c) and enthalpy (ΔH_c), Avrami exponent n, semi-crystallization time ($t_{1/2}$), incipient crystallization time (t_0) and time required to achieve 50% of the apparent crystallinity ($t_{1/2} + t_0$) of samples of sPP of different stereoregularity indicated as concentration of rrrr pentad.*

Samples	[*rrrr*] (%)	T_m (°C)	ΔH_m (J/g)	T_c (°C)	ΔH_c (J/g)	*n*	t_0 (s)	$t_{1/2}$(s)	$t_{1/2}+t_0$(s)
sRDG-2-1	95.5	149.9	-94.5	108.9	37	4	129.7	232	362
sPP2	95	149.8	-93.4	110.4	44.8	3.5	119.5	204	324
sPP3	94.2	147.1	-88.02	108.6	46.9	3.1	155.1	180	336
sPP4	92.5	142.9	-90.4	106.8	51.5	2.5	209.8	169	379
sPP5	91.5	158.2	-65.6	111.5	39.8	2.1	100	178	278
sPP6	90.7	125.9	-134.3	106.2	48.2	2.2	187.5	124	311
sPP7	88.6	127.9	-70	98.8	43.8	2.6	159.6	168	328
sPP8	87	147.2	--64.5	104.6	30.9	2.1	144.6	277	421
sPP9	78	127.8	-61.6	80.2	31.8	4	567.9	472	1040
sPP10	74.8	116.7	-64.3	75	31.9	4	562.8	394	957
sPP11	70.6	113.5	-34.6	60.4	6.2	2	72.7	366	438
sPP12	60.1	86	-37.2	/	/	/	/	/	/

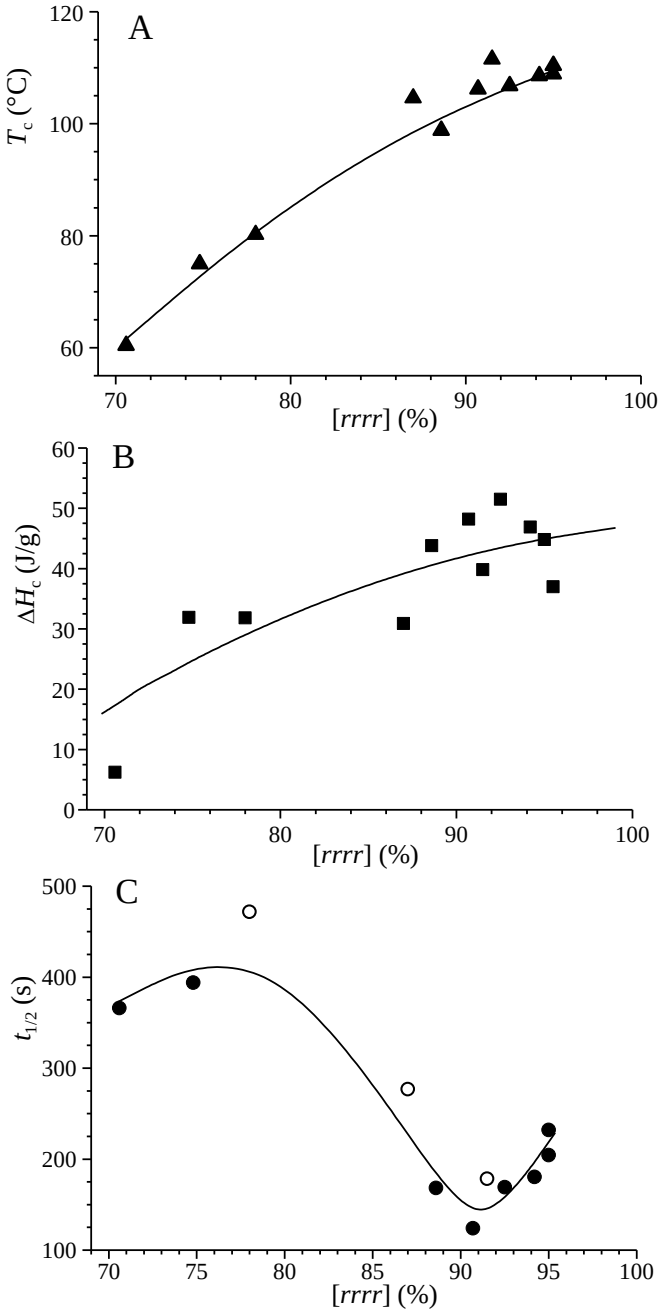

Figure 1.71. *Crystallization temperature (T_c) (A), crystallization enthalpy (ΔH_c) (B) and semi-crystallization time ($t_{1/2}$) (C) of samples of sPP of different stereoregularity as a function of rrrr pentad content.*

1.7.2. Crystallization kinetics of copolymers of sPP with ethylene

The DSC curves recorded during heating at 40 °C/min cooling from the melt at cooling rate of 2.5 °C/min of samples of sPPET copolymers with different ethylene content, the corresponding crystallization kinetics curves evaluated from the crystallization exotherms with the equation 1.1, and the fitting of these curves with the equation 1.2, are reported in Figures 1.72-1.78. Sample sPPET-3 presents multiple exothermic and endothermic peaks, indicating that the sample is probably partially degradated. Therefore, only the DSC curves are reported in Figure 1.73 and no evaluation of the crystallization kinetics has been attempted. The X-ray diffraction profiles of the samples crystallized in the DSC after the cooling scan of Figures 1.72A-1.78A are reported in Figure 1.79. The diffraction profiles of thin films crystallized from the melt in the same conditions at 2.5 °C/min for the POM observation have been shown in Figure 1.37C. These data indicate that all samples crystallize from the melt in the form I of sPP and for ethylene contents higher than 6-7 mol% in mixture with crystals of form II.[142c]

Table 1.12 reports the melting (T_m) and crystallization (T_c) temperatures, and the melting (ΔH_m) and crystallization (ΔH_c) enthalpies for all sPPET samples, whereas the values of crystallization temperature and enthalpy are reported in Figure 1.80A,B as a function of ethylene content. Since the heating is performed at 40 °C/min the values of melting temperature and enthalpy are not significant. Both crystallization temperature and enthalpy decrease with the decreasing of ethylene concentration. Some deviations have been observed for the samples sPPET-3, sPPET-4 and sPPET-9 with 2.6, 6.3, 13.2 mol% of ethylene, respectively, that appear partially degradated.

The parameters evaluated from the interpolation of the experimental data of Figures Figures 1.72A-1.78A with the Avrami equation 1.2, that is, the Avrami exponent n, the incipient crystallization time t_0, the semi-crystaliization time $t_{1/2}$ and the time required to achieve 50% of total apparent crystallinity ($t_{1/2} + t_0$) are reported in Table 1.12 . The values of Avrami exponent n are for almost all samples included in the range 1-2. Only the sample with the lowest ethylene content (AK-sPPET-2) shows the highest value of n (n = 2.7), indicating three-dimensional growth for heterogeneous nucleation or two-dimensional growth in case of homogeneous nucleation. Lower values of n (in the range 1-1.8) consistent with heterogeneous nucleation and growth in 1 direction have been observed for all other samples. The sample AK-sPPET-2 shows the lowest

value of the semi-crystallization time $t_{1/2}$ (140 s), while much higher values have been observed in the other samples (220-300 s) (Figure 1.80C).

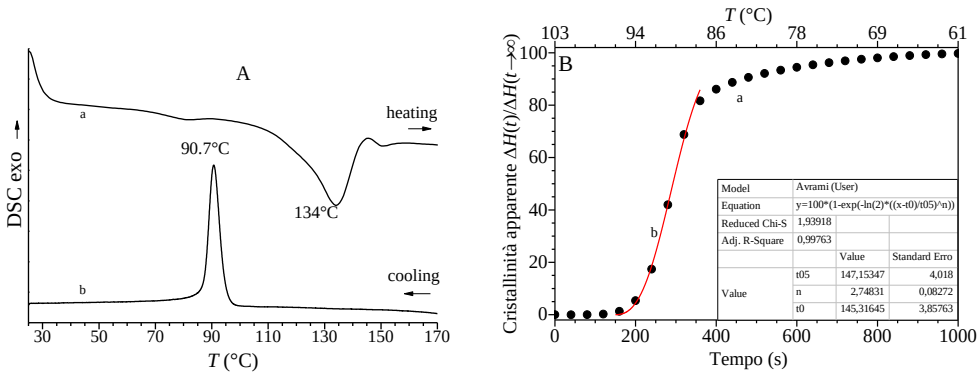

Figure 1.72. *DSC curves recorded during heating at 40°C/min from room temperature up to 180°C (a) and successive cooling to room temperature at 2.5°C/min (b) of the AK-sPPEt-2 (1.9 mol% of ethylene) (A). Degree of apparent crystallinity as a function of time and temperature evaluated from DSC curves using the equation 1.1 and interpolation with Avrami equation 1.2 (B).*

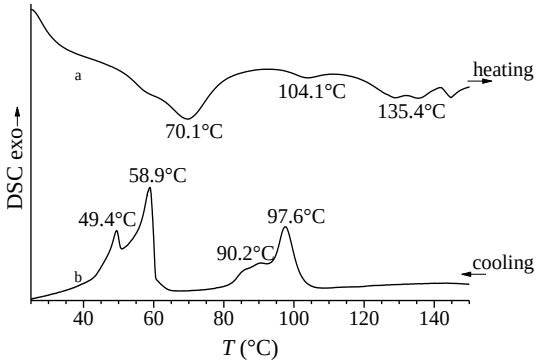

Figure 1.73. *DSC curves recorded during heating at 40°C/min from room temperature up to 160°C (a) and successive cooling to room temperature at 2.5°C/min (b) of the sPPET-3 (2.6 mol% of ethylene). The multiple melting and crystallization peaks are due to thermal degradation.*

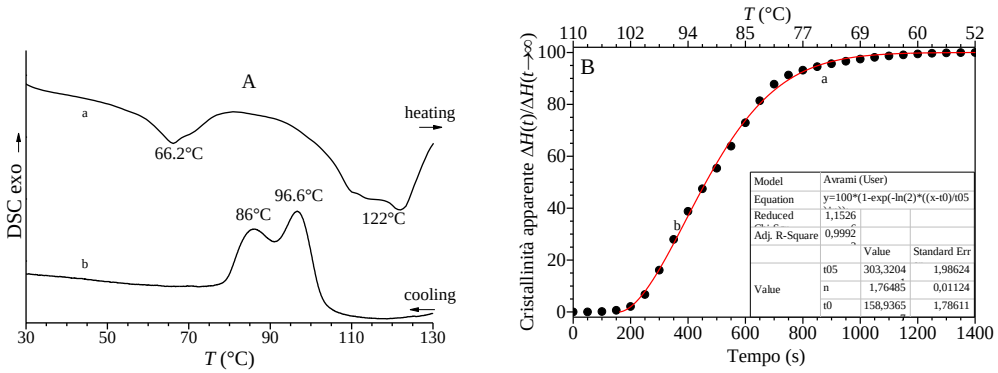

Figure 1.74. *DSC curves recorded during heating at 40°C/min from room temperature up to 140°C (a) and successive cooling to room temperature at 2.5°C/min (b) of the sPPET-4 (6.3 mol% of ethylene) (A). Degree of apparent crystallinity as a function of time and temperature evaluated from DSC curves using equation 1.1 and interpolation with Avrami equation 1.2 (B).*

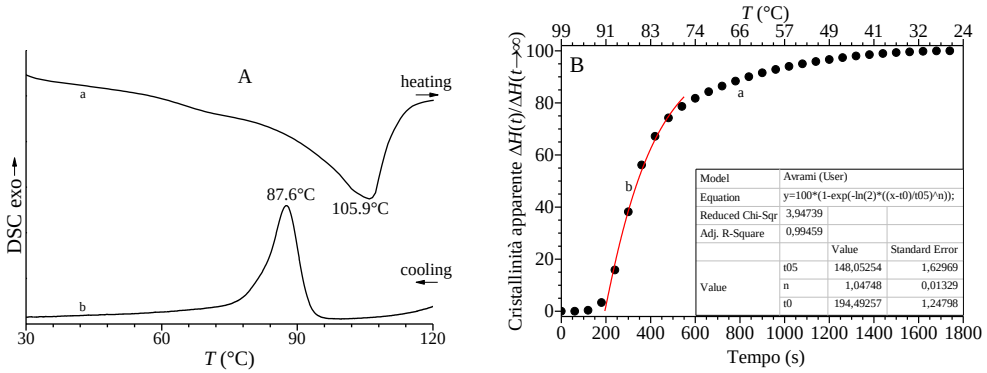

Figure 1.75. *DSC curves recorded during heating at 40°C/min from room temperature up to 130°C (a) and successive cooling to room temperature at 2.5°C/min (b) of the sPPET-6 (8.5 mol% of ethylene) (A). Degree of apparent crystallinity as a function of time and temperature evaluated from DSC curves using equation 1.1 and interpolation with Avrami equation 1.2 (B).*

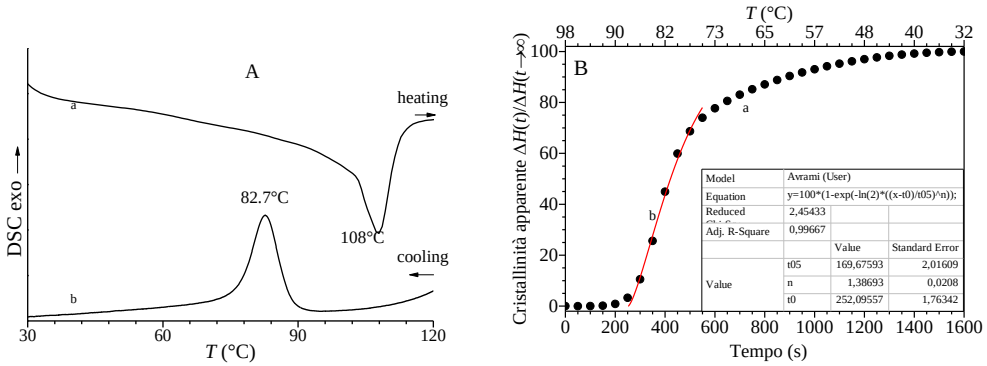

Figure 1.76. *DSC curves recorded during heating at 40°C/min from room temperature up to 130°C (a) and successive cooling to room temperature at 2.5°C/min (b) of the sPPEt-8 (9.8 mol% of ethylene) (A). Degree of apparent crystallinity as a function of time and temperature evaluated from DSC curves using equation 1.1 and interpolation with Avrami equation 1.2 (B).*

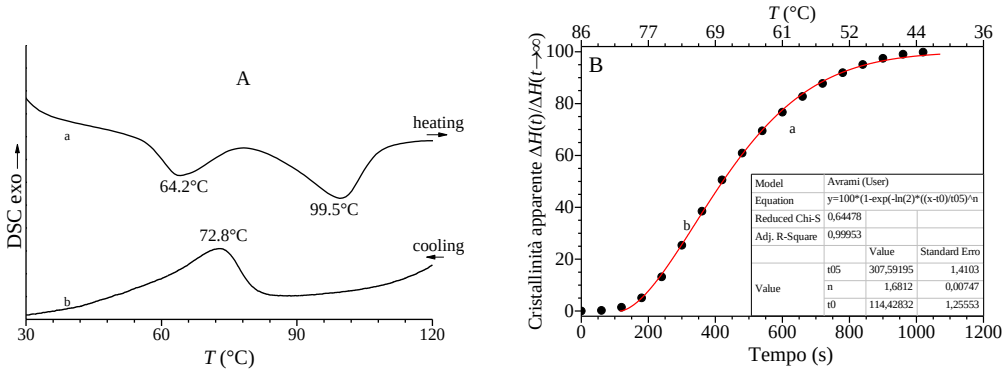

Figure 1.77. *DSC curves recorded during heating at 40°C/min from room temperature up to 130°C (a) and successive cooling to room temperature at 2.5°C/min (b) of the sPPEt-9 (13.2 mol% of ethylene) (A). Degree of apparent crystallinity as a function of time and temperature evaluated from DSC curves using equation 1.1 and interpolation with Avrami equation 1.2 (B).*

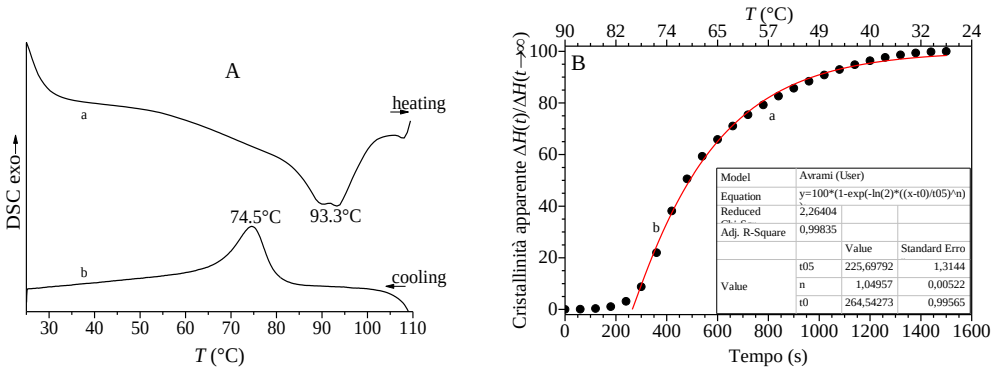

Figure 1.78. *DSC curves recorded during heating at 40°C/min from room temperature up to 110°C (a) and successive cooling to room temperature at 2.5°C/min (b) of the sPPEt-10 (14.3 mol% of ethylene) (A). Degree of apparent crystallinity as a function of time and temperature evaluated from DSC curves using equation 1.1 and interpolation with Avrami equation 1.2 (B).*

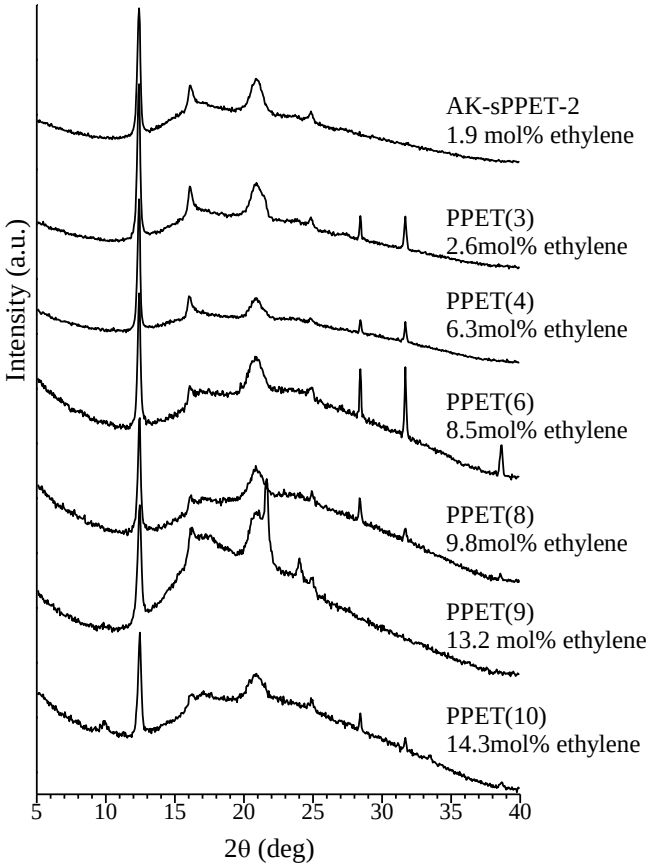

Figure 1.79. *X-ray powder diffraction profiles of samples of sPPET copolymers of different ethylene concentrations crystallized from the melt in DSC by cooling at 2.5 °C/min cooling rate (curves b of Figures 1.72A-1.78A).*

Table 1.12. *Melting temperature (T_m) and enthalpy (ΔH_m), crystallization temperature (T_c) and enthalpy (ΔH_c), Avrami exponent n, semi-crystallization time ($t_{1/2}$), incipient crystallization time (t_0) and time required to achieve 50% of the apparent crystallinity ($t_{1/2} + t_0$) for all sPPET copolymers with different ethylene content.*

Sample	(mol% ethylene)	T_m^I (°C)	T_m^{II} (°C)[b]	ΔH_m^I (J/g)	T_c^I (°C)	T_c^{II} (°C)	ΔH_c^I (J/g)	*n*	t_0 (s)	$t_{1/2}$(s)	$t_{1/2}+t_0$(s)
AK-sPPEt-2	1.9	134	/	-57.3	90.7	/	28.4	2.7	145	147	292
sPPEt-3[a]	2.6	70.1	135	-50.3	97.6	58.9	28.4	/	/	/	/
sPPEt-4 [a]	6.3	66.2	122	-11.5	96.6	86	27	1.8	159	303	462
sPPEt-6	8.5	105.9	/	-75.3	87.6	/	22.6	1	194	148	342
sPPEt-8	9.8	108	/	-58.8	82.7	/	19.4	1.4	252	170	429
sPPEt-9 [a]	13.2	99.5	64.2	-46.9	72.8	/	8.8	1.7	114	308	422
sPPEt-10	14.3	93.3	/	-41.8	74.5	/	9.3	1	264	226	490

[a]) The sample shows multiple esothermic and endothermic peaks. The main peaks are indicated as T_m^I e T_c^I, whereas the secondary peaks are indicated as T_m^{II} e T_c^{II}.

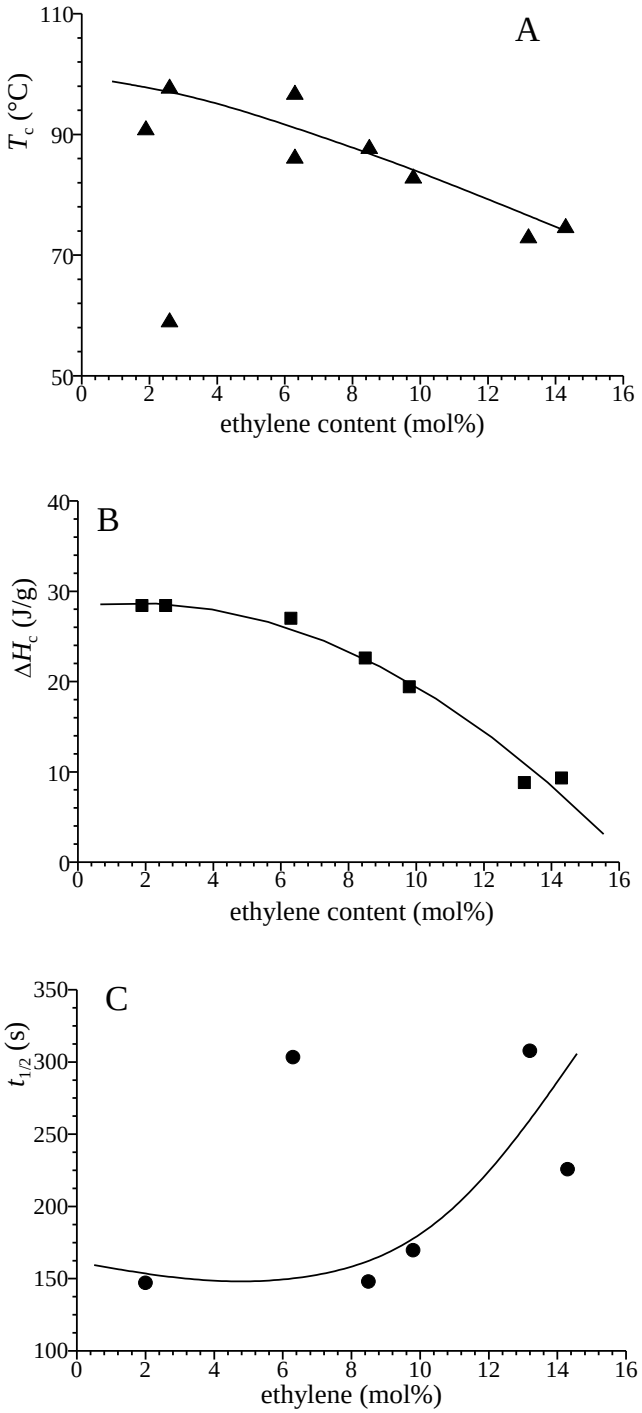

Figure 1.80. *Values of crystallization temperature (T_c) (A), crystallization enthalpy (ΔH_c) (B) and semi-crystallization time ($t_{1/2}$) (C) of sPPET copolymers as a function of ethylene content.*

1.7.3. Crystallization kinetics of copolymers of sPP with 1-butene

The DSC curves recorded during heating at 40 °C/min and cooling from the melt at cooling rate of 2.5 °C/min of samples of sPPBu copolymers with different 1-butene content, the corresponding crystallization kinetics curves evaluated from the crystallization exotherms with the equation 1.1, and the fitting of these curves with the equation 1.2, are reported in Figures 1.81-1.88. The X-ray diffraction profiles of the samples crystallized in the DSC after the cooling scan of Figures 1.81A-1.88A are reported in Figure 1.89. The diffraction profiles of thin films crystallized from the melt in the same conditions at 2.5 °C/min for the POM observation have already been shown in Figure 1.41B. As discussed in the secion 1.8, sPPBu samples are crystallized in disordered modifications of form I of sPP up to a content of 1-butene of 60-70 mol%,[140,143] and in structures similar to form I of sPB for contents of 1-butene higher than 70 mol% (Figure 1.89).[140] Samples with butene content higher than 30 mol% are amorphous just after cooling the melt but crystallize by aging at room temperature for several days (cold-crystallization).[143g] Therefore, for samples sPPBu-7, sPPBu-9, sPPBu-11 and sPPBu-12 only the DSC curves are reported in Figure 1.85-1.88. For these samples, the kinetics of cold-crystallization evaluated from the degree of crystallinity determined from the WAXS profiles recorded at different aging times has been reported in ref 143g. The values of apparent crystallinity, evaluated as:

$$\frac{x_c(t)}{x(end)} = x_c'(RX)$$

with $x_c(t)$ the X-ray diffraction crystallinity at the aging time t and x(end) the maximum crystallinity achieved upon aging, are reported in Figure 1.90 as a function of the aging time. Also the values of crystallinity developed by cold-crystallization have been interpolated with the Avrami equation 1.2 as shown by the fitting of Figure 1.90B.

Table 1.13 reports the melting (T_m) and crystallization (T_c) temperatures, and the melting (ΔH_m) and crystallization (ΔH_c) enthalpies for all sPPBu samples, whereas Figures 1.91A,B show the values of crystallization temperature (T_c) and enthalpy (ΔH_c) as a function of 1-butene content. The values of melting temperature and enthalpy reported in the Table 1.13 are not significant since the heating scans have been performed at 40°C/min. Both crystallization temperature and enthalpy decrease with decreasing of butene concentration in samples crystallizing from the melt.

The values of kinetic parameters evaluated from the interpolation of the experimental data of Figures 1.81-1.85 and the cold-crystallization data of Figure 1.90 with the Avrami equation 1.2, that is, the Avrami exponent *n*, the incipient crystallization time t_0, the semi-crystaliization time $t_{1/2}$ and the time required to achieve 50% of apparent crystallinity ($t_{1/2}$ + t_0), are also reported in Table 1.13. The values of Avrami exponent *n* are always included in the range 1-4. The sample with the lowest 1-butene content (sPPBu-1) exhibits n = 4, indicating three-dimensional growth for homogeneous nucleation. Lower values of *n* in the range 2.2-2.7, consistent with heterogeneous nucleation and growth in 2 directions or with homogeneous nucleation and growth in one direction, have been observed in samples with 1-butene content in the range 6-18 mol% (sPPBu-2, sPPBu-4, sPPBu-6). Samples with higher 1-butene concentration that crystallize upon aging display values of *n* lower than 1 (*n* in the range 1.1-1.9), probably indicating one-dimensional growth with heterogeneous nucleation. The semi-crystallization time $t_{1/2}$ reported in Figure 1.91C only for samples crystallizing from the melt are quite similar. Higher $t_{1/2}$ values have been observed in samples sPPBu-1 and sPPBu-6 (222 s and 295 s respectively), while lower values have been observed in samples sPPBu-2 and sPPBu-4 (130-183 s) (Figure 1.91C). In samples that crystallize upon aging, longer values of $t_{1/2}$ of the order of magnitude of days, have been evaluated from WAXS analysis.

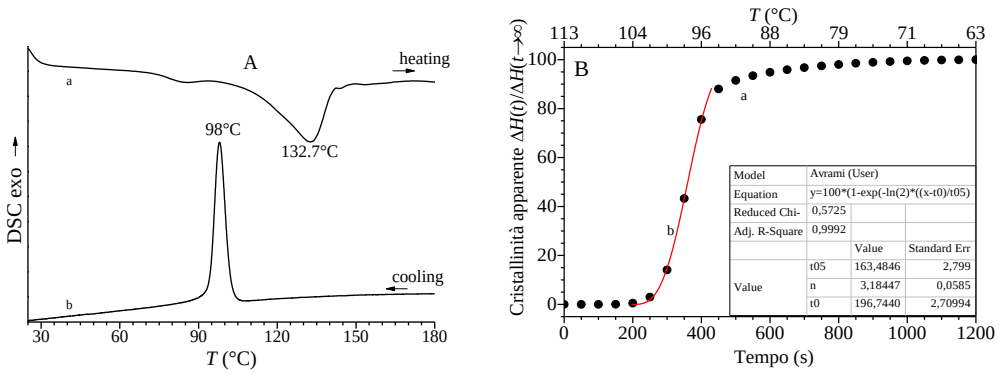

Figure 1.81. *DSC curves recorded during heating at 40°C/min from room temperature up to 190°C (a) and successive cooling to room temperature at 2.5°C/min (b) of the sPPBu-1 (3.2 mol% of 1-butene) (A). Degree of apparent crystallinity as a function of time and temperature evaluated from DSC curves using equation 1.1 and interpolation with Avrami equation 1.2 (B).*

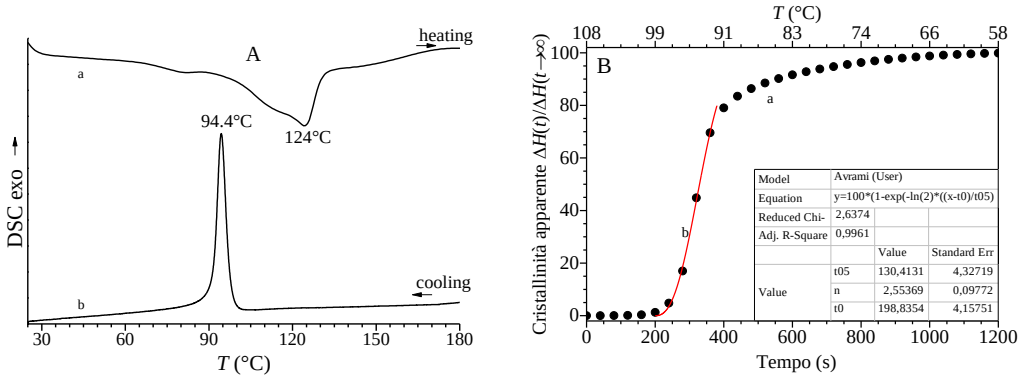

Figure 1.82. *DSC curves recorded during heating at 40°C/min from room temperature up to 190°C (a) and successive cooling to room temperature at 2.5°C/min (b) of the sPPBu-2 (6.1 mol% of 1-butene) (A). Degree of apparent crystallinity as a function of time and temperature evaluated from DSC curves using equation 1.1 and interpolation with Avrami equation 1.2 (B).*

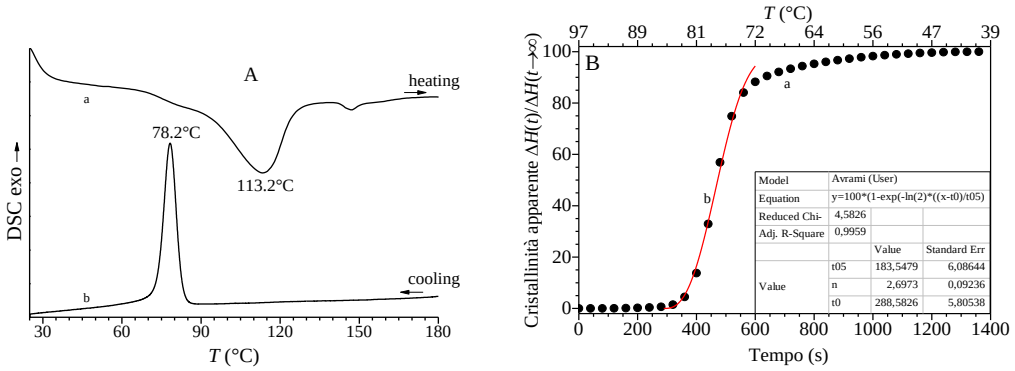

Figure 1.83. *DSC curves recorded during heating at 40°C/min from room temperature up to 190°C (a) and successive cooling to room temperature at 2.5°C/min (b) of the sPPBu-4 (11.2 mol% of 1-butene) (A). Degree of apparent crystallinity as a function of time and temperature evaluated from DSC curves using equation 1.1 and interpolation with Avrami equation 1.2 (B).*

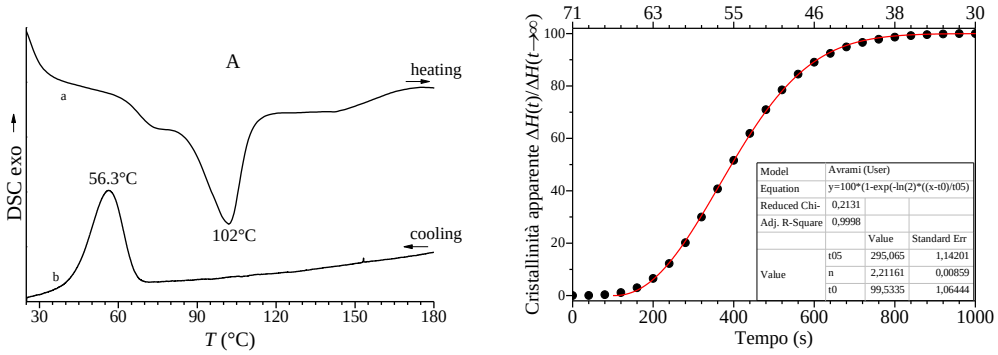

Figure 1.84. *DSC curves recorded during heating at 40°C/min from room temperature up to 190°C (a) and successive cooling to room temperature at 2.5°C/min (b) of the sPPBu-6 (18.2 mol% of 1-butene) (A). Degree of apparent crystallinity as a function of time and temperature evaluated from DSC curves using equation 1.1 and interpolation with Avrami equation 1.2 (B).*

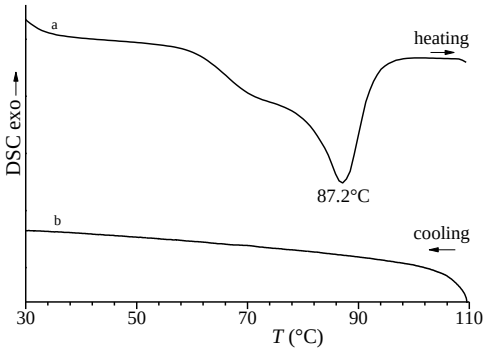

Figure 1.85. *DSC curves recorded during heating at 40°C/min from room temperature up to 110°C (a) and successive cooling to room temperature at 2.5°C/min (b) of the sPPBu-7 (31.5 mol% of 1-butene).*

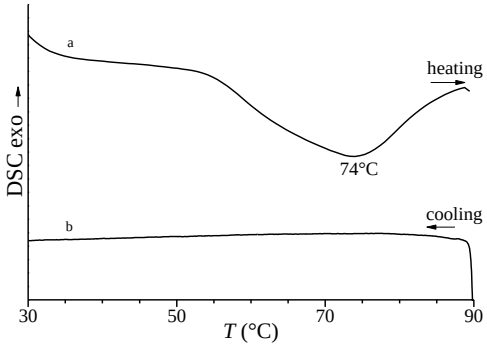

Figure 1.86. *DSC curves recorded during heating at 40°C/min from room temperature up to 90°C (a) and successive cooling to room temperature at 2.5°C/min (b) of the sPPBu-9 (51.7 mol% of 1-butene).*

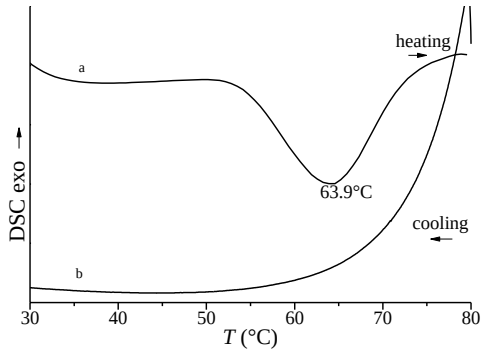

Figure 1.87. *DSC curves recorded during heating at 40°C/min from room temperature up to 80°C (a) and successive cooling to room temperature at 2.5°C/min (b) of the sPPBu-11 (69.9 mol% of 1-butene).*

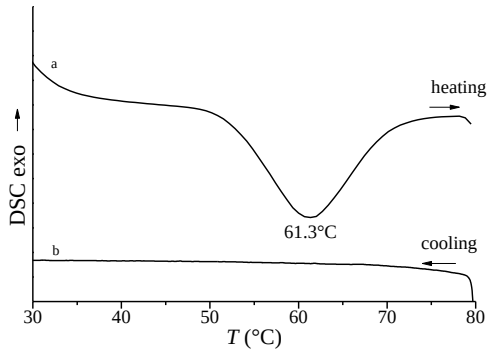

Figure 1.88. *DSC curves recorded during heating at 40°C/min from room temperature up to 80°C (a) and successive cooling to room temperature at 2.5°C/min (b) of the sPPBu-12 (89 mol% of 1-butene).*

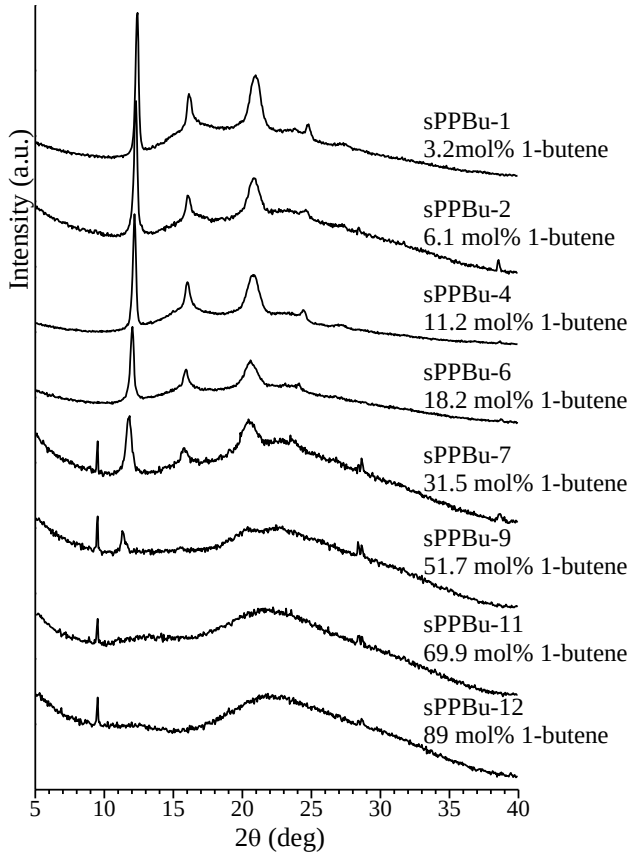

Figure 1.89. *X-ray powder diffraction profiles of samples of sPPBu copolymers of different butene concentrations crystallized from the melt in DSC by cooling at 2.5 °C/min cooling rate (curves b of Figures 1.81A-1.84A and 1.85-1.88.).*

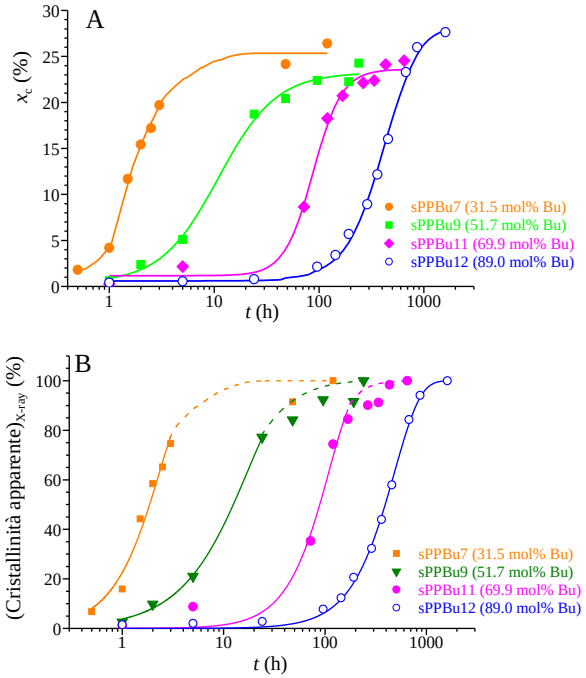

Figure 1.90. *Degree of crystallinity (A) and apparent crystallnity (B) as a function of aging time of samples sPPBu-7 (31.5 mol% of 1-butene), sPPBu-9 (51.7 mol% of 1-butene), sPPBu-11 (69.9 mol% of 1-butene), sPPBu-12 (89 mol% of 1-butene). The data have been evaluated by using the WAXS profile of ref 143g: The fitting of the kinetic curves with Avrami equation is also shown in B.*

Table 1.13. *Melting temperature (T_m) and enthalpy (ΔH_m), crystallization temperature (T_c) and enthalpy (ΔH_c), Avrami exponent n, semi-crystallization time ($t_{1/2}$), incipient crystallization time (t_0) and time required to achieve 50% of apparent crystallinity ($t_{1/2} + t_0$) for sPPBu copolymers with different 1-butene content.*

Sample	(mol % of 1-butene)	T_m (°C)	ΔH_m (J/g)	T_c (°C)	ΔH_c (J/g)	*n*	t_0 (s)	$t_{1/2}$(s)	$t_{1/2}+t_0$(s)
sPPBu-1	3.2	132.7	-82.6	98	43.3	4	141	222	363
sPPBu-2	6.1	124	-84.6	94.4	38.3	2.5	199	130	329
sPPBu-4	11.2	113.2	-82.2	78.2	37.5	2.7	289	183	472
sPPBu-6	18.2	102	-66.3	56.3	25	2.2	99	295	395
sPPBu-7[a]	31.5	87.2	-51.9	/	/	1.9	0	7×10^3	7×10^3
sPPBu-9[a]	51.7	74	-33.2	/	/	1.1	0	44×10^3	44×10^3
sPPBu-11[a]	69.9	63.9	-35.6	/	/	1.8	0	32×10^4	32×10^4
sPPBu-12[a]	89	61.3	-29.1	/	/	1.7	0	141×10^5	141×10^5

[a]) The kinetics parameters of these samples have been obtained by interpolation of crystallinity data evaluated fromWAXS analysis.

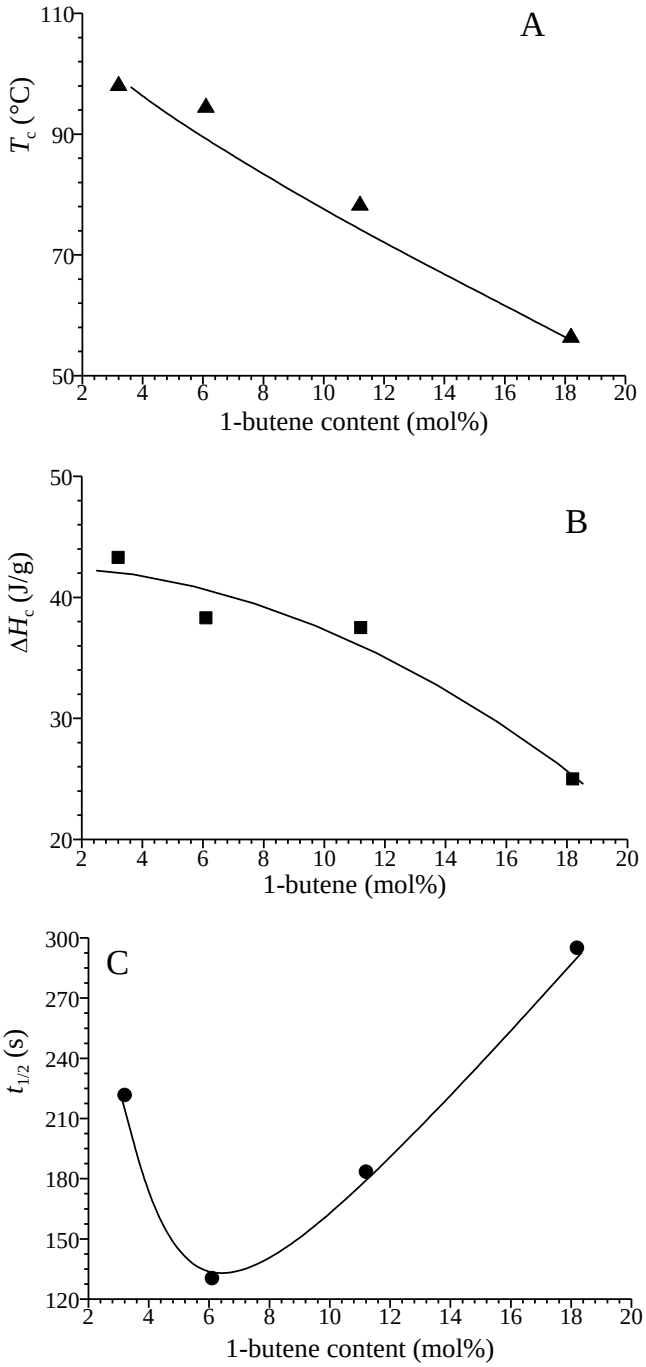

Figure 1.91. *Values of crystallization temperature (T_c) (A), crystallization enthalpy (ΔH_c) (B) and semi-crystallization time ($t_{1/2}$) (C) of sPPBu coplymers as a function of 1-butene content.*

1.7.4. Crystallization kinetics of copolymers of sPP with 4-methyl-1-pentene

The DSC curves recorded during heating at 40 °C/min and cooling from the melt at cooling rate of 2.5 °C/min of samples of sPP4M1P copolymers with different 4-methyl-1-pentene content, the corresponding crystallization kinetics curves evaluated from the crystallization exotherms with the equation 1.1, and the fitting of these curves with the equation 1.2, are reported in Figures 1.92-1.96. The X-ray diffraction profiles of the samples crystallized in the DSC after the cooling scan of Figures 1.92A-1.96A are reported in Figure 1.97. All samples crystallize from the melt in form I of sPP. Similar data have been reported for thin films crystallized from the melt in the same conditions at 2.5 °C/min for the POM observation in Figure 1.44B. The sample sPP4M1P-6 does not crystallize from the melt but crystallize upon aging at room temperature and therefore only the DSC curves are reported in Figure 1.96.

The values of the melting and crystallization temperatures and enthalpies for all sPP4M1P samples are reported in Table 1.14, whereas the values of crystallization temperature and enthalpy are reported in Figure 1.98A,B as a function of 4-methyl-1-pentene content. Also in this case, the crystallization temperature and the crystallization enthalpy decrease with decreasing comonomer concentration.

Table 1.14 also reports the kinetics parameters evaluated from the interpolation of the experimental data of Figure 1.92B-1.96B with Avrami equation 1.2, that is, the Avrami exponent *n*, the incipient crystallization time t_0, the semi-crystaliization time $t_{1/2}$ and the time required to achieve 50% of the total apparent crystallinity ($t_{1/2}$ + t_0) for all samples. The values of Avrami exponent *n* are quite similar for all samples and are always included in the range 1.6-2.5. Samples sPP4M1P-1 (1.8 mol% of 4-methyl-1-pentene), sPP4M1P-4 (12.9 mol% of 4-methyl-1-pentene) and sPP4M1P-5 (15.2 mol% of 4-methyl-1-pentene) show *n* values equal or higher than 2, indicating heterogeneous nucleation with growth in 2 dimensions or homogeneous nucleation with one-dimensional growth. Only the sample sPP4M1P-2 (4 mol% of 4-methyl-1-pentene) exhibits a value of *n* lower than 1 indicating heterogeneous nucleation with growth in one dimension. The semi-crystallization time $t_{1/2}$ reported in Figure 1.98C increases with increasing comonomer content from the value of 123s of the sample sPP4M1P-1 to the value of 267s of the sample sPP4M1P-5 (Figure 1.98C).

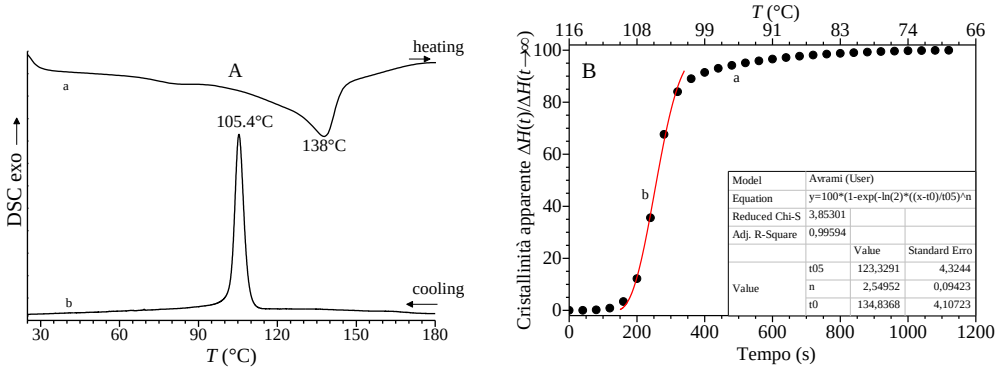

Figure 1.92. *DSC curves recorded during heating at 40°C/min from room temperature up to 190°C (a) and successive cooling to room temperature at 2.5°C/min (b) of the sPP4M1P-1 (1.8 mol% of 4-methyl-1-pentene) (A). Degree of apparent crystallinity as a function of time and temperature evaluated from DSC curves using equation 1.1 and interpolation with Avrami equation 1.2 (B).*

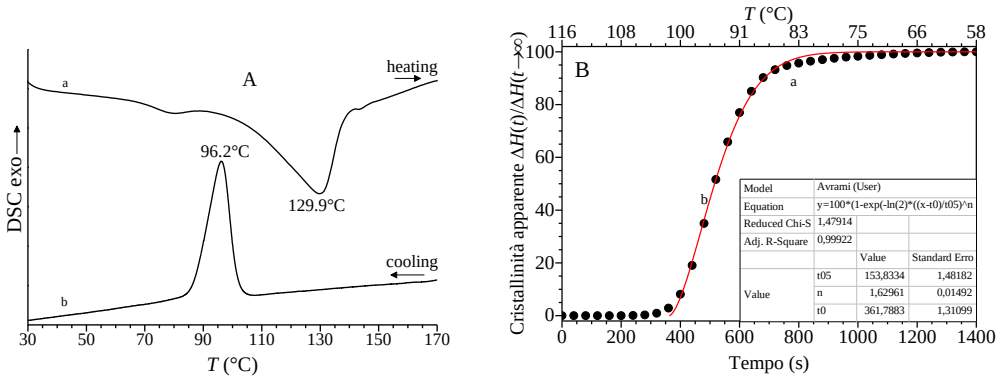

Figure 1.93. *DSC curves recorded during heating at 40°C/min from room temperature up to 180°C (a) and successive cooling to room temperature at 2.5°C/min (b) of the sPP4M1P-2 (4 mol% of 4-methyl-1-pentene) (A). Degree of apparent crystallinity as a function of time and temperature evaluated from DSC curves using equation 1.1 and interpolation with Avrami equation 1.2 (B).*

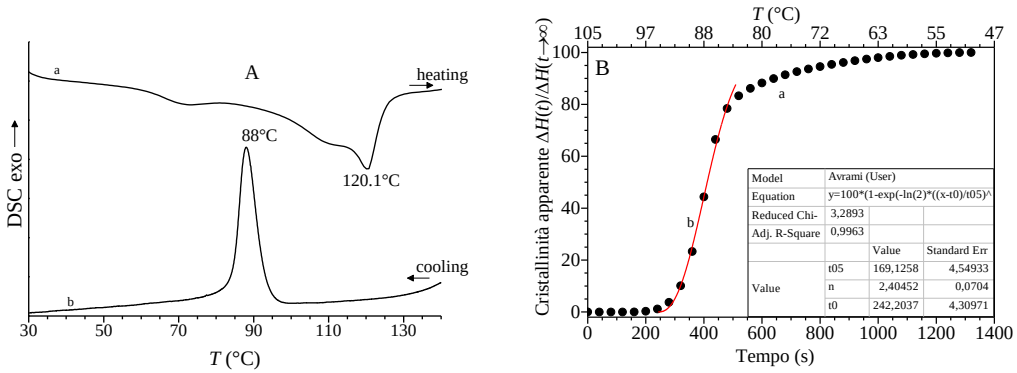

Figure 1.94. *DSC curves recorded during heating at 40°C/min from room temperature up to 150°C (a) and successive cooling to room temperature at 2.5°C/min (b) of the sPP4M1P-4 (12.9 mol% of 4-methyl-1-pentene) (A). Degree of apparent crystallinity as a function of time and temperature evaluated from DSC curves using equation 1.1 and interpolation with Avrami equation 1.2 (B).*

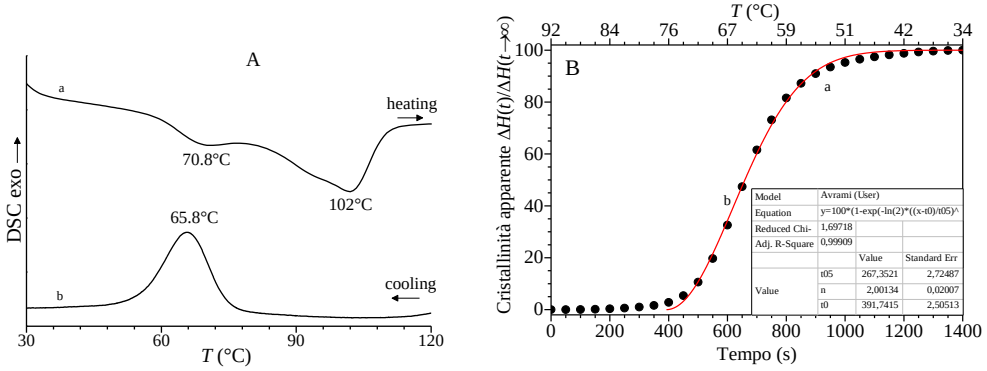

Figure 1.95. *DSC curves recorded during heating at 40°C/min from room temperature up to 130°C (a) and successive cooling to room temperature at 2.5°C/min (b) of the sPP4M1P-5 (15.2 mol% of 4-methyl-1-pentene) (A). Degree of apparent crystallinity as a function of time and temperature evaluated from DSC curves using equation 1.1 and interpolation with Avrami equation 1.2 (B).*

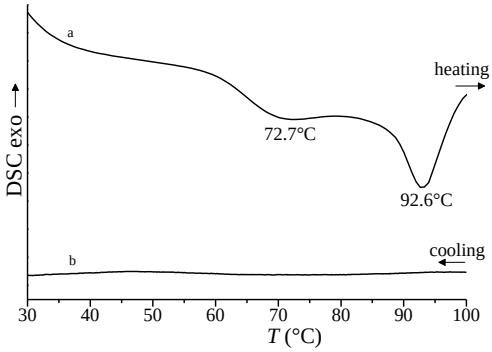

Figure 1.96. *DSC curves recorded during heating at 40°C/min from room temperature up to 110°C (a) and successive cooling to room temperature at 2.5°C/min (b) of the sPP4M1P-6 (20.5 mol% of 4-methyl-1-pentene).*

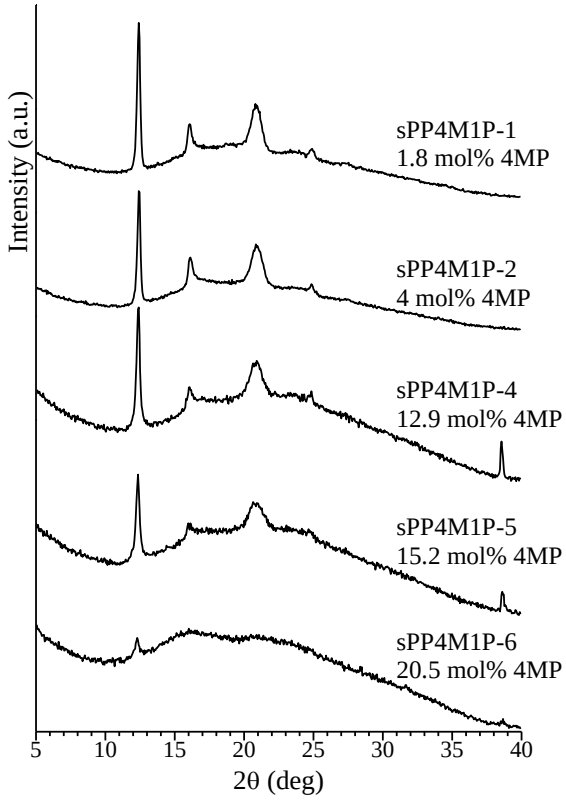

Figure 1.97. *X-ray powder diffraction profiles of samples of sPP4M1P copolymers of different 4-methyl-1-pentene concentrations crystallized from the melt in DSC by cooling at 2.5 °C/min cooling rate (curves b of Figures 1.92A-1.95A and 1.96).*

Table 1.14. *Melting temperature (T_m) and enthalpy (ΔH_m), crystallization temperature (T_c) and enthalpy (ΔH_c), Avrami exponent n, semi-crystallization time ($t_{1/2}$), incipient crystallization time (t_0) and time required to achieve 50% of the apparent crystallinity ($t_{1/2}+t_0$) for all sPP4M1P copolymers with different 4-methyl-pentene (4M1P) content.*

Samples	4M1P (mol%)	T_m (°C)	ΔH_m (J/g)	T_c (°C)	ΔH_c (J/g)	n	t_0 (s)	$t_{1/2}$ (s)	$t_{1/2}+t_0$ (s)
sPP-4MP-1	1.8	138	-102.9	105.4	47.3	2.5	134.8	123.3	258.1
sPP-4MP-2	4.0	129.9	-92.7	96.2	42.5	1.6	361.8	153.8	515.6
sPP-4MP-4	12.9	120.1	-74.5	88	30.6	2.4	242.2	169.1	411.3
sPP-4MP-5	15.2	102	-50.8	65.8	16.8	2	391.7	267.3	659
sPP-4MP-6	20.5	92.6	-39.5	/	/	/	/	/	/

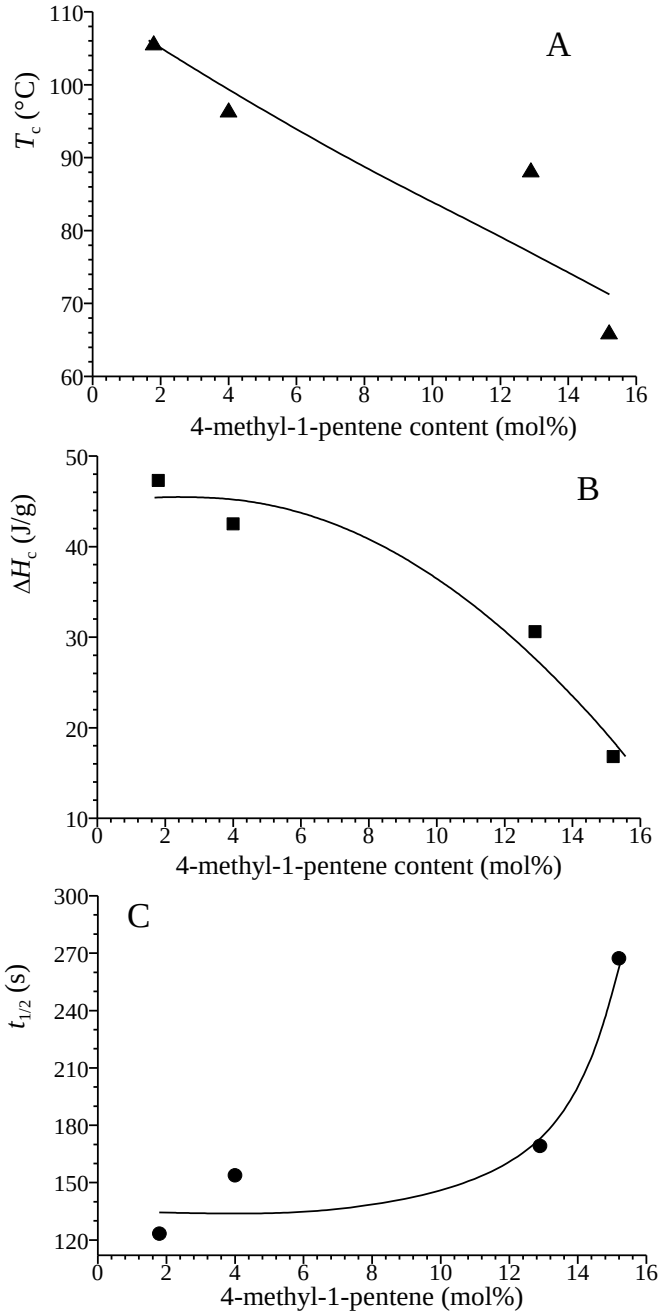

Figure 1.98. *Values of crystallization temperature (T_c) (A), crystallization enthalpy (ΔH_c) (B) and semi-crystallization time ($t_{1/2}$) (C) of sPP4M1P copolymers as a function of 4-methyl-1-pentene content.*

1.7.5. Crystallization kinetics of copolymers of sPP with 1-hexene

The DSC curves recorded during heating at 40 °C/min and cooling from the melt at cooling rate of 2.5 °C/min of samples of sPPHe copolymers with different 1-hexene content, the corresponding crystallization kinetics curves evaluated from the crystallization exotherms with the equation 1.1, and the fitting of these curves with the equation 1.2, are reported in Figures 1.99-1.103. The X-ray diffraction profiles of the samples crystallized in the DSC after the cooling scans of Figures 1.99-1.103 are reported in Figure 1.104. All samples crystallize from the melt in form I of sPP. Similar data have been reported for thin films crystallized from the melt in the same conditions at 2.5 °C/min for the POM observation in Figure 1.46B.

The sample sPPHe-6 with 9 mol% of hexene does not crystallize from the melt but crystallize upon aging at room temperature (cold-crystallization) and therefore only the DSC curves are reported for this sample in Figure 1.103. The values of crystallinity and apparent crystallinity as a function of aging time for the sample sPPHe-6 have been evaluated from WAXS profiles recorded during aging reported in ref 146, and are reported in Figure 1.105 as a function of the aging time. Also the values of crystallinity developed by cold-crystallization for the sample sPPHe-6 have been interpolated with the Avrami equation 1.2, as shown by the fitting of Figure 1.105B.

The values of the melting and crystallization temperatures and enthalpies for all sPPHe samples are reported in Table 1.15, whereas the values of crystallization temperature and enthalpy are reported in Figure 1.106A,B as a function of hexene content. Also in this case, the crystallization temperature and the crystallization enthalpy decrease with decreasing comonomer content.

The kinetics parameters evaluated from the interpolation of the experimental data of Figures 1.99B-1.102B and 1.105B with Avrami equation 1.2 are also reported in Table 1.15. The values of Avrami exponent *n* are very low, in the range 0.6-2.4. Only the samples sPPHe-1 (1.7 mol% of 1-hexene) and sPPHe-3 (3.9 mol% of 1-hexene) show *n* values close to 2, indicating heterogeneous nucleation with growth in 2 dimensions or homogeneous nucleation with one-dimensional growth. The other samples exhibit values of *n* lower than 1 indicating heterogeneous nucleation with growth in one dimension. The samples sPPHe-6 (9 mol% of 1-hexene) displays a very low *n* value. This value has been obtained byy interpolation of WAXS data and it is probably not reliable. The semi-crystallization time $t_{1/2}$ reported in Figure 1.106C initially decreases with increasing comonomer content from the value of 220 s of the

sample sPPHe-1 to the value of 134 s of the sample sPPHe-3, then increases again up to 180 s for the last sample sPPHe-5 (6.4 mol% of 1-hexene). The value of $t_{1/2}$ of the sample sPPHe-6 has been evaluated from WAXS analysis (Figure 1.105) and confirms that crystallinity develop by cold-crystallization in several days (Figure 1.106C).

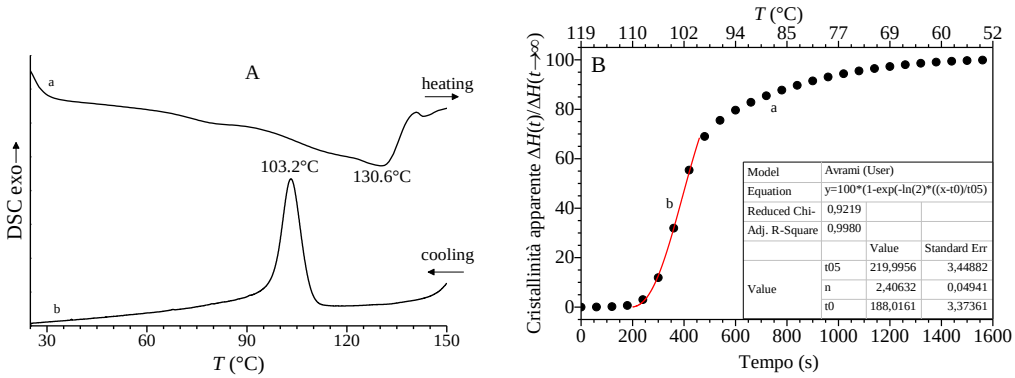

Figure 1.99. *DSC curves recorded during heating at 40°C/min from room temperature up to 155°C (a) and successive cooling to room temperature at 2.5°C/min (b) of the sPPHe-1 (1.7 mol% of 1-hexene) (A). Degree of apparent crystallinity as a function of time and temperature evaluated from DSC curves using equation 1.1 and interpolation with Avrami equation 1.2 (B).*

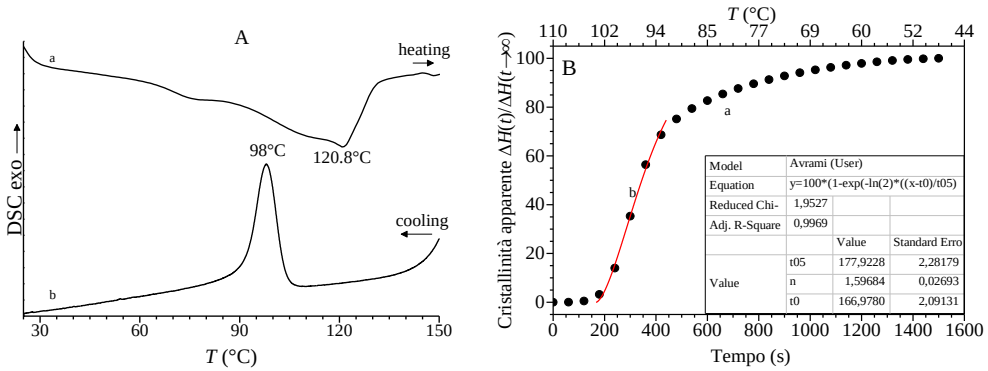

Figure 1.100. *DSC curves recorded during heating at 40°C/min from room temperature up to 155°C (a) and successive cooling to room temperature at 2.5°C/min (b) of the sPPHe-2 (3 mol% of 1-hexene) (A). Degree of apparent crystallinity as a function of time and temperature evaluated from DSC curves using equation 1.1 and interpolation with Avrami equation 1.2 (B).*

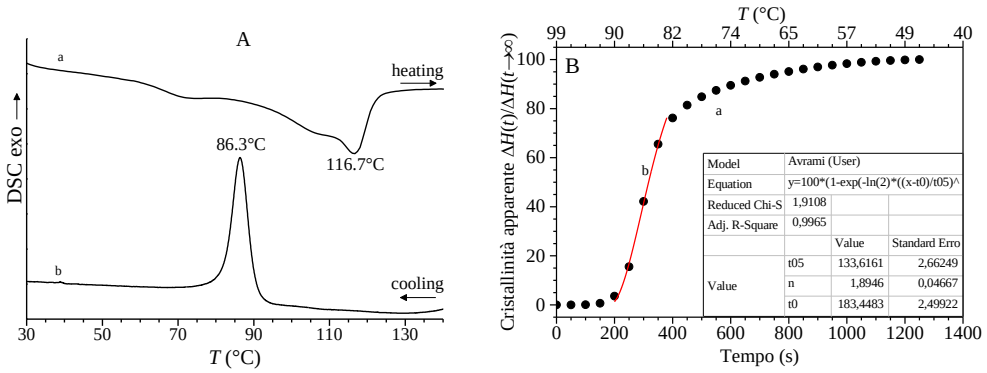

Figure 1.101. *DSC curves recorded during heating at 40°C/min from room temperature up to 150°C (a) and successive cooling to room temperature at 2.5°C/min (b) of the sPPHe-3 (3.9 mol% of 1-hexene) (A). Degree of apparente crystallinity as a function of time and temperature evaluated from DSC curves using equation 1.1 and interpolation with Avrami equation 1.2 (B).*

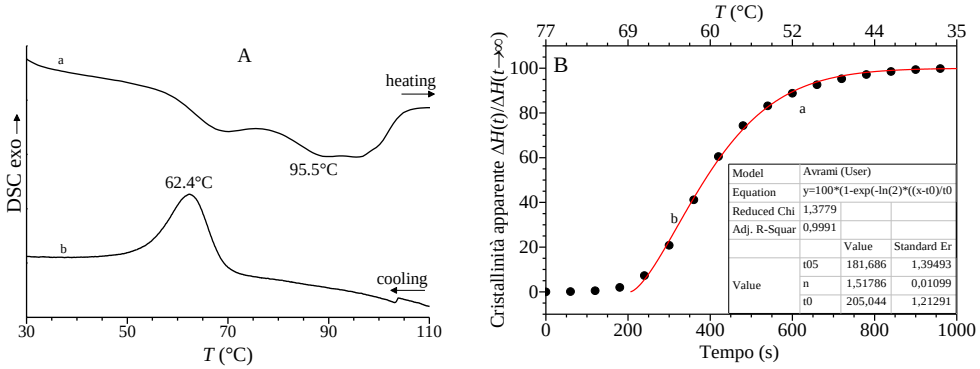

Figure 1.102. *DSC curves recorded during heating at 40°C/min from room temperature up to 120°C (a) and successive cooling to room temperature at 2.5°C/min (b) of the sPPHe-5 (6.4 mol% of 1-hexene) (A). Degree of apparent crystallinity as a function of time and temperature evaluated from DSC curves using equation 1.1 and interpolation with Avrami equation 1.2 (B).*

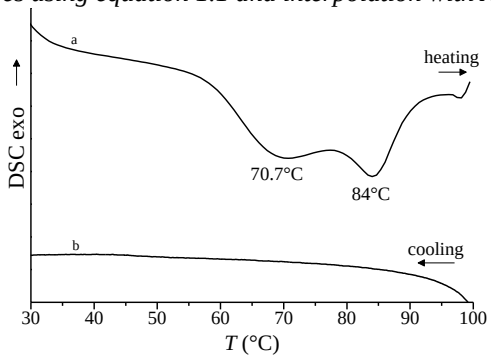

Figure 1.103. *DSC curves recorded during heating at 40°C/min from room temperature up to 100°C (a) and successive cooling to room temperature at 2.5°C/min (b) of the sPPHe-6 (9 mol% of 1-hexene) (A). Degree of apparent crystallinity as a function of time and temperature evaluated from DSC curves using equation 1.1 and interpolation with Avrami equation 1.2 (B).*

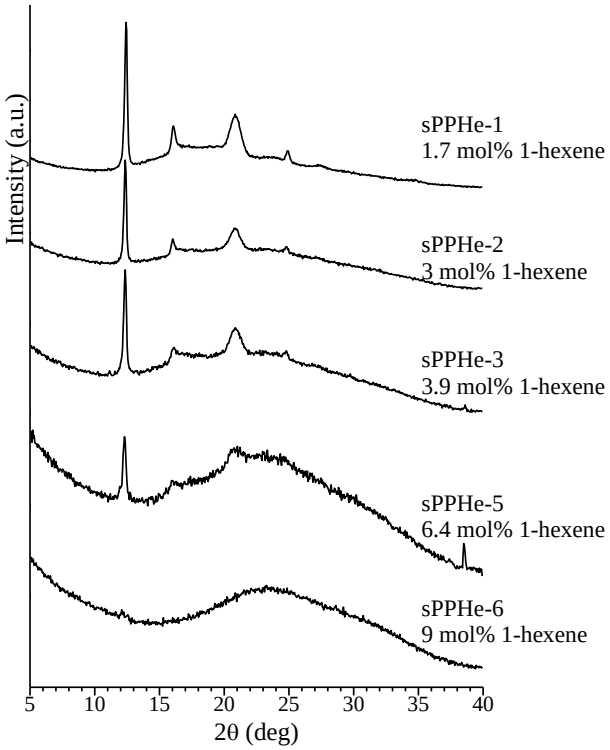

Figure 1.104. *X-ray powder diffraction profiles of samples of sPPHe copolymers of different 1-hexene concentrations crystallized from the melt in DSC by cooling at 2.5 °C/min cooling rate (curves b of Figures 1.99A-1.102A and 1.103).*

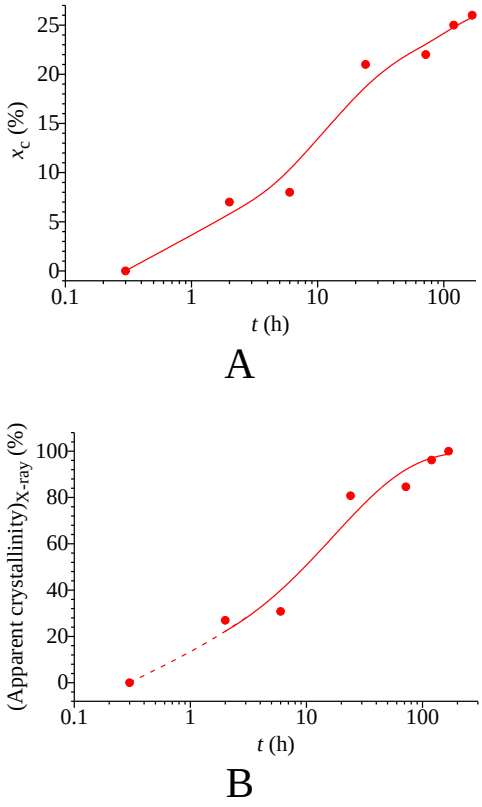

Figure 1.105 *Degree of crystallinity (A) and apparent crystallnity (B) as a function of aging time of sample sPPHe-6 (9 mol% of 1-hexene). The data have been evaluated by using the WAXS profile of ref 146. The fitting of the kinetic curves with Avrami equation is also shown in B.*

Table 1.15. *Melting temperature (T_m) and enthalpy (ΔH_m), crystallization temperature (T_c) and enthalpy (ΔH_c), Avrami exponent n, semi-crystallization time ($t_{1/2}$), incipient crystallization time (t_0)and time required to achieve 50% of the total apparent crystallinity ($t_{1/2} + t_0$) for all sPPHe copolymers with different 1-hexene content.*

Sample	1-hexene (mol%)	T_m (°C)	ΔH_m (J/g)	T_c (°C)	ΔH_c (J/g)	n	t_0 (s)	$t_{1/2}$(s)	$t_{1/2}+t_0$(s)
sPPHe-1	1.7	130.6	-88.3	103.2	35	2.4	188	220	408
sPPHe-2	3	120.8	-88.7	98	30.1	1.6	167	178	345
sPPHe-3	3.9	116.7	-71.1	86.3	30.2	1.9	183	134	317
sPPHe-5	6.4	95.5	-49.9	62.4	12	1.5	205	182	387
sPPHe-6[a]	9	84	-36.3	/	/	0.6	0	34×10^3	34×10^3

[a]) The kinetic parameters of this sample have been evaluated from WAXS analysis.

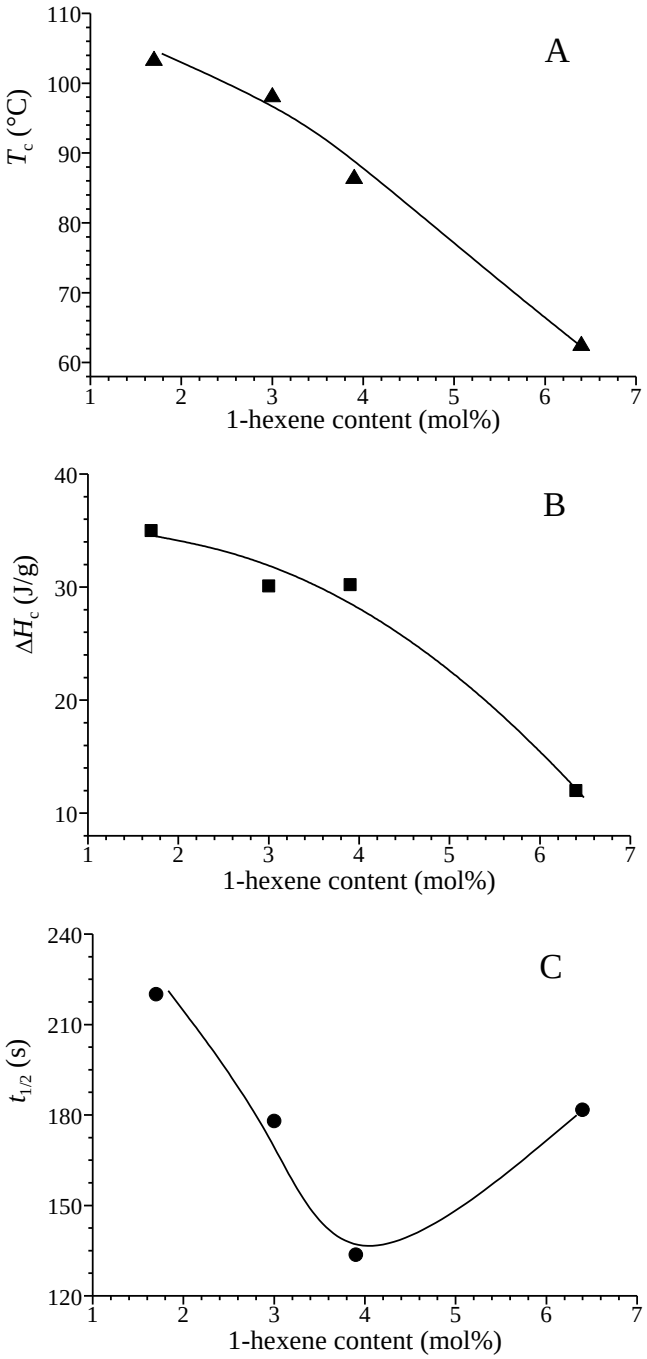

***Figure 1.106**. Values of crystallization temperature (T_c) (A), crystallization enthalpy (ΔH_c) (B) and half-crystallization time ($t_{1/2}$) (C) of sPPHe copolymers as a function of 1-hexene content.*

1.7.6. Crystallization kinetics of copolymers of sPP with 1-octene

The DSC curves recorded during heating at 40 °C/min and cooling from the melt at cooling rate of 2.5 °C/min of samples of sPPOt copolymers with different 1-octene content, the corresponding crystallization kinetics curves evaluated from the crystallization exotherms with the equation 1.1, and the fitting of these curves with the equation 1.2, are reported in Figures 1.107-1.112. The X-ray diffraction profiles of the samples crystallized in the DSC after the cooling scans of Figures 1.106A-1.109A and 1.110-1.111 are reported in Figure 1.113. All samples crystallize from the melt in form I of sPP. Similar data have been reported for thin films crystallized from the melt in the same conditions at 2.5 °C/min for the POM observation in Figure 1.47B. The samples sPPOt-7 and sPPOt-8 do not crystallize from the melt but cold-crystallize upon aging at room temperature and, therefore, only the DSC curves are reported in Figures 1.111 and 1.112. The values of crystallinity and apparent crystallinity as a function of aging time for the samples sPPOt-7 and sPPOt-8 have been evaluated from the WAXS profiles reported in ref 146 recorded during aging, and are reported in Figure 1.114 as a function of the aging time. Also the values of crystallinity developed by cold-crystallization for the sample sPPOt-7 and sPPOt-8 have been interpolated with the Avrami equation 1.2, as shown by the fitting of Figure 1.114B.

The values of the melting and crystallization temperatures and enthalpies for all sPPOc samples are reported in Table 1.16, whereas the values of crystallization temperature and enthalpy are reported in Figure 1.115A,B as a function of octene content. Also in this case, the crystallization temperature and the crystallization enthalpy decrease with decreasing comonomer content.

The kinetics parameters evaluated from the interpolation of the experimental data of Figures 1.107B-1.110B and 1.114B with the Avrami equation 1.2 are also reported in Table 1.16. The sample sPPOt-1 (1.9 mol% of 1-octene) shows two crystallization peaks in the DSC cooling scan of Figure 1.107A, corresponding to two crystallization processes characterized by different rates; the first process occurring at $T \approx 104$°C characterized by Avrami exponent $n = 2$, corresponding to a two-dimensional growth with heterogenous nucleation or one-dimensional growth with homogeneous nucleation, and semi-crystallization time $t_{1/2} = 130$ s, is followed by a slower second crystallization process at $T \approx 92$°C with $n = 4$, corresponding to growth in 3 dimensions with homogeneous nucleation, and $t_{1/2} = 207$ s (Figure 1.107). However, multiple crystallization peaks may also indicate that the sample has undergone partial degradation at

high temperature. Samples sPPOt-2 (2.7 mol% of 1-octene) and sPPOt-6 (6.1 mol% of 1-octene) show $n \approx 3$ (three-dimensional growth in case of heterogenous nucleation or two-dimesional growth in case of homogenous nucleation), while other samples exhibit n values lower than 1 (heterogeneous nucleation and one-dimensional growth). The values of semi-crystallization time $t_{1/2}$ reported in Figure 1.115C increases with increasing 1-octene content and long $t_{1/2}$ times have been obtained from WAXS analysis in samples sPPOt7 (9.3 mol% of 1-octene) and sPPOt8 (18.8 mol% of 1-octene) that cold-crystallize upon aging (Figure 1.115C).

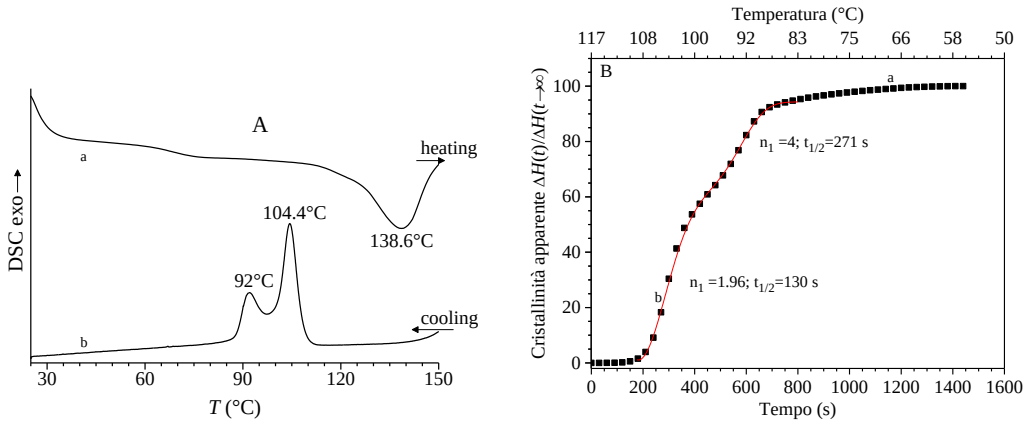

Figure 1.107. *DSC curves recorded during heating at 40°C/min from room temperature up to 155°C (a) and successive cooling to room temperature at 2.5°C/min (b) of the sPPOt-1 (1.9 mol% of 1-octene) (A). Degree of apparent crystallinity as a function of time and temperature evaluated from DSC curves using equation 1.1 and interpolation with Avrami equation 1.2 (B).*

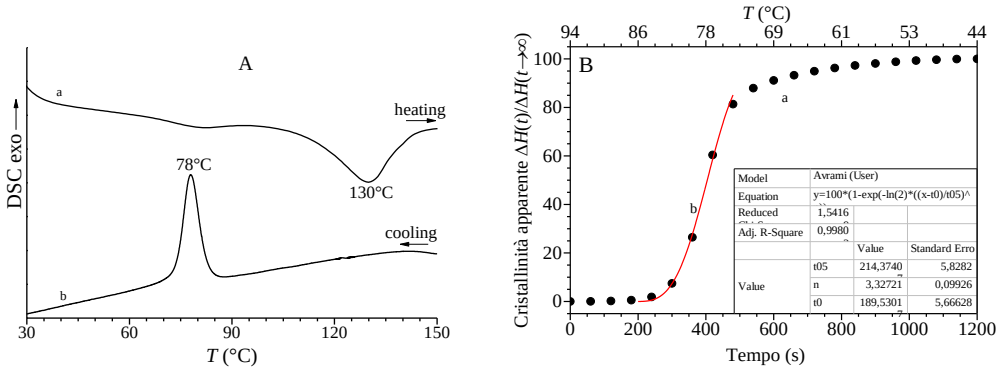

Figure 1.108. *DSC curves recorded during heating at 40°C/min from room temperature up to 155°C (a) and successive cooling to room temperature at 2.5°C/min (b) of the sPPOt-2 (2.7 mol% of 1-octene) (A). Degree of apparent crystallinity as a function of time and temperature evaluated from DSC curves using equation 1.1 and interpolation with Avrami equation 1.2 (B).*

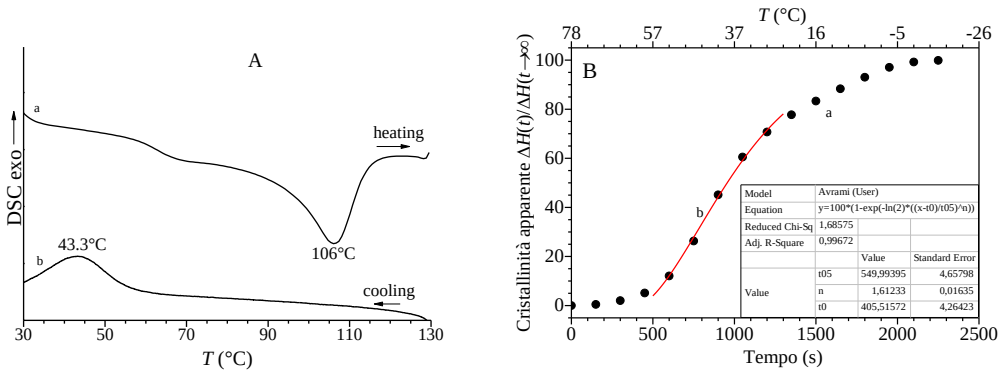

Figure 1.109. *DSC curves recorded during heating at 40°C/min from room temperature up to 130°C (a) and successive cooling to room temperature at 2.5°C/min (b) of the sPPOt-4 (4 mol% of 1-octene) (A). Degree of apparent crystallinity as a function of time and temperature evaluated from DSC curves using equation 1.1 and interpolation with Avrami equation 1.2 (B).*

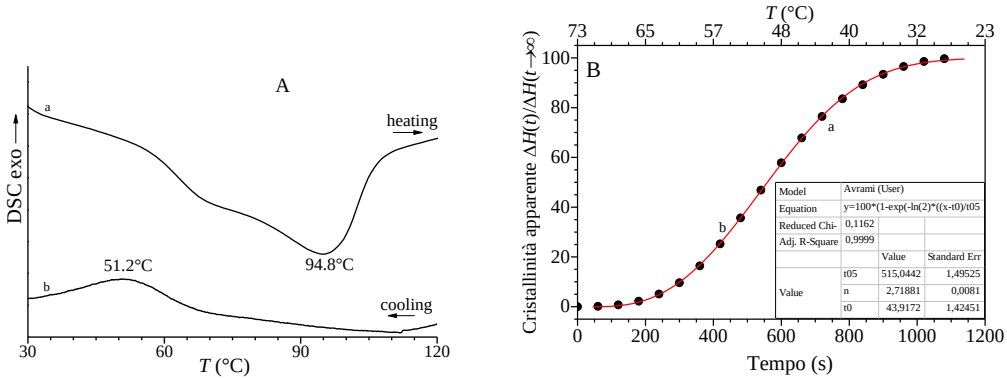

Figure 1.110. *DSC curves recorded during heating at 40°C/min from room temperature up to 130°C (a) and successive cooling to room temperature at 2.5°C/min (b) of the sPPOt-6 (6.1mol% of 1-octene) (A). Degree of apparent crystallinity as a function of time and temperature evaluated from DSC curves using equation 1.1 and interpolation with Avrami equation 1.2 (B).*

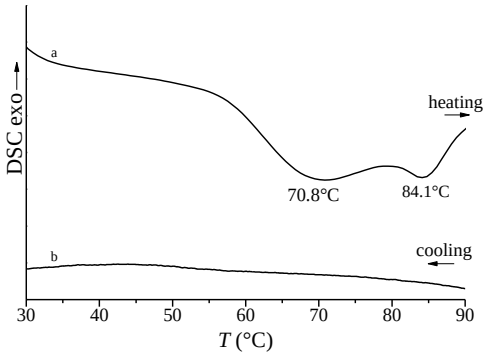

Figure 1.111. *DSC curves recorded during heating at 40°C/min from room temperature up to 100°C (a) and successive cooling to room temperature at 2.5°C/min (b) of the sPPOt-7 (9.3 mol% of 1-octene).*

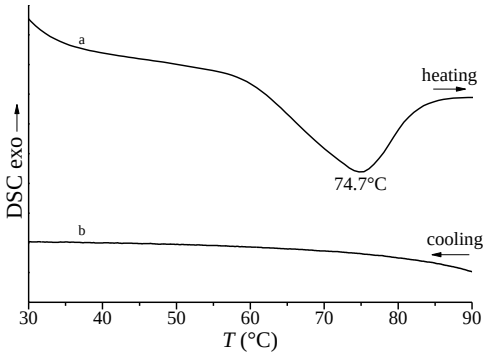

Figure 1.112. *DSC curves recorded during heating at 40°C/min from room temperature up to 100°C (a) and successive cooling to room temperature at 2.5°C/min (b) of the sPPOt-8 (18.8 mol% of 1-octene).*

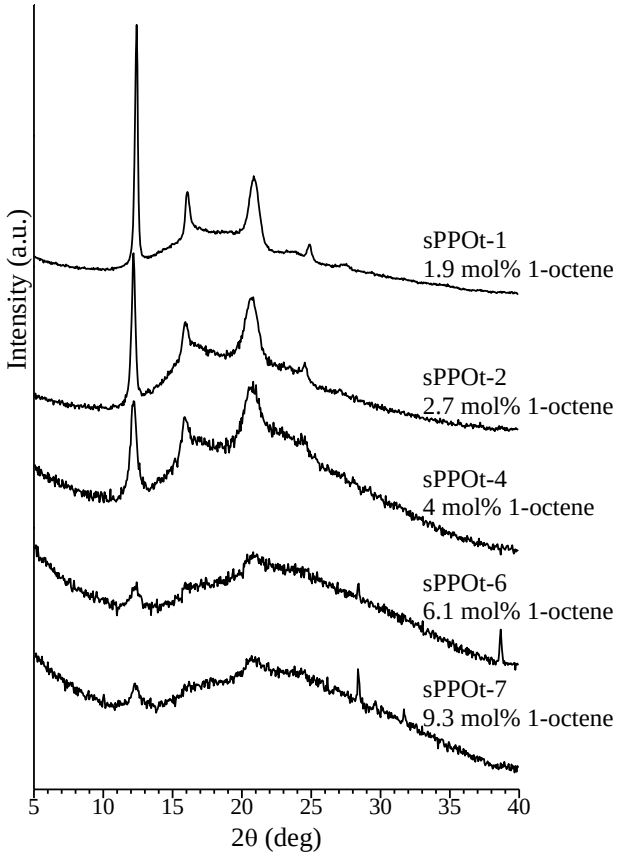

Figure 1.113.. *X-ray powder diffraction profiles of samples of sPPOc copolymers of different 1-octene concentrations crystallized from the melt in DSC by cooling at 2.5 °C/min cooling rate (curves b of Figures 1.107A-1.110A and 1.111-1.112).*

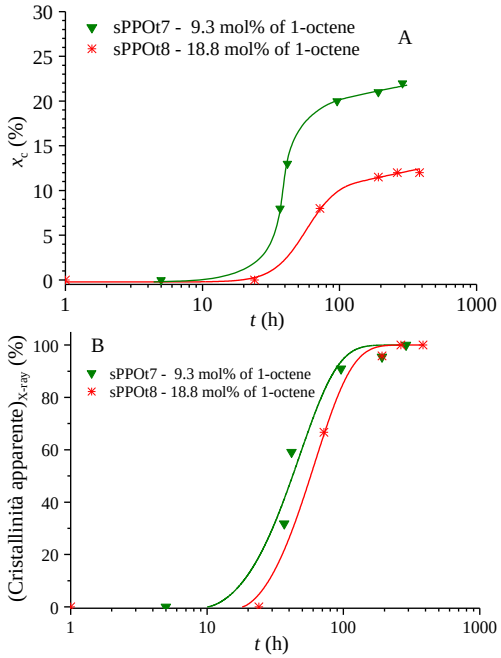

Figure 1.114. *Degree of crystallinity (A) and apparent crystallnity (B) as a function of aging time of samples sPPOt-7 (9.3 mol% of 1-octene) and sPPOt-8 (18.8 mol% of 1-octene). The data have been evaluated by using the WAXS profile of ref 146. The fitting of the kinetic curves with Avrami equation is also shown in B.*

Table 1.16. *Melting temperature (T_m) and enthalpy (ΔH_m), crystallization temperature (T_c) and enthalpy (ΔH_c), Avrami exponent n, semi-crystallization time ($t_{1/2}$), incipient crystallization time (t_0) and time required to achieve 50% of the total apparent crystallinity ($t_{1/2}+t_0$) for all sPPOt copolymers with different 1-octene content.*

Samples	1-octene (mol%)	T_m (°C)	ΔH_m (J/g)	T_c (°C)	ΔH_c (J/g)	*n*	t_0 (s)	$t_{1/2}$(s)	$t_{1/2}+t_0$(s)
sPPOt-1[a]	1.9	138.6	-76.5	104.4 92	43.7	2 4	177	130 207	307 384
sPPOt-2	2.7	130	-63	78	24	3.3	189.5	214	404
sPPOt-4	4	106	-54.9	43.3	11.9	1.6	405.5	550	955
sPPOt-6	6.1	94.8	-67.4	51.2	5.6	2.7	44	515	559
sPPOt-7[b]	9.3	70.8	-31.7	/	/	1.4	36000	115×10^3	151×10^3
sPPOt-8 [b]	18.8	74.7	-25	/	/	1.4	64800	140×10^3	205×10^3

[a]) This sample seems to have two different nucleation process. [b]) The kinetic parameters of this sample have been evaluated from WAXS analysis.

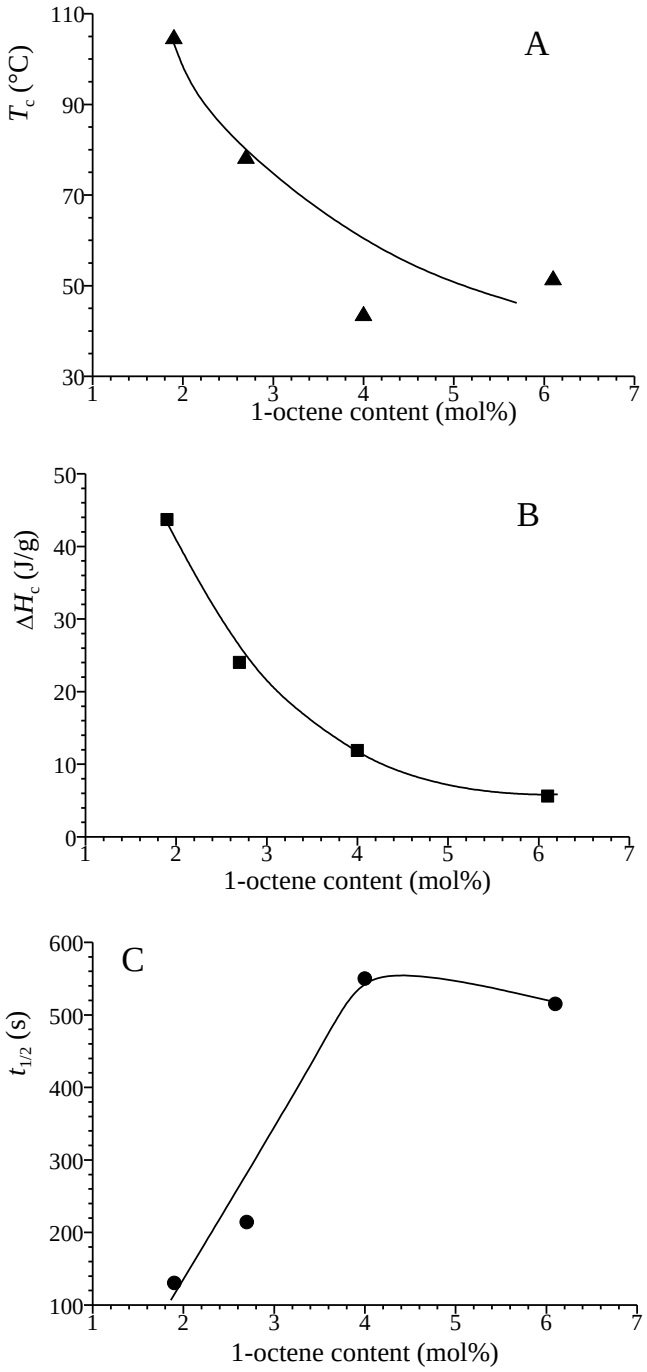

Figure 1.115. *Values of crystallization temperature (T_c) (A), crystallization enthalpy (ΔH_c) (B) and semi-crystallization time ($t_{1/2}$) (C) of sPPOt copolymers as a function of 1-octene content.*

1.7.7. Crystallization kinetics of copolymers of sPP with 1-dodecene

The DSC curves recorded during heating at 40 °C/min and cooling from the melt at cooling rate of 2.5 °C/min of samples of sPPC12 copolymers with different 1-dodecene content, the corresponding crystallization kinetics curves evaluated from the crystallization exotherms with the equation 1.1, and the fitting of these curves with the equation 1.2, are reported in Figures 1.116-1.120. The X-ray diffraction profiles of the samples crystallized in the DSC after the cooling scans of Figures 1.116A-1.120A are reported in Figure 1.121. All samples crystallize from the melt in form I of sPP. Similar data have been reported for thin films crystallized from the melt in the same conditions at 2.5 °C/min for the POM observation in Figure 1.50B.

The values of the melting and crystallization temperatures and enthalpies for all sPPC12 samples are reported in Table 1.17, whereas the values of crystallization temperature and enthalpy are reported in Figure 1.122A,B as a function of 1-dodecene content. Also in this case, the crystallization temperature and the crystallization enthalpy decrease with decreasing comonomer content.

Table 1.17 also reports all kinetics parameters evaluated from the interpolation of the experimental data of Figures 1.116B-1.120B with the Avrami equation 1.2. Only the sample sPPC12-1 (0.8 mol% of 1-dodecene) shows an Avrami exponent of ≈ 3 indicating three-dimensional growth with heterogeneous nucleation or two-dimensional growth with homogeneous nucleation. The other samples, that is sPPC12-2 (1.8 mol% of 1-dodecene), sPPC12-3 (2.7 mol% of 1-dodecene) and sPPC12-5 (6 mol% of 1-dodecene), exhibit *n* values around 2 (two-dimensional growth and hetrogenous nucleation or one-dimensional growth with homogeneous nucleation), while *n* value lower than 2 (one-dimensional growth with heterogeneous nucleation) has been observed in sample sPPC12-4 (4.2 mol% of 1-dodecene). Similar values of semi-crystallization time $t_{1/2}$, reported in Figure 1.122C as a function of dodecene content, have been observed in samples with low and intermediate comonomer concentrations (113-135 s), while a higher value has been observed in the sample with the highest 1-dodecene content (234 s) (Table 1.17 and Figure 1.122C).

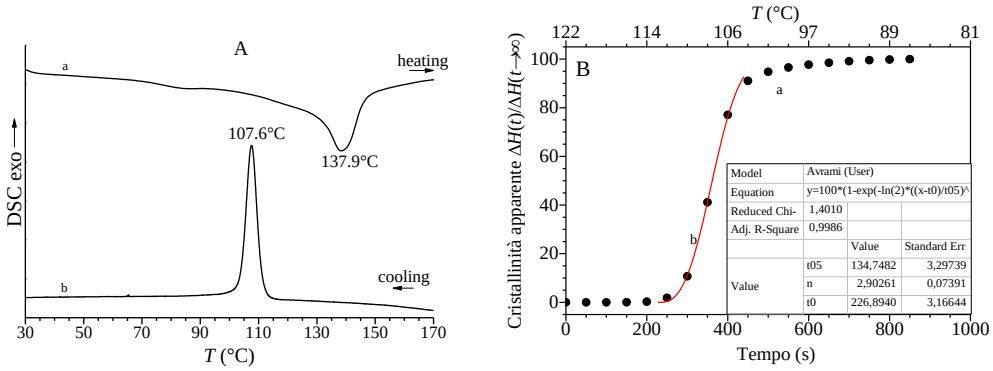

Figure 1.116. *DSC curves recorded during heating at 40°C/min from room temperature up to 180°C (a) and successive cooling to room temperature at 2.5°C/min (b) of the sPPC12-1 (0.8 mol% of 1-dodecene) (A). Degree of apparent crystallinity as a function of time and temperature evaluated from DSC curves using equation 1.1 and interpolation with Avrami equation 1.2 (B).*

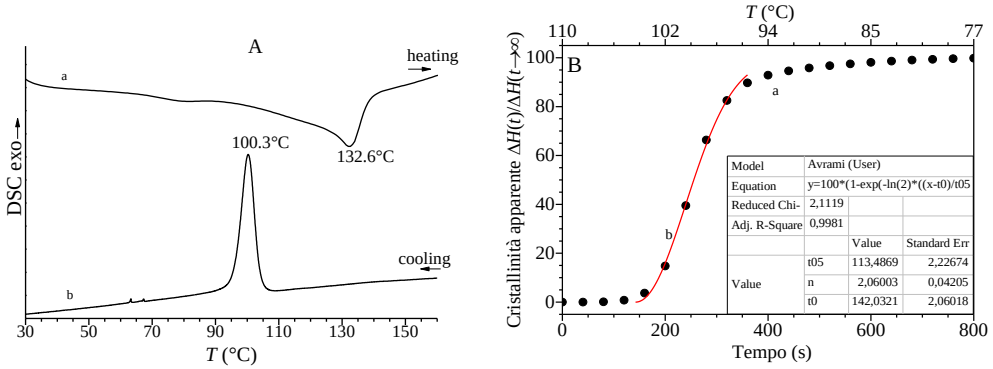

Figure 1.117. *DSC curves recorded during heating at 40°C/min from room temperature up to 170°C (a) and successive cooling to room temperature at 2.5°C/min (b) of the sPPC12-2 (1.8 mol% of 1-dodecene) (A). Degree of apparent crystallinity as a function of time and temperature evaluated from DSC curves using equation 1.1 and interpolation with Avrami equation 1.2 (B).*

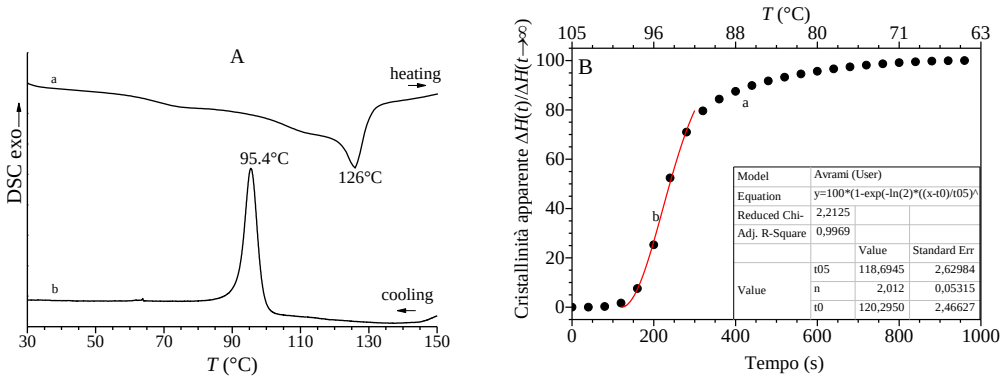

Figure 1.118. *DSC curves recorded during heating at 40°C/min from room temperature up to 160°C (a) and successive cooling to room temperature at 2.5°C/min (b) of the sPPC12-3 (2.7 mol% of 1-dodecene) (A). Degree of apparent crystallinity as a function of time and temperature evaluated from DSC curves using equation 1.1 and interpolation with Avrami equation 1.2 (B).*

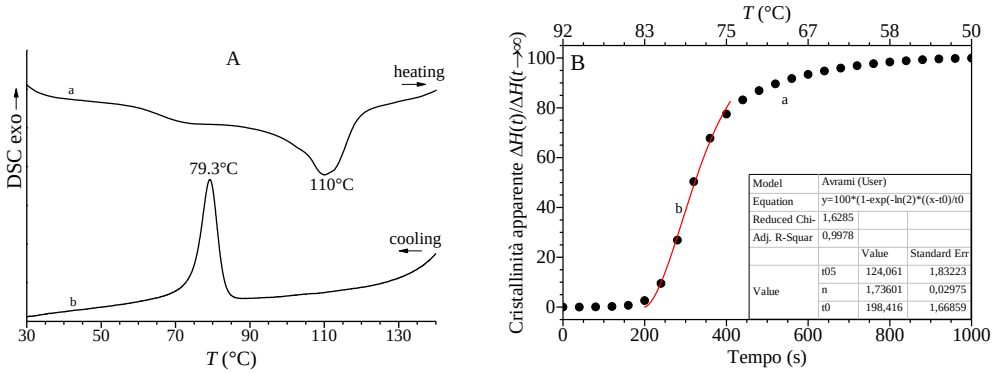

Figure 1.119. *DSC curves recorded during heating at 40°C/min from room temperature up to 150°C (a) and successive cooling to room temperature at 2.5°C/min (b) of the sPPC12-4 (4.2 mol% of 1-dodecene) (A). Degree of apparent crystallinity as a function of time and temperature evaluated from DSC curves using equation 1.1 and interpolation with Avrami equation 1.2 (B).*

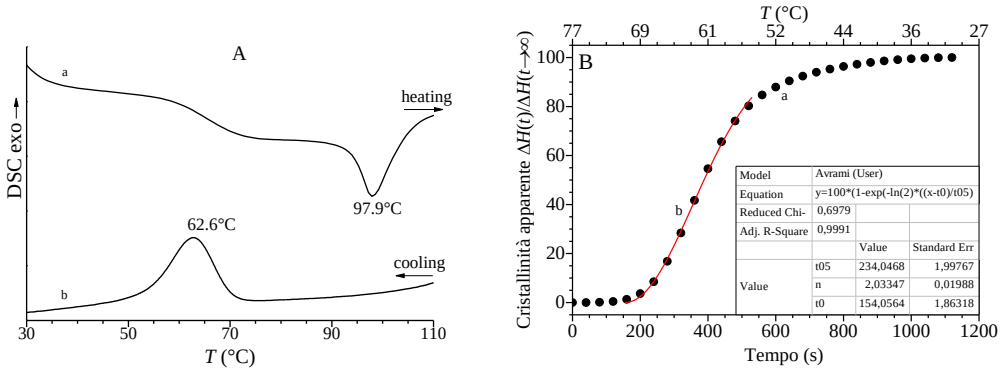

Figure 1.120. *DSC curves recorded during heating at 40°C/min from room temperature up to 120°C (a) and successive cooling to room temperature at 2.5°C/min (b) of the sPPC12-5 (6 mol% of 1-dodecene) (A). Degree of apparent crystallinity as a function of time and temperature evaluated from DSC curves using equation 1.1 and interpolation with Avrami equation 1.2 (B).*

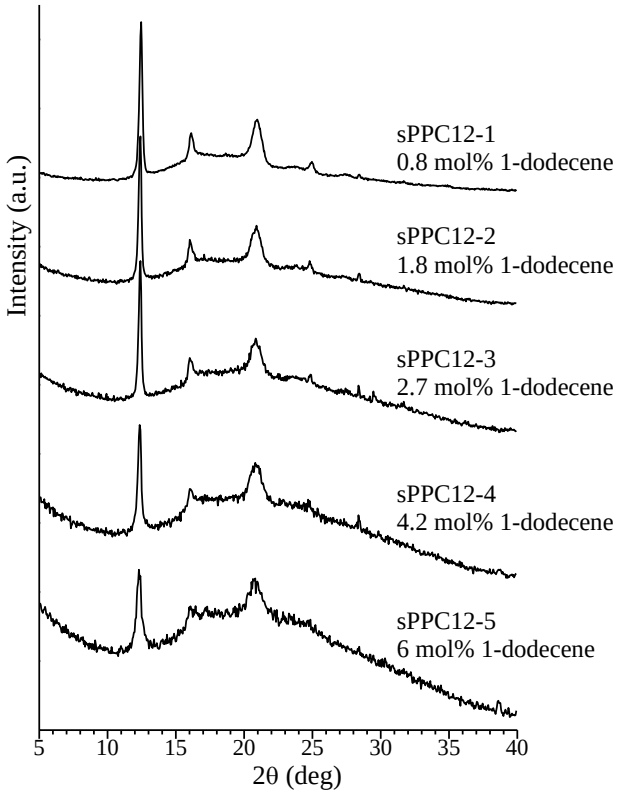

Figure 1.121. *X-ray powder diffraction profiles of samples of sPPC12 copolymers of different 1-dodecene concentrations crystallized from the melt in DSC by cooling at 2.5 °C/min cooling rate (curves b of Figures 1.116A-1.120A).*

Table 1.17. *Melting temperature (T_m) and enthalpy (ΔH_m), crystallization temperature (T_c) and enthalpy (ΔH_c), Avrami exponent n, semi-crystallization time ($t_{1/2}$), incipient crystallization time (t_0) and time required to achieve the 50% of the total apparent crystallinity ($t_{1/2}+t_0$) for all sPPC12 copolymers with different 1-dodecene content.*

Samples	1-dodecene (mol%)	T_m (°C)	ΔH_m (J/g)	T_c (°C)	ΔH_c (J/g)	n	t_0 (s)	$t_{1/2}$(s)	$t_{1/2}+t_0$(s)
sPPC12-1	0.8	137.9	-147.6	107.6	51.7	2.9	227	135	362
sPPC12-2	1.8	132.6	-98.3	100.3	44.6	2.1	142	113	255
sPPC12-3	2.7	126	-75.3	95.4	31.8	2	120	119	239
sPPC12-4	4.2	110	-74.3	79.3	22.1	1.7	198	124	322
sPPC12-5	6	97.9	-49	62.6	14.2	2	154	234	388

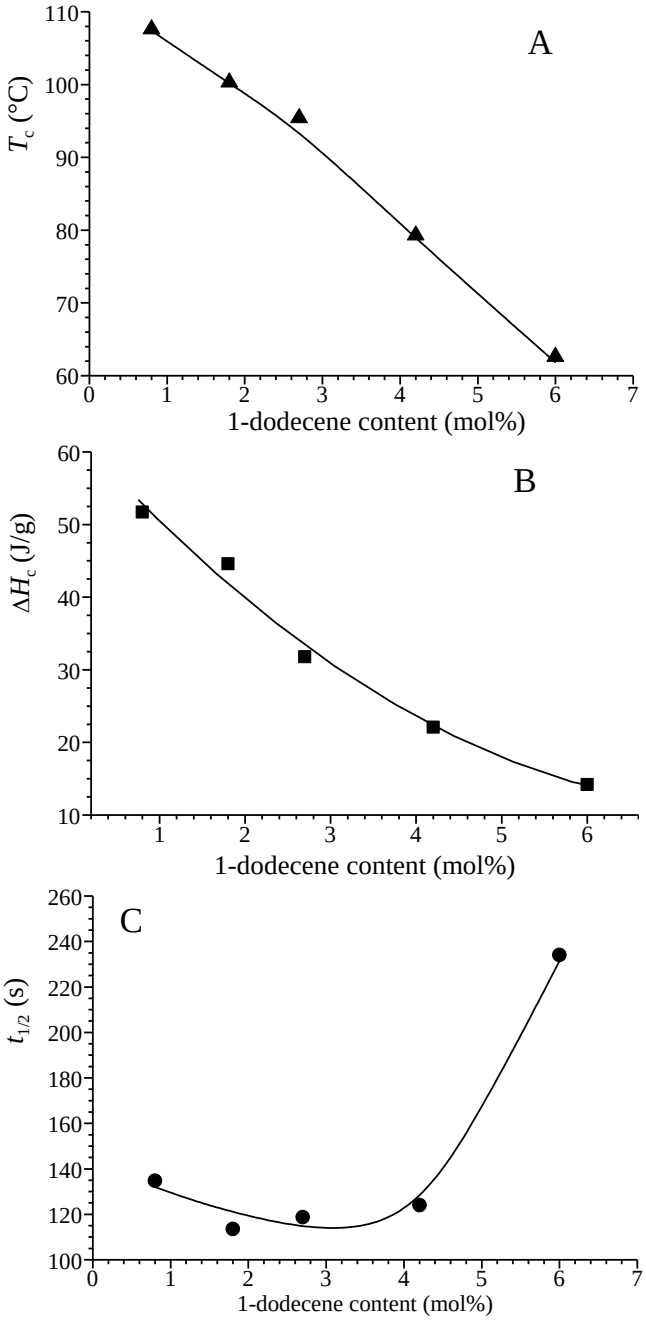

***Figure 1.122**. Values of crystallization temperature (T_c) (A), crystallization enthalpy (ΔH_c) (B) and semi-crystallization time ($t_{1/2}$) (C) of sPPC12 copolymers as a function of 1-dodecene content.*

1.7.8. Crystallization kinetics of copolymers of sPP with 1-octadecene.

The DSC curves recorded during heating at 40 °C/min and cooling from the melt at cooling rate of 2.5 °C/min of samples of sPPC18 copolymers with different 1-octadecene concentration, the corresponding crystallization kinetics curves evaluated from the crystallization exotherms with the equation 1.1, and the fitting of these curves with the equation 1.2, are reported in Figures 1.123-1.127. The X-ray diffraction profiles of the samples crystallized in the DSC after the cooling scans of Figures 1.123A-1.127A are reported in Figure 1.128. All samples crystallize from the melt in form I of sPP. Similar data have been reported for thin films crystallized from the melt in the same conditions at 2.5 °C/min for the POM observation in Figure 1.51B.

The values of the melting and crystallization temperatures and enthalpies for all sPPC18 samples are reported in Table 1.18, whereas the values of crystallization temperature and enthalpy are reported in Figure 1.129A,B as a function of 1-octadecene content. Also in this case, the crystallization temperature and the crystallization enthalpy decrease with decreasing comonomer content.

The values of the kinetics parameters evaluated from the interpolation of the experimental data of Figures Figures 1.123B-1.127B with the Avrami equation 1.2 are also eported in Table 1.18. The sample with the lowest 1-octadecene content (sPPC18a_iAc, 0.7 mol% of 1-octadecene) displays the highest value of Avrami exponent (n = 4) that indicates homogeneous nucleation and three-dimensional growth. Samples CA-sPPC18-4_iAc (0.9 mol% of 1-octadecene) and CA-sPPC18-12_iAc (1.7 mol% of 1-octadecene) show values of $n \approx 3$ indicating three-dimensional growth with heterogeneous nucleation or two-dimensional growth with homogeneous nucleation. Samples sPPC18-2_iAc (2.8 mol% of 1-octadecene) and sPPC18c_iAc (5.5mol% of 1-octadecene) exhibit n values in the range 2-3 that may indicate two-dimensional growth with heterogeneous nucleation or one-dimensional growth with homogeneous nucleation. The values of semi-crystallization time $t_{1/2}$ are reported in Figure 1.129C. Very different values of $t_{1/2}$ have been observed, from the lowest value of the sample CA-sPPC18-4_iAc (183 s) to the highest value of the sample sPPC18-2_iAc (518 s).

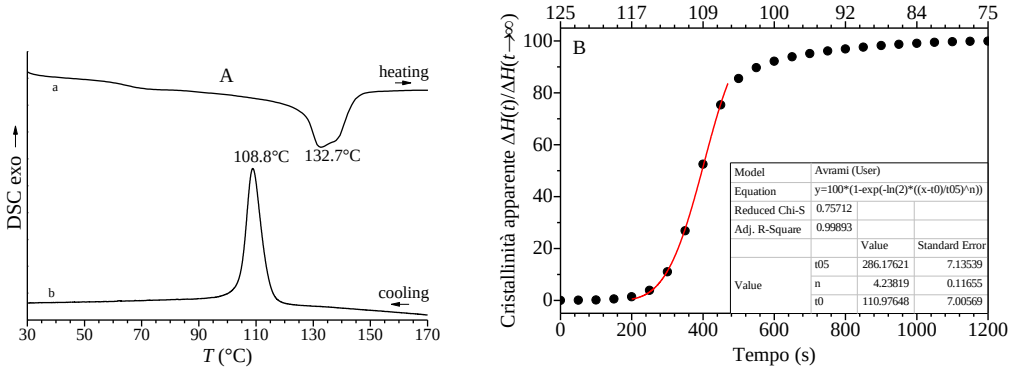

Figure 1.123 *DSC curves recorded during heating at 40°C/min from room temperature up to 180°C (a) and successive cooling to room temperature at 2.5°C/min (b) of the sPPC18-a_iAc (0.7 mol% of 1-octadecene) (A). Degree of apparent crystallinity as a function of time and temperature evaluated from DSC curves using equation 1.1 and interpolation with Avrami equation 1.2 (B).*

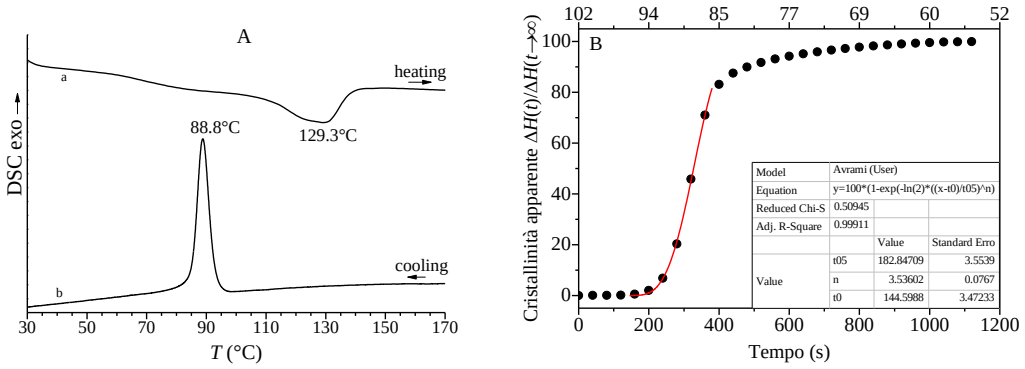

Figure 1.124 *DSC curves recorded during heating at 40°C/min from room temperature up to 180°C (a) and successive cooling to room temperature at 2.5°C/min (b) of the CA-sPPC18-4_iAc (0.9 mol% of 1-octadecene) (A). Degree of apparent crystallinity as a function of time and temperature evaluated from DSC curves using equation 1.1 and interpolation with Avrami equation 1.2 (B).*

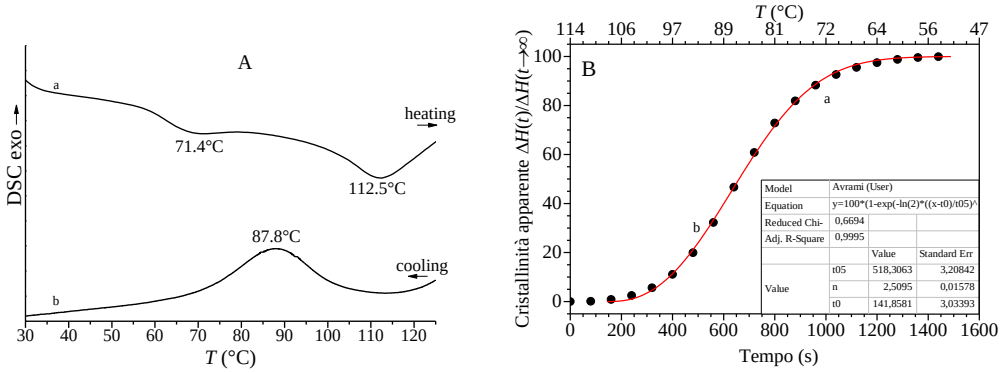

Figure 1.125 *DSC curves recorded during heating at 40°C/min from room temperature up to 130°C (a) and successive cooling to room temperature at 2.5°C/min (b) of the sPPC18-2_iAc (2.8 mol% of 1-octadecene) (A). Degree of apparent crystallinity as a function of time and temperature evaluated from DSC curves using equation 1.1 and interpolation with Avrami equation 1.2 (B).*

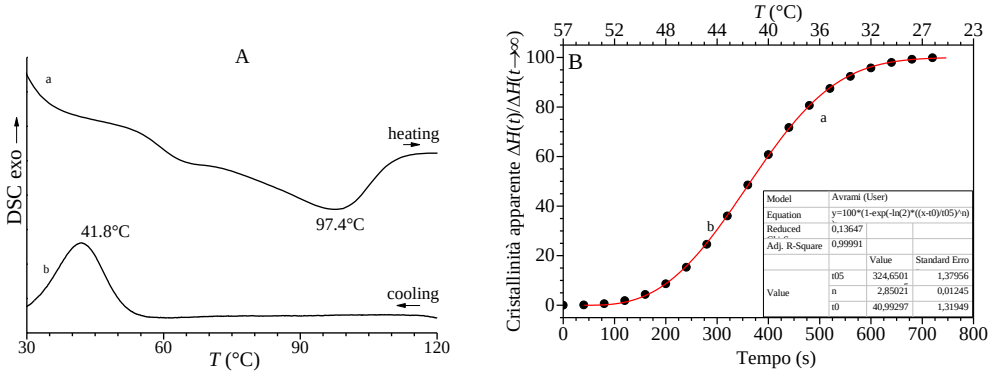

Figure 1.126 *DSC curves recorded during heating at 40°C/min from room temperature up to 130°C (a) and successive cooling to room temperature at 2.5°C/min (b) of the CA-sPPC18-12_iAc (4.2 mol% of 1-octadecene) (A). Degree of apparent crystallinity as a function of time and temperature evaluated from DSC curves using equation 1.1 and interpolation with Avrami equation 1.2 (B).*

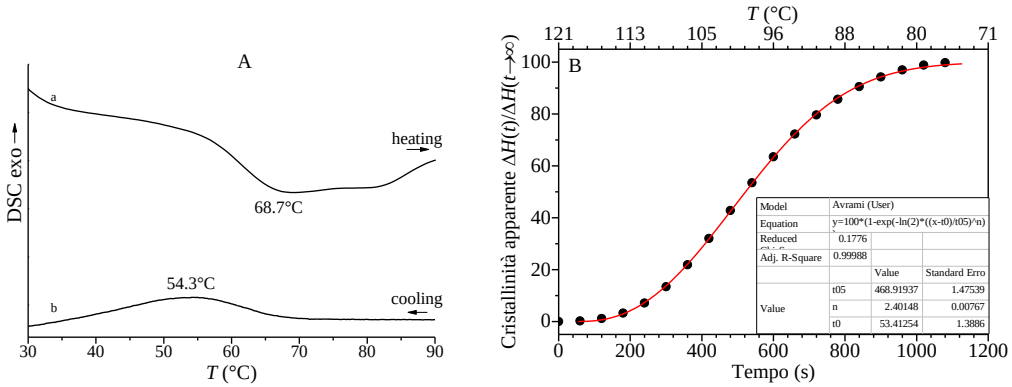

Figure 1.127 *DSC curves recorded during heating at 40°C/min from room temperature up to 100°C (a) and successive cooling to room temperature at 2.5°C/min (b) of the sPPC18-c_iAc (5.5 mol% of 1-octadecene) (A). Degree of apparent crystallinity as a function of time and temperature evaluated from DSC curves using equation 1.1 and interpolation with Avrami equation 1.2 (B).*

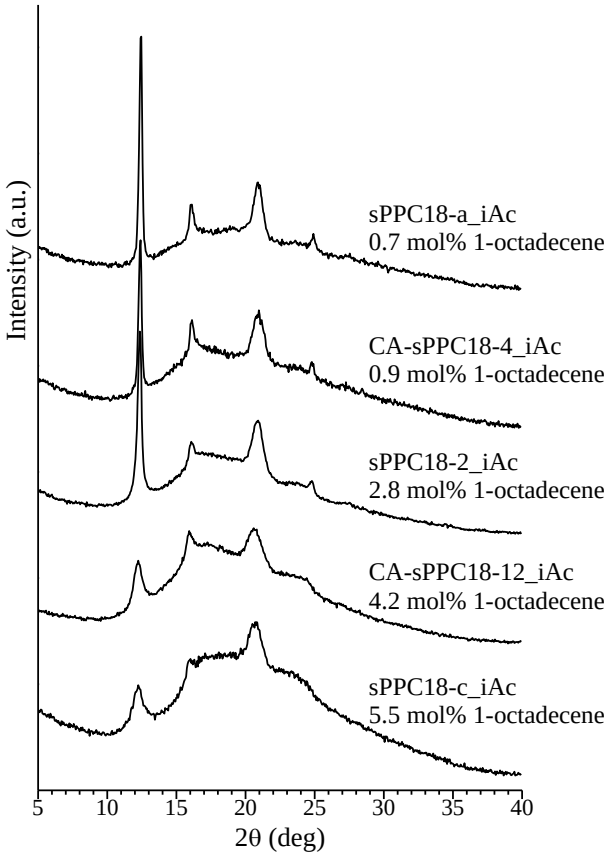

Figure 1.128. *X-ray powder diffraction profiles of samples of sPPC18 copolymers of different 1-octadecene concentrations crystallized from the melt in DSC by cooling at 2.5 °C/min cooling rate (curves b of Figures 1.123A-1.127A).*

Table 1.18. *Melting temperature (T_m) and enthalpy (ΔH_m), crystallization temperature (T_c) and enthalpy (ΔH_c), Avrami exponent n, semi-crystallization time ($t_{1/2}$), incipient crystallization time (t_0) and time required to achieved 50% of the total apparent crystallinity ($t_{1/2}+t_0$) for all sPPC18 copolymers with different 1-octadecene content.*

Samples	1-octadecene (mol%)	T_m (°C)	ΔH_m (J/g)	T_c (°C)	ΔH_c (J/g)	n	t_0 (s)	$t_{1/2}$(s)	$t_{1/2}+t_0$(s)
sPPC18a_iAc	0.7	132.7	-74.6	108.8	43.7	4	123	275	398
CA_sPPC18-4_iAc	0.9	129.3	-53.7	88.8	31.1	3.5	145	183	327
sPPC18-2_iAc	2.8	112.5	-31	87.8	15.5	2.5	142	518	660
CA_sPPC18-12_iAc	4.2	97.4	-38.2	41.8	14.1	2.8	41	325	366
sPPC18c_iAc	5.5	68.7	-25.1	54.3	/	2.4	53	469	522

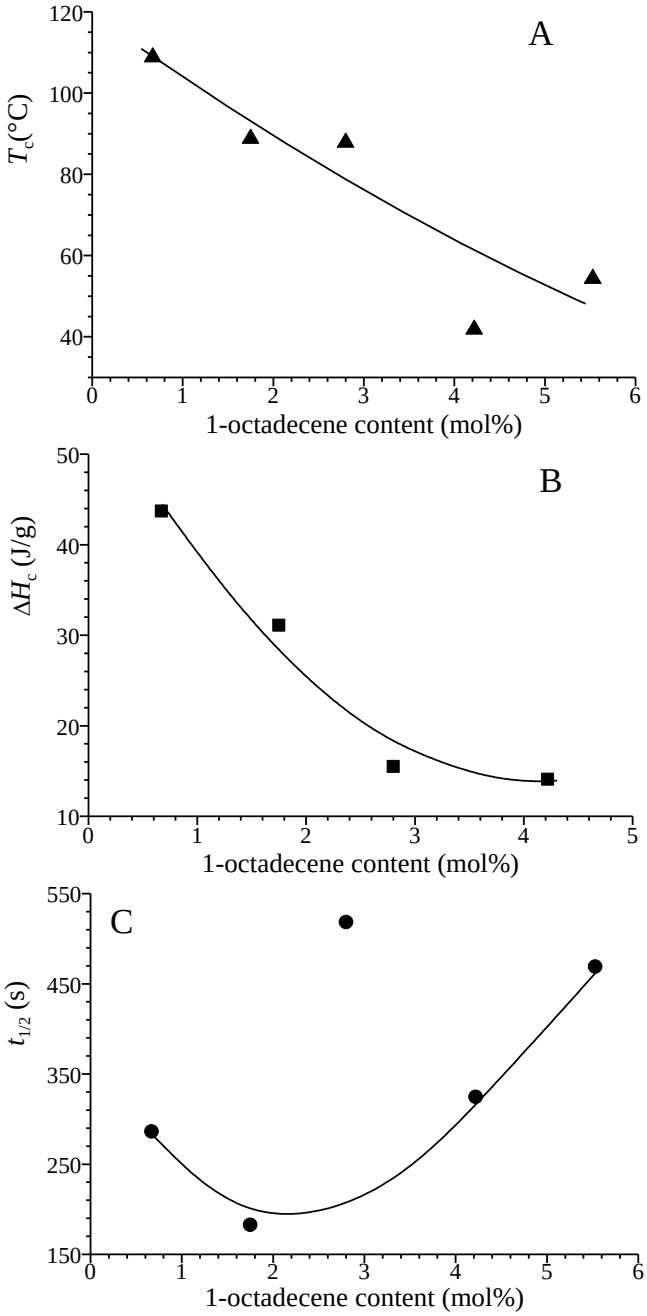

Figure 1.129. *Values of crystallization temperature (T_c) (A), crystallization enthalpy (ΔH_c) (B) and semi-crystallization time ($t_{1/2}$) (C) of sPPC18 copolymers as a function of 1-octadecene content.*

1.7.9. Crystallization kinetics of copolymers of sPP with 1-eicosene

The DSC curves recorded during heating at 40 °C/min and cooling from the melt at cooling rate of 2.5 °C/min of samples of sPPC20 copolymers with different 1-eicosene concentration, the corresponding crystallization kinetics curves evaluated from the crystallization exotherms with the equation 1.1, and the fitting of these curves with the equation 1.2, are reported in Figures 1.130-1.132. The X-ray diffraction profiles of the samples crystallized in the DSC after the cooling scans of Figures 1.130A-1.132A are reported in Figure 1.133. All samples crystallize from the melt in form I of sPP. Similar data have been reported for thin films crystallized from the melt in the same conditions at 2.5 °C/min for the POM observation in Figure 1.52B.

The values of the melting and crystallization temperatures and enthalpies for all sPPC20 samples are reported in Table 1.19, whereas the values of crystallization temperature and enthalpy are reported in Figure 1.134A,B as a function of 1-eicosene content. Also in this case, the crystallization temperature and the crystallization enthalpy decrease with decreasing comonomer content.

Table 1.19 also reports all kinetics parameters evaluated from the interpolation of the experimental data of Figures Figures 1.130B-1.132B with the Avrami equation 1.2. The values of semi-crystallization time $t_{1/2}$ are reported in Figure 1.134C. The samples sPPC20-2_iEE and sPPC20-3_iEE, with 0.7 and 1.6 mol% of 1-eicosene respectively, show very similar and high values of Avrami exponent ($n \approx 4$ corresponding to three dimensional growth with homogeneous nucleation) and also similar values of $t_{1/2}$ ($\approx$ 200 s) (Figure 1.134C). The sample sPPC20-5_iEE with 3.9 mol% of 1-eicosene exhibits n value of 3, corresponding to three-dimensional growth with heterogeneous nucleation or two-dimensional growth with homogeneous nucleation, and slightly higher value of $t_{1/2}$ (350 s).

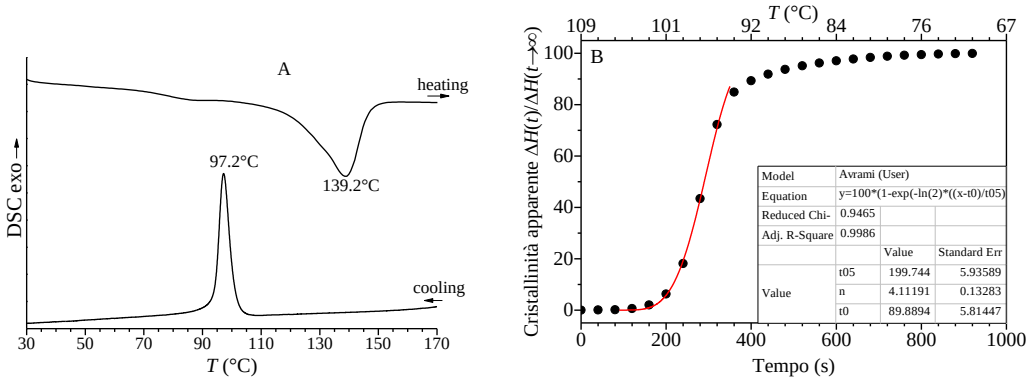

Figure 1.130. *DSC curves recorded during heating at 40°C/min from room temperature up to 180°C (a) and successive cooling to room temperature at 2.5°C/min (b) of the sPPC20-2_iEE (0.7 mol% of 1-eicosene) (A). Degree of apparent crystallinity as a function of time and temperature evaluated from DSC curves using equation 1.1 and interpolation with Avrami equation 1.2 (B).*

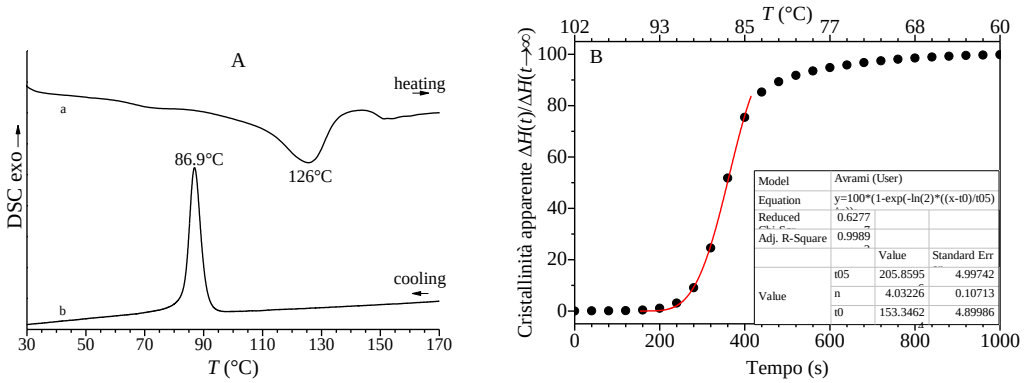

Figure 1.131. *DSC curves recorded during heating at 40°C/min from room temperature up to 180°C (a) and successive cooling to room temperature at 2.5°C/min (b) of the sPPC20-3_iEE (1.6 mol% of 1-eicosene) (A). Degree of apparent crystallinity as a function of time and temperature evaluated from DSC curves using equation 1.1 and interpolation with Avrami equation 1.2 (B).*

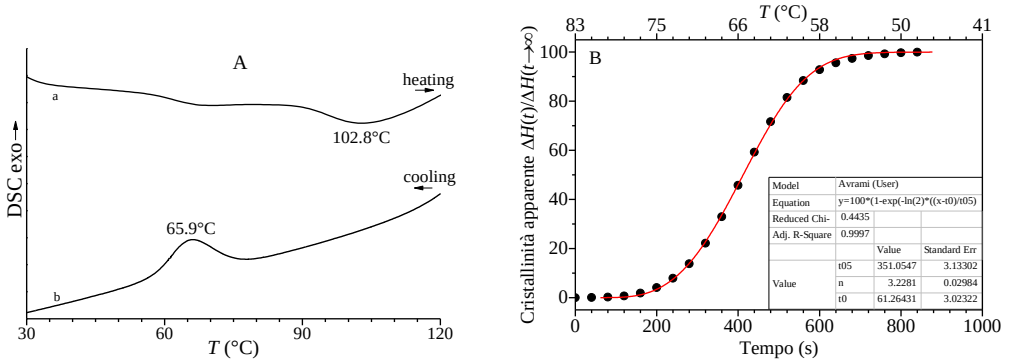

Figure 1.132. *DSC curves recorded during heating at 40°C/min from room temperature up to 130°C (a) and successive cooling to room temperature at 2.5°C/min (b) of the sPPC20-5_iEE (3.9 mol% of 1-eicosene) (A). Degree of apparent crystallinity as a function of time and temperature evaluated from DSC curves using equation 1.1 and interpolation with Avrami equation 1.2 (B).*

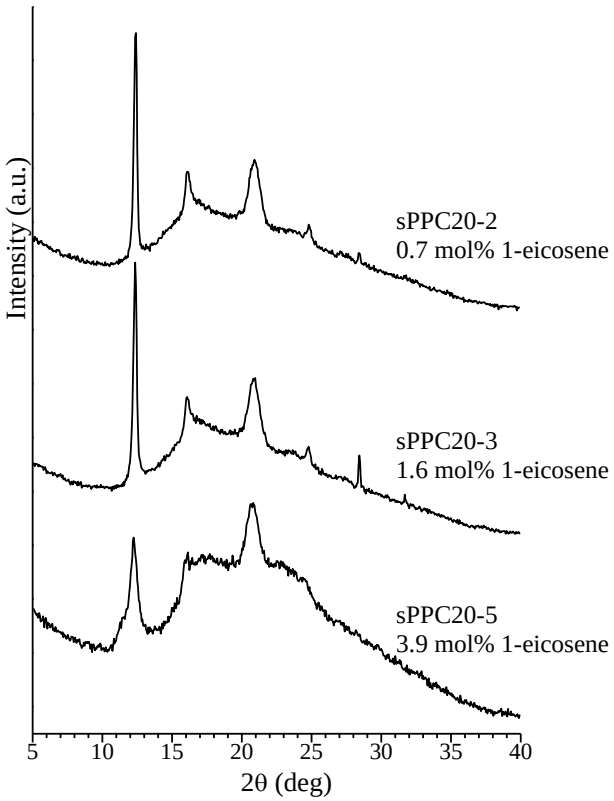

Figure 1.133. *X-ray powder diffraction profiles of samples of sPPC20 copolymers of different 1-eicosene concentrations crystallized from the melt in DSC by cooling at 2.5 °C/min cooling rate (curves b of Figures 1.130A-1.132A).*

Table 1.19. *Melting temperature (T_m) and enthalpy (ΔH_m), crystallization temperature (T_c) and enthalpy (ΔH_c), semi-crystallization time ($t_{1/2}$), incipient crystallization time (t_0) and time required to achieve 50% of the total apparent crystallinity ($t_{1/2}+t_0$) for all sPPC20 copolymers with different 1-eicosene content.*

Samples	1-eicosene (mol%)	T_m (°C)	ΔH_m (J/g)	T_c (°C)	ΔH_c (J/g)	n	t_0 (s)	$t_{1/2}$(s)	$t_{1/2}+t_0$(s)
sPPC20-2_iEE	0.7	139.2	-88.1	97.2	31.6	4.1	90	200	290
sPPC20-3_iEE	1.6	126	-68.2	86.9	31.9	4	153	206	359
sPPC20-5_iEE	3.9	102.8	-75.9	65.9	17	3.2	61	351	412

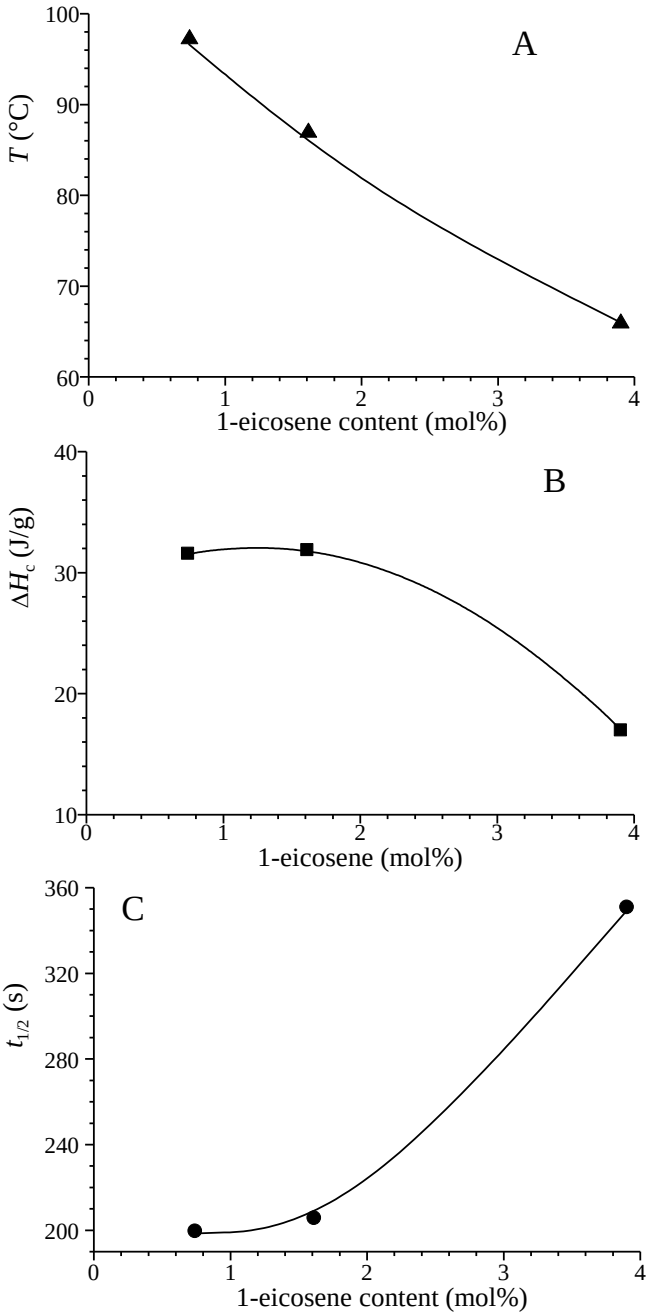

***Figure 1.134**. Values of crystallization temperature (T_c) (A), crystallization enthalpy (ΔH_c) (B) and semi-crystallization time ($t_{1/2}$) (C) of sPPC20 copolymers reported as a function of 1-eicosene content.*

1.7.10. Concluding remarks on the analysis of crystallization kinetics

It is well known that the Avrami equation provides more reliable indications of the mechanisms of nucleation and growth when it is applied in isothermal conditions. However, assuming that not integer values of the Avrami exponents are due to the factors discussed in section 1.14, the analysis of crystallization kinetics by using the Avrami approach in non-isothermal conditions has provided a rough indication of the influence of the stereo- and constitutional defects on the crystallization of the sPP and its random copolymers. In fact, the values of Avrami exponents approximated to the nearest integer number, generally, decrease with increasing concentration of defects (Table 1.20).

Although the value of the Avrami exponent is not directly related to the type and size of the final crystalline aggregate, the biggest aggregates, as bow-tie, bundles and other rare and irregular crystals have generally been observed in samples with the highest *n* value (Figure 1.125). In samples of sPP with different stereoregularity, *n* initially decreases from 4 to 2 with increasing concentration of stereodefects, according with the presence of a complex morphology, where bundles and bow-tie crystals, star structures and open irregular aggregates suggest a crystal growth in more than one dimension (Figure 1.125). The value of $n = 4$ observed in less stereoregular samples (sPP9 and sPP10 with [*rrrr*] =78 and 74.8% respectively) should be confirmed by additional measurements in isothermal conditions.

In copolymers of sPP with ethylene the highest observed value of *n* is 3 in the sample AK-sPPET-2 (1.9 mol% of ethylene) showing bow-tie crystals. In samples with higher concentration of ethylene Avrami exponent $n = 1$ has been observed, indicating one-dimensional growth according with the observed needle/granular morphology (Figure 1.126).

Copolymers of sPP with1-butene display *n* values bigger than those observed for sPPEt copolymers. This is probably related to the co-crystallization of propene and butene comonomeric units and the almost complete inclusion of butene units in the crystals of form I of sPP. The decrease of the Avrami exponent from the value of 4, observed in the sample with the lowest butene content, displaying the largest bow-tie aggregates (Figure 1.127), to the value of 2, observed in samples sPPBu-6 and sPPBu-7, and 1 for the sample sPPBu-9, is consistent with the changes observed in crystals morphology and the presence of thinner and thinner aggregates (Figure 1.127), that suggest lower tendency to branching.

Table 1.20. *Avrami exponent n, semi-crystallization time ($t_{1/2}$) of all samples of sPP of different stereoregularity and all random copolymers of sPP.*

Sample	Stereoregularity or mol% comonomer	*n*	$t_{1/2}$(s)
sRDG-2-1	95.5	4	232
sPP2	95.0	4	204
sPP3	94.2	3	180
sPP4	92.5	3	169
sPP5	91.5	2	178
sPP6	90.7	2	124
sPP7	88.6	3	168
sPP8	87.0	2	277
sPP9	78.0	4	472
sPP10	74.8	4	394
sPP11	70.6	2	366
AK-sPPEt-2	1.9	3	147
sPPEt-4	6.3	2	303
sPPEt-6	8.5	1	148
sPPEt-8	9.8	1	170
sPPEt-9	13.2	2	308
sPPEt-10	14.3	1	226
sPPBu-1	3.2	4	222
sPPBu-2	6.1	3	130
sPPBu-4	11.2	3	183
sPPBu-6	18.2	2	295
sPPBu-7	31.5	2	7×10^3
sPPBu-9[a]	51.7	1	44×10^3
sPPBu-11[a]	69.9	2	32×10^4
sPPBu-12[a]	89	2	141×10^5
sPP-4MP-1	1.8	3	123.3
sPP-4MP-2	4.0	2	153.8
sPP-4MP-4	12.9	2	169.1
sPP-4MP-5	15.2	2	267.3
sPPHe-1	1.7	2	220
sPPHe-2	3	2	178
sPPHe-3	3.9	2	134
sPPHe-5	6.4	2	182
sPPHe-6[a]	9	1	34×10^3
sPPOt-1[b]	1.9	2, 4	130, 207
sPPOt-2	2.7	3	214
sPPOt-4	4	2	550
sPPOt-6	6.1	3	515
sPPOt-7[a]	9.3	1	115×10^3
sPPOt-8 [a]	18.8	1	140×10^3
sPPC12-1	0.8	3	135
sPPC12-2	1.8	2	113
sPPC12-3	2.7	2	119
sPPC12-4	4.2	2	124
sPPC12-5	6	2	234
sPPC18a_iAc	0.7	4	275
CA_sPPC18-4_iAc	0.9	4	183
sPPC18-2_iAc	2.8	3	518
CA_sPPC18-12_iAc	4.2	3	325
sPPC18c_iAc	5.5	2	469
sPPC20-2_iEE	0.7	4	200
sPPC20-3_iEE	1.6	4	206
sPPC20-5_iEE	3.9	3	351

[a]) The kinetic parameters of this sample have been evaluated from WAXS analysis. [b]) This sample seems to have two different nucleation process.

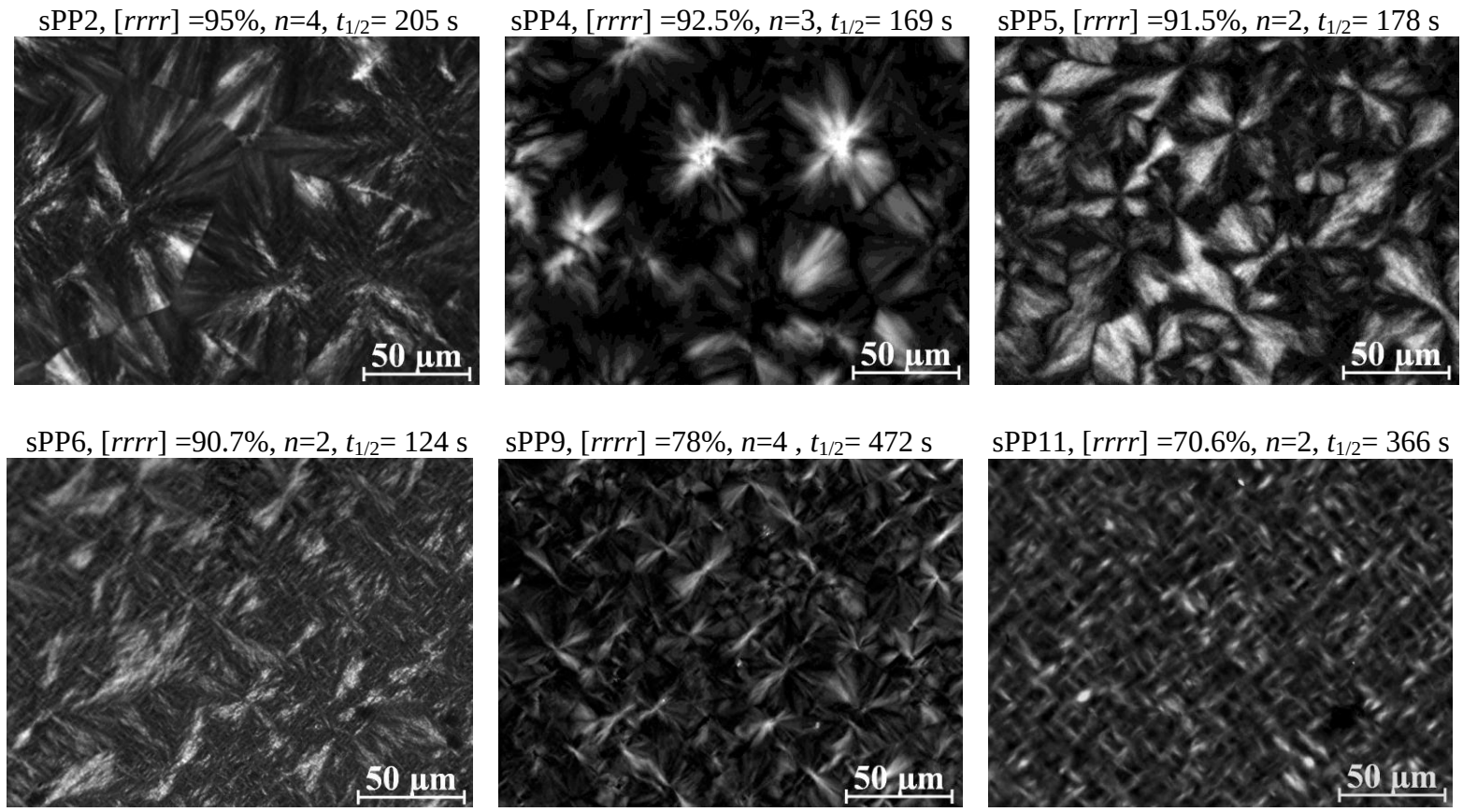

Figure 1.125. *Comparison of POM images of samples of sPP with the indicated [rrrr] pentad concentration and the corresponding Avrami exponent n and semi-crystallization time* $t_{1/2}$.

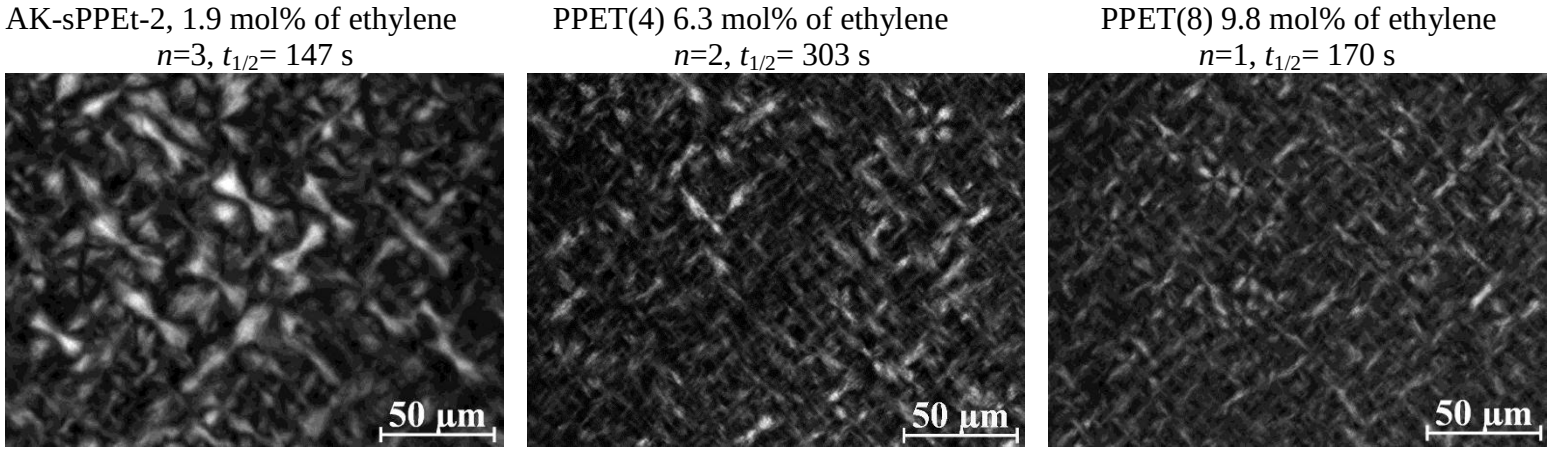

Figure 1.126. *Comparison of POM images of samples of sPPET with the indicated ethylene content and the corresponding Avrami exponent n and semi-crystallization time* $t_{1/2}$.

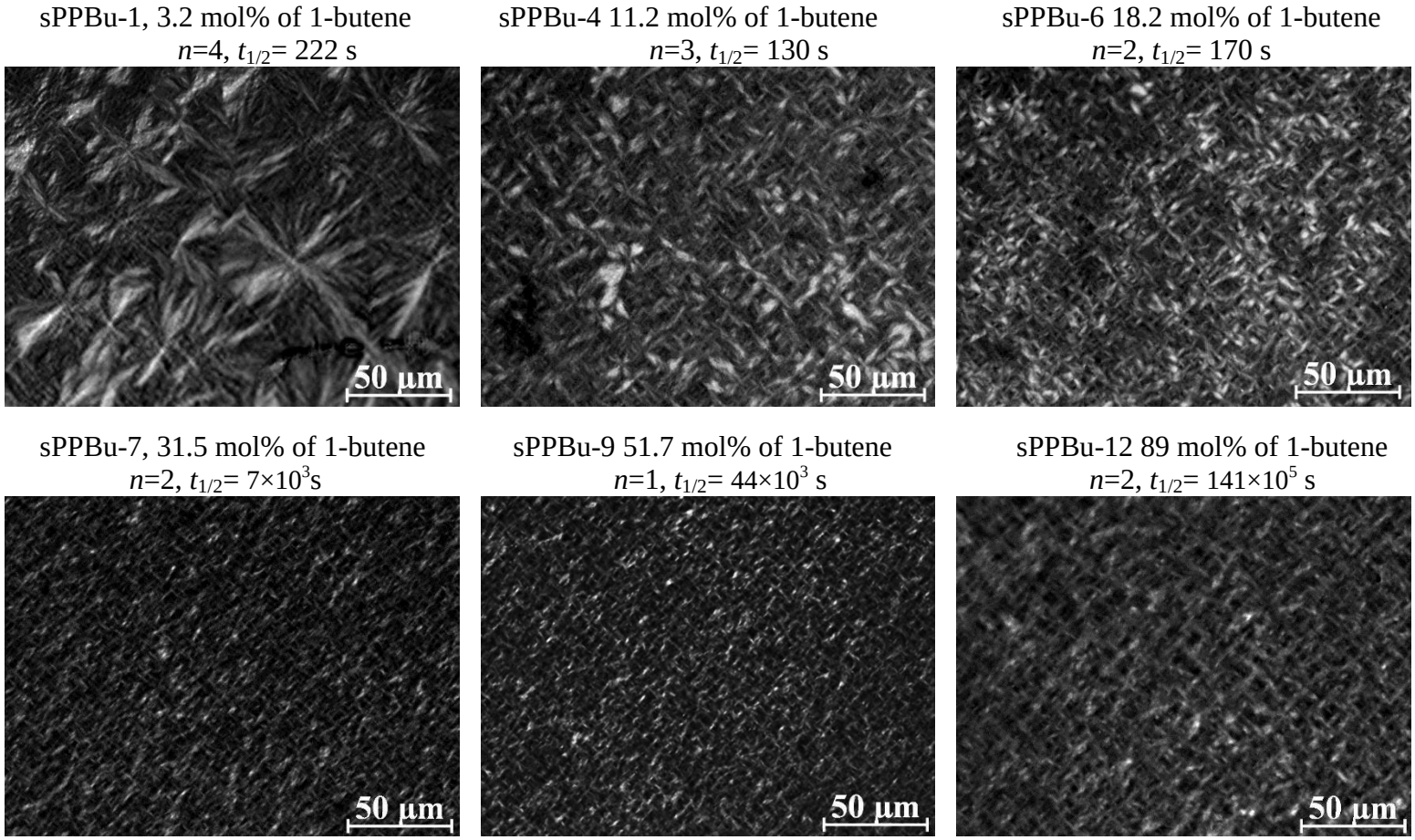

Figure 1.127. *Comparison of POM images of samples of sPPBu with the indicated 1-butene content and the corresponding Avrami exponent n and semi-crystallization time $t_{1/2}$.*

For further increase of butene content, increase of the Avrami exponent *n* to the values of 2 has been observed (sample sPPBu-12 with 89 mol% of butene), corresponding to the crystallization of form I of sPB and formation of slightly thicker crystals (Figure 1.127).

Not many differences have been observed in crystal morphology of random copolymers of sPP with 4-methyl-pentene. Correspondingly similar *n* values have been observed in all samples ($n = 2$) according with the co-existence of different types of slightly bigger aggregates in addition to the interwoven network (Figure 1.128). Only the sample with the lowest concentration of 4-methyl-1-pentene displays $n = 3$ (Figure 1.128). Probably in this sample the low comonomer content allows for the three- or two-dimensional growth of crystals which is prevented for higher comonomer concentrations.

All sPPHe copolymers exhibit $n = 2$ according with the observed similar morphology (Figure 1.128). For sPPOt copolymers values of *n* comprised between 2 and 1 have been observed, according with the similar morphology of thin and elongated crystals (Figure 1.129). Only in the case of the samples with the low octene concentrations higher values of *n*, in the range 3-4, have been observed according with the observation of thicker crystals (Figure 1.129).

Samples of copolymers with long comonomers (1-dodecene, 1-octadecene and 1-eicosene) exhibit crystalline aggregates very similar to those observed in more stereoregular sPPs (Figures 1.129 and 1.130). When the comonomer content is very low Avrami exponents $n = 3$, in the sample sPPC12-1, and $n = 4$, in the samples sPPC18a_iAc, CA-sPPC18-4_iAc, sPPC20-2_iEE and sPP20-3_iEE, have been observed according with the formation of thicker aggregates and the observed morphology, which seems to suggest a three-dimensional growth (Figures 1.129 and 1.130). Moreover, the values of *n* remain high also in sPPC18 and sPPC20 samples with higher comonomer content ($n = 3$ in samples sPPC18-2_iAc, CA-sPPC18-12_iAc and sPPC20-5_iEE) (Figure 1.130). This could be due to the very low values of the glass transition displayed by these samples, which induces a higher chain mobility, allowing a three- or two-dimensional crystal growth.

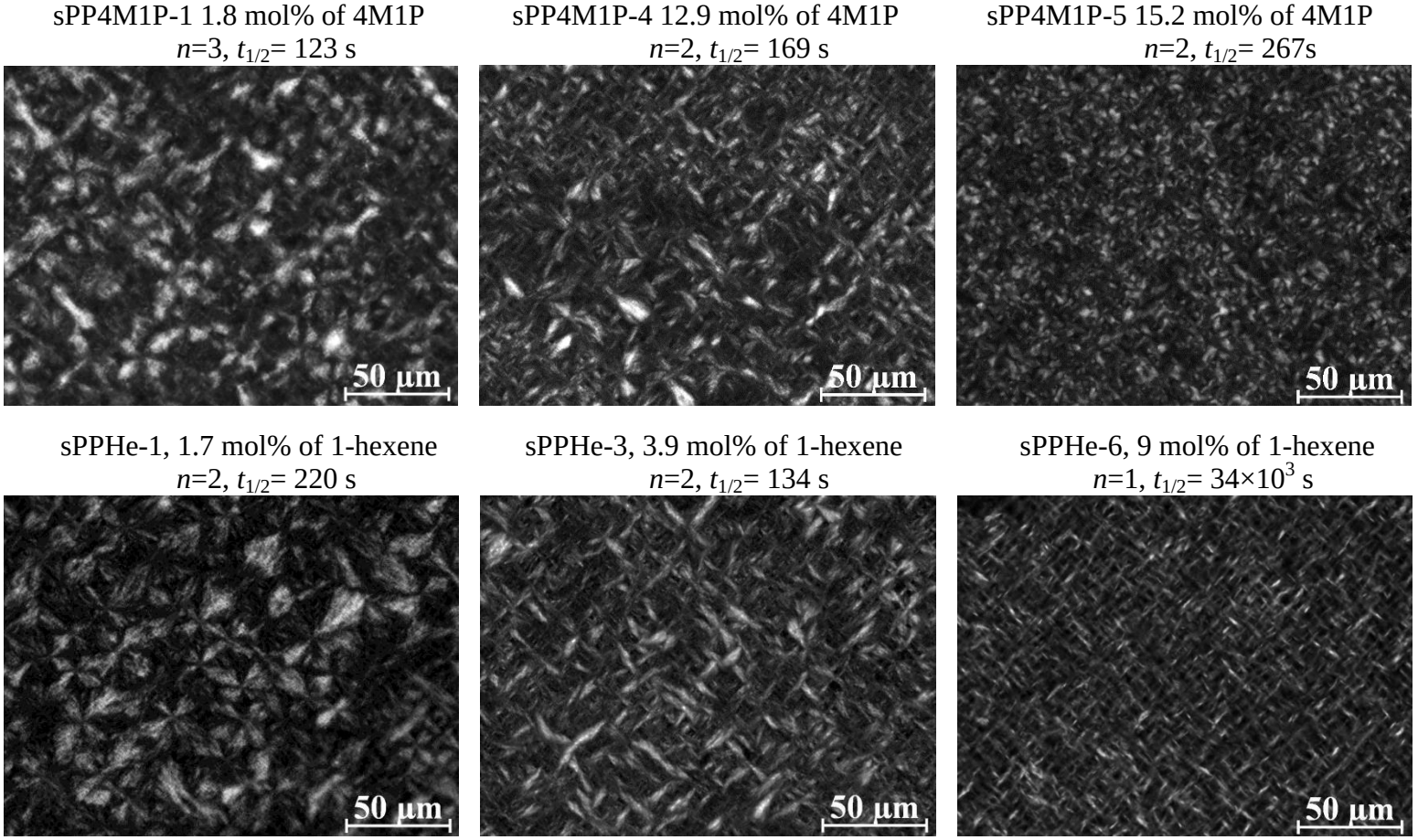

Figure 1.128. *Comparison of POM images of samples of sPP4M1P and sPPHe with the indicated comonomer content and the corresponding Avrami exponent n and semi-crystallization time* $t_{1/2}$.

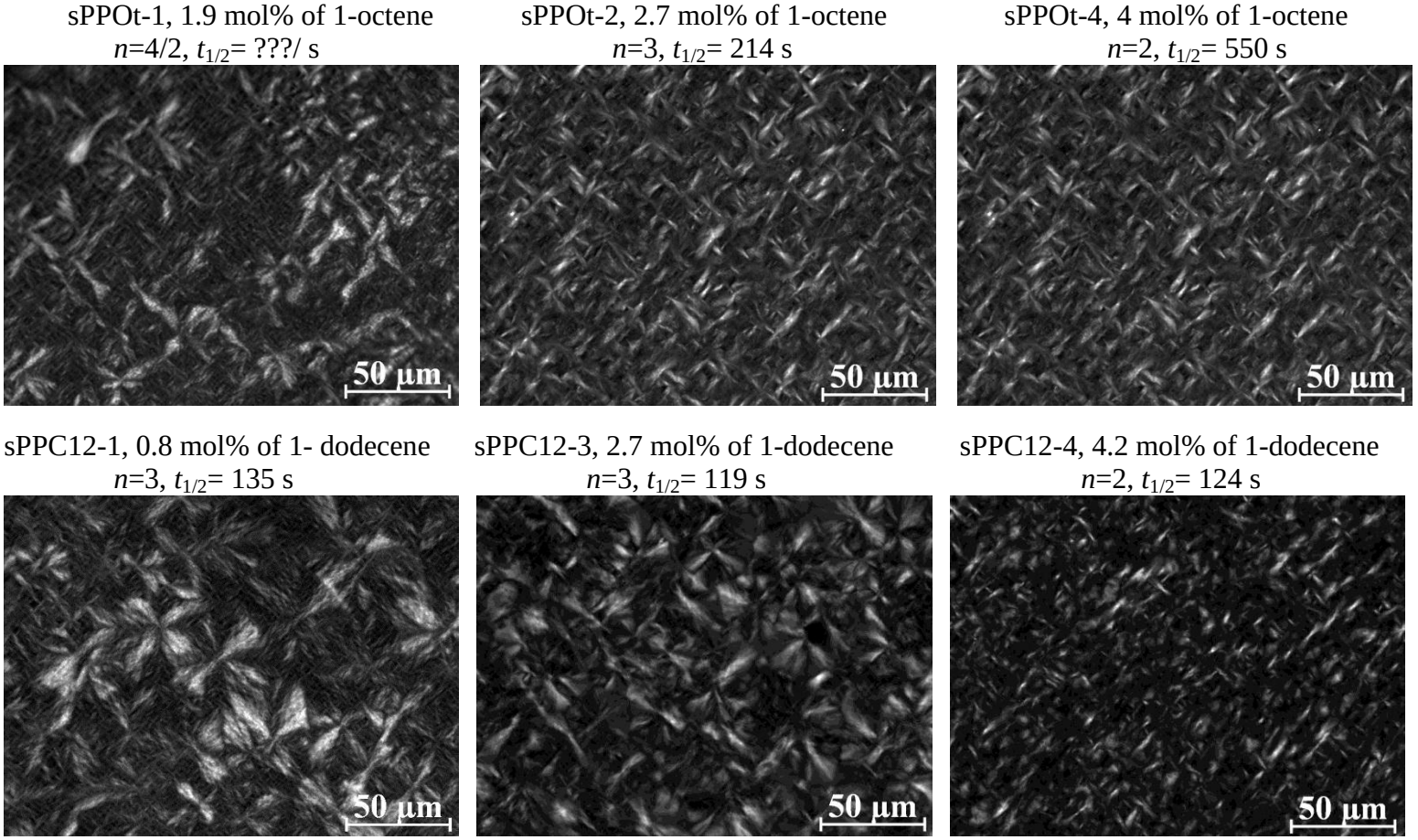

Figure 1.129. *Comparison of POM images of samples of sPPOt and sPPC12 with the indicated comonomer content and the corresponding Avrami exponent n and semi-crystallization time* $t_{1/2}$.

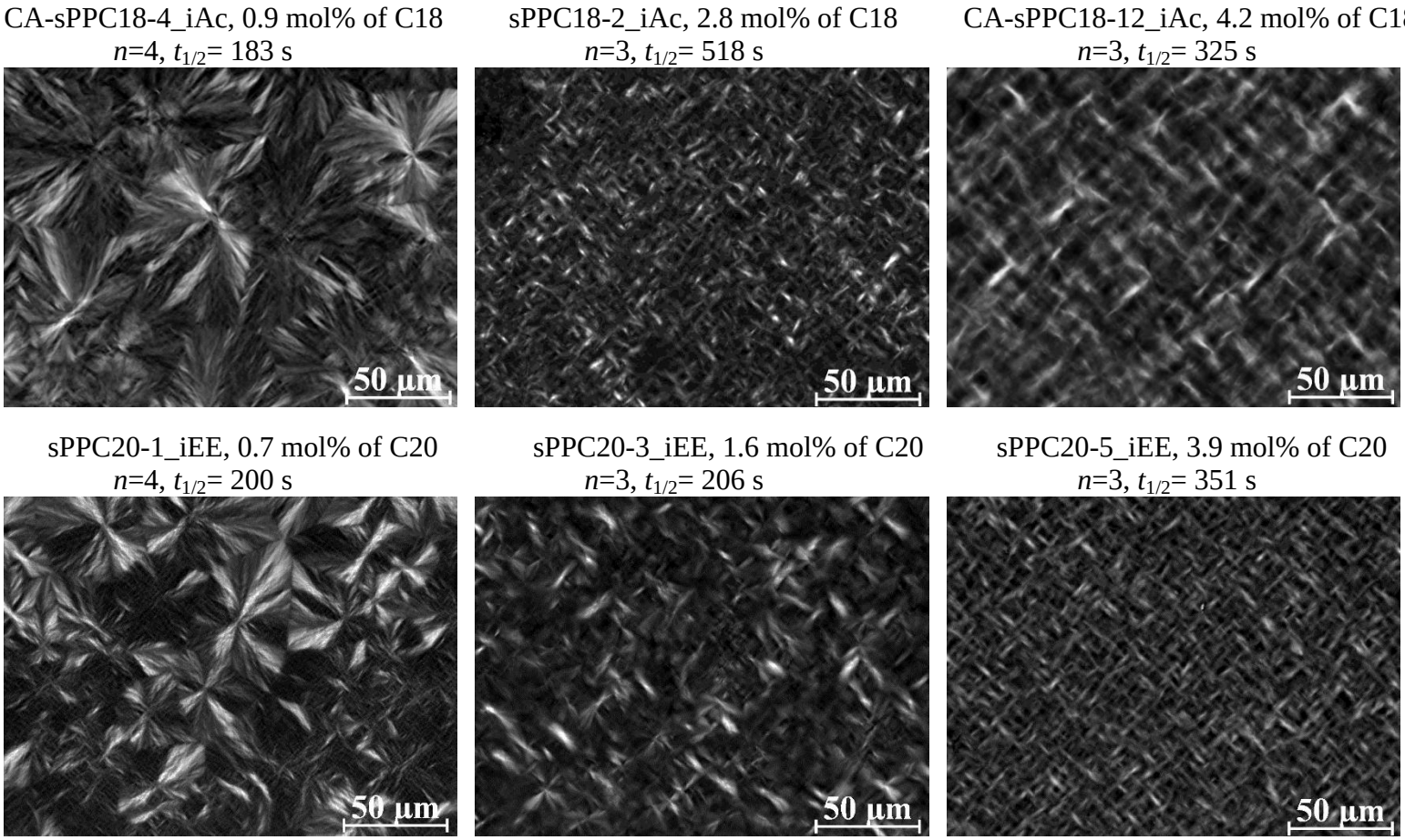

Figure 1.130. *Comparison of POM images of samples of sPPC18 and sPPC20 with the indicated comonomer content and the corresponding Avrami exponent n and semi-crystallization time* $t_{1/2}$.

1.8. Study of the crystal morphology by atomic force microscopy.

The correlation between morphology and mechanical properties has been studied in deep by Atomic Force Microscopy (AFM) and Small Angle X-ray Scattering (SAXS). These two techniques allow to investigate more in detail the inner structure of the crystalline aggregates described in previous sections. AFM measurements have been performed at room temperature, according with the procedure already described in section 1.5, on melt-crystallized thin films of samples of random copolymers of sPP with ethylene (sPPET) and 1-butene (sPPBu) selected from Tables 1.3 and 1.4. The observed morphology has been compared with the morphology of one sample of sPP of high steroregularity (sample sRDG-2-1, Table 1.1).

X-ray powder diffraction profiles of compression-molded samples of the sPP homopolymer and of sPPET and sPPBu copolymers analyzed by AFM are shown in Figures 1.131 and 1.132. The diffraction profiles of the samples as cooled from the melt (Figures 1.131A and 1.132A) and of the samples aged at room temperature (Figures 1.131B and 1.132B) are reported. The diffraction profiles of the aged samples are similar to those of thin films used for the POM experiments shown in Figure 1.37C for sPPET and Figure 1.41B for sPPBu.

For most of the samples the AFM images are recorded soon after the cooling from the melt, as explained in the experimental section 1.5, whereas for samples with high butene concentrations that crystallize by aging (Figure 1.132B), the AFM images are recorded also after long aging at room temperature.

The AFM images of compression-molded samples of the sPP homopolymer (sample sRDG-2-1) are reported in Figure 1.133, whereas those of the sPPET and sPPBu copolymers are shown in Figures 1.134 – 1.137 (for sPPET samples) and in Figures 1.138-1.145 (for sPPBu samples).

In the sPP homopolymer and in both sPPET and sPPBu copolymers with low concentration of comonomeric units the lamellar morphology typical of semi-crystalline polymers, with bundles of nearly parallel and stacked lamellae radiating from a nucleus, has been observed (Figures 1.133 – 1.135 and 1.138 – 1.139). At low magnifications the boundaries of spherulites are also apparent (Figures 1.133C,C' – 1.135C,C' and Figures 1.138C,C).

The lamellar morphology becomes more and more disordered with increasing comonomer concentration. In samples AK-sPPEt-15, sPPBu-4 and sPPBu-6 with 11.9 mol% of ethylene, 11.2 and 18.2 mol% of 1-butene respectively, indeed, smaller and thiner lamellae still radiating from a nucleus

are randomly oriented (Figures 1.136, 1.140-1.141) and only small bundles of parallel lamellae are visible (Figures 1.140B,B' - 1.141B,B').

The samples AK-sPPEt-25 with the highest ethylene concentration of 27.5 mol% is amorphous after cooling from the melt (profile h of Figure 1.131A) and does not crystallize after aging (profile h of Figure 1.131B). Accordingly, the AFM images of these samples of Figure 1.137 are featurless.

Samples of copolymers sPPBu-7, sPPBu-9, sPPBu-11, sPPBu-12 with 31.5, 51.7, 69.9 and 89 mol% of 1-butene respectively do not crystallize from the melt in bulk samples (profiles e-h of Figure 1.132A) but crystallize upon aging at room temperature (profiles e-h of Figure 1.132B).[143g] Samples sPPBu11 and sPPBu12, in particular, crystallize in structures similar to that of form I of sPB (Figure 1.132B curves g,h).[140] Nevertheless, when cooled from the melt in thin film for the AFM experiments the samples sPPBu-7 and sPPBu-11 display very short and irregular randomly oriented crystalline lamellae already soon after the cooling (Figures 1.142A,A' and 1.144). Little or no improvement of this disordered morphology has been observed after aging at room temperature (Figure 1.142 B,B'-C,C'). Only the images of the non aged samples, recorded soon after the cooling, are reported for the samples sPPBu9, sPPBu11 and sPPBu12 (Figures 1.143 - 1.145).

For samples sPPBu-9 and sPPBu-12 the AFM images are featurless or not well-resoved (Figures 1.143 and 1.145) so that no evident morphology has been observed, even after long aging time. This is also due to the extremely high roughness and stickiness of these samples that has hindered the acquisition of well resolved AFM images.

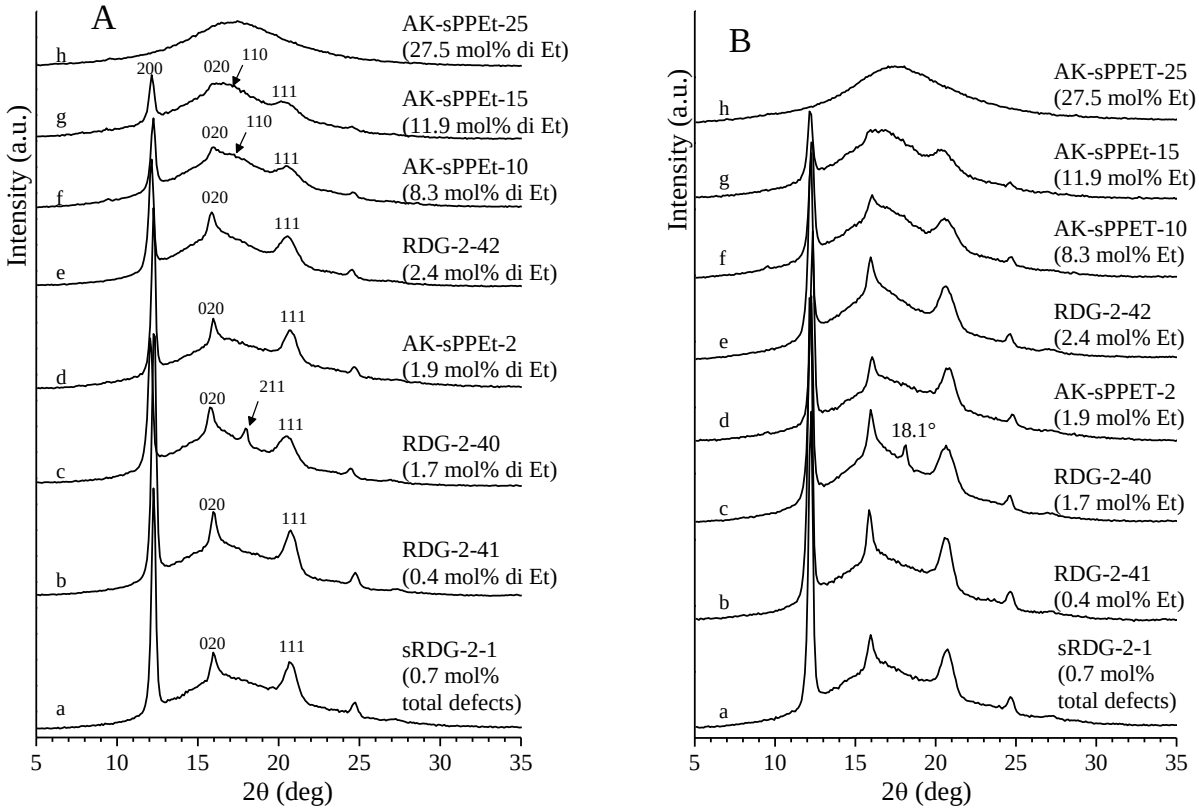

Figure 1.131. *X-ray powder diffraction profiles of as-prepared compression-moulded films slowly cooled from the melt (A) and aged at room temperature (B) of the sPP homopolymer (sRDG-2-1) and of selecets samples of sPPET copolymers of Table 1.3. The X-ray powder diffraction profiles of similar thin films used for the POM experiments have also been shown in Figure 1.37C.*

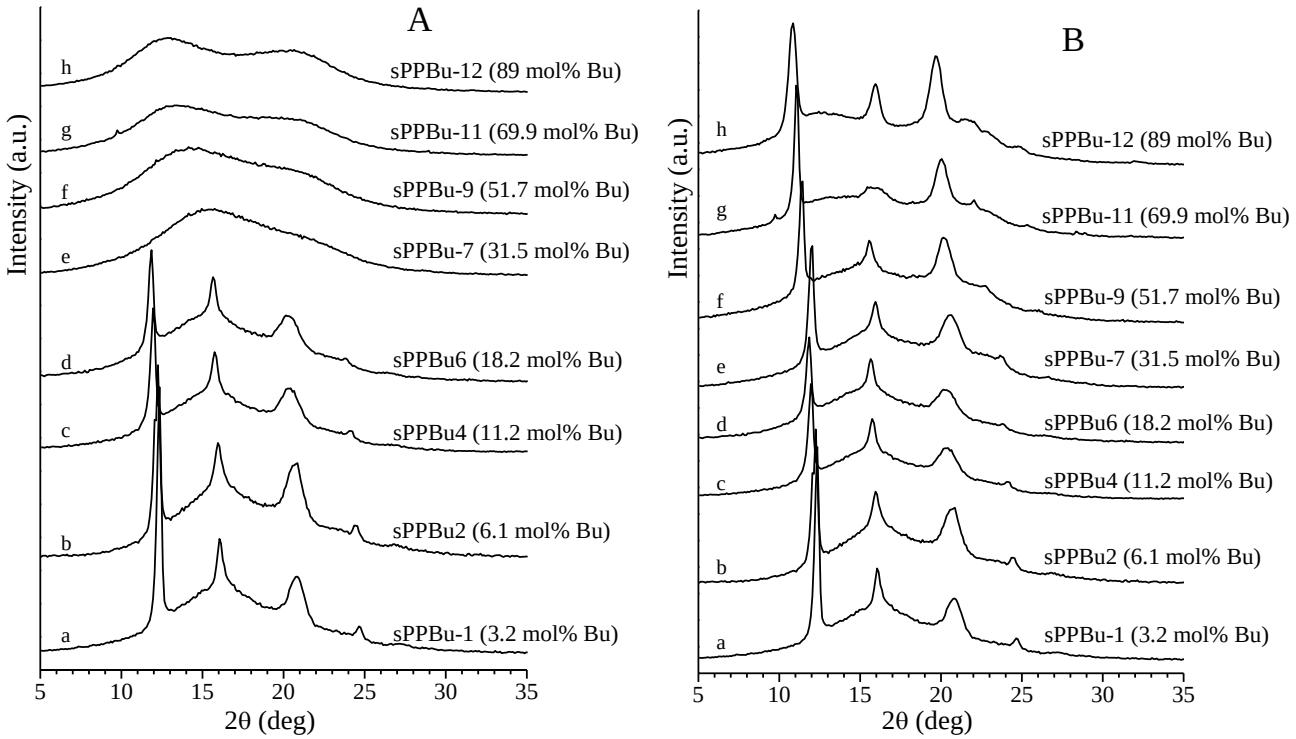

Figure 1.132. *X-ray powder diffraction profiles of as-prepared compression-moulded films slowly cooled from the melt (A) and aged at room temperature (B) of samples of sPPBu copolymers of Table 1.4. The X-ray powder diffraction profiles of similar thin films used for the POM experiments have also been shown in Figure 1.41B.*

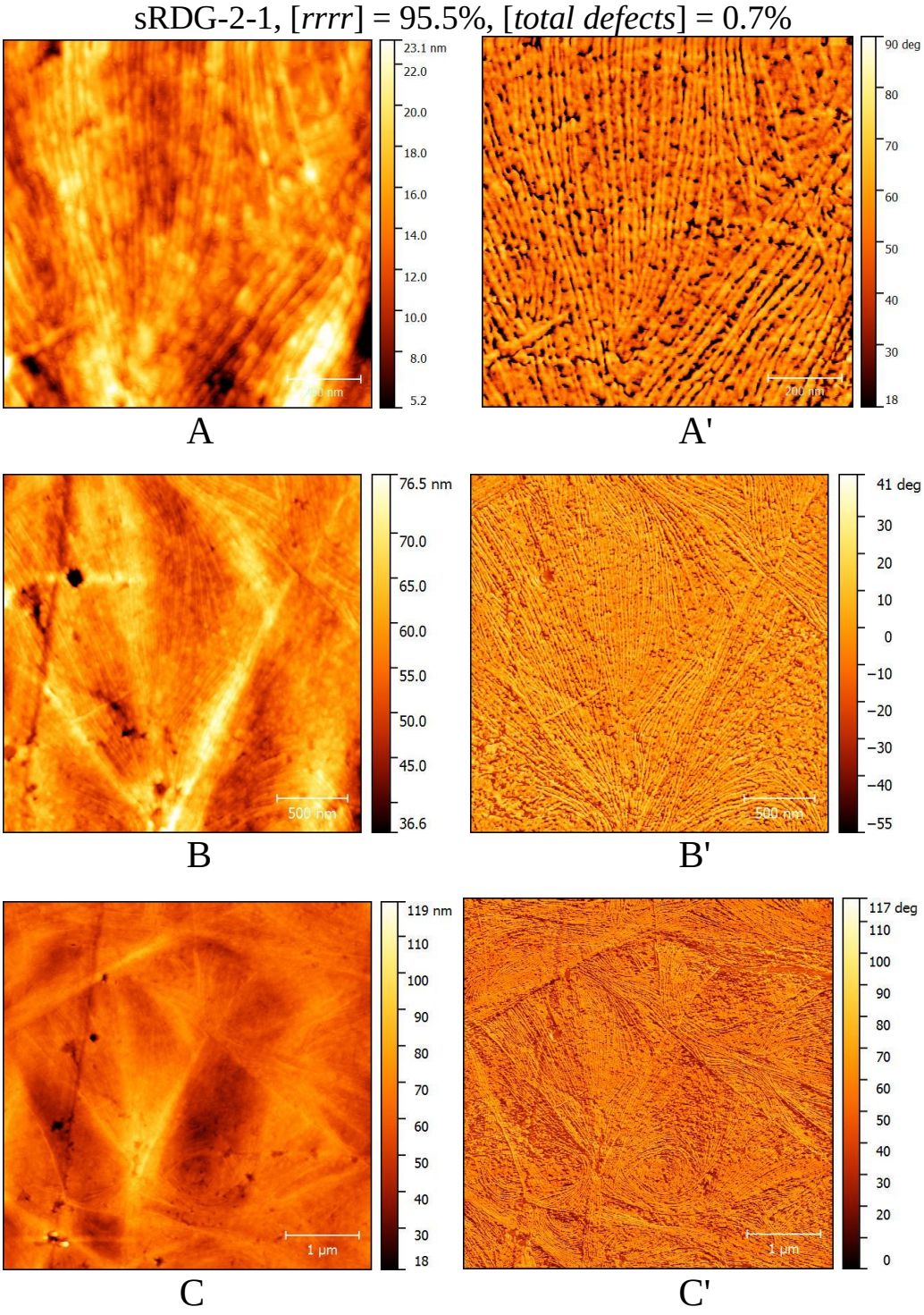

Figure 1.133. *AFM height (A,B,C) and phase images (A',B',C') of the thin film of the sample sRDG-2-1 with 0.7 mol% of total defects collected in tapping mode at room temperature with different scan sizes of 1 (A,A'), 2.5 (B,B') and 5 (C,C') µm.*

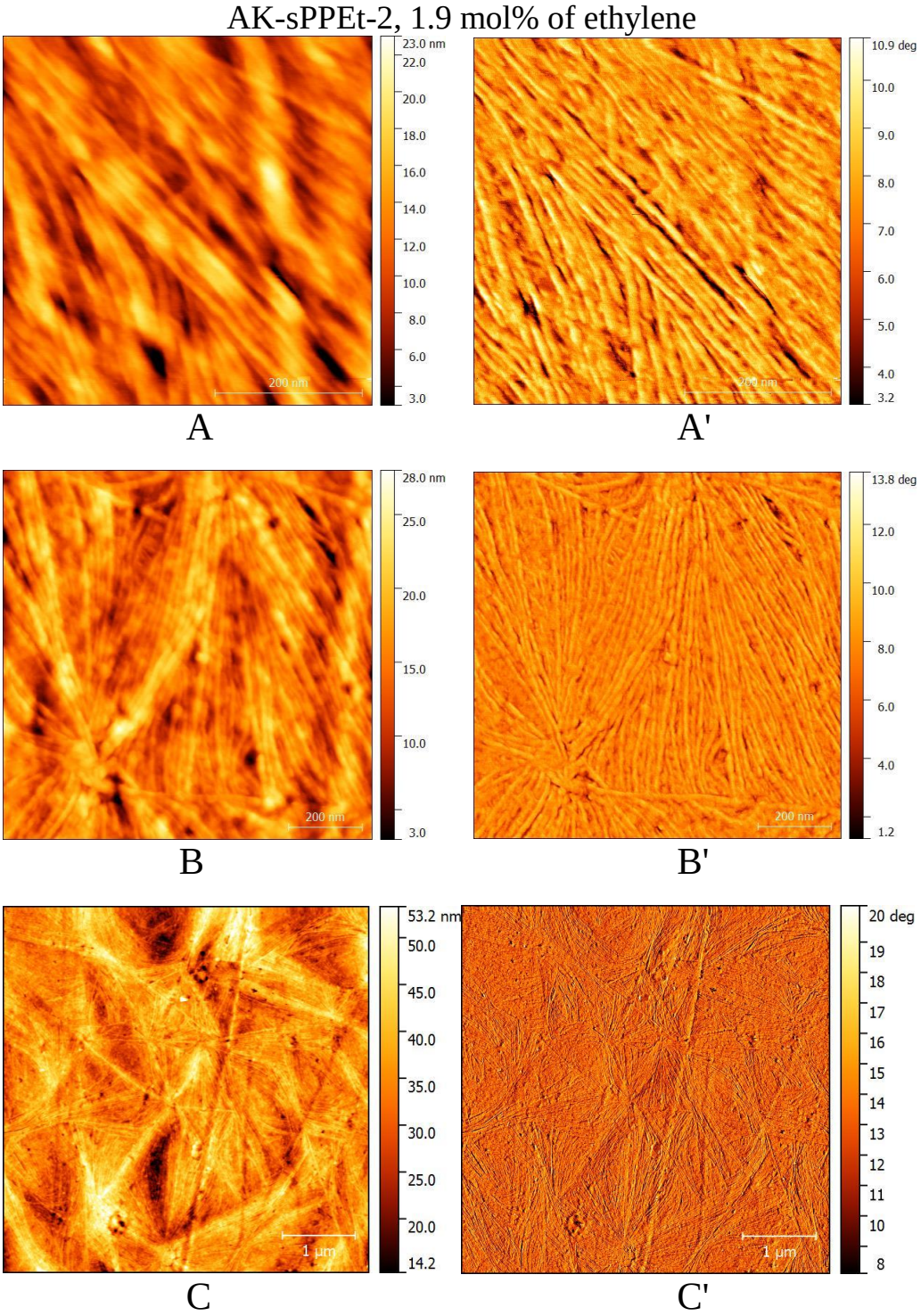

Figure 1.134. *AFM height (A,B,C) and phase images (A',B',C') of the thin film of the sample AK-sPPEt-2 with 1.9 mol% of ethylene collected in tapping mode at room temperature with different scan sizes of 500 nm (A,A'), 1 (B,B') and 5 (C,C') µm.*

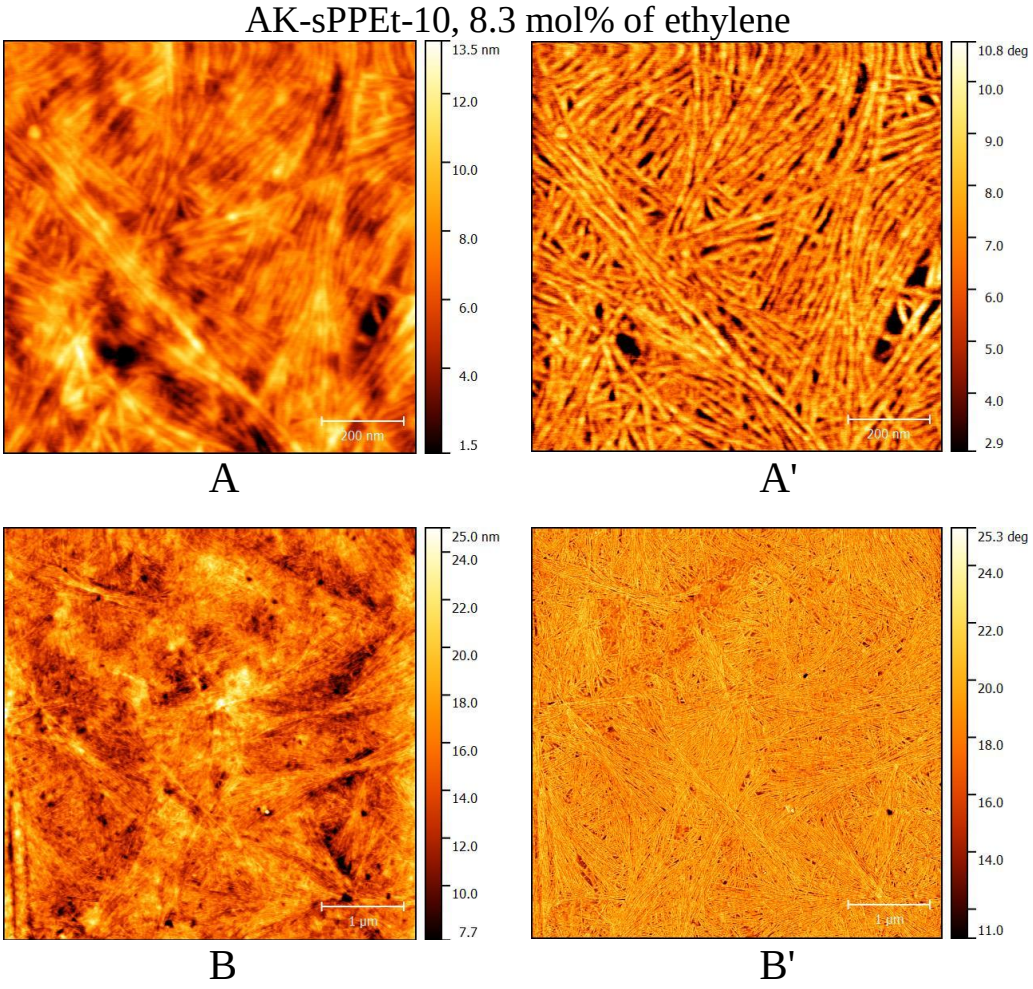

Figure 1.135. *AFM height (A, B) and phase images (A', B') of the thin film of the sample AK-sPPEt-10 with 8.3 mol% of ethylene collected in tapping mode at room temperature with different scan sizes of 1 (A,A')and 5 (B,B') µm.*

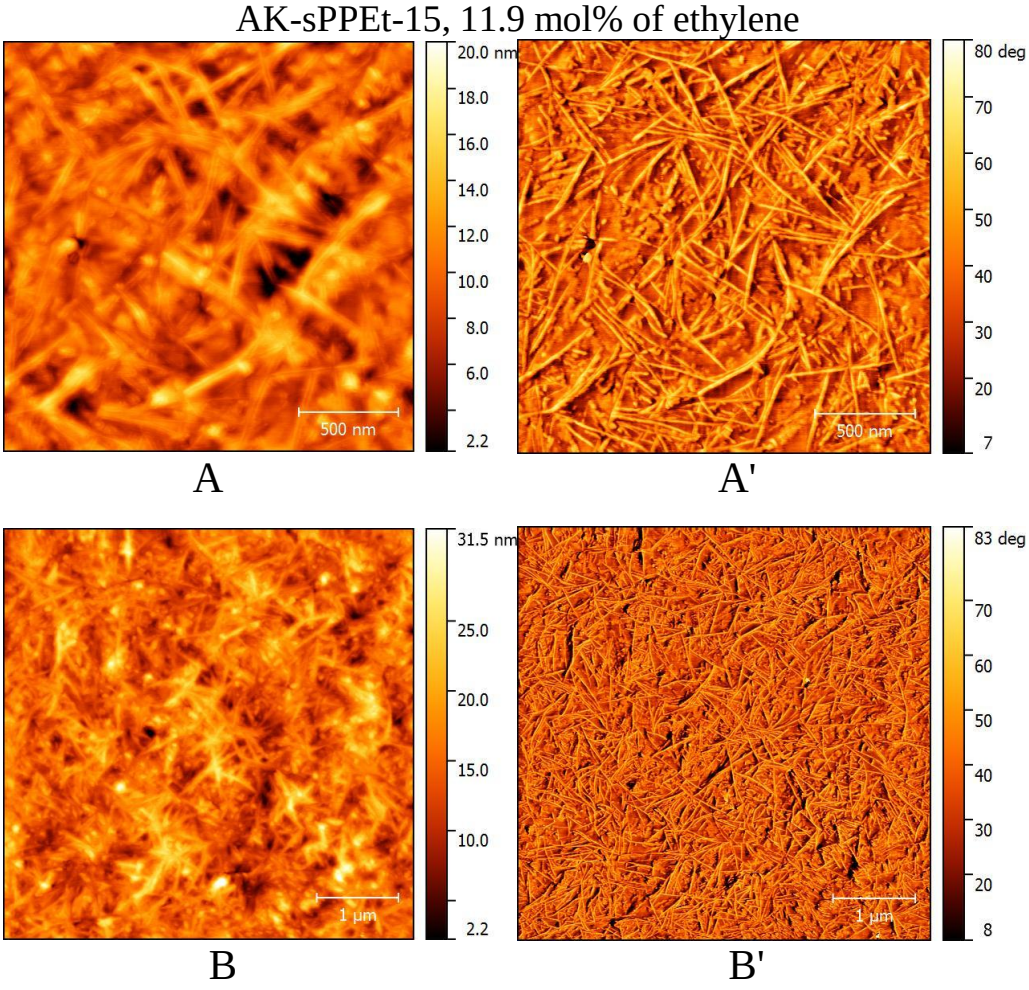

Figure 1.136. *AFM height (A,B) and phase images (A',B') of the thin film of the sample AK-sPPEt-15 with 11.9 mol% of ethylene collected in tapping mode at room temperature with different scan sizes of 2 (A,A') and 5 (B,B') µm.*

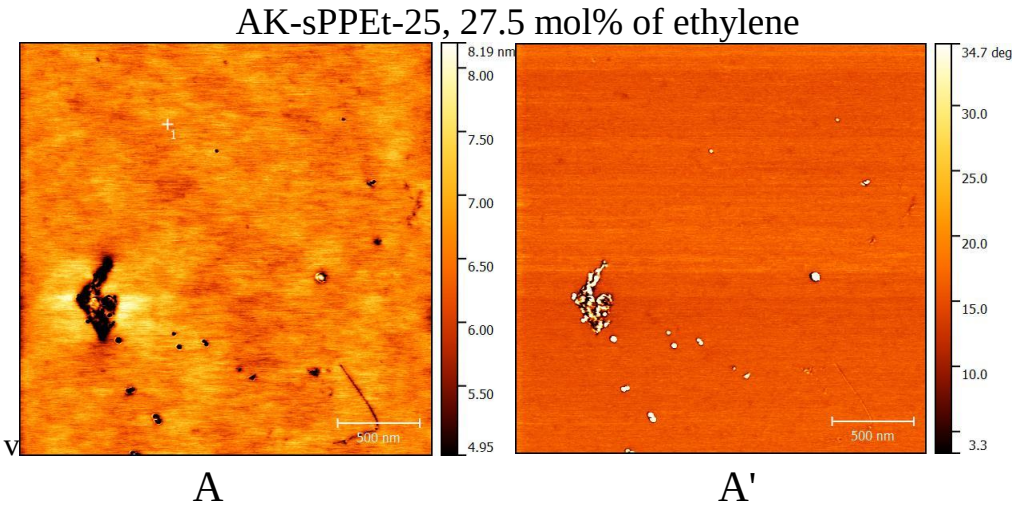

Figure 1.137. *AFM height (A) and phase images (A') of the thin film of the sample AK-sPPEt-25 with 27.5 mol% of ethylene collected in tapping mode at room temperature with scan size of 2 μm.*

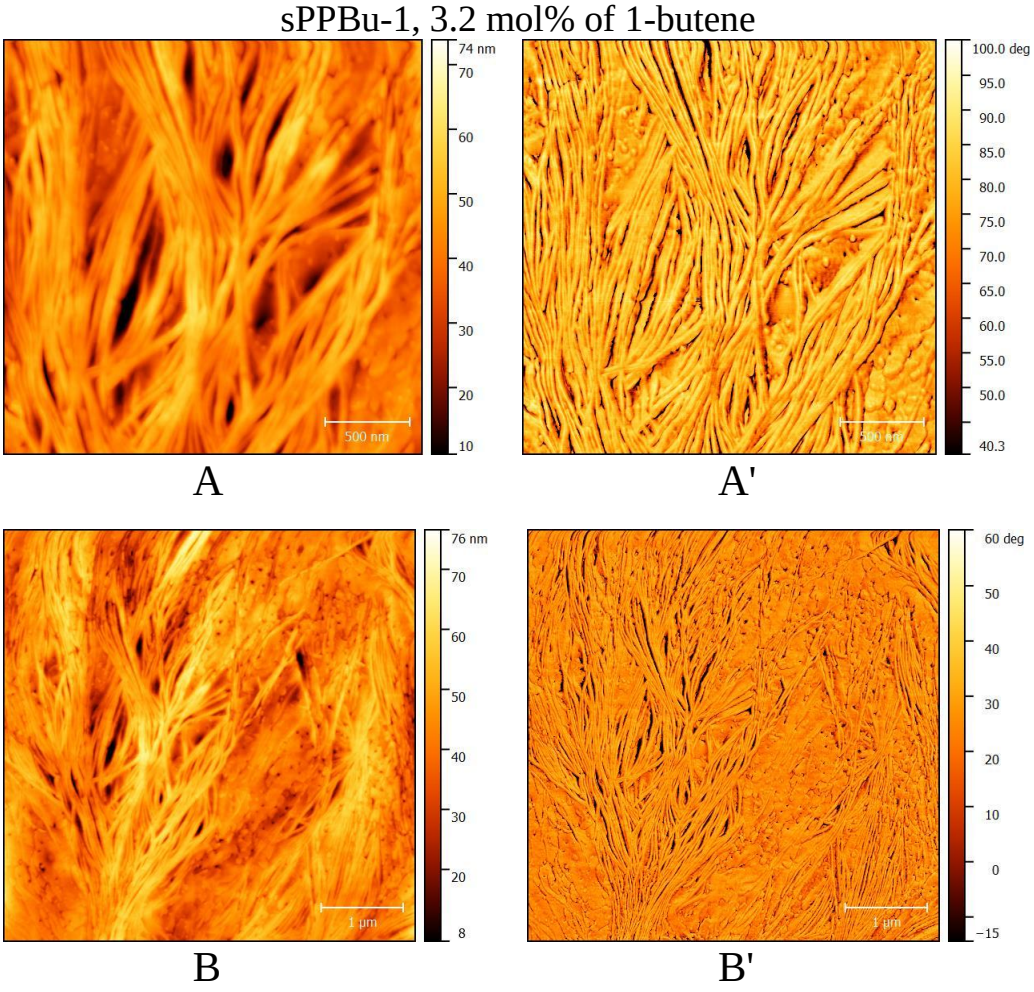

Figure 1.138. *AFM height (A,B) and phase images (A', B') of the thin film of the sample sPPBu-1 with 3.2 mol% of 1-butene collected in tapping mode at room temperature with different scan sizes of 2.5 (A,A') and 5 (B,B') µm.*

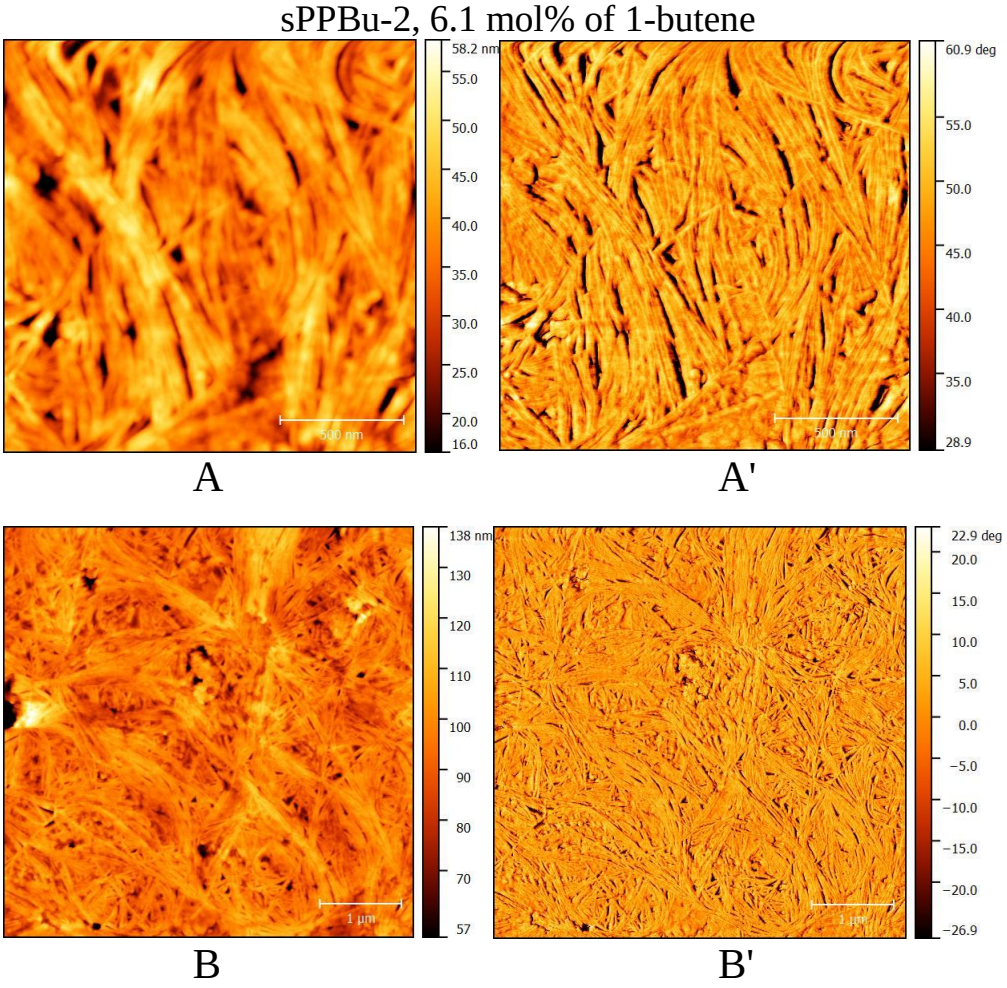

Figure 1.139. *AFM height (A,B) and phase images (A',B') of the thin film of the sample sPPBu-2 with 6.1 mol% of 1-butene collected in tapping mode at room temperature with different scan sizes of 1.7 (A,A') and 5 (B,B') µm.*

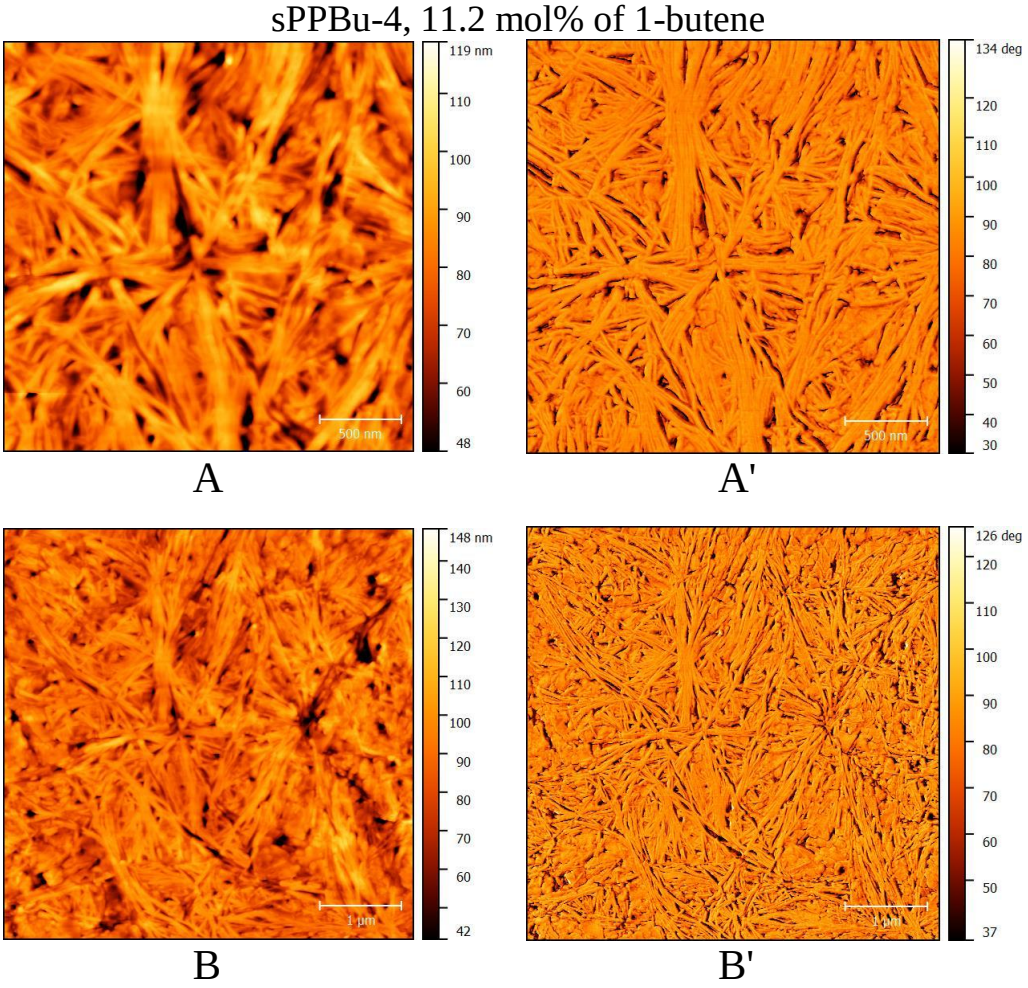

Figure 1.140. *AFM height (A,B) and phase images (A',B') of the thin film of the sample sPPBu-4 with 11.2 mol% of 1-butene collected in tapping mode at room temperature with different scan sizes of 2.4 (A,A') and 5 (B,B') µm.*

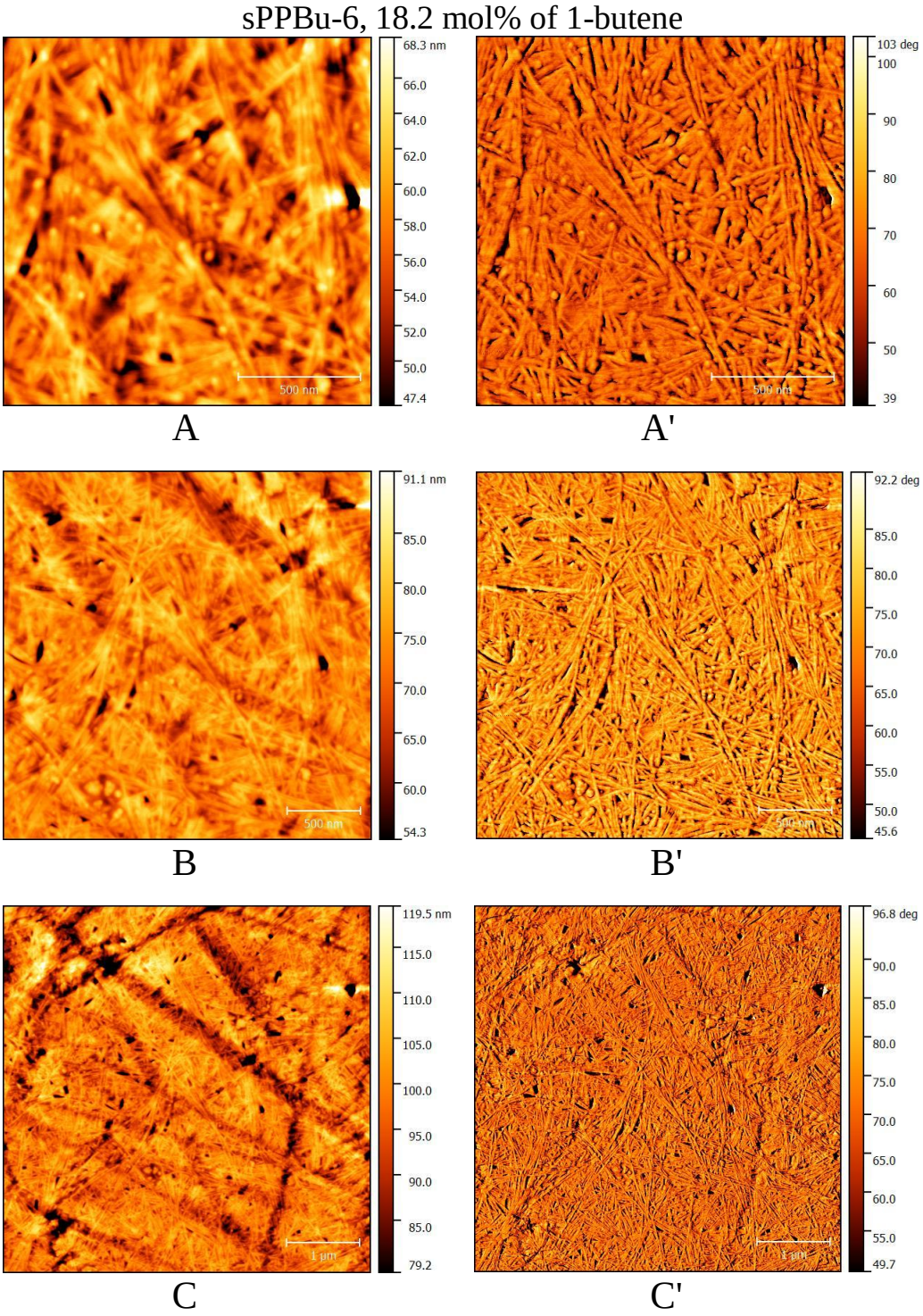

Figure 1.141. *AFM height (A,B,C) and phase images (A',B',C') of the thin film of the sample sPPBu-6 with 18.2 mol% of 1-butene collected in tapping mode at room temperature with different scan sizes of 1.5 (A,A',) 2.5 (B,B') and 5 (C,C')µm.*

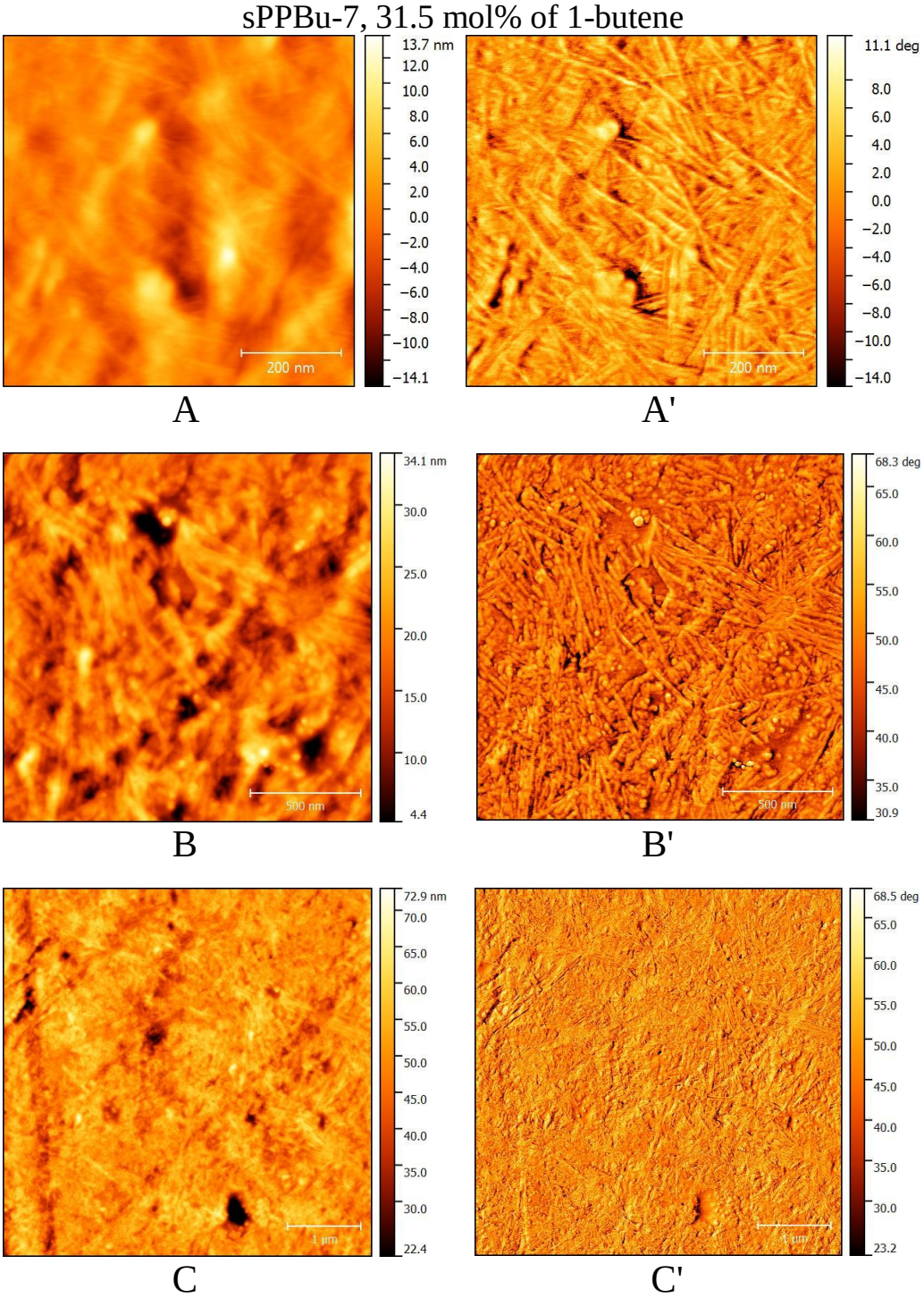

Figure 1.142. *AFM height (A,B,C) and phase images (A',B',C') of the as-crystallized (A,A') and aged (B,B',C,C') thin film of the sample sPPBu-7 with 31.5 mol% of 1-butene collected in tapping mode at room temperature with different scan sizes of 700 nm (A,A',) 1.7 (B,B') and 5 (C,C')µm.*

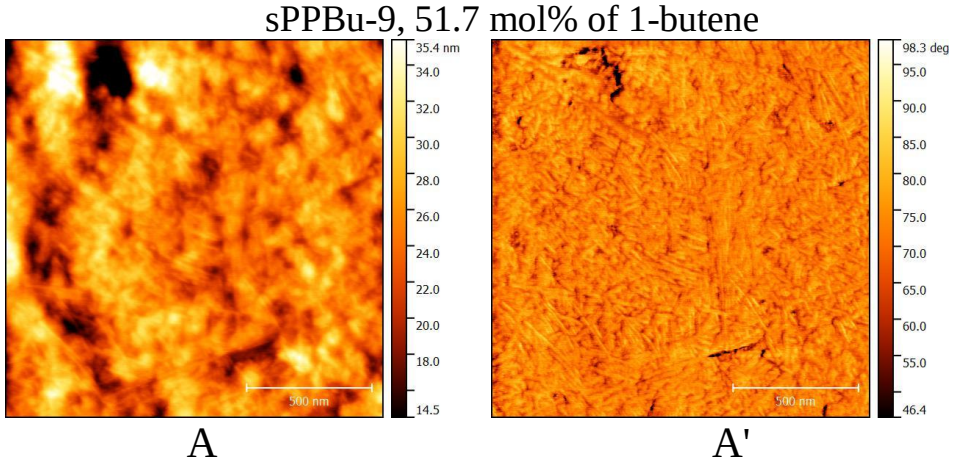

Figure 1.143. *AFM height (A) and phase images (A') of the thin film of the sample sPPBu-9 with 51.7 mol% of 1-butene recorded soon after the cooling from the melt in tapping mode at room temperature with scan size of 1.5 μm.*

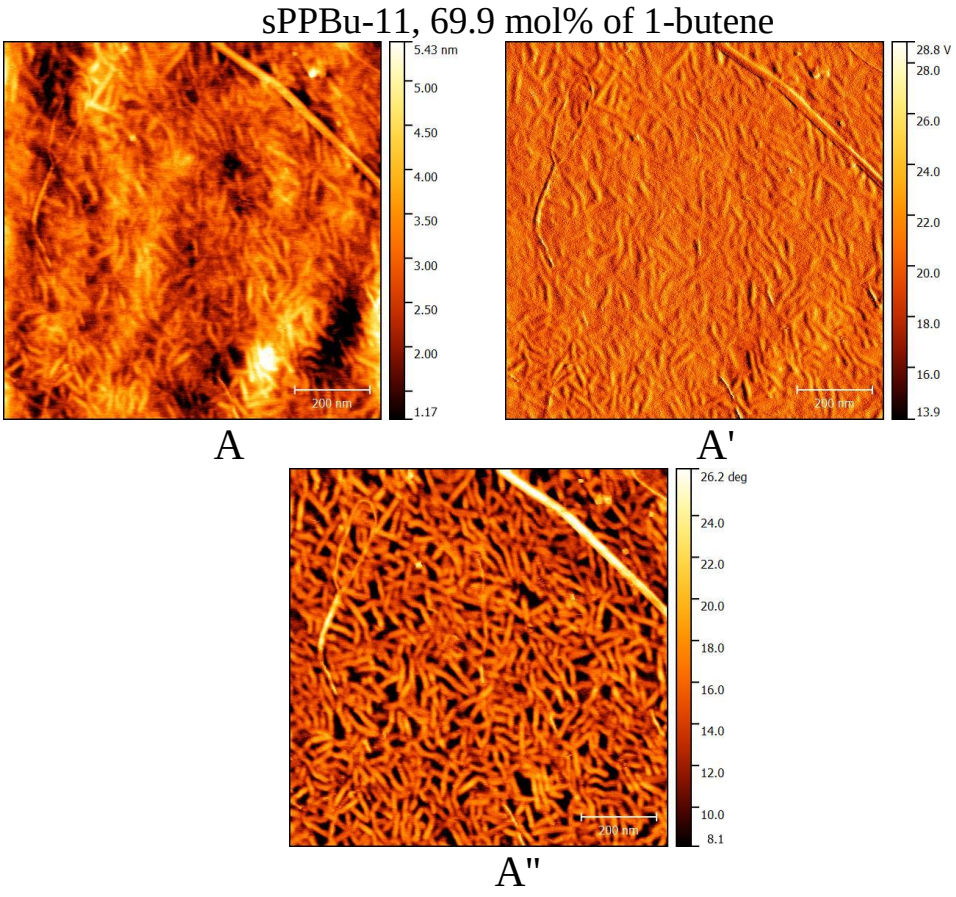

Figure 1.144. *AFM height (A), amplitude (A') and phase images (A'') of the thin film of the sample sPPBu-11 with 69.9 mol% of 1-butene recorded soon after the cooling from the melt in tapping mode at room temperature with scan size of 1 μm.*

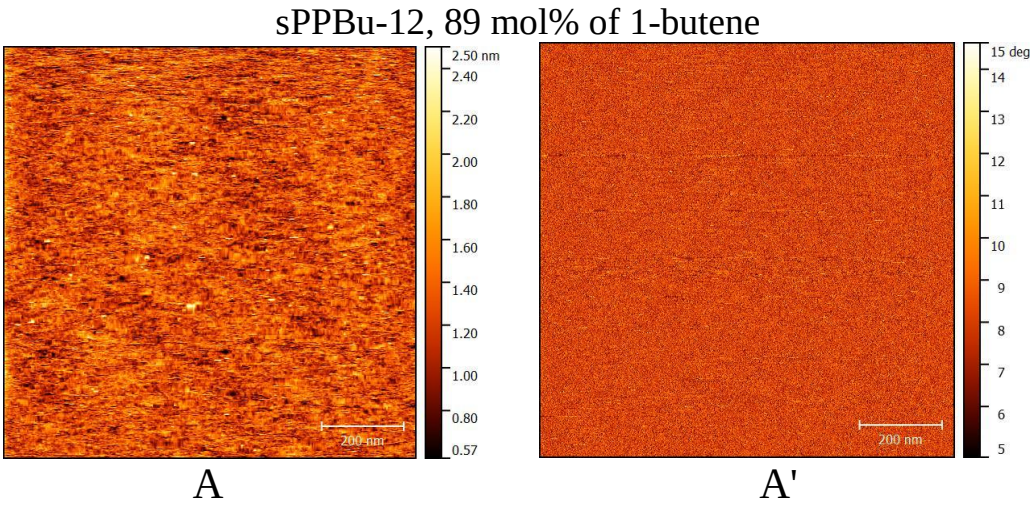

Figure 1.145. *AFM height (A) and phase images (A') of the thin film of the sample sPPBu-12 with 89 mol% of 1-butene recorded soon after the cooling from the melt in tapping mode at room temperature with scan size of 1 μm.*

1.9. Study of the crystal morphology by Small Angle X-ray Scattering.

In parallel to the AFM analysis, SAXS experiments have been performed on the same samples of sPP and sPPET and sPPBu copolymers for a better evaluation of the influence of the composition on the morphological parameters such as the lamellar thicknesses.

Aged compression moulded films of the sPP homopolymer (sample sRDG-2-1), sPPEt and sPPBu copolymers of Figures 1.131B and 1.132B have been analyzed at room temperature, in the molten state and soon after the cooling from the melt down to room temperature. The SAXS data have been collected using a Kratky compact camera in the slit collimation configuration, attached to a conventional X-ray source (CuKα, wavelength λ =1.5418 Å). The range of values of the analyzed scattering vector *s* is 0.01 $nm^{-1} \leq s \leq 0.9$ nm^{-1}, where $s = 2\pi \sin\theta/\lambda$ and 2θ is the scattering angle. The zero position of the primary beam has been evaluated from the maximum of the height intensity profile of the detector recorded placing a Zinc absorber in front of the X-ray source and placing an orizhontal slit 20 μm width and without beamstop. The intensity of the primary beam has been evaluated by measuring the counts per 60 seconds placing a vertical slit in fronto of the detector. Then, the scattering of the sample is measured removing the Zinc absorber and placing the beamstop and a orizhontal slit 100 μm width in front of the detector. Finally, after the measurement of the scattering from the sample, the background is measured recording the SAXS profile of the empty sample holder and is subtracted from the scattering of the sample.

After the subtraction of the background, the slit smeared data have been deconvoluted using a home-made QT/C++ program to obtain the corresponding pinhole scattering (desmeared) intensity distribution in absolute units.[163] The desmeared data have been processed with the MATLAB program *correlation_gui* developed in Prof. Thurn-Albrecht's group.[163]

1.9.1. Basic Formalism Describing the Relation between Real-Space Structure and Scattering Intensity in a SAXS Experiment.

The following section presents a short overview of the basic concepts of SAXS analysis/theory, as described in the ref 163.

In SAXS experiments, the incident X-ray beam with wavelength λ and flux J_0 irradiates a sample. The scattered beam with flux *J* is detected as a function of the scattering angle 2θ at a certain distance from the sample. Note that the term *Intensity* is generally used to denote a *flux J* in units of energy per unit area

and per unit time. More precisely, an incident plane wave with flux J_0 is scattered by the electrons in the sample. The scattered spherical waves interfere with each other, resulting in an angle-dependent flux J of scattered radiation. The flux J_0 of the incident plane wave corresponds to the energy transmitted per unit area and per unit time and the flux J of the scattered radiation to the energy transmitted per unit solid angle per unit time. Now the differential scattering cross section or scattered intensity is defined as the ratio between the flux J of the scattered beam and the flux J_0 of the incident beam:

$$I(\vec{s}) = \frac{d\sigma}{d\Omega} = \frac{J}{J_0} \tag{1.4}$$

where ($\vec{s}$) is the scattering vector defined as the difference between the wave vector ($\vec{k}$) of the scattered beam and the wave vector ($\vec{k}_0$) of the incident beam

$$\vec{s} = \frac{1}{2\pi}(\vec{k} - \vec{k}_0) \tag{1.5}$$

The absolute value of the scattering vector is

$$|\vec{s}| = \frac{2}{\lambda} sin\vartheta \tag{1.6}$$

An alternative parameter often used as scattering vector is $q = 2\pi s$.

The flux J of the scattered radiation is the square of the amplitude A of the scattered wave field.

$$J(\vec{s}) = |A(\vec{s})|^2 = A(\vec{s}) \times A(\vec{s})^* \tag{1.7}$$

$A(\vec{s})$ can be calculated as the sum of the amplitudes of the scattered waves originating from N scattering centers in the sample.

$$A(\vec{s}) = A_0 b_e \sum_{j=1}^{N} e^{-i2\pi\vec{s}\cdot\vec{r}} \tag{1.8}$$

Where A_0 is the amplitude of the incident beam and $b_e = r_e[(1+\cos^2 2\theta)/2]^{1/2}$ is the scattering length of an electron with r_e the radius of an electron $re = 2.818\times10^{-15}$ m and $p = (1+\cos^2 2\theta)/2$ is the polarization factor, which is approximately 1 for small angles ($2\theta \leq 8°$), and therefore $b_e \approx r_e$.

At the length scales investigated in small angle scattering experiments a continous electron density $\rho(\vec{r})$ is used to describe the structure of the sample instead of single scattering centers. Therefore, the sum in Equation 1.8 can be replaced by an integral.

$$A(\vec{s}) = A_0 b_e \int_V \rho(\vec{s})\, e^{-i2\pi\vec{s}\cdot\vec{r}} d\vec{r} \tag{1.9}$$

That is to say that the amplitude is proportional to the Fourier transform of the electron density $\rho(\vec{r})$.

In an experiment, a time-averaged intensity $I(\vec{s})$ is measured, which in an equilibrium system is equivalent to the ensemble average:

$$I(\vec{s}) = \frac{J(\vec{s})}{J_0} = < \frac{|A(\vec{s})|^2}{|A_0|^2} > = < |b_e \int_V \rho(\vec{s})\, e^{-i2\pi\vec{s}\cdot\vec{r}} d\vec{r}|^2 > \qquad (1.9a)$$

If $g(\vec{r})$ is the three dimensional electron density correlation function:

$$g(\vec{r}) = < \rho(\vec{r}')\rho(\vec{r}' + \vec{r}) >_{\vec{r}\prime} = \frac{1}{V}\int_V \rho(\vec{r}')\rho(\vec{r}' + \vec{r})\, d\vec{r'} \qquad (1.10)$$

Then:

$$I(\vec{s}) = b_e^2 V \int_V g(\vec{r})\, e^{-i2\pi\vec{s}\cdot\vec{r}} d\vec{r} \qquad (1.11)$$

That is to say that the intensity $I(\vec{s})$ is proportional to the Fourier transform of the three-dimensional electron density correlation function $g(\vec{r})$.

In SAXS experiments the fluctuations of the electron density are more significant that the electron density it self. Therefore $\rho(\vec{r})$ can be replaced by the deviation from the average electron density:

$$\delta\rho(\vec{r}) = \rho(\vec{r}) - \rho \qquad (1.12)$$

leading to:

$$g(\vec{r}) = < \delta\rho(\vec{r}')\delta\rho(\vec{r}' + \vec{r}) >_{\vec{r}\prime} + < \rho^2 > \qquad (1.13)$$

Finally, the absolute intensity $I_{abs}(\vec{s})$ is defined as the intensity normalized to the scattering of a single electron and to the irradiated volume. It describes the scattering power of a material per volume in units of [e.u./nm^3].

$$I_{abs}(\vec{s}) = \frac{1}{b_e^2 V}\frac{d\sigma}{d\Omega}(\vec{s}) = \int_V g(\vec{s}) e^{-i2\pi\vec{s}\cdot\vec{r}} d\vec{r} \qquad (1.14)$$

The morphology of semicrystalline polymers is generally described with the lamellar two-phase system consisting of crystalline and amorphous phases with different electron densities and with sharp boundaries between them. A model of lamellar stacks where crystalline layers of thickness d_c alternate with amorphous layers of thickness d_a and with an avareged periodicity L, is

generally accepted (Figure 1.146A). This structure gives rise to a peak in the scattering intensity at a scattering vector s_p from which the average long period $L = 1/s_p$ can be determined.

Typically, the lateral dimensions of the lamellar stacks in the sample are large compared to the interlamellar distance *L*; therefore, only the electron density distribution along the normal of the lamellar stacks, here denoted as *z*-direction, changes within the relevant length scale of a SAXS experiment (1 – 100 nm) (Figure 1.146B). Hence, $g(\vec{r})$ reduces to the one-dimensional correlation function *K*(*z*).

$$K(z) =< \delta\rho(z')\delta\rho(z'+z) >_{z'} \tag{1.15}$$

Inserting the equation 1.15 into the equation 1.14 leads to

$$I_{abs}(\vec{s}) = \int_{x,y,z} K(z)\, e^{-i2\pi\vec{s}\cdot\vec{r}} dxdydz \tag{1.16}$$

After integration over *x* and *y* with $\delta(t) = \frac{1}{2\pi}\int_{-\infty}^{\infty} e^{-i\omega t} d\omega$

$$I_{abs}(\vec{s}) = \delta(s_x)\delta(s_y) \int_{-\infty}^{\infty} K(z)\, e^{-i2\pi s_z z} dz \tag{1.17}$$

As the lamellar stacks are isotropically distributed inside the sample, the intensity in $\pm s_z$ direction is distributed over the surface of a sphere with radius s_z

$$I_{abs}(\vec{s}) = \frac{2}{4\pi s_z^2} \int_{-\infty}^{\infty} K(z)\, e^{-i2\pi s_z z} dz \tag{1.18}$$

The reverse Fourier transform gives

$$K(z) = \int_{-\infty}^{\infty} 2\pi s^2 I_{abs}(s) e^{-i2\pi s_z z} ds \tag{1.19}$$

Since *K*(*z*) and $I_{abs}(s)$ are both even function (*f*(*x*) = *f*(-*x*)), the Fourier transform becomes a cosine transform:

$$K(z) = 2\int_0^{\infty} 2\pi s^2 I_{abs}(s) \cos(2\pi s z)\, ds \tag{1.20}$$

that means that the one-dimensional correlation function *K*(*z*) can be calculated directly from *I*(*s*). The correlation function *K*(*z*) for an ideal lamellar stacks is shown in Figure 1.147A. The "self-correlation triangle" centered at the origin, reflects the electron density correlation within a lamella (Figure 147A). For a two-phase system, the maximum *Q* at *z* = 0 is

$$Q = K(0) = \delta\rho^2 = \Delta\rho^2\phi_a\phi_c \tag{1.21}$$

It depends only on the volume fractions of the two phases ϕ_c and ϕ_a and the electron density difference $\Delta\rho = \rho_c - \rho_a$, that is Q does not depend on the detailed structure. Therefore, it is called *invariant*.

From the maximum at the origin, $K(z)$ decreases linearly to a minimum value, namely, the baseline B, with the value

$$-B = -\phi_c{}^2\Delta\rho^2 = \frac{\phi_c}{1-\phi_c} \tag{1.22}$$

If the crystallinity is smaller than 50% ($\phi_c \leq 0.5$), this minimum position corresponds to the crystalline thickness d_c. Otherwise, it corresponds to the amorphous thickness d_a and ϕ_c has to be replaced by $\phi_a = (1-\phi_c)$, in accordance with Babinet's principle.

The slope of $K(z)$ at the origin is

$$\frac{dK}{dz} = -\frac{O_{ac}}{2}\Delta\rho^2 = \frac{\Delta\rho^2}{L} \tag{1.23}$$

with O_{ac} as the specific inner surface per unit volume of the interfaces between crystalline and amorphous regions.

$$O_{ac} = \frac{2}{L} = \frac{2\phi_c}{d_c} \tag{1.24}$$

The second maximum in $K(z)$ is located at the long period L. The crystallinity and the square of the electron density then follow by:

$$\phi_c = \frac{d_c}{L} = \frac{B}{B+Q} \tag{1.25}$$

$$\Delta\rho^2 = \frac{Q}{\phi_c(1-\phi_c)} = \frac{(B+Q)^2}{B} \tag{1.26}$$

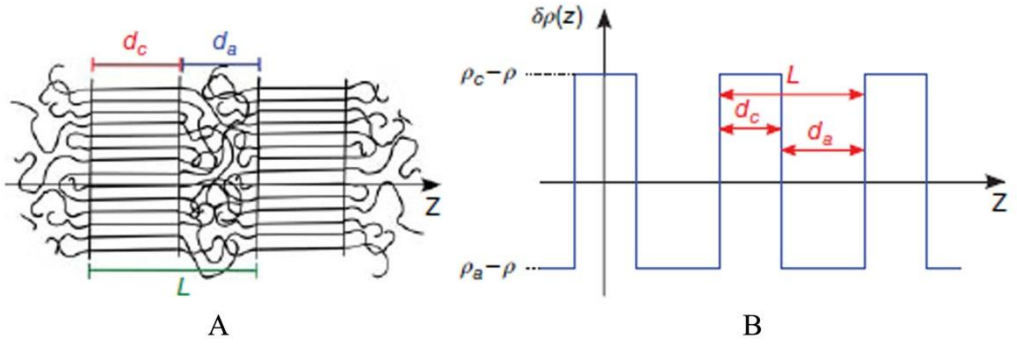

Figure 1.146. *Scheme of the ideal lamellar structure of a semicrystalline polymer (A), consisting of crystalline lamellae with thickness d_c and amorphous regions with thickness d_a alternating along the z-direction with periodicity $L=d_c+d_a$ and corresponding electron density difference along the z-direction (B).*

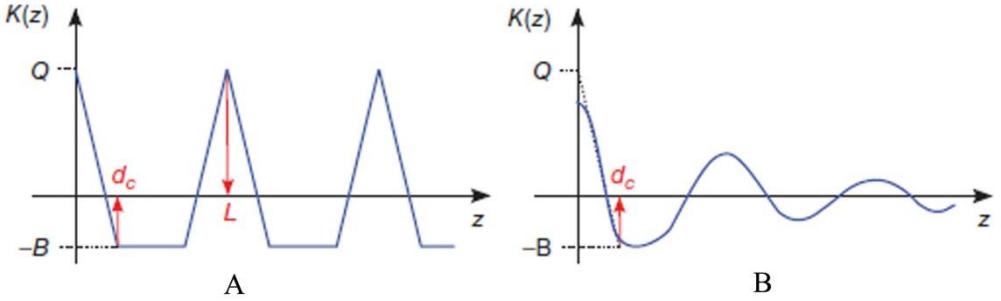

Figure 1.147. *Correlation function for an ideal lamellar stack (A) and effect of deviations from ideality (B).*

In a real system, deviations from the ideal structure exist, for example, variations of the lamellar and crystalline thicknesses or diffuse interphases. Figure 147B illustrates this case. Around the origin, $K(z)$ is flattened. The first minimum does not necessarily reach the value of the baseline anymore. In addition, higher order maxima of $K(z)$ are damped due to the thickness variations of the crystalline and amorphous phase, leading to an overestimated long period.[164]

Another way of analyzing SAXS data of a lamellar two-phase system is the interface distribution function $K''(z)$ (IDF) established by Ruland.[165] For an ideal lamellar two-phase system, the second derivative of the one-dimensional correlation function $K''(z)$ has only contributions (δ-functions) at positions that correspond to the distance of any two interphases, with the first three giving the structure parameters d_a, d_c, and L. Figure 1.148 shows the correlation function and the first and second derivative $K'(z)$ and $K''(z)$. Deviations from an ideal

lamellar structure, for example, varying amorphous and crystalline thicknesses, lead to a broadening of the δ-peaks (Figure 1.148).

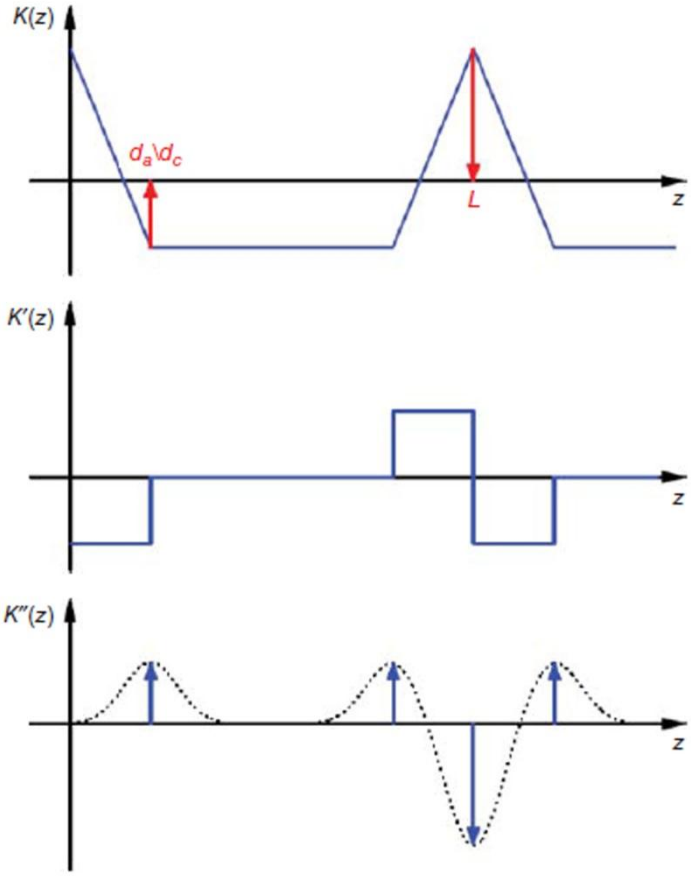

Figure 1.148. Correlation function $K(z)$ for an ideal lamellar stack and the first and second derivatives $K'(z)$ and $K''(z)$. Deviations from the ideal lamellar structure lead to a broadening (dotted line) of the δ-Peaks (arrows).

$K''(z)$ can be calculated directly from $I_{abs}(s)$ using the common expression for the Fourier transform of derivatives:[166]

$$\mathcal{F}[K''(z)] = (i2\pi s)^2 \mathcal{F}[K(z)] \qquad (1.27)$$

$$K''(z) = -8\pi^3 \int_{-\infty}^{\infty} s^4 I_{abs}(s) e^{i2\pi sz} ds \qquad (1.28)$$

The triangular shape of $K(z)$ around the origin leads to a δ-function for $K''(z)$ at $z = 0$, which gives a constant contribution in reciprocal space for $s \rightarrow \infty$, which has to be subtracted:[167]

$$\lim_{s\to\infty} I_{abs}(s)s^4 = \text{const} = \text{P} \qquad (1.29)$$

This means that for for $s \to \infty$ it is assumed that the experimental SAXS intensity responds to the Porod law:[168]

$$I_{abs}(s) = Ps^{-4} \qquad (1.29a)$$

The Porod parameter P is related to the specific inner surface O_{ac} and the electron density difference $\Delta\rho$:

$$P = \frac{O_{ac}\Delta\rho^2}{8\pi^3} \qquad (1.30)$$

A decrease of $I(s) \propto s^{-4}$ is characteristic for a two-phase system with sharp boundaries.[168] After subtracting the contribution at $z = 0$, Equation 1.28 yields:

$$K''(z) = 8\pi^3 \int_{-\infty}^{\infty} [\lim_{s\to\infty} I_{abs}(s)s^4 - s^4 I_{abs}(s)] e^{i2\pi sz} ds \qquad (1.31)$$

The inverse Fourier transform:

$$[\lim_{s\to\infty} I_{abs}(s)s^4 - s^4 I_{abs}(s)] = \int_{-\infty}^{\infty} \frac{K''(z)}{8\pi^3} e^{i2\pi sz} dz \qquad (1.32)$$

Since $K''(z)$ is an even function the latter equation is equivalent to

$$[\lim_{s\to\infty} I_{abs}(s)s^4 - s^4 I_{abs}(s)] = 2\int_0^{\infty} \frac{K''(z)}{8\pi^3} \cos(2\pi z) dz \qquad (1.33)$$

With $s^4 I_{abs}(s)$ being an even function, the Equation 1.33 becomes:

$$K''(z) = 16\pi^3 \int_0^{\infty} [\lim_{s\to\infty} I_{abs}(s)s^4 - s^4 I_{abs}(s)] \cos(2\pi sz)\ ds \qquad (1.34)$$

For an ideal system, $K''(z{=}0)$ as defined in Equation 1.34 is zero, corresponding to the fact that there are no interfaces with zero distance, as they would occur, for example, at the edges of lamellar crystals. For laterally extended lamellae, this contribution is negligible also in a real lamellar system.[169] The scattering intensity $I_{abs}(s)$ is measured in absolute unitsas defined in Equation 1.14. In addition to scattering, absorption takes place in the sample, following the Lambert–Beer law[170] as it does for visible light. For SAXS, the transmitted and the scattered beams are attenuated by the same amount. The transmission measured for the primary beam can therefore be used to correct

the scattering signal $I_{exp}(s)$ for absorption effects. The absorption factor A is the ratio of the primary beam intensity with and without the sample.

$$A = \frac{J_{0\,(Sample)}}{J_{0\,(Background)}} \tag{1.35}$$

$$I_{exp,abs}(s) = A^{-1} I_{exp}(s) \tag{1.36}$$

Absorption also needs to be taken into account when subtracting the background $I_{exp,BG}(s)$, caused, for example by the empty sample holder. This is the last step by which the experimental data have to be corrected before calculating the correlation function or the IDF.

$$I_{abs}(s) = I_{exp,abs}(s) - I_{exp,BG}(s) \tag{1.37}$$

1.9.2. Modeling the Interface Distribution Function for a 1D Lamellar Stack.

In an ideal lamellar structure the IDF has maxima or minima corresponding to the distance of interfaces between the two ideal crystalline and amorphous phases. In particular, there is a first maximum at d_a value, followed by a second maximum at d_c value (Figiure 1.148). A minimum follows these maxima at position $r = L = d_c + d_a$, which corresponds to the interface between couples of consecutive layers. Other maxima and minima are present at longer distances r corresponding to all possible third close interfaces ($r = d_c + d_a + d_c$ and $r = d_a + d_c + d_a$), fourth close interfaces etc.

Deviations from an ideal lamellar structure, for example, varying amorphous and crystalline thicknesses, lead to a broadening of the δ-peaks (Figure 1.148). Thus, $K''(z)$ can be described as a sum of distribution functions, where $h_c(z)$ denotes the distribution of crystalline thicknesses and $h_a(z)$ the distribution of amorphous thicknesses. $h_{ac}(z)$ is the distribution of the long period that is, one amorphous plus one crystalline thickness. Higher order distributions are defined analogously.

Therefore, in experimental cases the IDF must show two maxima at $r = l_a$ and l_c and a minimum at $r = l_c + l_a$ and it is not always possible to determine accurately the position of minima and/or maxima among more distant interfaces. Moreover, the nonideality of a real semicrystalline polymer can lead to a broadening and overlapping of the peaks in $K''(z)$, which makes it difficult to extract the correct structure parameters simply from the peak positions. The

one-dimensional paracrystalline stack has been suggested as an analytical model for the semicrystalline structure.[169,171,172] The procedure adopted by Prof. Thurn-Albrecht allows simulating and modeling the measured IDF based on this model. A simulated IDF $K''_{Sim}(z)$ is introduced:

$$K''_{Sim}(z) = \frac{O_{ac}\Delta\rho^2}{2}\left(h_a(z) + h_c(z) - 2h_{ac}(z) + h_{aca}(z) + h_{acc}(z) - \ldots\right) \quad (1.38)$$

for which $h_a(z)$ and $h_c(z)$ are taken to be normalized Gaussian functions, that is, the thicknesses $d_{a,c}$ have a Gaussian distribution with width $\sigma_{a,c}$

$$h_{a,c}(z) = \frac{1}{\sqrt{2\pi}\sigma_{a,c}} e^{-\frac{(z-d_{a,c})^2}{2\sigma_{a,c}^2}} \quad (1.39)$$

Higher order distributions $h_{aca}(z)$ are assumed to be convolutions ($*$) of $h_a(z)$ and $h_c(z)$, here the order of indices is irrelevant. Every Gaussian function has two free parameters ($d_{a,c}$ and $\sigma_{a,c}$); that is, all together, the model function has four free parameters. The cosine transform of $K''(z)$ (Eq. 1.33) is approximated by the real part $\Re$ of the Fourier transform of K'' ($_{Sim}(z)$)

$$\widetilde{K}''_{Sim}(s) = \Re(\mathcal{F}[K''_{Sim}(z)] \quad (1.40)$$

The calculation is simplified by the fact that the Fourier transform of a Gaussian function is again a Gaussian function

$$\mathcal{F}[h(z)] = \tilde{h}(s) = \int_{-\infty}^{\infty} h(z)e^{-i2\pi sz}dz = e^{-2\pi^2 s^2\sigma^2}\, e^{i2\pi sd} \quad (1.41)$$

and that the convolutions become products. The sum in Equation 1.38 can be represented as a geometric series and an analytical expression is obtained for $\widetilde{K}''_{Sim}(s)$, which can be fitted to the experimental data (for details, see ref 163):

$$\widetilde{K}''_{Sim}(s) = 16\pi^3[\lim_{s\to\infty} I_{abs}(s)s^4 - s^4 I_{abs}(s)] \quad (1.42)$$

Finally, the calculation of $K''_{Sim}(z)$ is realized by a cosine transform of $\widetilde{K}''_{Sim}(s)$. For the Fourier transform of the experimental data, it is necessary to multiply the right side of Equation 1.42, that is, $16\pi^3[\lim_{s\to\infty} I_{abs}(s)s^4 - s^4 I_{abs}(s)]$, abbreviated $16\pi^3[P - s^4 I_{abs}(s)]$ with a window function:

$$\omega(s) = e^{-4\pi\sigma^2 s^2} \quad (1.43)$$

to suppress contributions due to noise, which become very strong at high s due to the multiplication with s^4. Therefore, to compare the measurement with the simulation, both are multiplied with $\omega(s)$. This procedure is equivalent to a convolution of $K''(z)$ and $K''_{Sim}(z)$ with $\omega(z)$ in real space, resulting in a certain broadening of both. Typical values for σ are in the range between 1 and 2 nm. In addition, taking into account the finite resolution of the measuring instrument, the simulated $\widetilde{K}''_{Sim}(s)$ has to be convoluted with a resolution function

$$A(s) = \frac{1}{\sqrt{2\pi}\sigma_A} e^{-\frac{s^2}{2\sigma_A^2}} \tag{1.44}$$

For the data shown in next section, a value of σ_A = 0.00325 nm^{-1} was assumed. The final expression of the simulation function, in the following abbreviated with $\widetilde{K}''_{Sim,final}(s)$, is then

$$\widetilde{K}''_{Sim,final}(s) = A(s) * (\widetilde{K}''_{Sim}(s)\omega(s)) \tag{1.45}$$

The approach to take the real part $\Re$ of the Fourier transformation $\mathcal{F}$ as an approximation of the cosine transformation leads to an additional contribution for $K''_{Sim}(z)$ at small z. The light gray area in Figure 1.149 illustrates the additional contribution. One, therefore, has to make sure that this additional contribution is small. Here it has been adopted the criterion that the integrated contribution of the Gaussian function $h^{\omega}_{a}(z)$ (convoluted with the window function):

$$h_a^{\omega}(z) = \mathcal{F}\left(\tilde{h}_a(s)\omega(s)\right) = \frac{1}{\sqrt{2\pi}\sqrt{(\sigma_a^2+2\sigma^2)}} e^{-\frac{(z-d_a)^2}{2\sigma_a^2+4\sigma^2}} \tag{1.46}$$

for negative z is smaller than 5% of the whole area underneath $h^{\omega}_{a}(z)$.

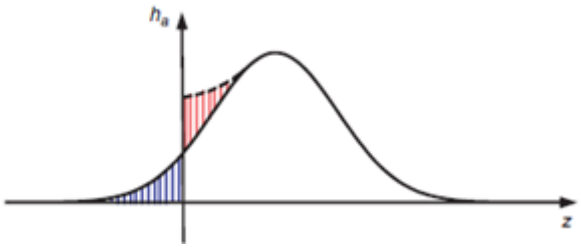

Figure 1.149. Gaussian function (black line) with nonzero values for $z \leq 0$ (dark gray area). Calculating the real part of the Fourier transformation instead of a cosine transformation leads to an additional contribution (light gray area) for $h(z \geq 0)$.

Since the calculation of the IDF is realized by a discrete cosine transform (DCT) applied to the discrete data points from the experiment, the *s*-range, over which experimental data are measured, sets the resolution with which the IDF is determined. For a given highest scattering vector s_{max}, the IDF is calculated with a distance between the data points $\Delta z = 1/s_{max}$. For a reliable analysis, Δz should be smaller than the scale of the smallest features to be determined, that is, d_a or d_c, whatever is smaller. Then the corresponding contribution in the IDF will be well-resolved. In reciprocal space, this requires that s_{max} is in the Porod range for which $I_{abs}(s) = Ps^{-4}$. If a smaller s_{max} is chosen, small-scale features in the IDF and also the correlation function are effectively averaged out with a resolution corresponding to $1/s_{max}$.

In the next section the calculation of $K''(z)$ will be demonstrated step by step only for the sample of the sPP homopolymer, as an example of the complete procedure. For all other samples of sPPET and sPPBu copolymers onlyy the results will be shown.

1.9.3. SAXS analysis on the sPP homopolymer sample.

SAXS desmeared profiles of the compression-moulded sample and aged at room temperature of the sPP homopolymer sRDG-2-1 recorded at 25 °C, after heating at 180 °C where the sample is melted and after successive cooling down to 25 °C allowing crystallization of the sample, are reported in Figures 1.150. The SAXS data have been recorded following the procedure described in sections 1.5 and at the beginning of the section 1.9. The corresponding WAXS profiles, recorded in separated experiments on compression molded films soon after the cooling from the melt and after aging at room temperature are reported in Figures 1.131A and B (profiles a), respectivey. Therefore, the SAXS profile of the sample sRDG-2-1 labeled 25°C start of Figure 1.150 corresponds to the WAXS diffraction profile a of Figure 1.131B of the compression-molded and aged sample. The SAXS profile labeled 25°C end of Figure 1.150 recorded soon after the cooling from the melt, corresponds to the WAXS diffraction profile a of Figure 1.131A of the as-prepared non-aged compression-molded sample.

The calculation of the interface distribution function (IDF), $K''(z)$, followed by the modeling of the data by the simulated IDF, $K''_{Sim,final}(s)$, in the reciprocal space is demonstrated in detail on the SAXS data of the sample sRDG-2-1 at room temperature before melting (Figure 1.151) and after melting and successive crystallization by cooling from 180 °C down to 25 °C (Figure 1.152).

The scattering intensity $I_{abs}(s)$ is measured in absolute units and describes the scattering power of the sample per volume in units of [e.u./nm^3]. For real data, the intensity contains, in addition, a constant contribution from thermal density fluctuations within the amorphous phase c_2 and a contribution proportional to s^2 from the amorphous halo. The latter term is often negligible. Thus, for large s:

$$I_{abs}(s) \approx Ps^{-4} + c_1 s^2 + c_2 \qquad (1.47)$$

To determine P, c_1 and c_2, the expression in Equation 1.47 is fitted to the data in the range of high values of the scattering vectors s and, as explained above, under the side condition $K''(0) = 0$:

$$K''(0) = 0 = 16\pi^3 P \int_0^{Smax} [P - (I_{abs}(s) - c_2)s^4 + c_1 s^6] \times e^{-4\pi^2\sigma^2 s^2} ds \qquad (1.48)$$

As the scattered intensity at $s = 0$ is not measurable, an extrapolation is required. The window function $e^{-4\pi^2\sigma^2 s^2}$ on the other hand, avoids truncation effects at large s due to the finite interval [0, s_{max}] and suppresses noise. As

shown in Figures 1.151A and 1.152A and by Equation 1.47, a range of s large enough is needed to determine c_2 correctly.

The value of the scattering vector s^* corresponding to the maximum SAXS intensity has been evaluated from the Lorentz corrected profiles $Is^2(s)$ corrected by subtraction of the background,[173] shown in Figures 1.151B and 1.152B. From both the Lorentz-corrected profiles of the sample at room temperature before melting (Figure 1.151B) and after melting and crystallization (Figure 1.152B) a similar value of $s^* \approx 0.08$ nm^{-1} has been evaluated. The experimental Lorentz-corrected profiles have been fitted with a Gaussian curve (red curves in Figures 1.151B and 1.152B) for a better evaluation of the maxima.

The correlation functions $K(z)$ are then calculated from the cosine transform of the intensity $I(s)$ (Eq.1.20) and are reported in Figures 1.151C and 1.152C for the data at room temperature before melting and after melting and crystallization, respectively.

The Interface Distribution Functions (IDF) $K''(z)$ are finally obtained performing the discrete cosine transform (DCT) of the function $16\pi^3[P\text{-}I_{abs}s^4]\omega$ (cf. Eq. 1.34). The profiles of the function $16\pi^3[P\text{-}I_{abs}s^4]\omega$ are shown in Figures 1.151D and 1.152D as black lines, whereas the profiles of the IDF evaluated from the transform of the scattering data are shown in Figure 1.151E and 1.152E as black curves. For the simulation, the values of the Porod constant, here $P = 0.876$ and 0.368 e.u./nm^7, was taken from the corresponding fit and for the window function a width of $\sigma = 1.0$ nm has been always chosen, that is, the same value as used during the calculation of the IDF (Figure 1.151E and 1.152E, black curves) from the scattering data. For the resolution function $A(s)$, a value of σ_A=0.00325 nm^{-1} has been taken. The four parameters d_a, d_c, σ_a, and σ_c are obtained from the fitting. The resulting model functions $16\pi^3[P\text{-}I_{abs}s^4]\omega$ are shown in Figures 1.151D and 1.152D as red curves.

The experimental IDF functions of Figures 1.151E and 1.152E (black curves) show a broad maximum followed by and a clear minimum. As explained above (Figure 1.148), the first broad maximum should be composed of two maxima corresponding to the two interphase distances d_a and d_c, whereas the position of the minimum clearly corresponds to the long period $L = d_a + d_c$. Therefore, the position of the first maximum should correspond to d_a or d_c and it is, in principle, difficult to distinguish between d_a and d_c. However, we assume that the peak position of the first maximum in Figures 1.151E and 1.152E corresponds to d_c , which is, therefore, lower than d_a, and, then, we calculate d_a from the long period L determined from the position of the

minimum, as $d_a = L - d_c$. The values of the parameters d_a, d_c and L determined from the experimental IDF of Figures 1.151E and 1.152E are reported in Tables 1.21 and 1.22 and are indicated as d_a(IDF), d_c(IDF) and L(IDF).

In a final step, the simulated IDF is calculated according to the Eq. 1.38. The profiles of the simulated IDF are shown in Figures 1.151E,F and 1.152E,F (red curves), in comparison with the IDF evaluated from the experimental data (black curves). The simulated IDF is composed of the contributions of the thicknesses distributions and the first three contributions h_a, h_c, and $-2h_{ac}$ are shown in Figure 1.151F and 1.152F, for the aged sample at room temperature, before melting and after melting and crystallization, respectively, as blue, pink and green dashed lines. It is apparent that, the amorphous and crystalline peaks in the IDF profiles strongly overlap due to the crystallinity of approximately 50% (measured by WAXS). This is an example where it is impossible to obtain the crystalline and amorphous thicknesses simply from the peak position of $K''(z)$. The separation into crystalline and amorphous contributions is only possible with the help of the simulation. However, it is also woth noting that one of the two distributions of thicknesses (corresponding to the thicknesses of amorphous or crystalline phases) is much broader (the blue curves in Figures 1.151F and 1.152F) than the other (red curves in in Figures 1.151F and 1.152F). This difference may be used to discriminate between the amorphous and crystalline contributions to the simulated IDF.

In general, to assign the two peaks of the IDF to the amorphous and crystalline contributions, additional information (e.g., about crystallinity) is needed. In the cases of the esamples of sPP homopolmer and of sPPET and sPPBu copolymers analyzed by SAXS, the crystallinity degree (x_c) has been determined from the WAXS profiles of Figures 1.131 and 1.132 by the ratio between the crystalline diffraction area (A_c) and the area of the whole diffraction profiles (A_t), $x_c = (A_c/A_t)\times 100$. The area of the crystalline diffraction A_c has been evaluated by subtracting the area of the amorphous halo from the area of the whole diffraction profiles A_t. However, the determination of crystallinity by WAXS is not always reliable, in particular when crystals contains high degrees of structural disorder, as in the case of sPP (see section 1.2), which is further increased in copolymers for the presence of constitutional defects. This uncertainty has serious consequences in samples of sPP homopolymers or sPPET and sPPBu copolymers with low comonomer concentrations for which the values of the degree of crystallinity are approximately around 50% (Figures 1.131 and 1.132), producing the overlap of

the amorphous and crystalline peaks in the IDF and preventing the assignment of the two peaks of the IDF to the amorphous and crystalline contributions. With the help of the simulation and determination of the simulated IDF a reliable choice may be assumed. Since the simulated IDF can be described as a sum of distribution functions of crystalline thicknesses h_c, of amorphous thicknesses h_a and of the values of the long period h_{ac} (Eq. 1.38), each distribution being characterized by a width σ_c, σ_a and σ_{ac}, we assume that the distribution of thicknesses h_i with lower width σ_i corresponds to that of the crystalline thickness h_c. This allows for the the assignment of the two peaks of the IDF to the amorphous and crystalline thichness d_c and d_a.

For the sample of the sPP homopolymer sRDG-2-1, a value of crystallinity x_c = 61% has been evaluated for both the as-prepared compression-molded samples (from the diffraction profile a of Figure 1.131A) and for the sample crystallized from the melt and aged at room temperature (from the diffraction profile a of Figure 1.131B) (Table 1.21 and 1.22). From this value of crystallinity, the values of parameters d_c = 4.59 nm, d_a = 6.39 nm, L = 10.98 nm, σ_c = 0.64 nm, σ_a = 3.56 nm, reported in Table 1.21 and in Figure 1.151E,F, have been obtained for the compression-molded and aged film (before melting) of the sample sRGD-2-1, and the parameters d_c = 3.62 nm, d_a = 6.58 nm, L = 10.22 nm, σ_c = 0.50 nm, σ_a = 3.62 nm, reported in Table 1.22 and in Figure 1.152E,F, have been obtained for the as-crystallized sample soon after the cooling from the melt.

The three contributions h_a, h_c, and $-2h_{ac}$ have been calculated by replacing the value of d_c, d_a, σ_a, σ_c resulting from the fitting function in the following equations:

$$h_a = (P \times 4\pi^3) \times \frac{1}{\sqrt{2\pi({\sigma_a}^2+2\sigma^2)}}\, e^{-\frac{(z-d_a)^2}{2{\sigma_a}^2+4\sigma^2}} \tag{1.49}$$

$$h_c = (P \times 4\pi^3) \times \frac{1}{\sqrt{2\pi({\sigma_c}^2+2\sigma^2)}}\, e^{-\frac{(z-d_c)^2}{2{\sigma_c}^2+4\sigma^2}} \tag{1.50}$$

$$h_{ac} = (-2P \times 4\pi^3) \times \frac{1}{\sqrt{2\pi(({\sigma_c}^2+2\sigma^2)+({\sigma_a}^2+2\sigma^2))}}\, e^{-\frac{(z-(d_c+d_a))^2}{2{\sigma_c}^2+4\sigma^2}} \tag{1.51}$$

The profiles of the three thickness distributions h_a, h_c, and $-2h_{ac}$ as contributions of the IDF are shown in Figures 1.151F and 1.152F. As mentioned above, it is apparent that the distributions of the amorphous thicknesses ha (blue curves in Figures 1.151F and 1.152F) are reasonably much broader than those of the crystalline thicknesses (red curves in Figures 1.151F and 1.152F).

The values of L, d_c and d_a evaluated from the modeled function and the simulated IDF have been compared with those evaluated from the Lorentz-corrected profiles (Figures 1.151B and 1.152B) and the correlation functions (Figures 1.151C and 1.152C). The parameters evaluated from the Lorentz-corrected profiles are defined with a * in the symbols (L^*), whereas the parameters evaluated form the correlation function are defined as L(cofun), d_c(cofun) and d_a(cofun).

The values of the long period L^* have been calculated as $L^* = 1/s^*$ from the positions of maxima of the Lorentz-corrected profiles s^* of Figure 1.151B and 1.152B and are reported in the Tables 1.21 and 1.22 for the compression-molded and aged film of the sample sRDG-2-1 and for the as-crystallized sample cooled from the melt, respectively. From the correlation functions $K(z)$ of Figure 1.151C and 1.152C, the value of the long period L(cofun) has been evaluated from the positions of first maximum of $K(z)$. According to the Eq. 1.23, from the slope of $K(z)$ at the origin the difference of the electronic densities of the two crystalline and amorphous phases has been evaluated. The information content of $K(z)$ is strongly limited due to the absence of the baseline and, as mentioned above, the uncertainty of the crystallinity, in particular when it is approximately around 50%. This makes it impossible to distinguish d_a from d_c. In addition, the information about the thickness distributions is hidden. Only the long period could be extracted from $K(z)$. However, in general, it is possible to evaluate the values of d_c and d_a, besides the long period, from the first correlation triangle at the origin of the correlation function (Figures 1.151C and 1.152C). In particular, the short side of the rectangle triangle, or the intersection point between the segment interpolating the first part of $K(z)$ at the origin (the hypotenuse of the triangle) and the tangent to the minimum of $K(z)$, gives the value of the minimum layer thickness d_{min} of the biphasic model, d_a or d_c and corresponds to the crystalline thickness d_c, if the degree of crystallinity evaluated by a different technique (for instance DSC or WAXS) is less than 50%, to the thickness of the amorphous layers d_a if the degree of crystallinity is higher than 50%. Since, from the simulated IDF the values of d_c results lower than d_a, we assume, for analogy with the IDF results, that the minimum thickness evaluated from the triangle of the correlation functions corresponds to the crystalline thickness d_c(cofun) (Figures 1.151C and 1.152C), even though the degrees of crystallinity have been evaluated from the WAXS profiles a of Figures 1.131A and B slightly higher

than 50%. Then, the value of d_a(cofun) has been calculated as L(cofun) - d_c(cofun).

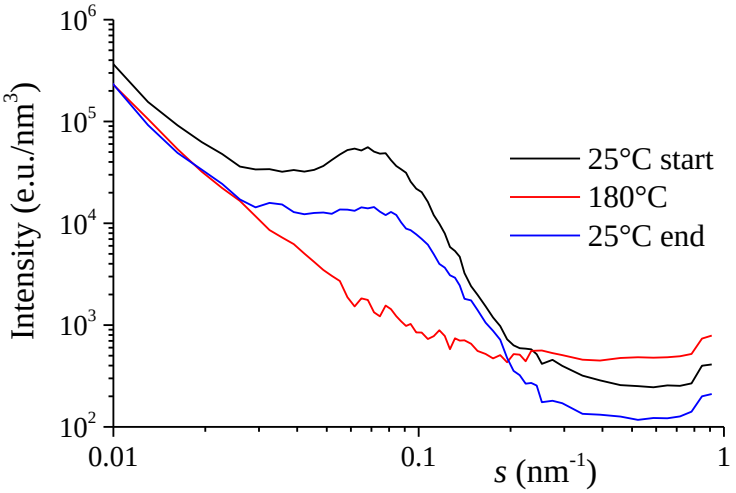

Figure 1.150. *SAXS intensity profiles of the sPP homopolymer sample sRDG-2-1 with 0.7 mol% of total defects recorded at room temperature for a compression-moulded melt-crystallized film aged at room temperature (black curve), recorded after heating at 180 °C where the sample is melted (red curve) and soon after the successive cooling from the melt to room temperature allowing crystallization (blue curve).*

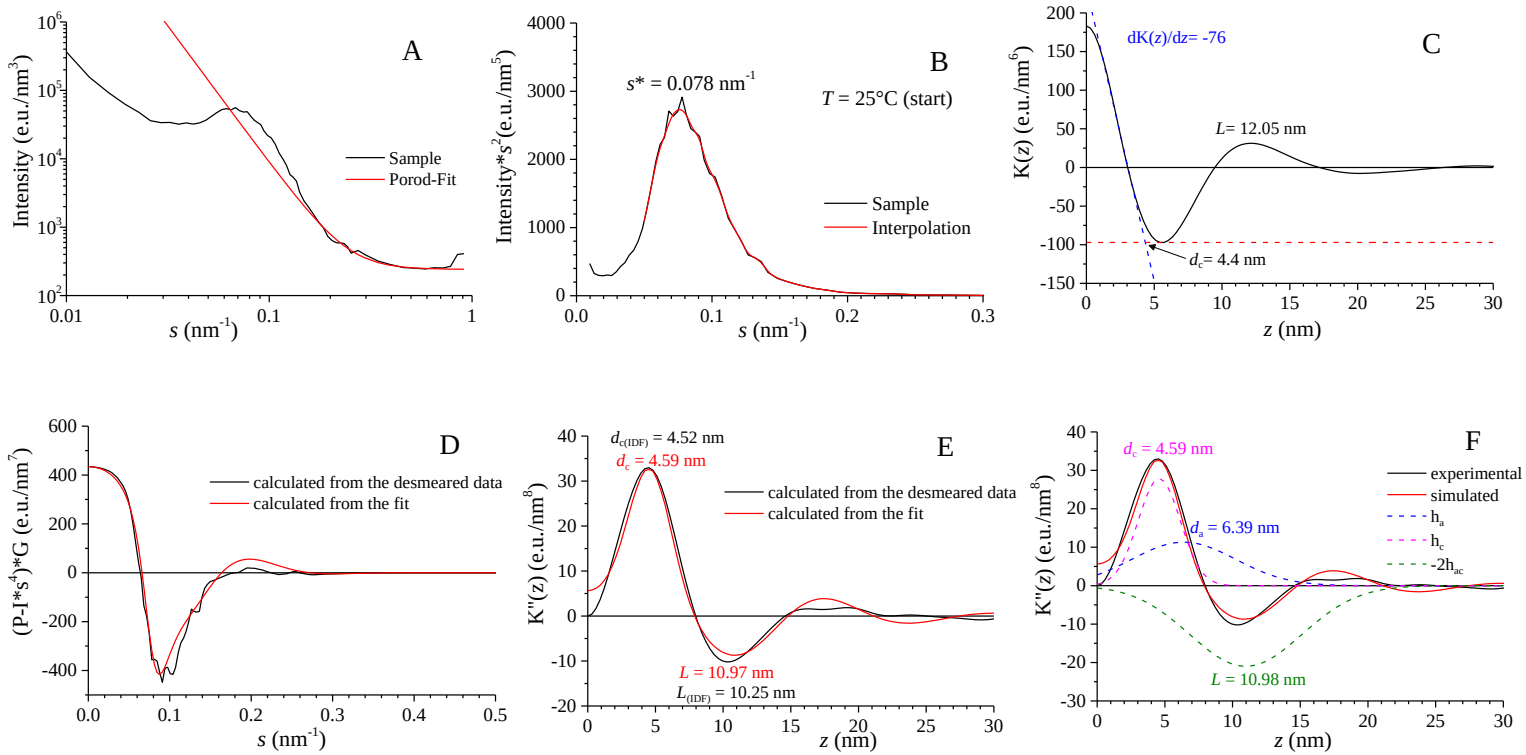

Figure 1.151. *A) SAXS intensity profiles of the aged compression molded film of the sample of sPP homopolymer sRDG-2-1 recorded at room temperature. The red line represents the Porod fit and gives the sum of the Porod scattering and a background due to density fluctuations. B) Lorentz-corrected SAXS intensity profile. The red curve represents the interpolation of the experimental data to evaluate the position of the peak s*. C) Correlation function K(z). The slope of initial part of the function at the origin and the correlation triangle at the origin are shown. The values of L and d_c, evaluated from the position of the first maximum of K(z) and from the short side of the correlation triangle, respectively, are indicated. D) Function $16\pi^3[P\text{-}I_{abs}s^4]\omega$ as calculated from I(s) (black line). The red curve is the result of the simulation. E) Experimental IDF function calculated from I(s) (black line), and simulated IDF function (red curve). F) Experimental and simulated IDF (continuous curves) and single contributions of the distributions of thicknesses h_c, h_a and h_{ac} to the IDF (dashed curves).*

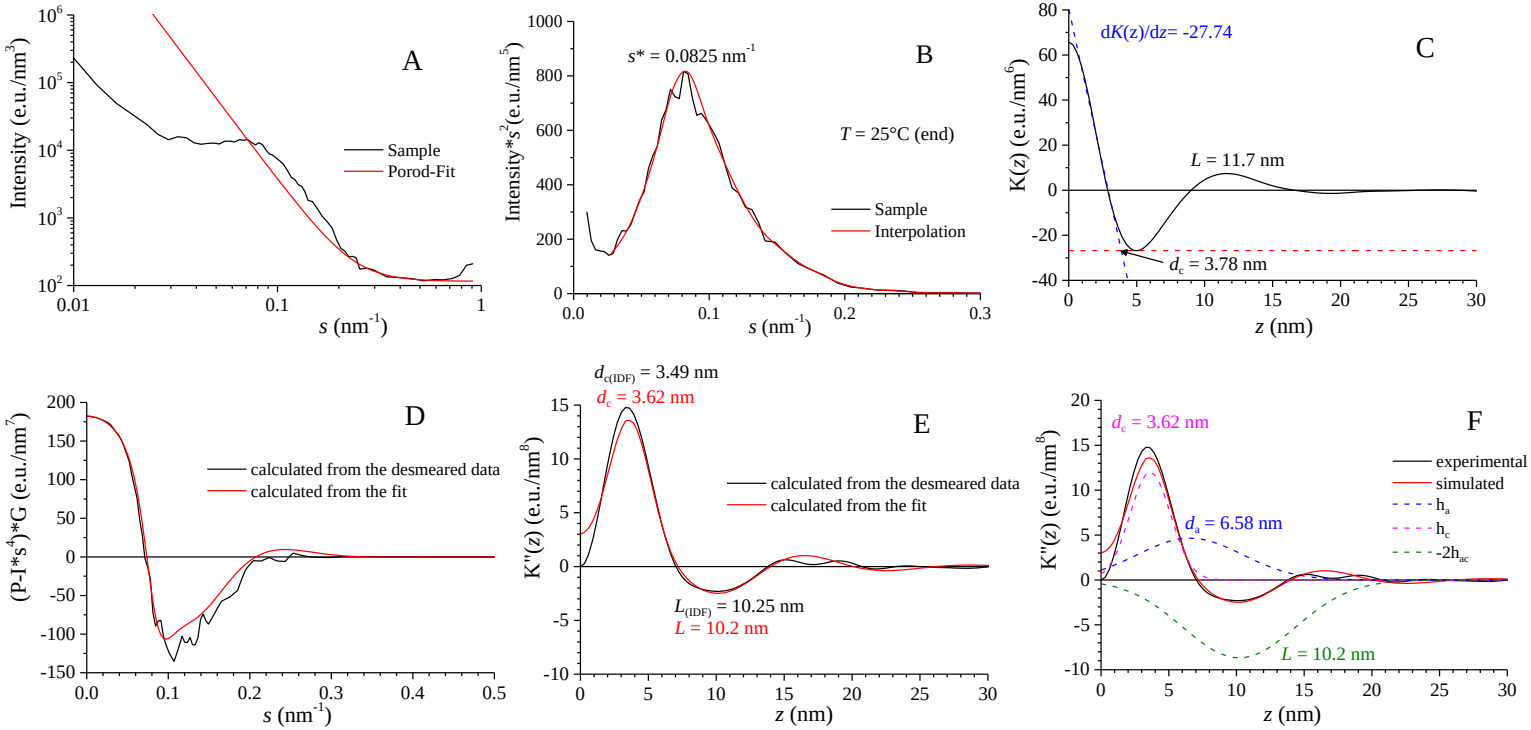

Figure 1.152. *A) SAXS intensity profiles of the as-prepared compression-molded film of the sample of sPP homopolymer sRDG-2-1 recorded soon after the cooling from the melt at room temperature. The red line represents the Porod fit and gives the sum of the Porod scattering and a background due to density fluctuations. B) Lorentz-corrected SAXS intensity profile. The red curve represents the interpolation of the experimental data to evaluate the position of the peak s*. C) Correlation function K(z). The slope of initial part of the function at the origin and the correlation triangle at the origin are shown. The values of L and d_c, evaluated from the position of the first maximum of K(z) and from the short side of the correlation triangle, respectively, are indicated. D) Function $16\pi^3[P\text{-}I_{abs}s^4]\omega$ as calculated from I(s) (black line). The red curve is the result of the simulation. E) Experimental IDF function calculated from I(s) (black line), and simulated IDF function (red curve). F) Experimental and simulated IDF (continuous curves) and single contributions of the distributions of thicknesses h_c, h_a and h_{ac} to the IDF (dashed curves).*

All values of the parameters evaluated from the Lorentz corrected profiles (s^* and L^*), from the experimental IDF (L(IDF), d_c(IDF) and d_a(IDF)), from the simulated IDF (L, d_c, d_a and the widths of thicknesses distributions σ_c and σ_a) and from the correlation function (L(cofun), d_c(cofun) and d_a(cofun)), are reported in Tables 1.21 and 1.22, for the compression-molded and aged film of the sample sRDG-2-1 and for the sample as-cooled from the melt, respectively. For both samples, the values of parameters evaluated from the experimental and simulated IDFs are very similar. Moreover, the values of the long period evaluated from the Lorentz-corrected profiles (L^*) and the correlation functions (L(cofun)) are only slighlty higher than the value evaluated from the modeled function and the simulated IDF (L), while the values of the thicknesses of the crystalline layers d_c and d_c(cofun) are very similar. Furthermore, only a slight difference in the thickness of the crystalline (d_c) and amorphous (d_a) layers and in the long period L between the aged (Figure 1.151) and the as-crystallized sample (Figure 1.152) has been observed. The higher value of d_c and, correspondingly, the lower value of d_a observed in the aged sample are probably due to secondary crystallization phenomena occurring during aging at room temperature. The aging also produces a higher contrast as suggested from the higher $\Delta\rho$ evaluated on the aged sample.

1.9.4. SAXS analysis on sPPET random copolymers.

The same analysis has been performed on random copolymers sPPET. For each sample the SAXS profiles of compression-molded samples aged at room temperature recorded 25 °C, at 180 °C in the melt and after cooling from the melt are reported. Then the SAXS analysis with the modeling of the IDF on SAXS data at room temperature before and after melting is shown (Figures 1.153-1.174). The corresponding WAXS profiles, collected in separated experiments on compression molded films soon after the cooling from the melt and after aging at room temperature are reported in Figures 1.131A and B, respectively. The values of the degree of crystallinity evaluated form the diffraction profiles of Figures 1.131 are reported in Tables 1.21 and 1.22. Values of crystallinity approximately around 50% have been obtained for all samples of sPPET copolymers with ethylene content up to 2.4 mol%. For these samples the analysis of the SAXS data and of the simulated IDF suffers of the same ambiguity to distinguish d_c from d_a, as in the case of the sPP homopolymer. The crystallinity decreases with increasing ethylene concentration and for high ethylene content the crystallinity is clearly lower than 50% (Tables 1.21 and 1.22).

The SAXS profiles of samples of sPPET copolymers with low ethylene concentration up to 2.4 mol% are very similar and are shown in Figures 1.153-1.164. A well-defined peak is visible in the SAXS profiles of the aged samples recorded before melting (black curves in Figures 1.153, 1.156, 1.159 and 1.162). Since all samples with low ethylene concentrations crystallize from the melt (Figure 1.131A), the SAXS peak reappears after the cooling from the melt (blue curves in Figures 1.153, 1.156, 1.159 and 1.162). The Lorentz corrected SAXS profiles, the correlation functions $K(z)$ and the experimental and simulated IDF of the four sPPET samples with ethylene concentrations up to 2.4 mol% are shown in the Figures 1.154-1.155, 1.157-1.158, 1.160-1.161 and 1.163-1.164. The values of the morphological parameters evaluated from the Lorentz corrected SAXS profiles (s^* and L^*), the correlation functions $K(z)$ (d_c(cofun), d_a(cofun) and L(cofun)), the experimental IDF (d_c(IDF), d_a(IDF) and L(IDF)), and the simulated IDF (d_c, d_a and L), are reported in Tables 1.21 and 1.22 for the aged compression-molded samples and for the samples as-crystallized from the melt by cooling from the melt to room temperature, respectively.

As in the homopolymer sRDG-2-1, L^* and L(cofun) are slightly higher than L and this difference become more evident in the as-crystallized samples. On

the contrary the values of d_c(cofun) are similar to those of d_c and d_c(IDF) for all samples before and after melting.

As in the case of the sample of the sPP homopolymer, higher values of the thickness of the crystalline d_c phase and of the long period L have been obtained for the aged samples (Table 1.21) compared to those of the as-crystallized samples (Table 1.22) of sPPET copolymers with ethylene concentration up to 2.4 mol%, whereas the the values of the thickness of the amorphous phase d_a on average remain nearly constant. This is probably due to secondary crystallization phenomena occurring during aging at room temperature.

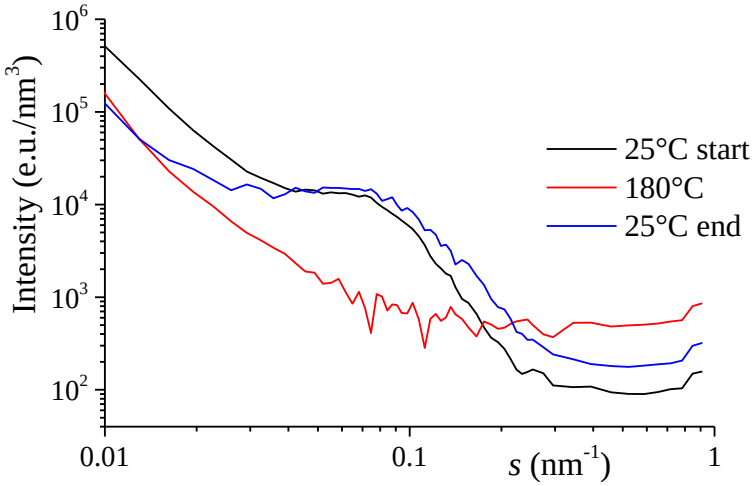

Figure 1.153. *SAXS intensity profiles of the sample of sPPET copolymer RDG-2-41 with 0.4 mol% of ethylene recorded at room temperature for a compression-molded melt-crystallized film aged at room temperature (black curve), recorded after heating at 180 °C where the sample is melted (red curve) and soon after the successive cooling from the melt to room temperature allowing crystallization (blue curve).*

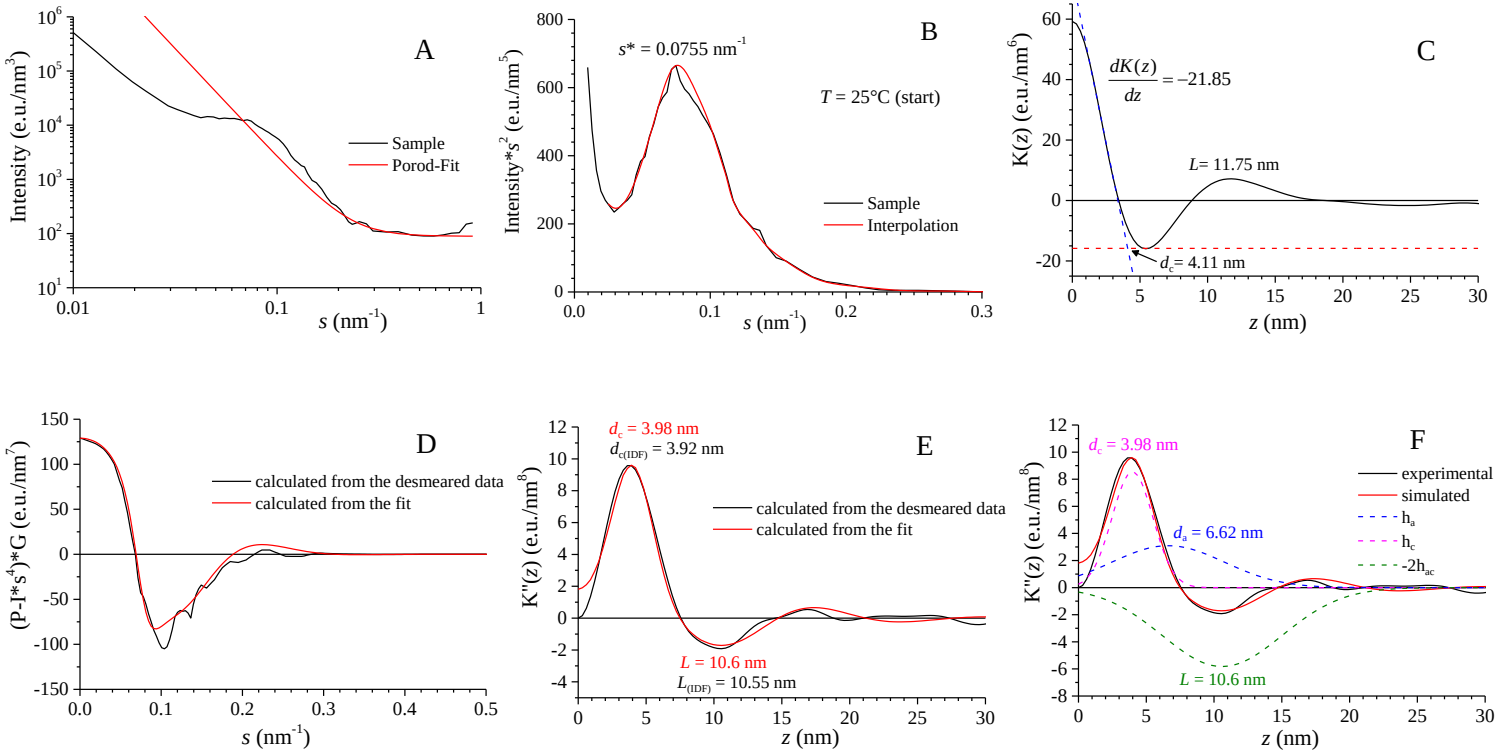

Figure 1.154. *A) SAXS intensity profiles of the aged compression molded film of the sample of sPPET copolymer RDG-2-41 with 0.4 mol% of ethylene recorded at room temperature. The red line represents the Porod fit and gives the sum of the Porod scattering and a background due to density fluctuations. B) Lorentz-corrected SAXS intensity profile. The red curve represents the interpolation of the experimental data to evaluate the position of the peak s*. C) Correlation function K(z). The slope of initial part of the function at the origin and the correlation triangle at the origin are shown. The values of L and d_c, evaluated from the position of the first maximum of K(z) and from the short side of the correlation triangle, respectively, are indicated. D) Function $16\pi^3[P\text{-}I_{abs}s^4]\omega$ as calculated from I(s) (black line). The red curve is the result of the simulation. E) Experimental IDF function calculated from I(s) (black line), and simulated IDF function (red curve). F) Experimental and simulated IDF (continuous curves) and single contributions of the distributions of thicknesses h_c, h_a and h_{ac} to the IDF (dashed curves).*

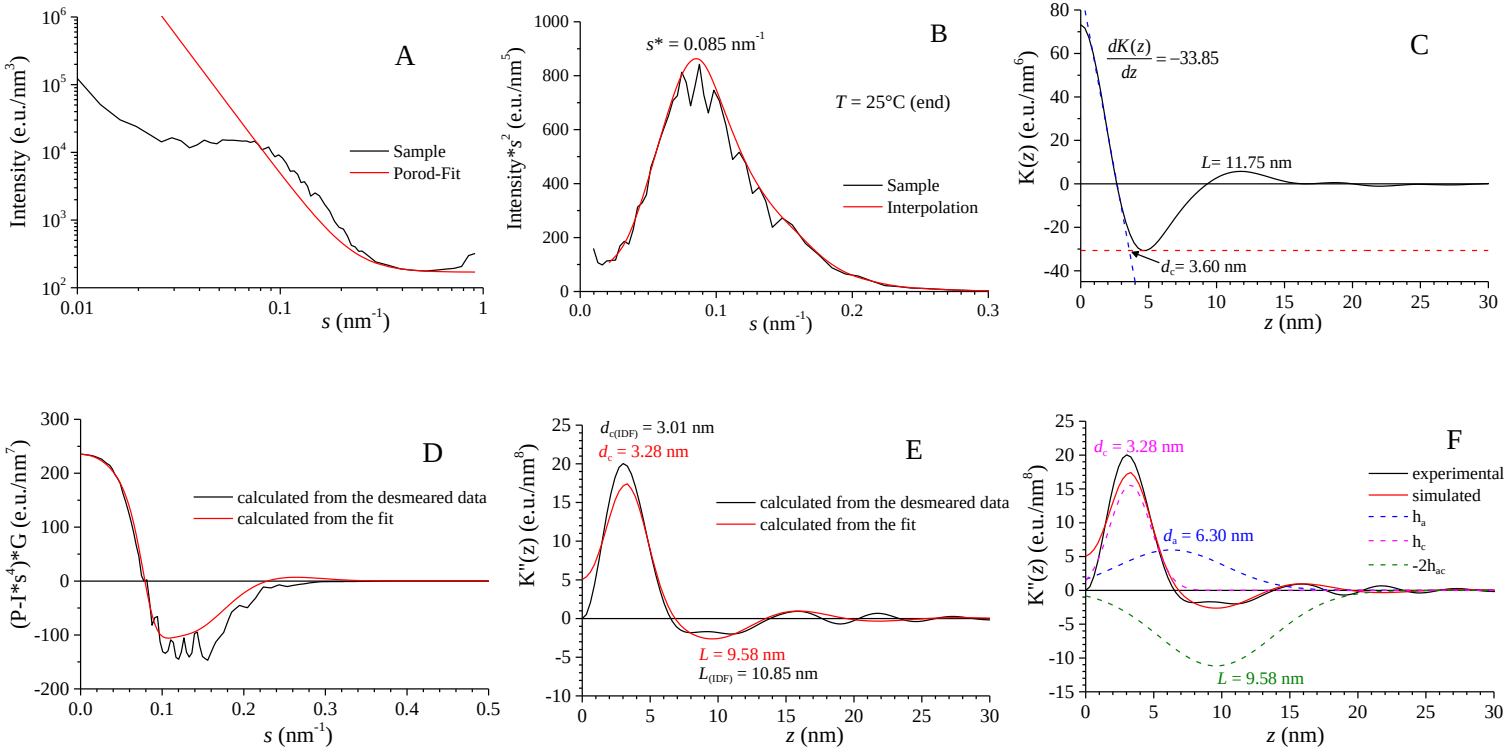

Figure 1.155. *A) SAXS intensity profiles of the as-prepared compression-molded film of the sample of sPPET copolymer RDG-2-41 with 0.4 mol% of ethylene recorded soon after the cooling from the melt at room temperature. The red line represents the Porod fit and gives the sum of the Porod scattering and a background due to density fluctuations. B) Lorentz-corrected SAXS intensity profile. The red curve represents the interpolation of the experimental data to evaluate the position of the peak s*. C) Correlation function K(z). The slope of initial part of the function at the origin and the correlation triangle at the origin are shown. The values of L and d_c, evaluated from the position of the first maximum of K(z) and from the short side of the correlation triangle, respectively, are indicated. D) Function $16\pi^3[P\text{-}I_{abs}s^4]\omega$ as calculated from I(s) (black line). The red curve is the result of the simulation. E) Experimental IDF function calculated from I(s) (black line), and simulated IDF function (red curve). F) Experimental and simulated IDF (continuous curves) and single contributions of the distributions of thicknesses h_c, h_a and h_{ac} to the IDF (dashed curves).*

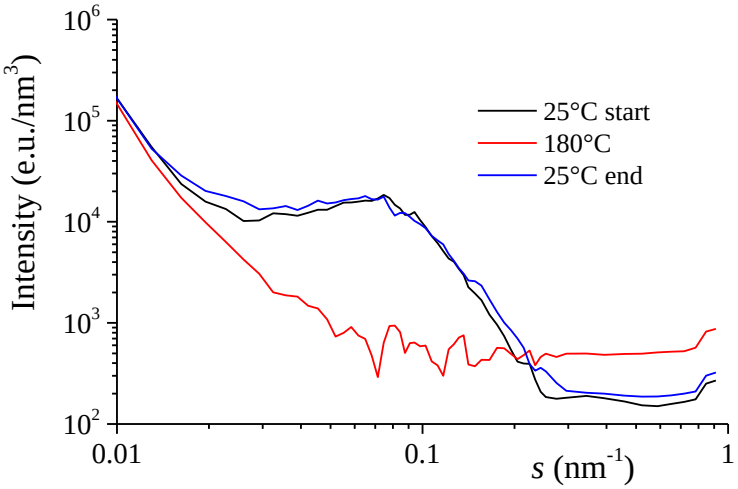

Figure 1.156. *SAXS intensity profiles of the sample of sPPET copolymer RDG-2-40 with 1.7 mol% of ethylene recorded at room temperature for a compression-molded melt-crystallized film aged at room temperature (black curve), recorded after heating at 180 °C where the sample is melted (red curve) and soon after the successive cooling from the melt to room temperature allowing crystallization (blue curve).*

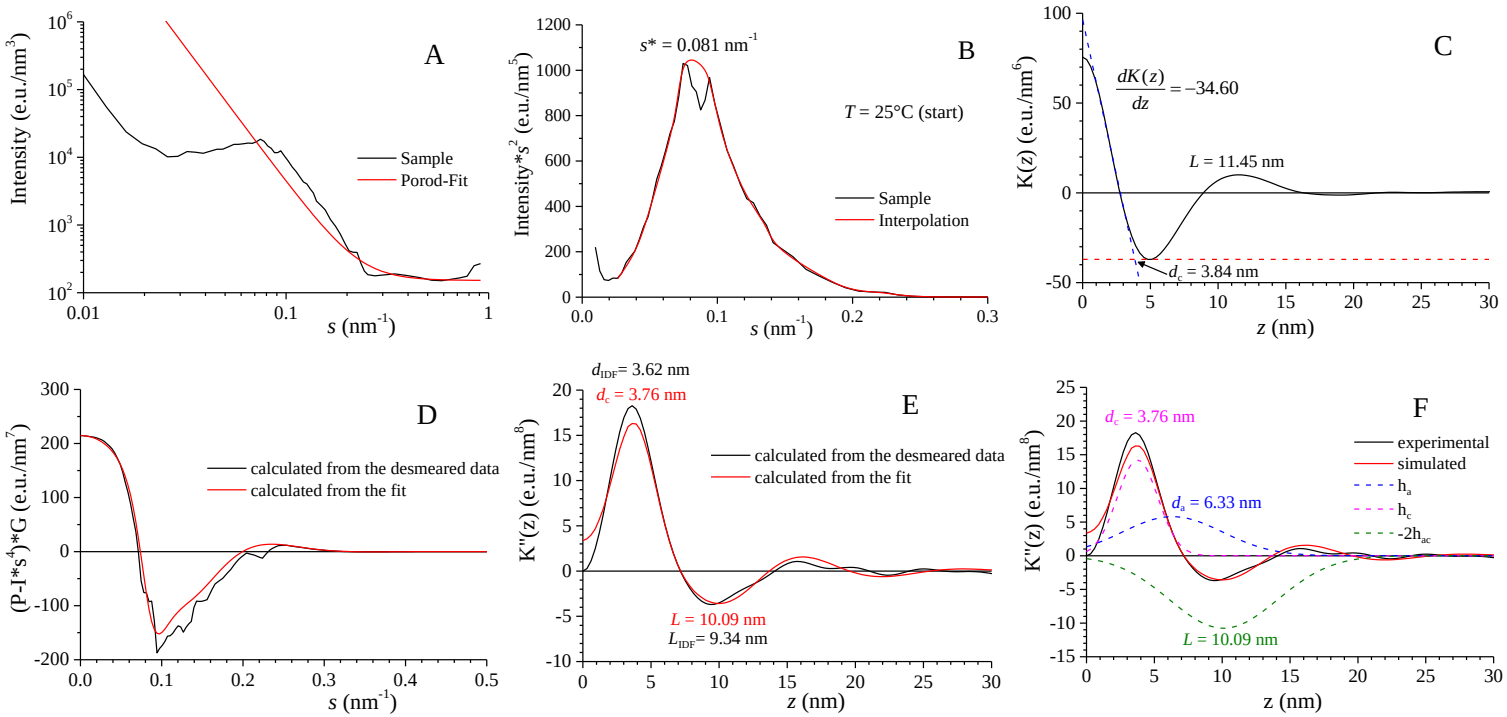

Figure 1.157. *A) SAXS intensity profiles of the aged compression molded film of the sample of sPPET copolymer RDG-2-40 with 1.7 mol% of ethylene recorded at room temperature. The red line represents the Porod fit and gives the sum of the Porod scattering and a background due to density fluctuations. B) Lorentz-corrected SAXS intensity profile. The red curve represents the interpolation of the experimental data to evaluate the position of the peak s*. C) Correlation function K(z). The slope of initial part of the function at the origin and the correlation triangle at the origin are shown. The values of L and d_c, evaluated from the position of the first maximum of K(z) and from the short side of the correlation triangle, respectively, are indicated. D) Function $16\pi^3[P\text{-}I_{abs}s^4]\omega$ as calculated from I(s) (black line). The red curve is the result of the simulation. E) Experimental IDF function calculated from I(s) (black line), and simulated IDF function (red curve). F) Experimental and simulated IDF (continuous curves) and single contributions of the distributions of thicknesses h_c, h_a and h_{ac} to the IDF (dashed curves).*

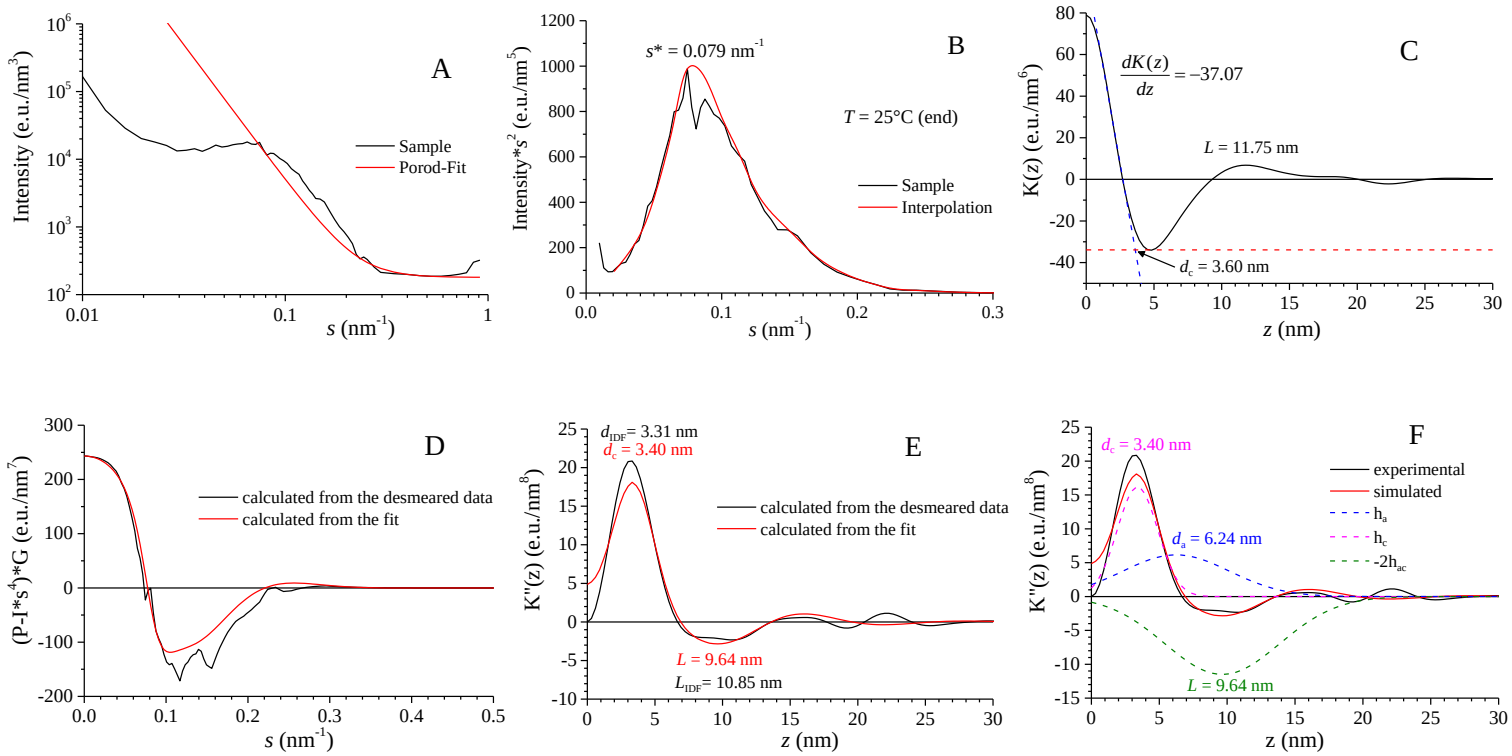

Figure 1.158. *A) SAXS intensity profiles of the as-prepared compression-molded film of the sample of sPPET copolymer RDG-2-40 with 1.7 mol% of ethylene recorded soon after the cooling from the melt at room temperature. The red line represents the Porod fit and gives the sum of the Porod scattering and a background due to density fluctuations. B) Lorentz-corrected SAXS intensity profile. The red curve represents the interpolation of the experimental data to evaluate the position of the peak s*. C) Correlation function K(z). The slope of initial part of the function at the origin and the correlation triangle at the origin are shown. The values of L and d_c, evaluated from the position of the first maximum of K(z) and from the short side of the correlation triangle, respectively, are indicated. D) Function $16\pi^3[P\text{-}I_{abs}s^4]\omega$ as calculated from I(s) (black line). The red curve is the result of the simulation. E) Experimental IDF function calculated from I(s) (black line), and simulated IDF function (red curve). F) Experimental and simulated IDF (continuous curves) and single contributions of the distributions of thicknesses h_c, h_a and h_{ac} to the IDF (dashed curves).*

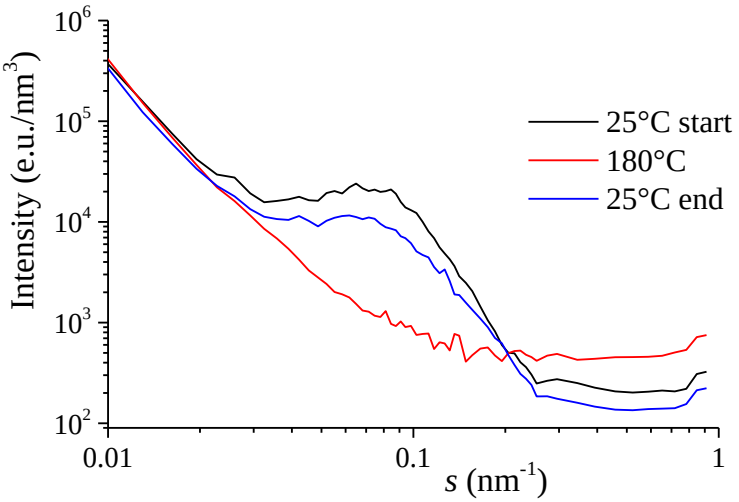

Figure 1.159. *SAXS intensity profiles of the sample of sPPET copolymer AK-sPPEt-2 with 1.9 mol% of ethylene recorded at room temperature for a compression-molded melt-crystallized film aged at room temperature (black curve), recorded after heating at 180 °C where the sample is melted (red curve) and soon after the successive cooling from the melt to room temperature allowing crystallization (blue curve).*

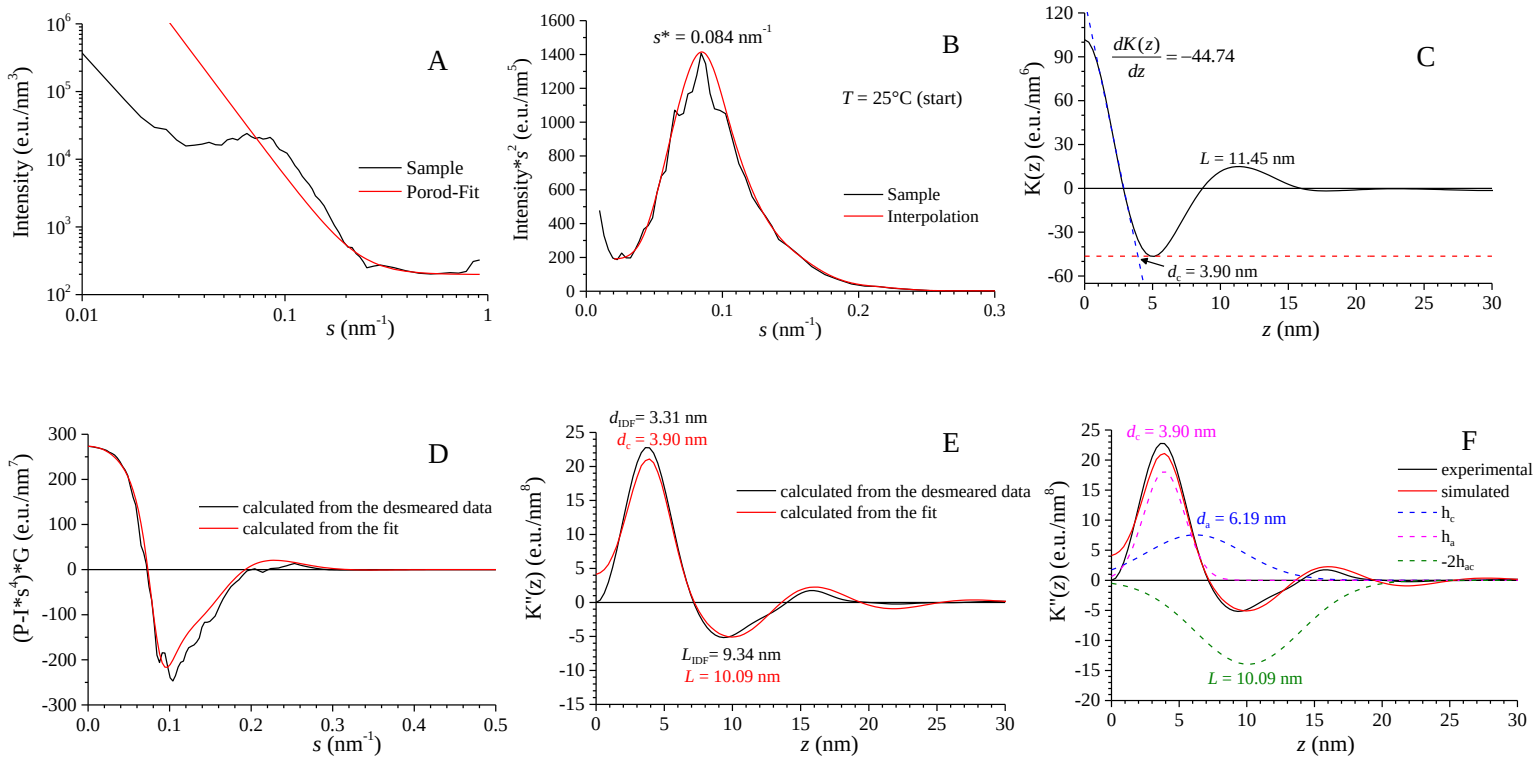

Figure 1.160. *A) SAXS intensity profiles of the aged compression molded film of the sample of sPPET copolymer AK-sPPEt-2 with 1.9 mol% of ethylene recorded at room temperature. The red line represents the Porod fit and gives the sum of the Porod scattering and a background due to density fluctuations. B) Lorentz-corrected SAXS intensity profile. The red curve represents the interpolation of the experimental data to evaluate the position of the peak s*. C) Correlation function K(z). The slope of initial part of the function at the origin and the correlation triangle at the origin are shown. The values of L and d_c, evaluated from the position of the first maximum of K(z) and from the short side of the correlation triangle, respectively, are indicated. D) Function $16\pi^3[P\text{-}I_{abs}s^4]\omega$ as calculated from I(s) (black line). The red curve is the result of the simulation. E) Experimental IDF function calculated from I(s) (black line), and simulated IDF function (red curve). F) Experimental and simulated IDF (continuous curves) and single contributions of the distributions of thicknesses h_c, h_a and h_{ac} to the IDF (dashed curves).*

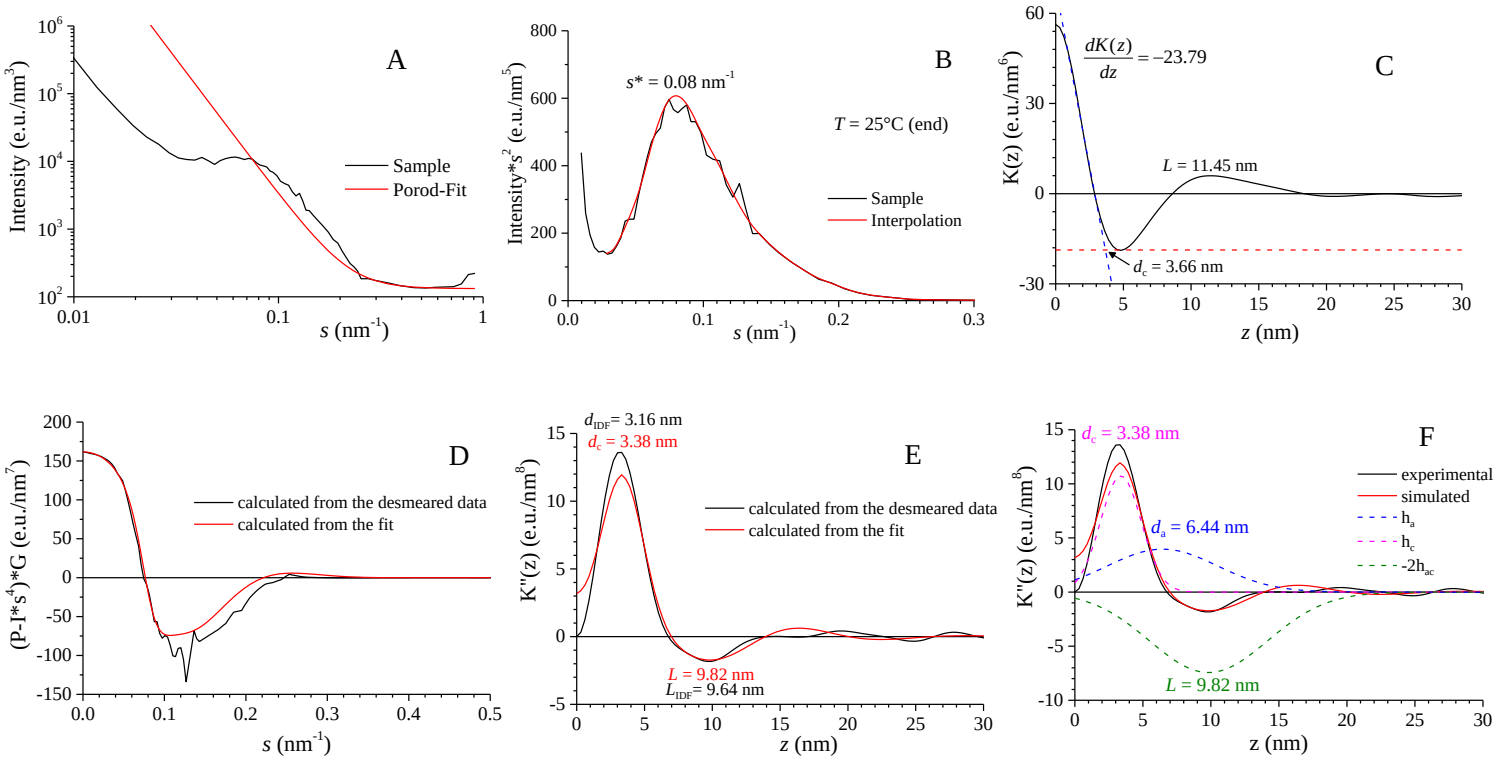

Figure 1.161. *A) SAXS intensity profiles of the as-prepared compression-molded film of the sample of sPPET copolymer AK-sPPEt-2 with 1.9 mol% of ethylene recorded soon after the cooling from the melt at room temperature. The red line represents the Porod fit and gives the sum of the Porod scattering and a background due to density fluctuations. B) Lorentz-corrected SAXS intensity profile. The red curve represents the interpolation of the experimental data to evaluate the position of the peak s*. C) Correlation function K(z). The slope of initial part of the function at the origin and the correlation triangle at the origin are shown. The values of L and d_c, evaluated from the position of the first maximum of K(z) and from the short side of the correlation triangle, respectively, are indicated. D) Function $16\pi^3[P\text{-}I_{abs}s^4]\omega$ as calculated from I(s) (black line). The red curve is the result of the simulation. E) Experimental IDF function calculated from I(s) (black line), and simulated IDF function (red curve). F) Experimental and simulated IDF (continuous curves) and single contributions of the distributions of thicknesses h_c, h_a and h_{ac} to the IDF (dashed curves).*

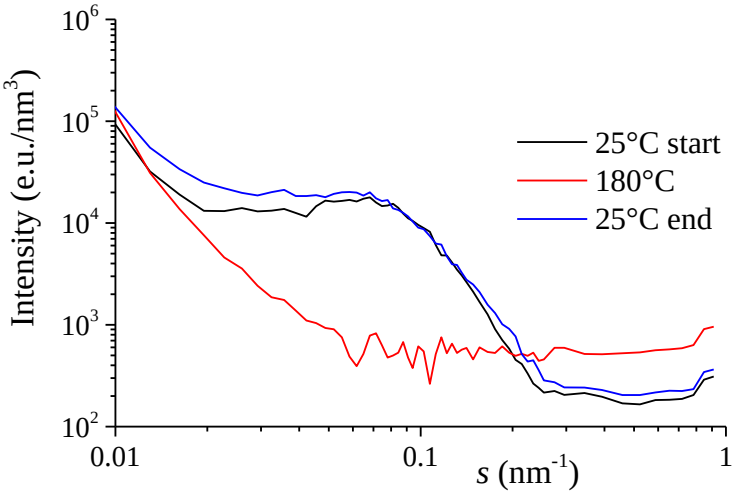

Figure 1.162. *SAXS intensity profiles of the sample of sPPET copolymer RDG-2-42 with 2.4 mol% of ethylene recorded at room temperature for a compression-molded melt-crystallized film aged at room temperature (black curve), recorded after heating at 180 °C where the sample is melted (red curve) and soon after the successive cooling from the melt to room temperature allowing crystallization (blue curve).*

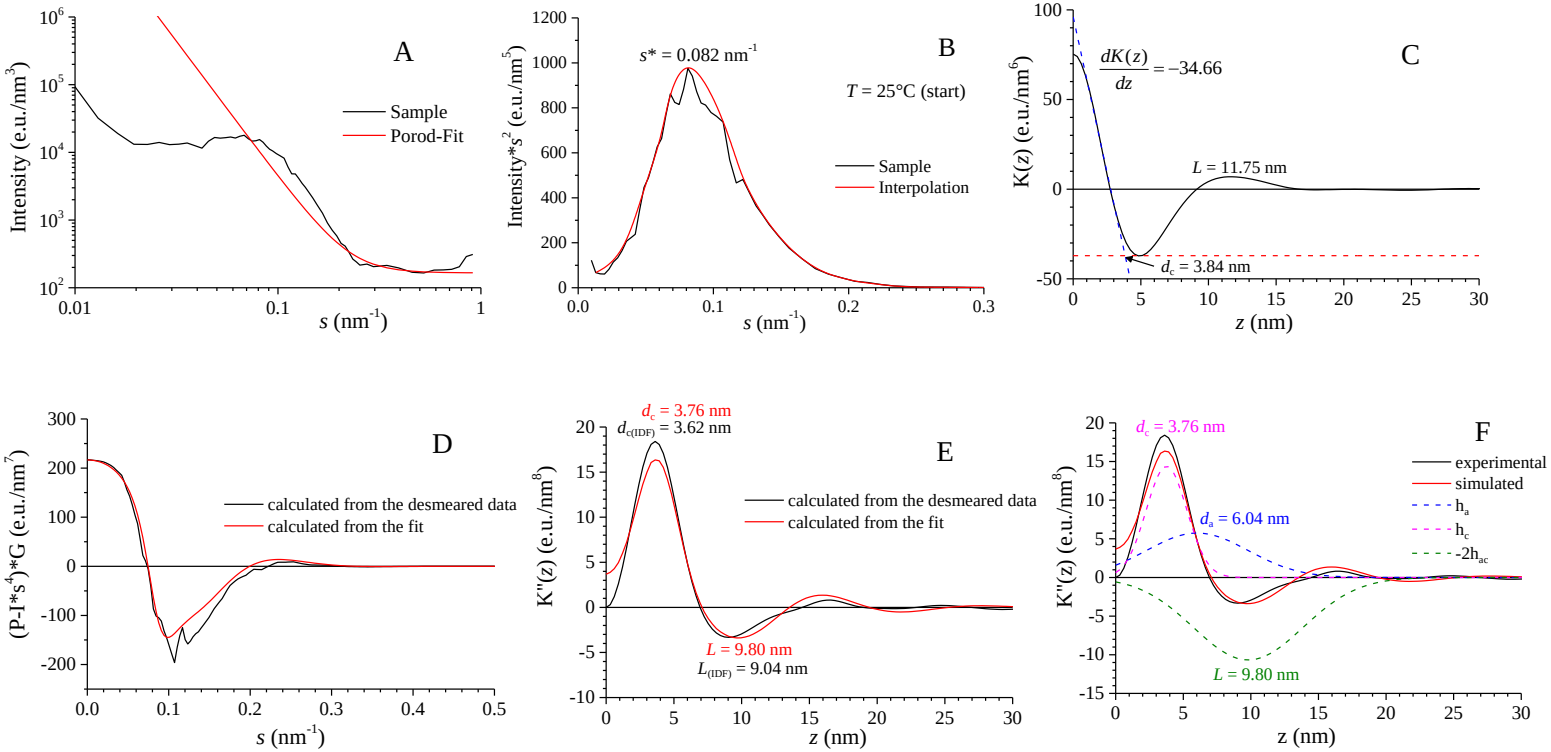

Figure 1.163. *A) SAXS intensity profiles of the aged compression molded film of the sample of sPPET copolymer RDG-2-42 with 2.4 mol% of ethylene recorded at room temperature. The red line represents the Porod fit and gives the sum of the Porod scattering and a background due to density fluctuations. B) Lorentz-corrected SAXS intensity profile. The red curve represents the interpolation of the experimental data to evaluate the position of the peak s*. C) Correlation function K(z). The slope of initial part of the function at the origin and the correlation triangle at the origin are shown. The values of L and d_c, evaluated from the position of the first maximum of K(z) and from the short side of the correlation triangle, respectively, are indicated. D) Function $16\pi^3[P\text{-}I_{abs}s^4]\omega$ as calculated from I(s) (black line). The red curve is the result of the simulation. E) Experimental IDF function calculated from I(s) (black line), and simulated IDF function (red curve). F) Experimental and simulated IDF (continuous curves) and single contributions of the distributions of thicknesses h_c, h_a and h_{ac} to the IDF (dashed curves).*

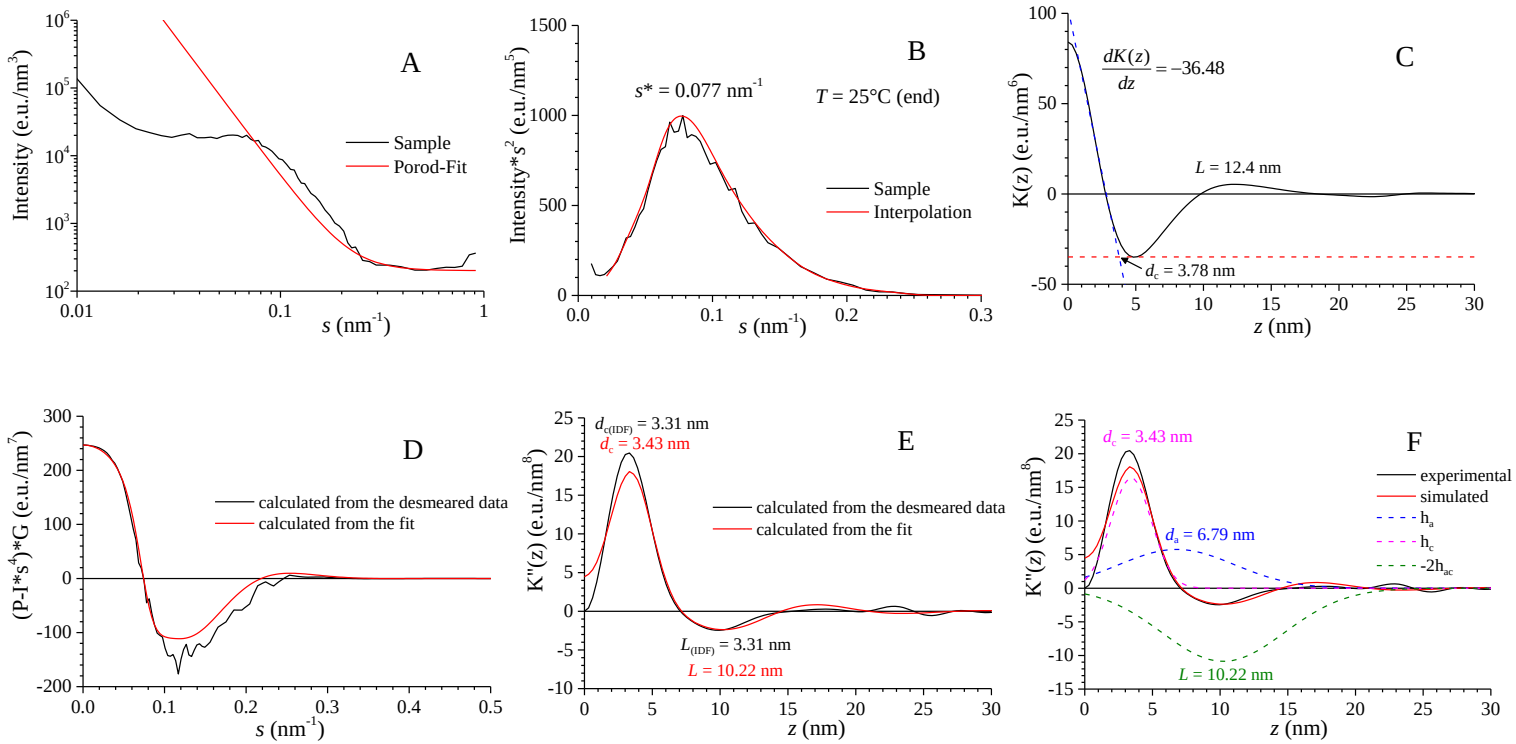

Figure 1.164. *A) SAXS intensity profiles of the as-prepared compression-molded film of the sample of sPPET copolymer RDG-2-42 with 2.4 mol% of ethylene recorded soon after the cooling from the melt at room temperature. The red line represents the Porod fit and gives the sum of the Porod scattering and a background due to density fluctuations. B) Lorentz-corrected SAXS intensity profile. The red curve represents the interpolation of the experimental data to evaluate the position of the peak s*. C) Correlation function K(z). The slope of initial part of the function at the origin and the correlation triangle at the origin are shown. The values of L and d_c, evaluated from the position of the first maximum of K(z) and from the short side of the correlation triangle, respectively, are indicated. D) Function $16\pi^3[P\text{-}I_{abs}s^4]\omega$ as calculated from I(s) (black line). The red curve is the result of the simulation. E) Experimental IDF function calculated from I(s) (black line), and simulated IDF function (red curve). F) Experimental and simulated IDF (continuous curves) and single contributions of the distributions of thicknesses h_c, h_a and h_{ac} to the IDF (dashed curves).*

For samples of sPPET copolymers with ethylene contents higher than 2.4 mol%, a less intense peak shifted to lower values *s* is observed in the SAXS profiles (Figures 1.165-1.174). Moreover the high intensity at low values of *s* (see Figures 1.165, 1.168, 1.171 and 1.174) hinders the SAXS analysis, in particular the evaluation of the correlation function and the modeling of the IDF, preventing the evaluation of the morphological parameters (see Figures 1.166A-F and 1.167A-F for the sample AK-sPPEt-10 with 8.3 mol% of ethylene). In fact, reasonable values of the thickness *d* and width of the distribution of the thicknesses σ have been obtained only for one of the two phases, while very low value of thickness *d* and high value of the distribution wodth σ have been obtained for the other phase, resulting in difficulty to distinguish d_c from d_a. The assumption that the crystalline contribution is characterized by the lowest value of the width of the distribution of the thicknesses σ leads to a very broad distribution of the thicknesses of the amorphous layers (Figures 1.166F and 1.167F). This could be consistent with the high comonomer content and the low degree of crystallinity of these samples. On the contrary, the assumption that the lower value of the thickness corresponds to d_a and, therefore, the value of *L* lower than in more crystalline samples appear contradictory, but could be explained with the presence of two different amorphous phases. The intra-lamellar amorphous phase consisting only of the amorphous layers alternating with crystalline layers in the model of Figure 1.146A is detected by the modeled IDF, but an extra-lamellar amorphous phase consisting of amorphous phase not organized in any morphological superstructure but only diffused in the matrix, may be also present. Nevertheless, the presence of a minimum at ≈ 9 - 10 nm in the experimental IDF evaluated from the experimental data (Figures 1.166E,F and 1.167 E,F, black curves) suggest that the system is more complex and cannot be treated as shown above for the sPP homopolymer and sPPET copolymers with lower ethylene concentrations.

The evaluation of the maximum in the Lorentz-corrected profiles is also difficult (Figures 1.166B and 1.167B for the sample AK-sPPEt-10 with 8.3 mol% of ethylene) because the maximum is not well-defined. A rough values of *s** and *L**, therefore, have been obtained by hypothesizing the presence of a correlation peak and building it with a Gaussian function centered at the value of *s** corresponding to the maximum of the supposed peak (Figures 1.166B and 1.167B).

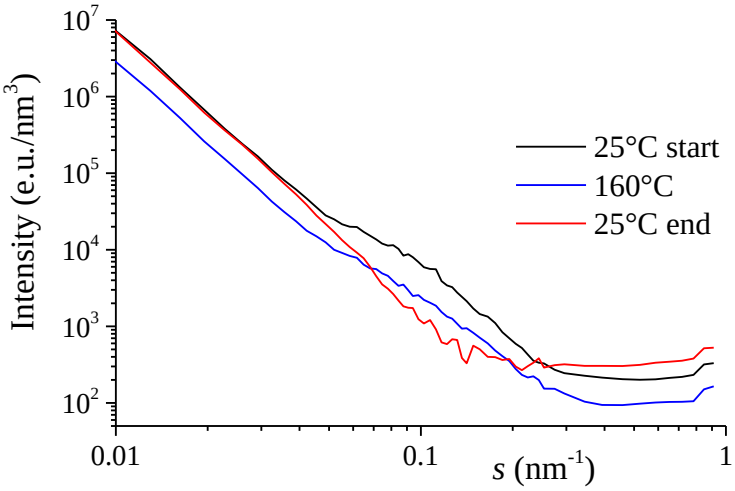

Figure 1.165.*SAXS intensity profiles of the sample of sPPET copolymer AK-sPPEt-10 with 8.3 mol% of ethylene recorded at room temperature for a compression-molded melt-crystallized film aged at room temperature (black curve), recorded after heating at 180 °C where the sample is melted (red curve) and soon after the successive cooling from the melt to room temperature allowing crystallization (blue curve).*

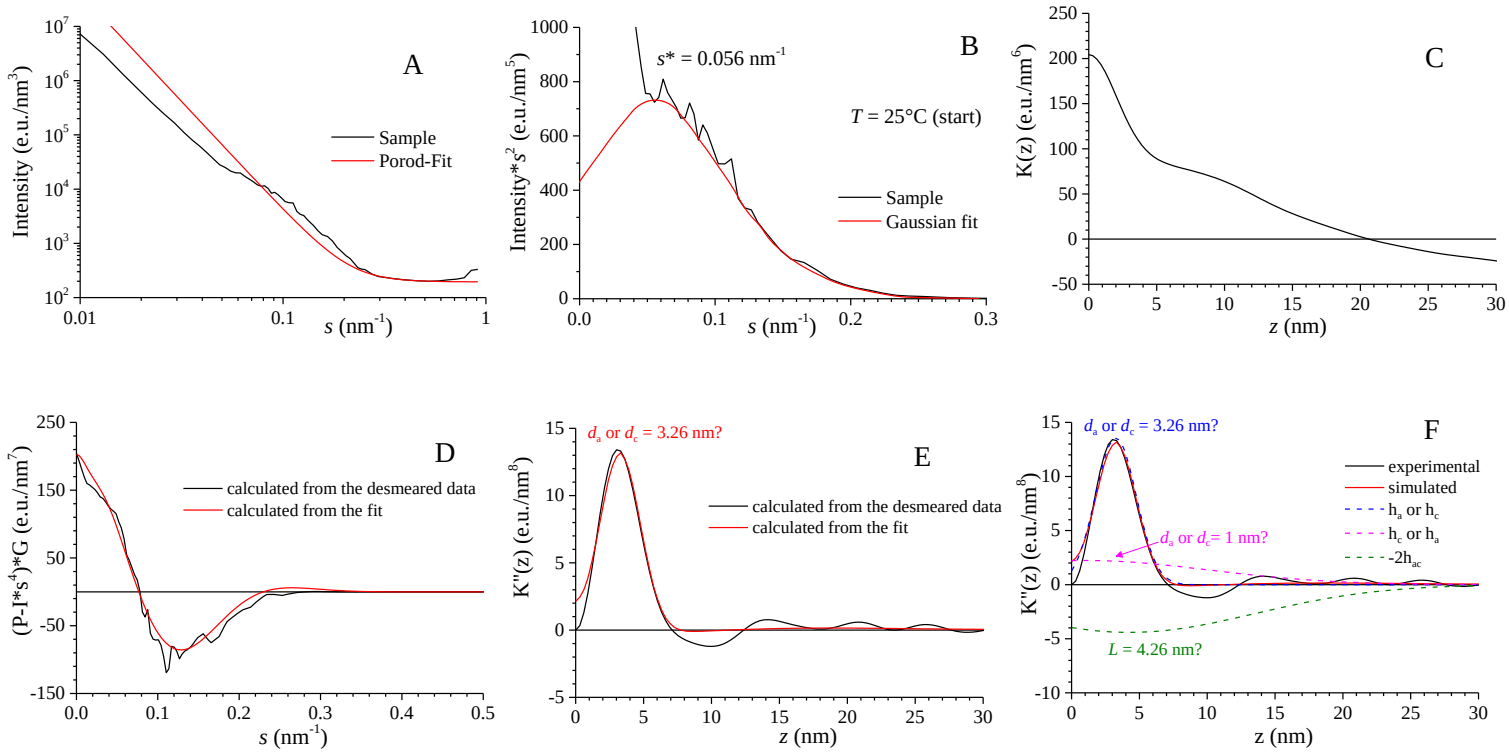

Figure 1.166. *A) SAXS intensity profiles of the aged compression molded film of the sample of sPPET copolymer AK-sPPEt-10 with 8.3 mol% of ethylene recorded at room temperature. The red line represents the Porod fit and gives the sum of the Porod scattering and a background due to density fluctuations. B) Lorentz-corrected SAXS intensity profile. The red curve represents the Gaussian function that simulates the correlation peak to evaluate the position of the peak s*. C) Correlation function K(z). D) Function $16\pi^3[P\text{-}I_{abs}s^4]\omega$ as calculated from I(s) (black line). The red curve is the result of the simulation. E) Experimental IDF function calculated from I(s) (black line), and simulated IDF function (red curve). F) Experimental and simulated IDF (continuous curves) and single contributions of the distributions of thicknesses h_c, h_a and h_{ac} to the IDF (dashed curves).*

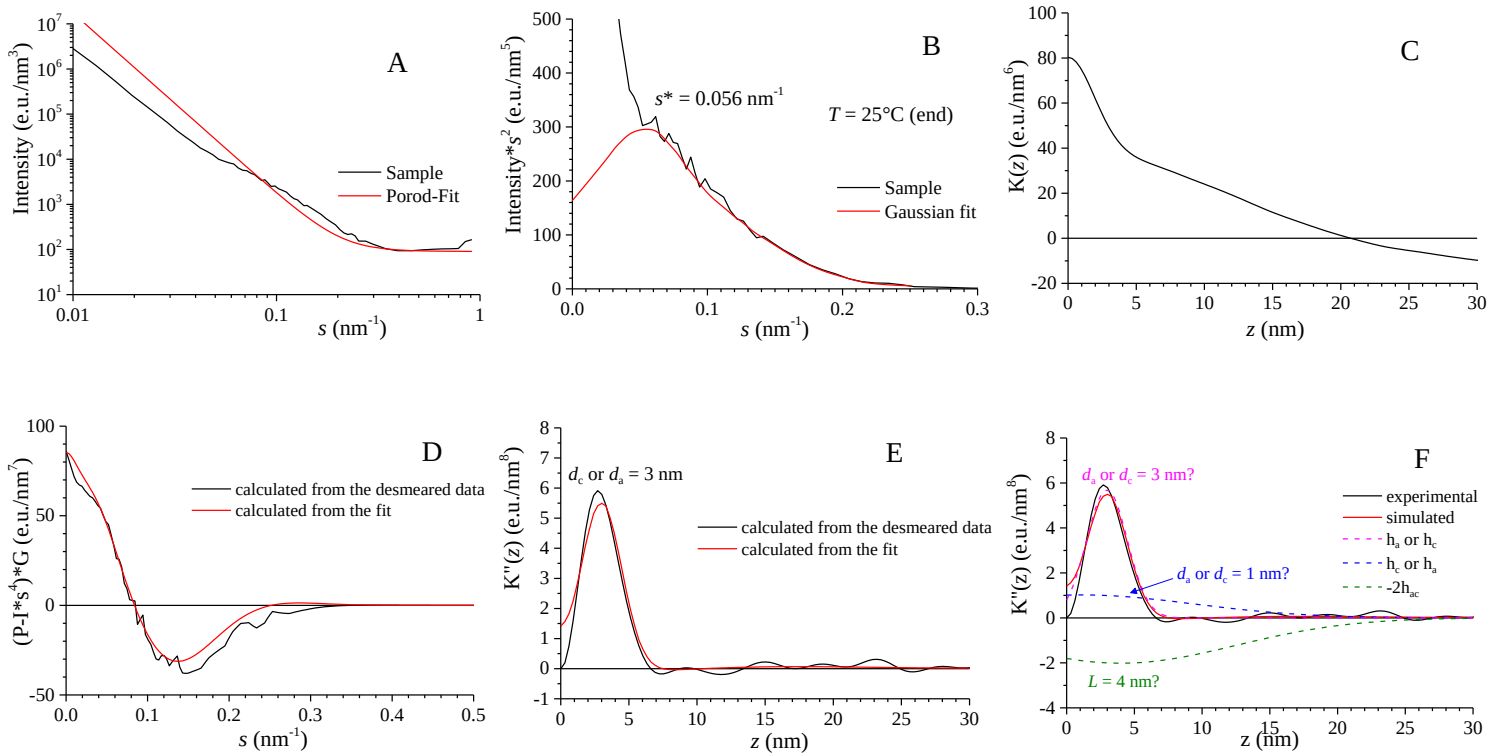

Figure 1.167. *A) SAXS intensity profiles of the as-prepared compression-molded film of the sample of sPPET copolymer AK-sPPEt-10 with 8.3 mol% of ethylene recorded soon after the cooling from the melt at room temperature. The red line represents the Porod fit and gives the sum of the Porod scattering and a background due to density fluctuations. B) Lorentz-corrected SAXS intensity profile. The red curve represents the Gaussian function that simulates the correlation peak to evaluate the position of the peak s*. C) Correlation function K(z). D) Function $16\pi^3[P\text{-}I_{abs}s^4]\omega$ as calculated from I(s) (black line). The red curve is the result of the simulation. E) Experimental IDF function calculated from I(s) (black line), and simulated IDF function (red curve). F) Experimental and simulated IDF (continuous curves) and single contributions of the distributions of thicknesses h_c, h_a and h_{ac} to the IDF (dashed curves).*

For these reasons, for the sPPET samples with high ethylene concentrations the original desmeared SAXS data have been treated before the processing with the program *correlation*_gui.[163].

The SAXS desmeared data $I_{obs}(s)$ have been extrapolated to $s = 0$ using the Debye−Bueche equation:[173]

$$I_{\mathrm{obs}}(s) = \frac{A}{\left(1 + B^2 s^2\right)^2} + c_2 \qquad (1.52)$$

where A and B are fitting parameters, while c_2 has been determined according with equation 1.47.

The use of the Debye-Bueche function at low values of s is justified by the fact that at distances $r >> L$ (and therefore $q << 2\pi q^*$) the X-ray scattering includes contributions from motifs (the lamellar stacks) characterized by correlation fading away with the distance r according with the exponential law $\exp(-r/\xi)$, where ξ is a correlation distance.[174] It has been demonstrated that the scattering intensity of these stacks has a dependence on s of the type indicated by the Equation 1.52.[174] Since the minimum experimental accessible value of s is 0.01 nm^{-1}, the precise determination of the correlation distance ξ would be affected by a too large error, so the parameters A and B of Equation 1.52 are treated as adjustable parameters which best reproduce the SAXS intensity in the region at values of s around s^* and slightly lower than s^*. The resulting Debye-Bueche functions that fit the experimental SAXS profiles at low values of s are shown in Figures 1.168A and B for the aged and as-crystallized samples of the copolymer AK-sPPEt-10 with 8.3 mol% of ethylene, along with the Porod finctions that fit the experimental profiles at high values of s.

The resulting corrected SAXS profile consists at low s of the Debye-Bueche profile that fits the experimental SAXS profile at values of s around s^* and slightly lower than s^*, the experimental profile at values of s around s^* and slightly higher than s^* and the Porod function the fits the experimental profile at high values of s. The SAXS profiles corrected for the Debye-Bueche function for the aged and the as-crystallized samples of the copolymer AK-sPPEt-10 with 8.3 mol% of ethylene are shown in Figures 1.169A and 1.170A. Starting from the these corrected Debye-Bueche SAXS profiles, the procedure for the calculations of the correlation function, the IDF and the simulated IDF has been repeated. The results for the the aged and the as-crystallized samples of the copolymer AK-sPPEt-10 with 8.3 mol% of ethylene are reported in Figures 1.169B-F and 1.170B-F.

It is apparent from Figures 1.169 and 1.170 and from the comparison with the data of Figures 1.166 and 1.167, obtained without the Debye-Bueche correction, that starting from the Debye-Bueche corrected SAXS profiles it has been possible to obtain reasonable and much better Lorentz corrected profiles (Figures 1.169B and 1.170B), correlation funtions $K(z)$ (Figures 1.169C and 1.170C) and experimental and simulated IDF (Figures 1.169E,F and 1.170E,F). In particular, correlation peak is more visible in the Lorentz corrected profiles (Figures 1.169C and 1.170C) from which the values of s^* and L^* have been evaluated. Moreover, a minimum and a broad maximum are now clearly present in the correlation function of both aged and as-crystallized samples (Figures 1.169C and 1.170C), from which it is possible to evaluate d_c and L, respectively, (and $d_a = L - d_c$). Finally, the experimental IDF presents a minimum, besides the clear broad maximum (Figures 1.169E and 1.170E), from which it has been possible to evaluated L and d_c, respectively, (and $d_a = L - d_c$), and the simulated IDF show the same features and more reasonable contributions of distributions of thicknesses (Figures 1.169F and 1.170F). All the parameters so obtained for the sample AK-sPPEt-10 with 8.3 mol% of ethylene, s^* and L^* (from the Lorentz corrected profiles), d_c(cofun), d_a(cofun) and L(cofun) (from the correlation function), d_c(IDF), d_a(IDF) and L(IDF) (from the experimental IDF), and d_c, d_a and L (from the simulated IDF) are reported in Table 1.21 and 1.22.

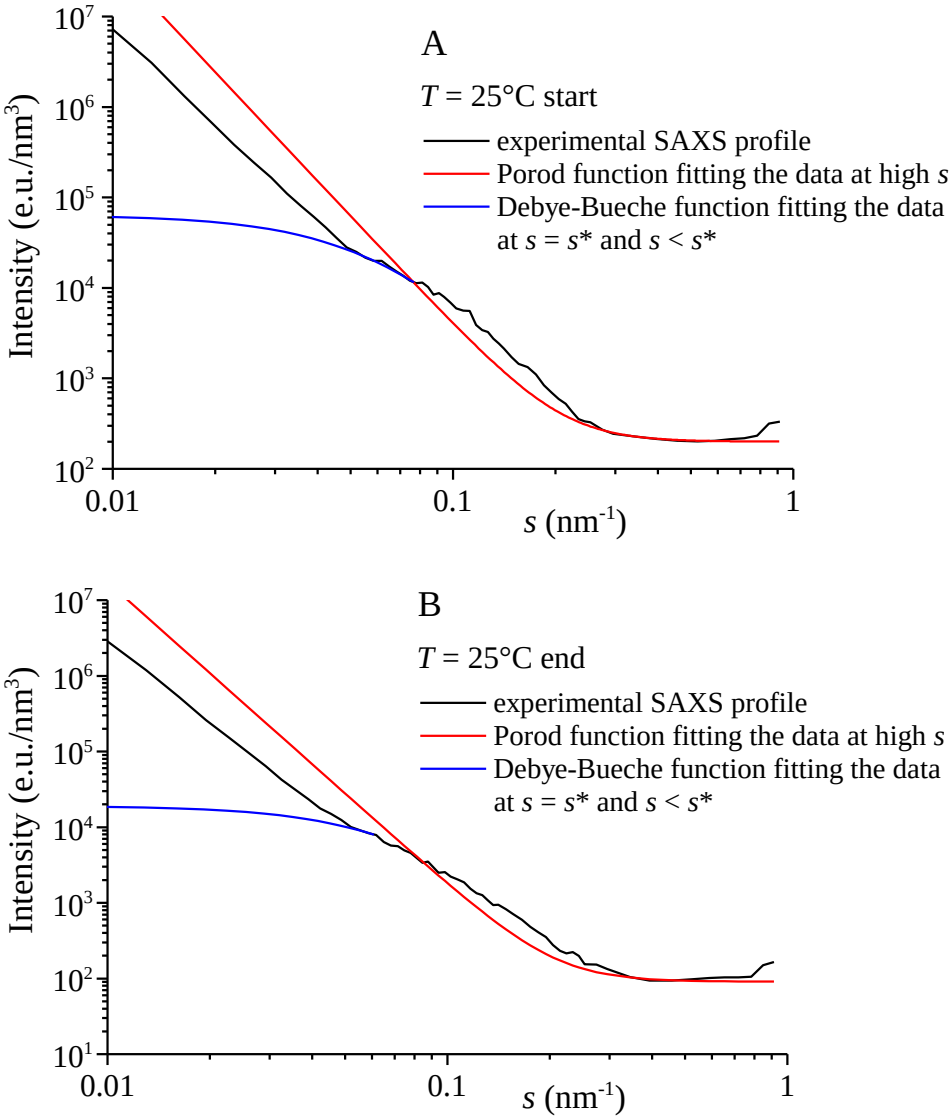

Figure 1.168. *Experimental SAXS intensity profiles (black curves) of the sample of sPPET copolymer AK-sPPEt-10 with 8.3 mol% of ethylene recorded at room temperature for a compression-molded melt-crystallized film aged at room temperature (A) and recorded after melting at 180 °C and successive cooling from the melt to room temperature allowing crystallization (B). The red line represents the Porod function that fits the experimental profiles at high values of s. The blue lines represent the Debye-Bueche function that fits the experimental profile at values s around the correlation peak s* and slightly lower than s*.*

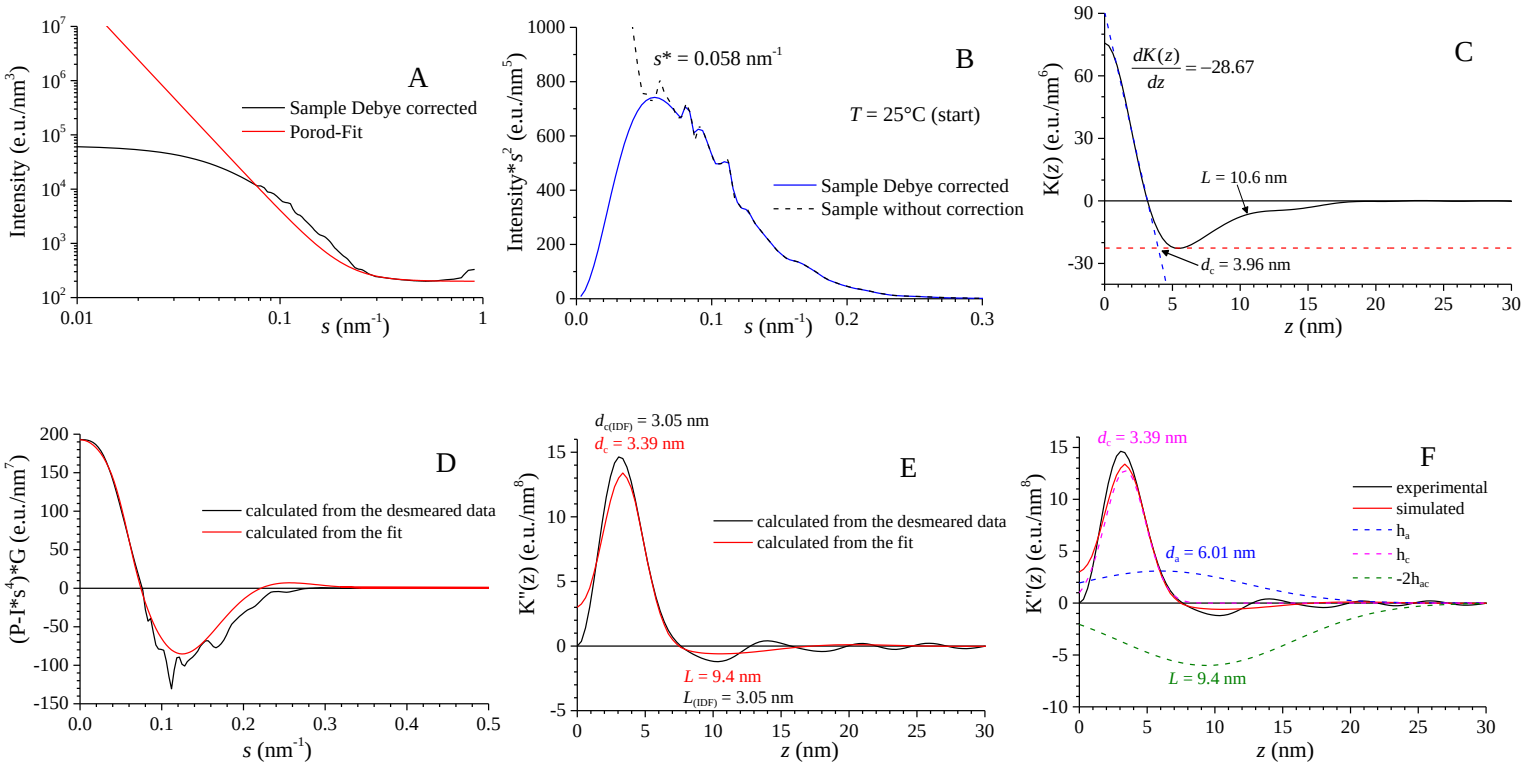

Figure 1.169. *A) SAXS intensity profiles of the aged compression molded film of the sample of sPPET copolymer AK-sPPEt-10 with 8.3 mol% of ethylene recorded at room temperature after correction for the Debye-Bueche function at low values of s (black curve). The red line represents the Porod fit and gives the sum of the Porod scattering and a background due to density fluctuations. B) Lorentz-corrected SAXS intensity profile. The black dashed curve represents the original Lorentz-corrected intensity profile, the blue curve represents the Lorentz-corrected profile after the Debye-Bueche correction. C) Correlation function K(z). The slope of K(z) at the origin and the values of L and d_c are indicated. D) Function $16\pi^3[P\text{-}I_{abs}s^4]\omega$ as calculated from I(s) (black line). The red curve is the result of the simulation. E) Experimental IDF function calculated from I(s) (black line), and simulated IDF function (red curve). F) Experimental and simulated IDF (continuous curves) and single contributions of the distributions of thicknesses h_c, h_a and h_{ac} to the IDF (dashed curves).*

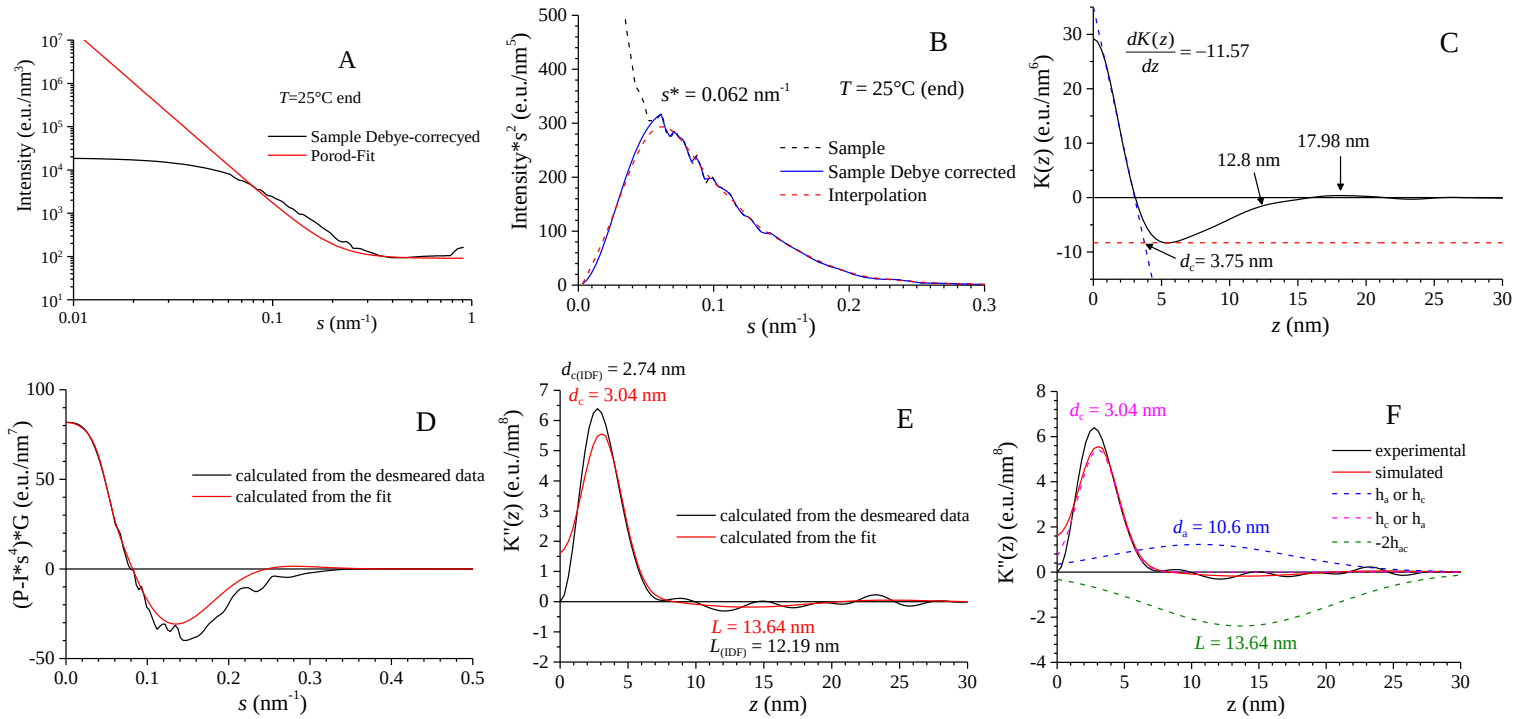

Figure 1.170. *A) SAXS intensity profiles of the as-prepared compression-molded film of the sample of sPPET copolymer AK-sPPEt-10 with 8.3 mol% of ethylene recorded soon after the cooling from the melt at room temperature, after correction for the Debye-Bueche function at low values of s (black curve). The red line represents the Porod fit and gives the sum of the Porod scattering and a background due to density fluctuations. B) Lorentz-corrected SAXS intensity profile. The black dashed curve represents the original Lorentz-corrected intensity profile, the blue curve represents the Lorentz-corrected profile after the Debye-Bueche correction and the red dashed curve represents the interpolation of the blue curve for a better evaluation of the position of the peak s*. C) Correlation function K(z). The slope of K(z) at the origin and the values of L and d_c are indicated. D) Function $16\pi^3[P-I_{abs}s^4]\omega$ as calculated from I(s) (black line). The red curve is the result of the simulation. E) Experimental IDF function calculated from I(s) (black line), and simulated IDF function (red curve). F) Experimental and simulated IDF (continuous curves) and single contributions of the distributions of thicknesses h_c, h_a and h_{ac} to the IDF (dashed curves).*

The sample AK-sPPEt-15 with 11.9 mol% of ethylene show a weak peak only in the SAXS profile of the aged compression molded film (Figure 1.171, black curve). The sample does not crystallize from the melt and no peaks are observed in the SAXS profile recorded soon after the cooling from the melt (Figure 1.171, blue curve). Therefore, the SAXS analysis and the modeling of the IDF have been performed only on the SAXS profile recorded at room temperature before melting (Figure 1.172). Even in this case the low intensity of the peak has prevented a correct evaluation of the morphological parameters (Figures 1.172A-F), therefore, a correction of the SAXS profile with the Debye-Bueche function at low values of *s* has been performed. The results are shown in Figures 1.173A-F. Also in this case the correction with the Debye-Bueche function produces an improvement of data with better correlation function and IDF that present clear minima and maxima, from which reasonable values of d_c, d_a and L have been determined (Table 1.21).

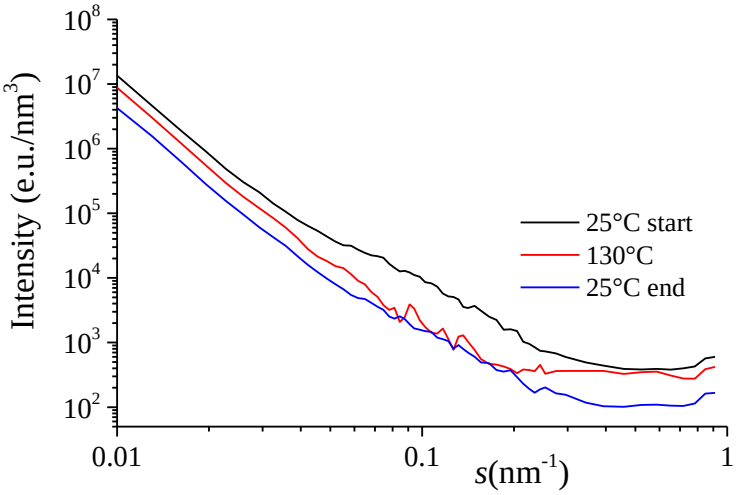

Figure 1.171. *SAXS intensity profiles of the sample of sPPET copolymer AK-sPPEt-15 with 11.9 mol% of ethylene recorded at room temperature for a compression-molded melt-crystallized film aged at room temperature (black curve), recorded after heating at 180 °C where the sample is melted (red curve) and soon after the successive cooling from the melt to room temperature (blue curve).*

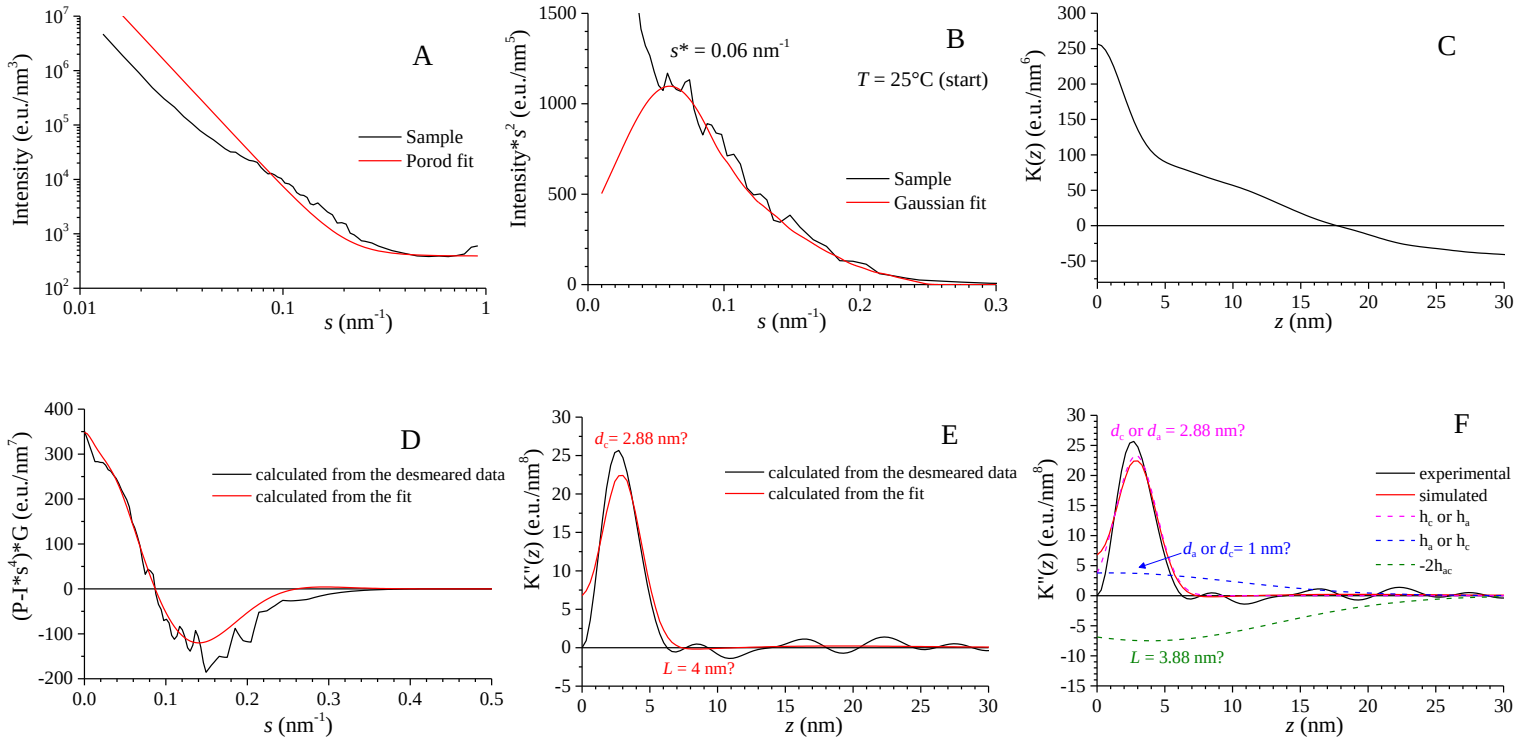

Figure 1.172. *A) SAXS intensity profiles of the aged compression molded film of the sample of sPPET copolymer AK-sPPEt-15 with 11.9 mol% of ethylene recorded at room temperature. The red line represents the Porod fit and gives the sum of the Porod scattering and a background due to density fluctuations. B) Lorentz-corrected SAXS intensity profile. The red curve represents the Gaussian function that simulates the correlation peak to evaluate the position of the peak s*. C) Correlation function K(z). D) Function $16\pi^3[P\text{-}I_{abs}s^4]\omega$ as calculated from I(s) (black line). The red curve is the result of the simulation. E) Experimental IDF function calculated from I(s) (black line), and simulated IDF function (red curve). F) Experimental and simulated IDF (continuous curves) and single contributions of the distributions of thicknesses h_c, h_a and h_{ac} to the IDF (dashed curves).*

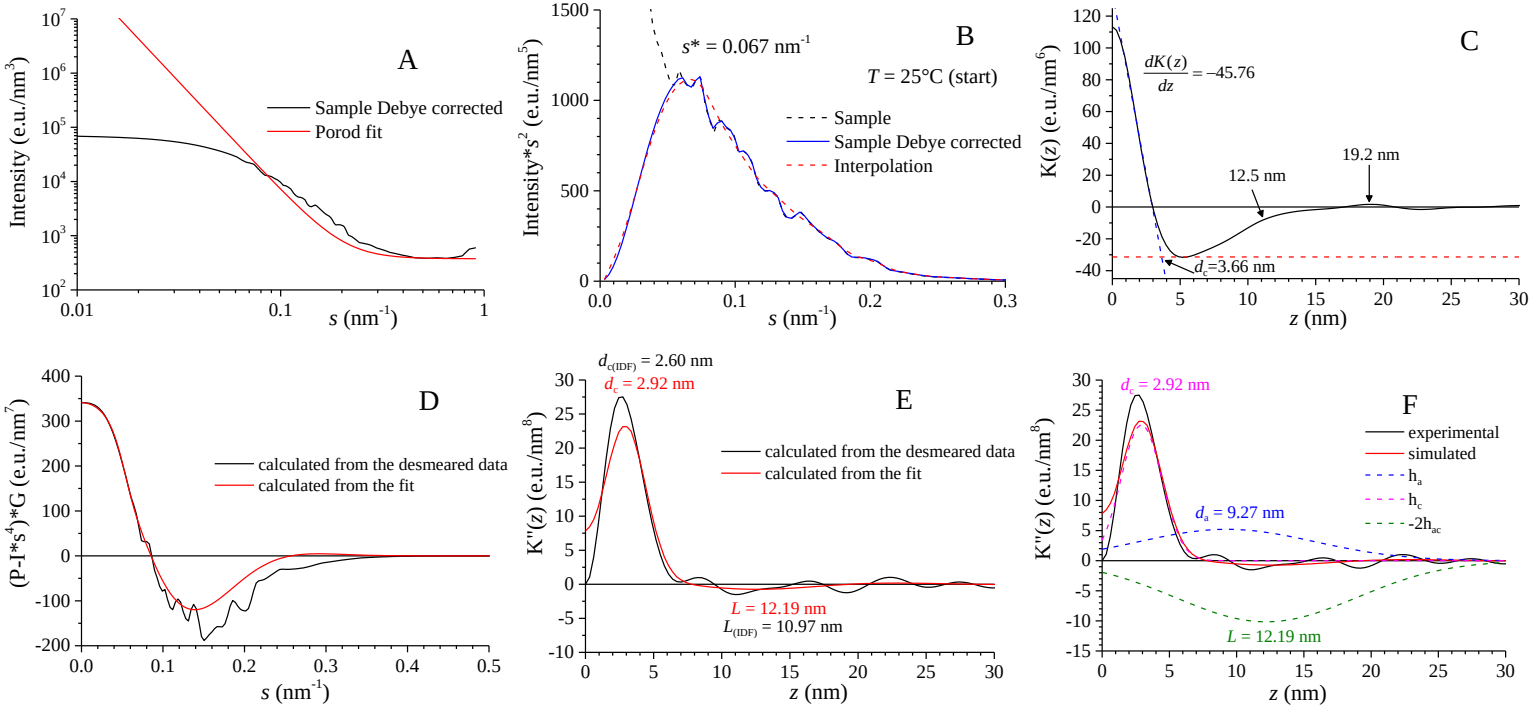

Figure 1.173. *A) SAXS intensity profiles of the as-prepared compression-molded film of the sample of sPPET copolymer AK-sPPEt-15 with 11.9 mol% of ethylene recorded soon after the cooling from the melt at room temperature, after correction for the Debye-Bueche function at low values of s (black curve). The red line represents the Porod fit and gives the sum of the Porod scattering and a background due to density fluctuations. B) Lorentz-corrected SAXS intensity profile. The black dashed curve represents the original Lorentz-corrected intensity profile, the blue curve represents the Lorentz-corrected profile after the Debye-Bueche correction and the red dashed curve represents the interpolation of the blue curve for a better evaluation of the position of the peak s*. C) Correlation function K(z). The slope of K(z) at the origin and the values of L and d_c are indicated. D) Function $16\pi^3[P\text{-}I_{abs}s^4]\omega$ as calculated from I(s) (black line). The red curve is the result of the simulation. E) Experimental IDF function calculated from I(s) (black line), and simulated IDF function (red curve). F) Experimental and simulated IDF (continuous curves) and single contributions of the distributions of thicknesses h_c, h_a and h_{ac} to the IDF (dashed curves).*

The sample AK-sPPEt-25 does not crystallize from the melt and remains completely amorphous even after long aging time (Figure 1.131A,B curves h) because of the high ethylene content. For this reason no peaks in both SAXS profiles collected before and after the melting are observed (Figure 1.174) and therefore SAXS analysis has not been performed on this sample.

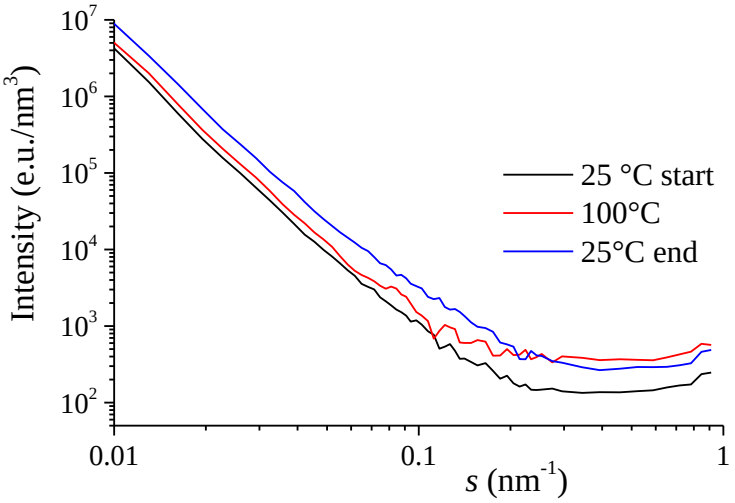

Figure 1.174. *SAXS intensity profiles of the sample of sPPET copolymer AK-sPPEt-25 with 27.5 mol% of ethylene recorded at room temperature for a compression-molded melt-crystallized film aged at room temperature (black curve), recorded after heating at 180 °C where the sample is melted (red curve) and soon after the successive cooling from the melt to room temperature (blue curve).*

Table 1.21. *Values of the degree of crystallinity x_c and morphological parameters evaluated from the analysis of the SAXS profiles recorded at room temperature of compression-molded melt-crystallized film aged at room temperature of samples of the sPP homopolymer sRDG-2-1 and sPPET copolymers of the indicated ethylene concentration (defects content). The values of the Porod costant (P), scattering vector corresponding to the maximum of the Lorentz-corrected profiles (s*), Long period (L), thickness of the crystalline lamellae (d_c) and of the amorphous layers (d_a) evaluated from the Lorentz-corrected profiles (L*), from the correlation functions K(z) (L(cofun), d_c(cofun) and d_a(cofun)), from the experimental IDF (L(IDF), d_c(IDF) and d_a(IDF)) and from the simulated IDF (L, d_c and d_a), slope of the first part of K(z) at the origin (dK/dz) and electron density difference ($\Delta\rho$) are reported. The widths of the distributions of thicknesses of crystalline lamellae (σ_c), thicknesses of amorphous phase (σ_a) evaluated from the simulated IDF are also reported.*

Sample	Defects content (mol%)	x_c (%)[a]	P (e.u./nm^7)	s^* (nm^{-1})	L^* (nm)	L (IDF) (nm)	d_c (IDF) (nm)	d_a (IDF) (nm)	d_c (nm)	σ_c (nm)	d_a (nm)	σ_a (nm)	L (nm)	L (cofun) (nm)	d_c (cofun) (nm)	d_a (cofun) (nm)	dK/dz	$\Delta\rho$
sRDG-2-1	0.7	45	0.876	0.078	12.82	10.25	4.52	5.73	4.59	0.64	6.39	3.56	10.98	12.05	4.40	7.65	-76	29
RDG-2-41	0.4	41	0.260	0.075	13.33	10.55	3.92	6.63	3.98	0.50	6.62	3.91	10.60	11.75	4.11	7.64	-21.85	15
RDG-2-40	1.7	40	0.433	0.081	12.35	9.34	3.62	5.72	3.76	0.50	6.33	3.40	10.09	11.45	3.84	7.61	-34.60	19
AK-sPPEt-2	1.9	40	0.551	0.084	11.90	9.34	3.31	6.03	3.90	0.50	6.19	3.32	10.09	11.45	3.90	7.55	-44.74	21
RDG-2-42	2.4	39	0.437	0.082	12.19	9.04	3.62	5.42	3.76	0.50	6.04	3.48	9.8	11.75	3.84	7.91	-34.66	18
AK-sPPEt-10	8.3	29	0.389	0.058	17.24	10.36	3.05	7.31	3.39	0.50	6.01	6.06	9.4	10.6	3.96	6.64	-28.67	16
AK-sPPEt-15	11.9	25	0.688	0.067	14.92	10.97	2.60	8.37	2.92	0.50	9.27	6.38	12.19	12.5	3.66	8.84	-45.76	24

[a]) evaluated from WAXS profiles

Table 1.22. *Values of the degree of crystallinity x_c and morphological parameters evaluated from the analysis of the SAXS profiles recorded at room temperature of as-prepared compression-molded melt-crystallized film of samples of the sPP homopolymer sRDG-2-1 and sPPET copolymers of the indicated ethylene concentration (defects content). The values of the Porod costant (P), scattering vector corresponding to the maximum of the Lorentz-corrected profiles (s*), Long period (L), thickness of the crystalline lamellae (d_c) and of the amorphous layers (d_a) evaluated from the Lorentz-corrected profiles (L*), from the correlation functions K(z) (L(cofun), d_c(cofun) and d_a(cofun)), from the experimental IDF (L(IDF), d_c(IDF) and d_a(IDF)) and from the simulated IDF (L, d_c and d_a), slope of the first part of K(z) at the origin (dK/dz) and electron density difference ($\Delta\rho$) are reported. The widths of the distributions of thicknesses of crystalline lamellae (σ_c), thicknesses of amorphous phase (σ_a) evaluated from the simulated IDF are also reported.*

Sample	Defects content (mol%)	x_c (%)[a]	P (e.u./nm^7)	s^* (nm^{-1})	L^* (nm)	L (IDF) (nm)	d_c (IDF) (nm)	d_a (IDF) (nm)	d_c (nm)	σ_c (nm)	d_a (nm)	σ_a (nm)	L (nm)	L (cofun) (nm)	d_c (cofun) (nm)	d_a (cofun) (nm)	dK/dz	$\Delta\rho$
sRDG-2-1	0.7	45	0.368	0.082	12.19	10.25	3.49	6.76	3.62	0.50	6.58	3.62	10.22	11.70	3.78	7.92	-27.74	17
RDG-2-41	0.4	41	0.474	0.085	11.76	10.85	3.01	7.84	3.28	0.50	6.30	3.66	9.58	11.75	3.60	8.15	-33.85	18
RDG-2-40	1.7	40	0.490	0.079	12.66	10.85	3.31	7.54	3.40	0.50	6.24	3.68	9.64	11.75	3.60	8.15	-37.07	19
AK-sPPEt-2	1.9	40	0.326	0.080	12.50	9.64	3.16	6.48	3.38	0.50	6.44	3.81	9.82	11.45	3.66	7.79	-23.79	15
RDG-2-42	2.4	39	0.498	0.077	12.99	9.94	3.31	6.63	3.43	0.50	6.79	4.03	10.22	12.40	3.78	8.62	-36.48	19
AK-sPPEt-10	8.3	29	0.165	0.062	16.13	12.19	2.74	9.45	3.04	0.50	10.60	6.52	13.64	12.80	3.75	9.05	-11.57	13
AK-sPPEt-15	11.9	25	/	/	/				/	/	/	/	/	/	/	/	/	/

[a]) evaluated from WAXS profiles

Tables 1.21 and 1.22 report the morphological parameters of all analyzed samples. For samples AK-sPPEt-10 and AK-sPPEt-15 only the parameters calculated on the SAXS profiles corrected with the Debye-Bueche function are reported. The values of the long period, the thickness of the crystalline lamellae and of the amorphous layers, evaluated from all the Lorentz corrected profiles, the correlation functions and the experimental and simulated IDF are reported in Figures 1.175-1.177 as a function of ethylene content. The values of the long period evaluated from the experimental and simulated IDF and from the correlation function are very similar in both aged and as-crystallized samples. In particular, they show the same behavior with increasing ethylene content. In fact, for aged samples, starting from the homopolymer, a slight decrease of long period is observed with increasing ethylene concentration up to 8.3 mol% (Figures 1.175A, 1.177A,A' and Table 1.21). With further increase of ethylene concentration a strong increase of the long period is observed (for the sample AK-sPPEt-15, 11.9 mol% of ethylene) (Figures 1.175A and 1.177A,A'). A similar trend is visible in the as-prepared melt-crystallized samples (Table 1.22 and Figure 1.176A): after some oscillations around an average constant value, an increase of the long period is observed when the comonomer content is higher than 2 mol% (Figures 1.176A and 1.177B,B', Table 1.22).

The values of the long period evaluated from the maximum of the Lorentz corrected SAXS profiles are higher than those evaluated from $K(z)$ and IDF and show a less regular trend with increasing ethylene content (Figures 1.175A, 1.176A). Because of the difficulty in the determination of s^* in less crystalline samples, these values are less reliable.

The thickness of crystalline lamellae d_c of sPPET copolymers is, as expected, lower than that of the homopolymer. It slightly decreases with increasing ethylene content in the melt-crystallized and aged samples (Figures 1.175B and 1.177A,A'), whereas it seems nearly constant for the as-crystallized samples (Figures 1.176B and 1.177B,B'), in particular when evaluated from the correlation function (Figure 1.177B'). As a consequence, the thickness of the amorphous layers d_a show changes with the ethylene concentration similar as that of the long period: for aged samples d_a slight decreases with increasing ethylene concentration up to 8.3 mol% of ethylene and then increases for higher ethylene concentration (Figures 1.175B and 1.177A,A', Table 1.21). For the as-prepared melt-crystallized samples (Table 1.22), the amorphous thickness is nearly constant for low ethylene concentrations and then increases for ethylene content higher than 2 mol% (Figures 1.176B and 1.177B,B', Table 1.22).

The comparison between Figures 1.177A and 1.177B and between Figures 1.177A' and 1.177B' shows, as already mentioned before, that aged samples have values of all morphological parameters higher than those of as-prepared melt-crystallized samples, probably because of the occurrence of secondary crystallization during aging. A comparison between Figures 1.177A and 1.177A'and between Figures 1.177B and 1.177B', instead, shows again that the morphological parameters evaluated from the correlation function are similar to those evaluated from the simulated and experimental IDF.

Even though some slight differences in the trends of L, d_c and d_a with the ethylene concentration have been observed for aged and as-crystallized samples, a clear obtained result is that at low ethylene concentration, up to 8 mol% for the aged samples and 2-3 mol% for the as-crystallized samples, the thickness of crystalline lamellae decreases with increasing ethylene concentration, while the thickness of the amorphous layers does not increase but, even, decrease (or it is nearly constant) with the increase of ethylene content (Figure 1.177A,A' and B). Correspondingly, the long period also decreases (Figure 1.177A,A') or it is nearly constant (Figure 1.177B,B') with increasing ethylene content. Only at high ethylene concentration (higher than to 8 mol% for the aged samples and higher than 2-3 mol% for the as-crystallized samples) a clear increase of the amorphous thickness and of long period occurs (Figure 1.177). The decrease of crystalline thickness is in agreement with the decrease of crystallinity with increasing ethylene concentration due to the presence of ethylene defects and increasing disorder in the crystalline phase. Moreover, it is worth recalling that ethylene units are only partially included into the crystals of sPP and an appreciable amount of ethylene units is also included in the noncrystalline phase of the copolymers.[142b] Therefore, most of the constitutional defects could be segregated in the extra-lamellar amorphous phase consisting of amorphous phase not organized in the lamellar stacks, and therefore, not visible by the modeling of the SAXS data. This could explain the result that, even though the fraction of the total amorphous phase, as evaluated by WAXS profiles, clearly increases with increasing ethylene content, the thickness of the amorphous layer in the model of lamellar stacks decreases. Only at high ethylene content also the fraction of amorphous phase in between the crystalline lamellae (in the lamellar stacks) increases, with corresponding increase of amorphous thickness and long period.

This result is in agreement with the results of the study of morphology of stereodefective sPP samples (Figures 1.32-1.36) and of copolymers of sPP with

ethylene (Figures 1.38-1.40) and other comonomers (Figures 1.56 and 1.57) by POM, that have revealed an interwoven morphology formed by bundle-like and needle-like crystals aggregates embedded in an amorphous matrix. In this morphology that explains the elastic properties of these materials even at high defects (stereodefects or comonomeric units) concentrations, the fraction of amorphous phase in the stacks of these thin crystals is necessarily lower than that of the matrix.

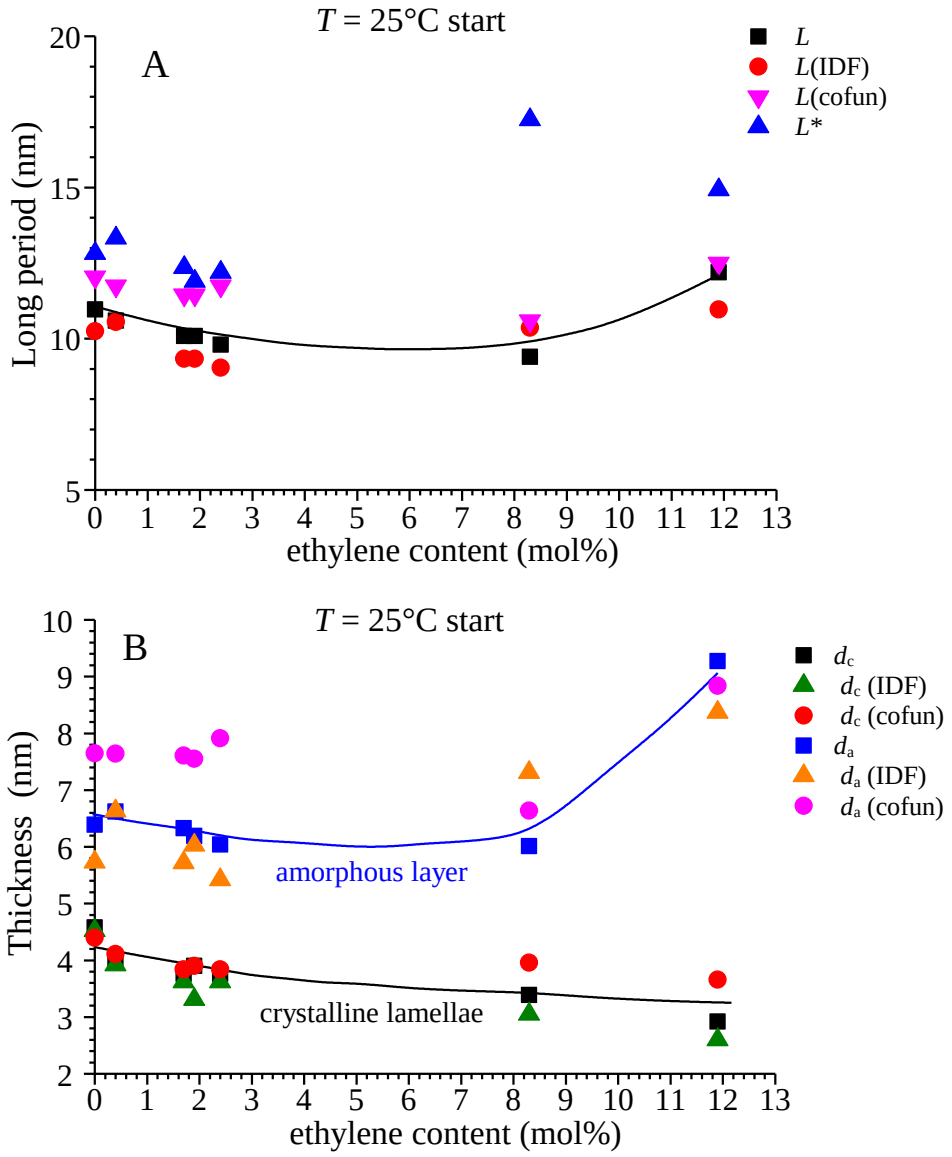

Figure 1.175. *A) Average values of the long period L (■) evaluated from the simulated IDF, L(IDF) (●) evaluated from the experimental IDF, L(cofun) (▼) evaluated from the correlation function, L* (▲) evaluated from the maximum s* of the Lorentz-corrected SAXS profile of the aged compression-molded samples of sPPET copolymers as a function of ethylene concentration. B) Average values of the of thickness of crystalline lamellae d_c (■), d_c (IDF) (▲), and d_c(cofun) (●), and amorphous layers d_a (■), d_a(IDF) (▲) and d_a(cofun) (●), evaluated from the simulated IDF (d_c, d_a), from the experimental IDF (d_c (IDF), d_a (IDF)) and from the correlation function (d_c(cofun), d_a(cofun)) of the aged samples of sPPET copolymers as a function of ethylene concentration (B). The morphological parameters of the homopolymer sRDG-2-1 (ethylene content =0) are also reported as a reference.*

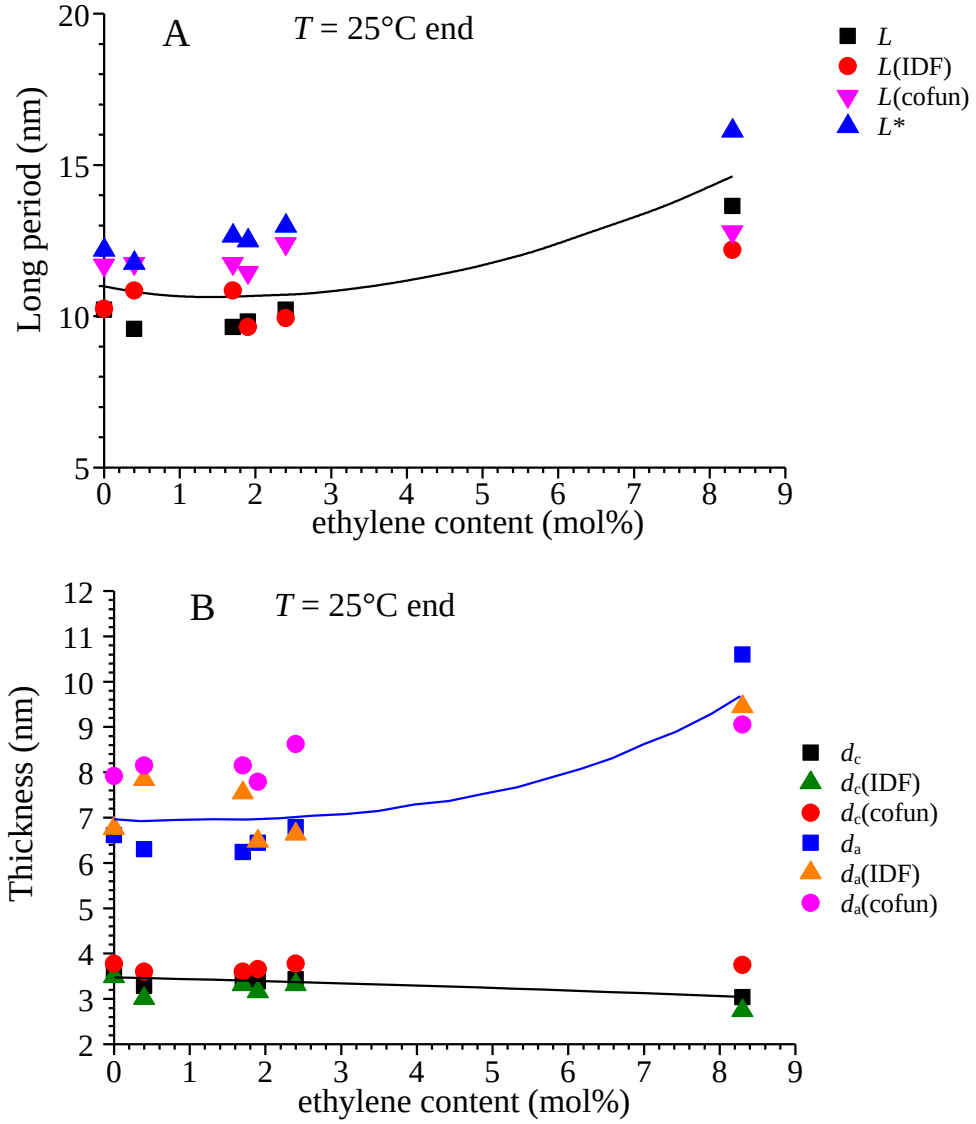

Figure 1.176. *A) Average values of the long period L (■) evaluated from the simulated IDF, L(IDF) (●) evaluated from the experimental IDF, L(cofun) (▼) evaluated from the correlation function, L* (▲) evaluated from the maximum s* of the Lorentz-corrected SAXS profile of the as-prepared melt-crystallized samples of sPPET copolymers as a function of ethylene concentration. B) Average values of the of thickness of crystalline lamellae d_c (■), d_c(IDF) (▲), and d_c(cofun) (●), and amorphous layer d_a (■), d_a(IDF) (▲) and d_a(cofun) (●), evaluated from the simulated IDF (d_c, d_a),* from the experimental IDF (*d_c(IDF), d_a(IDF)*) *and from the correlation function (d_c(cofun), d_a(cofun)) of the as-prepared melt-crystallized samples of sPPET copolymers as a function of ethylene concentration (B). The morphological parameters of the homopolymer sRDG-2-1 (ethylene content =0) are also reported as a reference.*

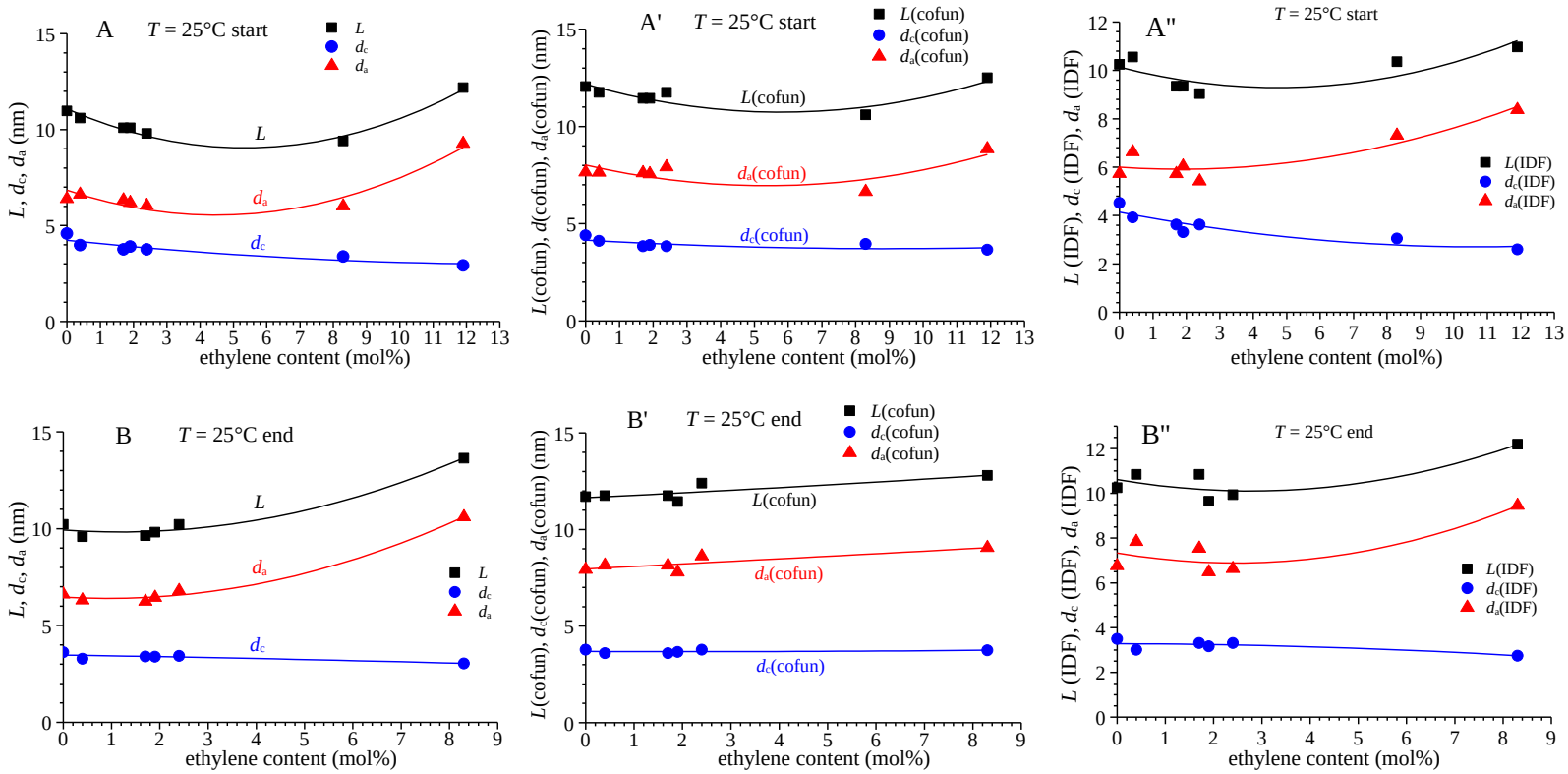

Figure 1.177. *Average values of the long period L (■), thickness of crystalline lamellae d_c (●), thickness of amorphous layers d_a (▲) evaluated from the simulated IDF (A,B), from the correlation function (A',B') and from the experimental IDF (A'',B'') of the aged compression-molded (A,A') and as-prepared melt-crystallized (B,B') samples of sPPET copolymers as a function of ethylene concentration.*

..

1.9.5. SAXS analysis on sPPBu random copolymers.

SAXS measurements have also been performed on the same samples of random copolymers of sPP with 1-butene already analyzed with AFM and POM, according with the procedure presented in section 1.5. For each sample the SAXS profiles of compression-molded samples aged at room temperature recorded 25 °C, at 180 °C in the melt and after cooling from the melt are reported. Then, the SAXS analysis with the modeling of the IDF on SAXS data at room temperature before and after melting is shown in Figures 1.178-1.197. The corresponding WAXS profiles, collected in separated experiments on compression molded films soon after the cooling from the melt and after aging at room temperature are reported in Figures 1.132A and B, respectively. The values of the degree of crystallinity evaluated form the diffraction profiles of Figures 1.132 are reported in Tables 1.21 and 1.22. Values of crystallinity approximately around 50% have been obtained for the sample of the sPPBu copolymer with 3.2 mol% of 1-butene. For this sample the analysis of the SAXS data and of the simulated IDF suffers of the same ambiguity to distinguish d_c from d_a, as in the case of the sPP homopolymer and sPPEt copolymers. Then, the crystallinity generally decreases with increasing butene content in both aged and melt-crystallized samples and it is always lower than 50%. Samples with butene content higher than 30 mol% do not crystallize from the melt but crystallize upon aging at room temperature. No significant increase of crystallinity has been observed upon aging in samples with low butene content. For aged compression-molded samples a small decrease of the crystallinity is observed with increasing butene concentrations up to a minimum of 30% observed in sample with 18.2 mol% of 1-butene and then a slight increase is observed in samples with butene content higher than 60 mol%, because of the crystallization of the form I of sPB. (Tables 1.23 and 1.24).

Because of the low amount of samples available, the SAXS profiles of the first two samples with 3.2 mol% and 6.3 mol% of butene have been collected on compression-molded samples using a SAXSLAB's GANESHA Instrument. This instrument presents several advantages with respect to the Kratky camera. The first one is the low amount of samples required. Then, the point collimation avoids the desmearing procedure at the end of the measurement. Finally, the high intensity of the source and the sensitivity of the detector allow obtaining SAXS 2D patterns and the corresponding 1D profile with high resolution in less time. Moreover, it is also possible to measure in different configurations such as ESAXS, SAXS, MAXS and WAXS. These SAXS data have been collected in

the q range of 0.007-0.25 Å with a distance sample-detector of 1050 mm. On the other hand, the intensity in arbitrary units introduces some difficulties in the SAXS analysis with the program *correlation_gui*. The 2D SAXS patterns recorded on the aged samples with 3.2 mol% and 6.3 mol% of butene at room temperature, in the melt and after cooling from the melt, and the corresponding SAXS profiles are shown in Figures 1.178 and 1.181. A well-defined peak is visible in the SAXS profiles of the aged samples recorded before melting (black curves in Figures 1.178D and 1.181D). Since all samples with low butene concentrations crystallize from the melt (Figure 1.132A), the SAXS peak reappears after the cooling from the melt (blue curves in Figures 1.178D and 1.181D). In particular, the sample sPPBu-1 with 3.2 mol% of 1-butene exhibits a more intense peak after the cooling from the melt.

For the modeling of the SAXS profiles and the calculation of the simulated IDF with the procedure described for the sPP homopolymer, the scattering vector q ($Å^{-1}$) is transformed in s (nm^{-1}). Then, because of the limited explored SAXS range, the tail of the SAXS profiles is not long enough for a correct evaluation of the Porod range. Therefore an additional WAXS measurement has been performed and the first data points (until s = 0.90 nm^{-1}) of the WAXS profiles have been patched to the tail of the SAXS profiles. Two examples of the resulting profiles are shown in Figures 1.178E and 1.181E.

The Lorentz corrected SAXS profiles, the correlation functions $K(z)$ and the experimental and simulated IDF of the two sPPBu samples with 1-butene concentrations of 2.3 and 6.3 mol% are shown in the Figures 1.179, 1.180, 1.182 and 1.183. The values of the morphological parameters evaluated from the Lorentz corrected SAXS profiles (s* and L*), the correlation functions $K(z)$ (d_c(cofun), d_a(cofun) and L(cofun)), the experimental IDF (d_c(IDF), d_a(IDF) and L(IDF)), and the simulated IDF (d_c, d_a and L), are reported in Tables 1.23 and 1.24 for the aged compression-molded samples and for the samples as-crystallized from the melt by cooling from the melt to room temperature, respectively. Since these SAXS profiles have been collected in arbitrary units, the evaluated Porod constant has no meaning. Similarly, the slope of the first part of the correlation function at the origin was not evaluated.

Unlike the homopolymer sRDG-2-1 and the sPPEt copolymers, all morphological parameters evaluated from the SAXS profiles of the melt-crystallized samples sPPBu1 and sPPBu-2 are higher than those evaluated from the SAXS profiles of the corresponding aged samples.

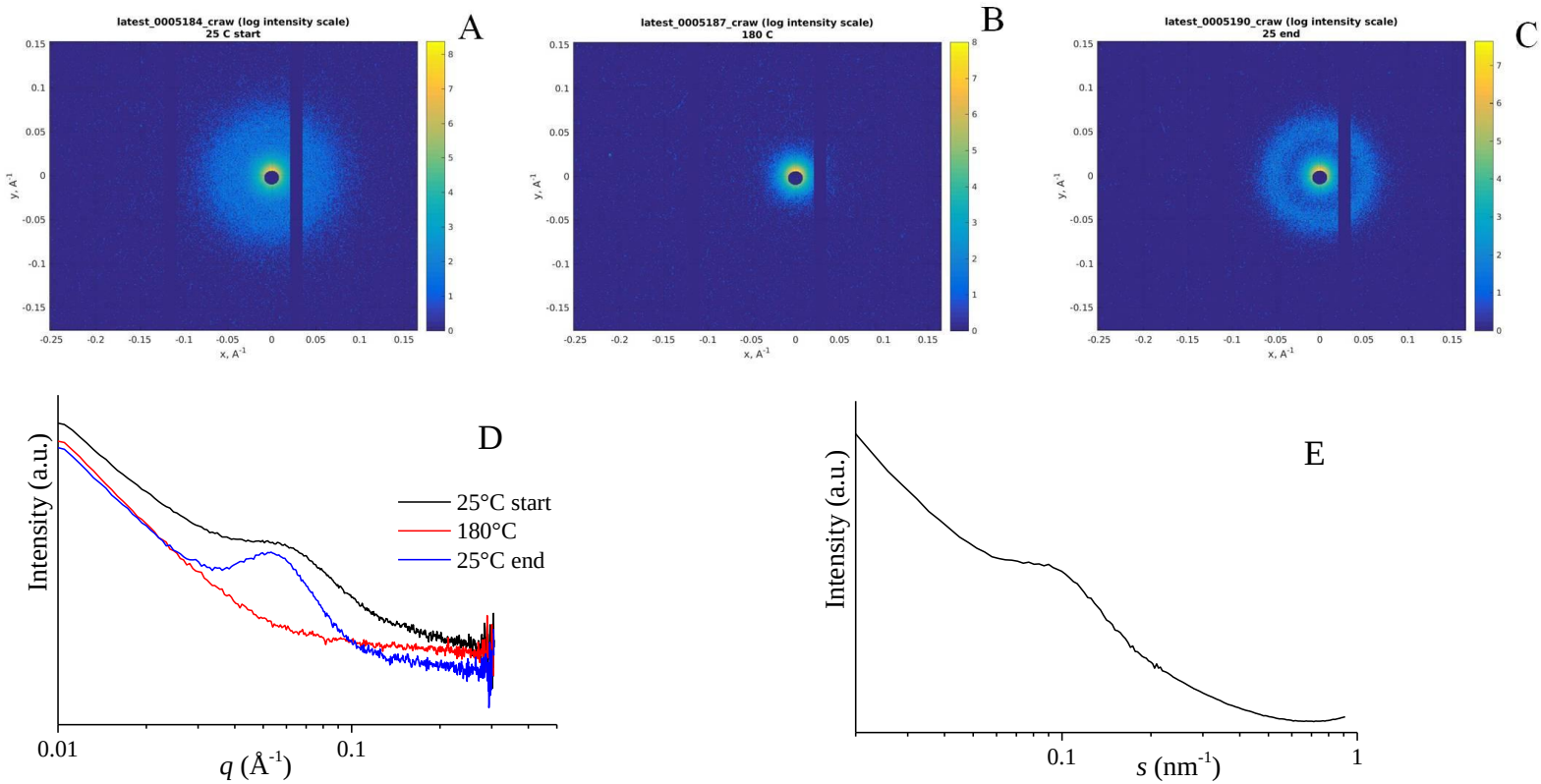

Figure 1.178. *SAXS 2D patterns (A-C) and corresponding one-dimensional profiles (D) of the sample sPPBu-1 with 3.2 mol% of 1-butene recorded at room temperature for a compression-molded melt-crystallized film aged at room temperature (A,D black curve), recorded after heating at 150 °C where the sample is melted (B, D red curve), and soon after the successive cooling from the melt to room temperature allowing crystallization (C, D blue curve). SAXS intensity profile of the same aged sample as a function of s (nm^{-1}) with longer tail resulting from the addition of several data points belonging to the WAXS profiles (E).*

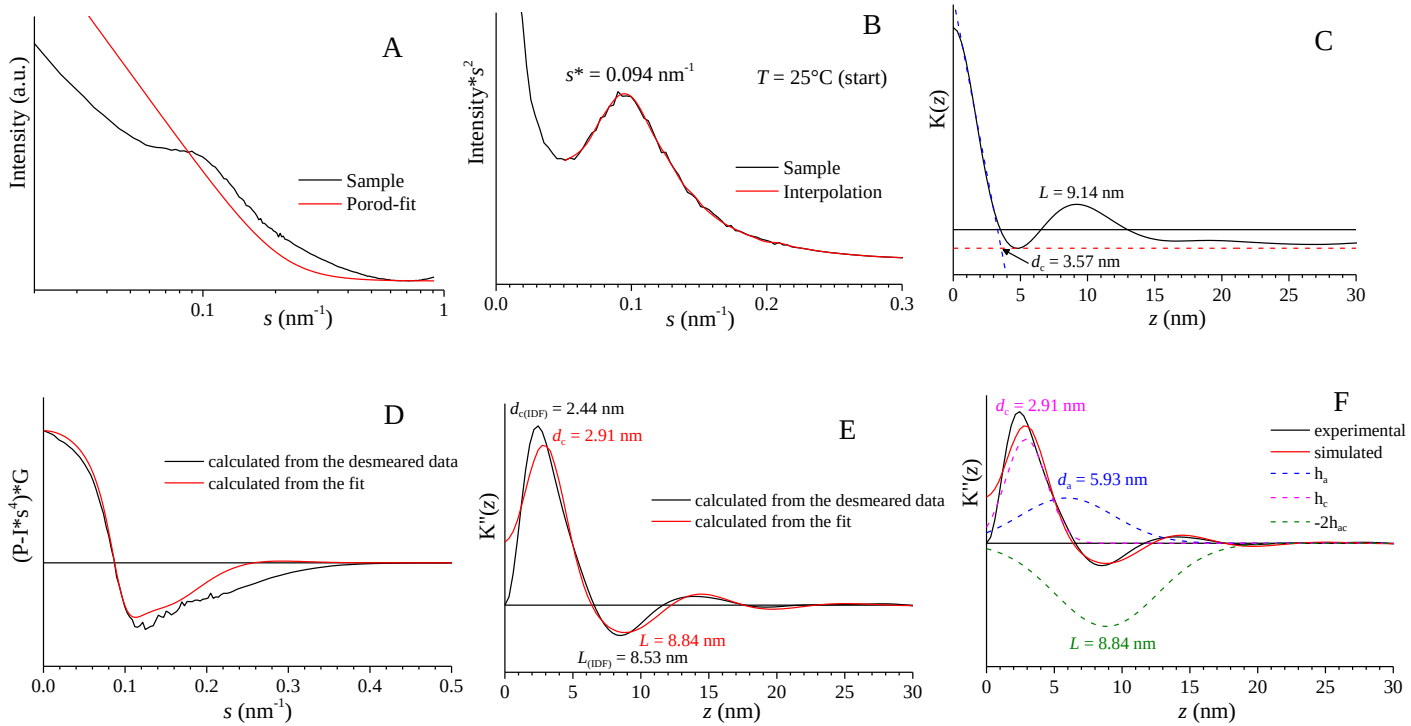

Figure 1.179. *A) SAXS intensity profiles of the aged compression molded film of the sample sPPBu-1 with 3.2 mol% of butene recorded at room temperature. The red line represents the Porod fit and gives the sum of the Porod scattering and a background due to density fluctuations. B) Lorentz-corrected SAXS intensity profile. The red curve represents the interpolation of the experimental data to evaluate the position of the peak s*. C) Correlation function K(z). The slope of initial part of the function at the origin and the correlation triangle at the origin are shown. The values of L and d_c, evaluated from the position of the first maximum of K(z) and from the short side of the correlation triangle, respectively, are indicated. D) Function $16\pi^3[P\text{-}I_{abs}s^4]\omega$ as calculated from I(s) (black line). The red curve is the result of the simulation. E) Experimental IDF function calculated from I(s) (black line), and simulated IDF function (red curve). F) Experimental and simulated IDF (continuous curves) and single contributions of the distributions of thicknesses h_c, h_a and h_{ac} to the IDF (dashed curves).*

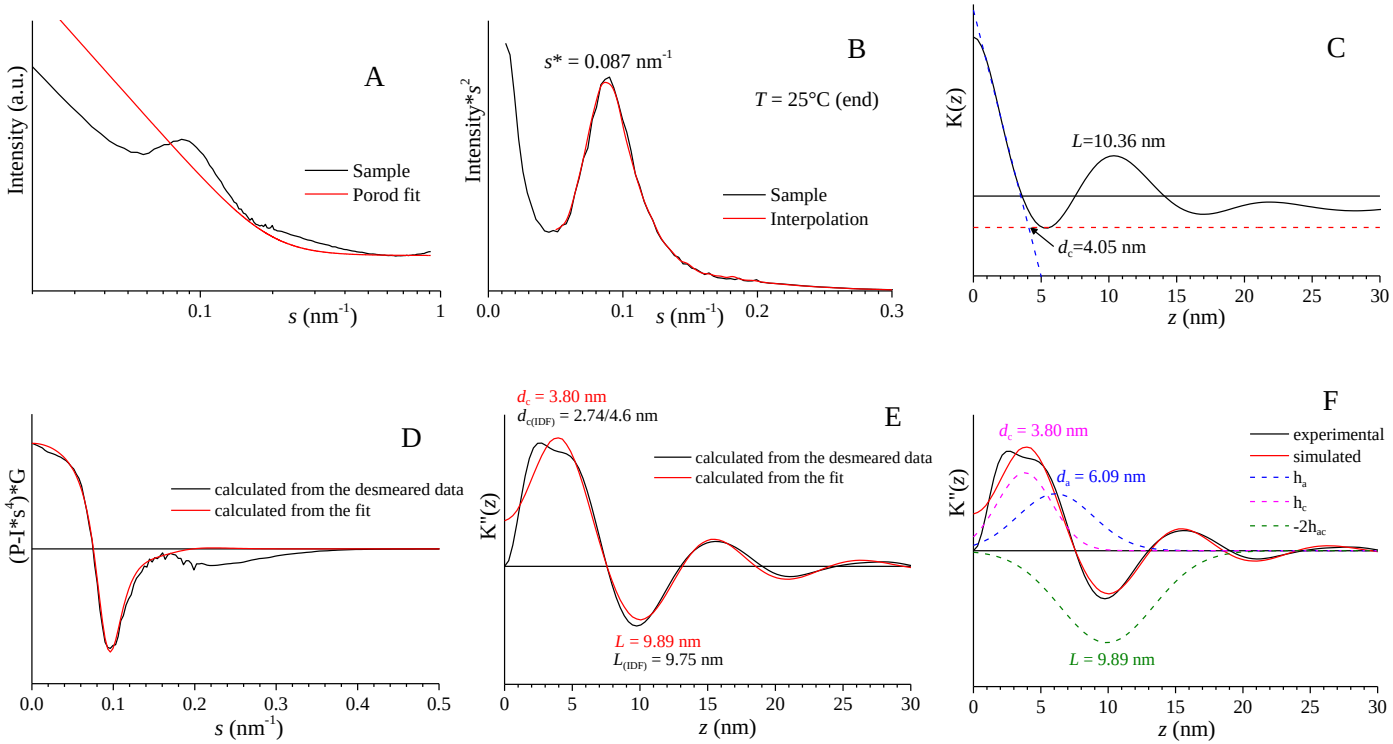

Figure 1.180. *A) SAXS intensity profiles of the as-prepared compression-molded film of the sample sPPBu-1 with 3.2 mol% of butene recorded at room temperature. The red line represents the Porod fit and gives the sum of the Porod scattering and a background due to density fluctuations. B) Lorentz-corrected SAXS intensity profile. The red curve represents the interpolation of the experimental data to evaluate the position of the peak s*. C) Correlation function K(z). The slope of initial part of the function at the origin and the correlation triangle at the origin are shown. The values of L and d_c, evaluated from the position of the first maximum of K(z) and from the short side of the correlation triangle, respectively, are indicated. D) Function $16\pi^3[P\text{-}I_{abs}s^4]\omega$ as calculated from I(s) (black line). The red curve is the result of the simulation. E) Experimental IDF function calculated from I(s) (black line), and simulated IDF function (red curve). F) Experimental and simulated IDF (continuous curves) and single contributions of the distributions of thicknesses h_c, h_a and h_{ac} to the IDF (dashed curves).*

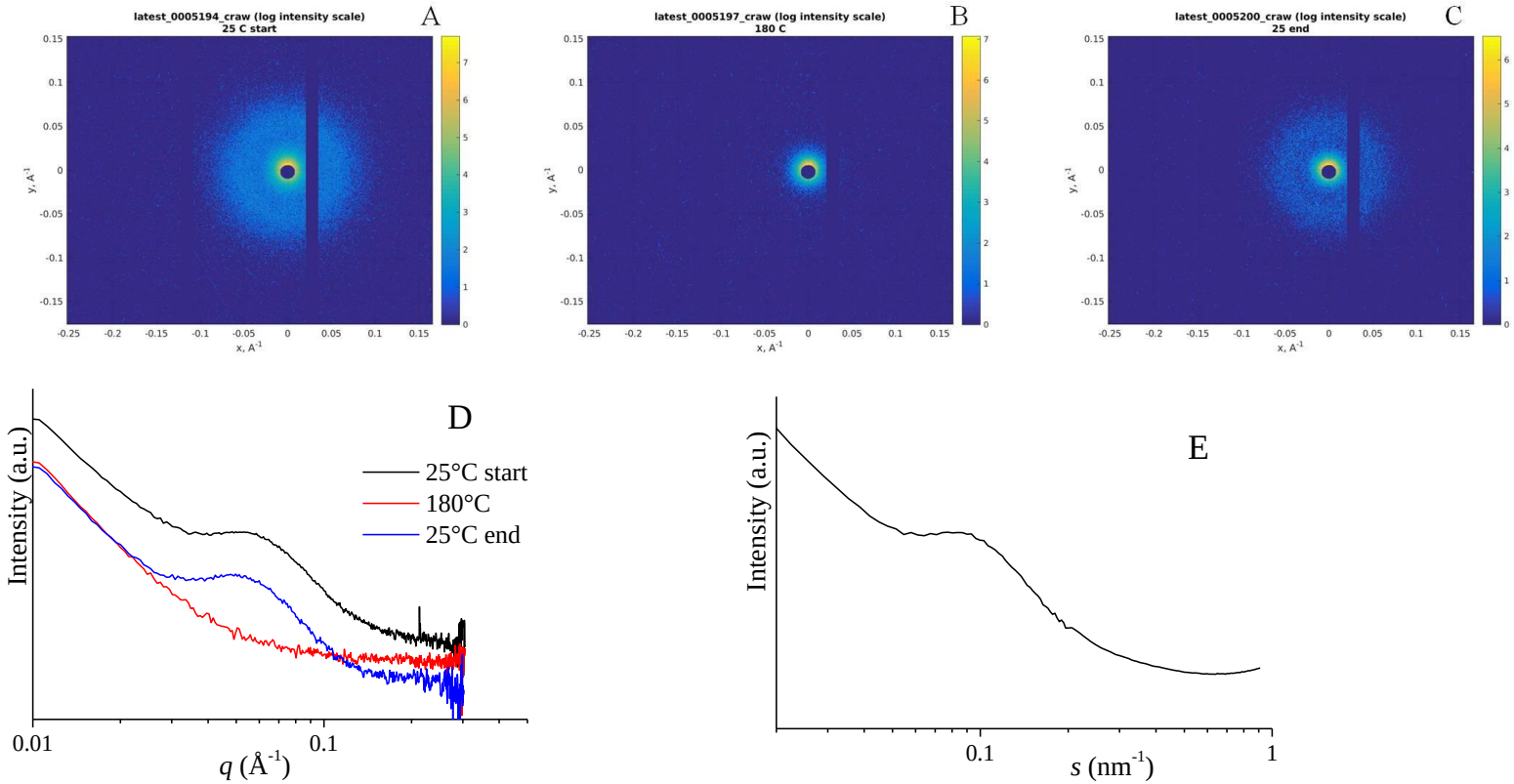

Figure 1.181. *SAXS 2D patterns (A-C) and corresponding one-dimensional profiles (D) of the sample sPPBu-2 with 6.3 mol% of 1-butene recorded at room temperature for a compression-molded melt-crystallized film aged at room temperature (A,D black curve), recorded after heating at 150 °C where the sample is melted (B, D red curve), and soon after the successive cooling from the melt to room temperature allowing crystallization (C, D blue curve). SAXS intensity profile of the same aged sample as a function of s (nm^{-1}) with longer tail resulting from the addition of several data points belonging to the WAXS profiles (E).*

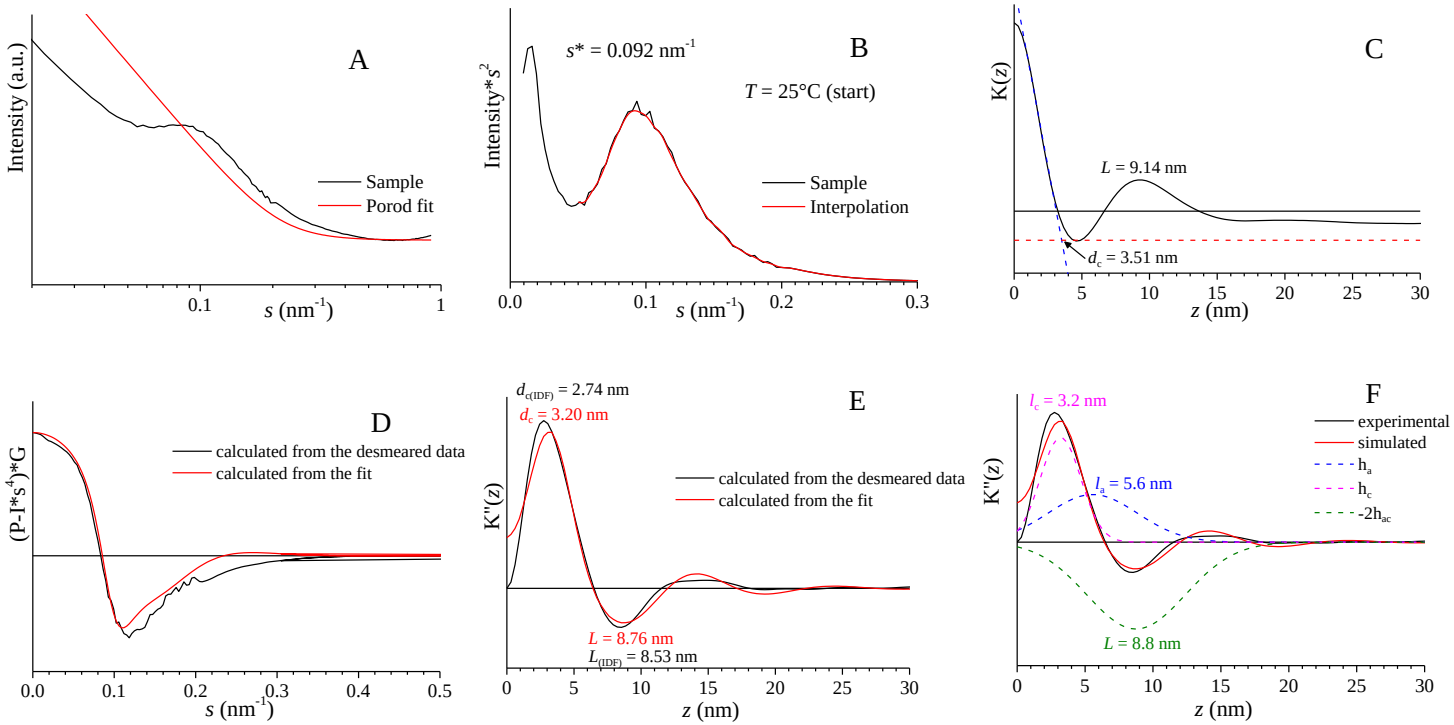

Figure 1.182. *A) SAXS intensity profiles of the aged compression molded film of the sample sPPBu-2 with 6.3 mol% of butene recorded at room temperature. The red line represents the Porod fit and gives the sum of the Porod scattering and a background due to density fluctuations. B) Lorentz-corrected SAXS intensity profile. The red curve represents the interpolation of the experimental data to evaluate the position of the peak s*. C) Correlation function K(z). The slope of initial part of the function at the origin and the correlation triangle at the origin are shown. The values of L and d_c, evaluated from the position of the first maximum of K(z) and from the short side of the correlation triangle, respectively, are indicated. D) Function $16\pi^3[P\text{-}I_{abs}s^4]\omega$ as calculated from I(s) (black line). The red curve is the result of the simulation. E) Experimental IDF function calculated from I(s) (black line), and simulated IDF function (red curve). F) Experimental and simulated IDF (continuous curves) and single contributions of the distributions of thicknesses h_c, h_a and h_{ac} to the IDF (dashed curves).*

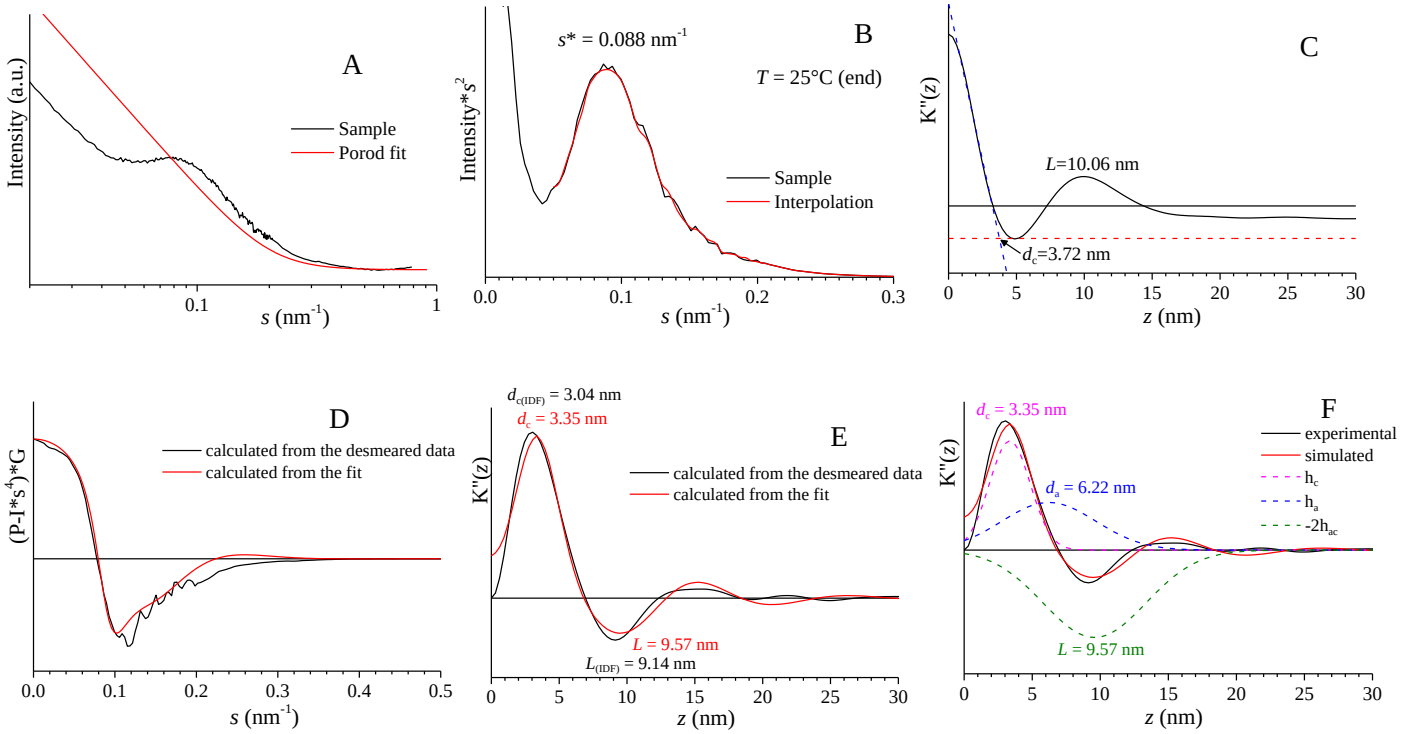

Figure 1.183. *A) SAXS intensity profiles of the as-prepared compression-molded film of the sample sPPBu-2 with 6.3 mol% of butene recorded at room temperature. The red line represents the Porod fit and gives the sum of the Porod scattering and a background due to density fluctuations. B) Lorentz-corrected SAXS intensity profile. The red curve represents the interpolation of the experimental data to evaluate the position of the peak s*. C) Correlation function K(z). The slope of initial part of the function at the origin and the correlation triangle at the origin are shown. The values of L and d_c, evaluated from the position of the first maximum of K(z) and from the short side of the correlation triangle, respectively, are indicated. D) Function $16\pi^3[P\text{-}I_{abs}s^4]\omega$ as calculated from I(s) (black line). The red curve is the result of the simulation. E) Experimental IDF function calculated from I(s) (black line), and simulated IDF function (red curve). F) Experimental and simulated IDF (continuous curves) and single contributions of the distributions of thicknesses h_c, h_a and h_{ac} to the IDF (dashed curves).*

The SAXS profiles of the melt-crystallized and aged sample sPPBu-4 with 11.2 mol% of 1-butene are shown in Figure 1.184. A peak is visible in the SAXS profiles recorded before melting (black curve in Figure 1.184) and also after melting and cooling from the melt to room temperature (blue curve in Figure 1.184), as expected since this sample still crystallizes from the melt (Figure 1.132A). The SAXS analysis performed on the aged melt-crystallized sample and the melt-crystallized sample as cooled from the melt are shown in Figures 1.185 and 1.186 and the resulting calculated morphological parameters are reported in Tables 1.23 and 1.24. Unlike the first two samples of the series, this sample exhibit slightly higher values of long period and thicknesses of amorphous and crystalline layers after aging at room temperature.

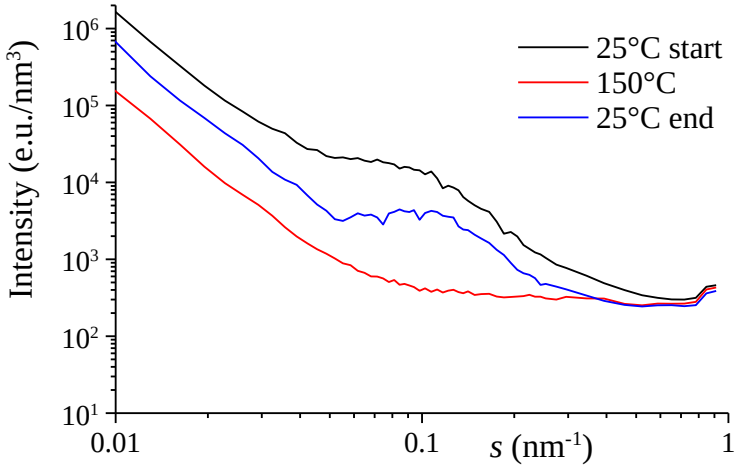

Figure 1.184. *SAXS intensity profiles of the sample of sPPBu-4 with 11.2 mol% of butene recorded at room temperature for a compression-molded melt-crystallized film aged at room temperature (black curve), recorded after heating at 150 °C where the sample is melted (red curve) and soon after the successive cooling from the melt to room temperature allowing crystallization (blue curve).*

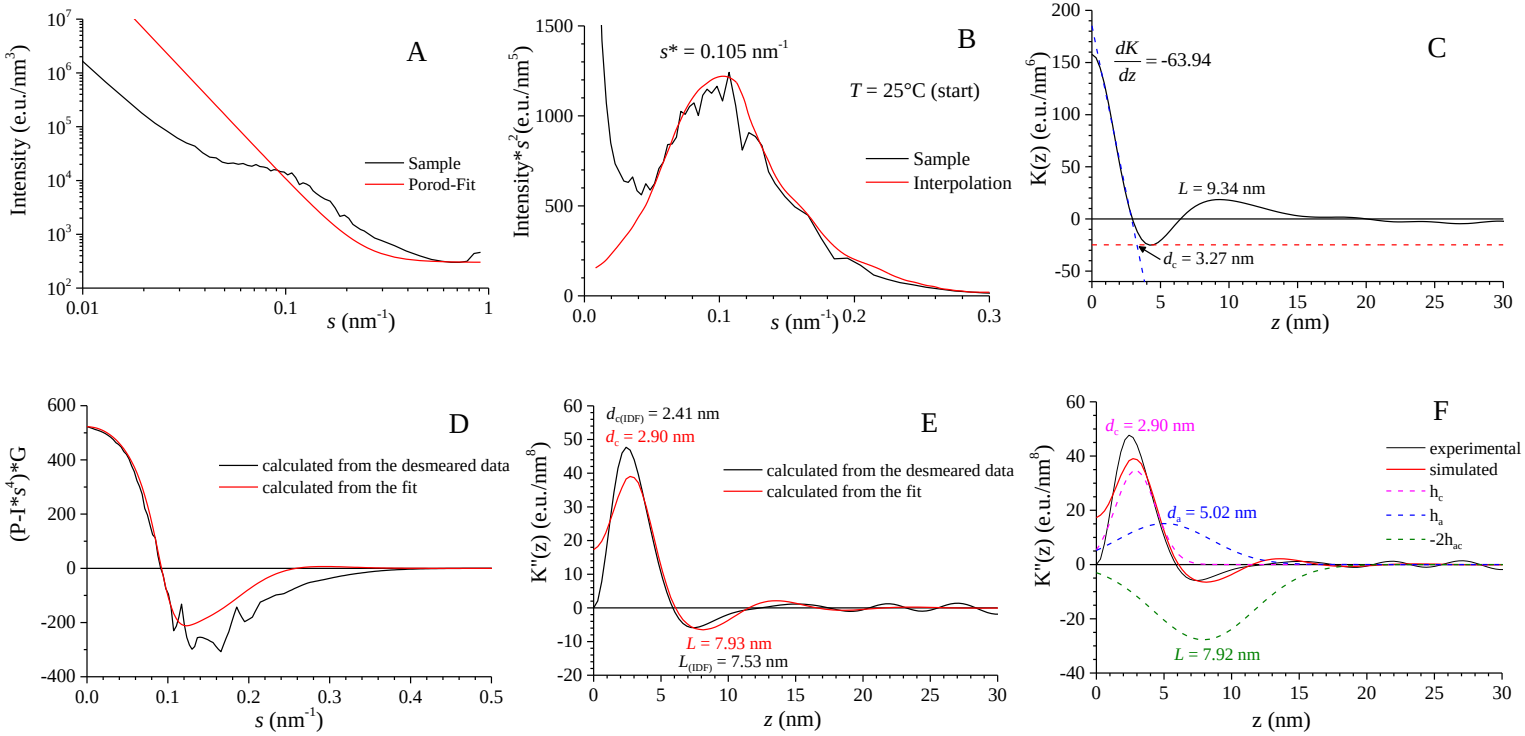

Figure 1.185. *A) SAXS intensity profiles of the aged compression molded film of the sample sPPBu-4 with 11.2 mol% of butene recorded at room temperature. The red line represents the Porod fit and gives the sum of the Porod scattering and a background due to density fluctuations. B) Lorentz-corrected SAXS intensity profile. The red curve represents the interpolation of the experimental data to evaluate the position of the peak s*. C) Correlation function K(z). The slope of initial part of the function at the origin and the correlation triangle at the origin are shown. The values of L and d_c, evaluated from the position of the first maximum of K(z) and from the short side of the correlation triangle, respectively, are indicated. D) Function $16\pi^3[P\text{-}I_{abs}s^4]\omega$ as calculated from I(s) (black line). The red curve is the result of the simulation. E) Experimental IDF function calculated from I(s) (black line), and simulated IDF function (red curve). F) Experimental and simulated IDF (continuous curves) and single contributions of the distributions of thicknesses h_c, h_a and h_{ac} to the IDF (dashed curves).*

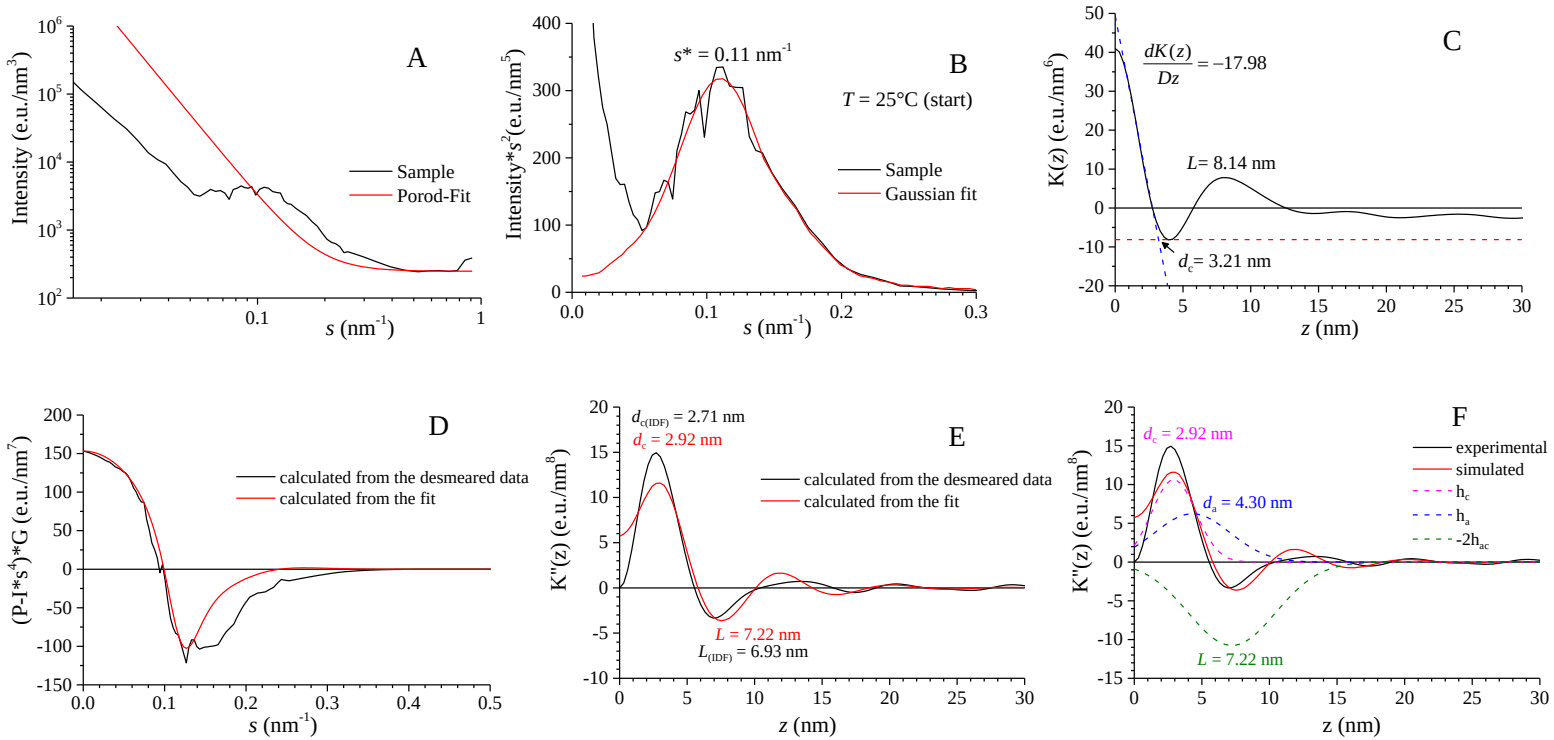

Figure 1.186. *A) SAXS intensity profiles of the as-prepared compression-molded film of the sample sPPBu-4 with 11.2 mol% of butene recorded at room temperature. The red line represents the Porod fit and gives the sum of the Porod scattering and a background due to density fluctuations. B) Lorentz-corrected SAXS intensity profile. The red curve represents the interpolation of the experimental data to evaluate the position of the peak s*. C) Correlation function K(z). The slope of initial part of the function at the origin and the correlation triangle at the origin are shown. The values of L and d_c, evaluated from the position of the first maximum of K(z) and from the short side of the correlation triangle, respectively, are indicated. D) Function $16\pi^3[P\text{-}I_{abs}s^4]\omega$ as calculated from I(s) (black line). The red curve is the result of the simulation. E) Experimental IDF function calculated from I(s) (black line), and simulated IDF function (red curve). F) Experimental and simulated IDF (continuous curves) and single contributions of the distributions of thicknesses h_c, h_a and h_{ac} to the IDF (dashed curves).*

Samples sPPBu-6, sPPBu-7, sPPBu-9 with 18.2, 31.5, 51.7 mol% of 1-butene, respectively, do not crystallize from the melt but crystallize upon aging at room temperature of several days. The aging time necessary for the complete crystallization increases with increasing butene concentration.[143]

The sample sPPBu-6 with 18.2 mol% of butene shows a slight peak only in the SAXS profile collected before melting, as shown in Figure 1.187 (black curve). Therefore the SAXS analysis has been performed only on this profile (see Figure 1.188). Because of the high intensity observed at low values of *s*, the SAXS profile has been corrected with the Debye-Beuche equation, as described in section 1.9.4 for sPPET copolymers with high ethylene content (see Figure 1.189). Although the shape of the IDF and simulated IDF ($K''(z)$ and $K''_{sim}(z)$) and the resulting morphological parameters do not significantly change (Figures 1.188E,F and 1.189E,F), this procedure improves the shape of the Lorentz-corrected profile (Figure 1.189B) and of the correlation function (Figure 1.189C), allowing the evaluation of the morphological parameters also from the correlation function.

No peak has been observed in the SAXS profiles of samples sPPBu-7 and sPPBu-9 with 31.5 and 51.7 mol% of 1-butene, respectively, as shown in Figures 1.190 and 1.191. These samples crystallize only upon long aging time. The aging time at the time of the measurements was probably not enough to observe some peaks in the SAXS profiles. Moreover, as expected, no peaks have been observed in the SAXS profiles of the samples as-cooled from the melt. All SAXS profiles perfectly overlap to the SAXS profiles recorded in the melt (Figures 1.190 and 1.191), which confirms that the sample are in the amorphous state. Therefore no SAXS analysis on has been performed on these samples.

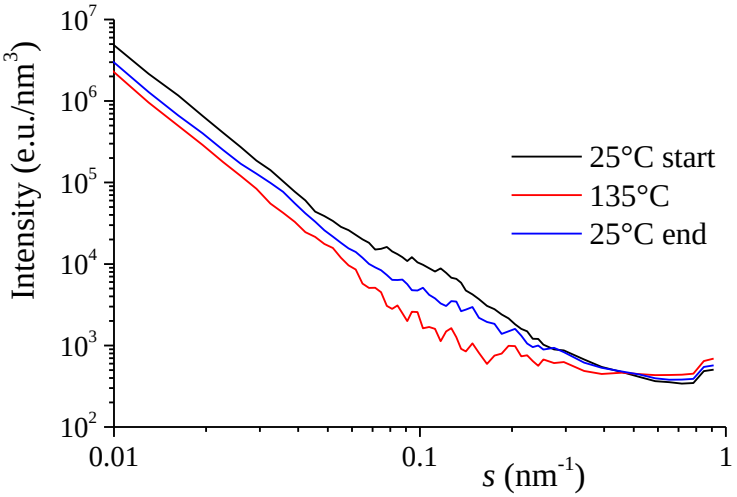

Figure 1.187.*SAXS intensity profiles of the sample of sPPBu-6 with 18.2 mol% of butene recorded at room temperature for a compression-molded melt-crystallized film aged at room temperature (black curve), recorded after heating at 135 °C where the sample is melted (red curve) and soon after the successive cooling from the melt to room temperature (blue curve).*

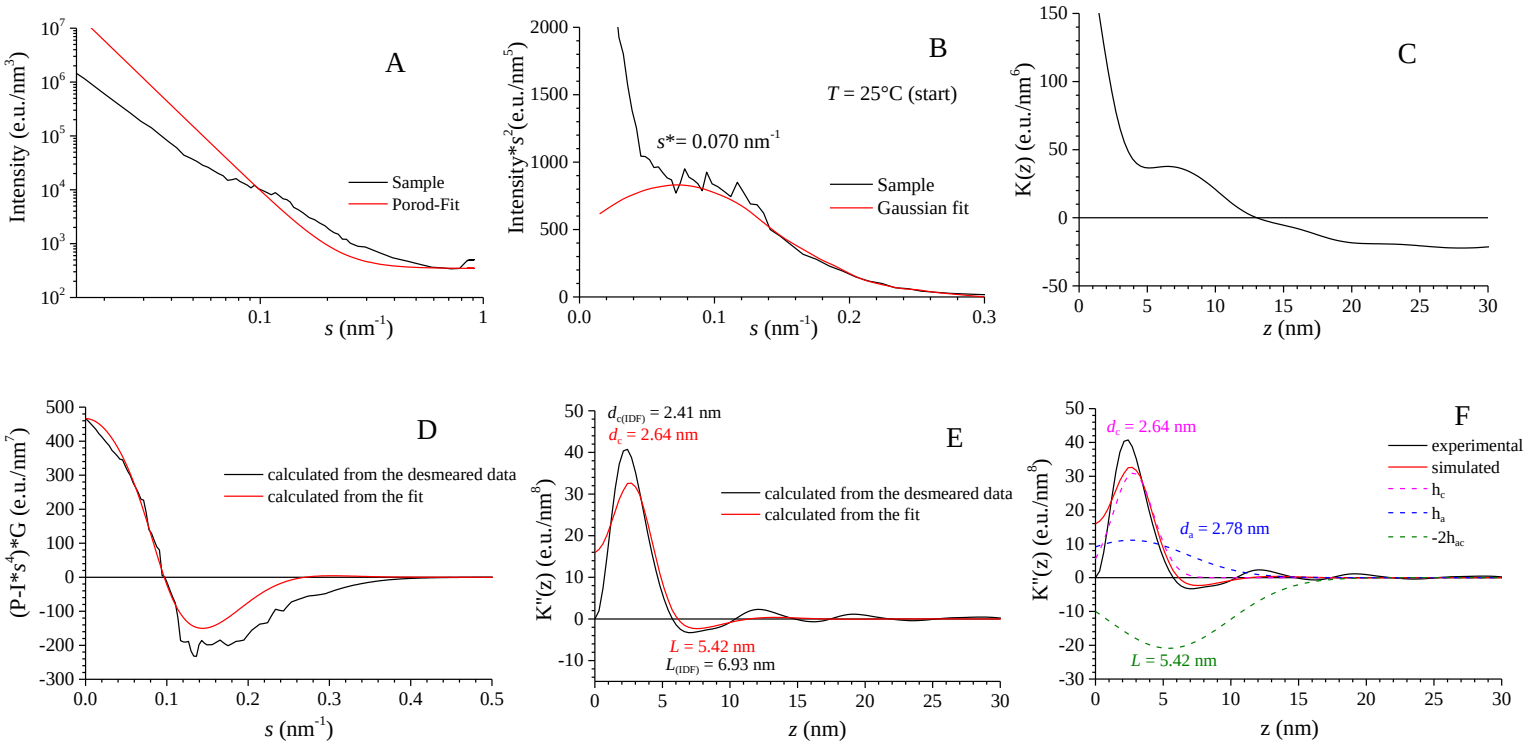

Figure 1.188. *A) SAXS intensity profiles of the aged compression molded film of the sample sPPBu-6 with 18.2 mol% of butene recorded at room temperature. The red line represents the Porod fit and gives the sum of the Porod scattering and a background due to density fluctuations. B) Lorentz-corrected SAXS intensity profile. The red curve represents the Gaussian function that simulates the correlation peak to evaluate the position of the peak s*. C) Correlation function K(z). D) Function* $16\pi^3[P\text{-}I_{abs}s^4]\omega$ *as calculated from I(s) (black line). The red curve is the result of the simulation. E) Experimental IDF function calculated from I(s) (black line), and simulated IDF function (red curve). F) Experimental and simulated IDF (continuous curves) and single contributions of the distributions of thicknesses* h_c, h_a *and* h_{ac} *to the IDF (dashed curves).*

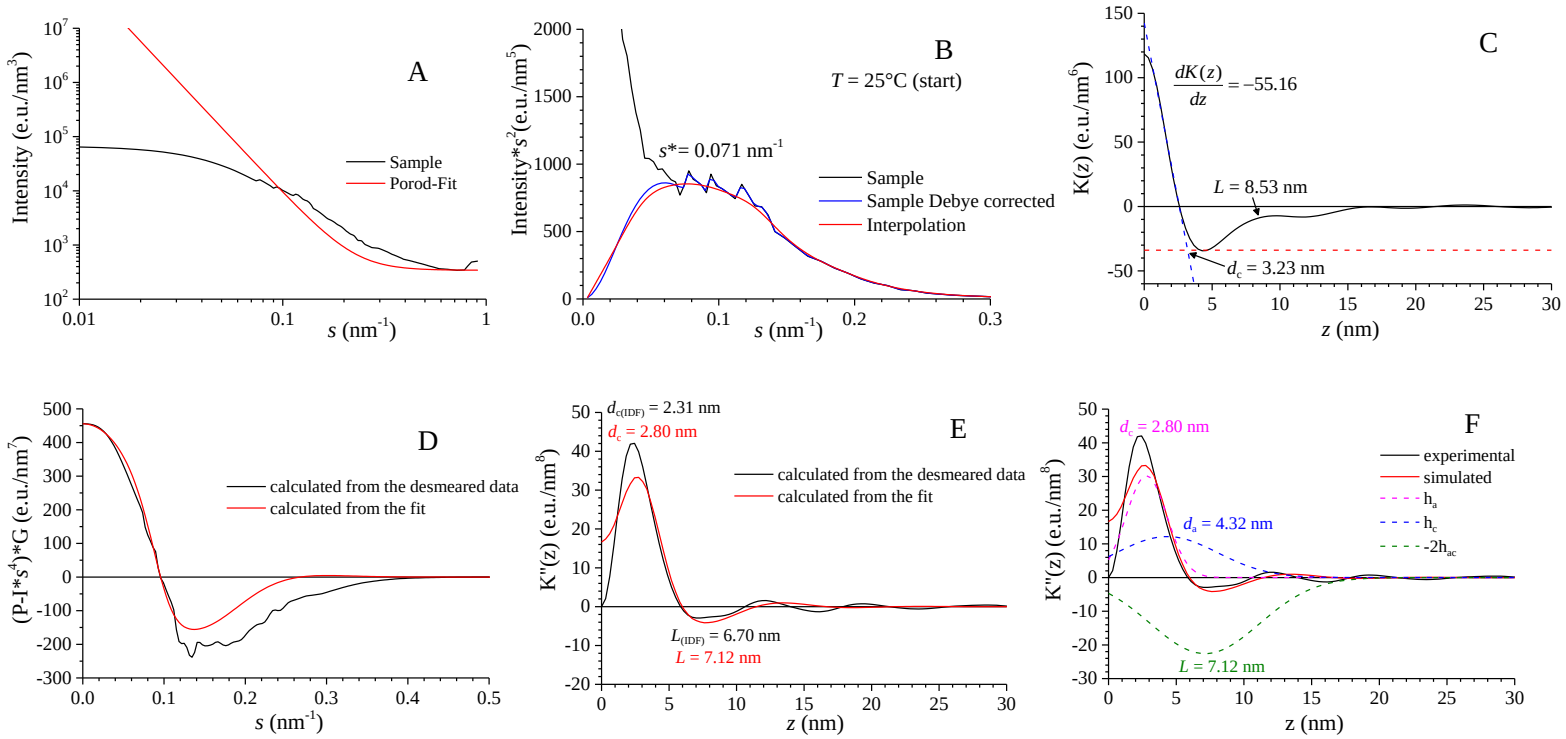

Figure 1.189. *A) SAXS intensity profiles of the aged compression molded film of the sample sPPBu-6 with 18.2 mol% of butene recorded at room temperature after correction for the Debye-Bueche function at low values of s (black curve). The red line represents the Porod fit and gives the sum of the Porod scattering and a background due to density fluctuations. B) Lorentz-corrected SAXS intensity profile. The black curve represents the original Lorentz-corrected intensity profile, the blue curve represents the Lorentz-corrected profile after the Debye-Bueche correction and the red curve represents the interpolation of the blue curve for a better evaluation of the position of the peak s*. C) Correlation function K(z). The slope of K(z) at the origin and the values of L and d_c are indicated. D) Function $16\pi^3[P\text{-}I_{abs}s^4]\omega$ as calculated from I(s) (black line). The red curve is the result of the simulation. E) Experimental IDF function calculated from I(s) (black line), and simulated IDF function (red curve). F) Experimental and simulated IDF (continuous curves) and single contributions of the distributions of thicknesses h_c, h_a and h_{ac} to the IDF (dashed curves).*

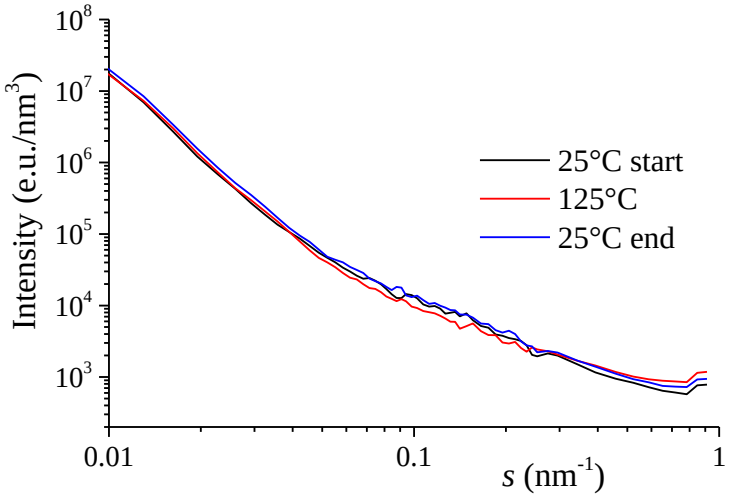

Figure 1.190. *SAXS intensity profiles of the sample of sPPBu-7 with 31.5 mol% of butene recorded at room temperature for a compression-molded melt-crystallized film aged at room temperature (black curve), recorded after heating at 125 °C where the sample is melted (red curve) and soon after the successive cooling from the melt to room temperature (blue curve).*

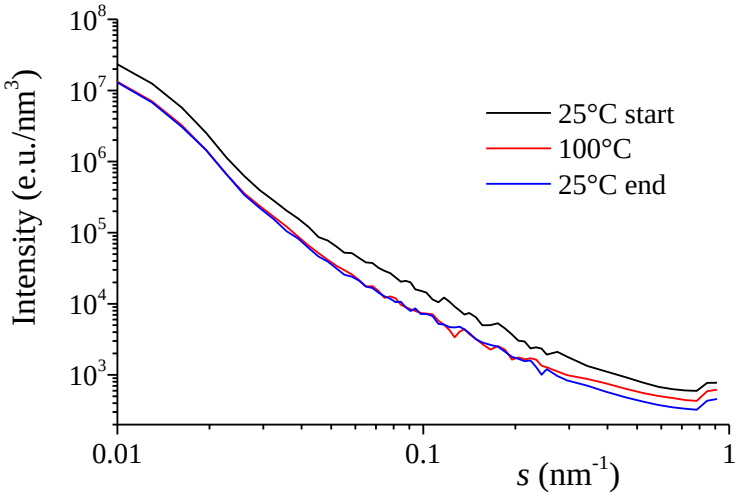

Figure 1.191. *SAXS intensity profiles of the sample of sPPBu-9 with 51.7 mol% of butene recorded at room temperature for a compression-molded melt-crystallized film aged at room temperature (black curve), recorded after heating at 100 °C where the sample is melted (red curve) and soon after the successive cooling from the melt to room temperature (blue curve).*

Samples sPPBu-11 and sPPBu-12 with 69.9 and 89 mol% of 1-butene, respectively, do not crystallize from the melt but crystallize upon aging in the form I of sPB.[143] (Figure 1.132B). Accordingly, the SAXS profiles of the compression-molded samples aged at room temperature of Figures 1.192 and 1.195 (black curves), whereas no peaks are present in the profiles of the samples after melting and cooling to room temperature without aging (blues curves of Figures 1.192 and 1.195). A more intense and defined peak has been observed in the SAXS profile of the sample sPPBu11. The SAXS analyses of these two samples are shown in Figures 1.193 and 1.196. As for the sample sPPBu-6 with 18.2 mol% of butene, the high intensity at low values of *s* has prevented a correct evaluation of the correlation function (Figure 1.193C and 1.196C) and, in particular for sample sPPBu12, the modeling of the IDF (Figure 1.196E,F) and the evaluation of the morphological parameters. Therefore, the SAXS analyses have been repeated after correction of the SAXS profiles at low *s* values with the Debye-Bueche function. The results are shown in Figures 1.194 and 1.197 and the evaluated morphological parameters are reported in Table 1.23.

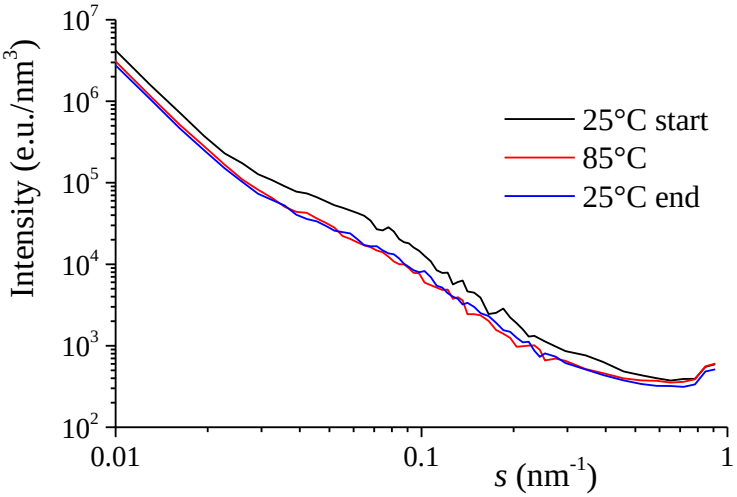

Figure 1.192. *SAXS intensity profiles of the sample of sPPBu-11 with 69.9 mol% of butene recorded at room temperature for a compression-molded melt-crystallized film aged at room temperature (black curve), recorded after heating at 85 °C where the sample is melted (red curve) and soon after the successive cooling from the melt to room temperature (blue curve).*

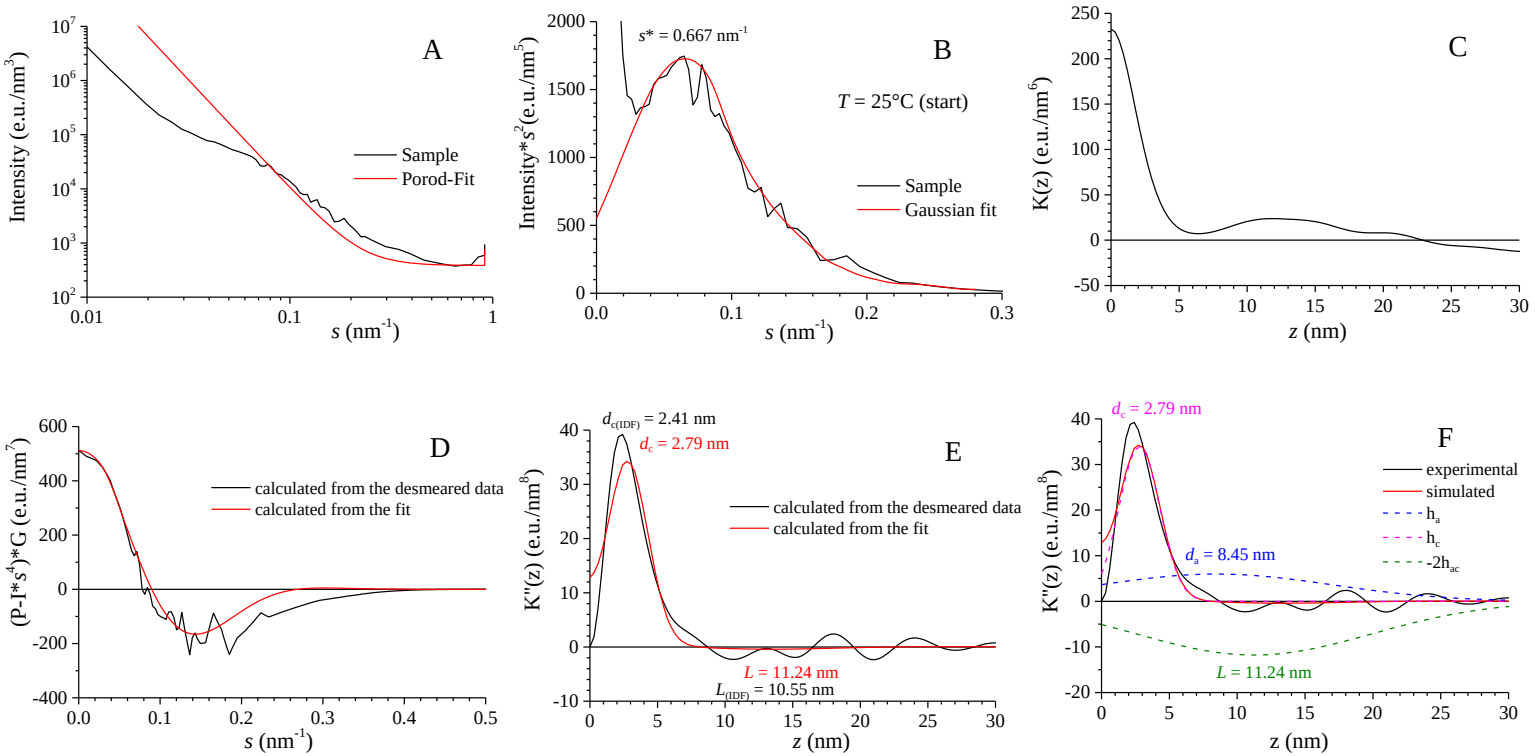

Figure 1.193. *A) SAXS intensity profiles of the aged compression molded film of the sample sPPBu-11 with 69.9 mol% of butene recorded at room temperature. The red line represents the Porod fit and gives the sum of the Porod scattering and a background due to density fluctuations. B) Lorentz-corrected SAXS intensity profile. The red curve represents the Gaussian function that simulates the correlation peak to evaluate the position of the peak s*. C) Correlation function K(z). D) Function* $16\pi^3[P\text{-}I_{abs}s^4]\omega$ *as calculated from I(s) (black line). The red curve is the result of the simulation. E) Experimental IDF function calculated from I(s) (black line), and simulated IDF function (red curve). F) Experimental and simulated IDF (continuous curves) and single contributions of the distributions of thicknesses* h_c, h_a *and* h_{ac} *to the IDF (dashed curves).*

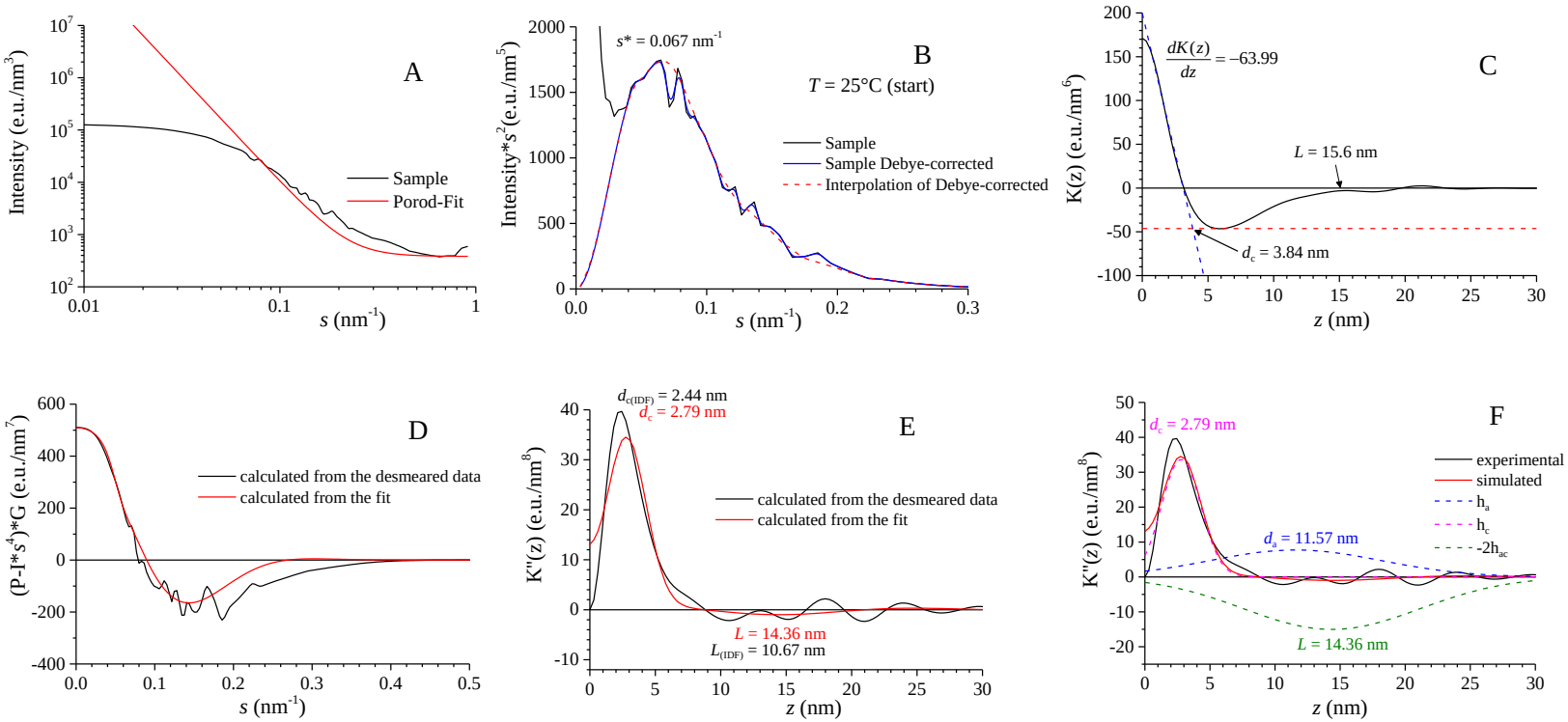

Figure 1.194. *A) SAXS intensity profiles of the aged compression molded film of the sample sPPBu-11 with 69.9 mol% of butene recorded at room temperature after correction for the Debye-Bueche function at low values of s (black curve). The red line represents the Porod fit and gives the sum of the Porod scattering and a background due to density fluctuations. B) Lorentz-corrected SAXS intensity profile. The black curve represents the original Lorentz-corrected intensity profile, the blue curve represents the Lorentz-corrected profile after the Debye-Bueche correction and the red dashed curve represents the interpolation of the blue curve for a better evaluation of the position of the peak s*. C) Correlation function K(z). The slope of K(z) at the origin and the values of L and d_c are indicated. D) Function $16\pi^3[P\text{-}I_{abs}s^4]\omega$ as calculated from I(s) (black line). The red curve is the result of the simulation. E) Experimental IDF function calculated from I(s) (black line), and simulated IDF function (red curve). F) Experimental and simulated IDF (continuous curves) and single contributions of the distributions of thicknesses h_c, h_a and h_{ac} to the IDF (dashed curves).*

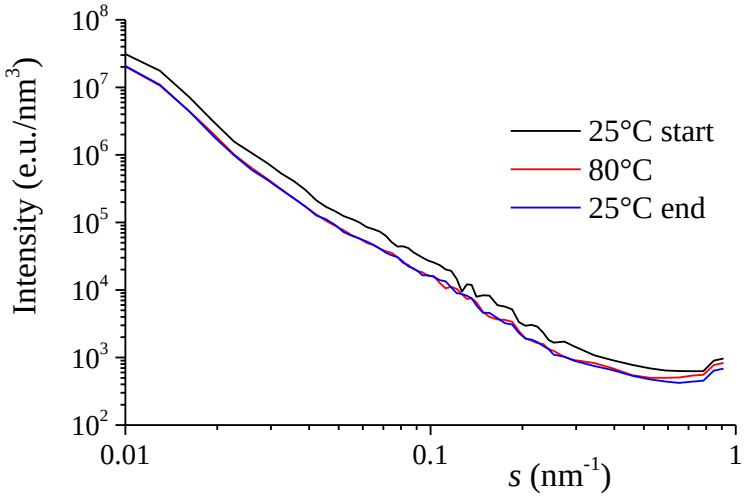

Figure 1.195. *SAXS intensity profiles of the sample of sPPBu-12 with 89 mol% of butene recorded at room temperature for a compression-molded melt-crystallized film aged at room temperature (black curve), recorded after heating at 80 °C where the sample is melted (red curve) and soon after the successive cooling from the melt to room temperature (blue curve).*

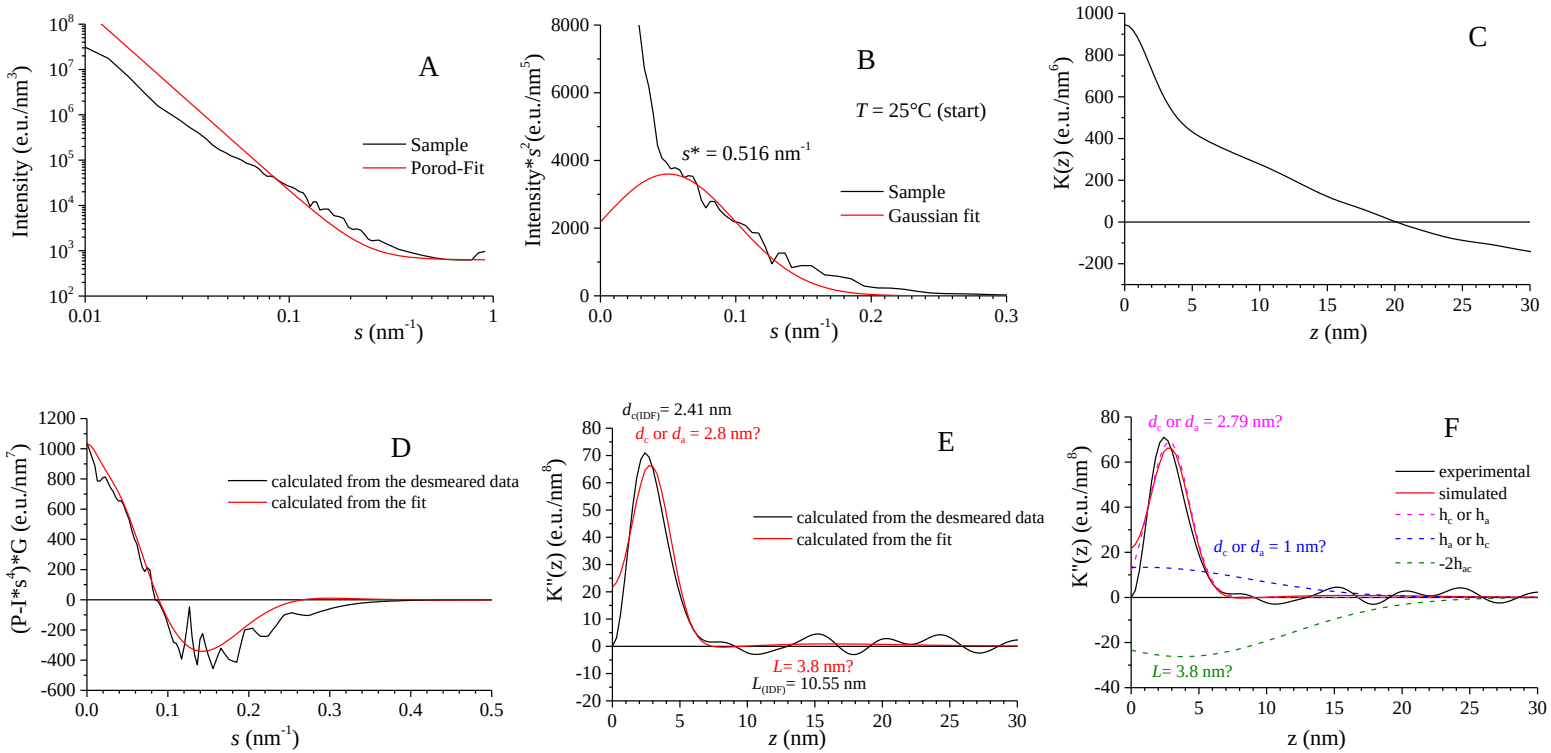

Figure 1.196. *A) SAXS intensity profiles of the aged compression molded film of the sample sPPBu-12 with 89 mol% of butene recorded at room temperature. The red line represents the Porod fit and gives the sum of the Porod scattering and a background due to density fluctuations. B) Lorentz-corrected SAXS intensity profile. The red curve represents the Gaussian function that simulates the correlation peak to evaluate the position of the peak s*. C) Correlation function K(z). D) Function $16\pi^3[P\text{-}I_{abs}s^4]\omega$ as calculated from I(s) (black line). The red curve is the result of the simulation. E) Experimental IDF function calculated from I(s) (black line), and simulated IDF function (red curve). F) Experimental and simulated IDF (continuous curves) and single contributions of the distributions of thicknesses h_c, h_a and h_{ac} to the IDF (dashed curves).*

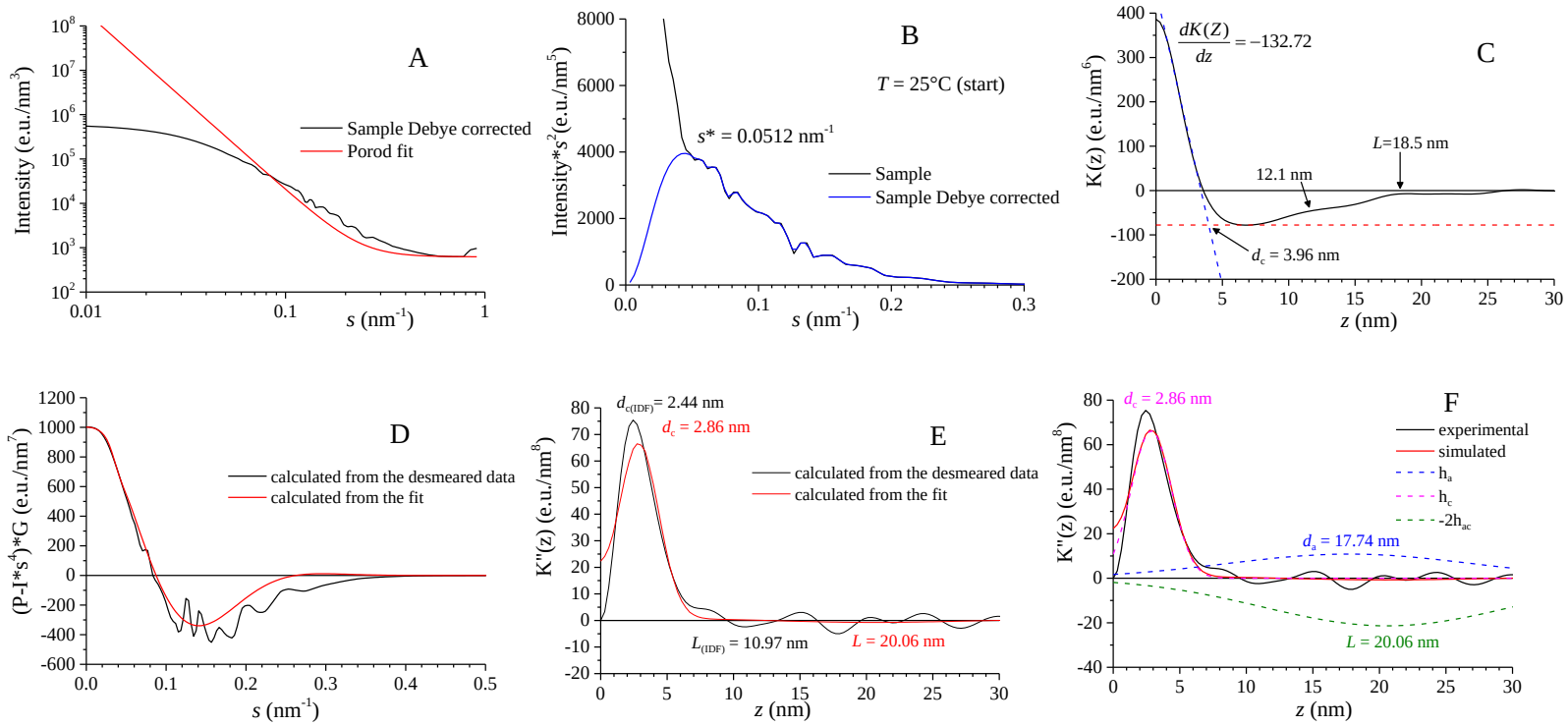

Figure 1.197. *A) SAXS intensity profiles of the aged compression molded film of the sample sPPBu-12 with 89 mol% of butene recorded at room temperature after correction for the Debye-Bueche function at low values of s (black curve). The red line represents the Porod fit and gives the sum of the Porod scattering and a background due to density fluctuations. B) Lorentz-corrected SAXS intensity profile. The black curve represents the original Lorentz-corrected intensity profile and the blue curve represents the Lorentz-corrected profile after the Debye-Bueche correction. C) Correlation function K(z). The slope of K(z) at the origin and the values of L and d_c are indicated. D) Function $16\pi^3[P\text{-}I_{abs}s^4]\omega$ as calculated from I(s) (black line). The red curve is the result of the simulation. E) Experimental IDF function calculated from I(s) (black line), and simulated IDF function (red curve). F) Experimental and simulated IDF (continuous curves) and single contributions of the distributions of thicknesses h_c, h_a and h_{ac} to the IDF (dashed curves).*

Tables 1.23 and 1.24 report the morphological parameters of all analyzed samples of sPPBu copolymers. For samples sPPBu6, sPPBu11 and sPPBu12 only the parameters calculated on the SAXS profiles corrected with the Debye-Bueche function are reported. The values of the long period, the thickness of the crystalline lamellae and of the amorphous layers, evaluated from the Lorentz corrected profiles, the correlation functions and the experimental and simulated IDF are reported in Figures 1.198 and 1.199 as a function of 1-butene content.

For the aged compression-molded samples, the long period and the thickness of the amorphous layers exhibit similar behavior with increasing butene content, as shown in Figure 1.198 A,C, and 1.199A-C. Starting from the homopolymer a decrease of L and d_a is observed in the first two samples sPPBu-1 (3.2 mol% of 1-butene) and sPPBu-2 (6.3 mol% of 1-butene). As the comonomer content further increases up to 20 mol% of butene a slight decrease of L and d_a (regardless of the method of evaluation) occurs, whereas a strong increase of L and d_a for high butene concentration, in correspondence of the samples sPPBu-11 andsPPBu-12 with 69.9 and 89 mol% of 1-butene, respectively, has been observed. The thickness of the crystalline lamellae also decreases with increasing butene content for low butene concentrations up to 20 mol%, then a slight increase of d_c for the samples sPPBu-11 and sPPBu-12 with 69.9 and 89 mol% of butene is observed (see Figures 1.198B and 1.199A-C). It is worth noting that a small decrease of the crystalline thickness occurs, whereas a strong increase of the amorphous thickness and of the long period is observed at high butene concentrations.

The same trend has been observed in as-prepared melt-crystallized samples in the range of butene concentrations for which the samples crystallize upon cooling from the melt. The long period and the thickness of the amorphous layers decrease with increasing butene concentration starting from the homopolymer, as shown in Figures 1.198A',C' and 1.199A'-C'. The thickness of the crystalline lamellae also decreases with the butene concentration and only that of the sample with 3.2 mol% of butene d_c seems to be higher than that of the homopolymer. For this sample the IDF gives two maxima corresponding to two different thicknesses of 2.7 nm and 4.6 nm (Figure 1.180E,F and Table 1.24), that cannot correspond to d_c and d_a because the long period evaluated from the minimum of the IDF is higher (9.75 nm) than their sum. On the other hand the simulated IDF gives a single maxima corresponding to a crystalline

thickness of 3.80 nm (Figure 1.180E,F and Table 1.24), in agreement with the value obtained from the correlation function (Figure 1.180C and Table 1.24).

A comparison between Figures 1.199A-C and 1.199A'-C' shows, as mentioned before, that the morphological parameters evaluated from the correlation function are similar to those evaluated from the simulated and experimental IDF.

All these data show that generally all morphological parameters decrease with increasing 1-butene concentration in samples that crystallize from the melt or upon aging in the form I of sPP. A small decrease of the crystalline thickness also occurs at high butene concentrations, when the samples crystallize upon aging at room temperature in form I of sPB, whereas correspondingly, for these samples a strong increase of the amorphous thickness and of the long period is observed. This is probably related to the fact that the crystallinity of these samples is very low and that, in the crystalline morphology of form I of sPB most of the amorphous phase is inside the lamellar stacks, resulting in high values of long period (20 nm), higher than that of analogous samples of sPPET copolymers of similar degrees crystallinity (12 nm, Tables 1.21 and 1.22).

It would be interesting to compare the morphological parameters evaluated by the analysis of the SAXS profiles with those that can be evaluated from the AFM images reported in the section 1.8 (Figure 1.133 for the sPP homopolymer sample, Figures 1.134 - 1.137, for sPPET samples and Figures 1.138 -1.145 for sPPBu copolymers). In particular, the thickness of the crystalline lamellae and a periodicity of the lamellar stacks can be determined from the AFM images that show bundles of nearly parallel and stacked lamellae radiating from a nucleus, or, for high defect concentration smaller and thinner randomly oriented lamellae still radiating from a nucleus (see Figures 1.136, 1.140-1.141).

The values of the thickness of the crystalline lamellae for sPPET copolymers measured from the AFM images are similar to those evaluated from the SAXS data (Tables 1.22). In the case of sPPBu copolymers the values of crystalline lamellae evaluated from AFM are slightly higher than those determined by SAXS analysis, probably due to resulting low resolution of the AFM images because of the too sticky samples.

Table 1.23. *Values of the degree of crystallinity x_c and morphological parameters evaluated from the analysis of the SAXS profiles recorded at room temperature of compression-molded melt-crystallized film aged at room temperature of samples of the sPP homopolymer sRDG-2-1 and sPPBu copolymers of the indicated butene concentration (defects content). The values of the Porod costant (P), scattering vector corresponding to the maximum of the Lorentz-corrected profiles (s*), Long period (L), thickness of the crystalline lamellae (d_c) and of the amorphous layers (d_a) evaluated from the Lorentz-corrected profiles (L*), from the correlation functions K(z) (L(cofun), d_c(cofun) and d_a(cofun)), from the experimental IDF (L(IDF), d_c(IDF) and d_a(IDF)) and from the simulated IDF (L, d_c and d_a), slope of the first part of K(z) at the origin (dK/dz) and electron density difference ($\Delta\rho$) are reported. The widths of the distributions of thicknesses of crystalline lamellae (σ_c), thicknesses of amorphous phase (σ_a) evaluated from the simulated IDF are also reported.*

Sample	Defects content (mol%)	x_c (%)[a]	P (e.u./nm^7)	s^* (nm^{-1})	L^* (nm)	d_c (IDF) (nm)	d_a (IDF) (nm)	L (IDF) (nm)	d_c (nm)	σ_c (nm)	d_a (nm)	σ_a (nm)	L (nm)	d_c (cofun) (nm)	d_a (cofun) (nm)	L (cofun) (nm)	dK/dz	$\Delta\rho$
sRDG-2-1	0.7	45	0.876	0.078	12.82	4.52	5.73	10.25	4.58	0.64	6.39	3.56	10.97	4.40	7.65	12.05	-76	29
sPPBu-1	3.2	44	/	0.094	10.64	2.44	6.09	8.53	2.91	0.50	5.93	3.16	8.84	3.57	5.57	9.14	/	/
sPPBu-2	6.3	42	/	0.092	10.87	2.74	5.79	8.53	3.20	0.50	5.56	2.98	8.76	3.51	5.63	9.14	/	/
sPPBu-4	11.2	41	1.053	0.105	9.52	2.41	5.12	7.53	2.90	0.50	5.03	3.14	7.93	3.27	6.07	9.34	-63.94	
sPPBu-6	18.2	39	0.919	0.071	14.08	2.31	4.39	6.70	2.80	0.50	4.32	3.46	7.12	3.23	5.3	8.53	-55.16	
sPPBu-11	69.9	28	1.028	0.067	14.93	2.44	8.23	10.67	2.79	0.50	11.57	6.44	14.36	3.84	11.76	15.6	-63.99	
sPPBu-12	89	32	2.020	0.051	19.61	2.44	8.53	10.97	2.86	0.50	17.74	9.11	20.60	3.96	8.14	12.10	-132.72	

[a]) evaluated from WAXS profiles

Table 1.24. *Values of the degree of crystallinity x_c and morphological parameters evaluated from the analysis of the SAXS profiles recorded at room temperature of as-prepared compression-molded melt-crystallized film of samples of the sPP homopolymer sRDG-2-1 and sPPBu copolymers of the indicated butene concentration (defects content). The values of the Porod costant (P), scattering vector corresponding to the maximum of the Lorentz-corrected profiles (s*), Long period (L), thickness of the crystalline lamellae (d_c) and of the amorphous layers (d_a) evaluated from the Lorentz-corrected profiles (L*), from the correlation functions K(z) (L(cofun), d_c(cofun) and d_a(cofun)), from the experimental IDF (L(IDF), d_c(IDF) and d_a(IDF)) and from the simulated IDF (L, d_c and d_a), slope of the first part of K(z) at the origin (dK/dz) and electron density difference ($\Delta\rho$) are reported. The widths of the distributions of thicknesses of crystalline lamellae (σ_c), thicknesses of amorphous phase (σ_a) evaluated from the simulated IDF are also reported.*

Sample	Defects content (mol%)	x_c (%)[a]	P (e.u./nm^7)	s^* (nm^{-1})	L^* (nm)	d_c (IDF) (nm)	d_a (IDF) (nm)	L (IDF) (nm)	d_c (nm)	σ_c (nm)	d_a (nm)	σ_a (nm)	L (nm)	d_c (cofun) (nm)	d_a (cofun) (nm)	L (cofun) (nm)	dK/dz	$\Delta\rho$
sRDG-2-1	0.7	45	0.368	0.082	12.19	3.49	6.76	10.25	3.62	0.50	6.58	3.62	10.22	3.78	7.92	11.70	-27.74	17
sPPBu-1	3.2	44	/	0.087	11.49	2.74/4.60	7.01	9.75	3.80	1.47	6.09	2.42	9.89	4.05	6.31	10.36	/	
sPPBu-2	6.3	42	/	0.088	11.36	3.04	6.1	9.14	3.35	0.51	6.22	3.15	9.57	3.72	6.34	10.06	/	
sPPBu-4	11.2	41	0.352	0.11	9.09	2.71	4.22	6.93	2.92	0.50	4.30	2.31	7.22	3.21	4.93	8.14	-17.98	12
sPPBu-6	18.2	39	/	/	/	/	/	/	/	/	/	/	/	/	/	/	/	/
sPPBu-11	69.9	0	/	/	/	/	/	/	/	/	/	/	/	/	/	/	/	/
sPPBu-12	89	0	/	/	/	/	/	/	/	/	/	/	/	/	/	/	/	/

[a]) evaluated from WAXS profiles

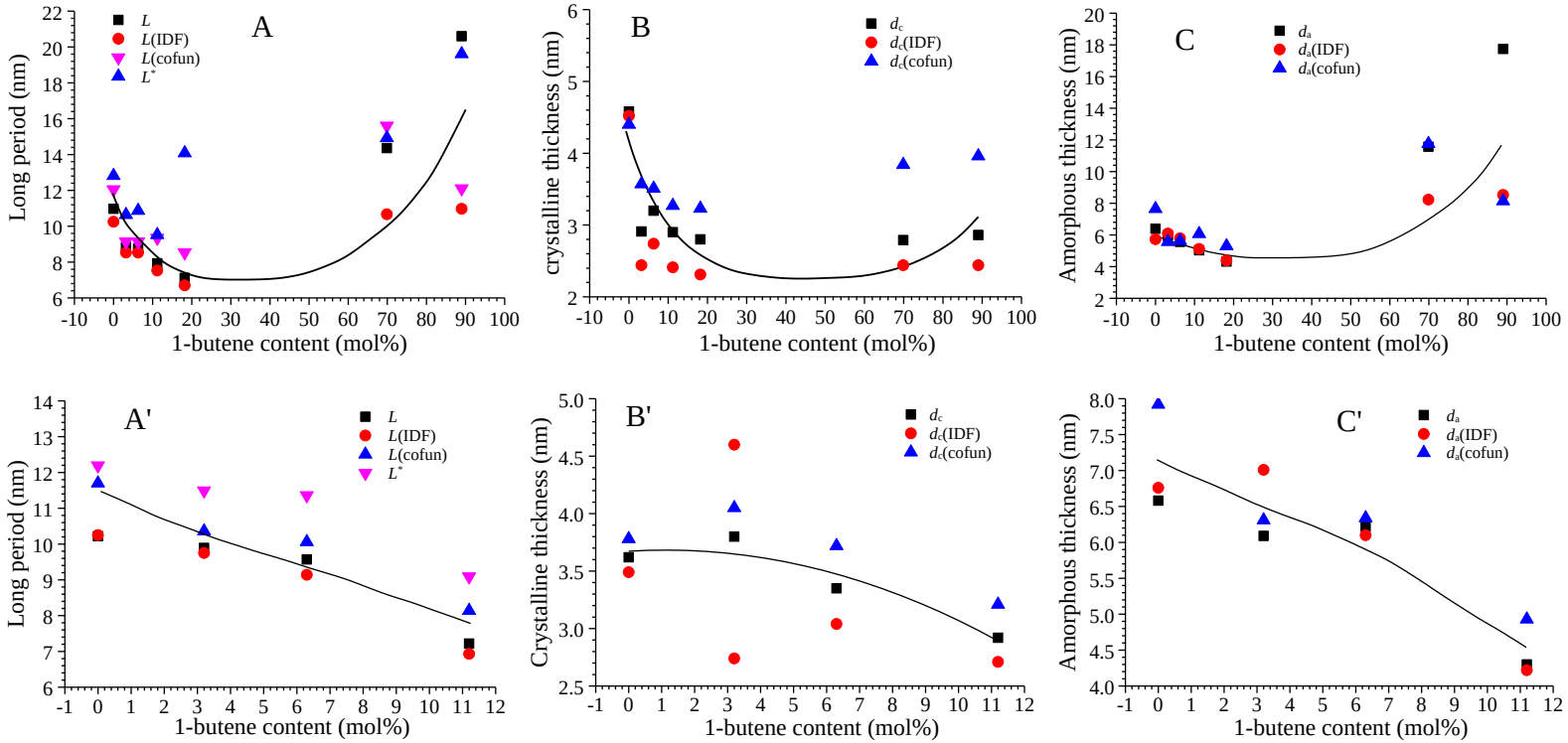

Figure 1.198. *Average values of the long period L (■) evaluated from the simulated IDF, L(IDF) (●) evaluated from the experimental IDF, L(cofun) (▲) evaluated from the correlation function, L* (▼) evaluated from maximum s* of the Lorentz-corrected SAXS profile, of the aged compression-molded melt-crystallized (A) and as-prepared melt-crystallized compression-molded (A') samples of sPPBu copolymers as a function of 1-butene concentration. Average values of the of thickness of crystalline lamellae (B,B') and amorphous layers (C,C'), d_c and d_a (■) evaluated from the simulated IDF, d_c(IDF) and d_a(IDF) (●) evaluated from the experimental IDF, d_c(cofun)and d_a(cofun) (▲) evaluated from the correlation function, of the aged (B,C) and melt-crystallized (B',C') compression-molded samples of sPPBu copolymers as a function of 1-butene concentration. The morphological parameters of the homopolymer sRDG-2-1 (ethylene content =0) are also reported as a reference.*

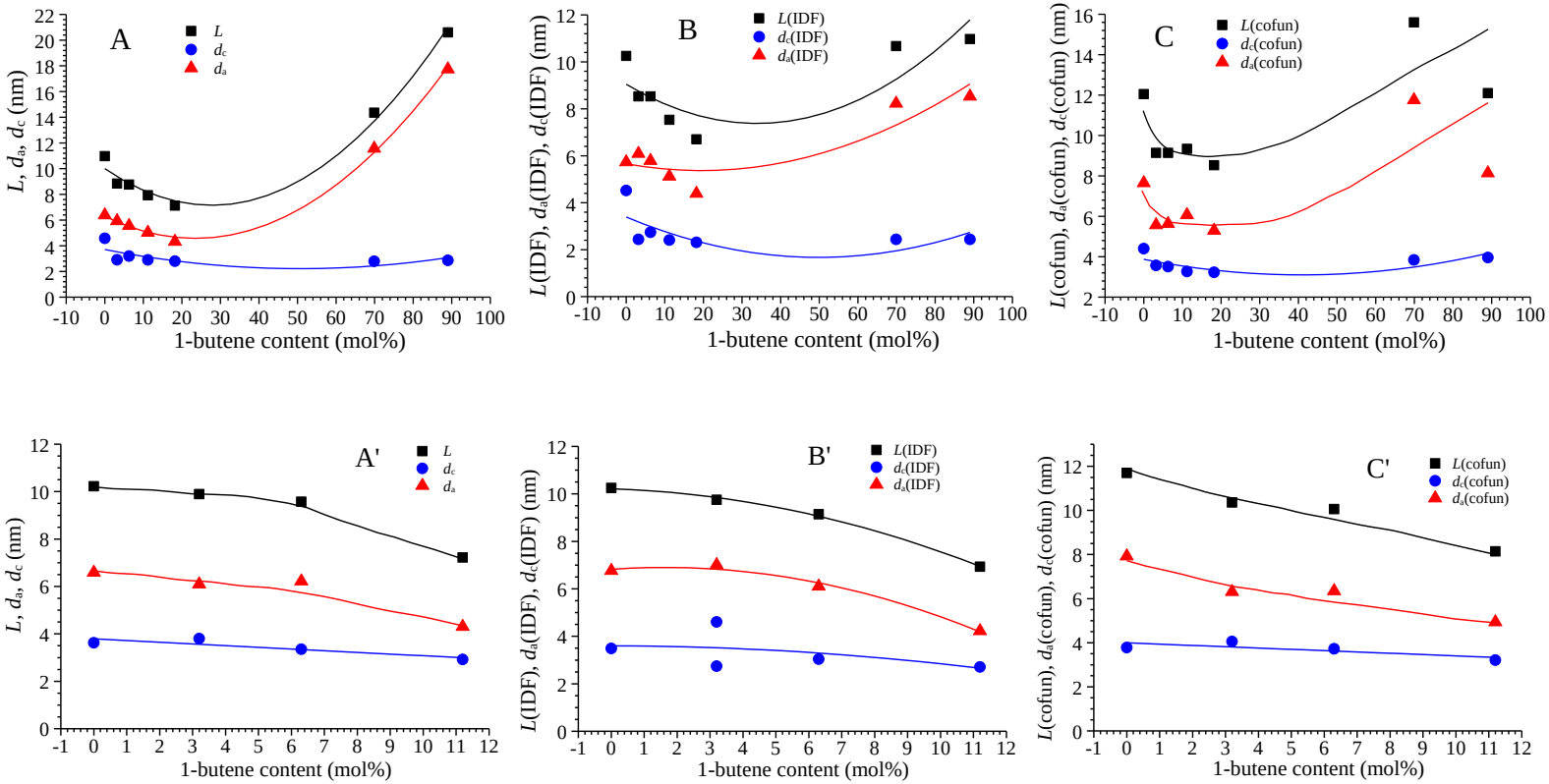

Figure 1.199. *Average values of the long period L (■), thickness of crystalline lamellae d_c (●), thickness of amorphous layers d_a (▲) evaluated from the simulated IDF (A,A'), from the experimental IDF (B,B') and from the correlation function (C,C') of the aged compression-molded (A,B,C) and as-prepared melt-crystallized (A',B',C') samples of sPPBu copolymers as a function of 1-butene concentration.*

1.9.6. Concluding remarks on SAXS and AFM analysis.

The results of the AFM and SAXS analysis on sPP-based copolymers are in good agreement and in according with the morphology observed by optical microscopy. In the case of sPPEt copolymer the decrease of crystalline thickness is in agreement with the decrease of crystallinity with increasing ethylene concentration due to the presence of ethylene defects and increasing disorder in the crystalline phase (Figura 1.200A). However, even though the fraction of the total amorphous phase clearly increases with increasing ethylene content (Figure 1.200A), the thickness of the amorphous layer in the model of lamellar stacks, evaluated by SAXS, decreases. Only at high ethylene content also the fraction of amorphous phase in between the crystalline lamellae (in the lamellar stacks) increases, with corresponding increase of amorphous thickness and long period. This can be explained recalling that ethylene units are only partially included into the crystals of sPP and an appreciable amount of ethylene units is also included in the noncrystalline phase of the copolymers. Therefore, most of the constitutional defects could be segregated in the extra-lamellar amorphous phase consisting of amorphous phase not organized in the lamellar stacks, and therefore, not visible by the modeling of the SAXS data.

The increasing disorder in the crystalline phase and the probable segregation of the constitutional defects in the extra-lamellar amorphous phase are in agreement with the lamellar morphology evidenced by AFM, characterized by bundles of nearly parallel and stacked lamellae radiating from a nucleus for low defect concentrations, and smaller and thinner randomly oriented lamellae still radiating from a nucleus for high defect concentration. These data suggest that the model of the perfectly alternated lamellar stacks is not a realistic model for the description of these disordered systems with high defect concentration and low crystallinity.

In the case of sPPBu copolymers all morphological parameters, crystalline and amorphous thicknesses and long period, decrease with increasing 1-butene concentration in samples that crystallize from the melt or upon aging in the form I of sPP. A small decrease of the crystalline thickness also occurs at high butene concentrations, when the samples crystallize upon aging at room temperature in form I of sPB, whereas correspondingly, for these samples a strong increase of the amorphous thickness and of the long period is observed.

The similar change of all morphological parameters evaluated by SAXS reflects the change of crystallinity with increasing butene concentration (Figure

1.200B). This suggests that the periodicity at nanometric scale changes as the variations occurring at atomic scale. This could be due to the fact that butene is regularly partitioned between crystalline and amorphous phase due to the complete co-crystallization of propylene and butene units in the syndiotactic copolymers. Therefore, although butene units are always included in the unit cell at any concentration, a fraction of butene units is always incorporated in the amorphous fraction. This results in similar changes of crystalline and amorphous thicknesses. Only when the sample crystallizes in form I of sPB a strong increase of the long period is obtained, probably because most of the amorphous phase is included in the lamellar stacks.

These results are in agreement with the results of the study of morphology of of these copolymers of sPP by POM, that have revealed an interwoven morphology formed by bundle-like and needle-like crystals aggregates embedded in an amorphous matrix. In this morphology that explains the elastic properties of these materials even at high defects (stereodefects or comonomeric units) concentrations, the fraction of amorphous phase in the stacks of these thin crystals is necessarily lower than that of the matrix.

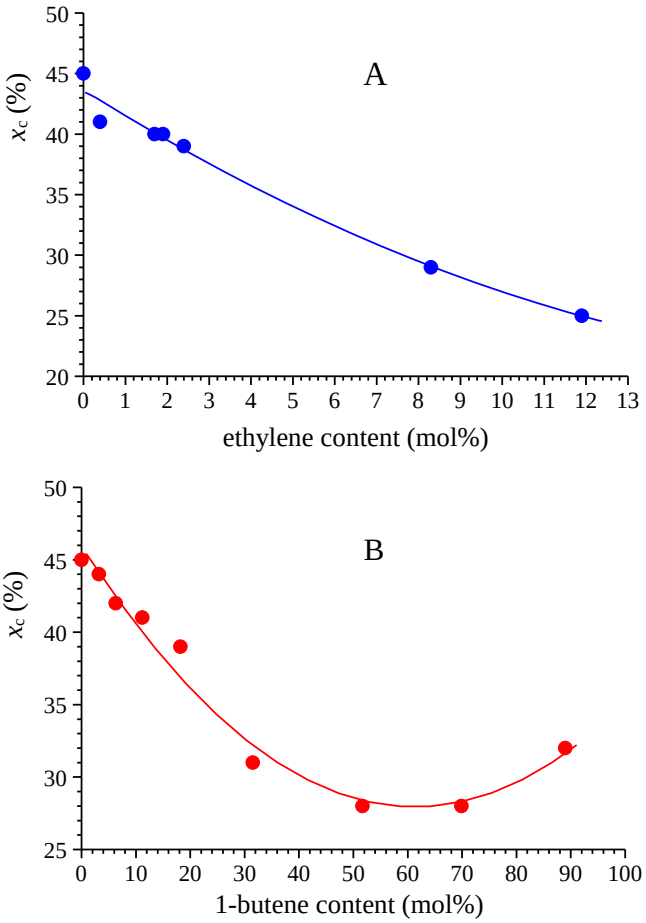

Figure 1.200. *Values of crystallinity of compression-molded melt-crystallized samples aged at room temperature of sPPET (A) and sPPBu (B) copolymers as a function of comonomer concentration.*

References Chapter I

1) C. De Rosa, F. Auriemma, *Prog. Polym. Sci.* **2006**, *31*, 145.

2) G. Natta, I. Pasquon I, P. Corradini, M. Peraldo, M. Pegoraro, A. Zambelli, *Rend Accad Naz Lincei* **1960**, *28*,539; *Chem. Abstr.* **1960**, *55*, 8923i.

3) A. Zambelli, C. Tosi, *Adv Polym Sci* **1974**, *15*, 31.

4) G. Natta, I. Pasquon, A. Zambelli, *J. Am. Chem. Soc.* **1962**, *84*, 1488. A. Zambelli, G. Natta, I. Pasquon, *J. Polym. Sci. Part C* **1963**, *4*, 411.

5) Y. Doi, S. Suzuki, K. Soga, *Makromol. Chem. Rapid Commun* **1985**, *6(10)*, 639.

6) A. Zambelli, G. Natta, I. Pasquon, R. Signorini, *J. Polym. Sci.* **1967**, *C16*, 2485.

7) A. Zambelli, I. Pasquon, R. Signorini, G. Natta, *Makromol. Chem.* **1968**, *112*, 160.

8) Y. Doi, M. Jakada, T. Keii, *Makromol. Chem*. **1979**, *180*, 57.

9) G. Natta, E. Lombardi, A. L. Segre, A. Zambelli, A. Marinangeli, *Chim Ind* (Milan) **1965**, *47*, 378.

10) A. Zambelli, M. G. Giongo, G. Natta, *Makromol. Chem.* **1968**, *112*, 183.

11) A. Zambelli, P. Locatelli, G. Bajo, F. A. Bovey, *Macromolecules* **1975**, *8*, 687.

12) A. Zambelli, G. Gatti, *Macromolecules* **1978**, *11*, 485.

13) A. Zambelli, P. Locatelli, E. Rigamonti, *Macromolecules* **1979**, *12*, 156.

14) A. Zambelli, G. Bajo, E. Rigamonti, *Makromol. Chem.* **1978**, *179*, 1249.

15) A. Zambelli, P. Locatelli, G. Bajo, *Macromolecules* **1979**, *12*, 154.

16) P. Locatelli, M. C. Sacchi, E. Rigamonti, A. Zambelli, *Macromolecules* **1984**, *17*, 123.

17) A. Zambelli, P. Longo, S. Terenghi, D. Recupero, G. Zannoni, *J. Mol. Catal A: Chem* **2000**, *152*, 25.

18) A. Zambelli, C. Tosi, M. C. Sacchi, *Macromolecules* **1972**, *5*, 649.

19) A. Zambelli, P. Locatelli, G. Zannoni, F. A. Bovey, *Macromolecules* **1978**, *11*, 923.

20) A: Zambelli, C. Wolfsgruber, G. Zannoni, F. A. Bovey, *Macromolecules* **1974**, *7*, 750.

21) a) P. Ammendola, X. Shijng, A. Grassi, A. Zambelli, *Gazz. Chim. Ital.* **1988**, *118*, 769. b) A. Grassi, P. Ammendola, P. Longo, E. Albizzati, L. Resconi, R. Mazzocchi, *Gazz. Chim. Ital.* **1988**, 118, 539. c) A. Zambelli, P. Ammendola, *Prog. Polym. Sci.* **1991**, *16*, 203.

22) A. Zambelli, I. Sessa, F. Grisi, R. Fusco, P. Accomazzi, *Macromol. Rapid. Commun*. **2001**, *22*, 297.

23) A. Zambelli, A. Lety, C. Tosi, I. Pasquon, *Makromol. Chem.* **1968**, *115*, 73.

24) S. Cesca, *Macromol Rev* **1975**, *10*, 1.

25) C. J. Carman, C. E. Wilkes, *Rubber Chem Techonol* **1971**, *44*, 781.

26) J. A. Ewen, *J. Am. Chem. Soc.* **1984**, *106*, 6355.

27) W. Kaminsky, K. Kulper, H. H. Brintzinger, F. R. W. Wild, *Angew. Chem.* **1985**, *97*, 507. *Angew, Chem, Int Ed Engl* **1985**, *24*, 507.

28) H. Sinn, W. Kaminsky, H. J. Vollmer, R. Woldt, *Angew. Chem. Int. Ed. Engl* **1980**, *92*, 396.

29) (a) J. A. Ewen, R. L. Jones, A. Razavi, J. D. Ferrara, *J .Am. Chem. Soc.* **1988**, *110*, 6255. (b) A. Razavi, J. A. Ewen, *US patent* 5,334,677. (c) J. A. Ewen, A. Razavi, *US patent* 5,476,914. (d) A. Razavi, J. A. Ewen, *US patent* 6184326. (e) A. Razavi, J. A. Ewen, *US patent* 4,892,851.

30) J. A. Ewen, M. J. Elder, R. L. Jones, S. Curtis, H. N. Cheng, In *Catalytic Olefin Polymerization*, T. Keii, K. Soga editors New York: Elsevier, 1989. p. 271.

31) a) A. Razavi, D. Baekelmans, V. Bellia, Y. De Brauwer, K. Hortmann, M. Lambrecht, O. Miserque, L. Peters, M. Slawinsky, S. Van Belle, in: Progress and Development of Catalytic Olefin Polymerisation, T. Sano, T. Uozumi, H. Nakatani, M. Terano, Eds., Technology and Education Publishers, Tokyo 2000, p. 176. b) A. Razavi, J. J. Ferrara, *J. Organomet. Chem*. **1992**, *435*, 299. c) A. Razavi, J. L. Atwood, *J. Organomet. Chem*. **1993**, *459*, 117. d) A. Razavi, U. Thewalt, *J. Organomet. Chem*. **1993**, *445*, 111. e) A. Razavi, L. Peters, L. Nafpliotis, D.Vereecke, K. DenDaw, *Macromol. Symp*. **1995**, *89*, 345. f) A. Razavi, J. L. Atwood, *J. Organomet. Chem*. **1996**, *520*, 115. g) A. Razavi, D. Vereecke, L. Peters, K. Den Daw, L. Nafpliotis, J. L. Atwood, in: ‘‘Ziegler Catalysts’’,G. Fink, R. Mulhaupt, H. H. Brintzinger, Eds., Springer-Verlag, Berlin 1993. h) R. Kleinschmidt, M. Reffke, G. Fink, *Macromol. Rapid Commun*. **1999**, *20*, 284.

32) K. Mislow, M. Raban, *Top. Stereochem.* **1967**, *1*, 1.

33) L. Cavallo, G. Guerra, M. Vacatello, P. Corradini, *Macromolecules* **1991**, *24*, 1784.

34) L. A. Castonguay, A. K. Rappé, *J. Am. Chem. Soc.* **1992**, *114*, 5832.

35) H. Kawamura-Kuribayashi, N. Koga, K. Morokuma, *J. Am. Chem. Soc.* **1992**, *114*, 8687.

36) T. Yu, J. C. W. Chien, *J. Polym. Sci.: Part A: Polym. Chem*. **1995**, 33, 1085.

37) Y. Van der Leek, K. Angermund, M. Reffke, R. Kleinschmidt, R. Goretzki, G. Fink, *Chem. Eur. J.* **1997**, *3*, 585..

38) L. Resconi, L. Cavallo, A. Fait, F. Piemontesi, *Chem. Rev.* **2000**, *100*, 1253.

39) H. H. Brintzinger, D. Fischer, R. Mülhaupt, B. Rieger, R. M. Waymouth, *Angew. Chem., Int. Ed. Engl.* **1995**, *34*, 1143.

40) P. Corradini, L. Cavallo, G. Guerra, In: Scheirs J, Kaminsky W editors. Metallocene-based polyolefins. Chichester: Wiley, 2000, vol.2, p. 3.

41) P. Longo, A. Proto, A. Grassi, P. Ammendola, *Macromolecules* **1991**, *24*, 4624.

42) J. A. Ewen, M. J. Elder, R. L. Jones, L. Haspelagh, J. L. Atwood, S. G. Bott, K. Robinson, *Makromol. Chem., Macromol. Symp*. **1991**, *48/49*, 253.

43) G. Balbontin, D. Dainelli, M. Galimberti, G. Paganetto, *Macromol. Chem.* **1992**, *193*, 693.

44) H. G. Alt, A. Koppl, *Chem Rev* **2000**, *100*, 1205.

45) A. Razavi, L. Peters, L. Nafpliotis, J. L. Atwood, In: Soga K, Terano M, editors, Catalyst design for tailor-made polyolefins. Tokyo: Kodansha, 1994 (supplement).

46) W. A. Herrmann, J. Rohrmann, E. Herdtweck, W. Spaleck, A. Winter, *Angew. Chem., Int. Ed. Engl.* **1989**, *28*, 1511.

47) T. Shiomura, M. Kohno, N. Inoue, T. Asanuma, R. Sugimoto, T. Iwatani, O. Uchida, S. Kimura, S. Harima, H. Zenkoh, E. Tanaka, *Macromol. Symp.* **1996**, *101*, 289.

48) S. A. Miller, J. E. Bercaw, 217th American Chemical Society National Meeting Poster INOR 151; Anaheim, CA; 1999.

49) a) A. Razavi, V. Bellia, Y. De Brauwer, K. Hortmann, L. Peters, S. Sirole, S. Van Belle, U. Thewalt, *Macromol Symp* **2004**, *213*,157. b) A. Razavi, V. Bellia, Y. De Brauwer, K.

Hortmann, L. Peters, S. Sirole, S. Van Belle, U. Thewalt, *Macromol Chem Phys* **2004**, *205*, 347.

50) E. Albizzati, L. Resconi, A. Zambelli, *Eur. Pat. Appl.* 387609 (Himont Inc.), 1991; *Chem.Abstr*. **1991**, *114*, 62980a.

51) F. Grisi, P. Longo, A. Zambelli, J. A. Ewen, *J. Mol. Catal. A Chem.* **1999**, *140*, 225.

52) a) L. Oliva, P. Longo, A. Zambelli, *Macromolecules* **1996**, *29*, 6383. b) A. Borriello, V. Busico, R. Cipullo, J. C. Chadwick, O. Sudmeijer, *Macromol. Rapid Commun*. **1996**, *17*, 589.

53) a) T. A. Herztog, L. Zubris, J. E. Bercaw, *J. Am. Chem. Soc*. **1996**, *118*, 11988; b) D. Veghini; J. E. Bercaw, *Polym. Prepr*. **1998**, *39*, 210; c) D. Veghini, L. M. Henling, T. J. Burkhardt, J. E. Bercaw, *J. Am. Chem. Soc*. **1999**, *121*, 564.

54) a) J. C. Stevens, F. J. Timmers, D. R. Wilson, G. F. Schmidt, P. N. Nickias, R. K. Rosen, G. W. Knight, S. Y. Lais, *Eur Pat Appl* 0416815, 1990 (Dow Chemical Company). b) J. C. Stevens, *Stud Surf Sci Catal* **1994**, *89*, 277.

55) J. Okuda, In *Metalorganic catalysts for synthesis and polymerization*, W. Kaminsky editor Berlin: Springer, 1999. p. 200.

56) A. L. McKnight, R. M. Waymouth, *Chem. Rev.* **1998**, *98*, 2587.

57) L. Resconi, In *Metallocene Catalysts*, W. Kaminsky, J. Scheirs editors, New York: Wiley. 1999. p. 467.

58) L. Resconi, I. Camurati, C. Grandini, M. Rinaldi, N. Mascellani, O. Traverso, *J. Organomet. Chem*. **2002**, *664*, 5.

59) J. A. M. Canich, *US Patent* 5504169 (Exxon), 1996. J. A. M. Canich, US Patent 5026798 (Exxon), 1991.

60) J. Okuda, F. J. Schattenmann, S. Wokadlo, W. Massa, *Organometallics* **1995**, *14*, 789.

61) T. Shiomura, T. Asakura, N. Inoue, *Macromol. Rapid Commun.* **1996**, *17*, 9. T. Shiomura, T. Asakura, T. Sunaga, *Macromol. Rapid Commun.* **1997**, *18*, 169.

62) H. Hagihara, T. Shiono, T. Ikeda, *Macromolecules* **1997**, *30*, 4783. H. Hagihara, T. Shiono, T. Ikeda, *Macromolecules* **1998**, *31*, 3184.

63) A. Razavi, V. Bellia, Y. De Brauwer, K. Hortmann, M. Lambrecht, O. Miserque, L. Peters, S. Van Belle, In *Metalorganic Catalysts for Synthesis and Polymerization*, W. Kaminsky editor Berlin: Springer-Verlag, 1999. A. Razavi, *Eur. Pat. Appl.* 96111127,5 (Atofina). A. Razavi, PCT/EP97/036449 (Atofina), *Int Appl WO* 98/02469, 1998. B. Haveaux, T. Coupin, PCT/EP99/00371 (Atofina), *Int Appl WO* 99/37711, 1999.

64) A. Razavi, U. Thewalt, *J. Organomet. Chem.* **2001**, *621*, 267. A. Razavi, (Atofina) PCT/EP00/08883, Int Appl WO 01/19877, 2001.

65) A. Razavi, V. Bellia, Y. De Brauwer, K. Hortmann, L. Peters, S. Sirole, S. Van Belle, V. Marine, J. Lopez, *J. Organomet. Chem.* **2003**, *684*, 206.

66) V. Busico, R. Cipullo, F. Cutillo, G. Talarico, A. Razavi, *Macromol. Chem. Phys.* **2003**, *204*, 1269.

67) C. Grandini, I. Camurati, S. Guidotti, N. Mascellari, L. Resconi, I. E. Nifant'ev, I. A. Kashulin, P. V. Ivchenko, P. Mercandelli, A. Sironi, *Organometallics* **2004**, *23*, 344.

68) L. Resconi, S. Guidotti, G. Baruzzi, C. Grandini, I. E. Nifant'ev, I. A. Kashulin, P. V. Ivchenko, *PCT Int Appl WO* 01/53360 (Basell: Italy), 2001.

69) L. K. Johnson, C. M. Killian, M. Brookhart, *J. Am. Chem. Soc*. **1995**, *117*, 6414.

70) M. Brookhart, L. K. Johnson, C. M. Killian, S. Mecking, J. Tempel, *Polym. Prepr. Am. Chem. Soc., Div. Polym. Chem.* **1996**, *37*, 254.

71) S. D. Ittel, L. K. Johnson, M. Brookhart, *Chem. Rev.* **2000**, *100*, 1169.

72) C. Pellecchia, A. Zambelli, *Macromol. Rapid Commun.***1996**, *17*, 333.

73) C. Pellecchia, A. Zambelli, M. Mazzeo, D. Pappalardo, *J. Mol. Catal. A: Chem*. **1998**, *128*, 229.

74) C. Pellecchia, A. Zambelli, L. Oliva, D. Pappalardo, *Macromolecules* **1996**, *29*, 6990.

75) B. L. Small, M. Brookhart, A. M. A. Bennett, *J. Am. Chem. Soc.* **1998**, *120*, 4049.

76) G. J. P. Britovsek, V. C. Gibson, B. S. Kimberley, P. J. Maddox, S. J. McTavish, G. A. Solan, A. J. P. White, D. J. Williams, *Chem.Commun.* **1998**, 849.

77) B. L. Small, M. Brookhart, *Polym. Prepr. Am. Chem. Soc., Div. Polym.Chem* **1998**, *39*, 213.

78) B. L. Small, M. Brookhart, *Macromolecules* **1999**, *32*, 2120.

79) C. Pellecchia, M. Mazzeo, D. Pappalardo, *Macromol. Rapid Commun.* **1998**, *19*, 651.

80) J. Tian, G. W. Coates, *Angew. Chem., Int. Ed.* **2000**, *39*, 3626.

81) J. Tian, P. D. Hustad, G. W. Coates, *J. Am. Chem. Soc.* **2001**, *123*, 5134.

82) P. D. Hustad, J. Tian, G. W. Coates, *J. Am. Chem. Soc.* **2002**, *124*, 3614.

83) T. Fujita, Y. Tohi, M. Mitani, S. Matsui, J. Saito,M. Nitabaru, K. Sugi, H. Makio, T. Tsutsui, (Mitsui Chemicals Inc.), EP 0874005, 1998, [Chem. Abstr. 1998, 129, 331166]. Matsui, S.; Mitani, M.; Saito, J.; Tohi, Y.; Makio, H.; Tanaka, H.; Fujita, T. *Chem. Lett.* **1999**, 1263-1264. Matsui, S.; Tohi, Y.; Mitani, M.; Saito, J.; Makio, H.; Tanaka, H.; Nitabaru, M.; Nakano, T.; Fujita, T. *Chem. Lett.* **1999**, 1065-1066. Matsui, S.; Mitani, M.; Saito, J.; Matsukawa, N.; Tanaka, H.; Nakano, T.; Fujita, T. *Chem. Lett.* **2000**, 554-555.

84) S. Matsui, M. Mitani, J. Saito, Y. Tohi, H. Makio, N. Matsukawa, Y. Takagi, K. Tsuru, M. Nitabaru, T. Nakano, H. Tanaka, N. Kashiwa, T. Fujita *J. Am. Chem. Soc.* **2001**, *123*, 6847.

85) S. Matsui, T. Fujita, *Catal. Today* **2001**, *66*, 63.

86) (a) S. Matsui, Y. Inoue, T. Fujita, *J. Synth. Org. Chem. Jpn.* **2001**, *59*, 232. (b) M. Mitani, R. Furuyama, J-I. Mohri, J. Saito, S. Ishii, H. Terao, T. Nakano, H. Tanaka, T. Fujita, *J. Am. Chem. Soc.* **2003**, *125*, 4293.

87) N. Matsukawa, S. Matsui, M. Mitani, J. Saito, K. Tsuru, N. Kashiwa, T. Fujita, *J. Mol. Catal. A-Chem.* **2001**, *169*, 99.

88) J. Saito, M. Mitani, J. Mohri, Y. Yoshida, S. Matsui, S. Ishii, S. Kojoh, N. Kashiwa, T. Fujita, *Angew. Chem., Int. Ed.* **2001**, *40*, 2918.

89) M. Mitani, Y. Yoshida, J. Mohri, K. Tsuru, S. Ishii, S. Kojoh, T. Matsugi, J. Saito, N. Matsukawa, S. Matsui, T. Nakano, H. Tanaka, N. Kashiwa, T. Fujita (Mitsui Chemicals Inc.), PCT Int. Appl. WO 2001055231 (Chem. Abstr. 2001, 135, 137852).

90) J. Saito, M. Mitani, M. Onda, J. I. Mohri, S. I. Ishii, Y. Yoshida, T. Nakano, H. Tanaka, T. Matsugi, S. I. Kojoh, N. Kashiwa, T. Fujita *Macromol. Rapid Commun.* **2001**, *22*, 1072.

91) A. Grassi, A. Zambelli, L. Resconi, E. Albizzati, R. Mazzocchi, *Macromolecules* **1988**, *21*, 617.

92) G. Natta G, P. Corradini, P. Ganis, *Makromol Chem* **1960**, *39*, 238.

93) G. Natta, P. Corradini, P. Ganis, *J. Polym. Sci.* **1962**, *58*, 1191.

94) G. Natta, M. Peraldo, G. Allegra, *Makromol Chem* **1964**, *75*, 215.

95) P. Corradini, G. Natta, P. Ganis, P. A. Temussi, *J. Polym. Sci. Part C* **1967**, *16*, 2477.

96) a) B. Pirozzi, R. Napolitano, *Eur. Polym. J.* **1992**, *28*, 703. b) P. Corradini, R. Napolitano, V. Petraccone, B. Pirozzi, A. Tuzi, *Macromolecules* **1982**, *15*, 1207. c) R. Napolitano, B. Pirozzi, *Polymer* **1997**, *38*, 4847. d) P. Corradini, C. De Rosa, G. Guerra, B. Pirozzi, V. Venditto, *Gazz. Chim. It.* **1992**, *122*, 305.

97) B. Lotz, A. J. Lovinger, R. E. Cais, *Macromolecules* **1988**, *21*, 2375.

98) A. J. Lovinger, B. Lotz, D. D. Davis, *Polymer* **1990**, *31*, 2253.

99) A. J. Lovinger, D. D. Davis, B. Lotz, *Macromolecules* **1991**, *24*, 552.

100) A. J. Lovinger, B. Lotz, D. D. Davis, F. J. Padden, *Macromolecules* **1993**, *26*, 3494. A. J. Lovinger, B. Lotz, D. D. Davis, *Polym. Prepr. Am. Chem. Soc.* **1992**, *33*, 552.

101) A. J. Lovinger, B. Lotz, D. D. Davis, M. Schumacher, *Macromolecules* **1994**, *27*, 6603.

102) W. Stocker, M. Schumacher, S. Graff, J. Lang, J. C. Wittmann, A. J. Lovinger, B. Lotz, *Macromolecules* **1994**, *27*, 6948.

103) M. Schumacher, A. J. Lovinger, P. Agarwal, J. C. Wittmann, B. Lotz, *Macromolecules* **1994**, *27*, 6956.

104) B. Lotz, J. C. Wittmann, A. J. Lovinger, *Polymer* **1996**, *37*, 4979.

105) A. J. Lovinger, B. Lotz, *J. Polym. Sci. Polym. Phys. Ed.* **1997**, *35*, 2523.

106) J. Zhang, D. Yang, A. Thierry, J. C. Wittmann, B. Lotz, *Macromolecules* **2001**, *34*, 6261.

107) Y. Chatani, H. Maruyama, K. Noguchi, T. Asanuma, T. Shiomura, *J. Polym. Sci., Part C* **1990**, *28*, 393.

108) Y. Chatani, H. Maruyama, T. Asanuma, T. Shiomura, *J. Polym. Sci., Polym. Phys.* **1991**, *29*, 1649.

109) C. De Rosa, P. Corradini, *Macromolecules* **1993**, *26*, 5711.

110) C. De Rosa, F. Auriemma, P. Corradini, *Macromolecules* **1996**, *29*, 7452.

111) C. De Rosa, F. Auriemma, V. Vinti, *Macromolecules* **1997**, *30*, 4137.

112) C. De Rosa, F. Auriemma, V. Vinti, *Macromolecules* **1998**, *31*, 7430.

113) C. De Rosa, F. Auriemma, V. Vinti, M. Galimberti, *Macromolecules* **1998**, *31*, 6206.

114) F. Auriemma, C. De Rosa, P. Corradini, *Macromolecules* **1993**, *26*, 5719.

115) F. Auriemma, C. De Rosa, P. Corradini, *Rend. Fis. Acc. Lincei* **1993**, *4*, 287.

116) F. Auriemma, R. Born, H. W. Spiess, C. De Rosa, P. Corradini, *Macromolecules* **1995**, *28*, 6902.

117) F. Auriemma, R. H. Lewis, H. W. Spiess, C. De Rosa, *Macromol. Chem. Phys.* **1995**, *196*, 4011.

118) F. Auriemma, C. De Rosa, O. Ruiz de Ballesteros, P. Corradini, *Macromolecules* **1997**, *30*, 6586.

119) F. Auriemma, C. De Rosa, O. Ruiz de Ballesteros, V. Vinti, *J. Polym. Sci., Polym. Phys.* **1998**, *36*, 395.

120) B. Lotz, C. Mathieu, A. Thierry, A. J. Lovinger, C. De Rosa, O. Ruiz de Ballesteros, F. Auriemma, *Macromolecules* **1998**, *31*, 9253.

121) C. De Rosa, F. Auriemma, O. Ruiz de Ballesteros, *Polymer* **2001**, *42*, 9729.

122) C. De Rosa, O. Ruiz de Ballesteros, M. Santoro, F. Auriemma, *Polymer* **2003**, *44*, 6267.

123) C. De Rosa, O. Ruiz de Ballesteros, M. Santoro, F. Auriemma, *Macromolecules* **2004**, *37*, 1816.

124) C. De Rosa, O. Ruiz de Ballesteros, F. Auriemma, *Macromolecules* **2004**, *37*, 7724.

125) F. Auriemma, O. Ruiz de Ballesteros, C. De Rosa, *Macromolecules* **2001**, *34*, 4485.

126) C. De Rosa, M. C. Gargiulo, F. Auriemma, O. Ruiz de Ballesteros, A. Razavi, *Macromolecules* **2002**, *35*, 9083.

127) F. Auriemma, C. De Rosa, *J. Am. Chem. Soc.* **2003**, *125*, 13143.

128) a) F. Auriemma, C. De Rosa, *Macromolecules* **2003**, *36*, 9396. b) F. Auriemma, C. De Rosa, S. Esposito, G. R. Mitchell, *Ang. Chem. Intern. Ed.* **2007**, *46*, 4325.

129) S. Rastogi, D. La Camera, F. van der Burgt, A. E. Terry, S. Z. D. Cheng, *Macromolecules* **2001**, *34*, 7730.

130) T. Nakaoki, Y. Ohira, H. Hayashi, F. Horii, *Macromolecules* **1998**, *31*, 2705.

131) V. Vittoria, L. Guadagno, A. Comotti, R. Simonutti, F. Auriemma, C. De Rosa, *Macromolecules* **2000**, *33*, 6200.

132) a) Y. Ohira, F. Horii, T. Nakaoki, *Macromolecules* **2000**, *33*, 1801. b) T. Nakaoki, T. Yamanaka, Y. Ohira, F. Horii, *Macromolecules* **2000**, *33*, 2718. c) Y. Ohira, F. Horii, T. Nakaoki, *Macromolecules* **2000**, *33*, 5566. d) Y. Ohira, F. Horii, T. Nakaoki, *Macromolecules* **2001**, *34*, 1655. e) T. Nakaoki, Y. Ohira, F. Horii, *Polymer* **2001**, *42*, 4555.

133) a) C. De Rosa, In *Materials Chirality, Topics in Stereochemistry*. M. M. Green, R. J. M. Nolte, E. W. Meijer editors, Hoboken: John Wiley & Sons Inc. 2003. vol. 24, p. 71. b) C. De Rosa, F. Auriemma, *Crystals and Crystallinity in Polymers*, Wiley, 2014.

134) C. De Rosa, F. Auriemma, O. Ruiz de Ballesteros, *Chem. Mater*. **2006**, *18*, 3523.

135) C. De Rosa, F. Auriemma, F.; Ruiz de Ballesteros, O. *Phys. Rev. Lett.* **2006**, *96 (16)*, 167801.

136) C. De Rosa, F. Auriemma, O. Ruiz de Ballesteros, L. Resconi, A. Fait, E. Ciaccia, I. Camurati, *J. Am. Chem. Soc.* **2003**, *125*, 10913.

137) C. De Rosa, F. Auriemma, O. Ruiz de Ballesteros, *Macromolecules* **2003**, *36*, 7607.

138) C. De Rosa, F. Auriemma, O. Ruiz de Ballesteros, *Macromolecules* **2004**, *37*, 1422.

139) A. Peterlin, In *Encyclopedia of Polymer Science and Engeneering*. New York: Wiley. 1987. vol. 10, p 26.

140) C. De Rosa, F. Auriemma, I. Orlando, G. Talarico, L. Caporaso, *Macromolecules* **2001**, *34*, 1663.

141) a) M. Kakugo, *Macromol. Symp*. **1995**, *89*, 545. b) N. Naga, K. Mizunuma, H. Sadatoshi, M. Kakugo, *Macromolecules* **1997**, *30*, 2197. c) N. Naga, K. Mizunuma, H. Sadatoshi, M. Kakugo, *Polymer* **2000**, *41*, 203.

142) a) C. De Rosa, F. Auriemma, V. Vinti, A. Grassi, M. Galimberti, *Polymer* **1998**, *39*, 6219. b) C. De Rosa, F. Auriemma, G. Talarico, V. Busico, L. Caporaso, D. Capitani, *Macromolecules* **2002**, *35*, 1314. c) C. De Rosa, F. Auriemma, E. Fanelli, G. Talarico, D.

Capitani, *Macromolecules* **2003**, *36*, 1850. d) C. De Rosa, F. Auriemma, *Adv. Mat.* **2005**, *17*, 1503. e) C. De Rosa, F. Auriemma, *Polymer* **2006**, *47*, 2179. f) C. De Rosa, F. Auriemma, *Macromolecules* **2006**, *39*, 249.

143) a) C. De Rosa, G. Talarico, L. Caporaso, F. Auriemma, O. Fusco, M. Galimberti, *Macromolecules* **1998**, *31*, 9109. b) C. De Rosa, F. Auriemma, L. Caporaso, G. Talarico, D. Capitani, *Polymer* **2000**, *41*, 2141. c) B. Zhang, D. Yang, C. De Rosa, S. Yan, *Macromolecules* **2002**, *35*, 4646. d) C. De Rosa, F. Auriemma, L. Caliano, G. Talarico, M. Corradi, *Macromolecules* **2008**, *41*, 5301. e) C. De Rosa, F. Auriemma, M. Corradi, L. Caliano, G. Talarico, *Macromolecules* **2008**, *41*, 8712. f) C. De Rosa, F. Auriemma, L. Caliano, M. Corradi, *Macromol. Mater. Eng*. **2008**, *293*, 810. g) C. De Rosa, F. Auriemma, M. Corradi, L. Caliano, O. Ruiz de Ballesteros, R. Di Girolamo, *Macromolecules* **2009**, *42*, 4728. h) S. Jiang, H. Li, C. De Rosa, F. Auriemma, S. Yan, *Macromolecules* **2010**, *43*, 1449.

144) E. D. Schwerdtfeger, S. A. Miller, *Macromolecules* **2007**, *40*, 5662.

145) J. Arranz-Andrés, J. L. Guevara, T. Velilla, R. Quijada, R. Benavente, E. Pérez, M. L. Cerrada, *Polymer* **46**, 12287 (2005).

146) C. De Rosa, F. Auriemma, R. Di Girolamo, G. Giusto, O. Ruiz de Ballesteros *Macromolecules* **2010**, *43*, 9802.

147) S. Jungling, R. Mulhaupt, D. Fisher, F. Langhauser, *Ang. Makromol. Chem.* **1995**, *229*, 93.

148) R. Thomann, J. Kressler, R. Mulhaupt, *Macromol. Chem. Phys.* **1997**, *198*, 1271. R. Thomann, J. Kressler, R. Mulhaupt, *Polymer* **1998**, *39*, 1907.

149) G. Hauser, J. Schmidtke, G. Strobl, *Macromolecules* **1998**, *31*, 6250.

150) S. M. Graef, U. M. Wahner, A. J. Van Reenen, R. Brull, R. D. Sanderson, H. Pasch, *J. Polym. Sci., Part A*, **2002**, *40*, 128.

151) C. De Rosa, V. Venditto, G. Guerra, B. Pirozzi, P. Corradini, *Macromolecules* **1991**, *24*, 5645.

152) C. De Rosa, V. Venditto, G. Guerra, P. Corradini, *Makromol. Chem*. **1992**, *193*, 1351.

153) C. De Rosa, G. Guerra, A. Grassi, *Macromolecules* **1996**, *29*, 471.

154) B. Zhang, D. Yang, C. De Rosa, S. Yan, J. Petermann *Macromolecules* **2001**, *34*, 5221.

155) C. De Rosa, F. Auriemma, *Polymer. Chem*. **2011**, *2*, 2155.

156) J. Brandrup, E. H. Immergut, E. A. Grulke, *Polymer Handbook;* John Wiley: New York, 1999.

157) R. Thomann, C. Wang, J. Kressler, S. Jüngling, R. Mülhaupt, *Polymer* **1995**, *36*, 3795.

158) N. Ahmad, R. Di Girolamo, F. Auriemma, C. De Rosa, N. Grizzuti, *Macromolecules* **2013**, *46*, 7940.

159) M. Avrami, *J. Chem. Phys*. **1939**, *7*, 1103; *J. Chem. Phys*. **1940**, *8*, 212; *J. Chem. Phys*. **1941**, *9*, 177.

160) a) A. N. Kolmogorov, *Bull. Acad. Sci. U.S.S.R. Phys. Ser*. **1937**, *3*, 555. b) A. M. Johnson, R. F. Mehl, *Trans. Am. Inst. Min. Engrs* **1939**, *135*, 417. c) N. X. Sun, X. D. Liu, K. Lu, *Scripta Materialia*, **1996**, *34*, 1201.

161) I. Shina, R. K. Mandal *Trans. Ind. Inst. Metals* **2008**, *61*, 131. I. Shina, R. K. Mandal *J. Non-Cryst. Solids* **2009**, *355*, 361.

162) D. W. Henderson, *J. Thermal Analysis*, **1979**, *15*, 325.

163) A. Seidlitz, T. Thurn-Albrecht, S*mall-angle X-ray scattering for morphological analysis of semicrystalline polymers*, in *Polymer Morphology: Principles, Characterization, and Processing*, Wiley, **2016**.

164) C. Santa Cruz, N. Stribeck, H. G. Zachmann, F. J. Baltá Calleja, *Macromolecules* **1991**, *24*, 5980.

165) W. Ruland, *Colloid Polym Sci* **1977**, *255*, 417.

166) T. Butz, *Fourier Transformation for Pedestrians*. Springer; **2006**.

167) G. Strobl, *The Physics of Polymers: Concepts for Understanding Their Structures and Behavior*, Berlin Heidelberg: Springer-Verlag, **2007**.

168) G. Porod, *Colloid Polym Sci*, **1951**, *124(2)*, 83.

169) T. Thurn-Albrecht, G. Strobl, *Macromolecules*, **1995**, *28*, 5827.

170) R. J. Roe, *Methods of X-Ray and Neutron Scattering in Polymer Science*, Oxford University Press, **2000**.

171) O. Glatter, O. Kratky, *Small Angle X-Ray Scattering*. London:Academic Press, **1982**.

172) R. Hosemann, S. N. Bagchi, *Direct Analysis of Diffraction by Matter*. Amsterdam: North-Holland, **1962**.

173) D. Debye and A. M. Beuche, *J. Appl. Phys*, **1949**, *20*, 518.

174) C. G. Vonk, *J. Appl. Cryst*., **1975**, *8*, 340.

CHAPTER II

Ethylene-Propylene Elastomers

2.1 Ethylene-propylene random copolymers

The relationships between microstructure, crystallinity and elastic properties of sPP and sPP-based copolymers and of semicrystalline block copolymers discussed in the chapters I and II, have been compared with those of conventional and commercial rubbers based on ethylene-propylene random copolymers (EPM).

EPM are elastomers based on ethylene and propene with ethylene content in the range 45 - 75 wt%. These polymeric materials and their derivatives are one of the most widely used synthetic rubbers for their properties and versatility. Amorphous or low crystalline grades have excellent low temperature flexibility with glass transition temperature of about -60°C. They are appreciable for their excellent resistance to heat, oxidation, ozone and weather aging due to their stable, saturated polymer backbone structure. As non-polar elastomers, they have good electrical resistivity, as well as resistance to polar solvents, such as water, acids, alkalies, phosphate esters and many ketones and alcohols. Heat aging resistance up to 130°C can be obtained with properly selected sulfur acceleration systems and heat resistance at 160°C can be obtained with peroxide cured compounds. Compression set resistance is good, particularly at high temperatures, if sulfur donor or peroxide cure systems are used.[1]

The versatility of EPM is due to the possibility to tailor their physical properties controlling the microstructure through different polymerization strategies. In fact, depending on the ethylene/propene ratio, the presence of a third monomer and/or fillers, different degree of crystallinity, crystallization behavior, thermal, mechanical and viscoelastic properties can be obtained.

Ethylene-propene copolymers were first synthesized by Giulio Natta and coworkers using stereospecific catalytic systems.[2] Based on the observation that "the exceptional properties of natural rubber are due to the fact that it hardly crystallizes", Natta and his coworkers developed the idea of introducing defects in the ordered chains of linear crystalline polymers, such as polyethylene (PE), to induce elastic properties. It is well known that PE does not show elastic properties notwithstanding the high flexibility of the chain because of his exceptional ability to crystallize. According to the Natta's idea, the controlled

incorporation of constitutional defects, as comonomeric units, in PE hinders the crystallization, keeping at the same time the high flexibility of the chains.[2]

One of the monomers used for introducing defects and controlled disorder is propene. In fact, besides the insertion of the ethylene unit, four different modes of insertion of propene are possible: 1,2 with *re* and *si* face or 2,1 with *re* and *si* face. The five different monomer insertions can be considered as five different repeating units present in the macromolecular chain (Figure 2.1).[3] Therefore, depending on the distribution and placement of propene units in the PE chains different degrees of disorder can be obtained (Figure 2.2). The presence of all the four possible modes of propene insertions is related to the stereoselectivity and regioselectivity of the Ziegler-Natta catalyst used in polymerization.[3]

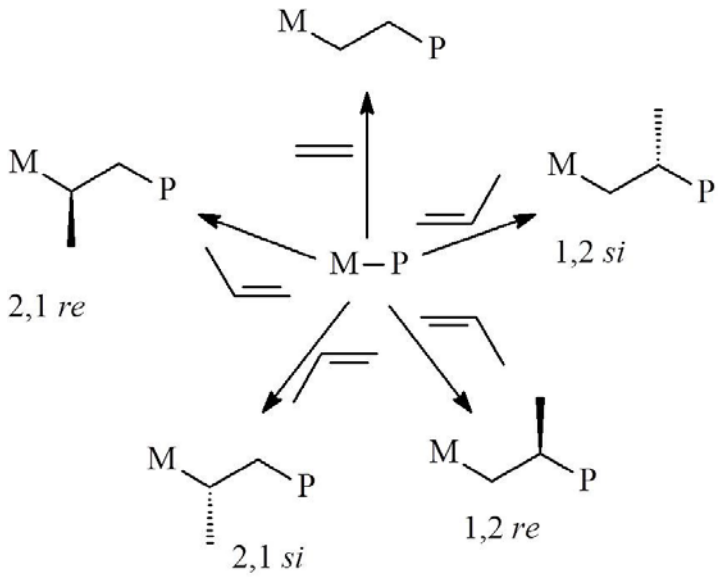

Figure 2.1. *Schematic representation of five different modes of insertion of monomers ethylene and propene in the M-P bond, where M is the metallic center of the catalyst and P represents the growing chain.*[3]

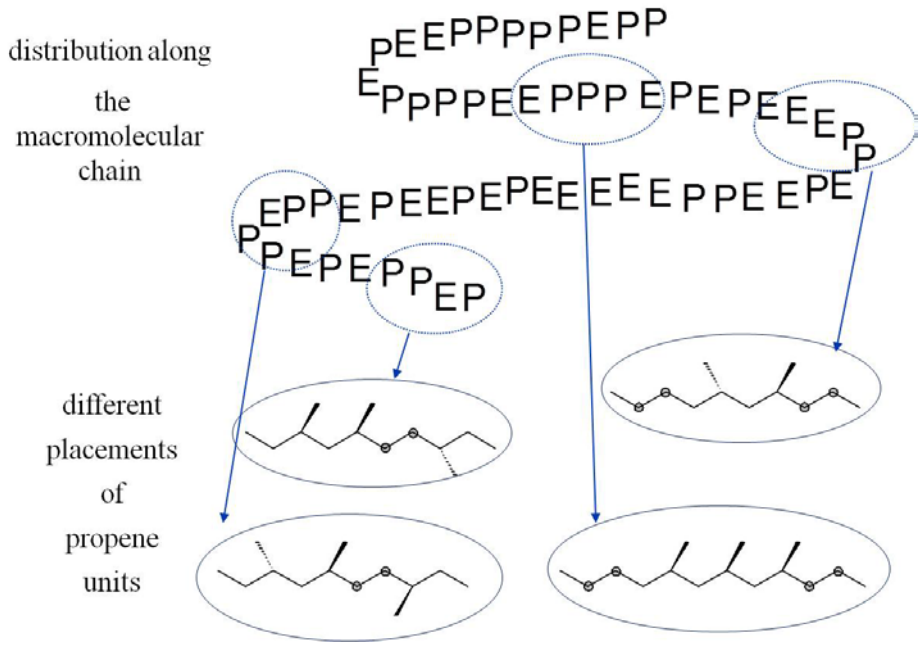

Figure 2.2. *Constitutional sequences and different configurations of propene units in ethylene-propene copolymers.*[3]

2.1.1 Ethylene-propene-diene random terpolymers (EPDM) and fillers

A saturated ethylene-propene copolymer can be crosslinked by using peroxides. However, a sulphur based vulcanization is beneficial to achieve better properties of the rubber and avoid side reactions promoted by the contemporary presence of radicals and tertiary carbon atoms, that leads to polymer degradation.[3] To allow a sulphur based vulcanization, double bonds have to be introduced in the macromolecular chain of an ethylene-propene copolymer. This is realized by introducing a diene as third co-monomer in the EPM copolymer, resulting in the EPDM terpolymer.

Three dienes have been used so far in the manufacture of EPDM:

- 5-ethylidene-2-norbornene (ENB)
- dicyclopentadiene (DCPD)
- 1,4-hexadiene (1,4-HD)

Their structures are shown in Figure 2.3. In these dienes, the double bond A inside the ring is reactive in polymerization, whereas the double bond B is unreactive (or very little reactive) in polymerization and is reactive in vulcanization.

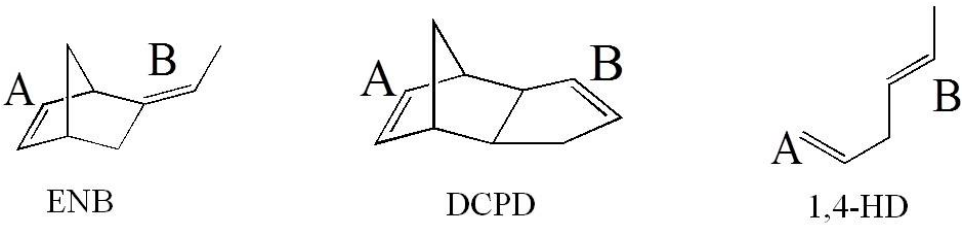

***Figure 2.3**. The main dienes used as termonomer in the production of EPDM. Double bond A is inserted in the polymer backbone and is highly reactive in polymerization. Double bond B is in the side chain and is not reactive or has a very low reactivity in polymerization, but it is reactive in vulcanization with a sulphur cure system.*[3]

5-ethylidene-2-norbornene (ENB) is a bicyclic nonconjugated diene. It presents two chiral centers: the two bridgehead carbon atoms 1 and 4 (Figure 2.4). For each *E* and *Z* isomers arising from the placement of the methyl group, there are two enantiomers, R,R or S,S (Figure 2.4).

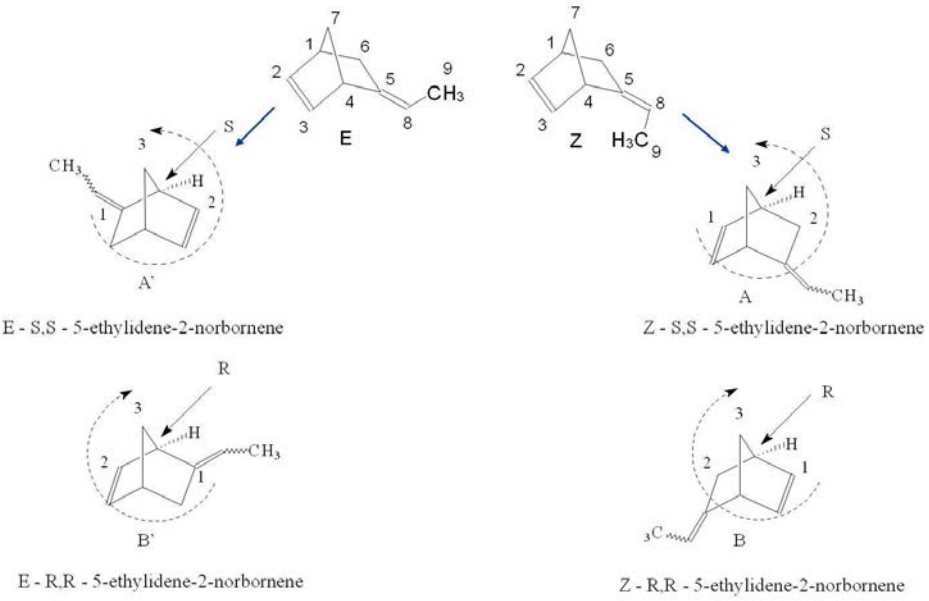

Figure 2.4. 5-ethylidene-2-norbornene presents two chiral centers: the two bridgehead carbon atoms 1 and 4. Structures A and A' correspond to the E or Z (S,S) isomer; analogously B and B' correspond to the E or Z (R,R) configuration.

ENB is industrially prepared in two steps:

1) Diels-Alder reaction between cyclopentadiene and 1,3-butadiene to give the endo-5-vinyl-2-norbornene and the exo-5-vinyl-2-norbornene in an isomeric mixture (Figure 2.5).

2) Catalytic isomerization promoted by a base of the *endo* and *exo*-5-vinyl-2-norbornene to give the (E) and (Z)-5-ethylidene-2-norbornene (Figure 2.6).

Therefore, the result is a mixture of 4 isomers and the isomeric composition depends on the synthetic approach used for its preparation.

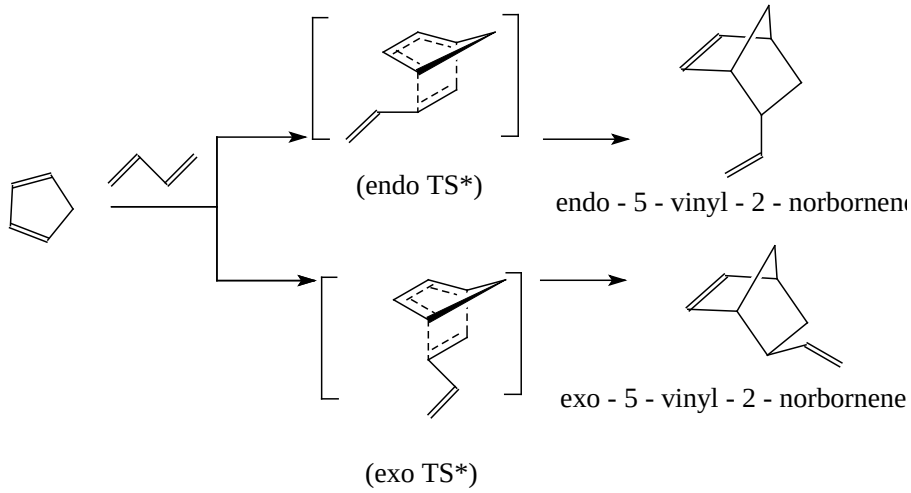

Figure 2.5*. Diels-Alder reaction between cyclopentadiene and 1,3-butadiene to give endo or exo 5-vinyl-2-norbornene.*

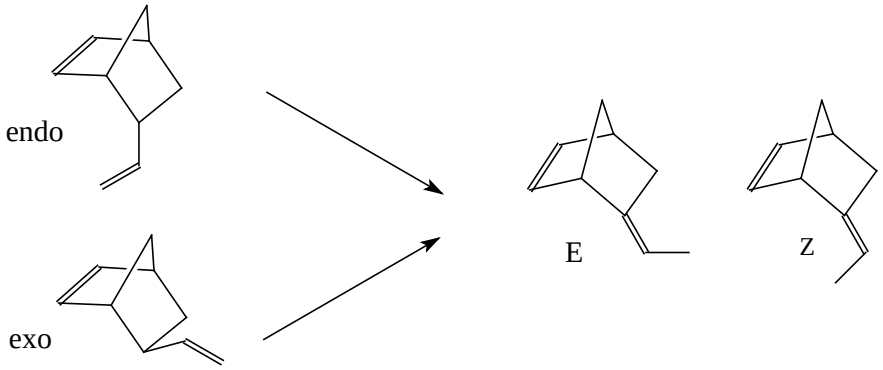

Figure 2.6. *Isomerization of 5-vinyl-norbornene to 5-ethylidene-2-norbornene.*

As mentioned before, the double bond that reacts in polymerization (double bond A in Figure 2.3) is that inside the ring. The addition of ENB during terpolymerization with ethylene and propylene may in principle occur through 2,3 or 3,2 insertion and with *exo* or *endo* addition. Therefore, many different situations may occur for the insertion of ENB in the growing chain. A different reactivity of the isomers (E-R,R / E-S,S / Z-R,R / Z-S,S) is generally not observed whatever the steric hindrance of the catalyst is.[3]

ENB may undergo reactions promoted by cationic catalysts. This is a relevant aspect because the catalytic systems most applied on industrial scale as the vanadium based catalysts, contain components with a known cationic catalytic capability. Catalytic side reactions can bring to the formation of branching of the polymer, presence of gels oligomers of the diene and broadening of molecular mass distribution. Similar side reaction can occur with other dienes.[3]

2.1.2 Curing agents and commercial fillers and their effect on mechanical properties of EPDM

Many applications of EPDM require a curing process in order to produce a crosslinked rubber. EPDM can be cured with sulphur and peroxide, depending on the requirements of the application. Peroxide cured rubbers are used for high temperature applications, in part due to the strong carbon-carbon cross-links, while sulphur-cured EPDM generally exhibit higher tear and tensile strength.[1] Curing by use of sulfur alone is a slow process, so curative agents are added to aid in curing. In sulfur curing systems, sulfur is first typically activated by zinc oxide and an accelerator. Accelerators, such as 2-mercaptobenzothiazole, speed up the sulfur curing process and act by forming an adduct with sulfur making it a more active species.[1]

Besides curative agents, non-curative ingredients are generally added for improving processing and mechanical performances. Non-curative agents are ingredients that will not participate directly in the curing of EPDM rubber. These ingredients include the processing aides, antioxidants, and fillers. Processing aides are petroleum based oils that are added to help when the polymer is cured inside a mold. The oils prevent the rubber from sticking to the mold surface, which could otherwise cause defects in the product or hinder its removal from the mold. Antioxidants are compounds that protect the final rubber product from degradation caused by heat, oxygen, ozone, UV radiation, etc. The antioxidants act by scavenging the radicals that are caused by the sources of degradation.[4] Reinforcing fillers include carbon blacks, silica and resins, which increase the strength of vulcanized rubber more than tenfold.[5-7]

Filling carbon blacks in elastomers and plastics also reduces the cost of the end product and modifies the electrical and optical properties of the polymer matrix.[8,9]

Reinforcement of rubber by carbon blacks has been intensively studied.[10-13] It is generally accepted that the reinforcement of elastomers and the

improvement of other properties are associated with the chemical and physical interactions between the polymer matrix and carbon blacks.[12-19] When the uncured EPDM is blended well with carbon black for a period of time, EPDM chains have a certain probability to contact with carbon black, and entangle or trap in the voids of carbon black aggregates. As shown in Figure 2.7, the rubber chains become highly immobilized and localized, and form a rubber shell, surrounding the carbon lack particles.[13] Figure 2.8 shows that those carbon black particles, whose surfaces were covered by entangled EPDM chains can be considered as physical cross-links.[12] The physical crosslinking hinders the mobility of rubber chains and restrains the deformation of rubber. Hence, it is understandable that development of a large polymer-filler interface is the most important factor for the degree of reinforcement provided by filler. Therefore, the surface area of carbon black is of great importance for the density of the physical cross-linking. As the surface area of carbon black increases, the number of rubber chains entangling with carbon black aggregates as well as that of the cross-links climbs up.[12,19]

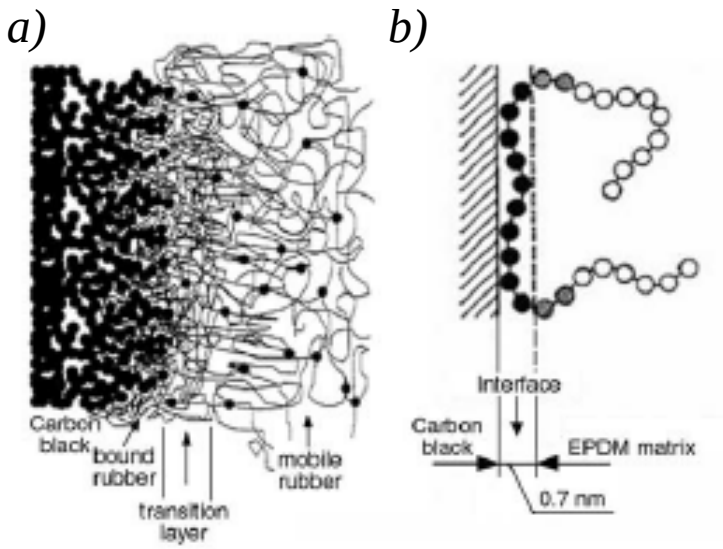

Figure 2.7. *Scheme of the interaction of rubber chains with carbon black: (a) The entanglement of EPDM chains on carbon black; (b) The interface between carbon black and EPDM matrix.*[12,13]

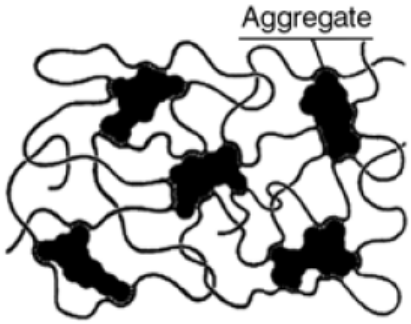

Figure 2.8. *Scheme of the physical network structure in a carbon black filled elastomers.*[12]

2.2 Catalytic systems used for the synthesis of EPM and EPDM

Three families of catalytic systems have been used so far for the preparation of EPDM: Titanium based catalysts, Vanadium based catalysts and Single Center Catalyst (metallocene or constrained geometry). Titanium based EPM grades were commercially available, but they are not anymore industrially produced. Vanadium based catalysts are largely applied for industrial production of EPDM. In the family of SCC, only those based on a constrained geometry have found application on a commercial scale for EPDM production.

2.2.1 Titanium based catalysts

The components of a typical Ziegler-Natta catalytic system are $TiCl_4$ supported on $MgCl_2$, a chlorinated aluminum alkyl $(C_2H_5)_3Al_2Cl_3$, $(C_2H_5)_2AlCl$ as cocatalyst and optionally aromatic esthers as electron donors. Titanium catalysts are well active at high and very high *T*, and also for long times (> 1 hour), however only for EPM. In fact they do not convert dienes also at higher temperature. As reported by Natta and coworkers, ethylene-propene random copolymers produced with this catalytic system generally show a product of the reactivity ratios r_1r_2 higher than 1,[20] indicating a blocky microstructure where ethylene and propene are not randomly distributed along the chain but form longer alternated ethylene and propylene sequencies. These catalysts are highly isospecific in the homopolymerization of propene and also in the case of EPM copolymers the sequences of propylene units are generally isotactic. However, for both iPP homopolymer and propylene-ethylene copolymers the different types of catalyst sites present on the surfaces of the heterogeneous Ziegler-Natta catalyst lead to mixtures of macromolecules having different molecular mass, different stereoregularities and non random distributions of comonomeric units. The comonomers are rather segregated in a fraction or more irregular

blocks. These EPM samples can be generally fractionated with conventional methods of extraction with boiling solvents in different fractions characterized by macromolecules having different composition, which reflect the different crystallinities and melting behavior.

Figure 2.9 shows the ^{13}C NMR spectra of two ethylene-propene random copolymers prepared with titanium based catalyst. The resonances $S_{\alpha\beta}$ and $S_{\beta\gamma}$ typical of 2,1 secondary propene units are not present, indicating a primary 1,2 insertion of propene.[21] The spectrum A of the sample with lower ethylene concentration shows a high intensity of the resonance of the methyl carbon in the isotactic *mmmm* pentad, indicating that this catalytic system remains isospecific also in the presence of ethylene. This seems no longer true in the case of the sample with higher ethylene concentration (spectrum B of Figure 2.9).[21]

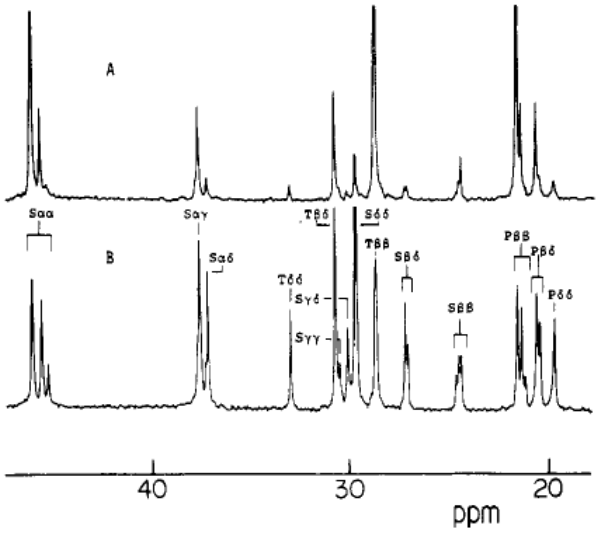

Figure 2.9. *^{13}C NMR spectra of two ethylene-propene random copolymers containing 16.7 and 53.8 mol % of ethylene, respectively.[21]*

Because of the non-random distribution of stereodefects and comonomeric units along the chains and their preferential segregation in blocks, ethylene or propylene sequences (depending on the composition) may be long enough to crystallize. This results in EP copolymers with physical properties different (for example a high melting temperature) from those of copolymers of similar composition but prepared with Vanadium-based catalysts or metallocene catalysts that produce more uniform and random distribution of comonomers and shorter ethylene or propene sequences.

2.2.2 Vanadium based catalysts

The homogeneous vanadium-based catalysts are of great importance and used commercially for the production of ethylene-propylene-diene (EPDM) rubber.[22,23] As discussed in the first chapter, this catalytic system comprises a variety of vanadium compounds, as VCl_4 or V(III)-β-diketonates (V(acetylacetonate)$_3$), an alkyl aluminum halide (typically $Al(C_2H_5)_2Cl$) and a Lewis base (e.g. anisole).[24-26] The precursors vanadium compounds are soluble in hydrocarbons and the oxidation state of vanadium is at least 3.[27] The catalytic systems are thermolabile and quickly decompose at room temperature producing poorly characterized precipitates containing Al, V(II) and Cl,[27,28] unable to promote polymerization. Therefore the polymerization has to be performed either at low temperature, or in the presence of a component able to continuously re-oxidate V(II) to a higher oxidation state during polymerization (for instance a chlorinated ester). This expedient is used for the commercial production of ethylene-propylene and ethylene-propylene-diene rubbers.[22]

These catalysts are soluble in aliphatic and aromatic hydrocarbons, in particular in solvents for industrial processes and remain active in polymerization for short time, less than 1 hour. Despite their critical stability at high temperature and a lower activity compared to other catalysts, they show the lowest decrease of catalytic activity in the presence of ENB, although the chlorinated aluminum alkyls promoter are powerful cationic catalysts for the diene. As discussed for sPP, regio and stereospecifity are not high for these catalysts: once a secondary 2,1 insertion of propene occasionally occurs, the 2,1 insertion tends to be maintained and sequences of secondary insertion much longer than the sequences of primary insertion are obtained. The sequences of secondary insertion lead to monomer sequences with a prevailingly syndiotactic arrangement.

The product of the reactivity ratios r_1r_2 is generally in the range 0.1-1, indicating a random distribution of ethylene and propene units in the chain. The possible presence of dienes does not affect the product of the reactivity ratios.[3] These catalysts introduce the highest degree of disorder in propene sequences allowing the contemporary presence of stereoirregularities and regioirregularities. As a result, the microstructure of the samples is rather complex for the presence of many different defects and the crystallinity that eventually develops from sequences of ethylene long enough is always very low due to the presence stereo- and regio-defects along with comonomeric propene units. The complex microstructure is demonstrated by the ^{13}CNMR

spectrum of a sample of EPM prepared with Vanadium catalyst shown in Figure 2.10. The region of the $S_{\alpha\gamma}$, $S_{\alpha\delta}$ and $S_{\alpha\gamma}$ resonances in the region 34.5-39.0 ppm is, in particular, complex. Moreover, six broad resonances are observed at higher fields, corresponding to both sequence and tacticity effects. In the $S_{\beta\gamma}$, $S_{\beta\delta}$ and $S_{\beta\beta}$ region (24-28 ppm), the effects of ethylene-propylene sequence placement and propylene tacticity are, therefore, mixed together. From the data in this region it is difficult to extract separate information on tacticity and sequence placements. Finally, the methyl region is also complex because many different types of methyl carbons belonging to different constitutional and confirgurational sequences are all squeezed into the 19.5-22.0 ppm region.[29]

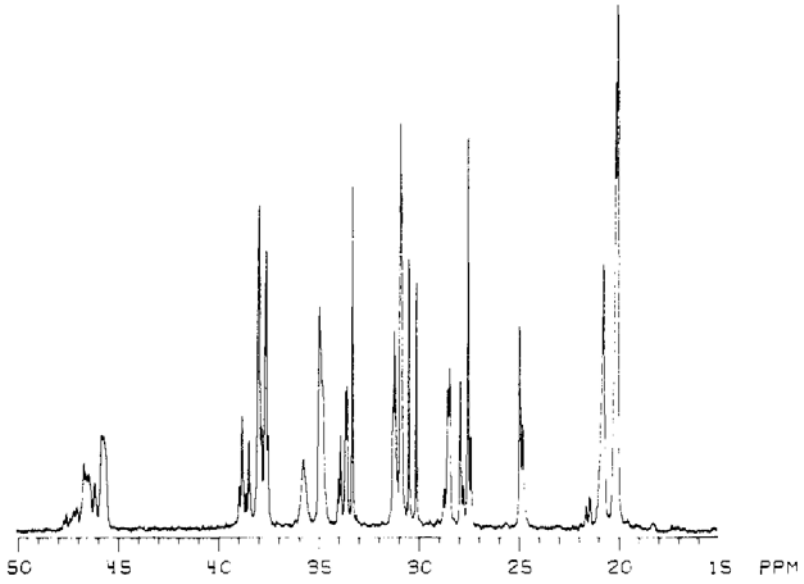

Figure 2.10. *^{13}C NMR spectrum of an ethylene-propene copolymer containing 40 mol % of ethylene prepared with a Vanadium catalyst.*[29]

2.2.3 Metallocene catalysts

As discussed in the first chapter, stereorigid zirconocenes and titanocenes with C_2 symmetry, such as *rac*-ethane(indenyl)$_2$MCl$_2$ (with M = Zr or Ti), in combination with methylaluminoxane (MAO),[30] produce isotactic polypropylene[31-32] (Chart 2.1).

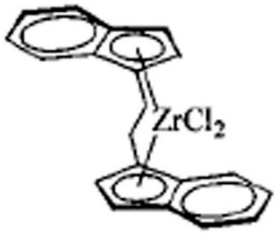

Chart 2.1

The catalytic site is pseudo-tetrahedral and cationic (Figure 2.11), with two indenyl ligands at two coordination sites and the growing polymer chain and a propene molecule at the two remaining coordination sites. The aromatic ligands are in the (*R*,*R*) or (*S*,*S*) configurations. Catalyst precursors are usually racemic mixtures of (*R*,*R*) and (*S*,*S*) species (*rac*-complex), and should be free of the (*R*,*S*) species (*meso*-complex) which is non-enantioselective. According to the chain migratory insertion mechanism,[33,34] the two sites occupied by the growing chains and the olefin are the active sites because after each insertion the growing chain will reside at the coordination site previously occupied by the monomer. The C_2 symmetry ensures the equivalence of the two active sites, which are homotopic. As a result, chain propagation is expected to be isotactic and site-controlled, with occasional *rr* stereodefects.[35]

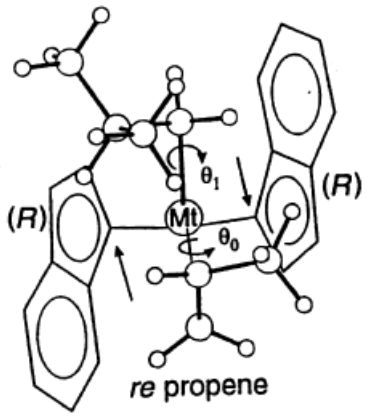

Figure 2.11. *Model of the active site in a C2 symmetric catalyst precursor rac-*ethane(indenyl)$_2$ZrCl$_2$. The active site is represented by the cation *[(R,R)-Me$_2$C(1-Ind)$_2$Mt(iso-Butyl)]$^+$ (Mt=Zr), with a re h^2-coordinated propene molecule and the iso-butyl group simulating a growing polypropylene chain.*[36]

Alumoxane or a Boron compounds are generally used as cocatalysts to promote the formation of the cationic complex.

In copolymerization of propene with ethylene, metallocene catalysts show high activity and sufficient stabillity at high temperature, but strong decrease of catalytic activity in the presence of a diene is observed.[3]

2.2.4 Half-metallocenes, "constrained geometry" catalysts

Constrained geometry (CG) catalysts of general formula $Me_2Si(Me_4Cp)(NR)MtX_2$ (Chart 2.2), with Mt = Ti or Zr, R = alkyl, X = alogen or alkyl[37,38] have been described in the first chapter. The absence of a second Cp ring and the short bridge results in a very open environment of the transition metal, allowing a much easier insertion of bulky monomers compared with bis-Cp systems. This feature is of special importance in the copolymerizations of ethylene with higher 1-alkenes.[35]

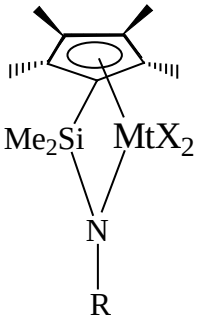

Chart 2.2

These catalysts are able to promote atactic propene sequences with some regioirregularity although to a minor extent with respect to Vanadium based catalysts and show high activity even at high temperatures. Figure 2.12 shows ^{13}C NMR spectra of five EP copolymer samples synthesized with a CG catalyst.[39] The presence of regiodefects due to head-to-head propene units is clearly indicated by the resonances of $S_{\alpha\beta}$, $T_{\gamma\gamma}$, $T_{\gamma\delta}$, and $T_{\beta\gamma}$ and $S_{\beta\gamma}$.[39] The spectra also show resonances similar to those present in the spectra of Vanadium-based EPM samples,[29,40] and indicate a random distribution of comonomers but with ethylene or propene sequences slightly longer than thos of vanadium-based samples.

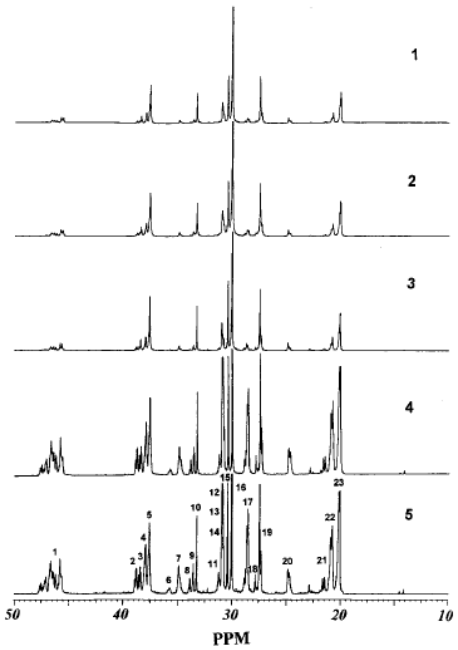

Table 1. ^{13}C NMR Assignment of Ethylene/Propylene Copolymer[a]

peak (no.)	carbon type	chemical shift (ppm)	integration limits (ppm)	area
1	$S_{\alpha\alpha}$	48.1−45.3	48.5−43.5	A
2	r-$S_{\alpha\gamma}$	38.8	39.8−36.1	B
3	r-$S_{\alpha\delta}$	38.4		
4	(m + other)-$S_{\alpha\gamma}$	37.9		
5	(m + other)-$S_{\alpha\delta}$	37.6		
6	r-$S_{\alpha\beta}$	35.7	36.1−34.3	C
7	(m + other)-$S_{\alpha\beta}$	34.9		
8	$T_{\gamma\gamma}$	33.8	34.3−32.4	D
9	$T_{\gamma\delta}$	33.5		
10	$T_{\delta\delta}$	33.2		
11	$T_{\beta\gamma}$	31.2	32.4−29.1	E
12	$T_{\beta\delta}$ (m)	30.9		
13	$S_{\gamma\gamma}$	30.85		
14	$T_{\beta\delta}$ (r)	30.8		
15	$S_{\gamma\delta}$	30.4		
16	$S_{\delta\delta}$	30.0		
17	$T_{\beta\beta}$	28.7, 28.6, 28.4	29.1−28.1	F
18	$S_{\beta\gamma}$	27.8	28.1−25.8	G
19	$S_{\beta\delta}$	27.45, 27.3		
20	$S_{\beta\beta}$	24.8, 24.7	25.8−23.8	H
21	$P_{\beta\beta}$(mm)	22.0−21.3	22.5−18.0	I
22	$P_{\beta\beta}$(mr) + $P_{\beta\gamma}$(m) + $P_{\beta\delta}$(m)	21.3−20.6		
23	$P_{\beta\beta}$(rr) + $P_{\beta\gamma}$(r) + $P_{\beta\delta}$(r) + $P_{\gamma\gamma}$	20.6−19.5		

[a] Referenced to isolated methylenes at 30.0 ppm.

Figure 2.12. *^{13}C NMR spectra of EPM copolymers prepared with CGC catalyst. Attributions are reported in the table on the right.*[39]

2.3 Crystallinity and physical properties of EPM and EPDM

Commercial EPM and EPDM grades are almost amorphous. Small level of crystallinity generally arises from crystallization of ethylene sequences.

EPM with ethylene content between 80 and 40 mol% are amorphous at room temperature,[41,42] but despite the irregular constitution, are able to crystallize at low temperatures or by stretching at room temperature.[41-53] In EP copolymers, propylene units are included in the crystalline lattice of the orthorhombic form of PE (lattice parameters a = 7.42 Å, b = 4.95 Å, and c (chain axis) = 2.54 Å (Figure 2.13),[54] inducing large disorder and decrease of degree of crystallinity. Accurate X-ray diffraction measurements have indicated that the dimension of the a-axis of the unit cell of PE increases almost linearly with increasing propylene content, whereas the b and c-axes practically retain the dimensions of the unit cell of the PE homopolymer. For propylene content around 25%, the a/b ratio approaches the value of $\sqrt{3}$ and the unit cell becomes pseudohexagonal.[41,43-49] In particular, the X-ray diffraction pattern of a stretched sample of an ethylene–propylene terpolymer with a low amount of diene (< 2 mol %), containing 75 mol % ethylene, could be interpreted in terms of an orthorhombic unit cell with parameters a_o = 8.66 Å, b_o = 5.0 Å, and

c_o(chain axis) = 2.54 Å (subscript "o" stands for orthorhombic); the unit cell is actually pseudohexagonal with $a_o/b_o = \sqrt{3}$.[41]

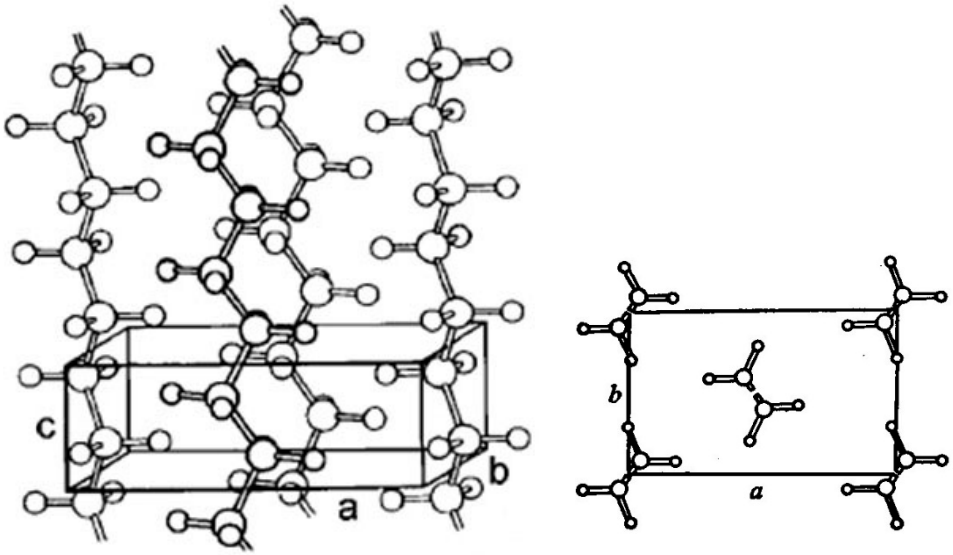

Figure 2.13. *Model of the crystal structure of the orthorhombic from of PE.*

The relationship between orthorhombic (a_o, b_o) and hexagonal (a_h, b_h) unit cell parameters is illustrated in Figure 2.14. The parameters of the hexagonal unit cell are $a_h = b_h = 5$ Å, whereas the c_h-axis coincides with the orthorhombic c_o parameter (subscript "h" stands for hexagonal).

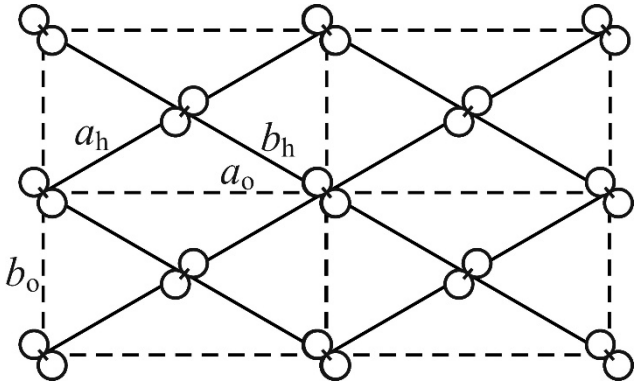

Figure 2.14. *Relationship between orthorhombic (a_o, b_o) and hexagonal (a_h, b_h) unit cell parameters in the structure of polyethylene. Chains of ethylene–propylene copolymers for propylene content close to 25% pack in a pseudohexagonal unit cell, with orthorhombic lattice parameters in the ratio $a_o/b_o = \sqrt{3}$.*

The X-ray fiber diffraction pattern of a stretched sample of EP copolymer in the pseudohexagonal form is shown in Figure 2.15.[55] The presence of the three

narrow diffraction peaks on the equator indicates a hexagonal lattice packing of chains with axis a_h = 4.94 Å and a long range order in the pseudo-hexagonal arrangement of chain axes. The well-defined layer lines indicate the nearly *trans*-planar conformation of the chains with periodicity c = 2.54 Å. The broadness of all the nonequatorial peaks and the diffuse nature of the diffraction halos along the layer lines indicates that a large amount of disorder is present in the pseudo-hexagonal packing of chains and that the coherent length of the ordered bundles of chains should be of the order of a few tens angstroms.[55]

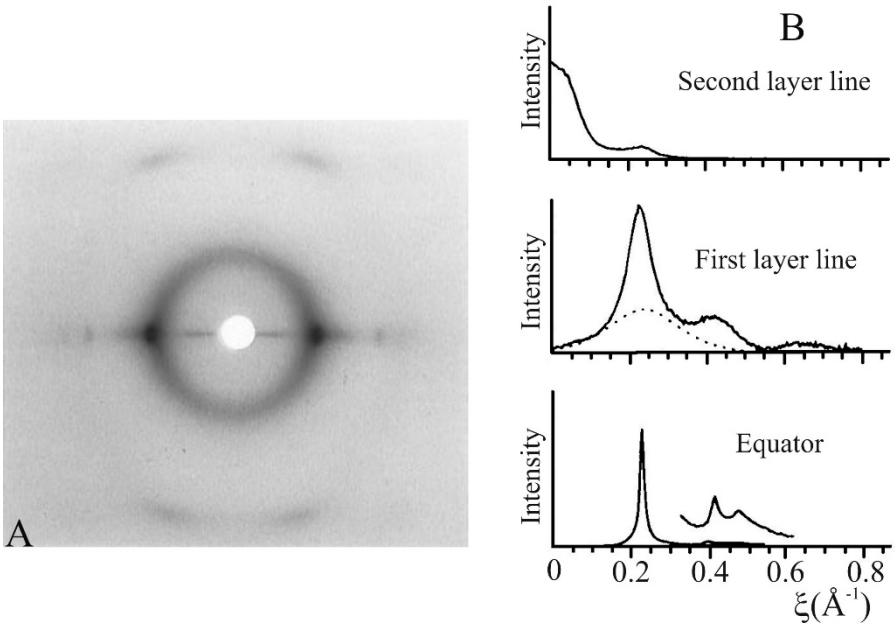

Figure 2.15. *X-ray fiber diffraction pattern (A) and corresponding profiles read along the equator, the first and the second layer lines (B) of a fiber of a sample of EP copolymer with an ethylene content of 75 mol % stretched at room temperature at 750% deformation.*[55]

The comparison between the experimental X-ray diffraction pattern in Figure 2.15 and the calculated Fourier transforms of various model structures has allowed clarification of several aspects concerning the nature of disorder that characterizes the mesomorphic pseudohexagonal form of ethylene–propylene copolymers.[55] Three limit ordered models, shown in Figure 2.16, were considered as possible ideal arrangements of EP chains in the mesomorphic bundles. In Figure 2.16A and B,B', the chains are arranged as in the orthorhombic[54] and monoclinic[56] polymorphs of PE, respectively. In Figure 2.16C and C', the chains are arranged as in the triclinic form of long-chain paraffins.[57] These models were chosen as reference, "ideal" limit ordered

structures, and disordered models were built starting from the ordered models introducing different kinds of disorder.

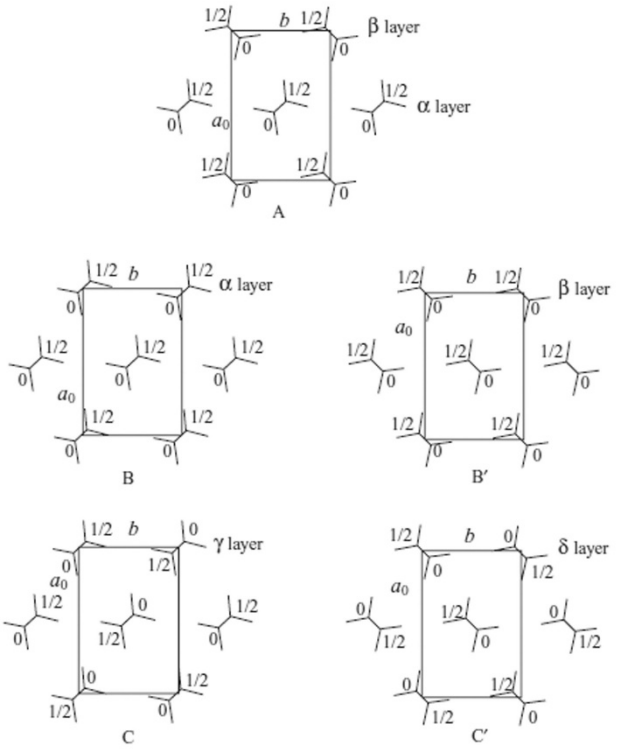

Figure 2.16. *Projections in the ab-plane of the limit ordered orthorhombic (A), monoclinic (B,B'), and triclinic (C,C') ideal model structures considered in the Fourier transform calculations for the pseudohexagonal form of EP copolymers.[55,58] The numbers indicate the fractional z coordinate of the backbone carbon atoms. α, β, γ, and δ layers indicate different kinds of b_oc_o layers of chains piled along the a_o lattice direction. The regular alternation of α and β layers along a_o characterizes the orthorhombic form (A), the regular succession along a_o of α layers or β layers produces the monoclinic form (B,B'), and the regular succession of γ or δ layers gives the triclinic form (C,C').[55]*

Possible structural disorders are the conformational disorder, consisting of small displacements from the *trans*-planar state of the backbone torsion angles close to the propylene units; translational intermolecular disorder along the chain axis; rotational intermolecular disorder around the chain axis; and disorder in the stacking of ordered layers of chains along one lattice direction (stacking faults).[55] In the ordered models, the regular alternation of α and β layers along a_o characterizes the orthorhombic form (Figure 2.16A); the regular succession along a_o of α layers or β layers produces the monoclinic form (Figure 2.16B,B') and the regular succession of γ or δ layers gives the triclinic

form (Figure 2.16C,C'). Structural disorder may develop, for instance, by defects in the regular succession of these b_oc_o layers of chains along a_o. Therefore, disordered models of the structure of the mesomorphic pseudohexagonal form may be characterized by small aggregates of EP copolymer chains characterized by a statistical succession along the a_o-axis of the different b_oc_o layers of chains of the kind in Figure 2.16 (α, β, γ, and δ layers), according to orthorhombic-like (Figure 2.16A), monoclinic-like (Figure 2.16B'), and triclinic-like (Figure 2.16C,C') ideal models, with probabilities p_o, p_m, and p_t, respectively.[55,58]

A comparison between the experimental X-ray diffraction profile along the first layer line and the diffraction profiles calculated for disordered models of structure characterized by the succession of b_oc_o layers of chains along a_o according to orthorhombic-like (Figure 2.16A), monoclinic-like (Figure 2.16B,B'), and triclinic-like (Figure 2.16C,C') ideal models, with probabilities p_o, p_m and p_t, respectively, is reported in Figure 2.17.[55,58]

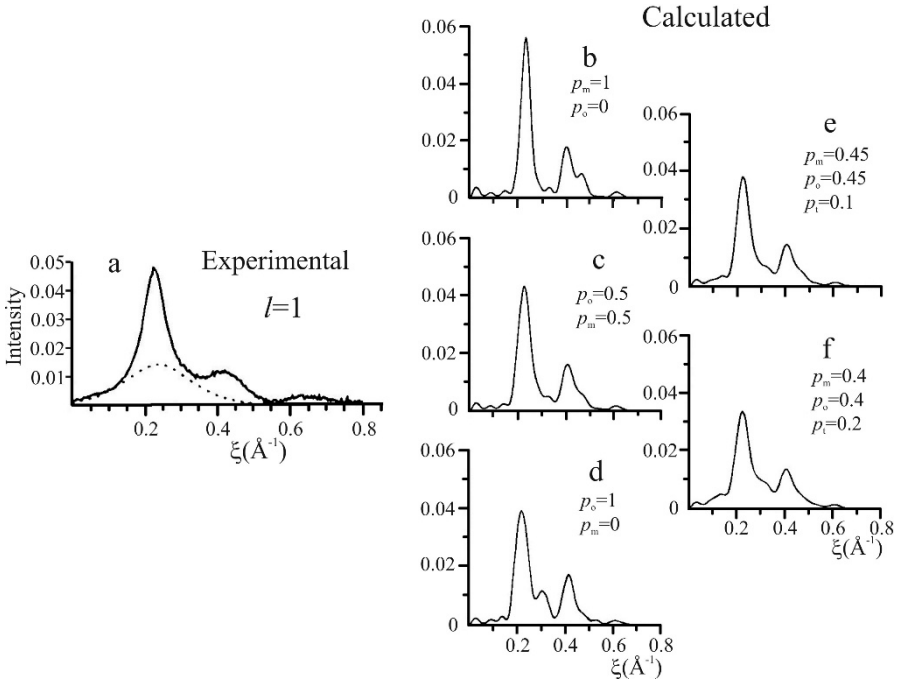

Figure 2.17. *(a) Experimental X-ray fiber diffraction profile along the first layer line (l = 1) of a stretched sample of EP copolymer in the pseudohexagonal mesomorphic form (solid line).*[55] *The dashed line indicates the contribution of the amorphous phase. (b–f) X-ray diffraction profiles along the first layer line calculated for small aggregates of EP copolymer chains, where consecutive b_oc_o layers of four to six chains of the kind shown in Figure 2.16 are faced along the axis a_o according to orthorhombic-like (Figure 2.16A), monoclinic-like (Figure 2.16B,B'), and triclinic-like (Figure 2.16C,C') models, with probabilities p_o, p_m, and p_t, respectively.*[55,58]

In all disordered models, a good agreement with the experimental intensity distribution data has been obtained, indicating that short-range correlations between the chains similar to those present in the orthorhombic, monoclinic, and triclinic models are present in the small aggregates of the mesomorphic form.[55] These correlations rapidly fade away as the interchain distances increase. In other terms, the mesomorphic form of EP copolymers may be described as aggregates of clusters of chains arranged as in the orthorhombic-, monoclinic-, or even triclinic-like structures, to form larger bundles, in a mosaiclike structure, as schematically shown in Figure 2.18.[58,59] The interference between different clusters in the mesomorphic aggregate would produce only a background on nonequatorial layer lines.[55] For all the considered models, the ratio between the integrated intensity of the main peaks on the first layer line and on the equator $I(l = 1)/I(l = 0)$ is nearly equal to 0.1 and is lower than the experimental value of about 0.18.[55] A better agreement has been obtained by introducing propylene units in the crystals and conformational disorder consisting in small displacements from the *trans*-planar conformation of the backbone torsion angles close to the propylene units. The presence of conformational disorder introduces some waviness in the chains and the experimental ratio $I(l = 1)/I(l = 0)$ has been reproduced with an average amplitude of the wave of $\Delta = 0.5$ Å for a copolymer with 25 mol % of propylene comonomer.[55] This implies deviations of the torsion angles smaller than □±20° from strictly 180° and deviations of the valence angles of □±2° from the common value of 112°, and substantially unaltered mean chain periodicity. The presence of the conformational disorder in the pseudohexagonal form of ethylene-propylene copolymers is a clear consequence of the constitutional disorder and of the inclusion of the methyl groups in the crystalline regions. The structure of the pseudohexagonal form is characterized by the following structural features:

1) Long-range positional order is maintained only for the positioning of the chain axes, which are placed at the nodes of a pseudohexagonal lattice. This long-range order accounts for the position and intensity of the reflections observed on the equator of the X-ray fiber diffraction patterns.

(2) The chains are essentially in *trans*-planar conformation. The methyl groups of the propylene units are included in the crystals and necessarily introduce some conformational disorder that consists in small deviations of the backbone torsion angles close to the pendant methyl groups from 180°. These

deviations from the *trans* state alleviate intramolecular and intermolecular strains and are easily digested in the pseudohexagonal lattice of EP copolymers. The portions of chain in the crystalline aggregates remain still extended, with a mean periodicity close to 2.5 Å, even in the presence of conformational defects, which introduce some waviness in the chains. Conformational disorder accounts for the experimental ratio between the integrated intensities of the main peaks on the first layer line and on the equator.

(3) Local correlations between neighboring chains similar to ideal orthorhombic- and monoclinic-like structures shown in Figure 2.16A, B, and B' are retained at short-range distances, up to few tens of angstroms (two to three times the lattice parameters). In other terms, on a local scale, the chains are arranged according to the orthorhombic-, monoclinic-, or triclinic-like models in Figure 2.16.

(4) Disorder in the relative heights of chains along the *c*-axis is present (translational disorder along *c*), as indicated by the broadness of nonequatorial diffraction peaks along the ξ-direction.[55,58,59]

(5) Disorder in the relative orientation of the chains around the chain axes is present (rotational disorder), as indicated by the presence of diffuse scattering subtending the Bragg reflections along the layer lines. The correlation in the relative angular position of couples of chains with respect to their “ideal” relative arrangement decreases with increasing their distance.[55,58,59] The comparison of experimental and calculated X-ray diffraction intensities of bundles of EP copolymer chains indicated that the range of angular displacement disorder of chains about their axis is very small.

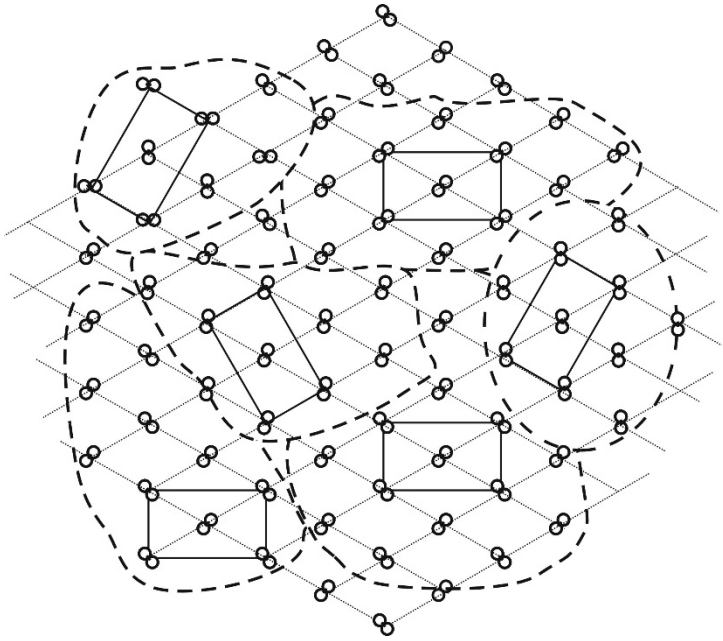

Figure 2.18. *Mosaiclike structure of crystalline microaggregates of EP copolymer chains in the mesomorphic pseudohexagonal form. In the different ordered domains, enclosed in the dashed lines, the chains are locally packed as in the orthorhombic-, monoclinic-, and triclinic-like model structures in Figure 2.16. The different domains are arranged in a mosaic structure so that long-range positional order of chain axes placed at nodes of a pseudohexagonal lattice is maintained. The unit cells of orthorhombic-, monoclinic-, and triclinicordered models are shown as continuous lines, whereas the hexagonal lattice is shown as dotted lines.*[59]

The small-sized crystals of the mesophase that includes large amounts of structural disorder play an important role in the elasticity of EP copolymers.[60-62] These small crystals form upon stretching and melt when the tension is released, or, for some particular compositions of the copolymers, are present in the bulk material as residual crystallinity. These crystals act as physical knots of the elastomeric network. Since they are highly interconnected via the entangled amorphous chains (tie chains), the formation of crystalline knots prevents viscous flow during application of tensile stress and ensures the recovery of the initial dimensions of the sample, upon releasing the tension.[63]

2.4 Aim of the study of crystallinity in EPM and EPDM

In this section the role played by crystals in the mechanical behavior of several commercial EPM and EPDM grades is analyzed. The first series of samples consists of EPM copolymers and EPDM terpolymers with different ethylene and diene content without filler (Table 2.1). The second series of samples consists of terpolymers with the same ethylene and diene content but different types and amount of commercial fillers (Table 2.2).

EPDM terpolymers with high ethylene contents (higher than 78-80 wt%) are generally crystalline whereas EPDM samples with ethylene concentration in the range 60-70 wt% appear amorphous in the undeformed state.[41,42,50,51,64] However, crystallization of ethylene sequences may occur during deformation. Small crystals can form upon stretching, acting as physical knots in the elastomeric network, resulting in increase of tensile strength of the rubber. In this chapter a study of the Stress-Induced Crystallization (SIC) in EPM copolymers and EPDM terpolymers of different ethylene concentrations is reported. Moreover, the possible presence of crystallinity in the underformed state (***faint or crypto crystallinity***) is analyzed in detail with different techniques of structural analysis in different length scales. The influence of ethylene content and of different commercial fillers on the SIC and on the presence of crystallinity in the underformed state is also analyzed. For comparison, ethylene/propylene copolymers prepared with different catalysts and with similar ethylene content are also analyzed.

2.5 Materials and methods

The analyzed samples includes EPDM terpolymers and EPM copolymers with ethylene concentration in the range 44-78 wt% provided by the company ARLANXEO under the global brand name Keltan®. Ethylene and diene contents, the used catalyst, the Mooney viscosity, the average molecular masses (M_w and M_n) are reported in Table 2.1. The samples have been synthesized with a Vanadium based catalyst, and with the new Keltan ACE^{TM} technology, based on a half-metallocene catalyst. The samples consist of three copolymers and seven terpolymers. Considering the ethylene content as the main difference among the samples, and neglecting the presence of the diene, the series can be regarded as three sets of samples of different ethylene concentration: the first set contains samples with ethylene content in the range 78-70 wt% (samples EPM from the pilot plant, K5170P, K5470P, K2070P); the second set includes samples with ethylene content in the range 67-64 wt% (samples K6260Q,

K5470C, K8570C, K6160D); the third set includes samples with ethylene content in the range 52-44 wt% (samples K4450C, K9950C, K3050). The sample EPM is not a commercial grade, but it has been synthesized in the pilot plant of the company, therefore several data such as the Mooney viscosity, the average molecular masses (M_w and M_n) are not known. All terpolymers contain ENB as the third comonomer, except the sample K6160D, which contains DCPD (Figure 2.3).

All these samples of Table 2.1 do not contain fillers except talc in some cases (samples in pellet morphology).

***Table 2.1**. Ethylene and diene content (wt%), Mooney viscosity (MU), catalyst, weight average molecular mass (M_w), number average molecular mass (M_n) of EPM copolymers and EPDM terpolymers.*

	Copolymers			Terpolymers							
Sample	EPM[(a)]	K2070P	K3050	K5170P	K5470P	K6260Q	K5470C	K8570C	K6160D[(e)]	K4450C	K9950C
Ethylene content (wt%)	78	73	49	71	70	67	66	66	64	52	44
Propylene content (wt%)	22	27	51	27.5	25.4	30.2	29.4	29	34.8	43.7	47
Diene content[(b)] (wt%)	-	-	-	1.5	4.6	2.8	4.6	5	1.2	4.3	9
Mooney viscosity ML (1+4) 125°C (MU)	n.a[(c)]	25	51	59	55	67	55	80	63	46	60
Catalyst	V[(d)]	V	V	V	V	V	ACE[(d)]	ACE	V	ACE	ACE
M_w (Kg/mol)	n.a	150	175	225	275	275	275	n.a.	250	200	300
M_n (Kg/mol)	n.a	40	80	100	100	100	100	n.a.	60	80	100

(a): sample from the company pilot plant;
(b): for all terpolymers the diene is 5-ethylidene-2-norbornene (ENB) (Figure 3.3). Only the sample K6160D contains dicyclopentadiene (DCPD) instead of ENB;
(c): data not available;
(d): V= Vanadium based catalyst; ACE= ACE catalyst (half-metallocene) patented by ARLANXEO
(e): the diene is DCPD instead of ENB

The structural organization of bulk samples in the undeformed state has been studied by Wide (WAXS) and Small Angle (SAXS) X-ray Scattering at different temperatures, and Differential Scanning Calorimetry (DSC).

X-ray powder diffraction patterns have been obtained with an automatic Philips diffractometer using Ni-filtered CuKα radiation.

Small Angle X-ray scattering measurements have been collected at room temperature using a Kratky compact camera SAXSess (Anton Paar, Graz, Austria) in the slit collimation configuration, attached to a conventional X-ray source (CuKα, wavelength λ =1.5418 Å). The scattered radiation was recorded on a BAS-MS imaging plate (FUJIFILM) and processed with a digital imaging reader Perkin Elmer Cyclone Plus (storage phosphor system).

Calorimetric measurements have been performed with a differential scanning calorimeter DSC Mettler 001 by Mettler Toledo at a scanning rates of 2.5, 10, 20 °C/min in a flowing N_2 atmosphere using liquid N_2 to reach temperatures below -60°C.

Unoriented films used for the structural and mechanical analysis have been obtained by compression molding. The as-prepared samples have been heated at ≈ 100 °C between flat Teflon plates under an hydraulics press at very low pressure (< 1 bar), kept at ≈ 100 °C for 5 min, and slowly cooled to room temperature (≈ 15 °C/min).

Mechanical tests have been performed at room temperature on compression-molded films with an Instron mechanical tester, following the standard test method for tensile properties of thin plastic sheeting ASTM D882-83. Rectangular specimens 5 mm long, 4 mm wide and 0.5 mm thick have been stretched up to the break or up to a given deformation $\varepsilon = [(L_f - L_0)/L_0] \times 100$, where L_0 and L_f are the initial and final lengths of the specimen, respectively. Two benchmarks have been placed on the test specimens and used to measure elongation. Values of tension set and elastic recovery have been measured after breaking. Ten minutes after breaking, the two pieces of the sample have been fit carefully together so that they are in contact over the full area of the break and the final total length L_r of the specimen has been obtained by measuring the distance between the two benchmarks. The tension set after breaking has been calculated as $t_b = [(L_r - L_0)/L_0]\times100$, whereas the elastic recovery has been calculated as $r_b = [(L_f - L_r)/L_r]\times100$ and the percentage of the total strain ($L_f - L_0$) that is recovered after breaking is calculated as $R_b = 100\times(L_f - L_r)/(L_f - L_0) = 100\times(\varepsilon_b - t_b)/\varepsilon_b$. In the mechanical tests, the ratio between the drawing rate and the initial length was fixed equal to 0.1 mm/(mm×min) for the

measurement of Young's modulus and 10 mm/(mm×min) for the measurement of stress−strain curves and the determination of the other mechanical properties (stress and strain at break and tension set). The reported values of the mechanical properties are averaged over at least five independent experiments.

The viscoelastic properties have been studied by Dynamic Mechanical Thermal Analysis (DMTA) with a TTDMA dynamic mechanical analyzer from Triton Technology, in double cantilever bending mode, imposing a frequency of 1Hz a displacement amplitude of 0.02mm and heating rate of 2 °C/min. This technique allows determining the values of the storage and loss moduli of the samples and the damping due to relaxation processes. The storage modulus value is a measure of the ability of the material to preserve energy, while the loss modulus indicates the energy needed to dissipate energy.

Possible occurrence of SIC has been analyzed by recording the two dimensional WAXS patterns during stretching and after relaxation of the specimens to verify whether crystals formed at high deformations melt during elastic recovery (reversible SIC). elastic recovery (reversible SIC). Fiber diffraction patterns have been collected with Ni-filtered CuKα radiation and recorded on a BAS-MS imaging plate (FUJIFILM) using a cylindrical camera and processed with a digital imaging reader Perkin Elmer Cyclone Plus (storage phosphor system).

Hysteresys cycles have been performed on stress-relaxed oriented fibers using a mechanical tester INSTRON, following the standard test method ASTM D412-87. In these cycles stress-relaxed oriented fibers of initial length L_r are stretched up to the final length L_f ($L_f = 5.5L_0$ or $5L_0$), that is, up to the maximum length achieved during the stretching of the starting unoriented film used for the preparation of the fibers (ε_{max} = 450% or 400%), so that the maximum deformation achieved during the first cycle ($\varepsilon = 100(L_f - L_r)/L_r$) for each sample is numerically equal to the elastic recovery $r(\varepsilon_{max})$ of the unoriented film. For each oriented film at least three consecutive hysteresis cycles have been recorded; each cycle has been performed 10 min after the end of the previous cycle.

Stress-relaxation tests were performed at room temperature on unoriented compression molded films following the procedure described in the standard test method ASTM D-2991-84. Instantaneous strains of 50% and 600% were applied and the values of stress were recorded as a function of time, while keeping constant the deformation.

2.6 Study of crystallinity in EPM copolymers and EPDM terpolymers

The study of the structure of EPM and EPDM samples, in particular the presence of crystallinity in the bulk samples in the undeformed state, has been performed by a parallel analysis of the wide-angle X-ray diffraction, small-angle X-ray scattering and calorimetric data. The crystallinity in the undeformed state has been compared with the crystallinity that develops during deformation by studying the structure that evolves during stretching by X-ray fiber diffraction.

2.6.1 Structural characterization

The X-ray powder diffraction profiles of samples of EPM copolymers and EPDM terpolymers of Table 2.1 as received from the company ARLANXEO are reported in Figure 2.19. All samples show quite similar WAXS profiles with a broad halo centered at $2\theta \approx 19°$ typical of amorphous EP copolymers. Only the sample EPM from the pilot plant, with 78 wt% of ethylene, shows an additional crystalline peak at $2\theta \approx 21°$ typical of PE in pseudohexagonal form. In samples K2070P, K5170P and K5470P this peak appears as a weak shoulder of the main broad halo at $2\theta \approx 19°$. Other small, narrow peaks at $2\theta \approx 9°$ and $2\theta \approx 29°$ are due to additives, in particular talc, as demonstrated by the comparison with the diffraction profiles of talc, ZnO and zinc stearate extract from the *database* PDF-ICDD-2014 and reported in Figure 2.20.

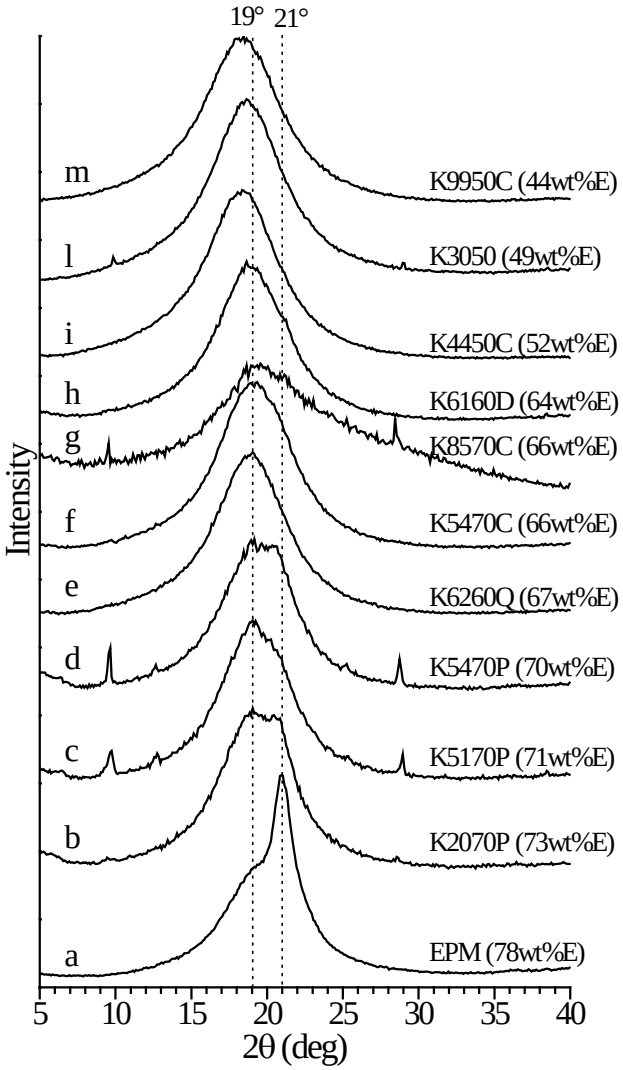

Figure 2.19. *X-ray powder diffraction profiles of samples of EPM copolymers and EPDM terpolymers as received from the company ARLANXEO.*

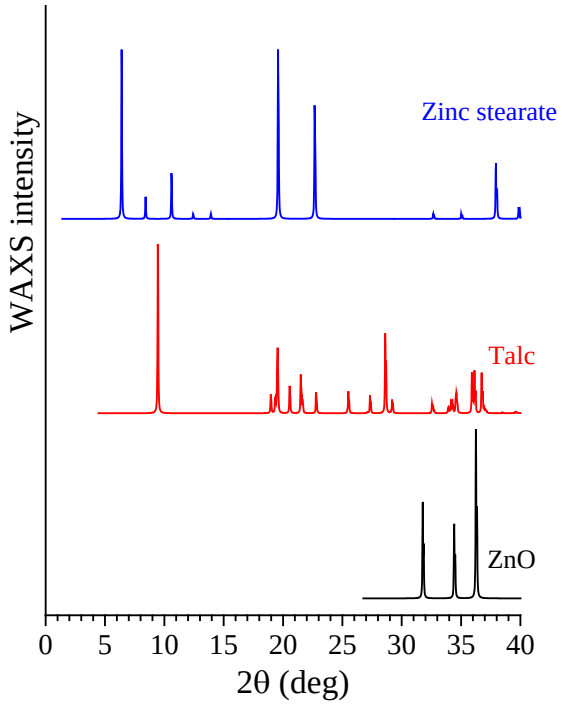

***Figure 2.20**. Main additives present in samples of EPM copolymers and EPDM terpolymers of both first and second series.*

The possible crystallization of the samples by cooling at low temperatures or by annealing has been verified performing WAXS measurements at different temperatures on samples with ethylene content in the range 78-64 wt% (first and second sets). WAXS profiles of samples EPM and K2070P are reported in figure 2.21A and 2.21B, respectively. The samples have been cooled from room temperature to -50°C, then heated up to 160°C, cooled again to -50°C and finally heated again up to 30°C. It is apparent that for the sample EPM (Figure 2.21A) during the cooling the reflection at $2\theta \approx 21°$ already present at room temperature become more evident, while a decrease of the amorphous halo at $2\theta \approx 19°$ at T = -60 °C is observed (Figure 2.21A). During the heating scan the intensity of the crystalline peak becomes lower and lower until it disappears at temperatures higher than 55-60 °C and only the amorphous halo can be observed (Figure 2.21A). The shift of the 2θ value of the peak of the amorphous halo to lower values at higher temperature is due to thermal expansion effects. During the second cooling other small peaks probably due to impurity present in the sample are visible in addition to the crystalline peak at $2\theta \approx 21°$.

Similar results have been obtained on the sample K2070P (73 wt% of ethylene) (Figure 2.21B). The main difference is that the crystalline peak at 2θ

≈ 21° at room temperature has intensity much lower than in the sample EPM. The intensity of this peak increases and that of the amorphous halo decreases at low temperature (T = -50 °C). These data indicate that for both samples, crystallinity increases by cooling at low temperature (T = -50 °C), due to the crystallization of short ethylene sequences, which are not able to crystallize at room temperature.

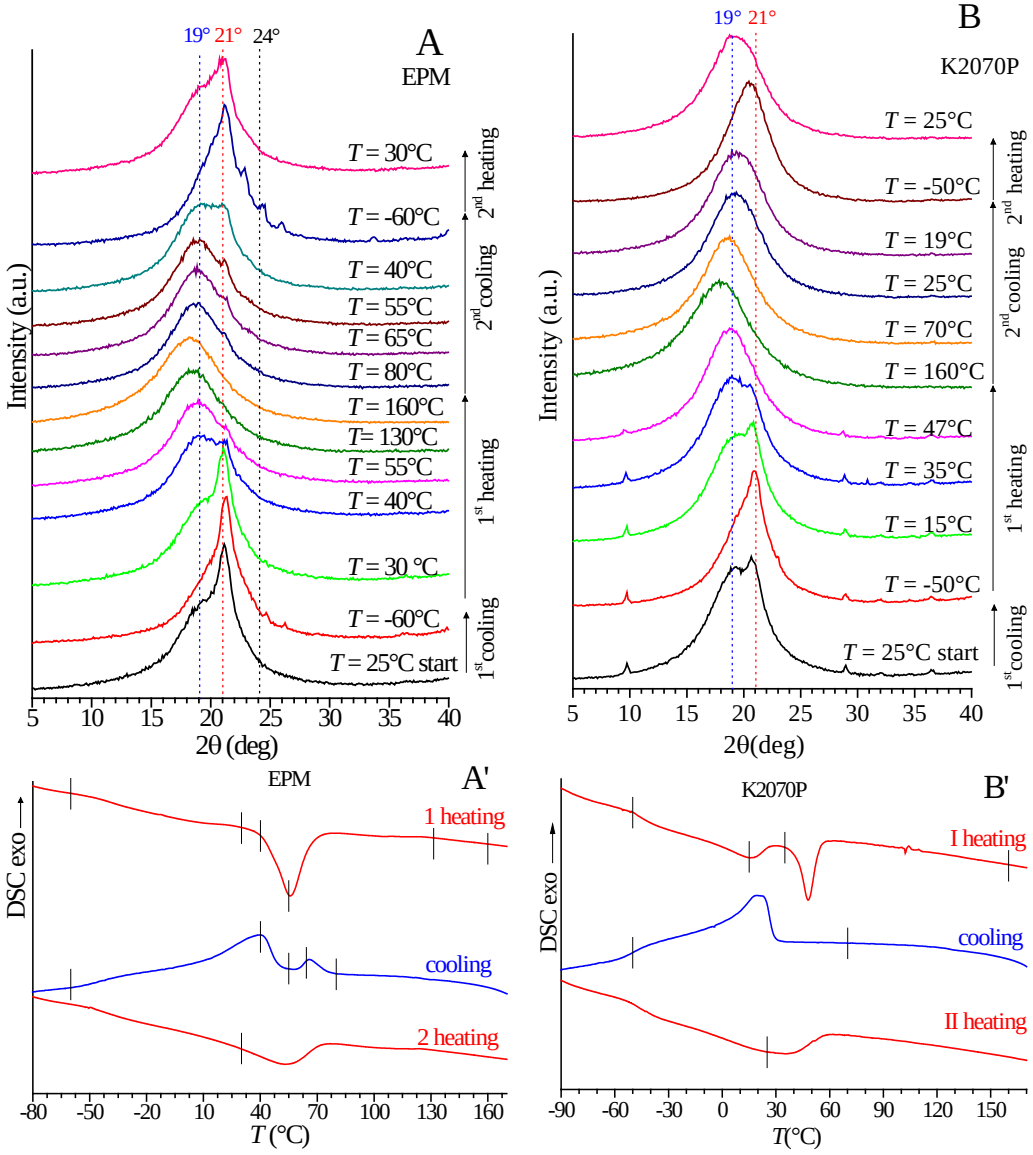

Figure 2.21. *WAXS profiles (A,B) recorded at the indicated temperatures and DSC curves (A',B') recorded during first heating, successive cooling and second heating of the samples EPM with 78 wt% of ethylene (A,A') and K2070P with 73 wt% of ethylene (B,B'). The vertical lines on the DSC curves indicate the temperatures of WAXS measurement.*

The same measurements have been performed on samples of EPDM terpolymers (Figure 2.22A-E). A similar behavior has been observed. Because of the ethylene content lower than that of the sample K2070P, only a weak peak at $2\theta \approx 21°$ is observed in some samples (K5170P and K5470P, Figure 2.22A,B), while in the other samples only the amorphous halo is visible. With decreasing temperature the amorphous halo becomes lower and a broad peak at $2\theta \approx 21°$ can be observed. In all samples this peak becomes less evident as the ethylene content decreases. Also in these samples, an increase of crystallinity at low temperature is observed, due to the crystallization of short ethylene sequences not able to crystallize at room temperature. Then, the small crystals formed at T = -50 °C melt during the heating scan.

In conclusion, from the WAXS analysis it is apparent that all these samples show similar crystallization behavior despite the different ethylene content, showing very low crystallinity also at low temperatures.

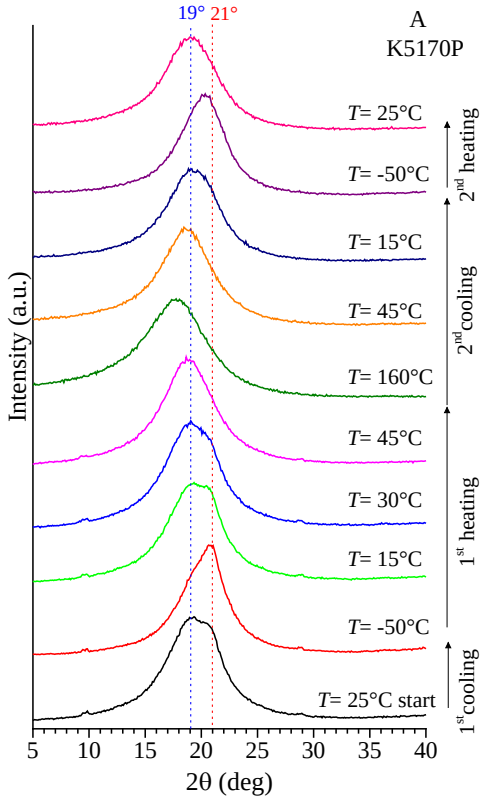
19° 21°
A
K5170P
T= 25°C
T= -50°C
T= 15°C
T= 45°C
T= 160°C
T= 45°C
T= 30°C
T= 15°C
T= -50°C
T= 25°C start
2nd heating
2nd cooling
1st heating
1st cooling
Intensity (a.u.)
5 10 15 20 25 30 35 40
2θ (deg)

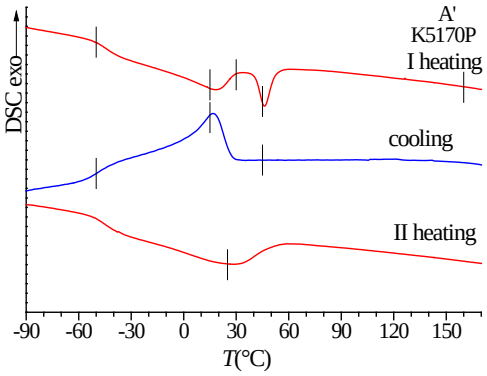
A'
K5170P
I heating
cooling
II heating
DSC exo
-90 -60 -30 0 30 60 90 120 150
T(°C)

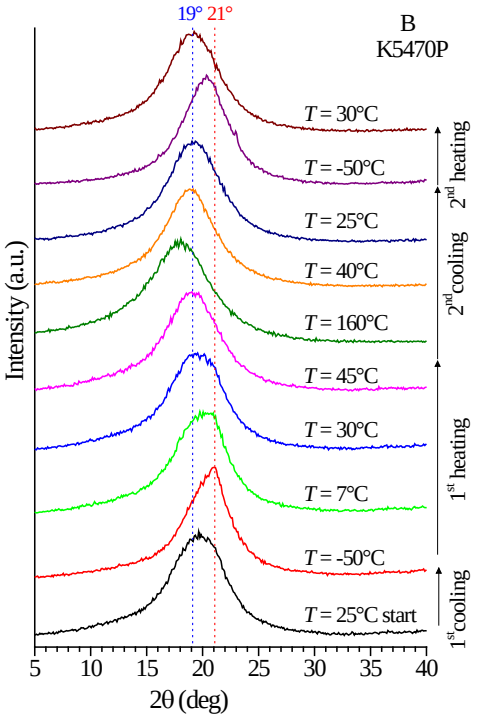
19° 21°
B
K5470P
T = 30°C
T = -50°C
T = 25°C
T = 40°C
T = 160°C
T = 45°C
T = 30°C
T = 7°C
T = -50°C
T = 25°C start
2nd heating
2nd cooling
1st heating
1st cooling
Intensity (a.u.)
5 10 15 20 25 30 35 40
2θ (deg)

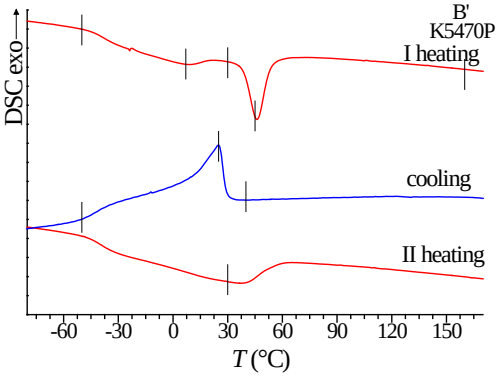
B'
K5470P
I heating
cooling
II heating
DSC exo
-60 -30 0 30 60 90 120 150
T (°C)

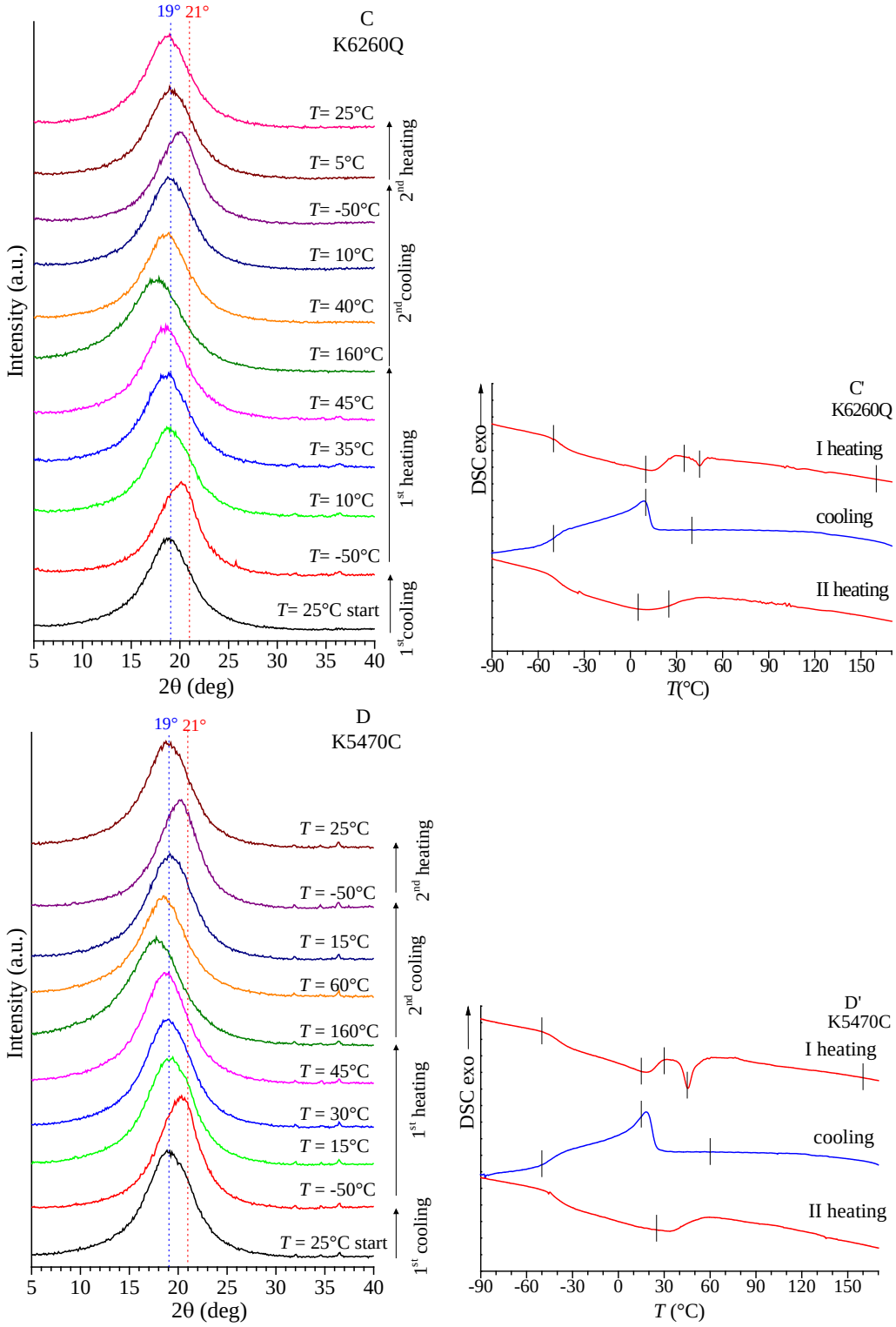
C
K6260Q
19°
21°
T= 25°C
T= 5°C
T= -50°C
T= 10°C
T= 40°C
T= 160°C
T= 45°C
T= 35°C
T= 10°C
T= -50°C
T= 25°C start
2nd heating
2nd cooling
1st heating
1st cooling
Intensity (a.u.)
2θ (deg)
C'
K6260Q
I heating
cooling
II heating
DSC exo
T(°C)
D
K5470C
T = 25°C
T = -50°C
T = 15°C
T = 60°C
T = 160°C
T = 45°C
T = 30°C
T = 15°C
T = -50°C
T = 25°C start
2nd heating
2nd cooling
1st heating
1st cooling
Intensity (a.u.)
2θ (deg)
D'
K5470C
I heating
cooling
II heating
DSC exo
T (°C)

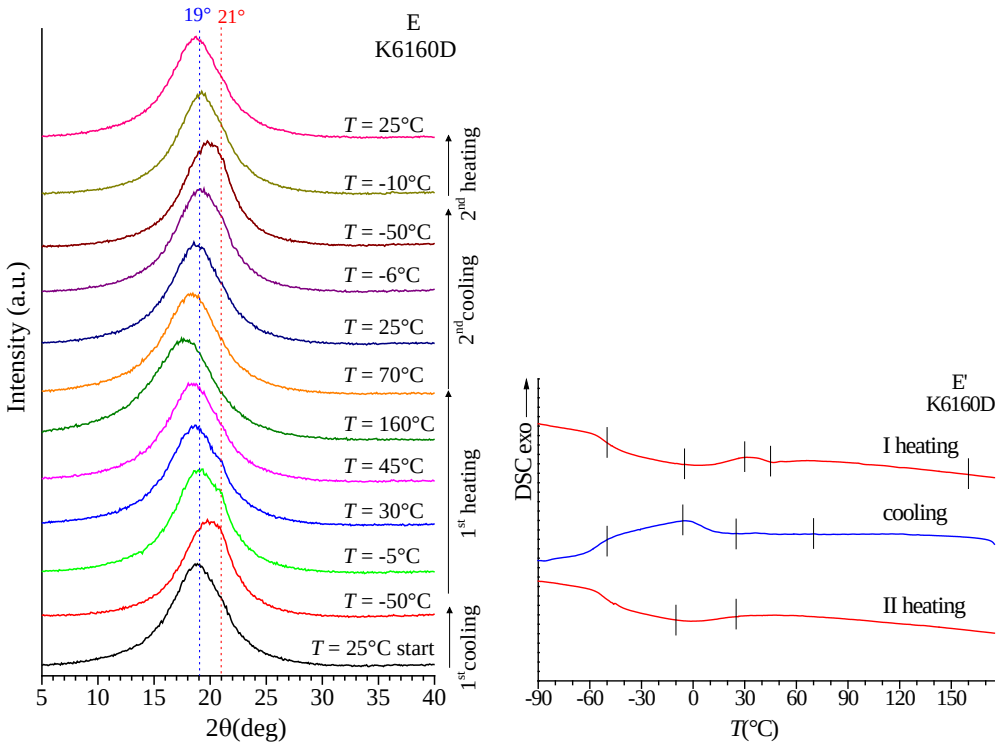

Figure 2.22. *WAXS profiles (A-E) recorded at the indicated temperatures and DSC curves (A'-E') recorded during first heating, successive cooling and second heating of the samples K5170P with 71 wt% of ethylene (A,A'), K5470P with 70 wt% of ethylene (B.B'), K6260Q with 67 wt% of ethylene (C,C'), K5470C with 66 wt% of ethylene (D,D'), K6160D with 64 wt% of ethylene (E,E'). The vertical lines on the DSC curves indicate the temperatures of WAXS measurement.*

2.6.2 Thermal analysis

The DSC curves of Figure 2.21 and 2.22 of samples of EPM copolymers and EPDM terpolymers, recorded during first heating from -100°C to 180°C, successive cooling from the melt to -100°C, and second heating of the melt-crystallized samples up to 180°C, all recorded at 10 °C/min, are reported for comparison in Figure 2.23A-C. The values of melting and crystallization temperatures and enthalpies are reported in Table 2.3.

Samples belonging to the first set with ethylene content in the range 78-70 wt%, that is EPM, K2070P (copolymers), K5170P and K5470P (terpolymers) show well defined melting peak during the first heating (curves a-d of Figure 2.23A), indicating the presence of crystallinity due to the crystallization of ethylene sequence long enough to crystallize at low temperature. For these samples, the melting temperature decreases with decreasing ethylene concentration (curves a-d of Figure 2.23A). The DSC data of the sample EPM

confirm the crystallinity observed with diffraction analysis with a sharp endothermic peak at the highest temperature (56 °C). This is due to the highest concentration of ethylene and the presence of longer ethylene sequences and, therefore, higher melting temperature. The same samples belonging to this first set also show clear exothermic peak in the DSC cooling curves a-d of Figure 2.23B, indicating crystallization by cooling from the melt. The crystallization temperature decreases with decreasing ethylene concentration, from 39 °C of the sample EPM with the highest ethylene content to nearly 17-20 °C of the samples with 70 wt% of ethylene (curves a-d of Figure 2.23B).

It is worth noting that the copolymer K2070P (73 wt% ethylene) and the terpolymers K5170P and K5470P (71 and 70 wt% of ethylene, respectively) show clear melting and crystallization peaks in the DSC curves b-d of Figure 2.23A and C notwithstanding they seem amorphous from the WAXS analysis because of the absence of sharp diffraction peaks (profiles b-d of Figure 2.19).

The DSC curves recorded during the first heating of samples of these first set also show a broad endothermic peak at low temperatures (curves a-d of Figure 2.23A) that can be attributed to the melting of small and imperfect crystals formed during the cooling at low temperature (-100 °C) or aging at room temperature. This broad endotherm is less evident in the sample EPM (curve a of Figure 2.23A) and its enthalpy increase with decreasing ethylene content (curves b-d of Figure 2.23A).

The presence of crystals of different sizes is also demonstrated by the DSC cooling curves of Figure 2.23B that show broad exothermic peaks with shoulders at low temperature and, in the case of the sample EPM, the cooling curve displays two separate peaks at 66 and 39 °C (curve a of Figure 2.23B), with the first one at temperature (66 °C) higher than the observed melting temperature of 55 °C (curve a of Figure 2.23A). This indicates that first longer ethylene sequences form thicker crystals at $T_c \approx 66$°C, then shorter sequences form thinner crystals at $T_c \approx 39$ °C.

Despite the lower ethylene content and WAXS profiles typical of amorphous materials, samples of the second set with ethylene content in the range 67-64 wt% also show a very broad endothermic peak at low temperatures followed by a narrower small peak at higher temperature (curves e-h of Figure 2.23A). The latter has enthalpy much lower than those of the main peaks observed in the samples of the first set (curves a-d of Figure 2.23A). Also for these samples the DSC cooling curves show well defined exothermic peaks that indicate

crystallization from the melt at low temperatures in the range -9°C - 18 °C (curves e-h of Figure 2.23B).

The first heating and the cooling scans of the samples K5470C and K8570C and are very interesting (curves f,g of Figure 2.23A,B). These samples have an ethylene concentration similar to that of the other two samples of the set (K6260Q and K6160D) and with only slightly higher content of the diene. Nevertheless, they show more defined endothermic peaks and higher crystallization temperature (curves f,g of Figure 2.23B) and seem more similar to the samples of the first set (curves b-d of Figure 2.23B). This is probably due to the presence of longer ethylene sequences formed by the different catalyst (ACE) used in the process synthesis. As discussed in paragraph 2.2.4, the CGC-based EP copolymers, have fewer alternating monomer units and more consecutive ethylene units than the vanadium-based EPM samples.

The samples belonging to the third series (ethylene content in the range 52-49 wt%) do not show any melting or crystallization peak, therefore they are really amorphous and show only the glass transition at low temperatures (nearly - 50 °C).

Data from thermal analysis are in contrast with data from diffraction analysis, revealing a crystallinity not detected by WAXS. We call this hidden crystallinity as “cryptocrystallinity”.

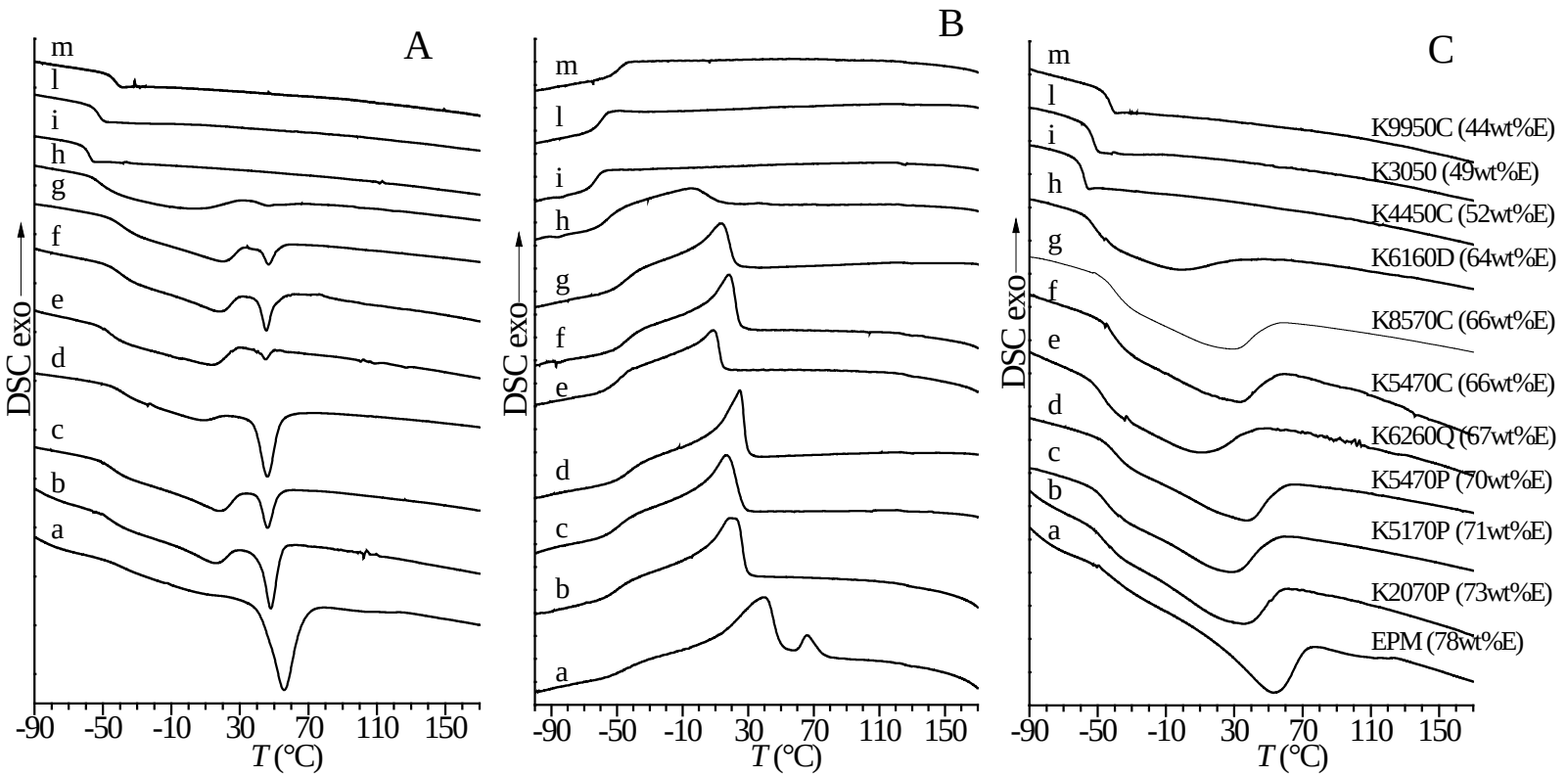

Figure 2.23. *DSC curves recorded at 10°C/min during first heating (A), successive cooling (B) and second heating scans (C) of samples of EPM copolymers and EPDM terpolymers as received from the company ARLANXEO.*

***Table 2.3**. Ethylene and diene concentrations in wt%, glass transition temperature (T_g), melting temperature (T_m^I) and melting enthalpy (ΔH_m^I) recorded during the first heating, crystallization temperature (T_c) and crystallization enthalpy (ΔH_c), melting temperature (T_m^{II}) and melting enthalpy (ΔH_m^{II}) recorded during the second heating and degree of crystallinity (x_c^{DSC}) evaluated from the melting enthalpy ΔH_m^I* measured from the DSC curves of the *first heating scans of Figure 2.23A of samples of EPM copolymers and EPDM terpolymers.*

Samples	Ethylene (wt%)	Diene (wt%)	T_g (°C)	T_m^I (°C)	T_c (°C)	T_m^{II} (°C)	ΔH_m^I (J/g)	ΔH_c (J/g)	ΔH_m^{II} (J/g)	x_c^{DSC}
EPM	78	0	-35	55.7	39.3 - 66	51.9	-76	74	-66	26
K2070P	73	0	-45.7	47.9	18.9	25.1	-38	38	-38	13
K5170P	71	1.5	-45.2	46.1	16.6	21.6	-37	36	-36	12
K5470P	70	4.6	-39.9	46.6	24.4	28.5	-41	37	-38	14
K6260Q	67	2.8	-46.2	45	8.5	4.1	-25	25	-29	8
K8570C	66	5	-40.5	46.7	13.4	24.7	-25	24	-25	8
K5470C	66	4.6	-40.3	45.3	18.1	21.3	-34	32	-32	11
K6160D	64	1.2	-50	46.3	-5.3	-8.7	-17	11	-14	6
K4450C	52	4.3	-58.6	/	/	/	/	/	/	/
K3050	49	0	-52.9	/	/	/	/	/	/	/
K9950C	44	9	-43	/	/	/	/	/	/	/

The values of the melting temperatures T_m, crystallization temperatures T_c and glass transition temperature T_g are reported in Figures 2.24, 2.25 and 2.26 respectively, as a function of ethylene and diene contents and of the total concentration of comonomeric units (ethylene + diene).

The values of melting temperature as a function of ethylene content (Figure 2.24A) are almost constant for all samples regardless the ethylene concentration and only a strong increase of T_m has been observed for the sample EPM, where the highest concentration of ethylene allows crystallization of small crystals of PE in pseudohexagonal form, as observed by WAXS. Similar behaviour can be observed reporting T_m as a function of diene content (Figure 2.24B). In fact the melting temperature decreases from the highest two values observed in the two copolymers EPM and K2070P to a constant value of ≈45 °C. Reporting the melting temperature as a function of the total concentration of comonomers (Figure 2.24C), a small increase of T_m with increasing the total comonomer concentration and a strong increase at higher concentration for the crystalline sample EPM have been observed.

The crystallization temperature also increases with increasing ethylene content (Figure 2.25A) and with increasing the total concentration of comonomers (Figure 2.25C), while no specific correlation between T_c and the diene content has been observed (Figure 2.25B). The sample K6160D indicated with a blue circle seems to be out of the correlations probably because it contains a different diene.

The correlation of the T_g with ethylene and diene concentrations is less evident (Figure 2.26). This is probably due to the difficulty of evaluating the exact values of the glass transition temperature from the DSC curves of Figure 2.23, where the broad melting endotherm and the glass transition are not well separated. Therefore, a better evaluation of the T_g has been obtained from DMTA measurements. (see section 2.6.4).

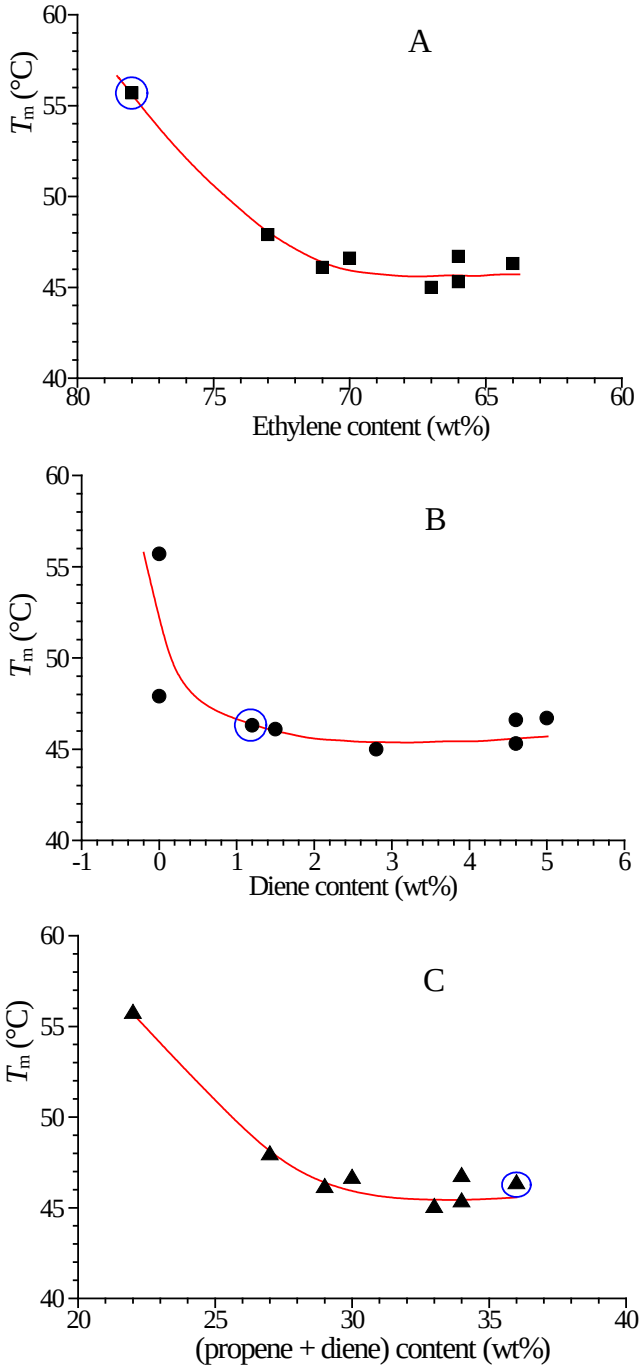

Figure 2.24 *Values of melting temperature (T_m) reported as a function of ethylene content (A), diene content (B) and total concentration of propylene and diene comonomeric units (C). The sample K6160D with DCPD instead of ENB as third monomer is indicated in the blue circle.*

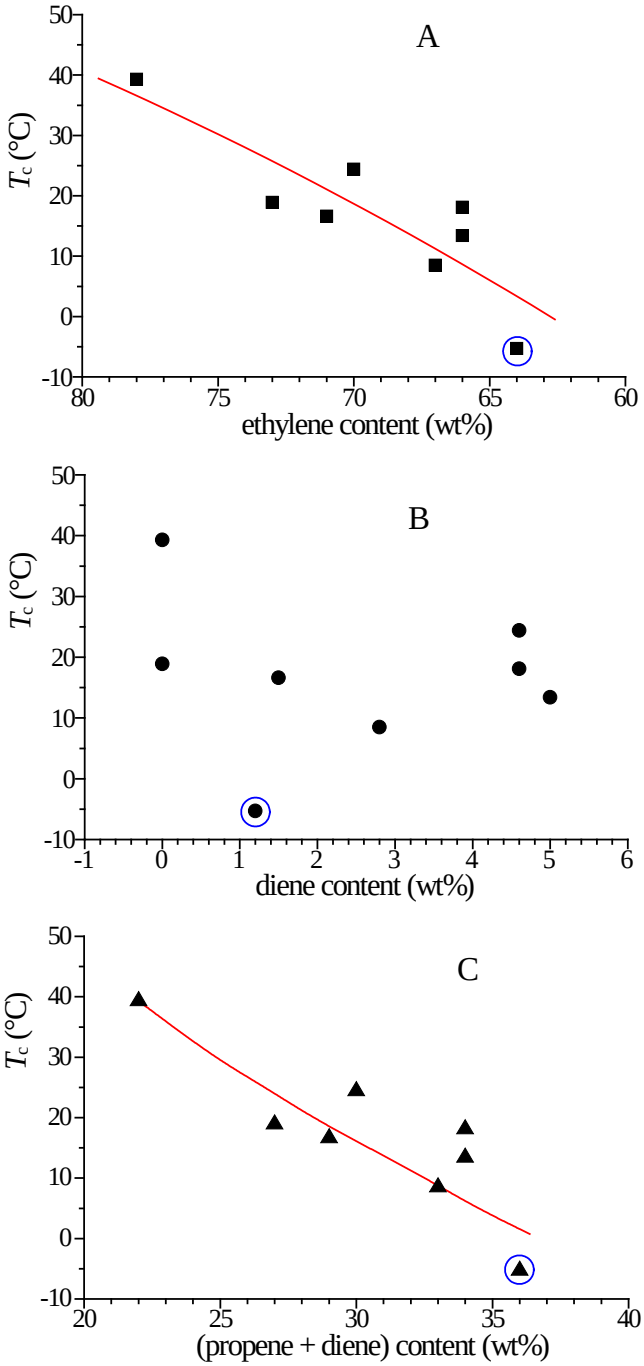

Figure 2.25 *Values of crystallization temperature (T_c) reported as a function of ethylene content (A), diene content (B) and total concentration of propylene and diene comonomeric units (C). The sample K6160D with DCPD instead of ENB as third monomer is indicated in the blue circle.*

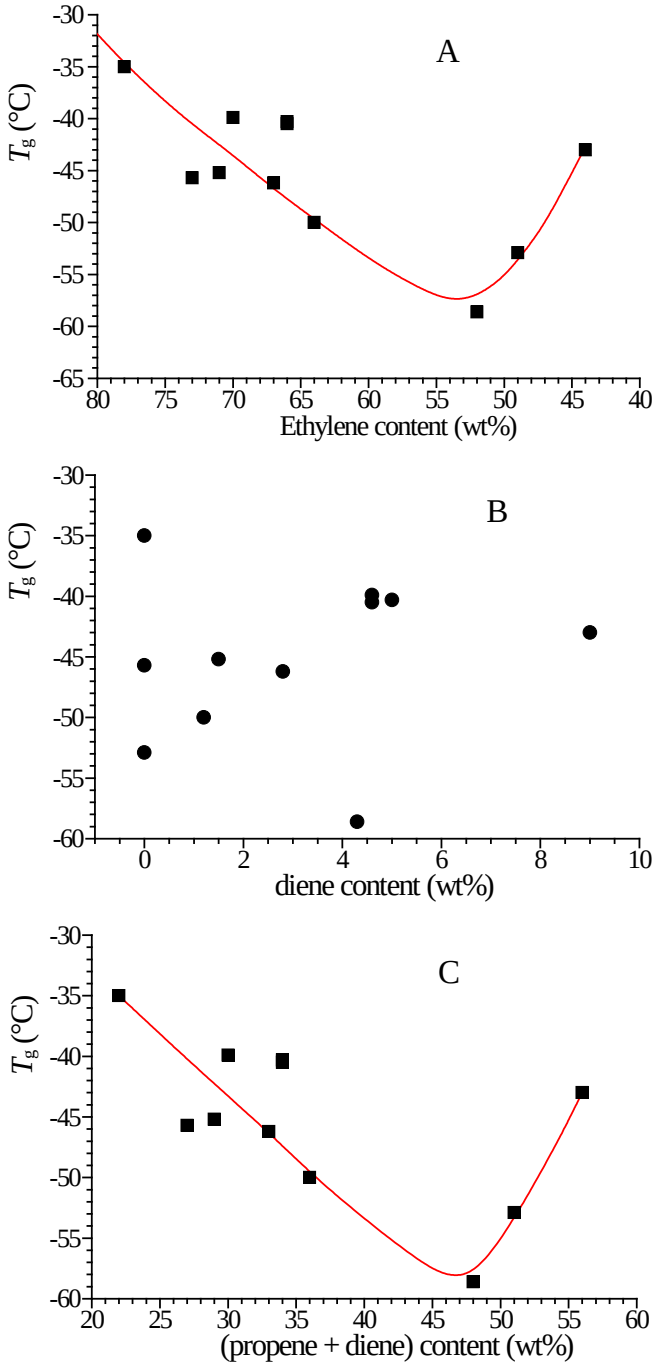

Figure 2.26 *Values of glass transition temperature (Tg) reported as a function of ethylene content (A), diene content (B) and total concentration of comonomeric units (C).*

Since crystallinity has been revealed better from DSC than from WAXS analysis, the evaluation of the degree of crystallinity has been performed using the values of melting enthalpy determined from the DSC curves of Figure

2.23A. Because of the broad melting peaks and the overlapping with the glass transition, the exact determination of the beginning of the melting endotherm is not immediate. As suggested by several methods reported in literature,[65] the extrapolation of the DSC curve to lower temperature from the melt (above 70 °C) has been used as the baseline for the melting peak. This curve also corresponds to the tangent for the glass transition evaluation. For all samples, the melting enthalpy ΔH_m has been evaluated integrating the area below the melting peak in the range -38 ÷ 70°C. Only for the sample EPM the range is -30 ÷ 70°C because of the higher T_g of this sample. The index of crystallinity x_c^{DSC} has been evaluated as:

$$x_c^{DSC} = \frac{\Delta H_m}{\Delta H_m^0}$$

where ΔH_m^0 = 297 J/g is the thermodinamic melting enthalpy of 100% crystalline PE.[66] The values of x_c^{DSC} are reported in Table 2.3 and in Figure 2.27A-C as a function of ethylene and diene contents and total concentration of comonomers. The sample EPM has the highest value of crystallinity then that decreases with decreasing ethylene concentration. The other three samples with high ethylene content (K2070P, K5170P, K5470P) show lower but similar values of crystallinity. This indicates that the crystallinity is mainly related to the ethylene concentration rather than the diene content. The samples of the second set with lower ethylene content (67 - 64 wt%) show similar and very low crystallinity (6 - 8%). The sample K5470C, prepared with the catalyst ACE, shows instead a slightly higher crystallinity, more similar to that of the samples of the first set. This indicates that with the catalyst ACE more crystalline samples with lower ethylene concentration can be obtained. This, in turn, demonstrates that in samples prepared with the ACE catalyst the sequences of ethylene units are longer than those in samples of similar ethylene concentration prepared with vanadium-based catalyst, as for example the sample K6260Q. However, the other sample prepared with the catalyst ACE (K8570C) having ethylene content similar to that of the sample K5470C shows lower crystallinity probably due to the higher concentration of diene.

For EPM and EPDM samples with ethylene contents in the range 78-64 wt% DSC experiments with different cooling rates have also been performed. Each experiment consists of a first heating scan from -100 to 180 °C at heating rate of 10°C/min, a cooling scan from 180 °C to -100 °C with variable cooling rates, and a second heating scan from -100 to 180 °C always at heating rate of 10°C/min. The selected cooling rates are 2.5, 10 and 20°C/min. The cooling

scans at the different cooling rates and the successive heating scans of the crystallized samples are shown in the Figures 2.28-2.30. For the copolymer samples EPM and K2070P with high ethylene content, as expected, the crystallization temperature decreases with increasing cooling rate (Figure 2.28A,B), while the corresponding melting temperature of the samples melt crystallized at different cooling rates increases with increasing cooling rate (Figure 2.28A',B'). Moreover, the sample EPM always presents two crystallization peaks, because of the coexistence of ethylene sequences of different length (Figure 2.28A): the peak at higher temperature corresponds to the crystallization of the longer sequences, the peak at lower temperature corresponds to the crystallization of shorter sequences.

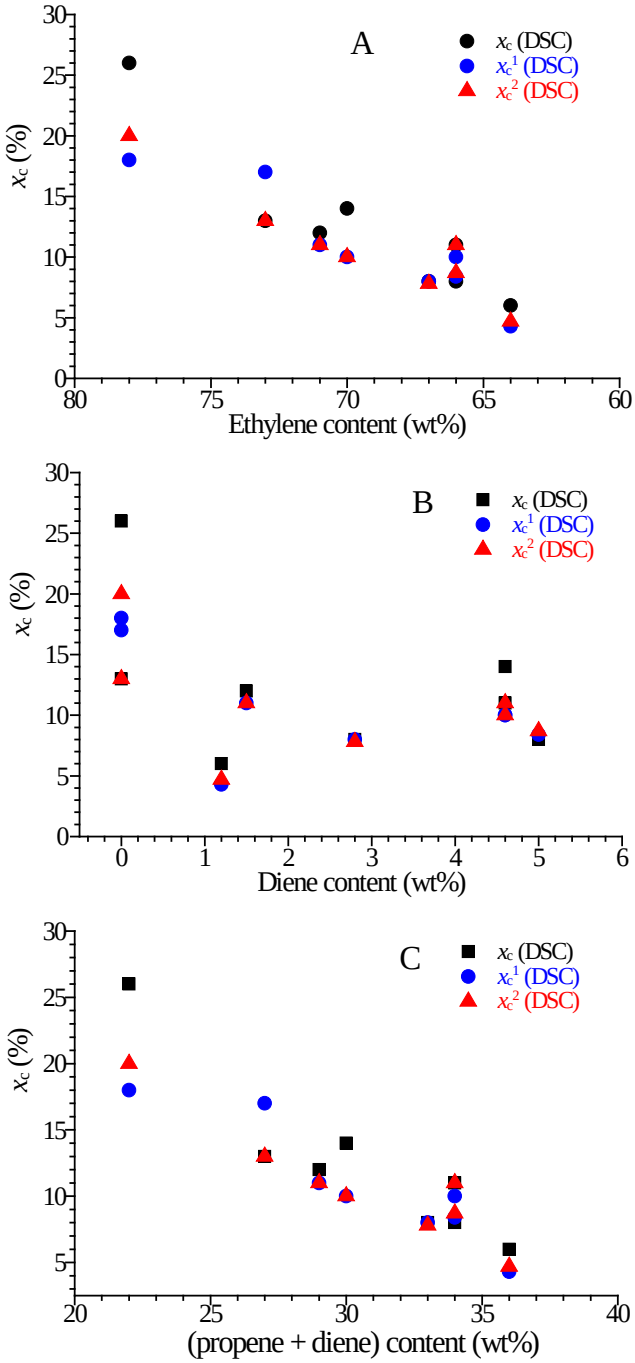

Figure 2.27. *Values of the degree of crystallinity evaluated from the first heating scan at 10°C/min of Figure 2.23A (x_c^{DSC}) (■), evaluated from the DSC cooling scan at 2.5°C/min of Figures 2.28-2.30 (x_c^1(DSC)) (●) and evaluated from the heating scan of the samples melt-crystallized at 2.5°C/min of Figures 2.28-2.30 (x_c^2(DSC)) (▲) of samples of EPM copolymers and EPDM terpolymers, as a function of ethylene content (A), diene content (B) and total concentration of comonomeric units (C).*

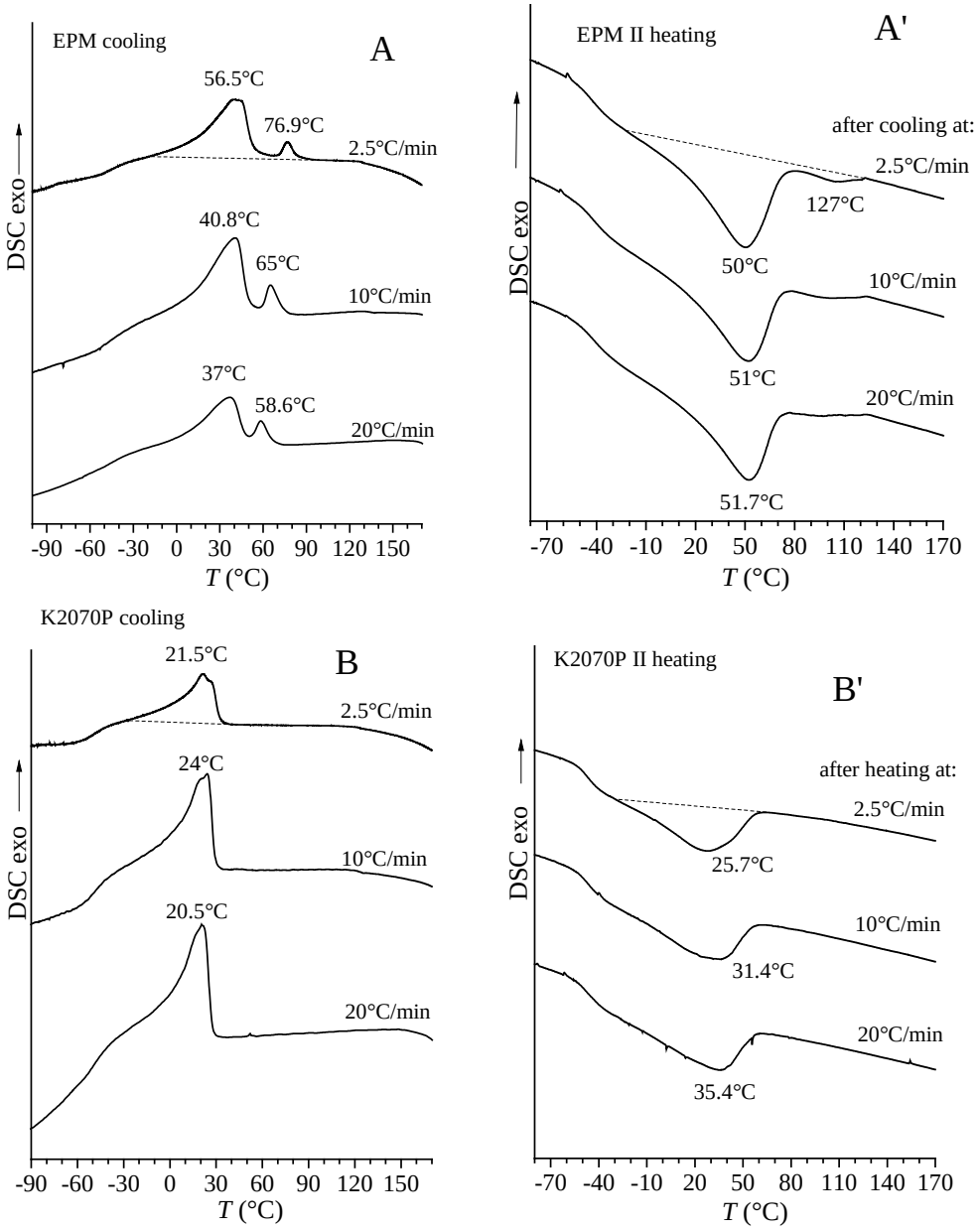

***Figure 2.28**. DSC cooling curves (A,B) recorded at the indicated cooling rates and corresponding DSC heating curves (A',B') recorded at heating rate of 10 °C/min of samples crystallized from the melt at the different cooling rates in A,B of EPM (A,A') and K2070P (B,B') copolymers.*

In the case of EPDM terpolymers, the cooling and corresponding heating scans are reported in Figure 2.29 for samples with ethylene content ≈ 70 wt% and in Figure 2.30 for samples with ethylene content in the range 67-64 wt%. In all samples, regardless the ethylene and diene contents, the crystallization temperature decreases and the corresponding melting temperature of the melt-

crystallized samples increases with increasing cooling rate, as for the copolymer samples of Figure 2.28.

The decrease of T_c with increasing cooling rates is due to supercooling effects. On the other hand, crystals formed at higher temperatures at low cooling rate should melt at higher temperature, and, instead, a decrease of the melting temperature at low cooling rate is observed. This can be explained considering that continuous melting and recrystallization phenomena occur during the melting of less stable crystals. Crystals formed at low crystallization temperatures at higher cooling rates (10 °C - 20 °C/min), indeed, are less stable and are subjected to reorganization phenomena during heating, resulting in increase of melting temperature. Crystals formed at higher crystallization temperatures at low cooling rate of 2.5°C/min are more stable, and, therefore, are not (or less) subjected to reorganization phenomena during heating. As a result, their melting temperatures are lower.

The values of the crystallization and melting temperatures and enthalpies and the degree of crystallinity x_c^1(DSC) calculated using the crystallization enthalpy evaluated from the cooling scan at 2.5°C/min of Figures 2.28-2.30, and the degree of crystallinity x_c^2(DSC) calculated using the melting enthalpy evaluated from the heating scans of the samples melt-crystallized at 2.5 °C/min, are reported in Table 2.4. The values of crystallinity x_c^1(DSC) and x_c^2(DSC) are also reported in Figure 2.27 in comparison with the values of crystallinity x_c^{DSC} of Table 2.3, evaluated from the melting enthalpy ΔH_m^I measured from the DSC curves of the first heating scans (Figure 2.23A). The values of crystallinity x_c^1(DSC) and x_c^2(DSC) are similar to the values x_c^{DSC}.

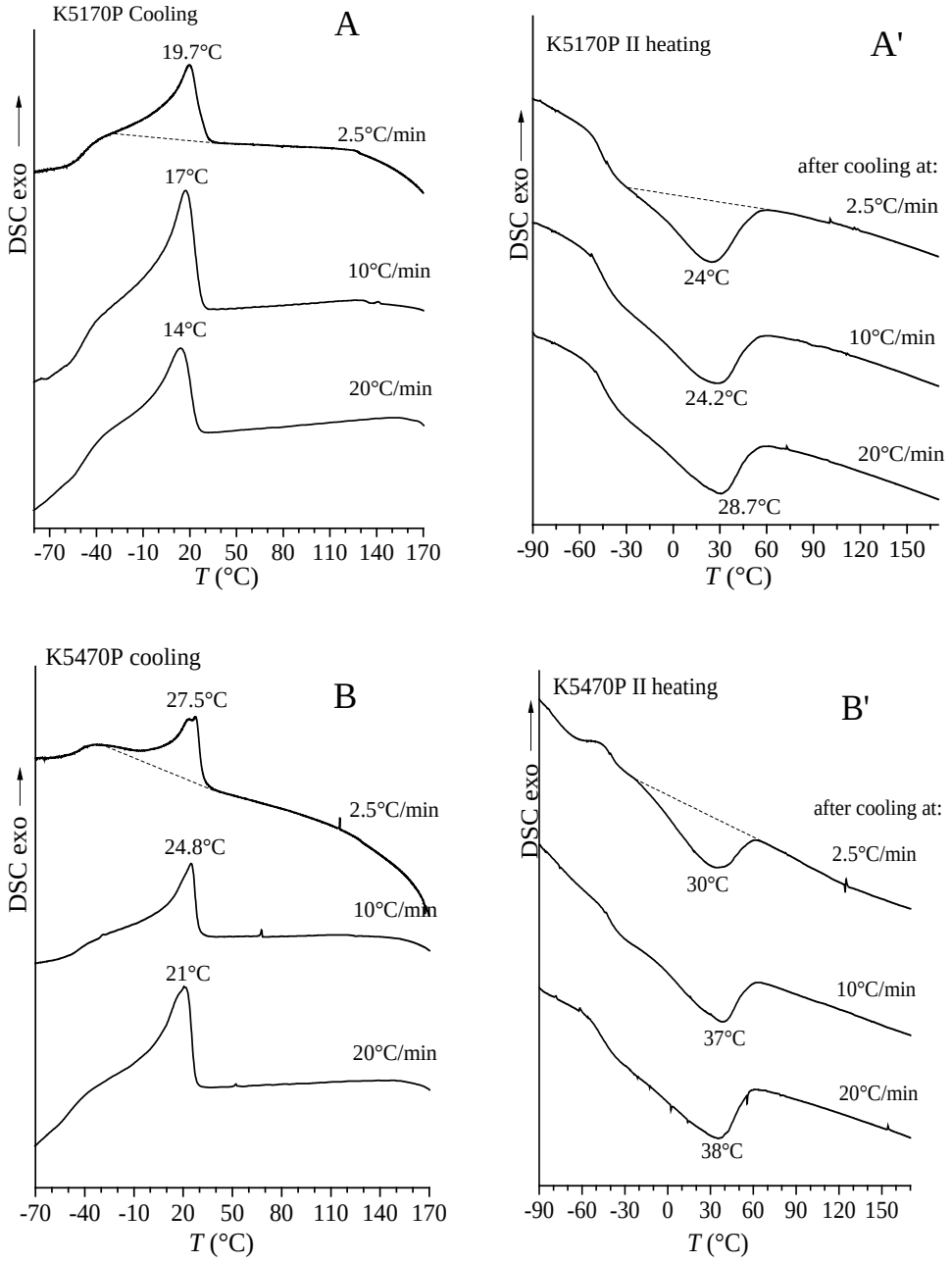

***Figure 2.29**. DSC cooling curves (A,B) recorded at the indicated cooling rates and corresponding DSC heating curves (A',B') recorded at heating rate of 10 °C/min of samples crystallized from the melt at the different cooling rates in A,B of samples K5170P (A,A') and K5470P (B,B').*

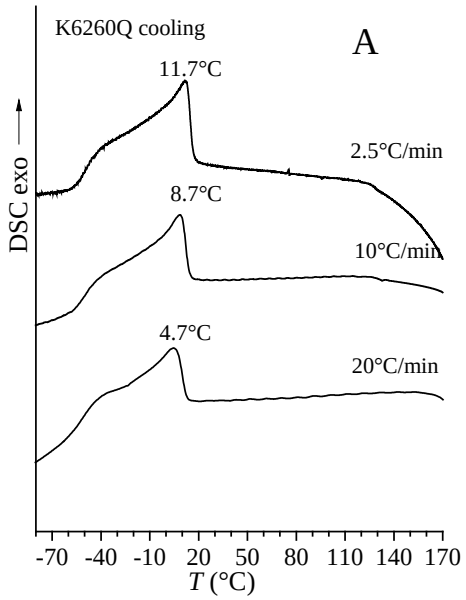
K6260Q cooling
A
11.7°C
2.5°C/min
8.7°C
10°C/min
4.7°C
20°C/min
DSC exo
-70 -40 -10 20 50 80 110 140 170
T (°C)

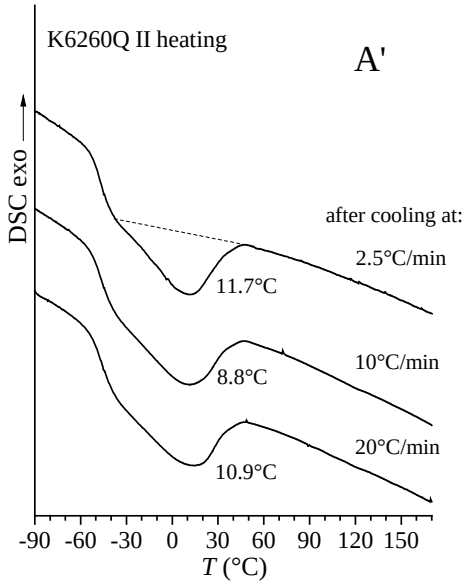
K6260Q II heating
A'
after cooling at:
2.5°C/min
11.7°C
10°C/min
8.8°C
20°C/min
10.9°C
DSC exo
-90 -60 -30 0 30 60 90 120 150
T (°C)

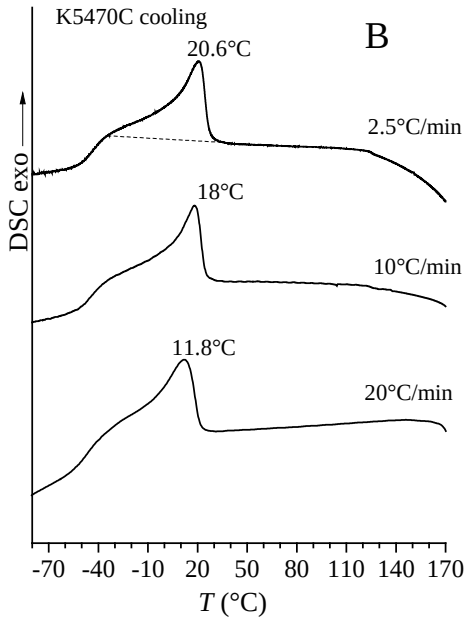
K5470C cooling
B
20.6°C
2.5°C/min
18°C
10°C/min
11.8°C
20°C/min
DSC exo
-70 -40 -10 20 50 80 110 140 170
T (°C)

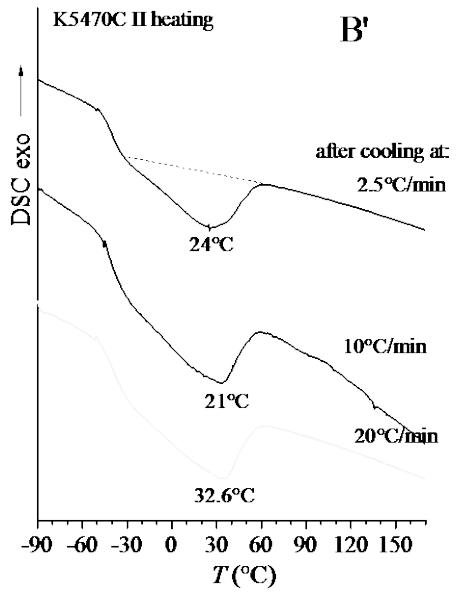
K5470C II heating
B'
after cooling at:
2.5°C/min
24°C
10°C/min
21°C
20°C/min
32.6°C
DSC exo
-90 -60 -30 0 30 60 90 120 150
T (°C)

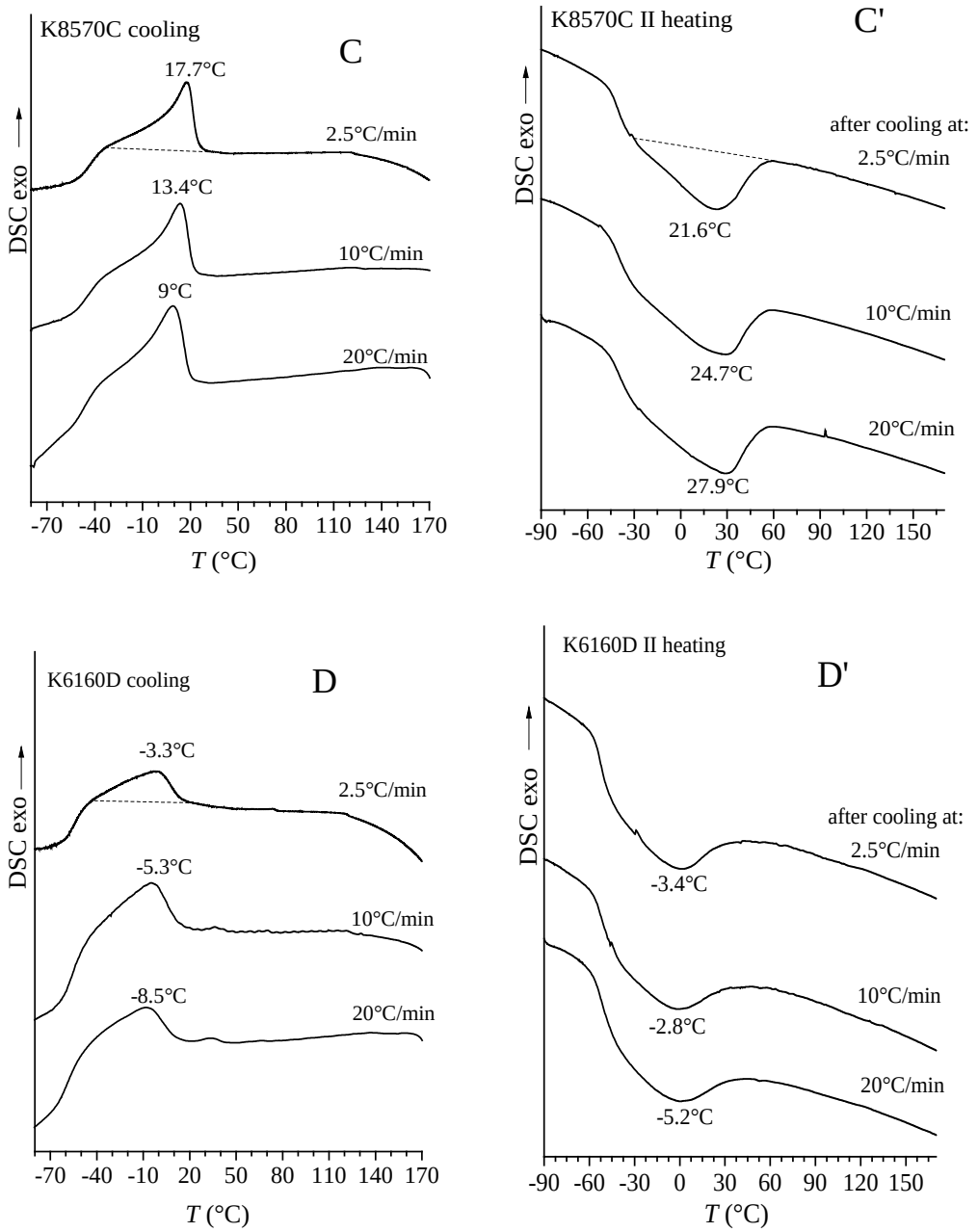

Figure 2.30. *DSC cooling curves (A-D) recorded at the indicated cooling rates and corresponding DSC heating curves (A'-D') recorded at heating rate of 10 °C/min of samples crystallized from the melt at the different cooling rates in A-D of samples K6260Q (A,A'), K5470C (B,B'), K8570C (C,C'), K6160D (D,D').*

Table 2.4. *Ethylene and diene contents, cooling rates, crystallization temperatures (T_c) and enthalpies (ΔH_c), melting temperatures (T_m) and enthalpies (ΔH_m), degree of crystallinity evaluated from the cooling scan at 2.5°C/min (x_c^1(DSC)) and from the successive heating scan (x_c^2(DSC)) of samples of EPM copolymers and EPDM terpolymers.*

Sample	Ethylene content (wt%)	Diene content (wt%)	Cooling rate	T_c (°C)	ΔH_c (J/g)	T_m (°C)	ΔH_m (J/g)	x_c^1(DSC)	x_c^2(DSC)
EPM	78	/	2.5°C/min	56.5, 106.5	52.9	50	59.8	18	20
			10°C/min	40.8, 65	51.4	51	41.8		
			20°C/min	37, 58.6	50	51.7	39		
K2070P	73	/	2.5°C/min	21.5	50	26	38.5	17	13
			10°C/min	24	41	31	40.7		
			20°C/min	20.5	40	35	40		
K5170P	71	1.5	2.5°C/min	20	34	24	34.5	11	11
			10°C/min	17	37	24.2	44		
			20°C/min	14	32	28.7	36		
K5470P	70	4.7	2.5°C/min	27.5	30	30	31.9	10	10
			10°C/min	24.8	38	37	30.6		
			20°C/min	21	40	38	25.5		
K6260Q	67	2.8	2.5°C/min	11.7	24.5	11.7	23.3	8	7.8
			10°C/min	8.7	23.7	8.8	23.6		
			20°C/min	4.7	21.5	10.9	22.5		
K5470C	66	4.6	2.5°C/min	20.6	30	20	33	10	11
			10°C/min	18	39.5	21	32		
			20°C/min	11.8	30.2	32.6	29.6		
K8570C	66	5.0	2.5°C/min	17.7	25	21.6	26	8.4	8.7
			10°C/min	13.4	24	24.7	25		
			20°C/min	9	26	27.9	26		
K6160D	64	1.2	2.5°C/min	-3.3	13	-3.4	14	4.3	4.7
			10°C/min	-5.3	13	-2.8	14		
			20°C/min	-8.5	13.3	-5.2	13.5		

2.6.3 Study of the morphology by Small Angle X-ray Scattering (SAXS)

The morphology of all EPM and EPDM samples has been studied by Small Angle X-ray Scattering to confirm the existence of the cryptocrystallinty found by DSC measurements but not visible by WAXS and to verify that these small crystals are able to arrange in ordered entities on the nanometer scale. The analysis has been performed on compression moulded films of samples of EPM copolymers and EPDM terpolymers aged for one month at room temperature to allow eventual slow crystallization of the samples. Moreover, for studying the possible influence of talc as nucleating agent, the same analysis has been also performed on the sample K5470NT that has the same composition as the sample K5470P but does not contain talc.

SAXS profiles of compression molded films aged for one month have been collected firstly at room temperature. The range of values of the analyzed scattering vector q is 0.1 $nm^{-1} \leq q \leq 2$ nm^{-1}, where $q = 4\pi \sin\theta/\lambda$ and 2θ is the scattering angle. After subtraction for dark current, the empty sample holder, and a constant background due to thermal density fluctuations, the slit smeared data have been de-convoluted with the primary-beam intensity distribution using the SAXSquant 2.0 software to obtain the corresponding pinhole scattering (desmeared) intensity distribution. Because of the finite range of accessible values of the scattering vector q, the scattering intensity has been extrapolated to very low (q = 0) and very high (q = ∞) values of q. In the assumption that SAXS intensity probes heterogeneities arising from a simple two phase structure at nanometer length scale, the SAXS desmeared data $I(q)$, after subtraction of the residual background intensity (approximated as a constant I_{back}) has been extrapolated to high q values with the Porod law:[67]

$$I(q) = Kq^{-4} \qquad (1)$$

in the hypothesis that no diffuse boundary between crystalline and amorphous layers occurs, by fitting the experimental intensity data $I_{obs}(q)$ in the high q region ($q > 1.2$ nm^{-1}) with Equation 2:

$$\lim_{q\to\infty}\left[I_{obs}(q) - I_b\right] = K_p q^{-4} \qquad (2)$$

where K_p is a quantity proportional to the Porod constant through a factor K due the fact that our intensity is in relative units. In this procedure the value of

K_p has been found by selecting of the value of background intensity I_{back} that maximizes the length of Porods's region.[67]

The SAXS desmeared data $I(q)$ have been extrapolated to q = 0 using the Debye−Bueche equation (Equation 3).[68]

$$I_{obs}(q) - I_b = \frac{B}{\left(1 + C^2 q^2\right)^2} \qquad (3)$$

where B and C are interpolation parameters.

Since the samples are isotropic with no preferred orientation of the crystals, the total scattered intensity $I(q)$ has been transformed into one-dimensional intensity by multiplication for the Lorentz factor equal to $4\pi(2\sin\theta/\lambda)^2 = q^2/\pi$.[67] The value of the scattering vector q of the maximum SAXS intensity (correlation peak) has been evaluated from the Lorentz corrected profiles as q^*.

The desmeared SAXS profiles of selected copolymer samples and the corresponding Lorentz corrected profiles are shown in Figure 2.31A and 2.31B, respectively. The SAXS profiles of the samples of the first set with ethylene concentration in the range 78-70 wt% show well defined correlation peaks. For the two copolymers with the highest ethylene contents, EPM (with 78 wt% of ethylene, Figure 2.31A,B curve *a*) and K2070P (with 73 wt% of ethylene, Figure 2.31A,B curve *b*), the correlation peaks are centered at q^* = 0.37 and 0.38 nm^{-1} respectively. Within this set of samples, changes in the position and intensity of the peaks are observed in EPDM terpolymers depending on the ethylene content. The SAXS profiles of the first two terpolymers, K5170P and K5470P with 71-70 wt% of ethylene show correlation peaks centered at q^* = 0.38 and 0.39 nm^{-1} respectively (curves c,d of Figure 2.31), as in the case of the two copolymers EPM and K2070P, notwithstanding the presence of the third monomer. The peak of the sample K5470P without talc, K5470NT, is less intense, broad and centered at q^* = 0.36 nm^{-1} (curve e of Figure 2.31).

SAXS profiles of samples K6260Q with 67 wt% of ethylene and K6160D with 64 wt% of ethylene (Figure 2.31A,B curves *f, h*) belonging to the second set of the series (ethylene content in the range 67-64 wt%) show very broad and weak correlation peaks centered at lower q values, 0.19 and 0.29 nm^{-1}, respectively. Once again, the sample K5470C (66 wt% of ethylene) is an exception in the set because of the well-defined peak centered at q^* = 0.40 nm^{-1}, very similar to those observed in SAXS profiles of samples of the first set with higher ethylene content. Moreover, SAXS profile of the sample K6260Q

(67 wt% of ethylene) shows an additional peak at higher *q* values probably due to impurities derived from the catalytic process (curve f of Figure 2.31B).

SAXS profiles of samples with lower ethylene content, that is the copolymer K3050 (49 wt% of ethylene) and the terpolymers K4450 (52 wt% of ethylene) and K9950C (44 wt% of ethylene) (Figure 2.31A,B curves *l, i, m,* respectively) do not show any correlation peak.

These data indicate that position and intensity of the correlation peak decrease within the first set of samples (78-70 wt% of ethylene) going from copolymers to terpolymers and further decrease in the second set (76-64 wt% ethylene) with decreasing ethylene concentration. No correlation peaks are observed for the third set of sample with lower ethylene content (52-44 wt%).

The WAXS profiles of the same compression-moulded and aged samples recorded suimultaneously to the SAXS data of Figure 2.31 are shown in Figure 2.32A. These data are similar to those reported in Figure 2.19 for the as-received samples and indicate that only the sample EPM with the highest ethylene concentration of 78 wt% is clearly crystalline with the presence of the reflection at $2\theta \approx 21°$ typical of the pseudohexagonal crystalline form of PE (profile a of Figure 2.32A). This also indicates that no increase of crystallinity upon aging at room temperature is revealed by WAXS. The DSC heating curves from room temperature to 180 °C of the same compression-molded samples are shown in Figure 2.32C. These data are similar to the DSC curves of samples cooled (crystallized) from the melt Figure 2.23C, recorded from -90 °C to 180 °C, and indicate that all samples with ethylene concentrations from 78 to 64 wt% present clear melting endothermic peaks, suggesting presence of crystallinity.

The presence of a correlation peak in the SAXS profiles of Figure 2.31 may be attributed to the presence of crystallinity. This is not surprising in the case of the sample EPM with the highest ethylene concentration that shows a clear Bragg reflection at $2\theta \approx 21°$ typical of PE in pseudohexagonal crystalline form in the WAXS patterns (profiles a of Figures 2.19 and 2.32A and in Figure 2.21A) and, in part, for samples K2070P, K5170P and K5470P with 73-70 wt% of ethylene, that show a weak shoulder of the main broad halo at $2\theta \approx 19°$ typical of amorphous EP copolymers (profiles b-d of Figure 2.19 and 2.32A). The presence of a correlation peaks in the SAXS profiles of the other samples with lower ethylene concentration (67-64 wt%) (curves f-h of Figure 2.31) that appear amorphous from the WAXS profiles (profiles e-h of Figure 2.19 and f-h of Figure 2.32A) is instead surprising. However, for these samples the presence

of crystallinity has been revealed by the presence of endothermic peaks in the DSC heating curves of Figures 2.23A and 2.32C and by the exothermic peaks in the DSC cooling scans from the melt of Figure 2.23B. The SAXS data of Figure 2.31 indicate that the cryptocrystallinity revealed by DSC analysis and not detected by WAXS is surprisingly confirmed by SAXS.

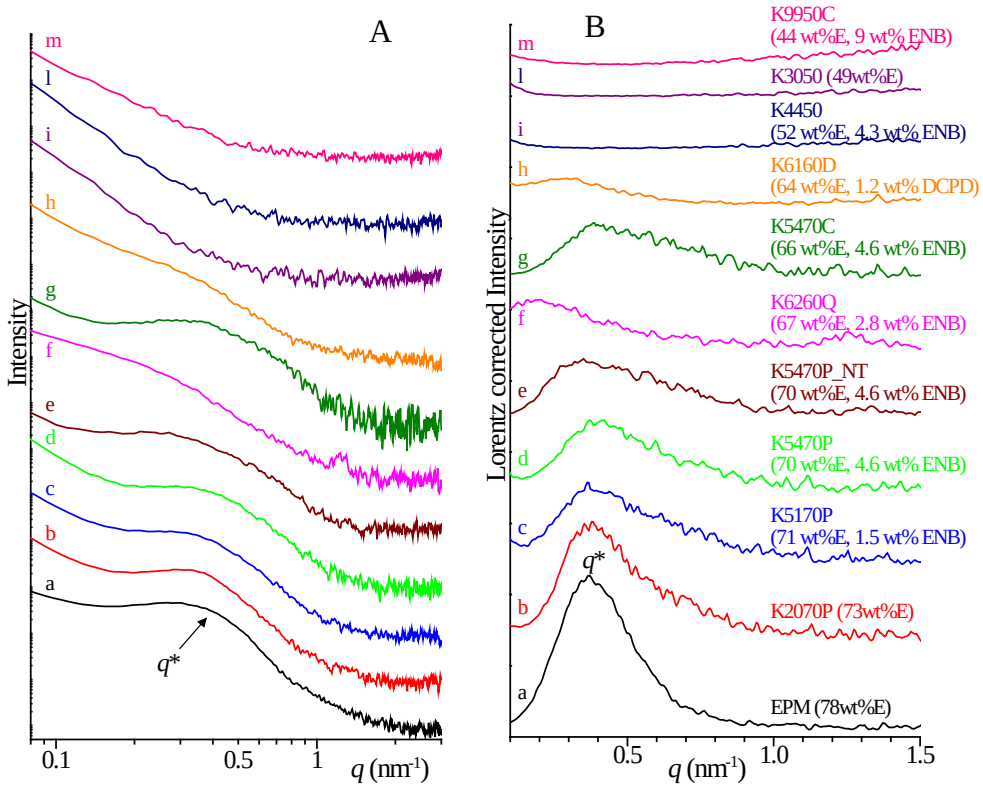

Figure 2.31. *SAXS intensity profiles (A) and Lorentz-corrected SAXS profiles (B) measured at room temperature of compression-moulded samples of EPM copolymers and EPDM terpolymers with the indicated concentration of ethylene and diene, aged at room temperature for 1 month.*

The SAXS data can be, in fact, interpreted in terms of a crystalline lamellar morphology (Figure 2.33) that presents large imperfections due to the presence of the propene and diene units, with amount of defects increasing with increasing propene and diene concentrations. The formation of distorted lamellar morphologies is, indeed, typical of copolymers.[69] Distorted lamellae having small lateral dimensions, large distributions of the thicknesses of the crystalline and amorphous layers in the lamellar stacks, the presence of single lamellar entities besides a population of periodic arrays of parallel lamellae are typical defects, in particular for copolymers.[70]

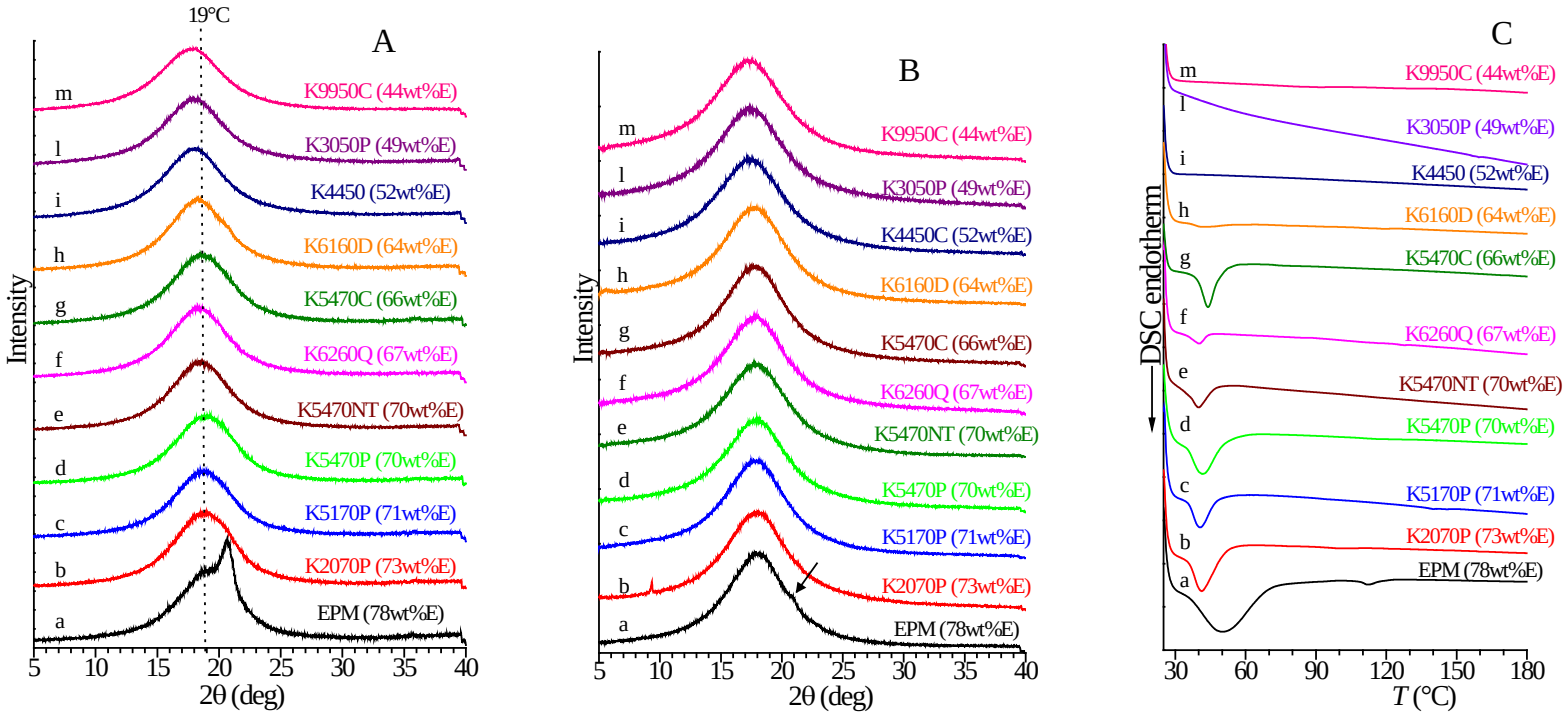

Figure 2.32. *WAXS profiles of aged compression moulded films of sample of EPM copolymers and EPDM terpolymers recorded simultaneously to SAXS profiles at room temperature (A) and at 90°C (B). DSC heating curves collected from room temperature to 180°C of aged compression moulded films of sample of EPM copolymers and EPDM terpolymers (C).*

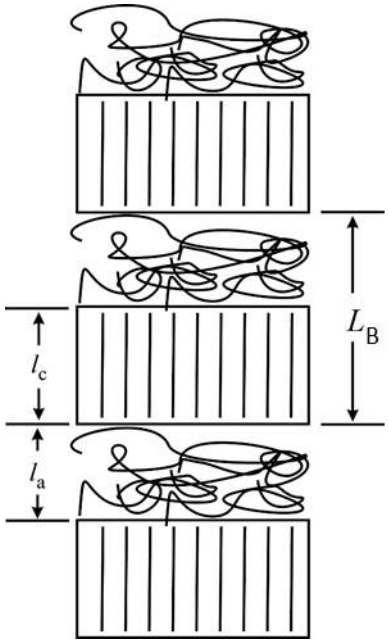

Figure 2.33. *Model of lamellar stacks for a two phase system with layers of lamellar crystals of thickness l_c alternating with layers of amorphous phase of thickness l_a. The long spacing L_B corresponds to l_a+l_c.*

The small intensity of SAXS scattering in samples with lower ethylene content and in particular, the steep increase of the intensity in the low q region of the SAXS profiles of samples with ethylene content lower than 70 wt% may be associated with the small lateral dimensions of the crystallites and the presence of non-negligible amount of extra-lamellar amorphous phase.

The morphological parameters of crystals of EPM copolymers and EPDM terpolymers, in particular the lamellar thickness, have been determined from the SAXS data of Figure 2.31. The average values of the lamellar long period L_B can be evaluated from the position q of the peak maxima (q^*) in the Lorentz corrected SAXS intensities of Figure 2.31B as $L_B = 2\pi/q^*$. The values of the long period have been used for a rough evaluation of the thicknesses of crystalline layers l_c (defined l_c^* because it is evaluated from the value of q^*) as $l_c^* = L_B\, x_c/100$ with x_c the crystallinity index determined from the wide angle X-ray powder diffraction profiles of Figure 2.32A.[67,69] The thickness of the amorphous layers, l_a^*, has been then evaluated as $l_a^* = L_B - l_c^*$. The crystallinity index x_c evaluated from the WAXS profiles of Figure 2.32A has been determined as the ratio between the crystalline diffraction area (A_c) and the area of the whole diffraction profiles (A_t), $x_c(\text{WAXS}) = (A_c/A_t)\times 100$. The crystalline diffraction area A_c has been evaluated by subtracting the area of the amorphous halo from the area of the whole diffraction profiles A_t. The

diffraction profiles collected at 90°C (Figure 2.32B) for each samples have been used as the diffraction profile of the amorphous phase. These diffraction profiles of the amorphous phases of each sample were then scaled and subtracted to the whole diffraction profiles of the samples at room temperature to obtain the crystalline diffraction area A_c.

The values of long period $L_{B,}$ of thicknesses of crystalline l_c* and amorphous layers l_a* are reported in Table 2.5 and in Figure 2.34 as a function of ethylene and diene concentrations and of total concentration of comonomers. The values of crystallinity x_c(WAXS) are also reported in Table 2.5.

Table 2.5. Values of the scattering vector corresponding to the maxima of SAXS intensity (q^*), long period L_B, thickness of crystalline lamellae l_c^*, thickness of amorphous layers l_a^* evaluated from the SAXS intensity profiles of Figure 2.31B and degree of crystallinity x_c(WAXS) evaluated from the WAXS profiles of Figure 2.32A. The value of L_B has been evaluated as $L_B = 2\pi/q^*$, whereas the values of l_c^* and l_a^* have been calculated as $l_c^* = L_B x_c/100$ and $l_a^* = L_B - l_c^*$. Values of long period L, thickness of crystalline l_c and amorphous l_a layers and degree of crystallinity x_c(cofun) = l_c/L, evaluated from the correlation function $\gamma(z)$ are also reported.

Sample	wt% ethylene	wt% diene	q^* (nm^{-1})	L_B (nm)	x_c(WAXS) (%)	l_c^* (nm)	l_a^* (nm)	L (nm)	l_c (nm)	l_a (nm)	x_c(cofun) (%)
EPM	78	-	0.37	17.0	16	2.7	14.3	15.7	5.1	10.6	32
K2070P	73	-	0.38	16.5	12	2.0	14.6	16.5	4.1	12.4	25
K5170P	71	1.5	0.38	16.5	10	1.7	14.9	17.4	3.7	13.7	21
K5470P	70	4.6	0.39	16.1	8	1.3	14.8	15.3	3.8	11.5	25
K5470NT	70	4.6	0.36	17.5	6	1.0	16.4	18.1	4.2	13.9	23
K6260Q	67	2.8	0.19	33.1	5	1.7	31.4	27.5	3.4	24.1	12
K5470C	66	4.6	0.40	15.7	6	0.9	14.8	16.0	3.4	12.6	21
K6160D	64	1.2	0.29	21.7	3	0.6	21.0	23.6	5.3	18.3	22

It is apparent from Figure 2.34A that the long spacing L_B slightly decreases from the value of 17 nm of the most crystalline sample EPM (78 wt% of ethylene) to the values of 16.5 nm of the copolymer K2070P (73 wt% of ethylene) and the first terpolymer K5170P (71 wt% of ethylene) to 16.1 nm of the terpolymer K5470P (70 wt% of ethylene). The sample K5470NT shows L_B value higher than that of the sample K5470P notwithstanding the same concentration of ethylene and diene. The samples with lower ethylene contents K6260Q (67 wt% of ethylene) and K6160D (64 wt% of ethylene) show the highest L_B values (33.1 and 21.7 nm respectively), while the L_B value of the sample K5470C with 66 wt% of ethylene is lower (15.7 nm) and very similar to the values of samples of the first group. The samples with lowest ethylene content do not show any correlation peak in SAXS profile, therefore the evaluation of morphological parameter is not possible.

The thickness of the crystalline layers l_c* decreases with decreasing ethylene concentration (Figure 2.34A) from the value of 2.7 nm of the sample EPM (78 wt% of ethylene) to about 2-1.0 nm of the copolymers K2070P (73 wt% of ethylene) and terpolymers K5170P(71 wt% of ethylene) and K5470P (70 wt% of ethylene) and K5470NT (70 wt% of ethylene). The different values of L_B and l_c* in the sample K5470NT with respect to the sample K5470P, despite the same composition, may be explained with the absence of talc, which probably acts as nucleating agent in sample K5470P and in all other samples. In samples with ethylene contents in the range 67-64 wt%, l_c* further decreases down to the lowest values of 0.9 and 0.6 nm for samples K5470C and K6160D, respectively. The thickness of the amorphous layers l_a* increases from the value of 14.3 nm of the sample EPM (78 wt% of ethylene) to the values of 14.6-14.9 nm of samples of copolymer K2070P (73 wt% of ethylene) and terpolymers K5170P (71 wt% of ethylene) and K5470P (70 wt% of ethylene), according with the decrease of crystallinity. The sample K5470NT show a l_a* value higher than that of the sample K5470P despite the same composition. This value along with the lower l_c* and higher L_B seems to confirm the nucleating capacity of talc. In this sample talc is absent, therefore cristallinity and l_c* are lower than in the same sample with talc (K5470P), while L_B is higher because of the higher value of l_a*. The maximum value of l_a* of 31.4 nm is observed in the sample K6260Q (67 wt% of ethylene). The sample K5470C (66 wt% of ethylene) is again an exception in the group, since the value of l_a* is 14.8 nm, very similar to samples with the highest ethylene content. The sample K6160D (64 wt% of ethylene) show higher l_a* value according with the lower ethylene content, but lower than that of the sample K6260Q.

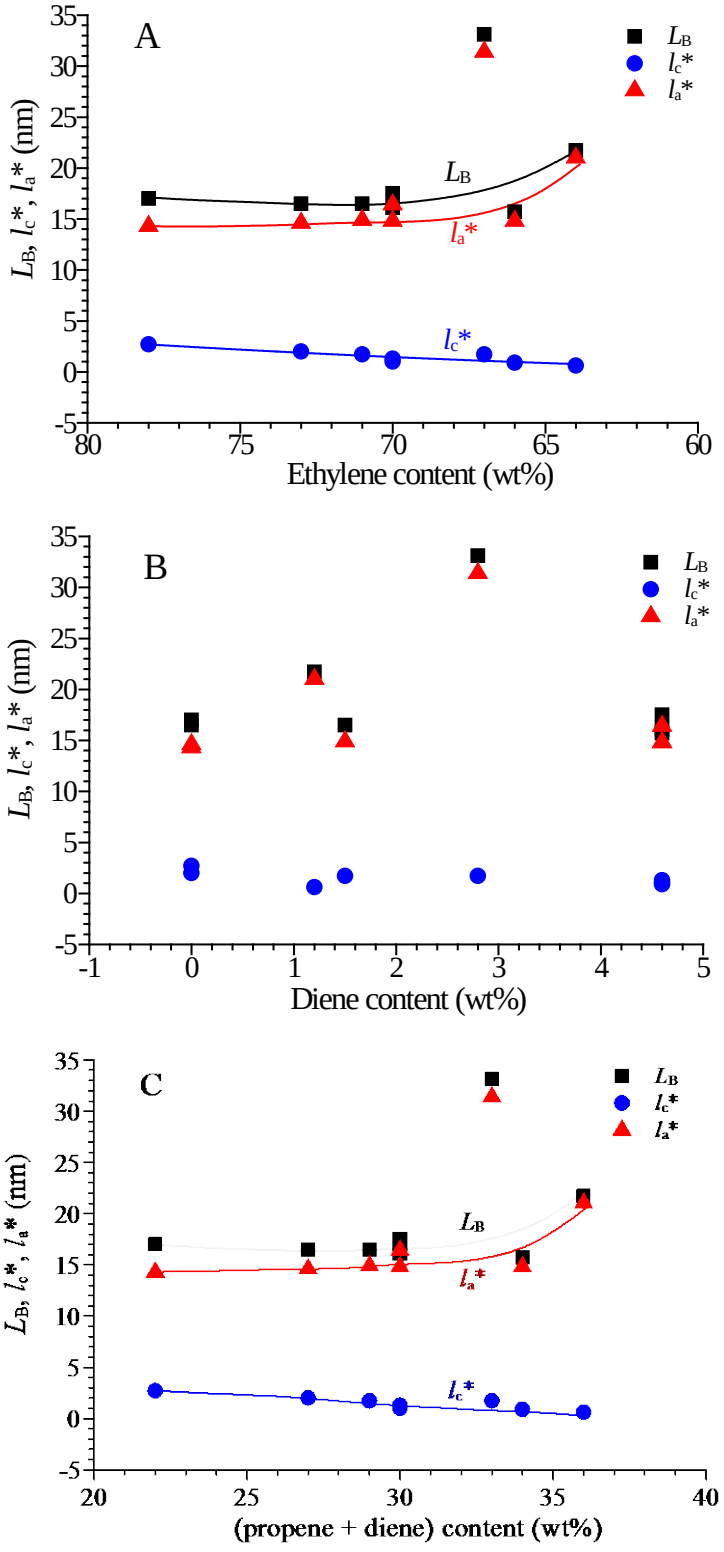

Figure 2.34. *Average values of the long period L_B (■), and of thickness of crystalline lamellae l_c^*(●) and amorphous layer l_a^* (▲) of melt-crystallized compression molded samples of EPM copolymers and EPDM terpolymers as a function of ethylene (A), diene (B) and total concentration of comonomeric units (C) evaluated from the SAXS data of Figure 2.31A,B.*

Therefore, the long period is almost constant with the ethylene concentration in the first set of samples and then increases due to the increase of l_a* as a consequence of the decrease of crystallinity. The values of morphological parameters L_B, l_c* and l_a* seem to be not dependent on the diene concentration (Figure 2.34B,C).

As mentioned above, the DSC heating scans of Figure 2.32C of of the melt-crystallized compression molded and aged samples with ethylene concentration from 78 wt% to 66 wt% show rather sharp endothermic peaks (curves a-g of Figure 2.32C). Compared to the DSC heating curves of Figure 2.23C of samples crystallized from the melt by cooling the melt down to -100 °C, the compression-molded sample of Figure 2.32C have been crystallized by cooling the melt down to room temperature. Therefore, the endothermic peaks of Figure 2.32C correspond to the melting of crystals formed at crystallization temperatures higher than or close to the room temperature (Figure 2.23B). These data, therefore, demonstrate that crystals are already present at room temperature. The cooling to -100°C allows only further crystallization and formation of smaller crystals melting at temperature lower than room temperature (Figures 2.23C), resulting in endothermic peaks in Figure 2.23C much broader than those of Figure 2.32C.

From the melting enthalpies of the DSC curves of Figure 2.32C the degree of crystallinity x_c^{aged}(DSC) has been evaluated and compared to the values determined from the WAXS profiles x_c(WAXS) of the same compression-molded samples of Figure 2.32A and Table 2.5. The values of crystallinty x_c(WAXS) and x_c^{aged}(DSC) of the melt-crystallized and aged samples and the values of crystallinity of the as-prepared samples x_c^{DSC} of Table 2.4, evaluated from the melting enthalpy in the DSC curves of the first heating scans of Figure 2.23A, are compared in Table 2.6. The values of melting temperatures (T_m^I) and melting enthalpies (ΔH_m^I) evaluated from the single heating scans of Figure 2.32C are also reported in Table 2.6. The values of crystallinty x_c(WAXS) and x_c^{aged}(DSC) are very similar whereas those x_c^{DSC} of the as-prepared samples are slightly higher.

Table 2.6 *Ethylene and diene contents, melting temperature (T_m^I), melting enthalpy (ΔH_m^I) and degree of crystallinity (x_c^{aged}) evaluated from the DSC heating curves of Figure 2.32C of aged compression molded samples of EPM copolymers and EPDM terpolymers. The degree of crystallinity x_c(WAXS) of the aged compression-molded samples evaluated from the WAXS profiles of Figure 2.32A and of table 2.5 and the degree of crystallinity x_c^{DSC} of as prepared samples of table 2.4, evaluated from the DSC first heating curves of Figure 2.23A, and, are also reported as a comparison.*

Samples	Ethylene (wt%)	Diene (wt%)	x_c(WAXS) (%)	T_m^I (°C)	ΔH_m^I (J/g)	x_c^{aged}(DSC) (%)	x_c^{DSC} (%) (as-prepared, from table 2.3
EPM	78	-	16	50.2; 112	-43	14	26
K2070P	73	-	12	41.2	-19	6	13
K5170P	71	1.5	10	40.4	-12	4	12
K5470P	70	4.6	8	41.5	-20	7	14
K5470NT	70	4.6	6	39.8	-8	3	8
K6260Q	67	2.8	5	40.1	-3	1	8
K5470C	66	4.6	6	43.9	-13	4	11
K6160D	64	1.2	3	41.6	-2	1	6
K4450	52	4.3	-	-	-	-	-
K3050	49	-	-	-	-	-	-
K9950C	44	9	-	-	-	-	-

SAXS measurements at different temperatures on samples with ethylene concentrations in the range 78-64 wt% have also been performed to verify whether the corrlation peaks observed in the SAXS profiles at room temperature are really related to the presence of crystallinity or could be attributed to some other heterogeneity. In Figure 2.35A,B the SAXS profiles of samples of copolymers EPM (78 wt% of ethylene) and K2070P (73 wt% of ethylene) recorded at 25°C and at 90°C and after cooling to room temperature are reported in Figure 2.35A,B. It is apparent that the correlation peaks observed at room temperature for both samples partially disappear at 90 °C and reappear after successive cooling to room temperature. This confirms that the correlation peaks are really due to the presence of crystals arranged in lamellar stacks morphology that melt at 90 °C and that for both samples crystallization occurs againg upon cooling (Figure 2.35A,B). After cooling the correlation peaks appear less defined and less intense, in particular for the sample K2070P (Figure 2.35B), and their position are slightly shifted at lower q^* values. This indicates higher long period values, probably due to an increase of l_a values. This can be explained with an incomplete crystallization leading to layers of lamellar crystals separated by thicker amorphous layers.

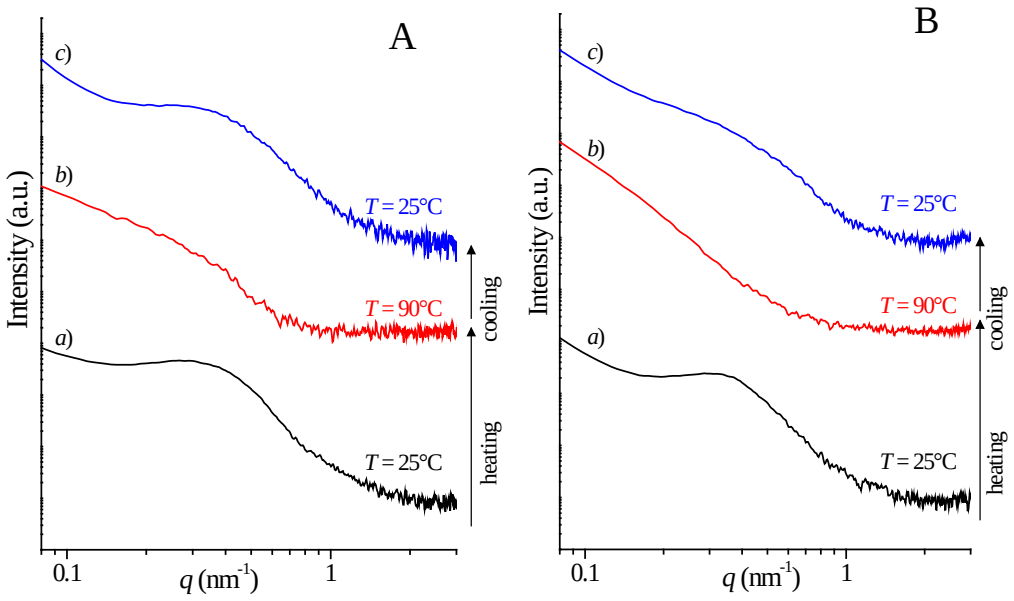

Figure 2.35. *SAXS profiles of samples EPM (A) and K2070P (B) recorded at 25°C (a), after heating up to 90 °C (b) and after cooling down to 25 °C (c).*

Similar results have been obtained for EPDM terpolymers of the first set of the series with ethylene concentration ≈71-70 wt% (Figure 2.36A-C). The correlation peak observed in SAXS profiles recorded at room temperature disappears at 90°C and reappears after the cooling at 25°C. Also in this case,

less defined peaks after heating and cooling and their shift to lower *q* values, heve been observed. The crystallization of these samples, indeed, is complete at temperature lower than room temperature (see Figure 2.23, 2.28, 2.29), whatever the cooling rate from the melt.

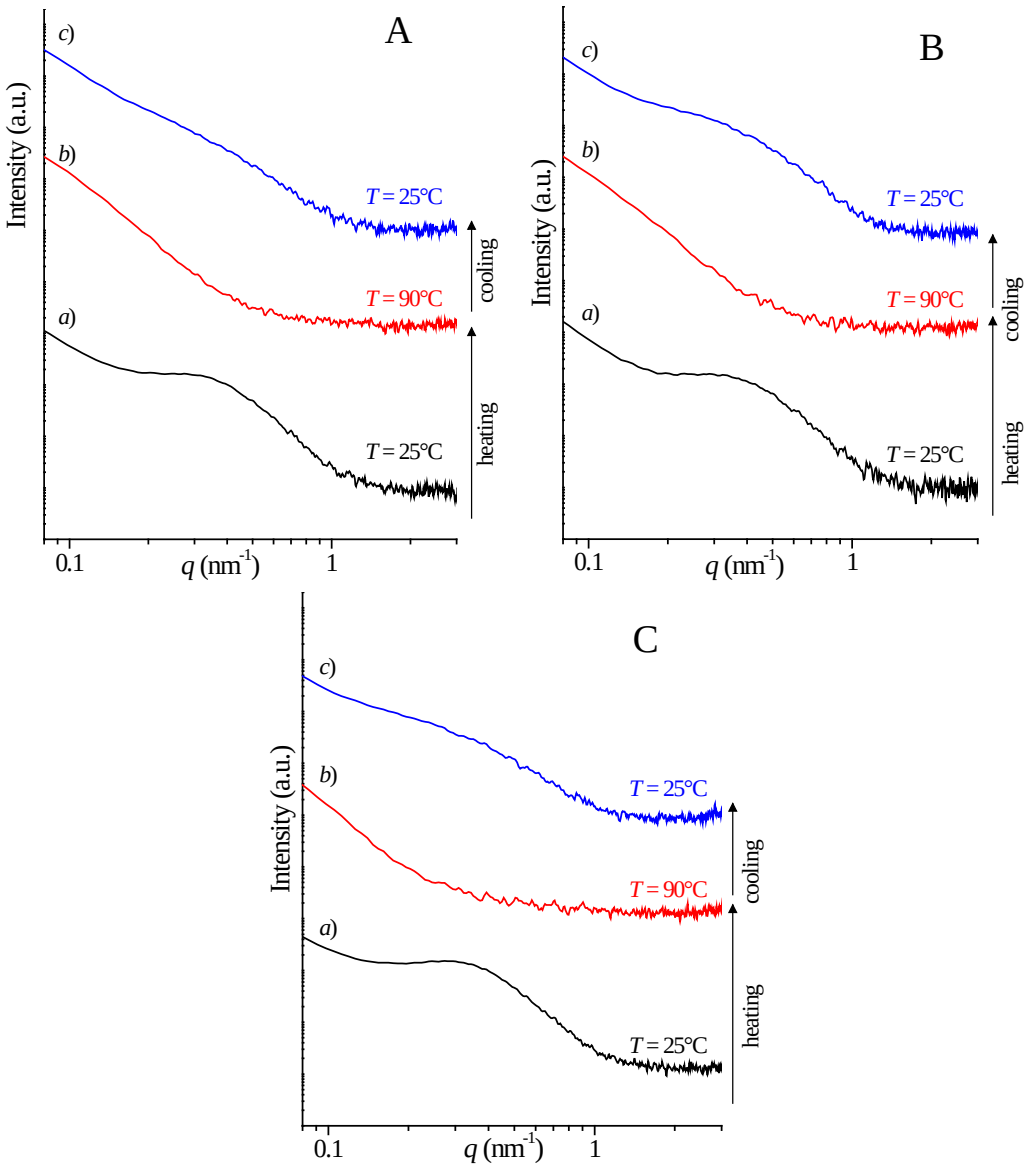

Figure 2.36. *SAXS profiles of samples K5170P (A), K5470P (B) and K5470PNT (C) recorded at 25°C (a), after heating up to 90°C (b) and after cooling down to 25°C (c).*

SAXS profiles collected at different temperatures of samples with ethylene content in the range 67-64 wt% are showed in Figure 2.37A-C. Also in these samples the correlation peaks displayed at room temperature disappear at 90 °C and appear again after the cooling, although both peaks, before and after the

heating, are very weak. This confirms that, also in this case, the correlation peaks are really due to the presence of crystals arranged in lamellar stacks morphology.

The SAXS profile of the sample K6260Q show an additional peak at higher *q* values (Figure 2.37A). This peak does not disappear at 90°C and it is probably due to impurities present in the samples. This sample, indeed, is the only one synthesized using a slurry process, while all other samples have been synthesized in solution. The different synthetic process and the residual impurities may explain the presence of this peak also at 150°C (curve *b'* in Figure 2.37A) and after the cooling from 150°C to 25°C.

As mentioned above, the sample K5470C is more similar to samples of the first set than to samples with similar ethylene content. However, after the heating at 90°C and successive cooling to room temperature the correlation peak appears much broader than the initial peak (Figure 2.37B). Also in this case the reason is that at 25°C the crystallization is not complete because the sample crystallizes at temperature lower than that of the samples of the first set.

Samples with lower ethylene content, that is, the copolymer K3050 (49 wt% of ethylene) and the terpolymers K4450 (52 wt% of ethylene) and K9950C (44 wt% of ethylene), do not show any correlation peak at room temperature, at 90°C and after cooling at 25°C, indicating these samples are really amorphous (Figure 2.38A-C).

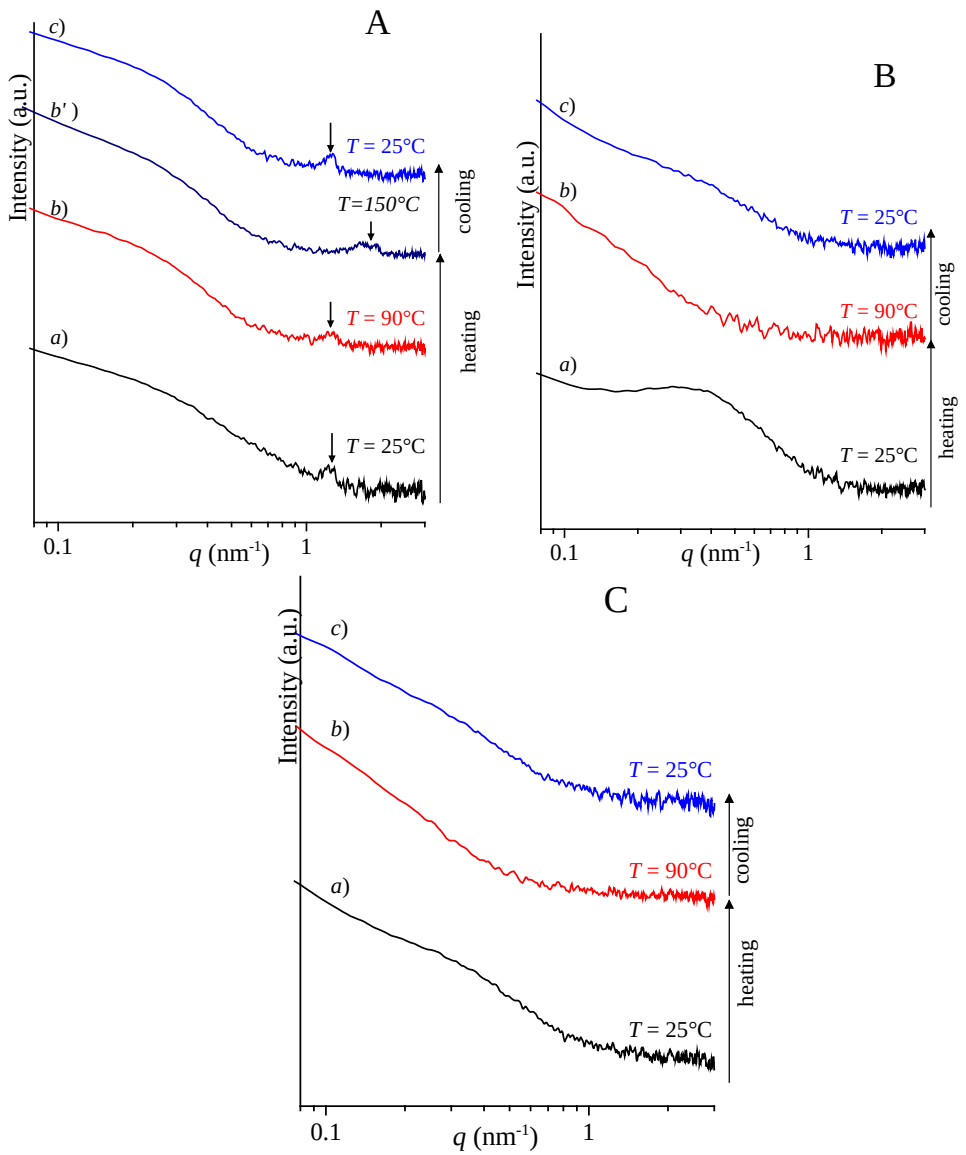

Figure 2.37. *SAXS profiles of samples K6260Q (A), K5470C (B) and K6160D (C) recorded at 25 °C (a), after heating up to 90 °C (b) and after cooling down to 25 °C (c.) The SAXS profile at 150 °C of the sample K6260Q is also reported in A (b').*

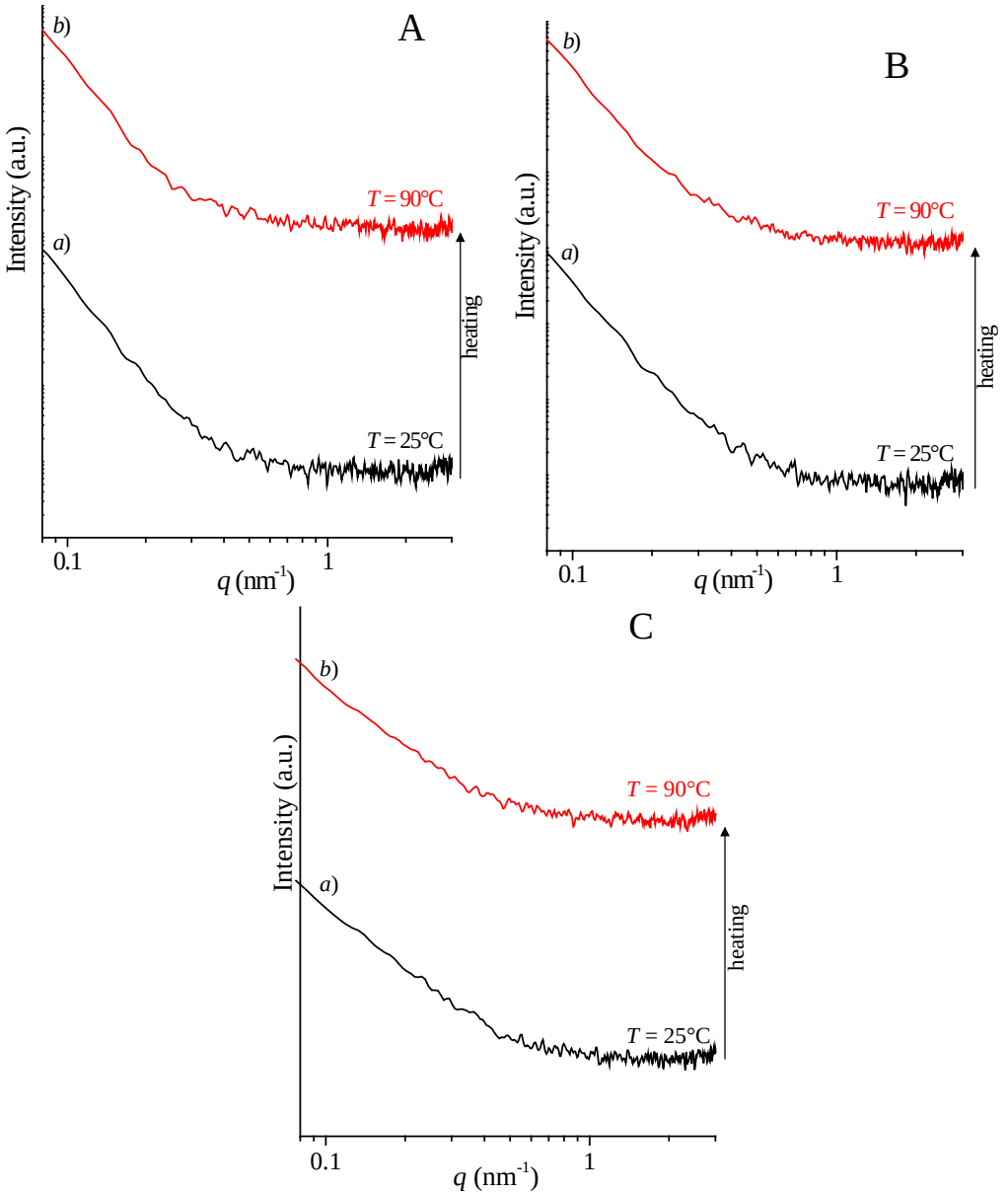

Figure 2.38. *SAXS profiles of samples K3050 (A), K4450 (B) and K9950C (C) recorded at 25 °C (a) and after heating up to 90 °C (b).*

The hypothesis that the systems under study can be modeled as stacks of laterally extended crystallites, of average thickness l_c repeating at average distance L and separated by amorphous layers of thickness l_a (Figure 2.33), allows relating the scattering intensity to the one-dimensional correlation of electron density $\gamma_1(z)$ defined as:[71]

$$\gamma_1(z) = \left\langle \left(\rho(z) - \langle\rho\rangle\right)^2 \right\rangle \left\langle \left(\rho(0) - \langle\rho\rangle\right)^2 \right\rangle = \left\langle \rho(z)\rho(0) - \langle\rho\rangle^2 \right\rangle \quad (4)$$

with $\rho(z)$ the electron density in the direction parallel to the layer normal. The function $\gamma_1(z)$, after normalization for the scattering invariant Q (in relative K units):

$$Q = \frac{1}{2\pi^2}\int_0^\infty I(q)q^2 dq \quad (5)$$

corresponds to the normalized correlation of electron density fluctuations $\gamma(z)$, and can be directly obtained by a Fourier transformation of the scattering intensity in arbitrary units as:[67]

$$\gamma(z) = \frac{\int_0^\infty \cos(qz)I(q)q^2 dq}{\int_0^\infty I(q)q^2 dq} \quad (6)$$

With $I_c(q) = I(q) - I_{back}$ and I_{back} found from equation (2).

The normalized correlation function $\gamma(z)$ is composed of a sequence of contributions due to the correlations within a single layer, next neighboring layers, second neighboring layers, etc. The most important part corresponds to the "self-correlation triangle" ABC located at the origin (Figure 2.39A), where $\gamma(z)$ assumes its maximum value, that is, $\gamma(0) = 1$, then decreases with slope $s = [\phi_c(1 - \phi_c)L]^{-1}$ up to become negative, with a minimum at $\gamma(z_{min}) = \phi_c/(1 - \phi_c)$ where ϕ_c is the volume fraction of the minority phase. The secondary maximum corresponds to the average periodicity L of the layered structure whereas the minimum layer thickness in the stacks corresponds to the abscissa of the intersection point between the line AD and the horizontal line AC fitting the

minimum of $\gamma(z)$. Since our systems have crystallinity index less than 0.5 (see Tables 2.6) the minimum thickness corresponds to the average thickness l_c of lamellar crystals. It has been checked that the values of linear crystallinity ϕ_c calculated independently as $\phi_c = l_c/L$, from the slope s and from the absolute minimum of $\gamma(z)$ are identical within the experimental error. The values of crystallinity x_c(cofun) = $\phi_c = l_c/L$ are reported in Table 2.5 in comparison with the values x_c(WAXS) evaluated from the WAXS profiles of Figure 2.32A.

The correlation functions $\gamma(z)$ calculated fom the SAXS profiles of samples of EPM copolymers and EPDM terpolymers are reported in Figure 2.39. The values of the l_c, l_a and L evaluated from the correlation function are reported in Table 2.5 and in Figure 2.40A-C as a function of the ethylene and diene concentration and total concentration of comonomers.

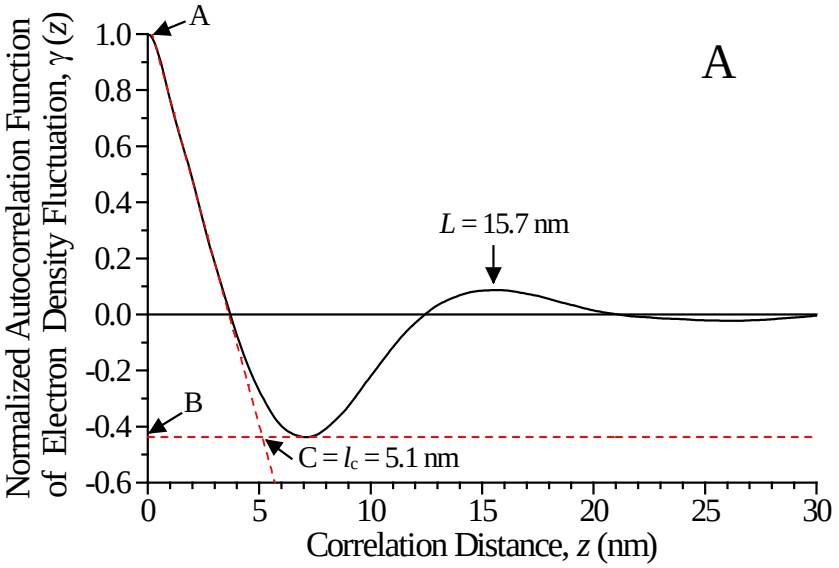
A
B
C = l_c = 5.1 nm
L = 15.7 nm
Normalized Autocorrelation Function of Electron Density Fluctuation, γ (z)
Correlation Distance, z (nm)
1.0
0.8
0.6
0.4
0.2
0.0
-0.2
-0.4
-0.6
0
5
10
15
20
25
30

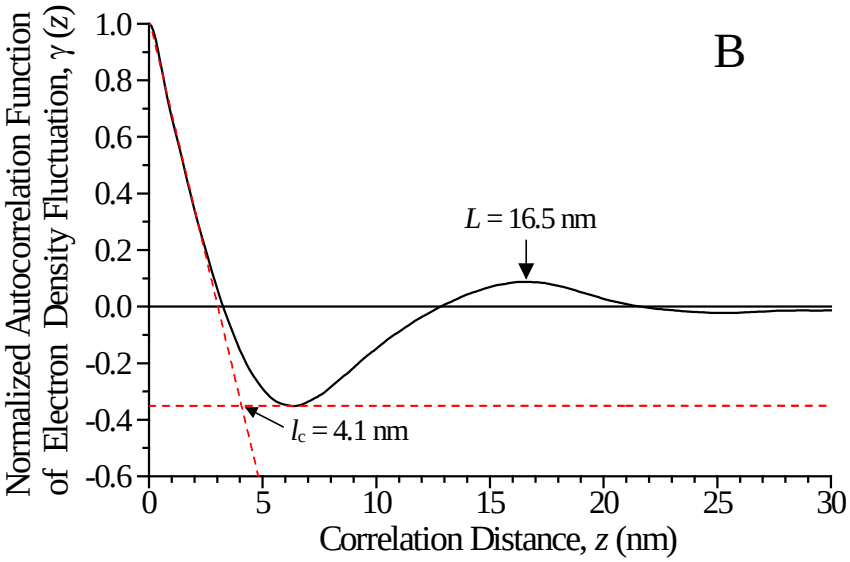
B
L = 16.5 nm
l_c = 4.1 nm
Normalized Autocorrelation Function of Electron Density Fluctuation, γ (z)
Correlation Distance, z (nm)
1.0
0.8
0.6
0.4
0.2
0.0
-0.2
-0.4
-0.6
0
5
10
15
20
25
30

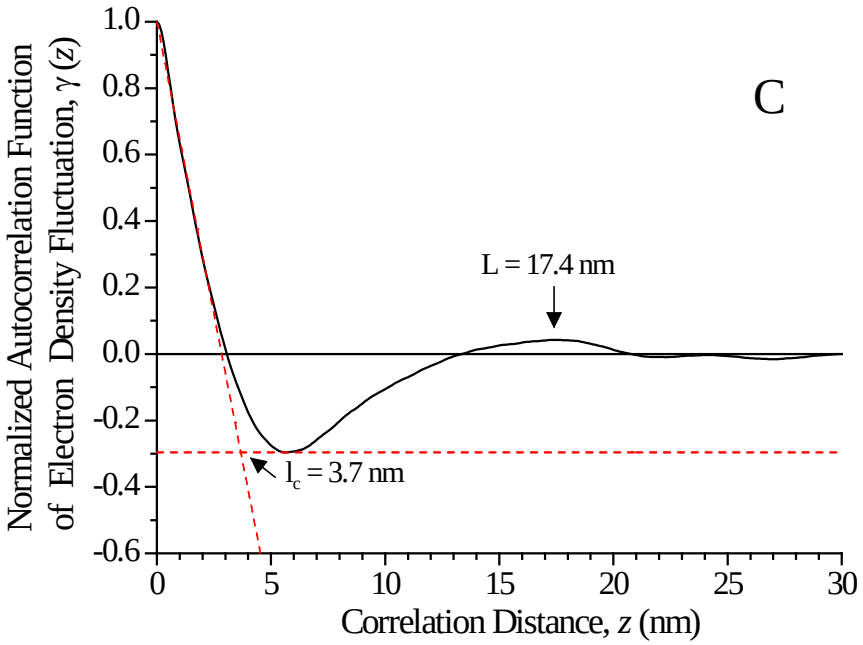
C
Normalized Autocorrelation Function of Electron Density Fluctuation, γ (z)
1.0
0.8
0.6
0.4
0.2
0.0
-0.2
-0.4
-0.6
L = 17.4 nm
l_c = 3.7 nm
0
5
10
15
20
25
30
Correlation Distance, z (nm)

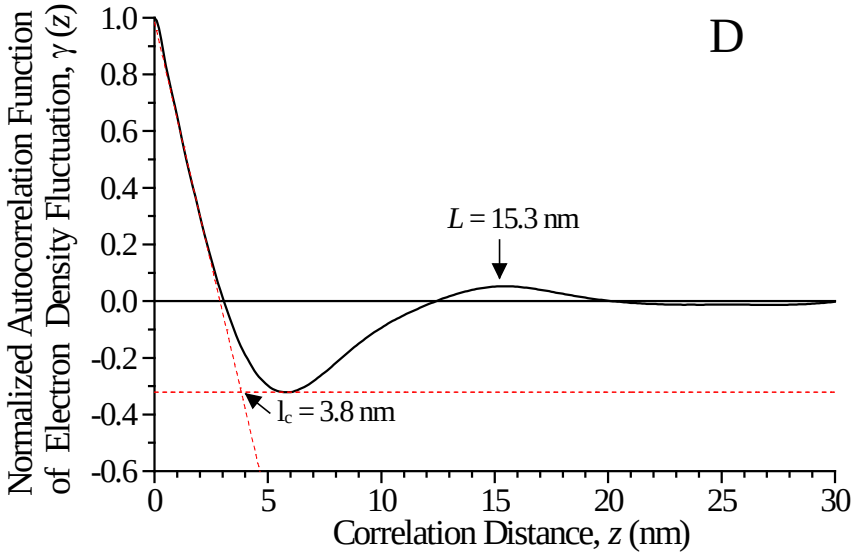
D
Normalized Autocorrelation Function of Electron Density Fluctuation, γ (z)
1.0
0.8
0.6
0.4
0.2
0.0
-0.2
-0.4
-0.6
L = 15.3 nm
l_c = 3.8 nm
0
5
10
15
20
25
30
Correlation Distance, z (nm)

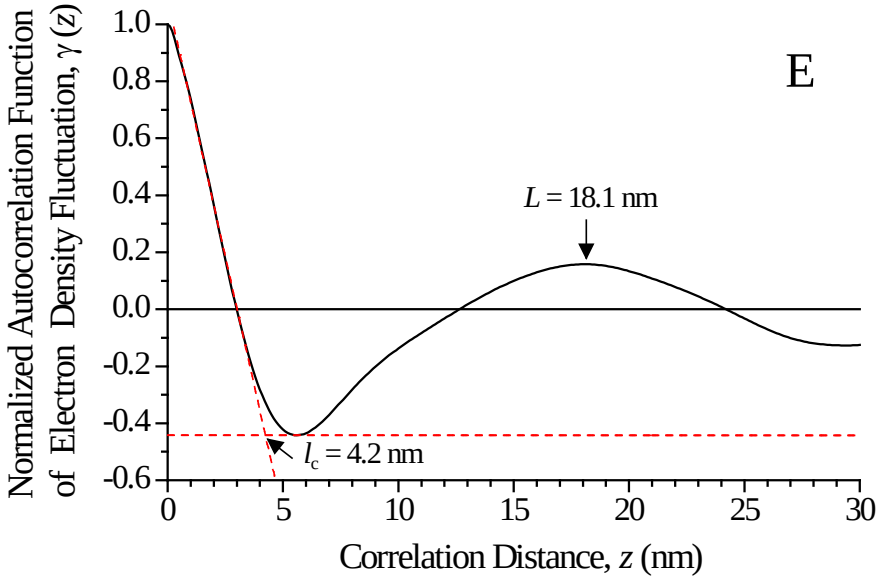
E
Normalized Autocorrelation Function of Electron Density Fluctuation, γ (z)
1.0
0.8
0.6
0.4
0.2
0.0
-0.2
-0.4
-0.6
0
5
10
15
20
25
30
L = 18.1 nm
l_c = 4.2 nm
Correlation Distance, z (nm)

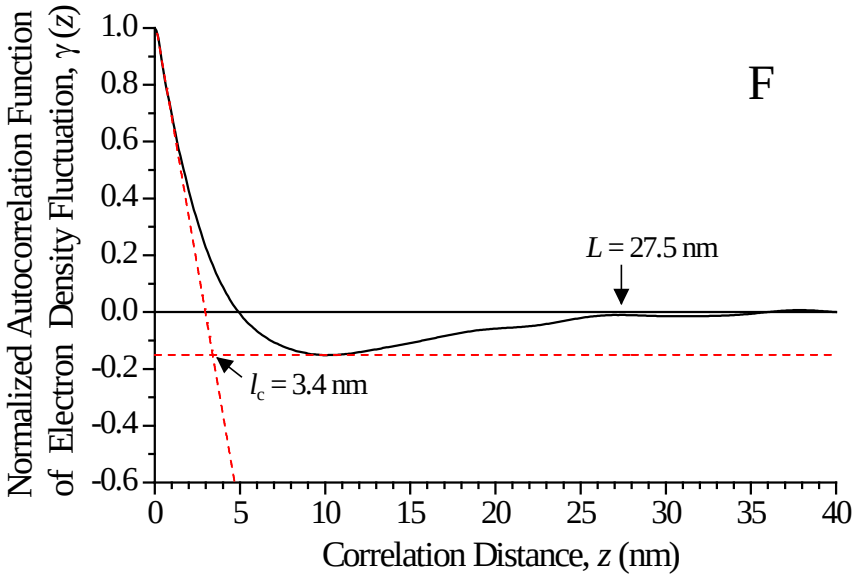
F
Normalized Autocorrelation Function of Electron Density Fluctuation, γ (z)
1.0
0.8
0.6
0.4
0.2
0.0
-0.2
-0.4
-0.6
0
5
10
15
20
25
30
35
40
L = 27.5 nm
l_c = 3.4 nm
Correlation Distance, z (nm)

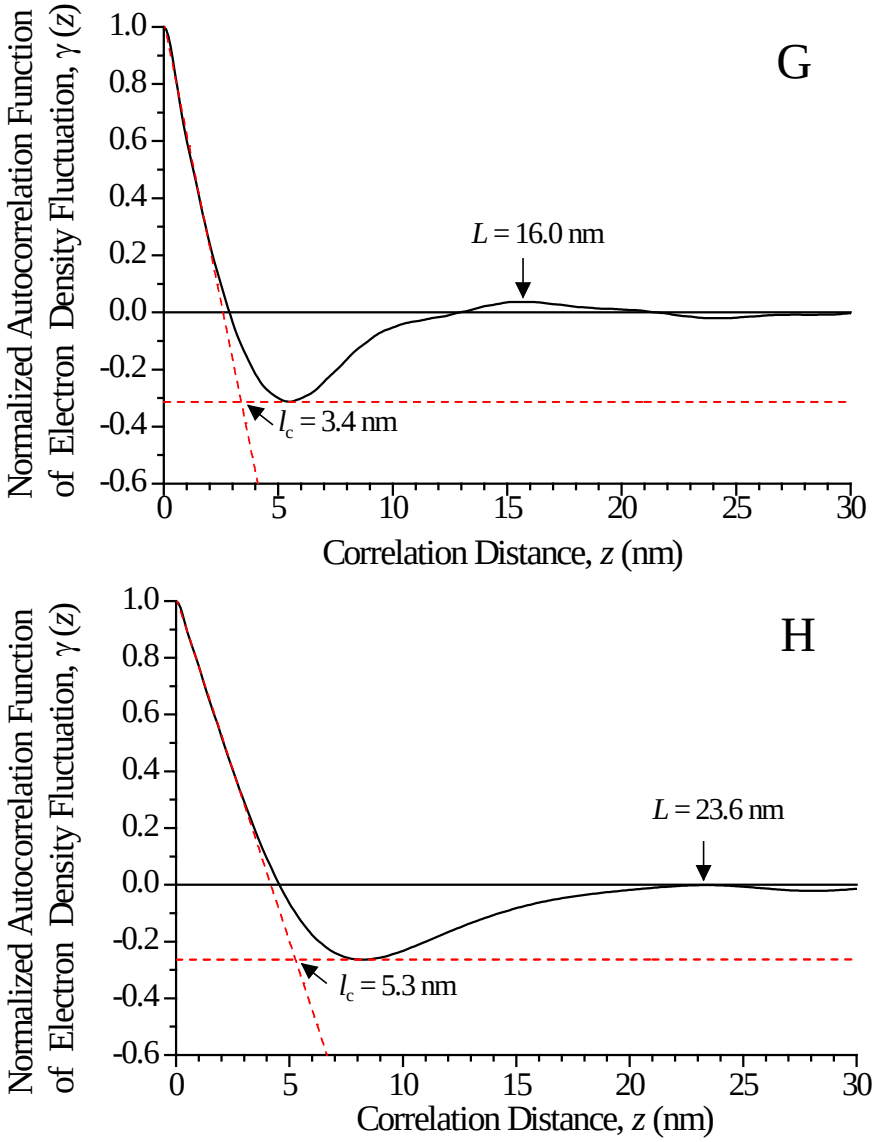

Figure 2.39. *Normalized correlation function of electron density of samples EPM (A), K2070P (B), K5170P (C), K5470P (D), K5470NT (E), K6260Q (F), K5470C (G), K6160D (H) extracted from SAXS data measured at room temperature of Figure 2.31. The average periodicity L of the layer structure and the thickness of the crystalline layer l_c are indicated. The main self-correlation triangle ABC is indicated in A.*

All samples show correlation function typical of the lamellar morphology (Figure 2.33). As in the case of Figure 2.34, the values of long period L and the thickness of the amorphous layer l_a evaluated from the correlation function $\gamma(z)$ are constant for the samples of the first set (ethylene content in the range 78-70 wt%) and then increase with further decreasing ethylene content, while l_c remains almost constant (Figure 2.40A). The values of morphological parameters L, l_c and l_a seem not to be dependent on the diene concentration (Figure 2.40B).

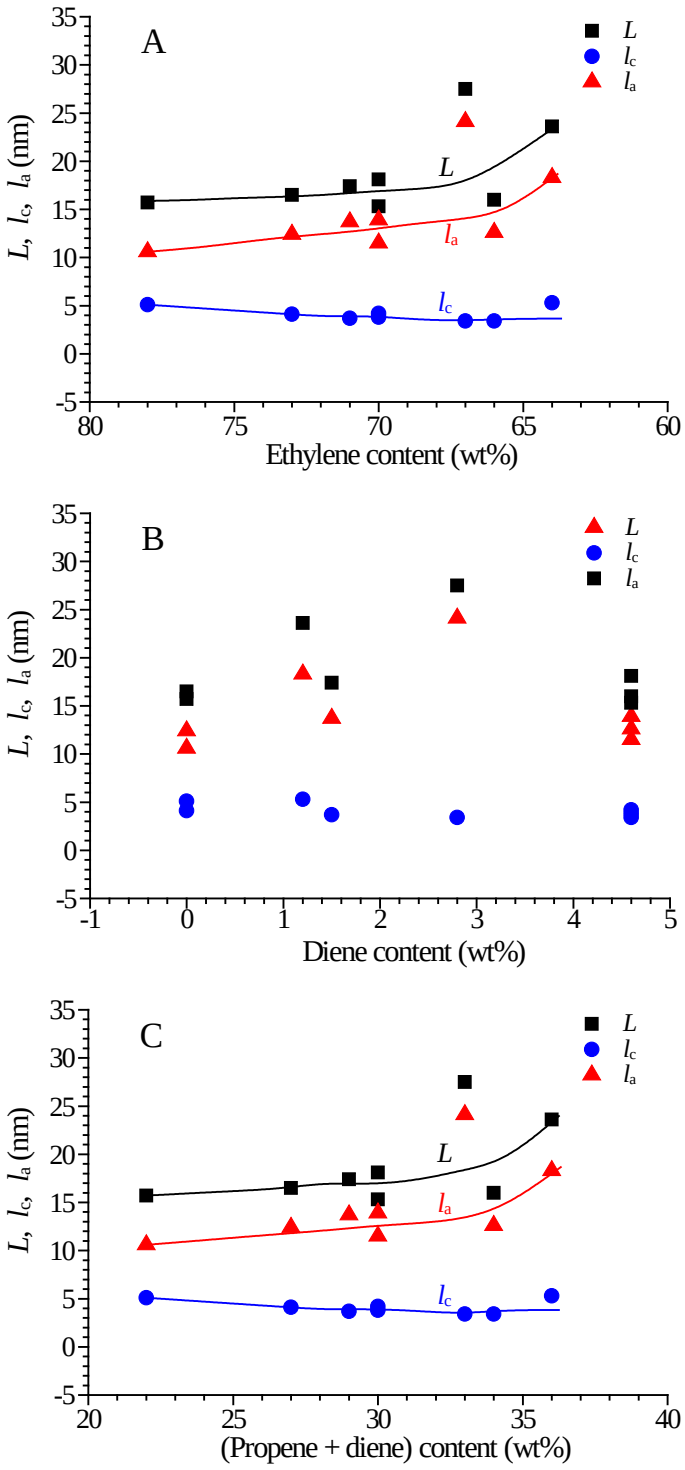

Figure 2.40. *Average values of the long period L (■), and of thicknesses of crystalline lamellae l_c (●) and amorphous layer l_a (▲) of melt-crystallized compression molded and aged samples of EPM copolymers and EPDM terpolymers, evaluated from the normalized correlation functions of electron density γ(z) of Figures 2.39A-H, as a function of ethylene concentration (A), diene concentration (B) and total amount of comonomeric units (C).*

A comparison between the morphological parameters evaluated from SAXS profiles of Figure 2.31B and those evaluated from the correlation function $\gamma(z)$ of Figures 2.39A-H is reported in Figures 2.41A-C and 2.42A-C as a function of ethylene (A), diene (B) and total concentration of comonomers (C). The values of the degree of crystallinty evaluated from the WAXS profiles of Figure 2.32A, x_c(WAXS), and from the correlation function x_c(cofun), are also compared in Figure 2.43A-C. It is apparent that the values of L, l_c, l_a and x_c(cofun) evaluated from the correlation functions are slightly different from the values L_B, l_c*, l_a* and x_c(WAXS) evaluated from the SAXS data of Figure 2.31A and WAXS profiles of Figure 2.32A. The difference is probably due to the presence of two different amorphous phases. The intra-lamellar amorphous phase consisting only of the amorphous layers alternating with crystalline layers in the model of Figure 2.33 is detected by the correlation function of electron density by construction. On the other hand, an extra-lamellar amorphous phase consisting of amorphous phase not organized in any morphological superstructure but only diffused in the matrix, may be also present. The signal obtained by a SAXS measurement includes both contributions of the intra and extra-lamellar amorphous phases. Therefore, the evaluation of the morphological parameters and of the degree of crystallinity evaluated from the SAXS correlation peak is affected by an error because of the impossibility to distinguish the single contributions. As a result, while the values of the long period L and L_B are quite similar, the values of the thickness of the amorphous layers evaluated from the correlation function are slightly lower than those evaluated from the SAXS profiles. In particular, a strong difference between L_B and L and between l_a* and l_a is observed in the sample K6260Q. It might be that the slurry process and, at the same time, the low amount of ethylene lead to the formation of a big amount of extra-lamellar amorphous phase. According with the hypothesis of two different amorphous phases, the values of thickness of the crystalline layers and of the degree of crystallinity evaluated from the correlation function are slightly higher than those evaluated from the SAXS profiles because they are based on a lower fraction of amorphous phase.

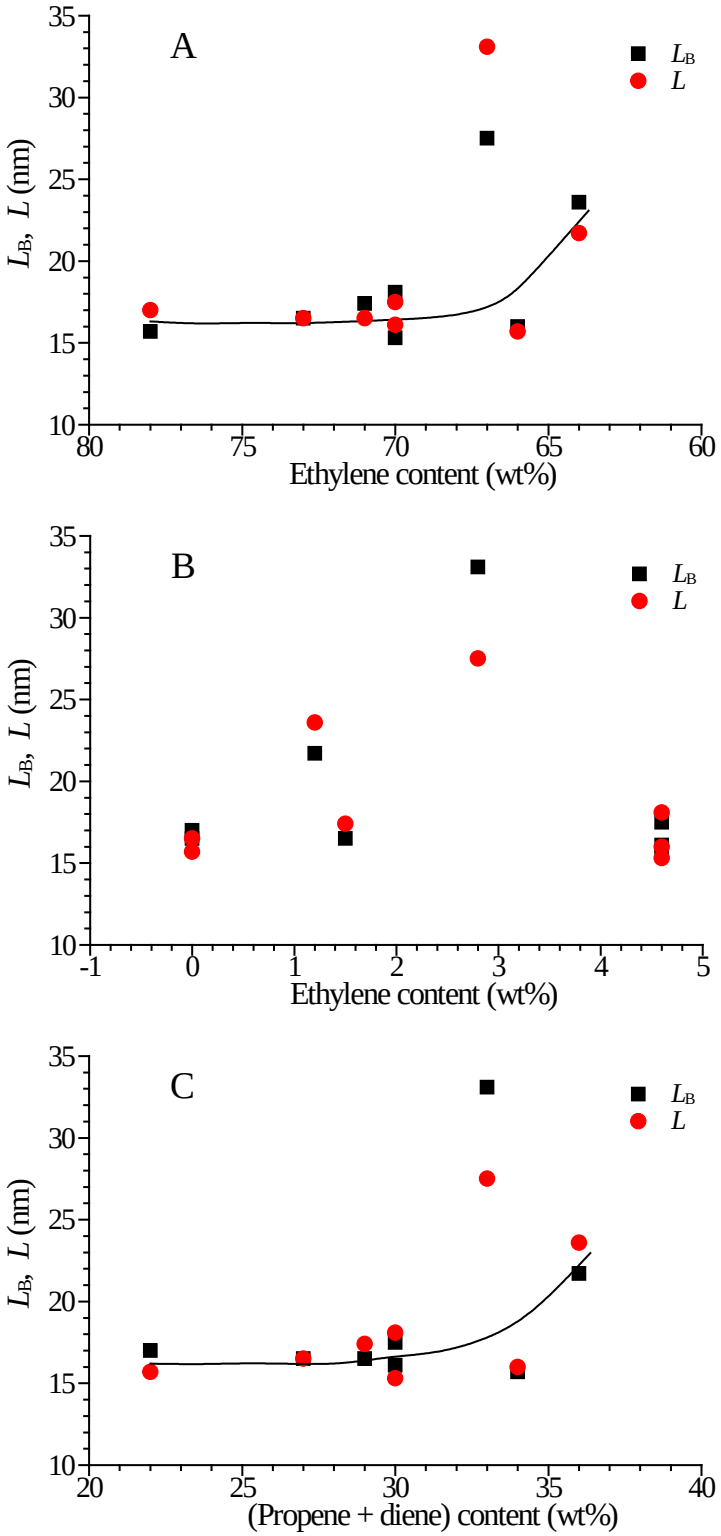

Figure 2.41. *Average values of the long period L_B (■) and L (●) of melt-crystallized compression molded and aged samples of EPM copolymers and EPDM terpolymers, evaluated from the SAXS data of Figure 2.31B and the normalized correlation functions of electron density γ(z) of Figures 2.39A-H, as a function of ethylene concentration (A), diene concentration (B) and total amount of comonomeric units (C).*

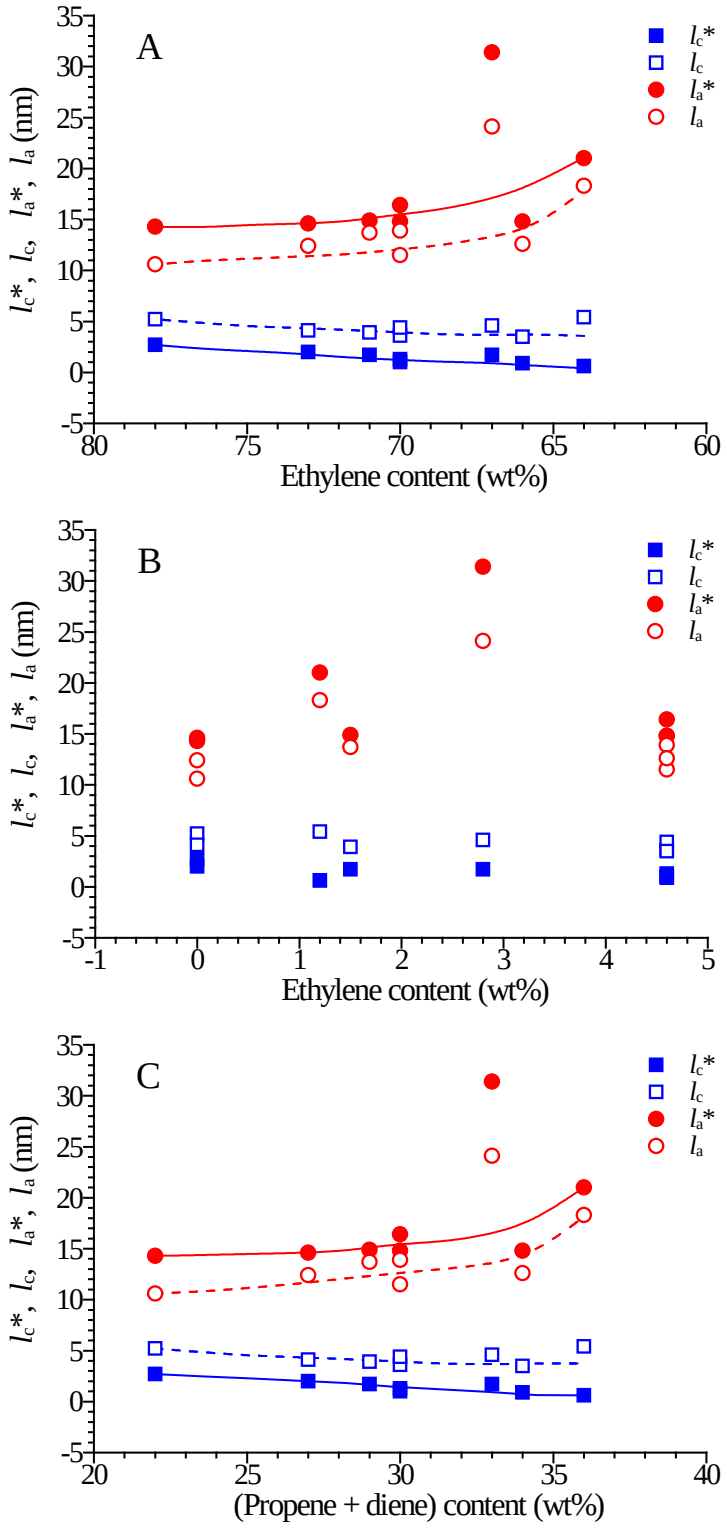

Figure 2.42. *Average values of thickness of crystalline lamellae l_c^* (■) and l_c (□) and amorphous layer l_a* (●) and l_a (○) of melt-crystallized compression molded and aged samples of EPM copolymers and EPDM terpolymers, evaluated from the SAXS data of Figure 2.31B and the correlation functions of electron density γ(z) of Figures 2.39A-H, as a function of ethylene concentration (A), diene concentration (B), total amount of comonomeric units (C).*

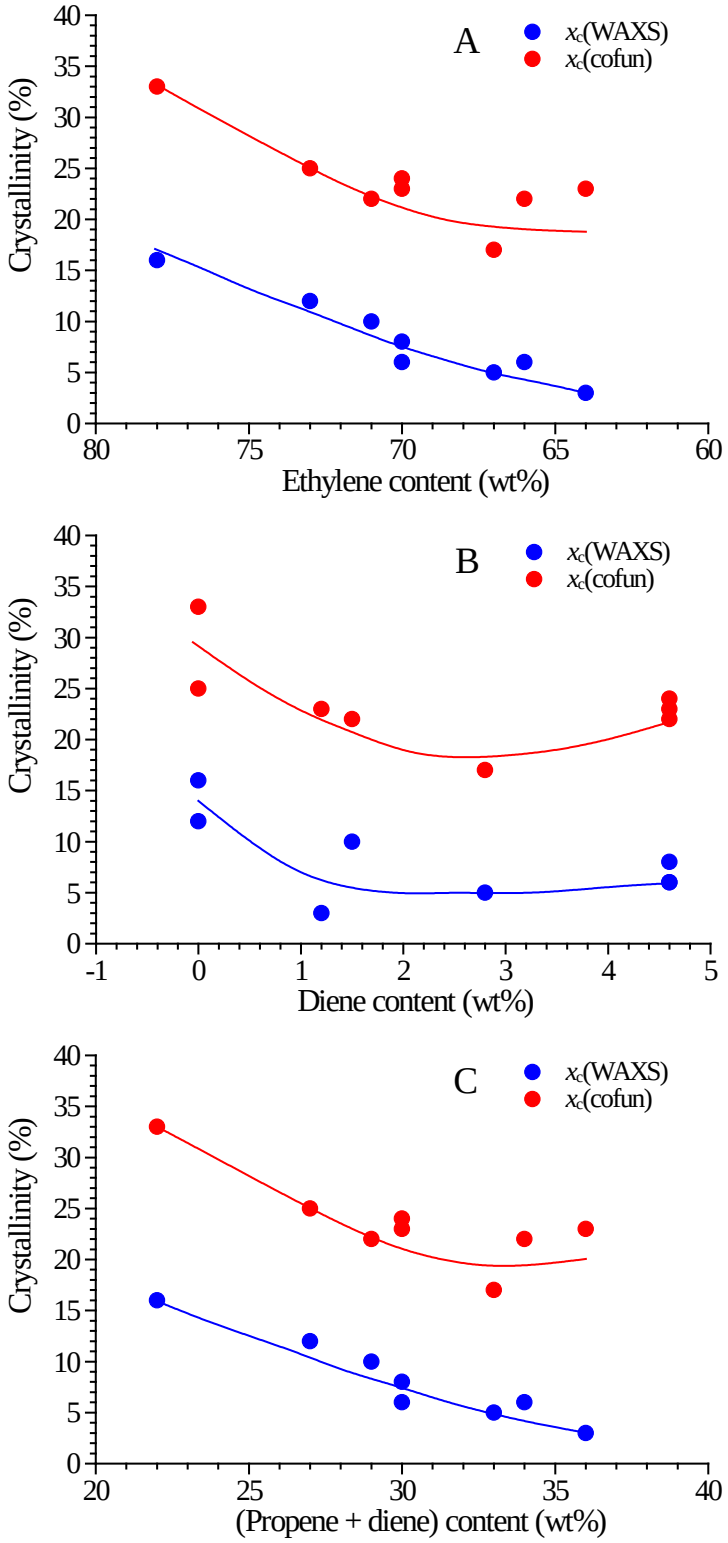

Figure 2.43. *Degree of crystallinity of melt-crystallized compression molded and aged samples of EPM copolymers and EPDM terpolymers, evaluated from the SAXS data of Figure 2.31B (●) and the correlation functions of electron density γ(z) (●) of Figures 2.39A-H, as a function of ethylene concentration (A), diene concentration (B), total amount of comonomeric units (C).*

In conclusion, SAXS analysis indicates that in EPM samples with ethylene content in the range 64-78 wt% crystallinity arising from crystallization of ethylene sequences is present. This crystallinity is not evident from WAXS data but it is revealed by DSC and SAXS measurements. The absence of Bragg peaks may be attributed to the small coherent length of the crystals and the high degree of structural disorder present in the crystals because of inclusion of propene units in the unit cell.[41,55]

2.6.4 Dynamic Mechanical Thermal Analysis (DMTA)

A study of the viscoelastic properties of EPM copolymers and EPDM terpolymers have been performed by using Dynamic Mechanical Thermal Analysis. This analysis have allowed a better evaluation of the glass transition (T_g) besides of the evaluation of the conservative (G') and loss modulus (G''). DMTA measurements have been performed on compression moulded films 1-1.2 mm thick, 11-12 mm long, with a free length of 5 mm, working in the temperature range of –120°C - 80 °C with a cooling rate of 5 °C/min. Bending deformation has been applied working in Dual Cantilever at a frequency of 1Hz and deformation width of 0.02 mm.

DMTA curves of all EPM copolymers and EPDM terpolymers are reported in Figure 2.44A-M. All samples show high values of the conservative modulus G' at low temperatures in the glassy state (10^9 Pa). The values of the loss modulus G'' are also high but lower than those of G'. In the glassy region at low temperature a slow decrease of both G' and G'' with increasing temperature occurs. At the glass transition temperature T_g a fast decrease of the conservative modulus G' of 3-4 order of magnitude is observed while the loss modulus G''decreases more slowly and the tanδ curve shows a maximum in correspondence of the T_g (Figure 2.44A-M).

In a typical DMTA curve of semicrystalline polymers, since the glass transition involves only the amorphous fraction, the value of the conservative modulus G' generally remains higher than that of the loss modulus with increasing temperature, even through the glass transition, because the elastic conservative contribution to the elastic modulus prevails and the elastic and conservative response of the sample prevails over the dissipative response. In these cases at T_g the maximum of tanδ is lower than 1. In the case of amorphous polymers, instead, along with the decrease of G' and G'' with increasing temperature a crossover between G' and G'' at temperatures close to the glass transition is generally observed and the loss modulus G'' becomes higher than

the conservative modulus G' because the dissipative contribution to the modulus due to the viscous behavior prevails after the T_g and the dissipative response of the sample prevails over that conservative. In these cases at T_g the maximum of tanδ is higher than 1. With further increase of temperature a second crossover between G' and G'' is observed and the conservative modulus G' becomes again higher than the loss modulus G'' achieving the rubbery plateau, because in this region the elastic rubbery behavior prevails.

This general behavior is observed in almost all samples of EPM and EPDM of Figure 2.44A-M. In particular, absence of cross over and values of G' higher than G'' in the whole temperature range have been observed in the samples EPM (78 wt% ethylene, Figure 2.44A), K5170P (71 wt% ethylene, Figure 2.44C), K5470P (70 wt% ethylene, Figure 2.44D), K5470NT (70 wt% ethylene, Figure 2.44E), K6260Q (67 wt% ethylene, Figure 2.44F), K5470C (66 wt% ethylene, Figure 2.44G), K8570C (66 wt% ethylene, Figure 2.44H) and K6160D (64 wt% ethylene, Figure 2.44I) and confirm that these samples are semicrystalline, as evidenced by DSC (Figure 2.32C) and SAXS (Figure 2.31) and not by WAXS (Figure 2.32A). The sample K2070P (73 wt% ethylene, Figure 2.44B) is an exception because it shows the crossover between G' and G'' but SAXS and DSC data have shown that this sample is crystalline. The DMTA curves of samples K3050 (49 wt% ethylene, Figure 2.44L) and K9950C (44 wt% ethylene, Figure 2.44M) show the crossover between G' and G'' and confirm that these samples are really amorphous.

At high temperatures approaching the rubbery plateau, the presence of secondary relaxation phenomena in case of amorphous samples, or the occurrence of melting process in case of crystalline samples, produces oscillations or additional peaks in the DMTA curves of amorphous and crystalline samples, respectively, avoiding the complete achievement of the rubbery plateau. In particular, in the curve of tanδ of the samples EPM (Figure 2.44A), K5170P (Figure 2.44C), K5470P (Figure 2.44D), K5470NT (Figure 2.44E) and K6260Q (Figure 2.44F), after the peak corresponding to the glass transition, a clear peak at higher temperature is present att temperatures (40-50 °C) similar to the DSC melting endotherm of Figure 2.32C. This suggests that the second peak in the tanδ curve probably correspond to the melting of the crystalline samples.

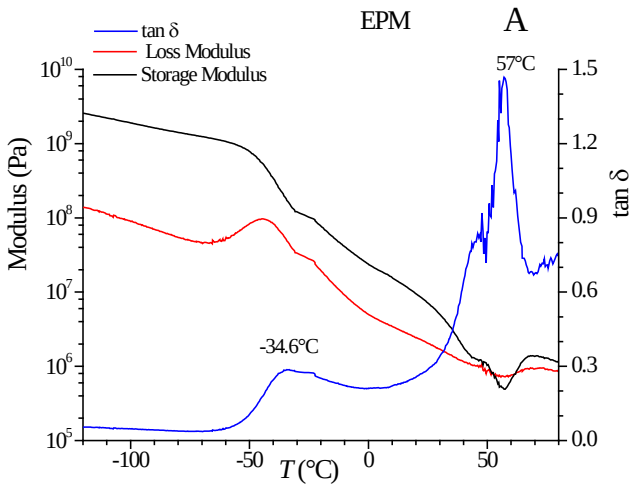
EPM
A
tan δ
Loss Modulus
Storage Modulus
57°C
-34.6°C
Modulus (Pa)
tan δ
T (°C)

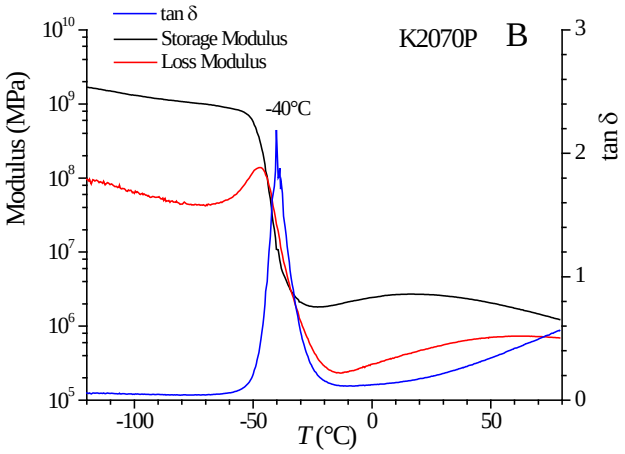
K2070P
B
tan δ
Storage Modulus
Loss Modulus
-40°C
Modulus (MPa)
tan δ
T (°C)

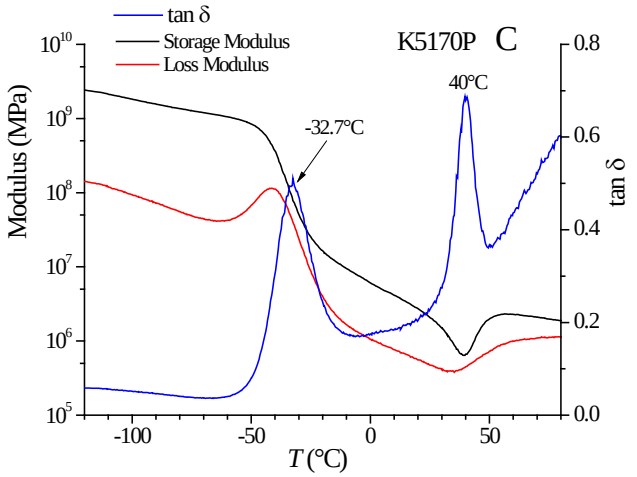
K5170P
C
tan δ
Storage Modulus
Loss Modulus
40°C
-32.7°C
Modulus (MPa)
tan δ
T (°C)

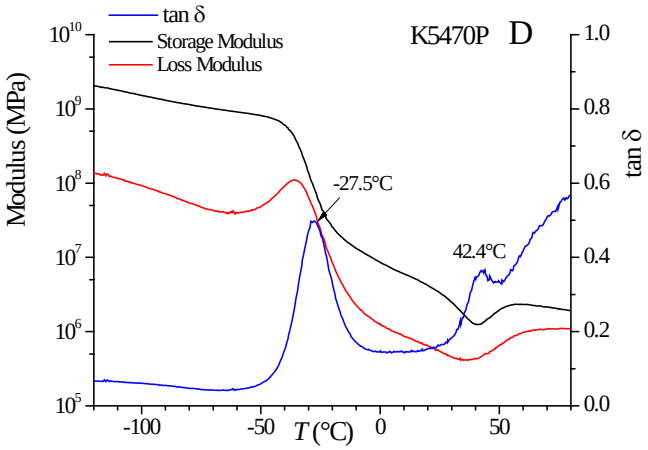
K5470P
D
tan δ
Storage Modulus
Loss Modulus
-27.5°C
42.4°C
Modulus (MPa)
tan δ
T (°C)

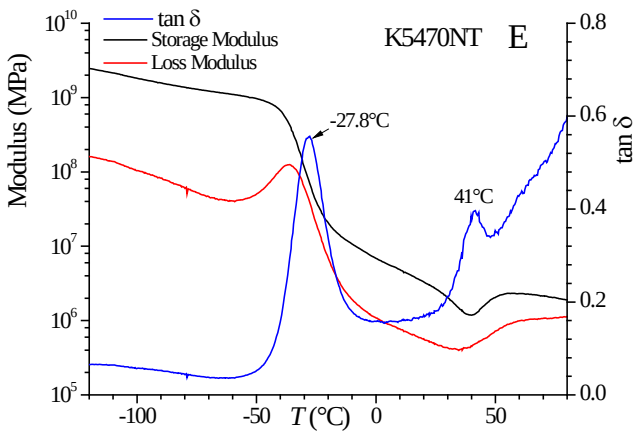
tan δ
Storage Modulus
Loss Modulus
K5470NT E
-27.8°C
41°C
Modulus (MPa)
tan δ
T (°C)

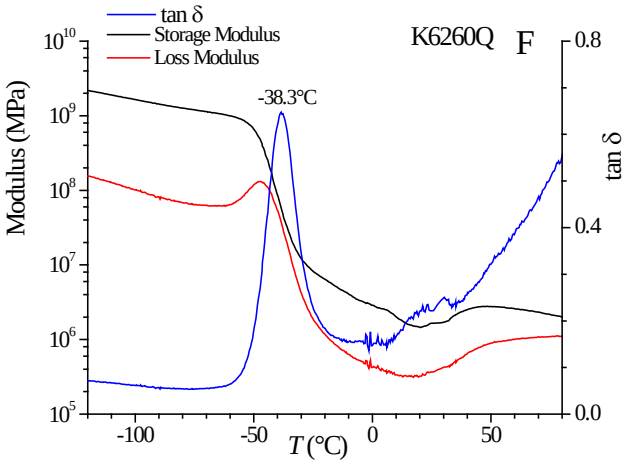
tan δ
Storage Modulus
Loss Modulus
K6260Q F
-38.3°C
Modulus (MPa)
tan δ
T (°C)

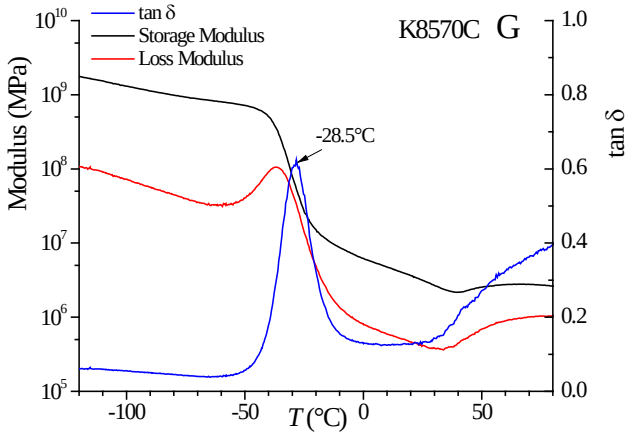
tan δ
Storage Modulus
Loss Modulus
K8570C G
-28.5°C
Modulus (MPa)
tan δ
T (°C)

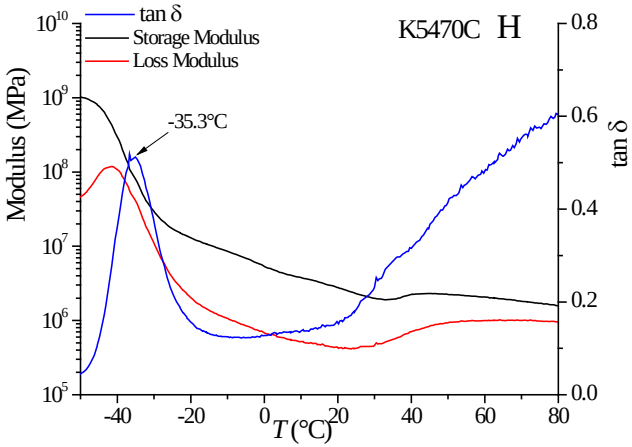
tan δ
Storage Modulus
Loss Modulus
K5470C H
-35.3°C
Modulus (MPa)
tan δ
T (°C)

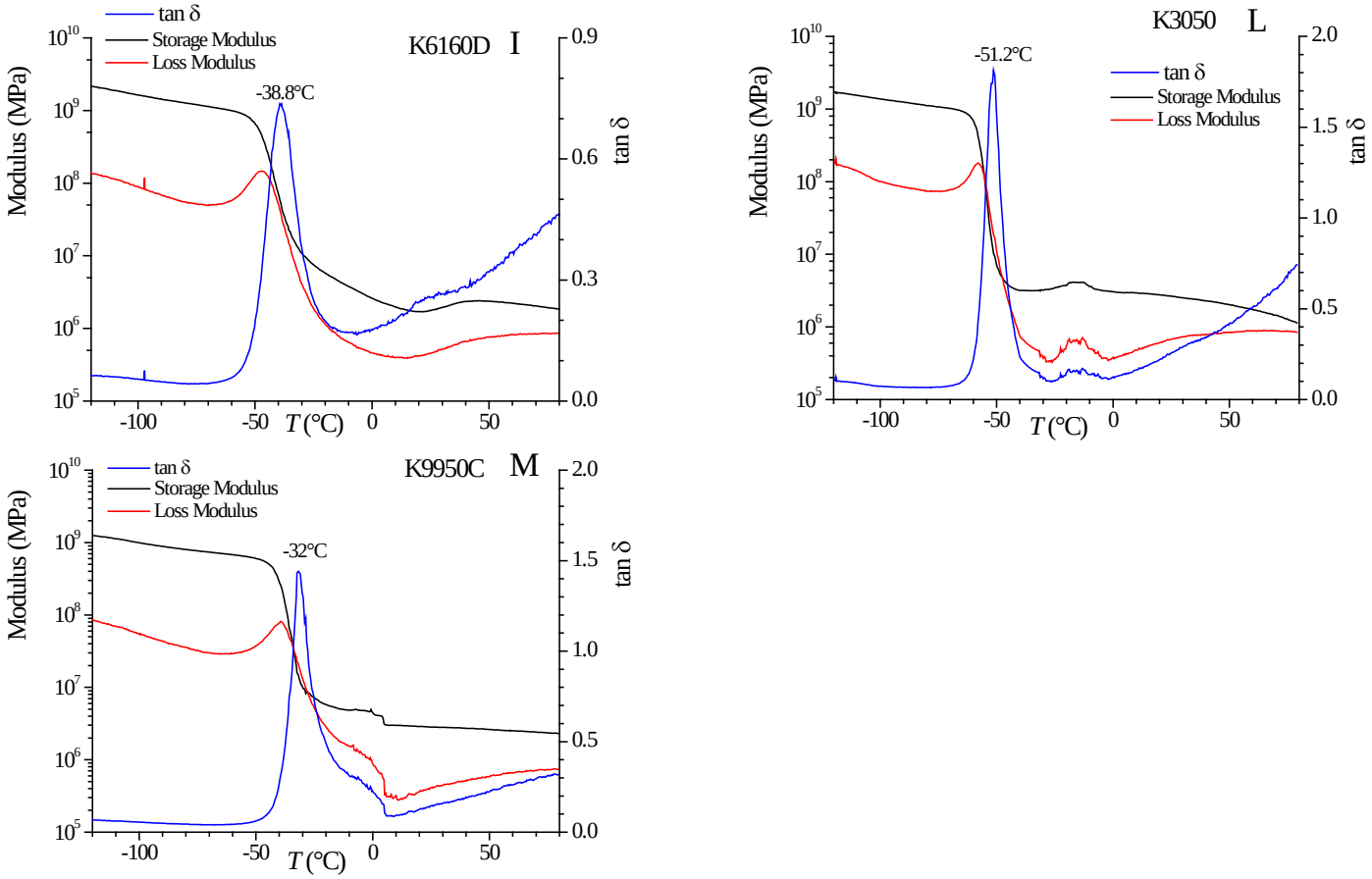

Figure 2.44. *DMTA curves of compression-molded and aged samples EPM with 78 wt% ethylene (A), K2070P with 73 wt% ethylene (B), K5170P with 71 wt% ethylene (C), K5470P with 70 wt% ethylene (D), K5470NT with 70 wt% ethylene (E), K6260Q with 67 wt% ethylene (F), K5470C with 66 wt% ethylene (G), K8570C with 66 wt% ethylene (H), K6160D with 64 wt% ethylene (I), K3050 with 49 wt% ethylene (L) and K9950C with 44 wt% ethylene (M).*

The values of G’ and G’’ at the temperatures of -100 °C and 25 °C, the value of the glass transition temperature T_g evaluated from the first maximum in the tanδ curve, the value of tanδ at the maximum peak corresponding to the glass transition temperature and the temperature of the second peak (second relaxation) in the tanδ curve are reported in Table 2.7. The values of glass transition and melting temperature of Table 2.3, determined from the DSC heating curves of Figure 2.23A, are also reported in Table 2.7 for comparison. This comparison confirms that the second relaxation peaks in the tanδ curves occur at temperatures similar to the melting temperature. Therefore, these second peaks can be reasonably attributed to the melting of the samples.

Figure 2.45 reports the values of G’ and G’’ at room temperature (Figure 2.45A,B) and at T = -100°C (Figure 2.45C,D) for all EPM copolymers and EPDM terpolymers also reported in Table 2.7). No specific dependence of the conservative and loss modulus on the ethylene content has been observed. At room temperature in the rubbery state the values G’ and G’’ of the more crystalline sample EPM are significantly higher than those of the other samples. This difference is less evident at -100 °C where all samples show similar G’ and G’’ values.

A comparison between the values of the T_g evaluated from the DSC heating curves of Figure 2.23 (Table 2.3) (T_g(DSC) and from the tanδ curve of DMTA experiments (T_g(DMTA)) is shown in Figure 2.46. The values determined from DMTA are always higher than those evaluated from DSC and no specific dependence on the ethylene content is observed.

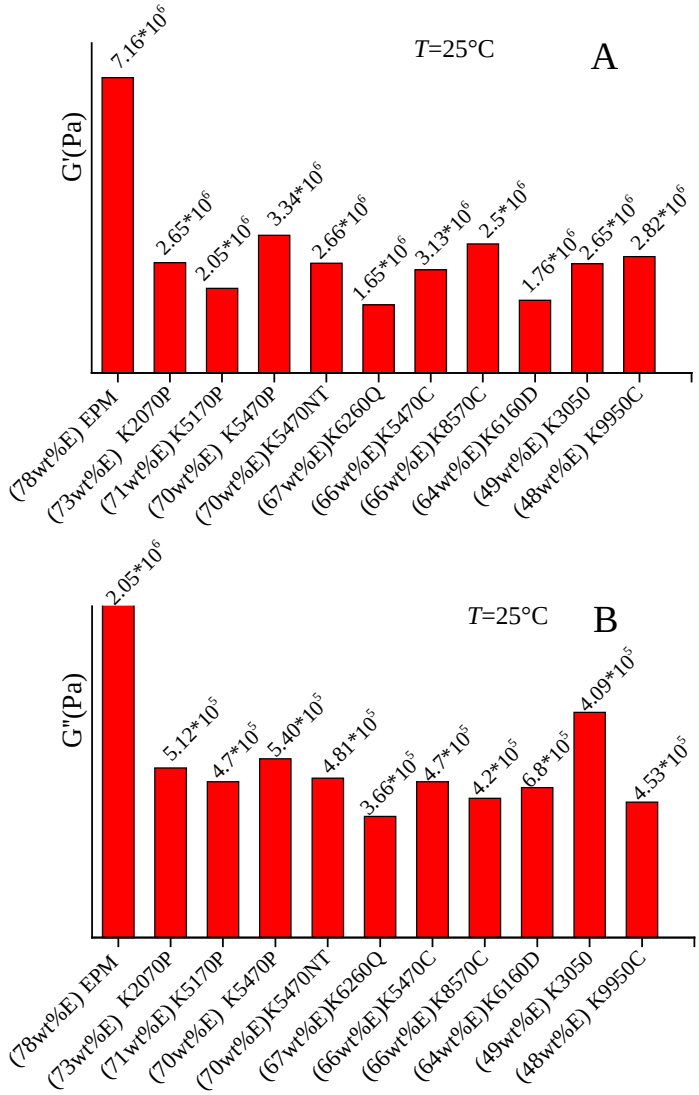
T=25°C
A
G'(Pa)
7.16*10^6
2.65*10^6
2.05*10^6
3.34*10^6
2.66*10^6
1.65*10^6
3.13*10^6
2.5*10^6
1.76*10^6
2.65*10^6
2.82*10^6
(78wt%E) EPM
(73wt%E) K2070P
(71wt%E)K5170P
(70wt%E) K5470P
(70wt%E)K5470NT
(67wt%E)K6260Q
(66wt%E)K5470C
(66wt%E)K8570C
(64wt%E)K6160D
(49wt%E) K3050
(48wt%E) K9950C
T=25°C
B
G"(Pa)
2.05*10^6
5.12*10^5
4.7*10^5
5.40*10^5
4.81*10^5
3.66*10^5
4.7*10^5
4.2*10^5
6.8*10^5
4.09*10^5
4.53*10^5
(78wt%E) EPM
(73wt%E) K2070P
(71wt%E)K5170P
(70wt%E) K5470P
(70wt%E)K5470NT
(67wt%E)K6260Q
(66wt%E)K5470C
(66wt%E)K8570C
(64wt%E)K6160D
(49wt%E) K3050
(48wt%E) K9950C

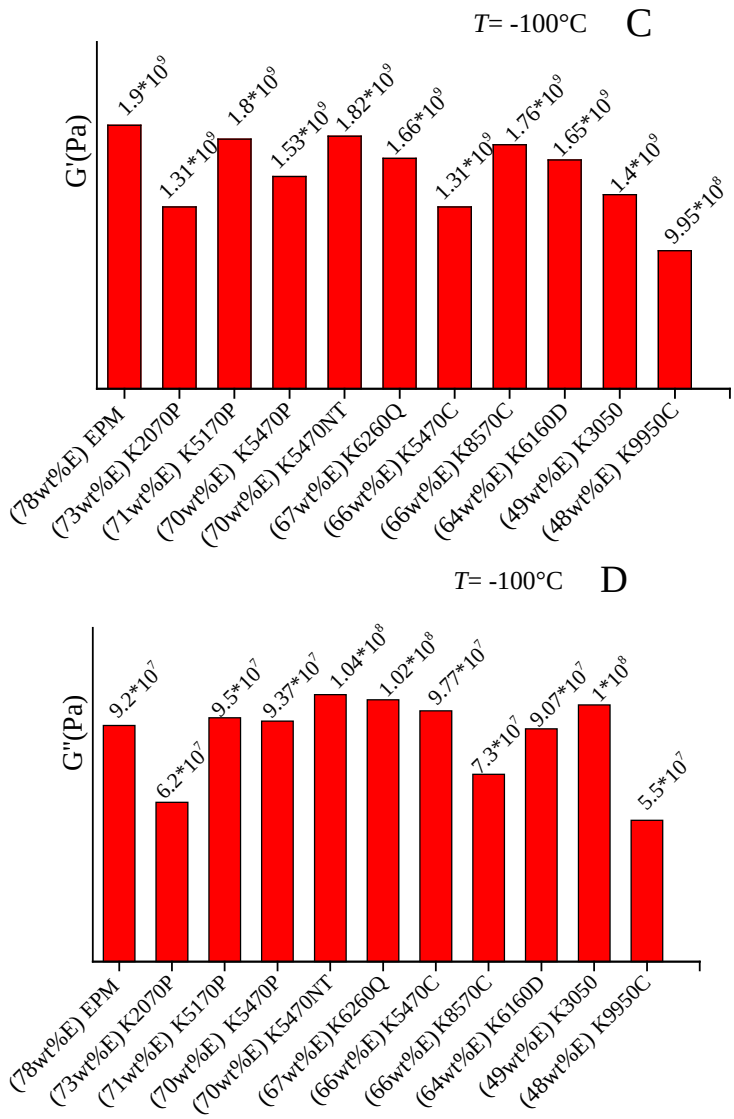

Figure 2.45. *Values of the conservative modulus G' (A,C) and of the loss modulus G'' (B,D) at room temperature (A,B) and at -100°C (C,D) of EPM and EPDM samples.*

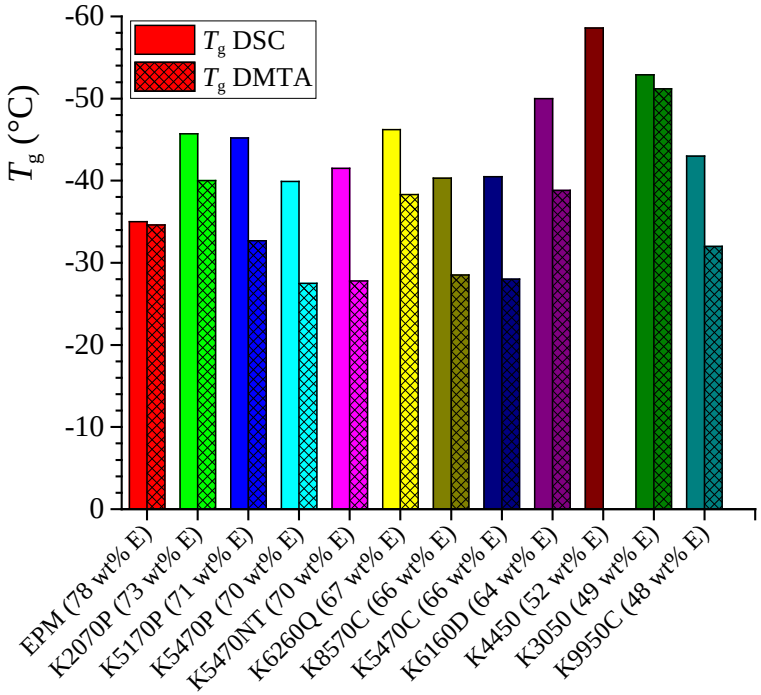

Figure 2.46. *Comparison between the values of the glass transition temperatures evaluated from DSC (T_g(DSC)) and DMTA measurements (T_g(DMTA)).*

As mentioned above, when crossover between G' and G'' occurs, G'=G'' and then tanδ = G''/G' = 1. Therefore, for amorphous samples in correspondence of the T_g, G'' is higher than G' and the values of tanδ are higher than 1. On the contrary, for crystalline samples the cross-over between G' and G'' does not occur and the values of tanδ close to the T_g are always lower than 1. Hence, the values of tanδ at the maximum peak corresponding to the glass transition temperature, higher or lower than 1, can be used for individuating amorphous or crystalline (or cryptocrystalline) samples. This method is shown in Figure 2.47 for EPM and EPDM samples and confirms that the samples EPM (78 wt% ethylene), K5170P (71 wt% ethylene), K5470P (70 wt% ethylene), K5470NT (70 wt% ethylene), K6260Q (67 wt% ethylene), K5470C (66 wt% ethylene), K8570C (66 wt% ethylene) and K6160D (64 wt% ethylene) are crystalline, as evidenced by DSC (Figure 2.32C) and SAXS (Figure 2.31) and not by WAXS (Figure 2.32A), whereas the samples K3050 (49 wt% ethylene) and K9950C (44 wt% ethylene) are really amorphous.

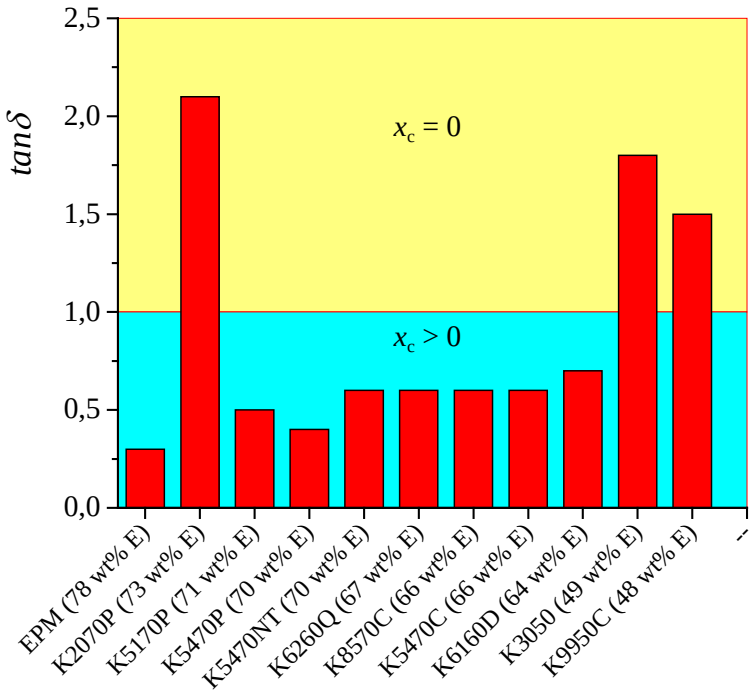

Figure 2.47. *Values of tanδ at the maximum peak corresponding to the glass transition temperature. Different colored backgrounds separate crystalline or cryptocrystalline samples for which tanδ < 1(blue background) from really amorphous samples for which tanδ > 1 (yellow background).*

***Table 2.7**. Values of conservative modulus (G') and loss modulus (G'') at -100 °C and 25 °C, glass transition temperature evaluated from the first maximum in the tanδ curves (T_g(DMTA)) and from the DSC heating curves of Figure 2.23A (Table 2.3) (T_g(DSC)), values of tanδ at the maximum peak corresponding to the glass transition temperature, temperature of the second peak (second relaxation) in the tanδ curve ($T_{II\ relaxation}$), melting temperatures evaluated from DSC heating curves of Figure 2.23A (Table 2.3) (T_m^I) and degree of crystallinity evaluated from the SAXS correlation functions (x_c(cofun) of EPM and EPDM samples.*

Sample	Ethylene content (wt%)	Diene content (wt%)	G' (MPa)		G''(MPa)		tanδ	T_g(DMTA) (°C)	T_g(DSC) (°C)	x_c(cofun) (%)	$T_{II\ relaxation}$ (°C)	T_m^I (°C)
			25°C	-100°C	25°C	-100°C						
EPM	78	0	7.16×10^6	1.90×10^9	2.05×10^6	9.20×10^7	0.3	-34.6	-35	32	56.7	55.7
K2070P	73	0	2.67×10^6	1.31×10^9	5.12×10^5	6.20×10^7	2.1	-40	-45.7	25	-	47.9
K5170P	71	1.5	2.05×10^6	1.80×10^9	4.70×10^5	9.50×10^7	0.5	-32.7	-45.2	21	40	46.1
K5470P	70	4.6	3.34×10^6	1.53×10^9	5.40×10^5	9.37×10^7	0.4	-27.5	-39.9	25	42.4	46.6
K5470NT	70	4.6	2.66×10^6	1.82×10^9	4.81×10^5	1.04×10^8	0.6	-27.8	-41.5	23	41	44.5
K6260Q	67	2.8	1.65×10^6	1.66×10^9	3.66×10^5	1.02×10^8	0.6	-38.3	-46.2	12	-	45
K8570C	66	5.0	3.13×10^6	1.31×10^9	4.20×10^5	7.30×10^7	0.6	-28.5	-40.5	-	-	46.7
K5470C	66	4.6	2.50×10^6	1.76×10^9	4.70×10^5	9.77×10^7	0.6	-28	-40.3	21	44	45.3
K6160D	64	1.2	1.76×10^6	1.65×10^9	4.53×10^5	9.07×10^7	0.7	-38.8	-50	22	-	46.3
K3050	49	0	2.65×10^6	1.40×10^9	6.80×10^5	1.0×10^8	1.8	-51.2	-52.9	-	-	-
K9950C	48	9	2.82×10^6	9.95×10^8	4.09×10^5	5.50×10^7	1.5	-32	-43	-	-	-

2.6.5 Mechanical properties

The analysis of the mechanical properties of samples of EPM copolymers and EPDM terpolymers has been performed on melt-crystallized compression molded films and on compression-molded films aged at room temperature for one week. The WAXS profiles of compression molded films, prepared as described in the section 2.5, soon after the cooling at room temperature (fresh compression-molded) and after aging at room temperature for one week are reported in Figure 2.48 A and B, respectively. WAXS profiles of compression-molded samples aged for one month at room temperature have been already reported in Figure 2.32A (recorded simultaneously to the SAXS profiles of Figure 2.31). There are no significant differences between WAXS profiles of fresh and aged compression molded samples of Figure 2.48A and B. Moreover, the WAXS profiles of Figure 2.48 are also similar to those of the compression-molded and aged samples of Figure 2.32A and those of the as-prepared samples of Figure 2.19. Only the sample EPM show a slightly sharper peak at $2\theta = 21°$ in the profiles of Figure 2.48 A and B. This indicates that a possible increase of crystallinity upon aging is not well revealed by WAXS. Small and sharp extra-reflections present in the profiles of Figure 2.48 are due to the additives, in particular talc as discussed in section 2.6.1.

Stress-strain curves of fresh and aged compression molded films of EPM and EPDM samples are reported in Figure 2.49A-M. The values of the mechanical parameters evaluated from stress-strain curves are reported in Table 2.8. All samples with ethylene contents in the range 78-66 wt% (Figure 2.49A-H) show mechanical properties typical of elastomers: low Young modulus, continuous deformation without evident yielding, high ductility with high values of deformation at break in the range 1000-2000% and in some cases higher than 2000%, and remarkable strain hardening. The Young modulus decreases with decreasing ethylene concentration (Table 2.8), according to the decrease of crystallinity (Figures 2.27 and 2.43 and Tables 2.3-2.6), from the value of 11-15 MPa of the most crystalline sample EPM with 78 wt% of ethylene to very low values, lower than 1 MPa, for the amorphous samples with ethylene concentration in the range 55-44 wt% (Table 2.8). The tensile strength is generally high thanks to strain-hardening with values of stress at break of 6-12 MPa for samples with ethylene content in the range 78-64 wt%.

An increase of modulus and tensile strength and a more defined yielding point and similar ductility and flexibility are observed in the samples aged at room temperature (dashed curves in Figure 2.49A-H). Almost all EPM and EPDM samples, indeed, show higher values of stress at any strain after aging. In the case of samples K2070P (73 wt% ethylene) and K6160D (64 wt%

ethylene) (Figures 2.49 B and I, respectively) a slight increase of deformation at break is also observed after aging. Samples with low ethylene content (55-44wt%) show stress-strain curves typical of soft materials with very low values of stress and strain at break. For these samples no improvement of mechanical properties is observed upon aging. The compression moulded film of sample K9950C with 44 wt% ethylene shrinks upon aging, therefore the corresponding stress-strain curve could not be recorded.

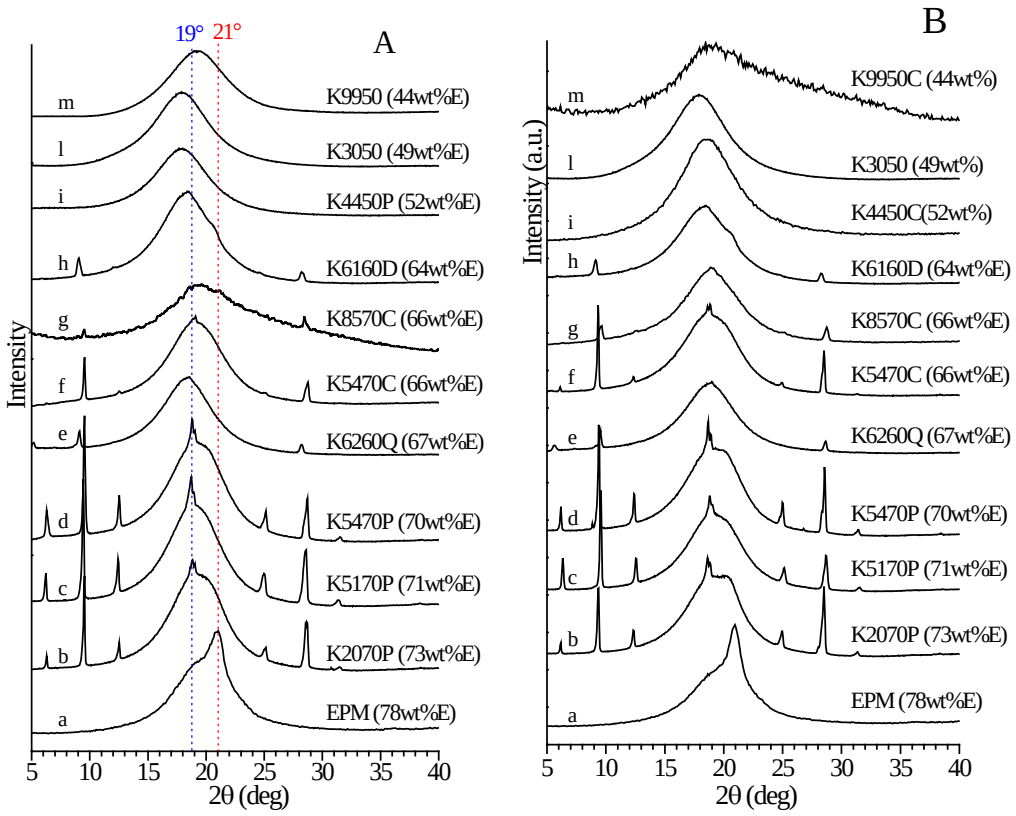

Figure 2.48. *X-ray powder diffraction profiles of fresh (A) and aged at room temperature for one week (B) compression molded films of samples of EPM copolymers and EPDM terpolymers.*

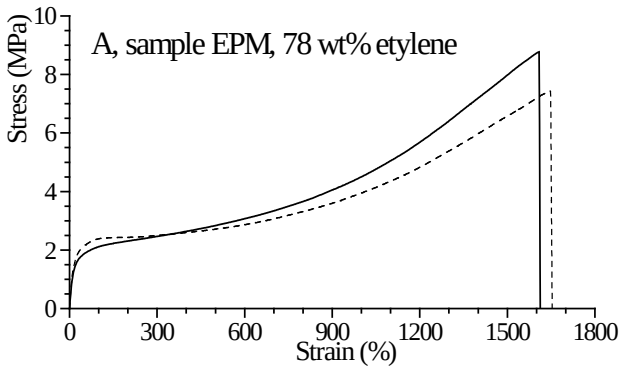
A, sample EPM, 78 wt% etylene
Stress (MPa)
Strain (%)
0
2
4
6
8
10
0
300
600
900
1200
1500
1800

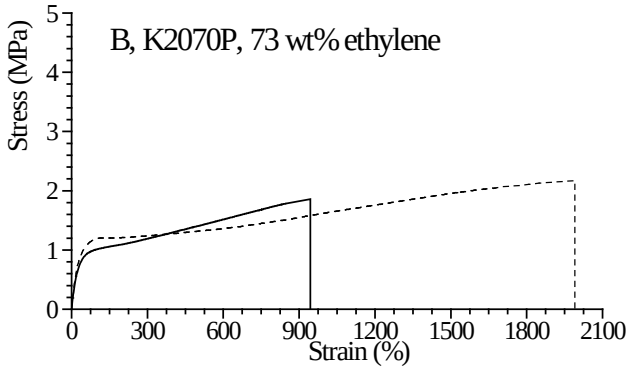
B, K2070P, 73 wt% ethylene
Stress (MPa)
Strain (%)
0
1
2
3
4
5
0
300
600
900
1200
1500
1800
2100

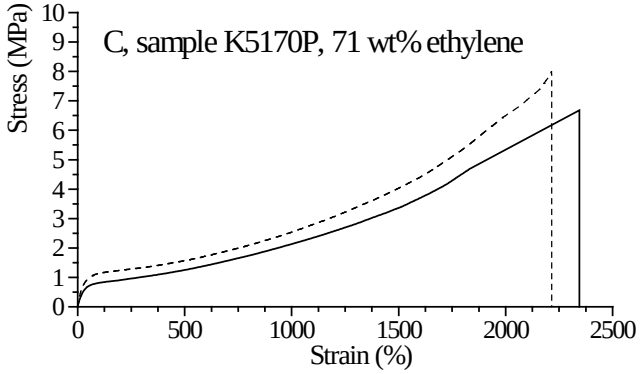
C, sample K5170P, 71 wt% ethylene
Stress (MPa)
Strain (%)
0
1
2
3
4
5
6
7
8
9
10
0
500
1000
1500
2000
2500

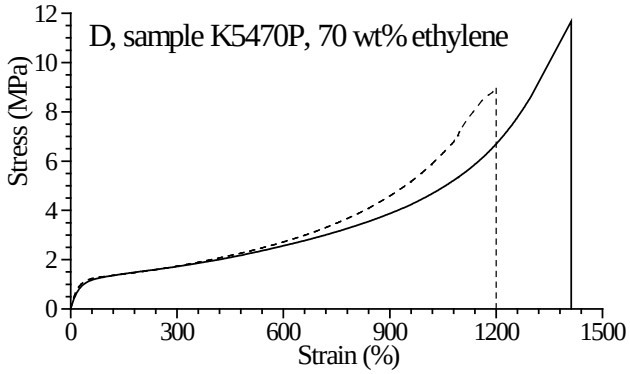
D, sample K5470P, 70 wt% ethylene
Stress (MPa)
Strain (%)
0
2
4
6
8
10
12
0
300
600
900
1200
1500

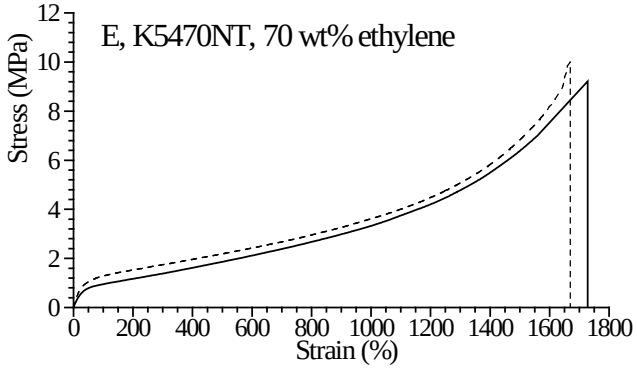
E, K5470NT, 70 wt% ethylene
Stress (MPa)
Strain (%)
0
2
4
6
8
10
12
0
200
400
600
800
1000
1200
1400
1600
1800

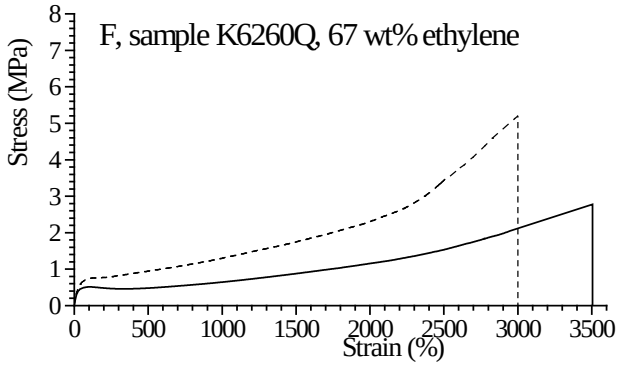
F, sample K6260Q, 67 wt% ethylene
Stress (MPa)
Strain (%)
0
1
2
3
4
5
6
7
8
0
500
1000
1500
2000
2500
3000
3500

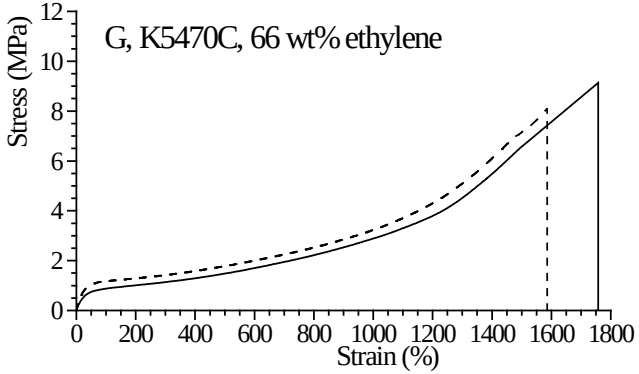
G, K5470C, 66 wt% ethylene
Stress (MPa)
Strain (%)
0
2
4
6
8
10
12
0
200
400
600
800
1000
1200
1400
1600
1800

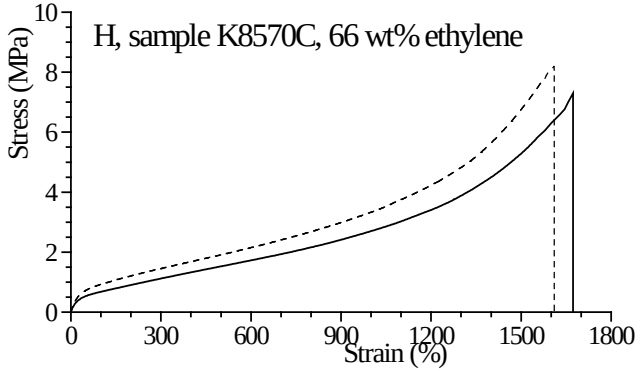
H, sample K8570C, 66 wt% ethylene
Stress (MPa)
Strain (%)
0
2
4
6
8
10
0
300
600
900
1200
1500
1800

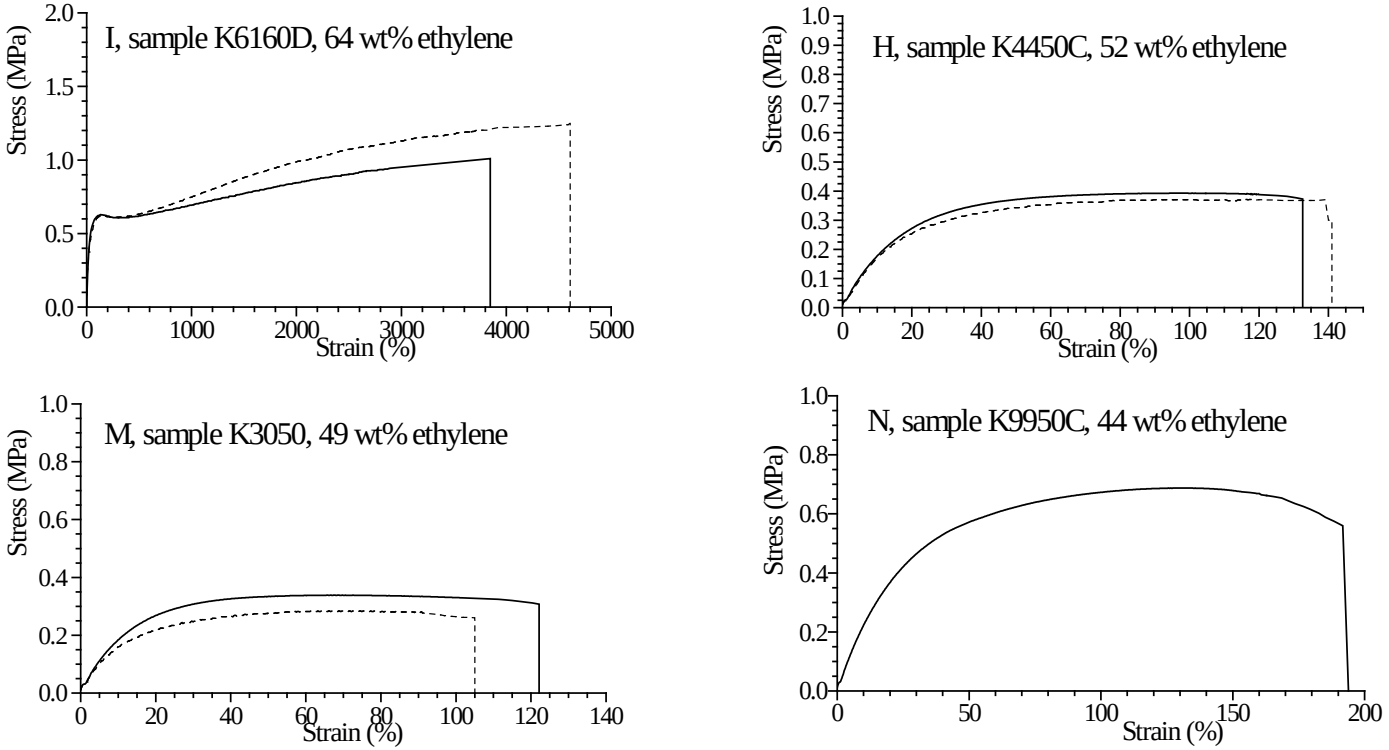

Figure 2.49. *Stress-strain curves of fresh (continuous curves) and aged (dashed curves) compression molded films of samples EPM with 78 wt% ethylene (A), K2070P with 73 wt% ethylene (B), K5170P with 71 wt% ethylene (C), K5470P with 70 wt% ethylene (D), K5470NT with 70 wt% ethylene (E), K6260Q with 67 wt% ethylene (F), K5470C with 66 wt% ethylene (G), K8570C with 66 wt% ethylene (H), K6160D with 64 wt% ethylene (I), K4450 with 52 wt% ethylene (L), K3050 with 49 wt% ethylene (M) and K9950C with 44 wt% ethylene (N).*

A comparison of the stress-strain curves of fresh and aged compression molded film of all samples is shown in Figure 2.50. As expected, the most crystalline sample (EPM, 78 wt% of ethylene) shows the highest values of modulus and stress at yield.

As mentioned above, the stress-strain curves of the crystalline samples EPM with 78 wt% ethylene, K5170P with 71 wt% ethylene, K5470P with 70 wt% ethylene, K5470NT with 70 wt% ethylene, K6260Q with 67 wt% ethylene, K5470C with 66 wt% ethylene and K8570C with 66 wt% ethylene show strain-hardening at high deformation (Figure 2.49A,C-H). The entity of strain-hardening is different in the various samples, for example it is low in the sample K2070P with 73 wt% ethylene (Figure 2.49B) and is absent in the amorphous samples with low ethylene content (52-44wt%), K4450 with 52 wt% ethylene (Figure 2.49L), K3050 with 49 wt% ethylene (Figure 2.49M) and K9950C with 44 wt% ethylene (Figure 2.49N). It is known that strain hardening in elastomers is often associated with crystallization induced by stretching. Therefore, we can hypothesize that strain-hardening in EPM and EPDM sample could be due to the stress-induced crystallization (SIC). In particular, initially crystalline samples show strain-hardening and hence further crystallization occurs by stretching at high deformation, whereas initially amorphous samples with low ethylene content in the range 52-44wt% are also not able to crystallize upon stretching. This hypothesis will be demonstrated in the next section by analysis of the X-ray diffraction patterns recorded during deformation. This results in improvement of strength upon deformation and in a remarkable ductility of samples with ethylene concentration in the range 78-64 wt% as initial crystals and those that develop during deformation create an efficient elastomeric network preventing viscous flow.

Within this general behavior some differences in the mechanical properties of the samples may be due to the different molecular mass. In particular, the sample K2070P with 73 wt% ethylene shows lower deformation at break and strength (Figure 2.49B) probably due to the lower molecular mass and less amount of SIC.

Slight differences have been also observed in the stress-strain curves of samples of the second set with similar ethylene concentration of 64-67 wt% (Figure 2.49F-I). The samples K6260Q (67 w% of ethylene, Figure 2.49F) and K6160D (64 w% of ethylene, Figure 2.49I) show very high deformation at break (3000-4000%) and low strain-hardening probably due to low SIC and some viscous flow at high deformation. Moreover, they show a defined yielding point due probably to the presence of initial crystallinity. The other two samples belonging to the same set with similar ethylene content, K5470C (66 w% of

ethylene, Figure 2.49G) and K8570C (66 wt% of ethylene, Figure 2.49H) show mechanical properties more similar to samples with higher ethylene concentration with strong strain-hardening and high strength. This behavior may be related, as discussed above, to the fact that these samples have been prepared with the catalyst ACE that produces chains with non-random distribution of comonomers and formation of longer ethylene sequences with less ethylene concentration. As a result, these two samples show stress-strain curves similar to samples with higher ethylene content.

After aging at room temperature all samples show higher values of modulus, stress at yield and at break. In some cases, as for the samples K2070P (Figure 2.49B) and K6160D (Figure 2.49I) aging also produces a slight increase of deformation at break. As a matter of fact, no great differences between stress-strain curves of fresh and aged samples can be observed.

Finally, as shown in the comparison of Figure 2.50C,D, samples with low ethylene content (52-44wt%) show stress-strain curves with very low values of stress and strain at break in both fresh and aged samples, and therefore, no improvement of mechanical properties is observed upon aging.

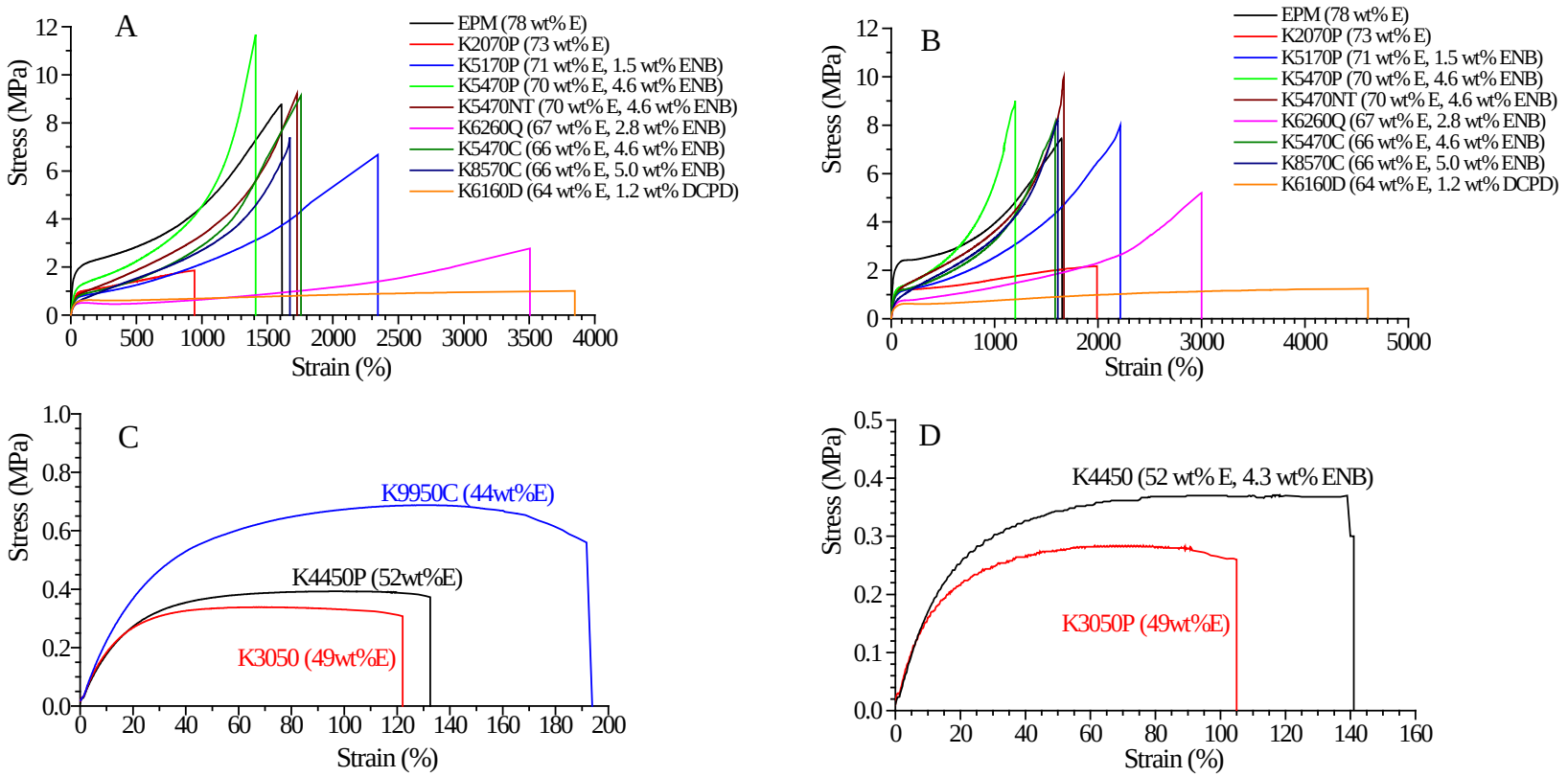

Figure 2.50. *Stress-strain curves of fresh (A,C) and aged (B,D) compression molded films of samples with ethylene content in the range 78-64 wt% (A,B) and 52-44 wt% (C,D).*

Table 2.8. Values of Young's modulus (E), stress (σ_b) and strain (ε_b) at break, stress (σ_y) and strain (ε_y) at the yield point, tension set at break (t_b) of fresh and aged compression molded films of EPM copolymers and EPDM terpolymers.

Sample	Ethylene (wt%)	Diene (wt%)	E (MPa)		ε_b (%)		σ_b (MPa)		ε_y (%)		σ_y(MPa)		t_b (%)	
			fresh	aged	fresh	aged	fresh	aged	fresh	aged	fresh	aged	fresh	aged
EPM	78	-	11±2	14±1	1410±230	1824±195	6.6±1.4	8.3±0.8	19±2	22±7	1.8±0.1	2.4±0.1	390±8	360±17
K2070P	73	-	3.1±0.2	3±1	945±75	1990±200	2.0±0.1	2.1±0.2	38±2	110±8	1.0±0.1	1.2±0.1	103±17	100±0.01
K5170P	71	1.5	2.4±0.2	4.0±0.2	2340±380	2215±150	6.7±1.2	8.0±0.8	38±4	40±1	0.8±0.1	1.1±0.1	90±3	80±10
K5470P	70	4.6	3.3±0.3	5.0 ±0.3	1410±90	1200±50	12.0±2.5	9.0±0.8	35±5	26±2	1.1±0.1	1.2±0.1	85±7	102±3
K5470NT	70	4.6	2.6±0.2	4.0±0.2	1730±105	1670±103	9±1	10±1	34±2	36±1	0.81±0.05	1.0±0.1	82±5	57±4
K6260Q	67	2.8	0.7±0.2	2.0±0.4	3500±380	3000±430	3.0±0.4	5.0±0.9	102±7	67±1	0.50±0.02	40±2	110±7	40±1
K5470C	66	4.6	3.3±0.3	4.0±0.2	1760±190	1586±110	9.0±0.5	8.0±0.2	40±3	35±3	0.80±0.05	1.1±0.1	80±5	79±1
K8570C	66	5.0	1.7±0.8	2.4±0.1	1700±100	1610±70	7.4±0.9	8±2	19.0±0.1	29±2	0.45±0.04	0.8±0.1	50±10	41±0.2
K6160D	64	1.2	1.1±0.1	1.5±0.1	3850±730	4610±490	1.0±0.1	1.2±0.3	140±25	160±25	0.60±0.02	0.6±0.1	180±7	50±4
K4450	52	4.3	0.6±0.1	0.7±0.1	130±11	141±17	0.40±0.03	0.3±0.1	-	-	-	-	17.0±0.2	-
K3050	49	-	0.25±0.03	0.4±0.1	120±18	105±15.5	0.30±0.02	0.2±0.1	-	-	-	-	25±3	-
K9950C	44	9.0	0.75±0.08	-	194±21	-	0.60±0.08	-	-	-	-	-	17±3/	-

The mechanical parameters evaluated from the stress-strain curves of fresh and aged samples of EPM copolymers and EPDM terpolymers are reported in Figure 2.51 as a function of ethylene concentration. Different colors have been used in background to mark different range of ethylene content.

Fresh samples in blue region (ethylene content in the range 78-70 wt%) show similar values of strain at break ε_b, except the sample K2070P with 73 wt% of ethylene that shows lower strain at break probably because of the lower molecular mass (Figure 2.51A). The two fresh samples in the pink region (K6260Q and K6160D, with 67 and 64 wt% of ethylene, respectively) show the highest values of ε_b, while the samples K5470C and K8570C displays ε_b values similar to samples in the blue region (Figure 2.51A), indicating that ACE catalyst provides ethylene sequences with length comparable to samples with higher ethylene content. Samples in the yellow zone show similar and very low values of strain and stress at break (Figure 2.51A,B). A similar trend is observed after aging at room temperature, with the exception of the sample K2070P, which shows much higher values of strain at break ε_b.

The samples of the blue region show the highest values of strength with higher values of the stress at break (Figure 2.51B), which is almost constant in this range except the sample K2070P with 73 wt% of ethylene, which shows lower stress at break because of the low strain-hardening probably due to the low molecular mass that prevents deformation at high strain. The stress at break decreases with decreasing ethylene concentration (Figure 2.51B), moving from the blue region to the pink and then to the yellow regions of the plot of Figure 2.51B. Similar trend is observed for aged samples. Analogously, the Young modulus decrease with decreasing ethylene concentration (Figure 2.51F), from the value of 11-15 MPa of the most crystalline sample EPM to very low values, lower than 1 MPa, for the amorphous samples with ethylene concentration in the range 55-44 wt%, according to the decrease of crystallinity (Figures 2.27 and 2.43 and Tables 2.3-2.6).

The strain at yield increases and the stress at yield decreases with decreasing ethylene content (Figure 2.51C,D) (moving from the blue region to the pink region of Figure 2.51C,D). The same trend is observed in the aged samples. The yellow region is not showed because the samples with lower ethylene content do not show any yielding point.

All samples show relatively low values of tension set at break (Table 2.8 and (Figure 2.51E), compared to the high values of the achieved deformation at breaking (higher than 1000%), indicating elastic recovery after breaking. The tension set at break decreases with decreasing ethylene content (Figure 2.51E). The most crystalline sample EPM with 78 wt% ethylene shows the highest

value of tension set (390% and 360% for the fresh and aged samples, respectively), due to the non-negligible irreversible plastic deformation that the sample experiences upon stretching. A fast decrease of the tension set is observed already for small decrease of ethylene concentration and all samples with ethylene content in the range 73-64% show similar low values of tension set, lower than 100% (Table 2.8 and Figure 2.51E). Therefore, in this range of ethylene concentration, between the two vertical dashed lines in Figure 2.51E, the presence of initial crystallinity, the occurrence of strain-hardening and the low values of tension set give the best elastic properties associated with remarkable strength. For amorphous samples with further lower ethylene concentration in the range 44-55 wt%, the tension set further decreases to values close to zero.

The same behavior is observed after aging. In particular, in the case of the samples K6260Q and K6160D with 67 and 64 wt% of ethylene, that present in the fresh specimens slightly higher values of tension set of 110 and 180%, respectively, a decrease of the tension set to values of 40 and 50%, similar to those of the other samples, is observed.

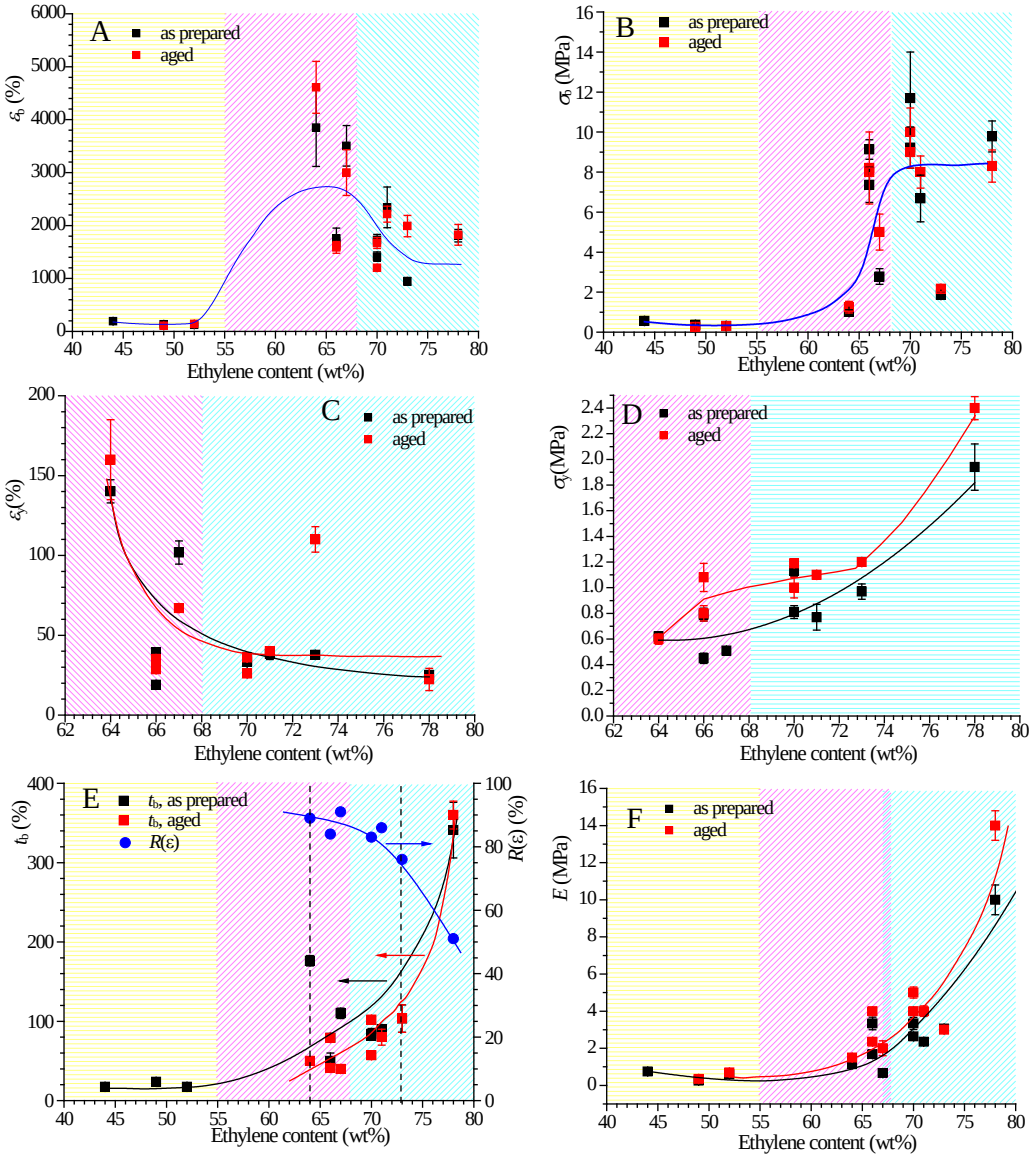

Figure 2.51. *Values of strain ε_b (A) and stress σ_b (B) at break, strain ε_y (C) and stress σ_y (D) at yeld point, tension set at break t_b (E), percentage of the deformation ε which is recovered after removing the tension from deformation ε R(ε) (E) and Young's modulus E (F) of fresh* (■) *and aged* (■) *compression molded films of EPM copolymers and EPDM terpolymers.*

The elastic behavior of EPM and EPDM samples has been better investigated performing mechanical cycles of stretching and relaxation on oriented stress-relaxed fibers and recording the corresponding stress-strain curves. Oriented fibers of EPM copolymers and EPDM terpolymers have been prepared by stretching compression-molded films of initial length L_0 up to the final length L_f comprised in the range $7.8L_0$-$25L_0$ (ε = 680% - 2400%) and then removing the tension allowing the relaxation of the fibers up to the relaxed length L_r. The values of the maximum deformation ε achieved in the

preparation of fibers and the corresponding values of tension set $t(\varepsilon)$, elastic recovery $r(\varepsilon)$ and percentage of the deformation ε which is recovered $R(\varepsilon)$ measured after releasing the tension are reported in Table 2.9. It is apparent that the achieved deformation is almost completely recovered after removing the tension, even when the deformation is very high (higher than 2000%), the percentage of recovered deformation *R* being 80-90% for samples with ethylene concentration in the range 70-64 wt% (Table 2.9 and Figure 2.51E), indicating a perfect elastic behavior. The recovered deformation increases with decreasing ethylene concentration, from 51% of the most crystalline sample EPM up to nearly 90% for the sample with 67-64 wt% (Table 2.9 and Figure 2.51E).

The stress-strain hysteresis cycles, composed of the curves recorded during the stretching and the successive relaxation at controlled rate, of stress-relaxed oriented fibers are reported in Figure 2.52. In these cycles stress-relaxed oriented fibers of initial length L_r are stretched up to the maximum length achieved during the stretching of the starting unoriented film used for the preparation of the fibers (ε_{max} in the range 680 to 2400%), so that the maximum deformation achieved during the first cycle ($\varepsilon = 100(L_f - L_r)/L_r$) for each sample is numerically equal to the elastic recovery $r(\varepsilon)$ of the unoriented film reported in Table 2.9. For each oriented film at least three consecutive hysteresis cycles have been recorded; each cycle has been performed 10 min after the end of the previous cycle. The values of tension set and the values of percentage of dissipated energy during each cycle are reported in Table 2.9.

It is apparent from Figure 2.52 and Table 2.9 that the values of tension set measured in the mechanical cycles are very low and decrease after the first cycle (Table 2.9), indicating a perfect elastic recovery, the hysteresis curves successive to the first cycle being nearly coincident. Furthermore the stress-strain curves of all stress-relaxed fibers present non null hysteresis (Figure 2.52), the values of the percentage of dissipated energy being lower than 70% for the first cycle, and tend to decrease for the successive cycles, achieving values lower than 60%. These data indicate that, regardless of the value of maximum deformation ε achieved for the preparation of the stress-relaxed fibers, all fiber samples show good elastic properties in a non trivial deformation range comprised between 85 and 700%. The good elastic behavior of the unoriented films is, therefore, improved in the oriented fibers. This is due to the fact that, while the unoriented films experience irreversible plastic deformation during stretching because of the small crystallinity, the stress-relaxed fibers are stretched in a deformation range without undergoing further plastic deformation.

A strong difference between stress-strain hysteresis cycles of the most crystalline sample EPM and of the other samples can be observed in Figure 2.52A,A' and B,B'. As demonstrated by X-ray fiber diffraction reported in next section, stretching induces orientation of crystals of pseudo-hexagonal form of PE already present in the undeformed state of the sample EPM. This orientation is partially lost after releasing the tension but residual crystallinity is present in the stress-relaxed fibers. As a result, stress-relaxed fibers of the sample EPM show values of stress higher than those of the stress-relaxed fibers of all other samples in both first and successive hysteresis cycles. This effect is even more evident when hysteresis cycles of sample EPM are compared with those of samples with ethylene content in the range 73-70wt% (Figure 2.52B,B'). Although the undeformed films of these samples show similar values of stress and strain at break (Figure 2.49A-E), the mechanical behavior of stress-relaxed fibers is different. All samples with 73-70 wt % of ethylene appear amorphous or very low crystalline in the undeformed state (see next section) but crystallize upon stretching. After releasing the tension a partial melting of crystals formed upon stretching occurs and the residual crystallinity after relaxation is lower than in the sample EPM. This transformation is reversible. The continuous crystallization and melting phenomena occurring during stretching and relaxation allow development of good elastic properties associated with a remarkable strength. The mechanical strength of these samples is lower than that of the sample EPM that, however, shows less elasticity.

A comparison of first and successive hysteresis cycles of stress-relaxed fibers of all samples, excluded the sample EPM, is shown in Figure 2.52C, C'. Stress-relaxed fibers of samples K6260Q and K6160D with 67 and 64 wt% of ethylene, respectively, show higher elastic recovery than samples with ethylene content in the range 73-70 wt%. Also in this case, the stress-strain curves of stress-relaxed fibers of the sample K5470C are similar to the curves of samples with higher ethylene content.

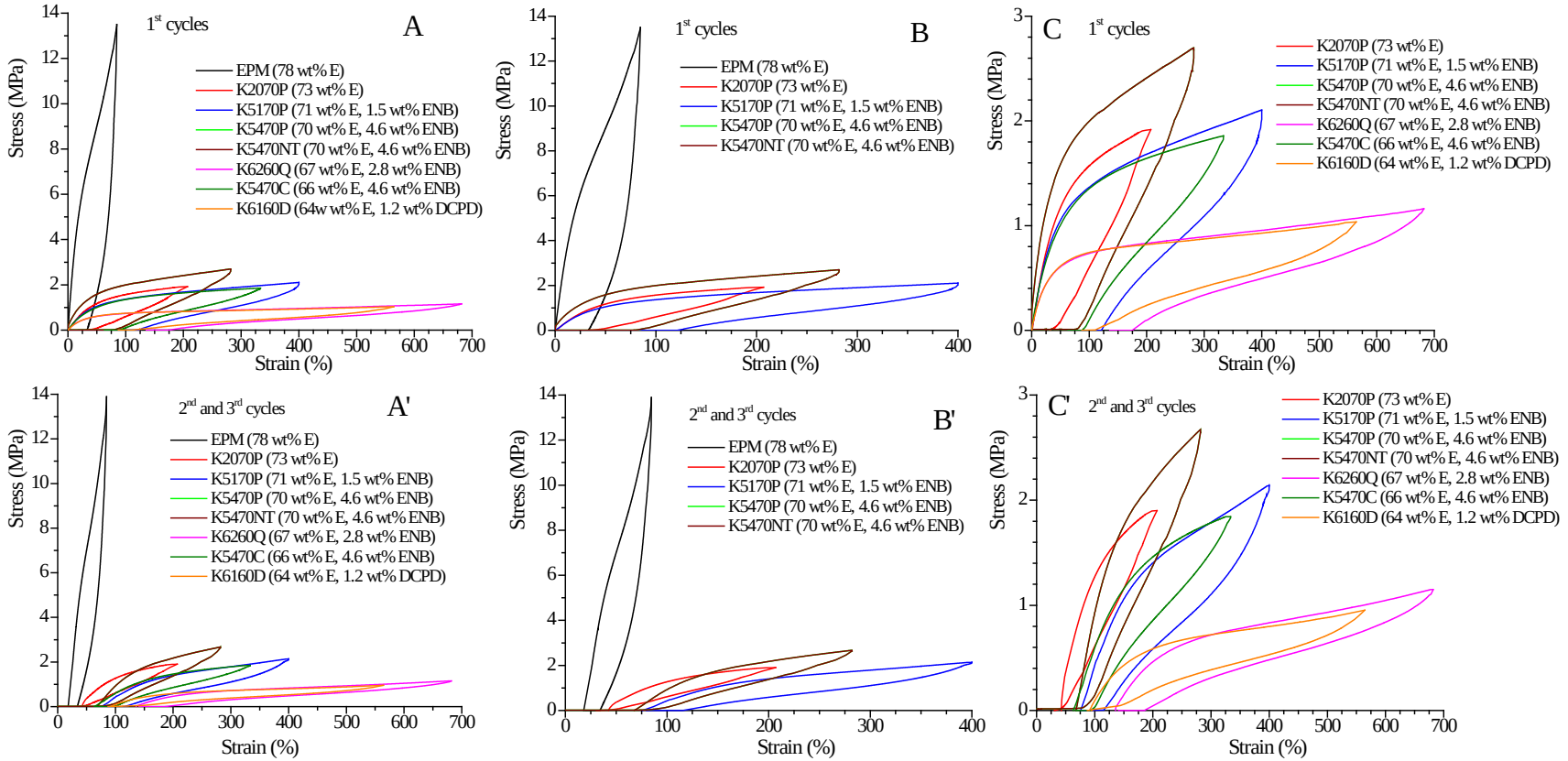

Figure 2.52. *Stress-strain hysteresis cycles of stress-relaxed fibers of EPM and EPDM samples with ethylene content in the range 78-64 wt%. The first hysteresis cycle (A,B,C) and curves averaged for at least 2 cycles successive to the first one (A',B',C') are reported. Comparisons among the hysteresis cycles of all samples (A,A'), of the more crystalline samples with ethylene content in the range 78-70 wt% (B,B') and of all samples excluded the sample EPM (C,C') are shown.*

***Table 2.9**. Values of the maximum deformation ε achieved during stretching of unoriented compression-molded films for the preparation of fibers, values of tension set ($t_s(\varepsilon)$), elastic recovery ($r(\varepsilon)$) and percentage of the deformation ε which is recovered ($R(\varepsilon)$) measured after releasing the tension from the deformation ε for the preparation of the stress-relaxed fibers, and values of tension set (t_s), elastic recovery (r) and percentage of dissipated energy (E_{diss}) measured after I, II and III cycle in the hysteresis stress-strain curves of Figure 2.52 of stress-relaxed fibers of the samples EPM and EPDM.*

Sample	Ethylene content (wt%)	Diene content (wt%)	ε (%)	$t_s(\varepsilon)$ (%)	$r(\varepsilon)$ (%)	$R(\varepsilon)$ (%)	$t_s^{\text{I cycle}}$ (%)	$r^{\text{I cycle}}$ (%)	$t_s^{\text{II-III cycles}}$ (%)	$r^{\text{I-II cycles}}$ (%)	$E_{diss}^{\text{I cycle}}$ (%)	$E_{diss}^{\text{I-II cycles}}$ (%)
EPM	78	/	1000	495 ± 23	85 ± 4	51 ± 2	18 ± 2	57 ± 6	1. 6 ± 0.8	54 ± 27	71 ± 2	58 ± 2
K2070P	73	/	680	160 ± 24	200 ± 30	76 ± 10	43 ± 5	110 ± 13	< 1	110	53 ± 3	37 ± 2
K5170P	71	1.5	1450	210 ± 4	400 ± 8	86 ± 2	76 ± 21	184 ± 50	4 ± 2	173 ± 87	59 ± 2	43 ± 2
K5470P	70	4.6	800	137 ± 15	280 ± 30	83 ± 10	70 ± 5	123 ± 10	< 1	123	60 ± 3	40 ± 5
K5470NT	70	4.6	1000	175 ± 3	300 ± 5	83 ± 2	70 ± 16	135 ± 30	< 1	135	50 ± 3	30 ± 2
K6260Q	67	2.8	2400	217 ± 3	682 ± 8	91 ± 1	136 ± 22	235 ± 38	5.3 ± 2.8	217 ± 115	54 ± 5	38 ± 1
K5470C	66	4.6	1100	176 ± 3	334 ± 6	84 ± 1	63 ± 6	167 ± 16	4.0 ± 1.8	156 ± 70	38 ± 2	36 ± 2
K6160D	64	1.2	2100	231 ± 12	564 ± 30	89 ± 5	87 ± 20	255 ± 60	7.4 ± 2.1	230 ± 65	54 ± 1	41.0 ± 0.2

The stress-strain curves of the stress-relaxed fibers of EPM copolymers and EPDM terpolymers that have experienced at least three consecutive hysteresis cycles of the kind of Figure 2.52 are reported in Figure 2.53. The Young modulus and the stress and strain at break evaluated from the stress-strain tests of Figure 2.53 are reported in Table 2.10. It is apparent that the stress-relaxed fibers exhibit an increase of mechanical strength and Young's modulus with respect to the corresponding unoriented films (Figure 2.49), regardless of the value of the deformation ε achieved for their preparation. In particular, the sample EPM show the highest values of modulus and stress at any strain. In the case of the sample K5470C, the relaxed fibers exhibit higher flexibility and ductility with respect to the corresponding unoriented films (Figure 2.53C). The values of tension set at break of all the oriented fibers are much lower than the corresponding unoriented films, indicating a perfect elastic recovery after breaking (Figure 2.10).

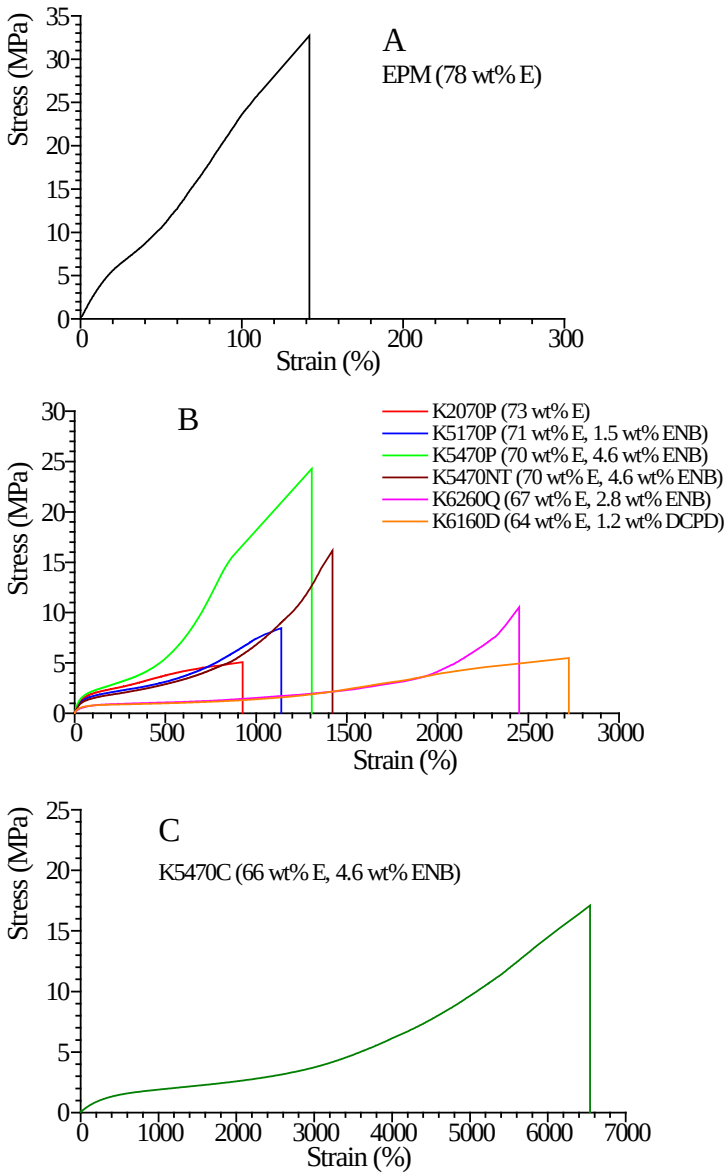

Figure 2.53. *Stress-strain curves of stress-relaxed fibers of samples of EPM and EPDM with ethylene content in the range 78-64 wt% recorded after having experienced at least three hysteresis cycles as in Figure 2.52.*

***Table 2.10**. Values of Young's modulus (E), stress (σ_b) and strain (ε_b) at break, stress (σ_y) and strain (ε_y) at the yield point, tension set at break (t_b) of stress-relaxed fibers of EPM copolymers and EPDM terpolymers.*

Sample	Ethylene content (wt%)	Diene content (wt%)	*E* (MPa)	ε_b (%)	σ_b (MPa)	ε_y (%)	σ_y(MPa)	t_b (%)
EPM	78	/	34 ± 5	140 ± 45	32 ± 1	15 ± 1	4.9 ± 0.6	10 ± 1
K2070P	73	/	4.6 ± 1.3	925 ± 230	5 ± 1	53 ± 3	1.8 ± 0.5	9 ± 5
K5170P	71	1.5	4.5 ± 0.7	1140 ± 110	8 ± 2	50 ± 3	1.8 ± 0.5	< 1
K5470P	70	4.6	6.5 ± 0.5	1300 ± 500	24 ± 1	40 ± 8	2.0 ± 0.1	10 ± 2
K5470NT	70	4.6	6.4 ± 0.4	1420 ± 70	16 ± 1	37 ± 5	1.4 ± 0.4	10 ± 6
K6260Q	67	2.8	2.4 ± 0.6	2450 ± 200	11 ± 2	60 ± 10	0.8 ± 0.1	12 ± 4
K5470C	66	4.6	3.3 ± 0.3	6540 ± 800	17.1 ± 0.5	330 ± 15	1.4 ± 0.1	9 ± 1
K6160D	64	1.2	1.1 ± 0.1	2700 ± 450	6 ± 1	59 ± 9	0.8 ± 0.1	28 ± 8

2.6.6 Stress Induced Crystallization (SIC)

Stress Induced Crystallization (SIC) is a well known phenomenon occurring in many elastomers. SIC was discovered in 1925 by Katz,[72] who was the first to show the X-ray diffraction pattern of a uniaxially stretched sample of natural rubber (NR).[73] The general molecular mechanism proposed for SIC involves the formation of crystals upon stretching and the complete or partial melting of these crystals during relaxation (Figure 2.54). In fact, stretching induces alignment of chains along the stretching direction and forces the chains to assume more extended conformations (Figure 2.54B) starting from the disordered random coil conformation they assume in the undeformed state (Figure 2.54A). In these conditions crystallization can take place even though the starting sample is completely amorphous. (Figure 2.54C). New crystallites oriented along the stretching direction form, providing an increase of tensile strength of the elastomer. This generally results in observation of strong strain-herdening at high deformation in the stress-strain curves of elastomers. When the tensile stress is removed, the elastic recovery of the material is associated generally with the loose of orientation of crystals formed upon stretching followed by partial or complete melting (Figure 2.54D). This mechanism also occurs in crosslinked elastomers, as in natural rubber cured with peroxides or sulphur.

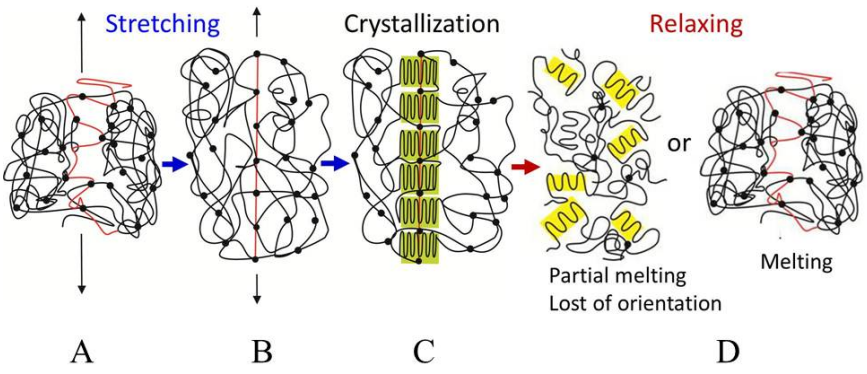

***Figure 2.54**. Scheme of SIC and melting upon releasing the tension.*

As reported in the case of natural rubber, the crystallization under stress has been studied with many different experimental techniques, in particular, volume change,[74-77] stress-relaxation,[76] transmission electron microscopy,[78,79] differential scanning calorimetry,[80] birefringence,[63,81] nuclear magnetic resonance,[82,83] or Raman spectroscopy.[84] The present section will be focused on

studies of SIC by using Wide Angle X-ray Diffraction. In the next section, a correlation between the occurrence of SIC and the results of stress-relaxation experiments will be presented.

Figure 2.55 shows the X ray fiber diffraction patterns of samples of NR recorded during stretching and relaxation.[85] The sample of NR is initially amorphous as indicated by the broad halo in the diffraction profile recorded at zero strain. The occurrence of SIC during stretching can be clearly seen from the appearance of several reflections in the bidimensional X-ray diffractions pattens recorded during deformation (strain $\neq$ 0). During the recovery (stress$\rightarrow$0) these reflections gradually disappear and only the amorphous halo is visible when the stress is totally removed.

More complex and detailed mechanisms have been proposed during the years for SIC in NR for a better understanding of the relationships between the outstanding mechanical properties of NR and SIC. Nevertheless, the general model depicted in Figure 2.55 is enough for a non trivial correlation of mechanical properties and crystallization induced by stretching not only in NR, but also in other elastomers, such as EPM and EPDM rubbers.

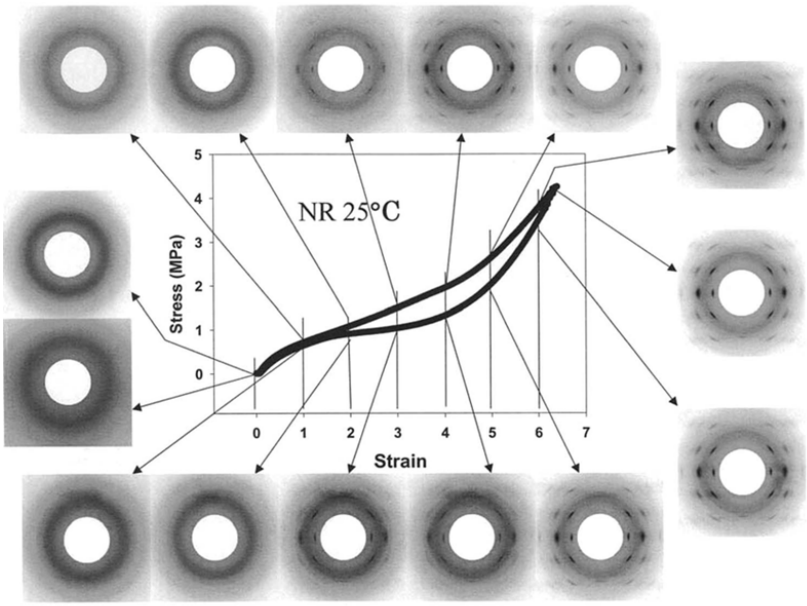

***Figure 2.55**. Stress-strain curve and corresponding diffraction patterns recorded simultaneously for a vulcanized NR (1.5phr sulfur).*[85]

X-ray fiber diffraction patterns have been recorded during deformation and after releasing the tension of all samples of EPM copolymers and EPDM terpolymers. Rectangular specimens cut from fresh compression moulded films

have been analysed before stretching and after stretching up to different degree of deformation ($\varepsilon = 500\%$ and $\varepsilon = \varepsilon_{max}$) without controlling the stretching rate and after releasing the tension. The diffraction patterns of the relaxed fibers have been recorded several hours after the release of the tension.

Since in samples of the third set (ethylene content in the range 52-44 wt%) viscous flow occurs during deformation, this analysis has been performed only on samples belonging to the first and second set, with ethylene concentration in the range 78-64 wt%.

For each deformation of all samples the bidimensional X-ray diffraction pattern, the equatorial profile and the equatorial profile integrated over the azimuthal coordinate are reported. Equatorial profiles have been evaluated reading the intensity along the equatorial line of the bidimensional patterns with the digital imaging reader. The integrated profiles have been calculated integrating the intensity along the azimuthal coordinate χ of the bidimensional patterns by using the software FIT2D (Figure 2.56). On samples stretched at the maximum deformation and relaxed an evaluation of the variation in degree of crystallinity (Δx_c) has been made by comparing the crystallinity achieved upon stretching and after relaxation with respect to the crystallinity visible in the same unoriented sample before stretching. The evaluation of Δx_c has been made by comparing integrated profiles of stretched and relaxed samples instead of the corresponding equatorial profiles. This method guarantees that also the contribution of other non-equatorial reflections possible present visible in the diffraction patterns is taken into account. In order to obtain integrated profiles, bidimensional patterns have been processed with FIT2D resulting in a three dimensional pattern of diffracted intensity as a function of the azimuthal coordinate χ and the radial distance from the center of the fiber pattern (Figure 2.56B). For each value of the radial distance the intensity is averaged over the azimuthal coordinate and the result is reported as a one dimensional profile as a function of the radial distance (Figure 2.56C). After the transformation of radial distance in the Bragg angle 2θ a monodimensional profile of the Intensity as a function of 2θ is obtained (Figure 2.56D).

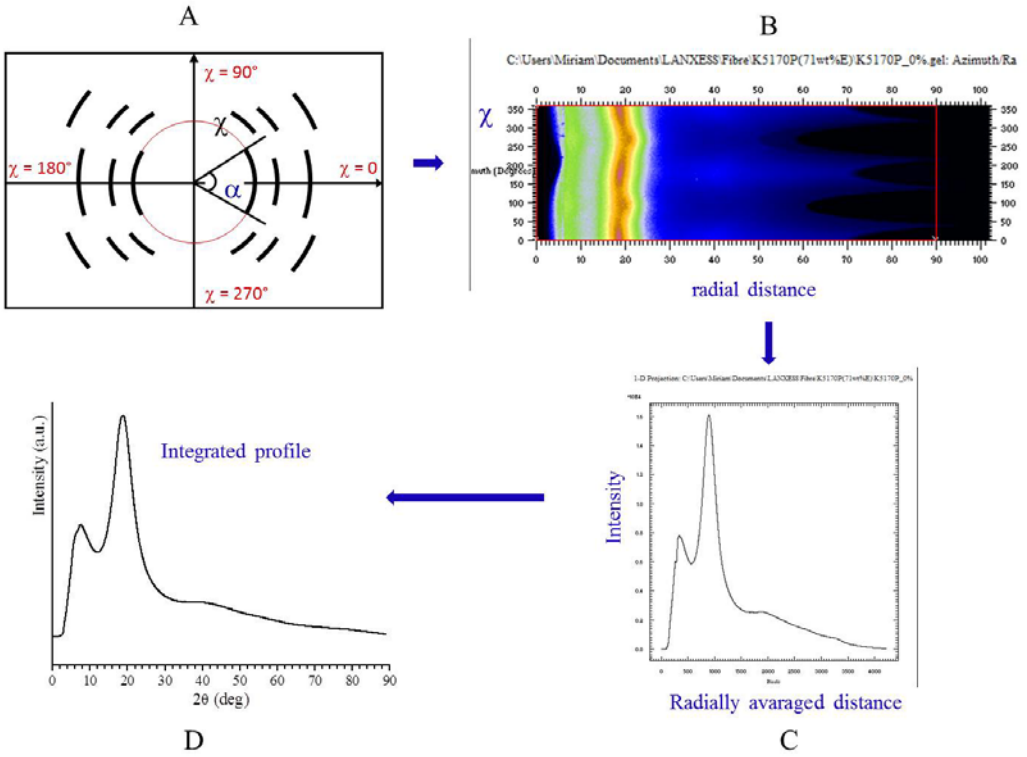

Figure 2.56*. Scheme of the procedure used to calculate the integrated diffracted intensity profiles as a function of 2θ. The intensity along the azimuthal coordinate χ is read (A); a 3D pattern of diffracted intensity as a function of the azimuthal coordinate χ and the radial distance from the center of the fiber pattern is obtained (B); for each value of the radial distance the intensity is averaged over the azimuthal coordinate giving the monodimensional intensity profile as a function of the radial distance (C); after the transformation of the radial distance in 2θ, the final integrated profile of Intensity as a function of 2θ is obtained (D).*

In order to eliminate the background a baseline has been subtracted from the integrated profile (Figure 2.57A). The degree of crystallinity of the fibers stretched at the various deformations has been evaluated from the integrated diffraction profiles. To this end, the integrated diffraction profile of the amorphous phase should be subtracted from the integrated diffraction profiles obtained at each degree of deformation to obtain the crystalline diffraction area A_c. The degree of crystallinity could be then evaluated by the ratio between the crystalline diffraction area (A_c) and the area of the whole diffraction profiles (A_t), $x_c = (A_c/A_t)\times 100$. For most of the analyzed samples, in particular those with ethylene concentrations lower than 78 wt% (in the range 73-64 wt%), the diffraction profile of the amorphous phase is not easily distinguishable from the whole diffraction profile of the un-stretched samples, even though the presence of cryptocrystallinity in these sample in the unoriented specimens has been

demonstrated by DSC and SAXS. For this reason, the integrated profile of the unstretched sample (after subtraction of the baseline (Figure 2.57A)) has been subtracted to the integrated profiles of fibers stretched at the different deformations and of relaxed fibers (Figure 2.57B,C), instead of subtracting the diffraction profile of the amorphous phase. This procedure allows evaluating the excess of crystallinity in the stretched fibers with respect to the unstretched samples. Since it is not clear if the unstretched samples are really amorphous or show faint crystallinity, the so evaluated degree of crystallinity is not an absolute value, but it is rather an evaluation of the eventual increase of crystallinity Δx_c during stretching, that is, the increase of crystallinity observed in the stretched fibers from that of the unstretched state.

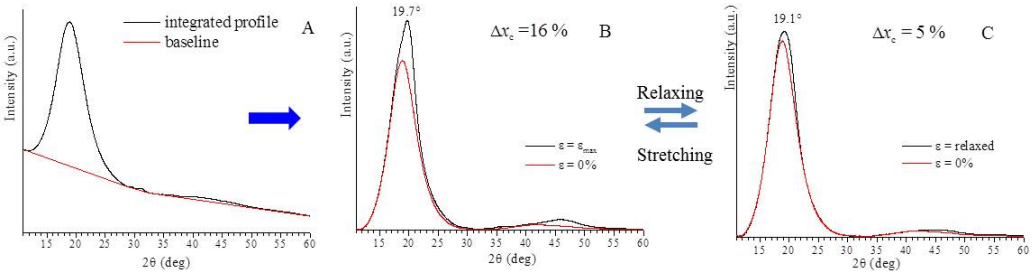

***Figure 2.57**. Scheme of the procedure used to calculate the increase of crystallinity Δx_c achieved upon stretching.*

The bidimensional X-ray diffraction patterns, and the corresponding equatorial and integrated profiles, of the undeformed samples (at ε = 0%) and of fibers stretched at the maximum deformation (ε = ε_{max}) and after releasing the tension (relaxed), of all samples of EPM copolymers and EPDM terpolymers are shown in Figures 2.58-2.66. The sample EPM is clearly already crystalline in the undeformed state, as already shown in diffraction profiles of as-prepared samples of Figures 2.19 and of compression-moulded samples cooled from the melt of Figures 2.32A and 2.48. In fact, the X-ray diffraction pattern of the undeformed sample at ε = 0% (Figure 2.58A) shows the typical reflection of the pseudo-hexagonal form of PE at 2θ = 21°, as also evident in the equatorial profile of Figure 2.58B where the equatorial reflection at 2θ ≈ 21° is clearly visible on the broad amorphous halo at 2θ ≈ 18-19°. Stretching produces orientation of crystals of the pseudo-hexagonal form, as indicated by the polarization of the reflection 2θ = 21° on the equator at deformation of 500% (Figure 2.58B,B'), while other weak reflections appear on the equator at 2θ = 25.7 and 35.7°, corresponding to the hexagonal form of PE, and on the first layer line, corresponding to the trans-planar periodicity of PE (2.5 Å) (Figure

2.58B). With increasing deformation up to ε = 1500%, improvement of orientation of crystals is observed with increase of polarization of equatorial reflections and increase of the intensity and sharpness of the reflection at 2θ = 21° (Figure 2.78C,D). Correspondingly, a polarization of the amorphous halo at 2θ = 18-19° close to the equator and a decrease of its intensity are observed (Figure 2.78B-D). This indicates that crystals of the pseudo-hexagonal form of PE already present in the unstretched sample are improved upon stretching and, probably, further crystallization seems to occur at high deformation.

After releasing the tension, only a slight decrease of the degree of orientation of crystals achieved upon stretching has been observed (Figure 2.58E), as indicated by the broadening of the equatorial reflections along the azimuthal coordinate. Melting of crystals upon relaxation seems not to occur. This is confirmed by the presence in the patterns of Figure 2.58E,E' of all equatorial reflections observed in the diffraction patterns of the stretched sample and by the fact that the intensity of the amorphous halo at 2θ ≈ 18-19° does not increase after relaxation.

EPM, 78 wt% of ethylene

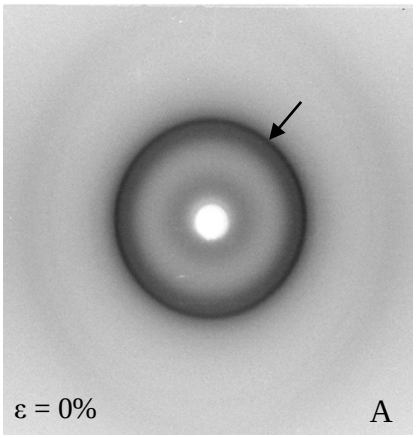

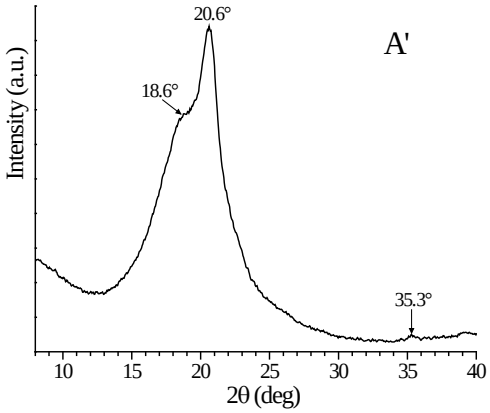

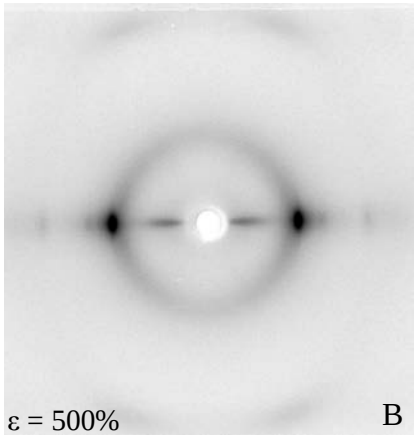

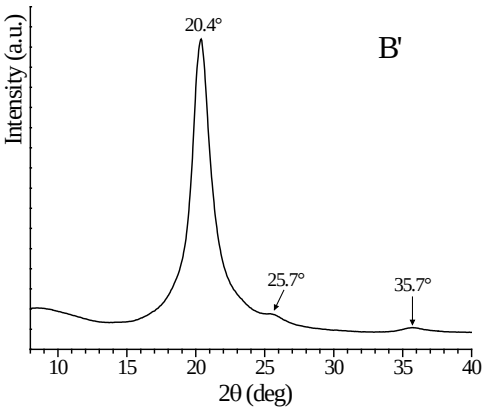

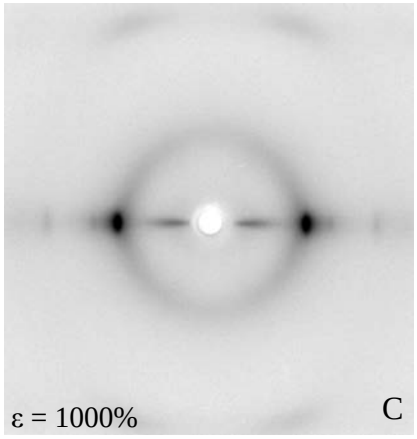

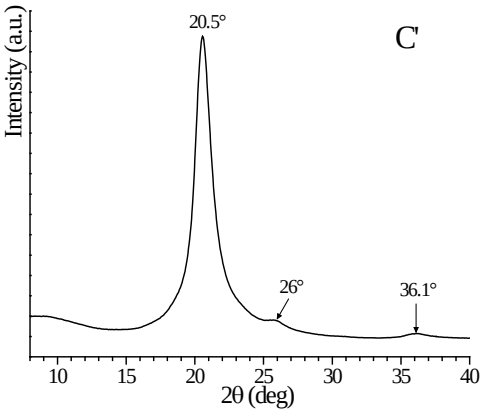

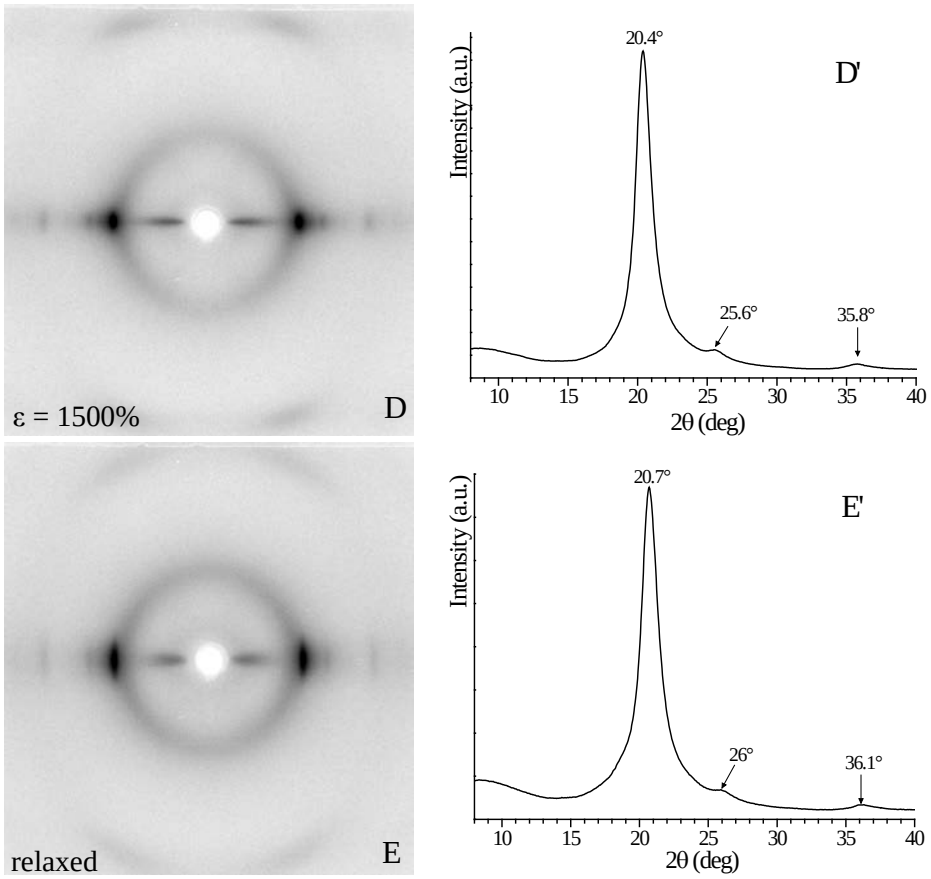

Figure 2.58. *X-ray fiber diffraction patterns (A-E), and corresponding equatorial profiles (A'-E'), of the sample EPM (78 wt% of ethylene) recorded at ε = 0% (A,A'), ε = 500% (B,B'), ε = 1000% (C,C'), ε = 1500% (D,D') and after releasing the tension (E,E').*

Figures 2.59-2.62 show the X-ray fiber diffraction patterns (A-D), and the equatorial (A'-D') and integrated (A''-D'') profiles of samples belonging to the first set of samples (ethylene content in the range 73-70 wt%). As mentioned in the discussion of the WAXS profiles of as-prepared samples (Figure 2.19) and of compression-molded samples cooled from the melt (Figures 2.32A and 2.48), all samples appear amorphous in the undeformed state from the analysis of the WAXS data. In fact, a broad halo at $2\theta \approx 18\text{-}19°$ can be observed in X-ray diffraction patterns and the corresponding equatorial and integrated profiles of the undeformed samples at ε = 0% (Figures 2.59-2.62A, A', A''). The equatorial profiles are, indeed, very similar to all WAXS profiles recorded at room temperature of compression-molded samples of Figures 2.32A and 2.48A,B.

In all samples, the diffraction patterns of fibers stretched at relatively low deformation (at ε = 500%) of Figure 2.59B,B'-2.62B,B' show that the broad

amorphous halo becomes less evident and the typical equatorial reflection of the pseudohexagonal form of PE at 2θ = 20.5-21° already appears. With increasing degree of deformation (at ε = ε_{max}) the reflection at 2θ = 20.5-21° becomes sharper and more intense (Figure 2.59-2.62C,C'). This indicates that in these samples crystallization of the pseudohexagonal form of PE occurs during stretching. Therefore, stress-induced crystallization (SIC) takes place either whether the undeformed samples are really amorphous or whether they present initial not visible cryptocrystallinity. In the latter case, stretching induces improvement of the initial cryptocrystallinity and/or further crystallization. At the maximum degree of deformation (at ε = ε_{max}) a high orientation of crystals of pseudohexagonal form is achieved, as indicated by the strong polarization of the reflection at 2θ = 21° on the equator (Figure 2.59-2.62C,C'). In the case of the sample K5170P with 71 wt% of ethylene the broad amorphous halo has still high intensity on the equator at ε = 500% (Figure 2.60B). This indicates that for this sample lower amount of SIC occurs upon stretching.

The occurrence of crystallization in these samples, or further crystallization with respect to the unstretched samples, is also clearly demonstrated by the comparison of the integrated profiles of fibers stretched at ε = ε_{max} (Figures 2.59C''-2.62C'') and those of the undeformed samples (ε = 0, Figures 2.59A''-2.62A''). A direct comparison between integrated profiles of fibers stretched at ε^{max} and of unstretched samples is shown in Figures 2.59C''-2.62C''. It is apparent that the integrated profiles of the unstretched samples show a main peak at 2θ = 18.9-19.3° and a very weak peak at 2θ = 41-42°, while the integrated profiles of the stretched samples show a main peak at slightly higher values of 2θ, 2θ = 19.3-20°, and a second weak peak at 2θ ≈ 45°. Therefore, the cryptocrystallinity hidden in the unstretched samples, not visible from the WAXS pattern and the integrated profiles (Figures 2.59-2.62A,A',A''), develops more clearly in the stretched fibers and evidenced by the increase of diffracted intensity at 2θ ≈ 20° and 45° in the integrated profiles of Figures 2.59C''-2.62C'').

The values of crystallinity increment Δx_c with respect to crystallinity eventually present in the unstretched samples, evaluated as described above (Figure 2.57), are very similar for the samples of the first set with ethylene contents in the range 73-70 wt%, that is the copolymer K2070P with 73 wt% of ethylene (Δx_c = 16%) and the terpolymers K5170P with 71 wt% of ethylene

(Δx_c = 15%), K5470P with 70 wt% of ethylene (Δx_c = 17%) and K5470NT with 70 wt% of ethylene (Δx_c = 16%).

After releasing the tension from the maximum deformation, the intensity of the broad amorphous halo at 2θ ≈ 18-19° increases (Figure 2.59D-2.62D) and reappears in the equatorial profiles of Figures 2.59D'-2.62D'as a shoulder of the main peak. This indicates that a partial melting of the crystals formed upon stretching, and a decrease of the orientation of the remaining crystals, occur after removing the tension and upon relaxation of the fibers. The amount of melting and of the loss of crystal orientation is different in the various samples. The integrated profiles of the relaxed samples and the corresponding integrated profiles of the unstretched samples are more similar but they do not coincide perfectly because the main crystalline reflection at 2θ ≈ 19-20° is still present in the integrated profiles of the relaxed fibers (Figures 2.59D''-2.62D''), indicating that a residual crystallinity is still present upon relaxation. The residual crystallinity increment in the sample K2070P (Δx_c = 10%) is higher than in the terpolymers K5170P, K5470P and K5470NT, which show similar values of Δx_c. (5-6%).

K2070P, 73 wt% of ethylene

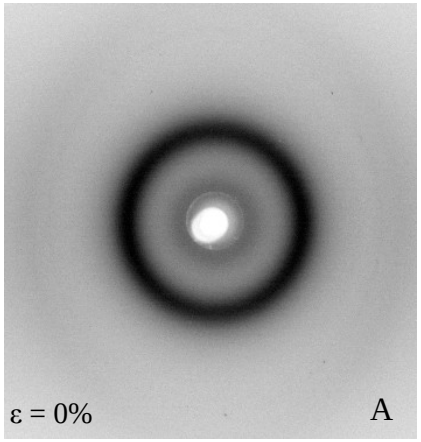

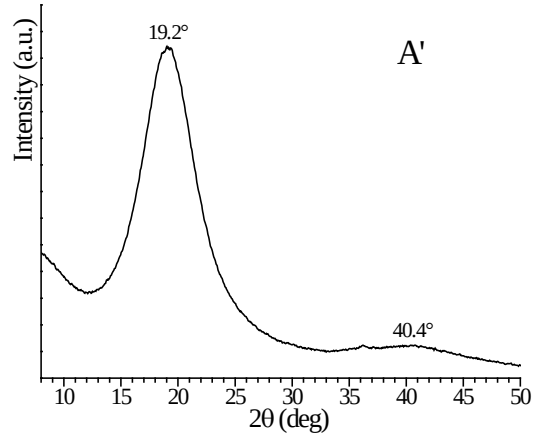

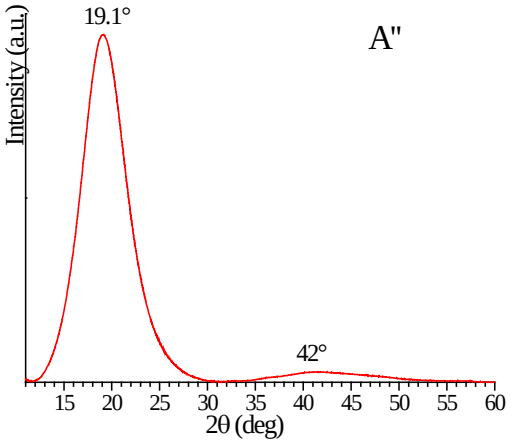

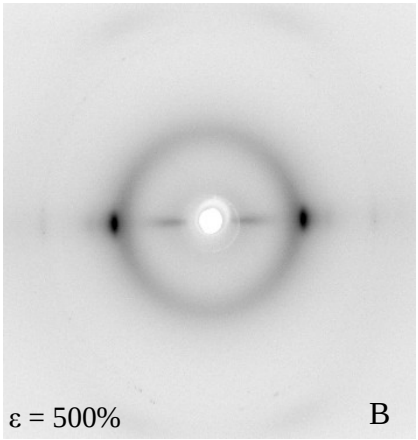

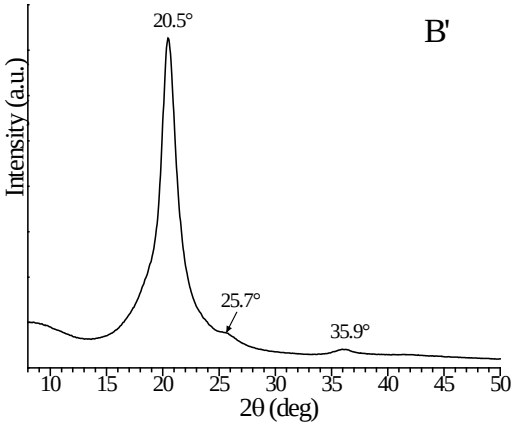

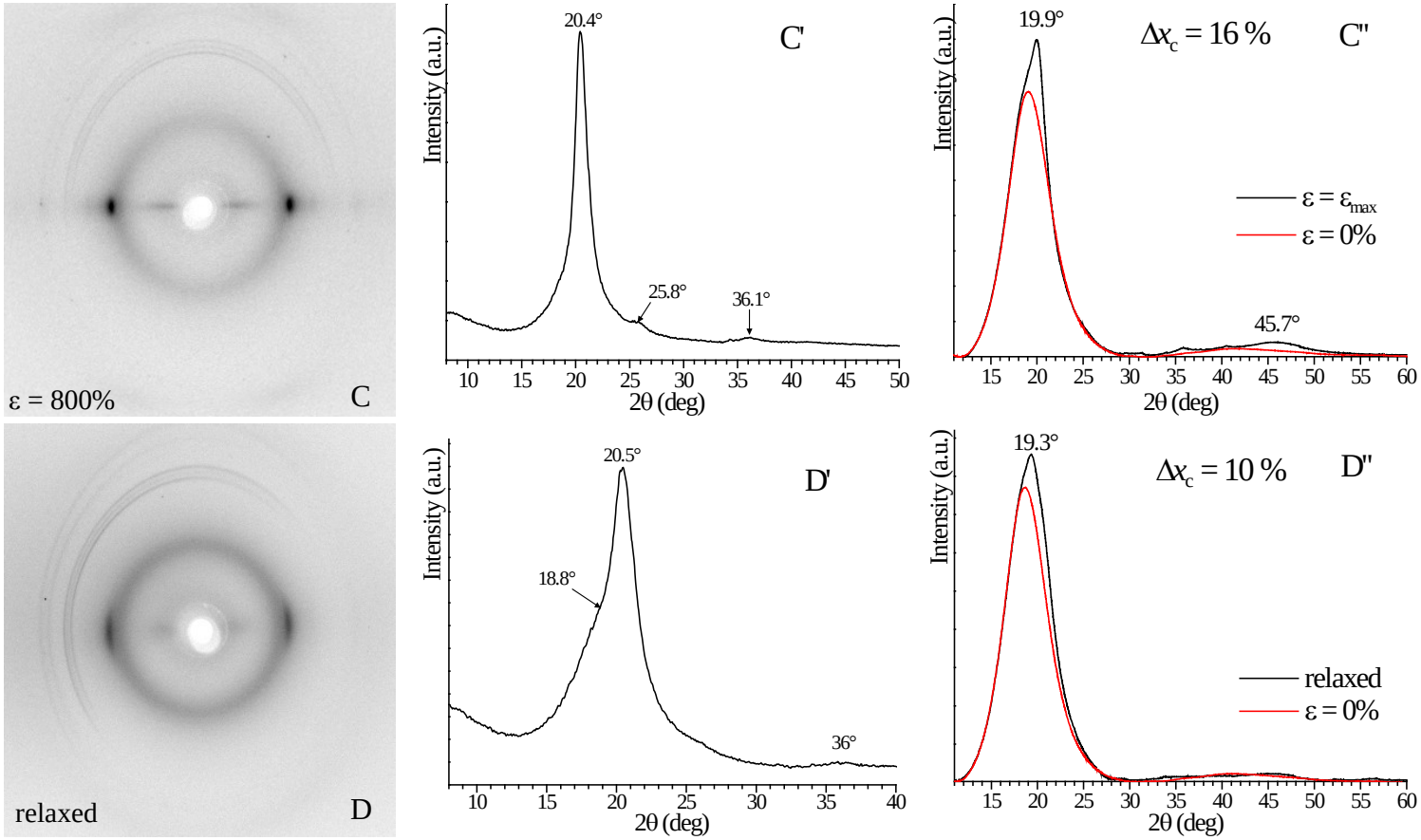

Figure 2.59. *X-ray fiber diffraction patterns (A-D) of sample K2070P (73 wt% of ethylene) and corresponding equatorial (A'-D') and integrated (A''-D'') profiles recorded at ε = 0% (A,A'), ε = 500% (B,B'), ε = 800% (C,C') and after releasing the tension (D, D').*

K5170P, 71 wt% of ethylene

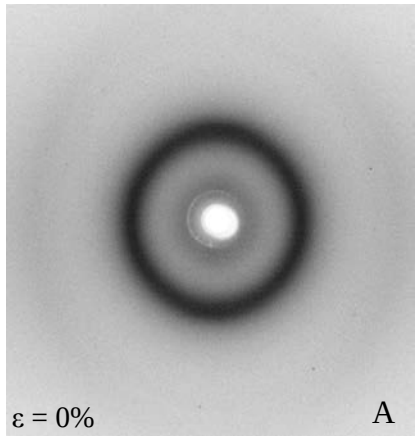

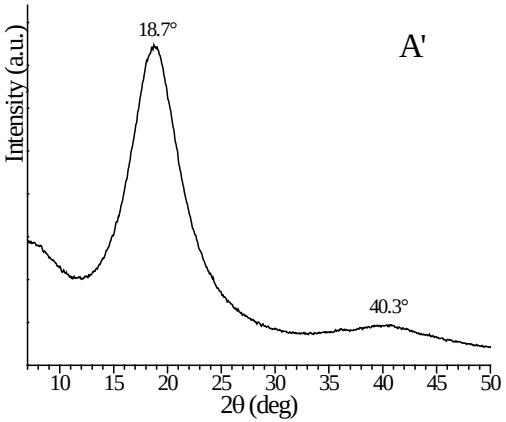

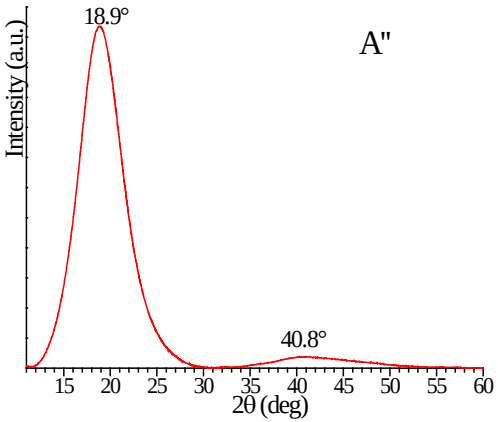

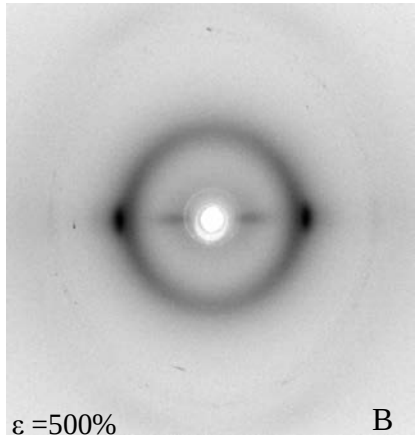

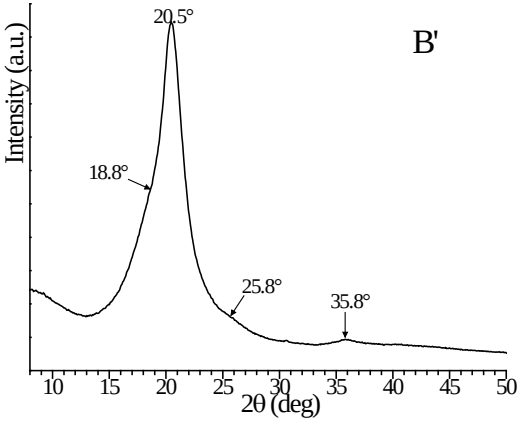

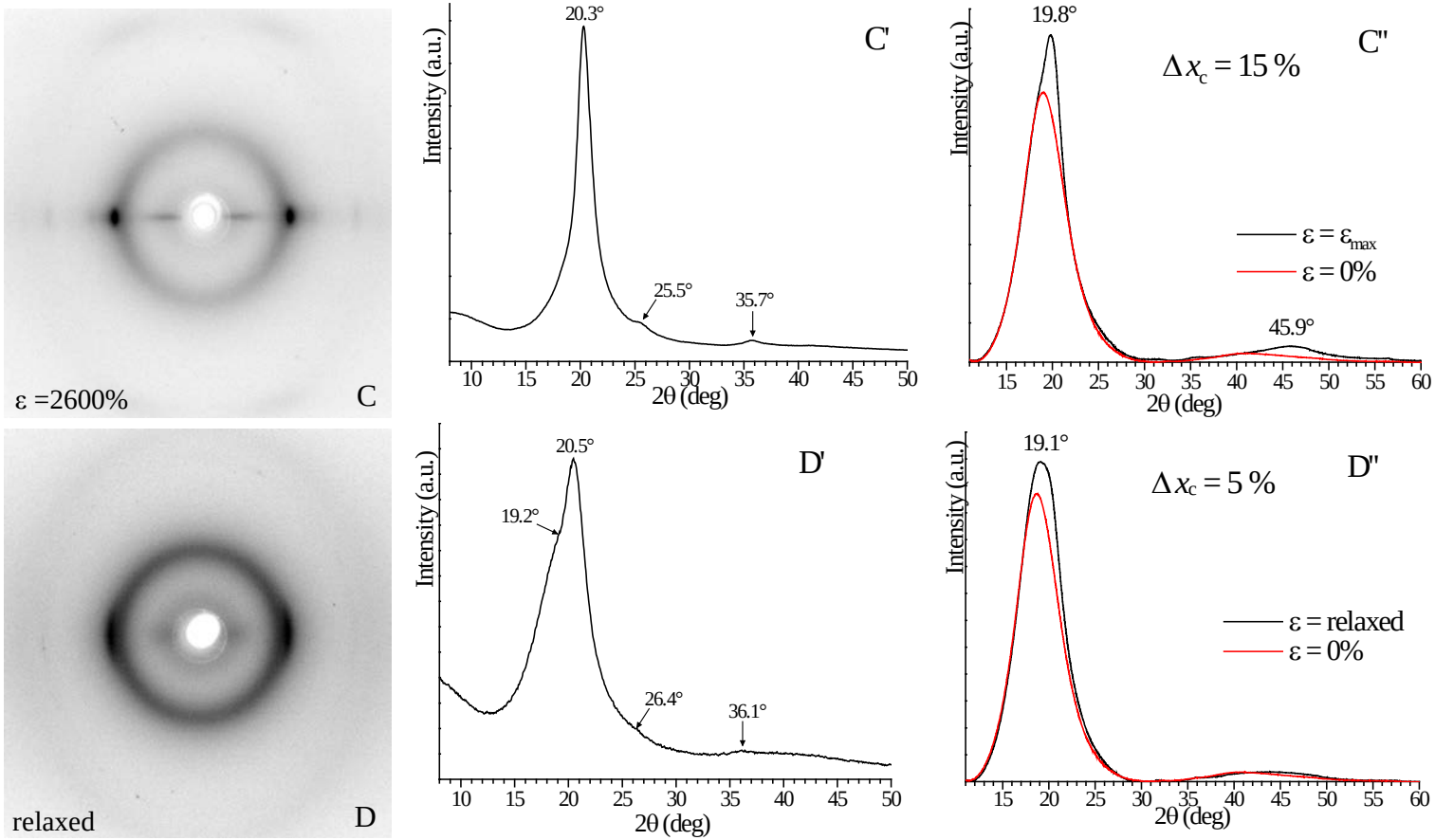

Figure 2.60. *X-ray fiber diffraction patterns (A-D) of sample K5170P (71 wt% of ethylene) and corresponding equatorial (A'-D') and integrated (A''-D'') profiles recorded at ε = 0% (A,A'), ε = 500% (B,B'), ε = 2600% (C,C') and after releasing the tension (D, D').*

K5470P, 70 wt% of ethylene

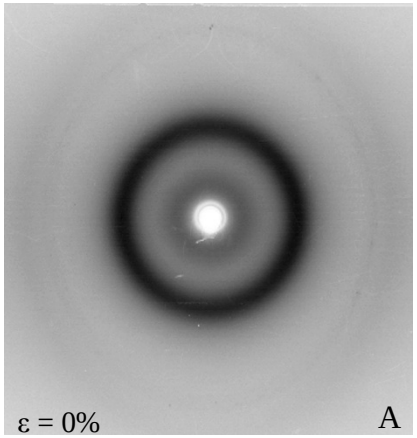

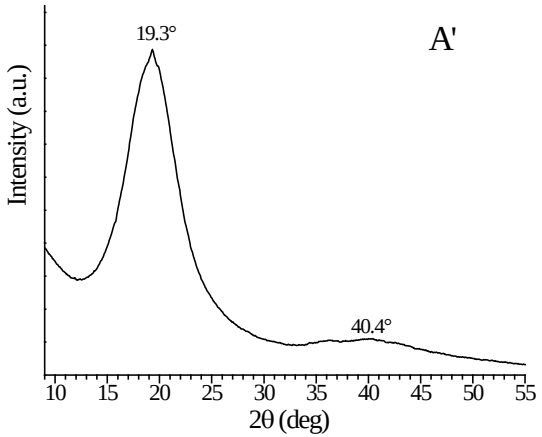

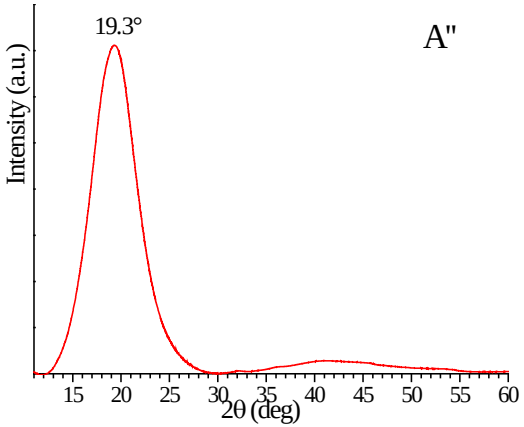

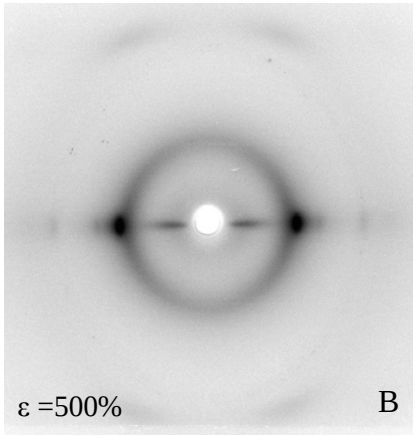

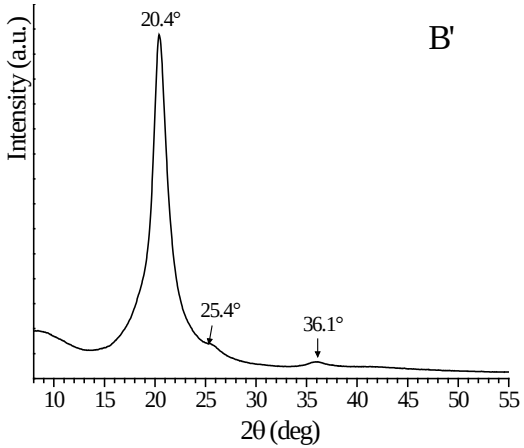

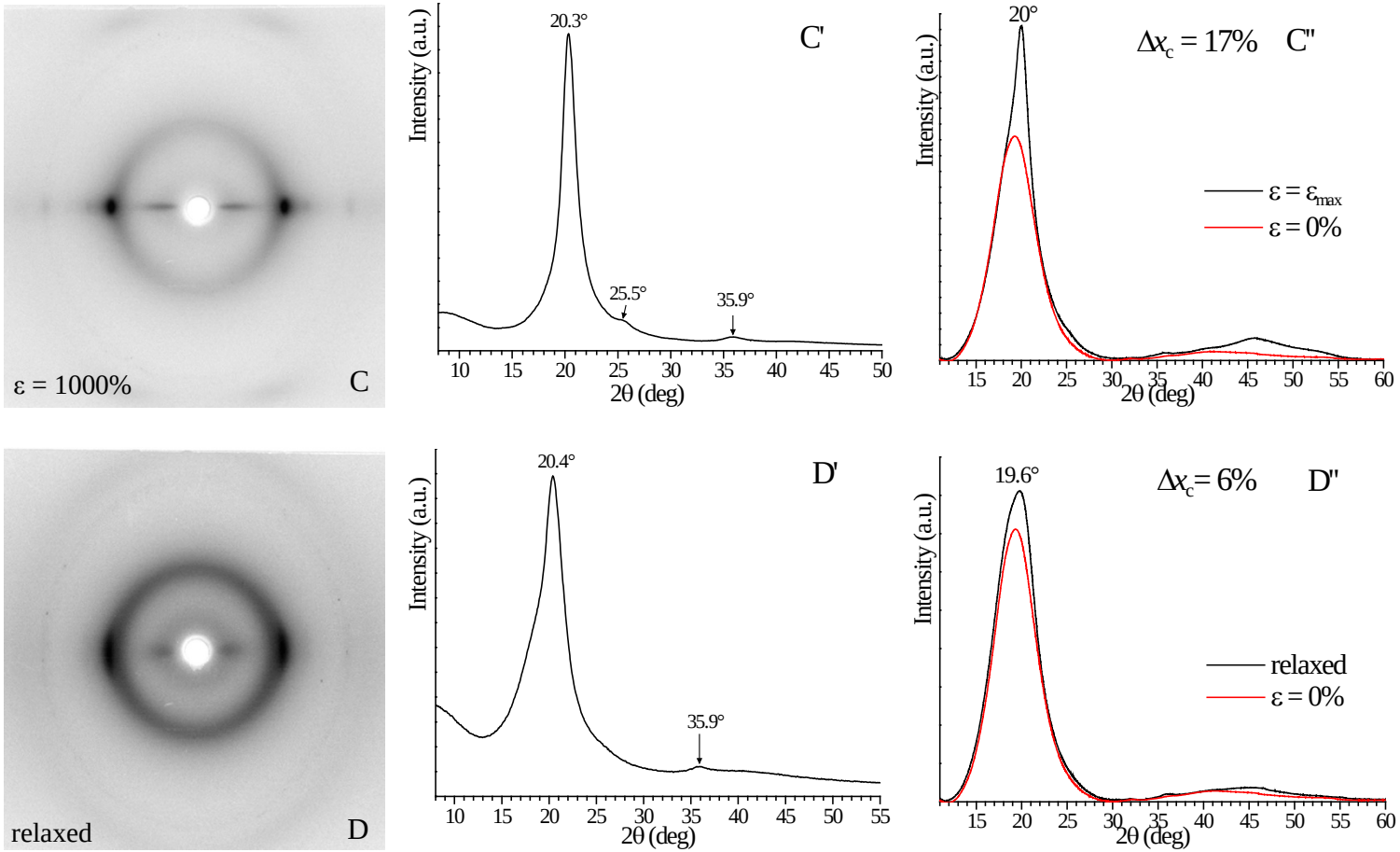

Figure 2.61. *X-ray fiber diffraction patterns (A-D) of sample K5470P (70 wt% of ethylene) and corresponding equatorial (A'-D') and integrated (A''-D'') profiles recorded at ε = 0% (A,A'), ε = 500% (B,B'), ε = 1000% (C,C') and after releasing the tension (D, D').*

K5470NT,70 wt% of ethylene

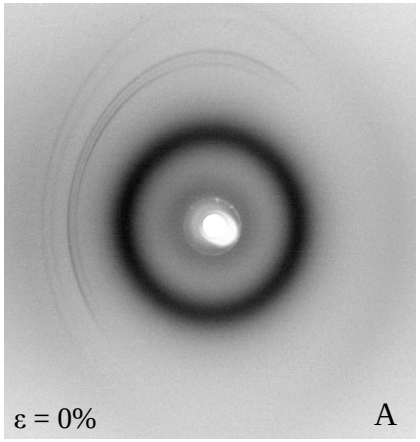

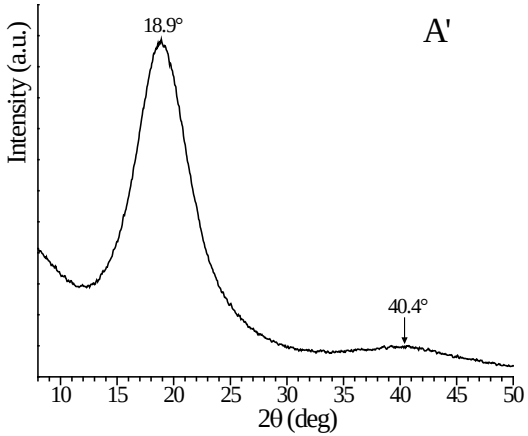

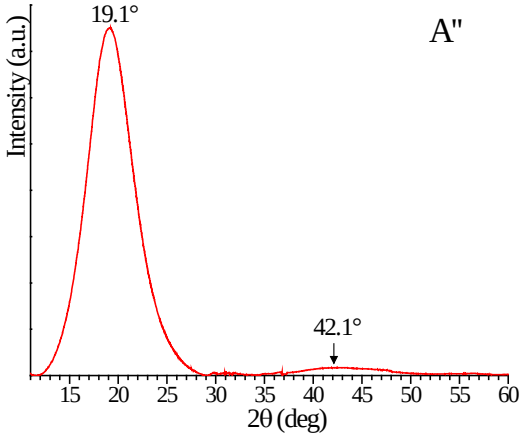

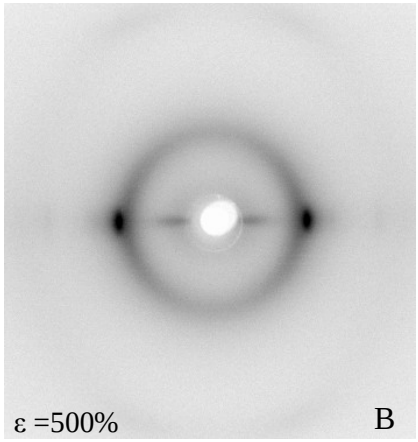

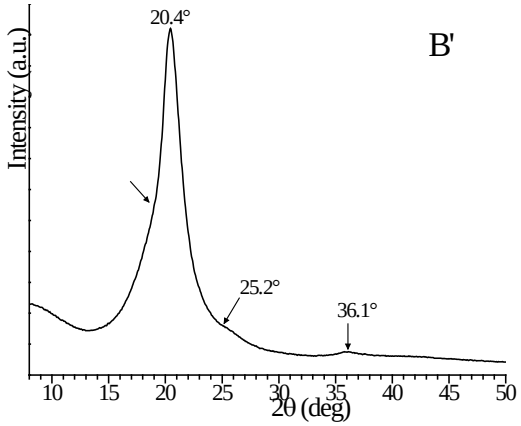

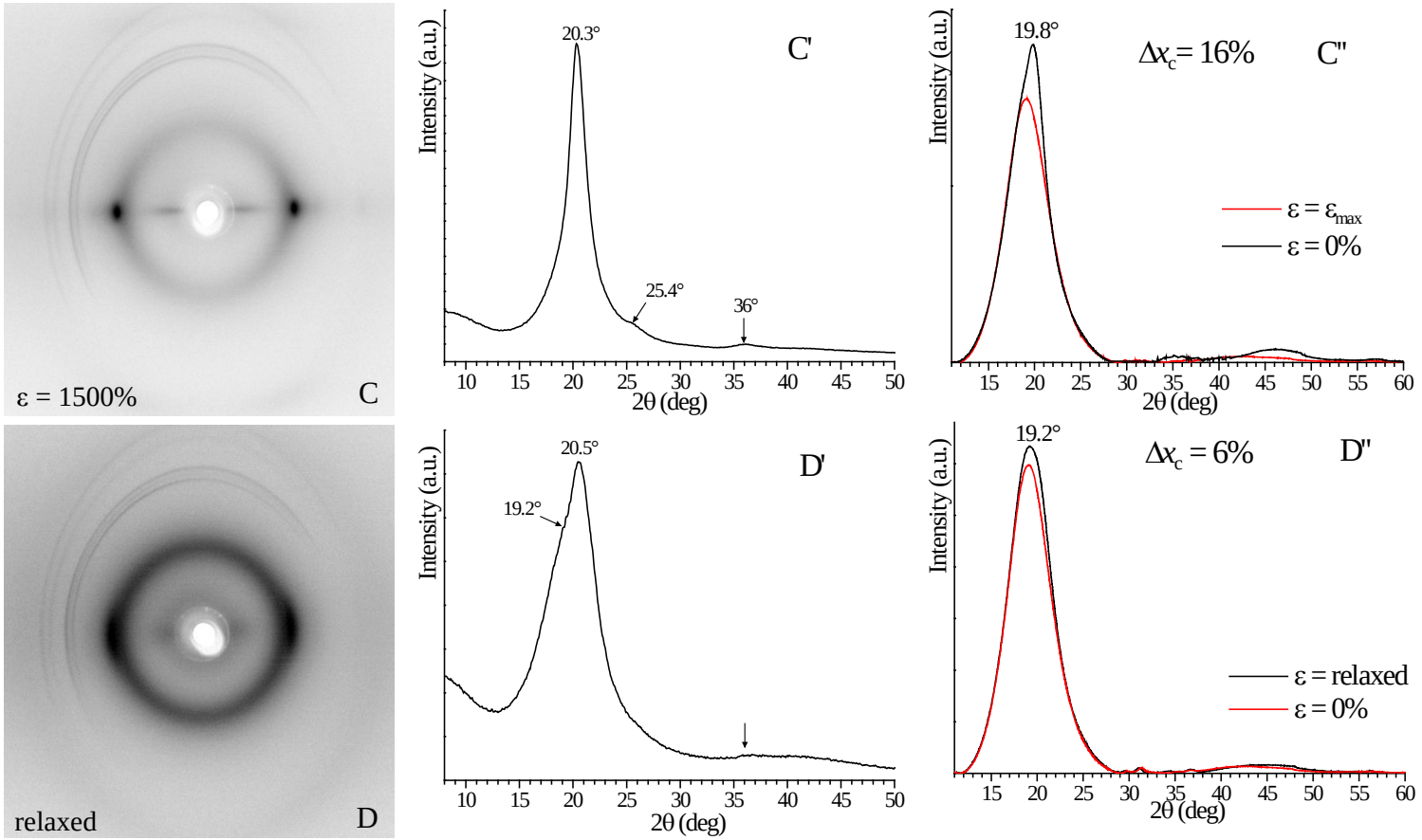

Figure 2.62. *X-ray fiber diffraction patterns (A-D) of sample K5470NT (70 wt% of ethylene) and corresponding equatorial (A'-D') and integrated (A''-D'') profiles recorded at ε = 0% (A,A'), ε = 500% (B,B'), ε = 1500% (C,C') and after releasing the tension (D, D').*

A similar behavior has been observed for samples of the second set with ethylene concentration in the range 67-64 wt%, even though different amount of SIC occurs depending on ethylene concentration. The X-ray diffraction patterns and the equatorial and integrated profiles of these samples are shown in Figures 2.63-2.66. Also for this case, all the undeformed samples appear amorphous or with not evident cryptocrystallinity, as indicated by the presence of the broad halo at $2\theta \approx 18\text{-}19°$ in the diffraction patterns and the equatorial profiles of Figures 2.63A,A'-2.66A.A'. In all samples the appearance of the reflection at $2\theta = 20\text{-}21°$ and its polarization on the equator of the diffraction patterns of fibers of Figures 2.63B,B'-2.66B,B' indicate that SIC occurs by stretching already at low deformations of $\varepsilon = 500\%$. At this low deformation the broad amorphous halo is still present in the diffraction patterns and equatorial profiles of samples K6260Q with 67 wt% of ethylene (Figure 2.63B,B') and K6160D with 64 wt% of ethylene (Figure 2.66B,B'), whereas it is less evident in the diffraction patterns and equatorial profiles of samples K8570C with 66 wt% of ethylene (Figure 2.64B,B') and K5470C with 66 wt% of ethylene (Figure 2.65B,B'). The samples K6260Q and K6160D show the broad halo also at the highest deformation, notwithstanding the very high values of ε_{max} (Figure 2.63C,C' and 2.66C,C'). This indicates that different amounts of SIC occur in these samples, the samples K6260Q and K6160D with 67 and 64 wt% of ethylene, respectively, show lower SIC than the samples K8570C and K5470C both with 66 wt% of ethylene. This is confirmed by the comparison of integrated profiles of stretched and unstretched samples in Figures 2.63C''-2.66C''. In fact for the samples K6260Q and K6160D the integrated profile of the fiber stretched at the maximum deformation present only an additional small peak at $2\theta \approx 19°$ with respect to the profiles of the unstretched samples (Figure 2.63C'' and 2.66C''). On the contrary, samples K8570C and K5470C both with 66 wt% of ethylene at the highest deformation show diffraction patterns (Figures 2.64C'' and 2.65C'') similar to those of stretched samples with higher ethylene concentrations (Figures 2.59-2.62).

The value of crystallinity increment Δx_c with respect to crystallinity eventually present in the unstretched samples, evaluated from the integrated profiles, is $\Delta x_c = 16\%$ for both samples K8570C and K5470C, which is higher than the values evaluated for samples K6260Q and K6160D ($\Delta x_c = 12\%$ and 10%, respectively).

A slight different behavior of these samples has been observed also after removing the tension. In all samples melting of crystals developed upon stretching and loss of their orientation occur upon relaxation but different

amounts of crystals melt in the different samples. In the case of samples samples K6260Q and K6160D, crystals formed upon stretching melt almost completely upon releasing the tension. The diffraction patterns and equatorial profiles of Figures 2.63D,D',D'' and 2.66D,D'D'' of the relaxed fibers of these samples are, indeed, very similar to those of the unstretched samples (Figure 2.63A and 2.66A). The intensity of the broad halo at $2\theta \approx 18\text{-}19°$ increases, while the main reflection of the pseudohexagonal form at $2\theta \approx 21°$ disappears (Figures 2.63D and 2.66D). The integrated profiles of the relaxed fibers and of the unstretched samples are very similar and very low values of residual crystallinity increment of Δx_c = 3% and 1% have been evaluated for the samples K6260Q and K6160D, respectively (Figures 2.63D'' and 2.66D''), indicating almost complete melting of crystals upon relaxation. In the case of samples K8570C and K5470C only partial melting of crystals and a decrease of crystal orientation is observed upon releasing the tension (Figures 2.64D'' and 2.65D''). The values of the residual crystallinity increment are, indeed, Δx_c = 4% and 5% for the samples K8570C and K5470C, respectively, which are slightly higher than those in samples K6260Q and K6160D.

All these differences among the samples belonging to this set of samples are due to the different molecular structure of these samples, in term of different distribution of comonomeric units along the chain. SIC depends on the presence and on the length of crystallizable ethylene sequences. As already discussed, with the same ethylene concentration in the copolymer chains, ACE catalyst allows obtaining ethylene sequences longer than those produced by Vanadium based catalyst. Samples K8570C and K5470C are presumably characterized by chains with ethylene sequences longer than those in the chains of samples K6260Q and K6160D, even though the ethylene concentration is basically the same in the four samples. This results in higher amount of SIC in samples K8570C and K5470C, which show crystallinity increment Δx_c very similar to the values exhibited by samples of the first group with higher ethylene concentrations.

It is worth noting that difference in SIC can explain differences in the mechanical properties among the samples. A more complete discussion about the relationships between SIC and mechanical properties will be presented in section 2.6.8.

K6260Q, 67 wt% of ethylene

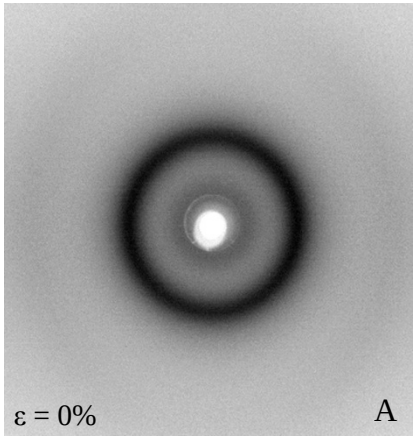

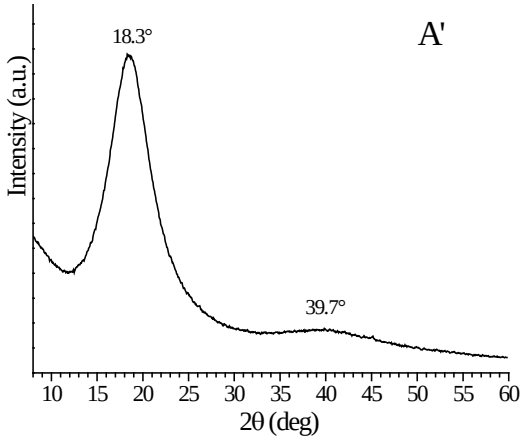

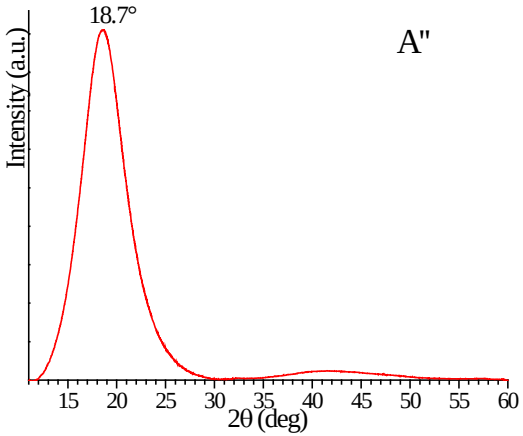

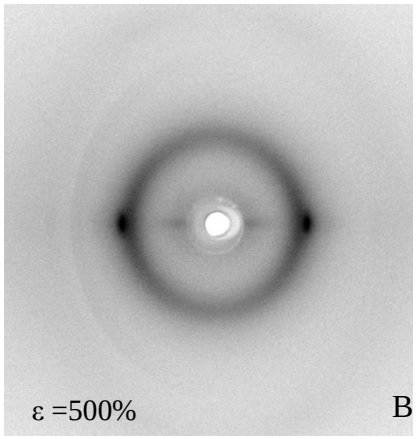

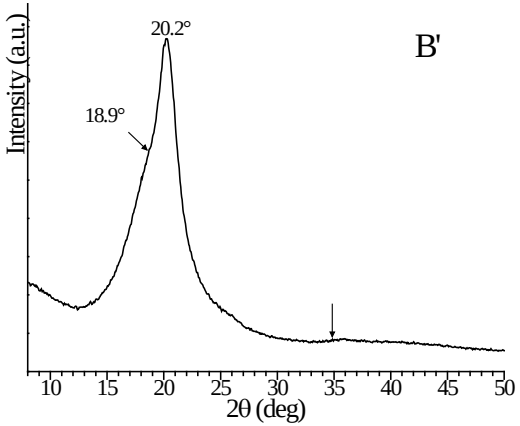

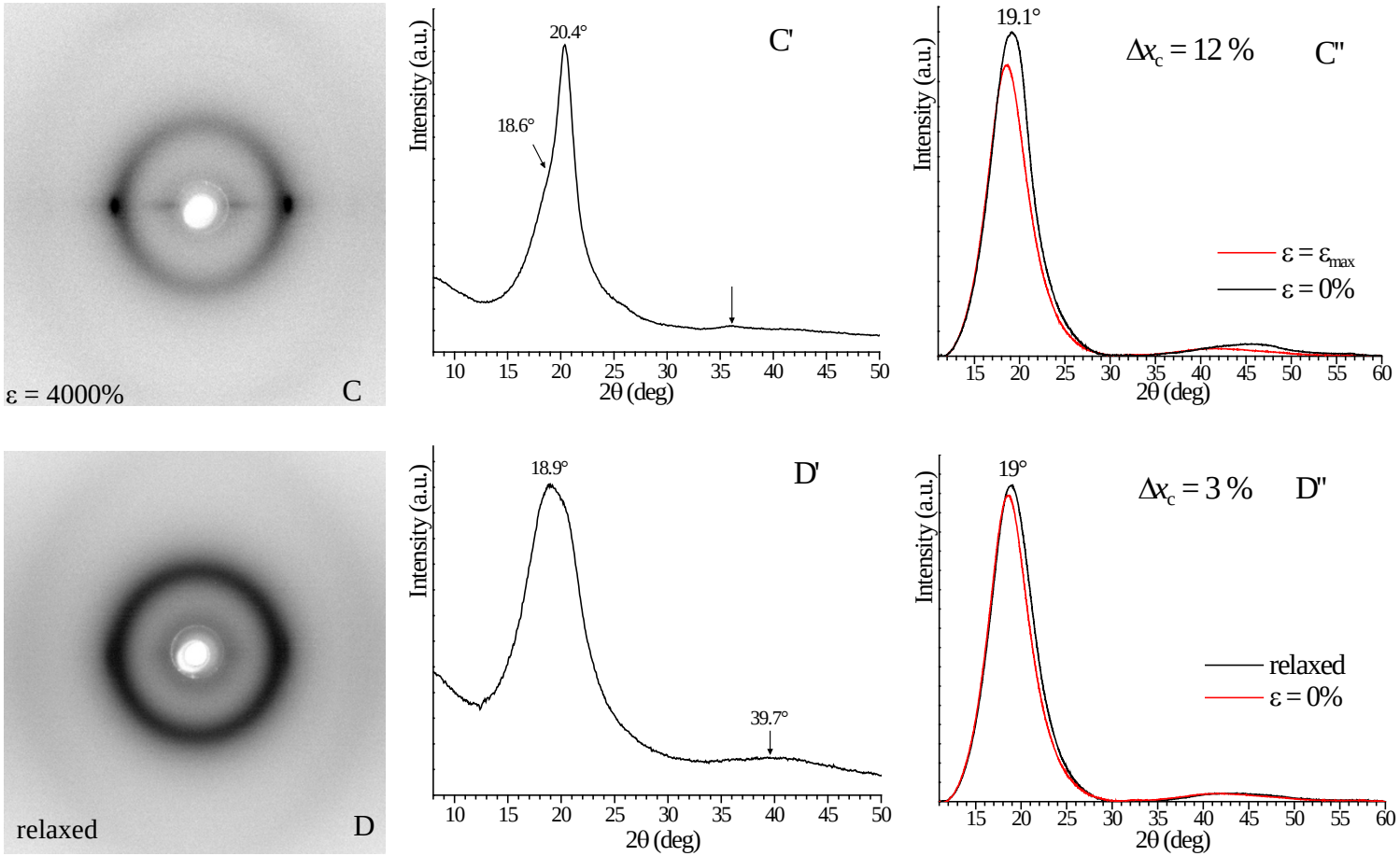

Figure 2.63. *X-ray fiber diffraction patterns (A-D) of sample K6260Q (67 wt% of ethylene) and corresponding equatorial (A'-D') and integrated (A''-D'') profiles recorded at ε = 0% (A,A'), ε = 500% (B,B'), ε = 4000% (C,C') and after releasing the tension (D, D').*

K8570C, 66 wt% of ethylene

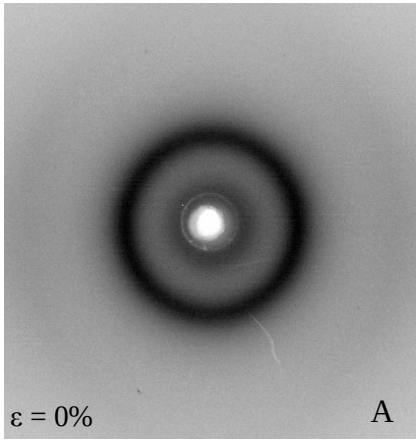

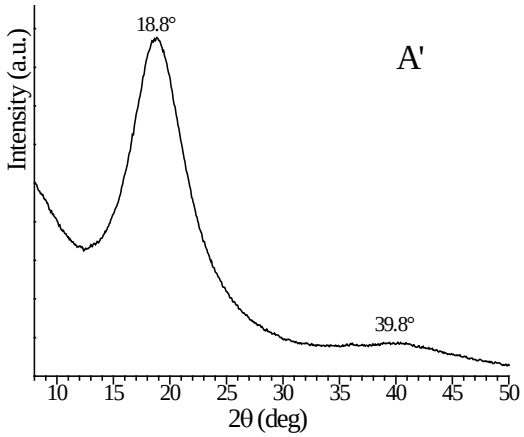

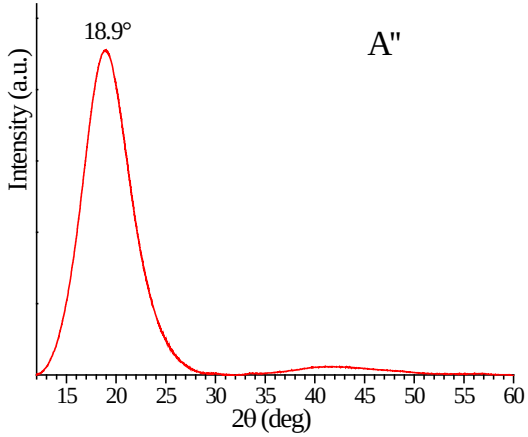

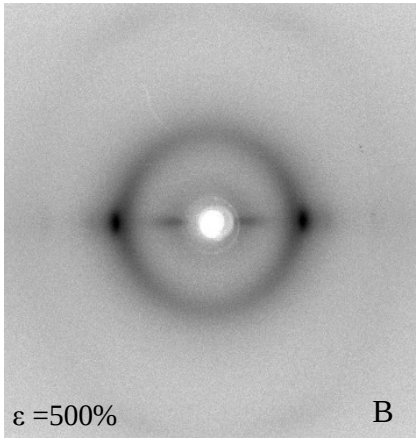

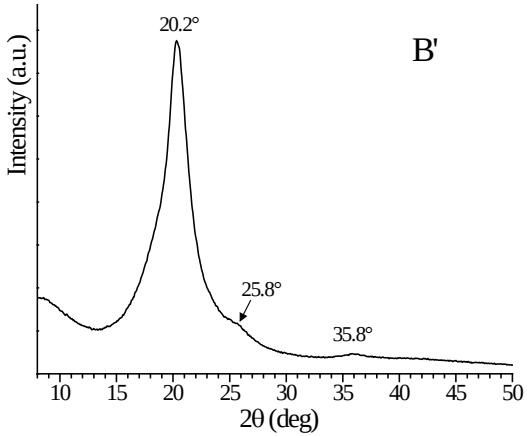

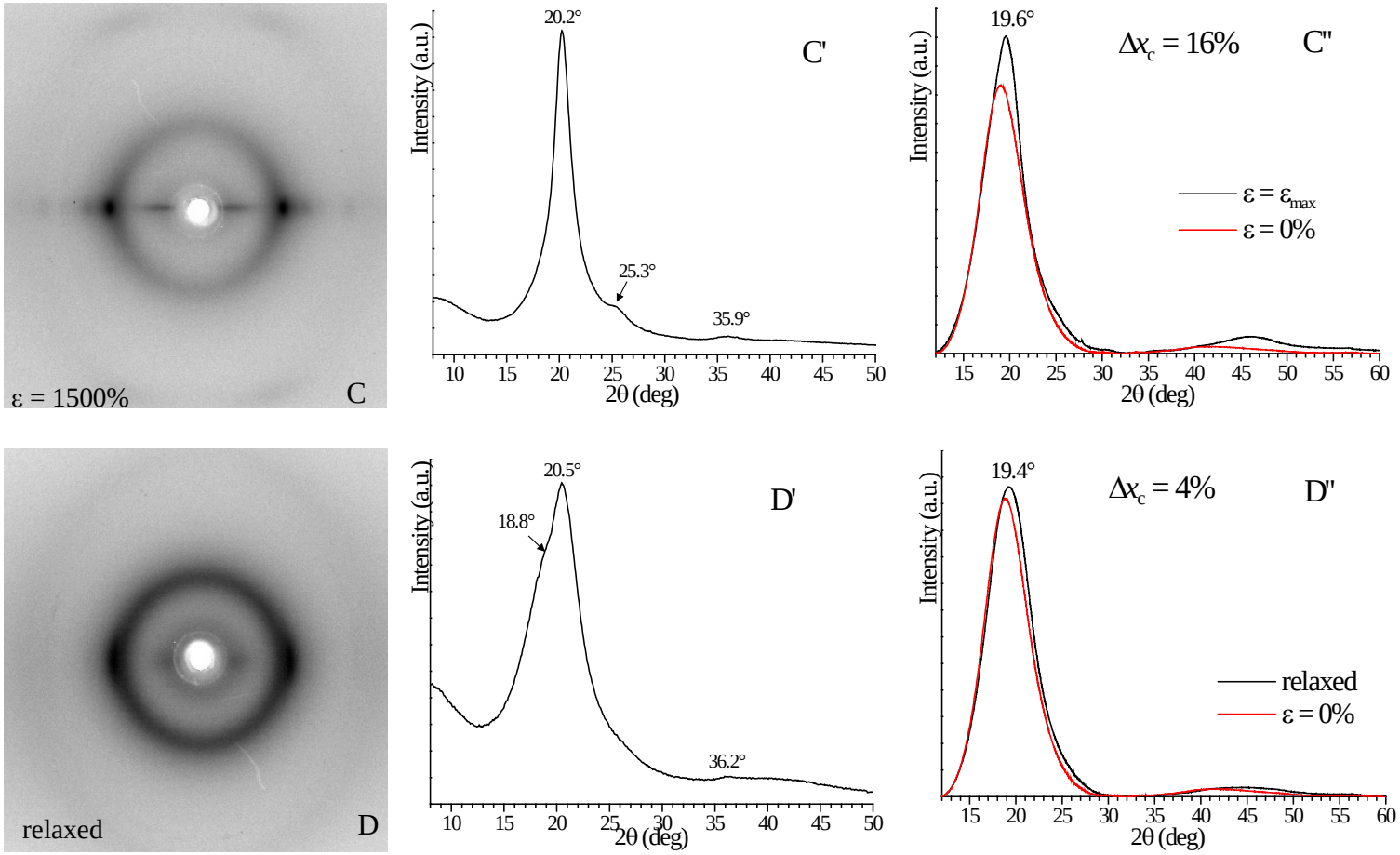

Figure 2.64. *X-ray fiber diffraction patterns (A-D) of sample K8570C (66 wt% of ethylene) and corresponding equatorial (A'-D') and integrated (A''-D'') profiles recorded at ε = 0% (A,A'), ε = 500% (B,B'), ε = 1500% (C,C') and after releasing the tension (D, D').*

K5470C, 66 wt% of ethylene

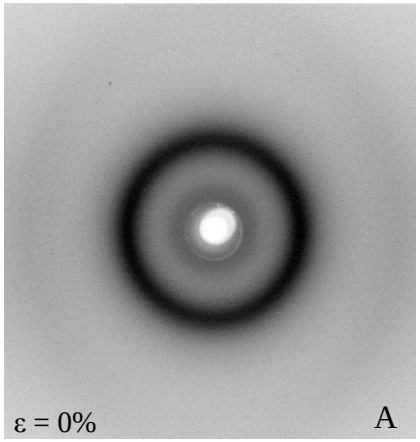

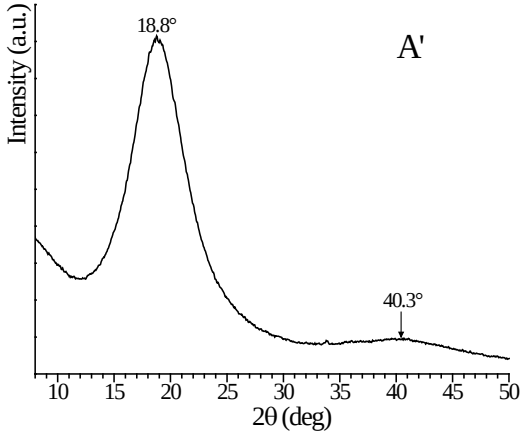

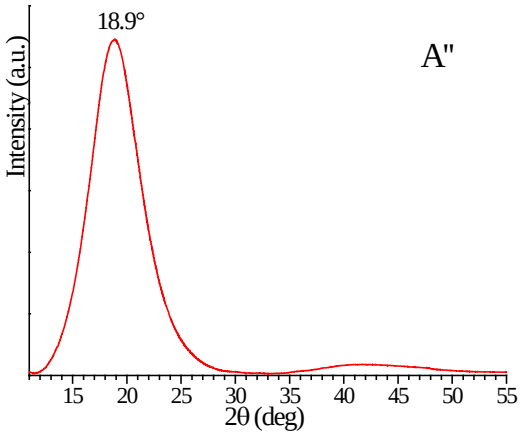

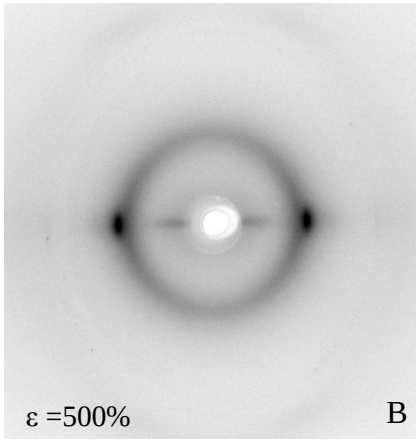

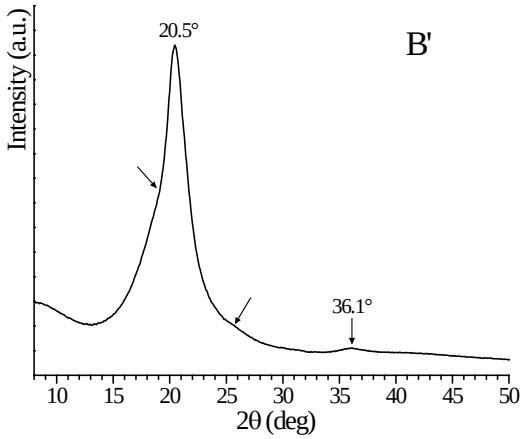

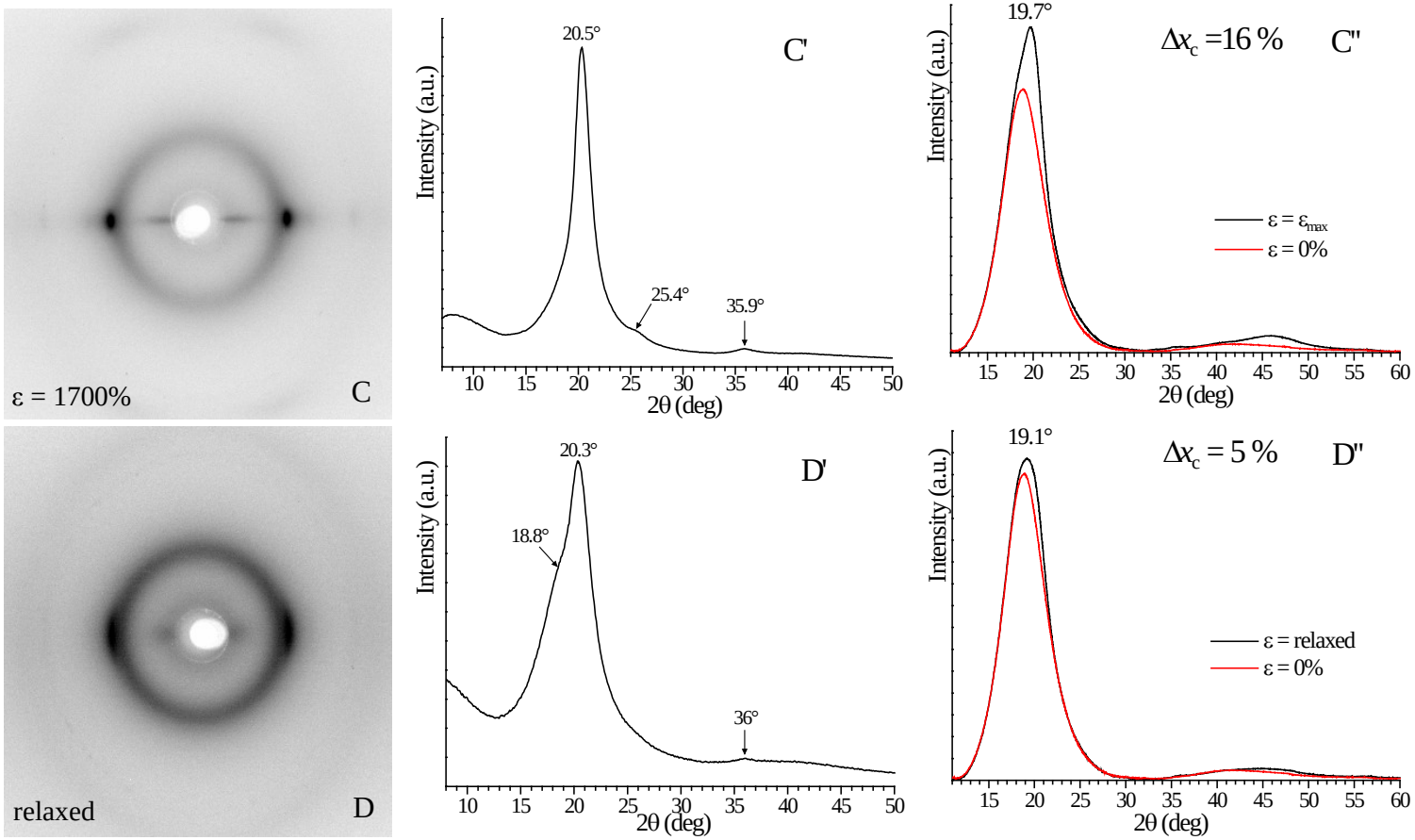

Figure 2.65. *X-ray fiber diffraction patterns (A-D) of sample K5470C (66 wt% of ethylene) and corresponding equatorial (A'-D') and integrated (A''-D'') profiles recorded at ε = 0% (A,A'), ε = 500% (B,B'), ε = 1700% (C,C') and after releasing the tension (D, D').*

K6160D, 64 wt% of ethylene

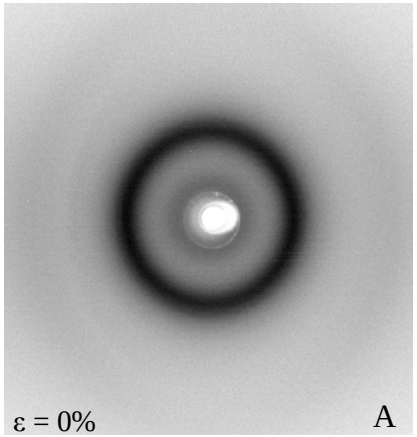

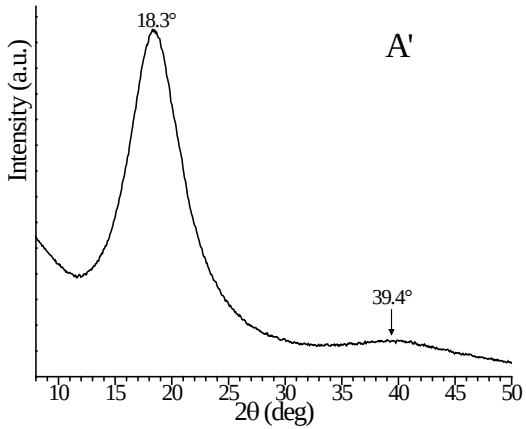

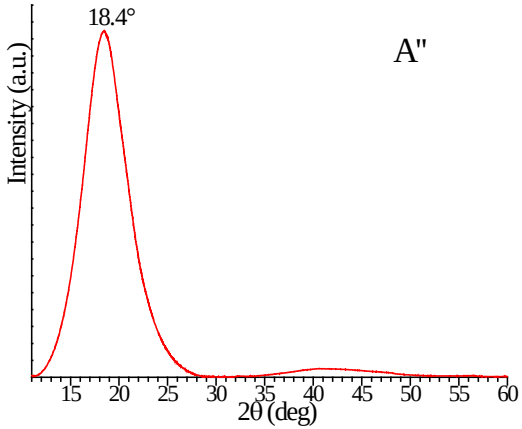

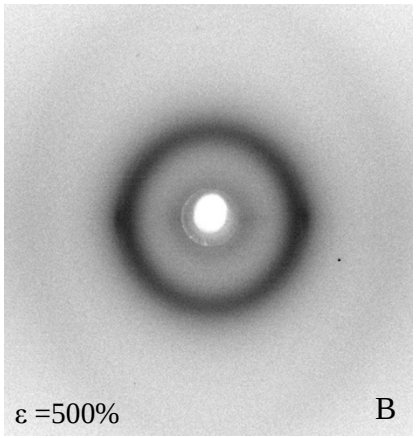

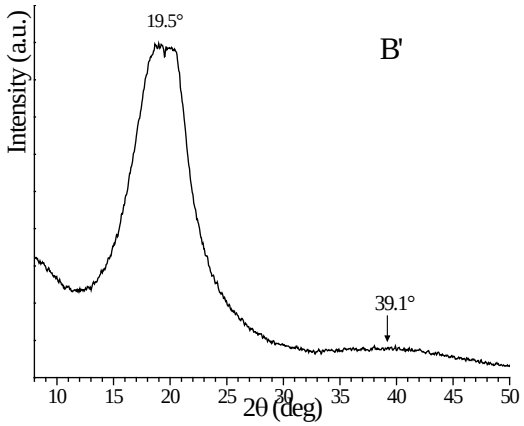

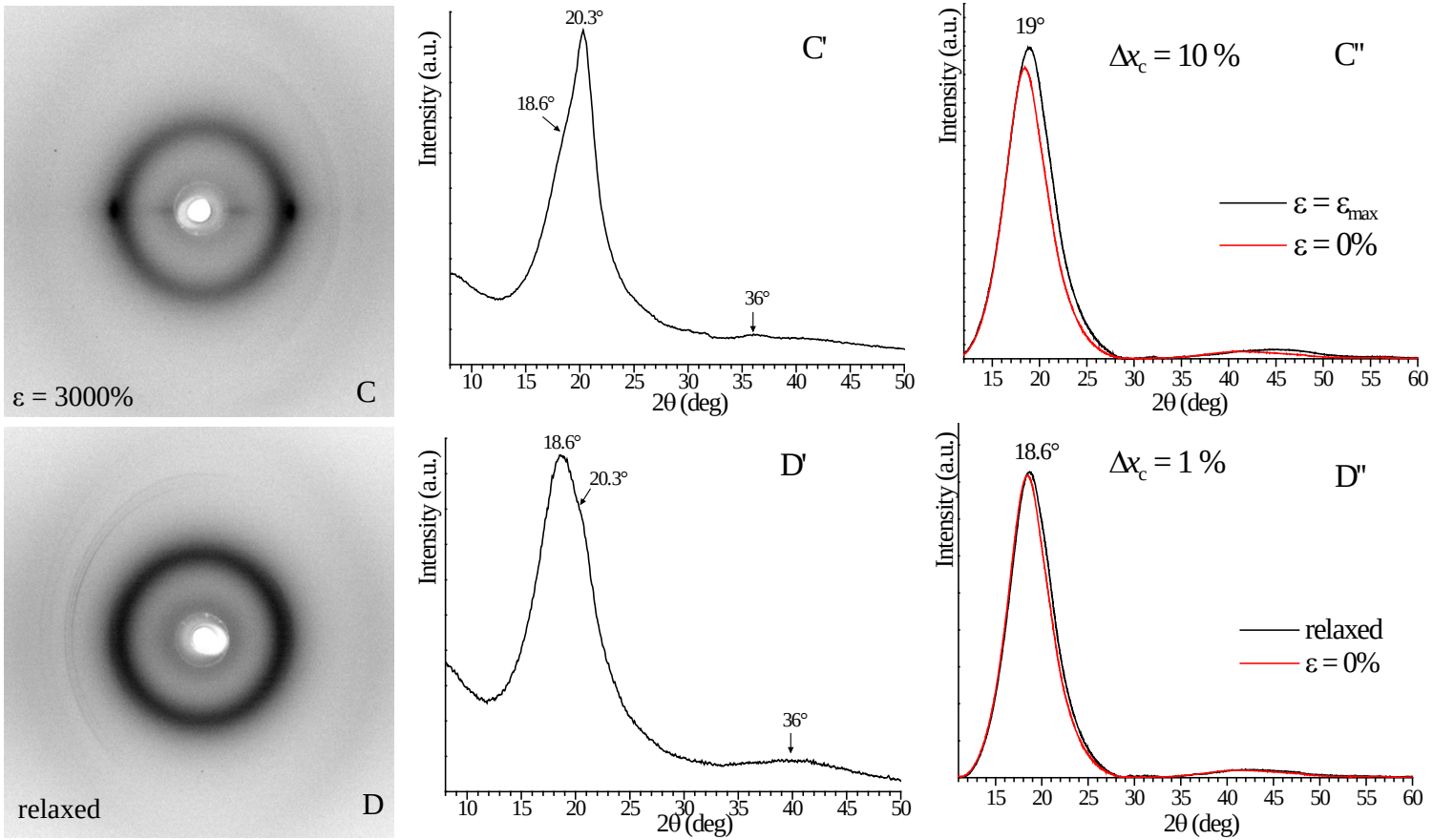

Figure 2.66. *X-ray fiber diffraction patterns (A-D) of sample K6160D (64 wt% of ethylene) and corresponding equatorial (A'-D') and integrated (A''-D'') profiles recorded at ε = 0% (A,A'), ε = 500% (B,B'), ε = 3000% (C,C') and after releasing the tension (D, D').*

A comparison of WAXS powder profiles recorded on compression moulded films of all samples (Figures 2.32A and 2.48A,B) with X-ray diffraction patterns and the corresponding equatorial and integrated profiles recorded before stretching (ε=0%) (Figures 2.58-2.66A,A',A'') may help to individuate the real structure existing at room temperature in the most crystalline samples. In fact, the average position of the maximum in the diffraction profile is at values of $2\theta \approx 19°$ in the most crystalline samples with the highest ethylene content (78-70 wt%) belonging to the first set. Then, the position of the maximum decreases up to $2\theta \approx 18.5°$ in less crystalline samples of the second set (ethylene content in the range 67-64 wt%) and a further decrease up to $2\theta \approx 18°$ is observed in the really amorphous samples belonging to the third set (ethylene content in the range 52-44 wt%). This might confirm that the broad halo observed in all WAXS profiles at room temperatures and in that of the unstretched state of samples of the first and second sets does not correspond to a real amorphous halo but include the contributions of an amorphous phase and of a crystalline disordered phase (the mesomorphic hexagonal form of PE). Therefore, only the WAXS profiles of the samples with the lowest ethylene content (52-44 wt%) correspond to the profiles of the real amorphous phase. Further indication may come from the comparison of WAXS profiles of samples K8570C and K5470C (Figures 2.64 and 2.65) with those of the samples K6260Q and K6160D (Figures 2.63 and 2.66): the position of the diffraction peak of the samples K8570C and K5470C with 66 wt% of ethylene (Figures 2.64 and 2.65) is slightly shifted to values of 2θ comparable with the values observed for the peak positions of the samples with higher ethylene concentration (78-70 wt%) (Figures 2.58-2.62), which are the most crystalline samples as clearly demonstrated by DSX and SAXS data. These considerations confirm that the parameters Δx_c defined as a ***crystallinity increment*** is really a relative increment of the degree of crystallinity with respect to the undeformed sample and does not represent an absolute value of crystallinity.

The values of the crystallinity increment Δx_c for all samples in the stretched and relaxed state are reported in Table 2.11 and in Figures 2.67 as a function of ethylene content and total concentration of comonomeric units. Δx_c in both stretched and unstretched state decreases with decreasing ethylene content and increasing total concentration of comonomeric units. This also indicates that the presence of the diene does not influence the SIC.

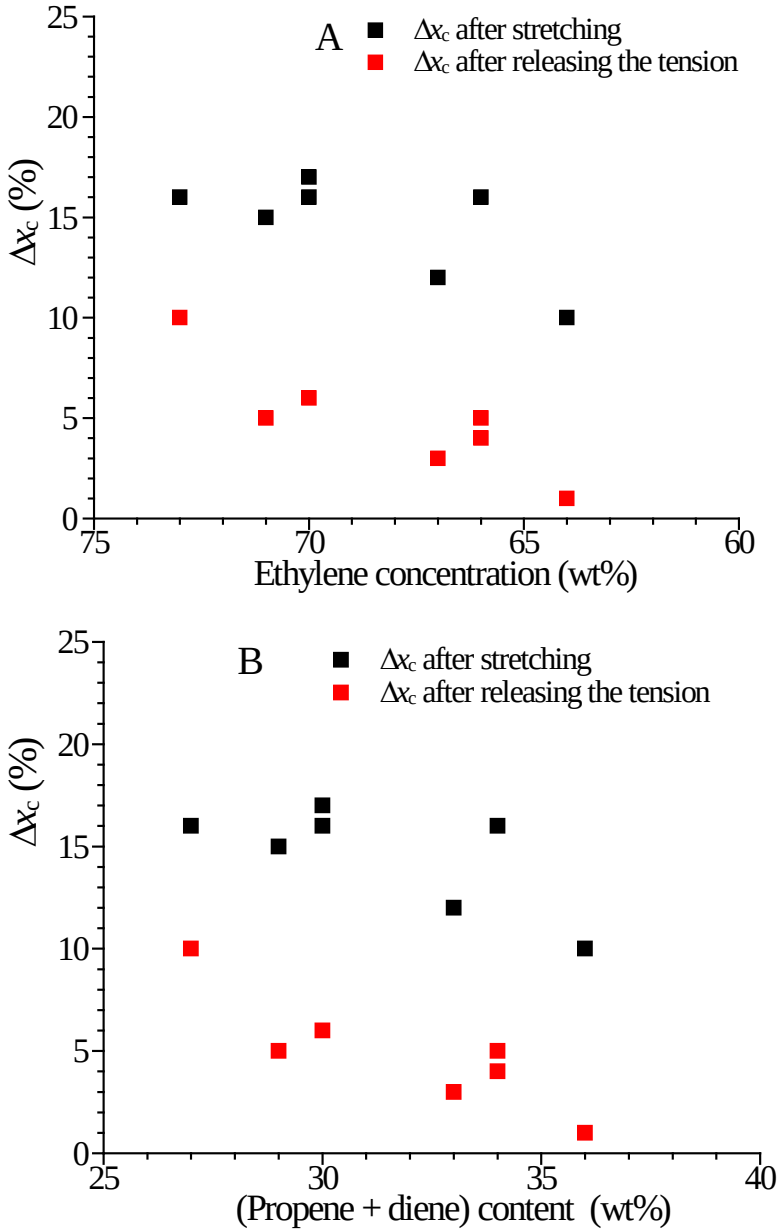

Figure 2.67. *Values of crystallinity increment Δx_c evaluated after stretching and after releasing the tension reported as a function of ethylene (A) and total concentration of comonomeric units (B).*

***Table 2.11**.Ethylene content (wt%), diene content (wt%), total concentration of comonomeric units (propene + diene) (wt%) and values of the crystallinty increment Δxc (%) evaluated in the stretched and relaxed state of samples of EPM and EPDM.*

Sample	Ethylene content (wt%)	Diene content (wt%)	Total concentration of comonomeric units (wt%)	Δx_c after stretching	Δx_c after relaxing
K2070P	73	/	27	16	10
K5170P	71	1.5	29	15	5
K5470P	70	4.6	30	17	6
K5470NT	70	4.6	30	16	6
K6260Q	67	2.8	33	12	3
K8570C	66	5	34	16	4
K5470C	66	4.6	34	16	5
K6160D	64	1.2	36	10	1

2.6.7 Stress-relaxation

Stress-relaxation experiments have been performed on specimens cut from fresh compression moulded films. The samples have been quickly deformed up to the constant deformations of 50% and 600% and the values of the stress necessary to maintain the constant deformation have been recorded for 7250s. The specimens have thickness of 0.70 mm, width of 5 mm and lengths of 15 mm for the test at 50% deformation, and 10 mm for the test at 600% deformation. Samples have been stretched up to the constant deformation ε_{cost} of 50% and 600% at deformation rates of 450 mm/min and 720 mm/min, respectively. The stress necessary to maintain the constant deformation decreases over time due to the relaxation of the sample. The relative drop of the applied load has been evaluated for all samples by using the equation:

$$\frac{\sigma_{in}-\sigma_{fin}}{\sigma_{in}} \times 100 = \frac{\Delta\sigma}{\sigma_{in}} \times 100 \qquad (1)$$

where σ_{in} and σ_{fin} are the stress measured at the beginning and at the end (after 7250s) of the experiment, respectively.

Stress-relaxation curves have been modeled in term of the Maxwell model (an elastic spring and dash-pot in series), for which the viscoelastic behavior of a material after application of a deformation is represented as a decay of the stress over the time and described with a single relaxation time τ:

$$\sigma(t) = \sigma_0 \exp\left(-\frac{t}{\tau}\right) \qquad (2)$$

with σ_0 the stress applied at t = 0 s and τ the relaxation time. According to this model upon application of a constant deformation the initial stress σ_o decays over time with exponential law. The relaxation time is the time needed for the initial stress σ_o to decrease by 1/e, that is, 37% of σ_o; the shorter the relaxation time, the more rapid the stress relaxation.

More realistic material responses can be modeled using models composed of more Maxwell elements in series. For the analyzed samples of EPM and EPDM the stress-relaxation experiments have been modeled with two relaxation times τ_1 and τ_2 corresponding to two Maxell models connected in series, according to the equation:

$$\sigma(t) = \sigma_{01}\exp\left(-\frac{t}{\tau_1}\right) + \sigma_{02}\exp\left(-\frac{t}{\tau_2}\right) \quad (3)$$

Equation (3) can be rearranged in the form:

$$\sigma(t) = \sigma_0\left(\varphi_1\exp\left(-\frac{t}{\tau_1}\right) + \varphi_2\exp\left(-\frac{t}{\tau_2}\right)\right) \quad (4)$$

with $\sigma_0 = \sigma_{01} + \sigma_{02}$ and $\varphi_1 = \frac{\sigma_{01}}{\sigma_0}$; $\varphi_2 = \frac{\sigma_{02}}{\sigma_0}$; $\varphi_1 + \varphi_2 = 1$

In other words the parameters φ_1 e φ_2 represent the relative weight of the two hypothesized relaxation mechanisms to the experimental phenomenon of stress-relaxation of our samples

The stress-relaxation curves of samples of EPM and EPDM with ethylene concentrations in the range 78-70 wt%, obtained imposing the constant deformation of ε_{cost}= 50% and 600%, are reported in Figures 2.68-2.72, in linear (Figures 2.68A,B-2.72A,B) and logarithmic Figures 2.68A',B'-2.72A'B') scales. The experimental data have been fitted with the equation (4) (blue curves). The experimental values of stress and of the drop of the stress and the values of the parameters of equation 4 that give the best fit are reported in the Tables 2.12-2.13.

With the exception of sample EPM, in all samples the drop of stress is unexpectedly higher in experiments performed at ε_{cost}= 50% than in experiments performed at ε_{cost}= 600% (Figure 2.69-2-72). This is due to the occurrence of stress induced crystallization (SIC) at the high deformation of 600%. In the previous section it has been demonstrated that SIC occurs already at ε=500%, therefore when samples are stretched up to ε_{cost}= 600% crystals formed upon stretching act as physical knots in the elastomeric network preventing the viscous flow and limiting the drop of stress in the stress-relaxation. This is also confirmed by the results obtained on the sample EPM (78 wt% of ethylene). In this case, as expected, the load drop is higher in the experiments performed at ε_{cost}= 600% than in those performed at ε_{cost}= 50% (Figure 2.68). The reason is that in this already crystalline sample, as discussed in the previous section, further crystallization under stretching (SIC) does not occur. This sample is already crystalline in the undeformed state and stretching produces only a better orientation of crystals in pseudohexagonal form of PE already present before stretching.

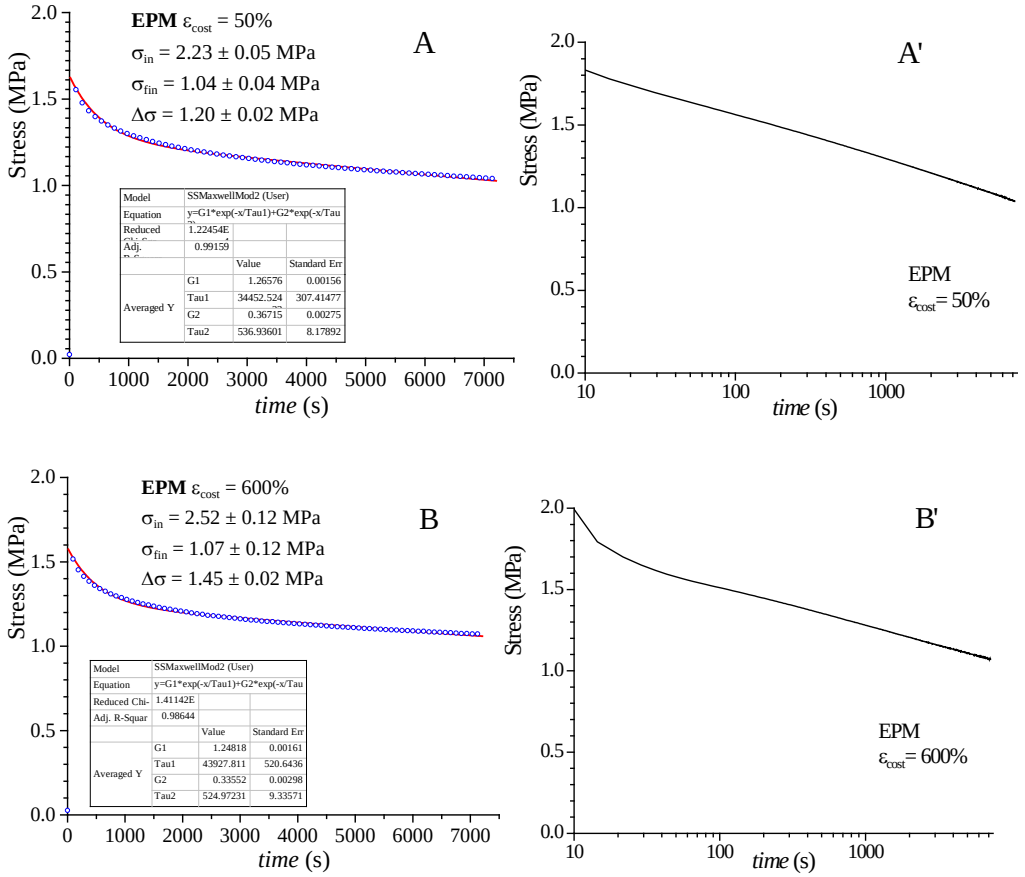

Model	SSMaxwellMod2 (User)		
Equation	y=G1*exp(-x/Tau1)+G2*exp(-x/Tau		
Reduced Chi-Sqr	1.22454E		
Adj. R-Squar	0.99159		
		Value	Standard Err
Averaged Y	G1	1.26576	0.00156
	Tau1	34452.524	307.41477
	G2	0.36715	0.00275
	Tau2	536.93601	8.17892

Model	SSMaxwellMod2 (User)		
Equation	y=G1*exp(-x/Tau1)+G2*exp(-x/Tau		
Reduced Chi-	1.41142E		
Adj. R-Squar	0.98644		
		Value	Standard Err
Averaged Y	G1	1.24818	0.00161
	Tau1	43927.811	520.6436
	G2	0.33552	0.00298
	Tau2	524.97231	9.33571

Figure 2.68. *Stress relaxation curves of sample EPM (78 wt% of ethylene) obtained at ε_{cost}= 50% (A,A') and 600% (B,B') as a function of time in linear (A,B) and in logarithmic (A',B') scales. The fitting curve according with the equation 4 is also reported (blue curve in A,B).*

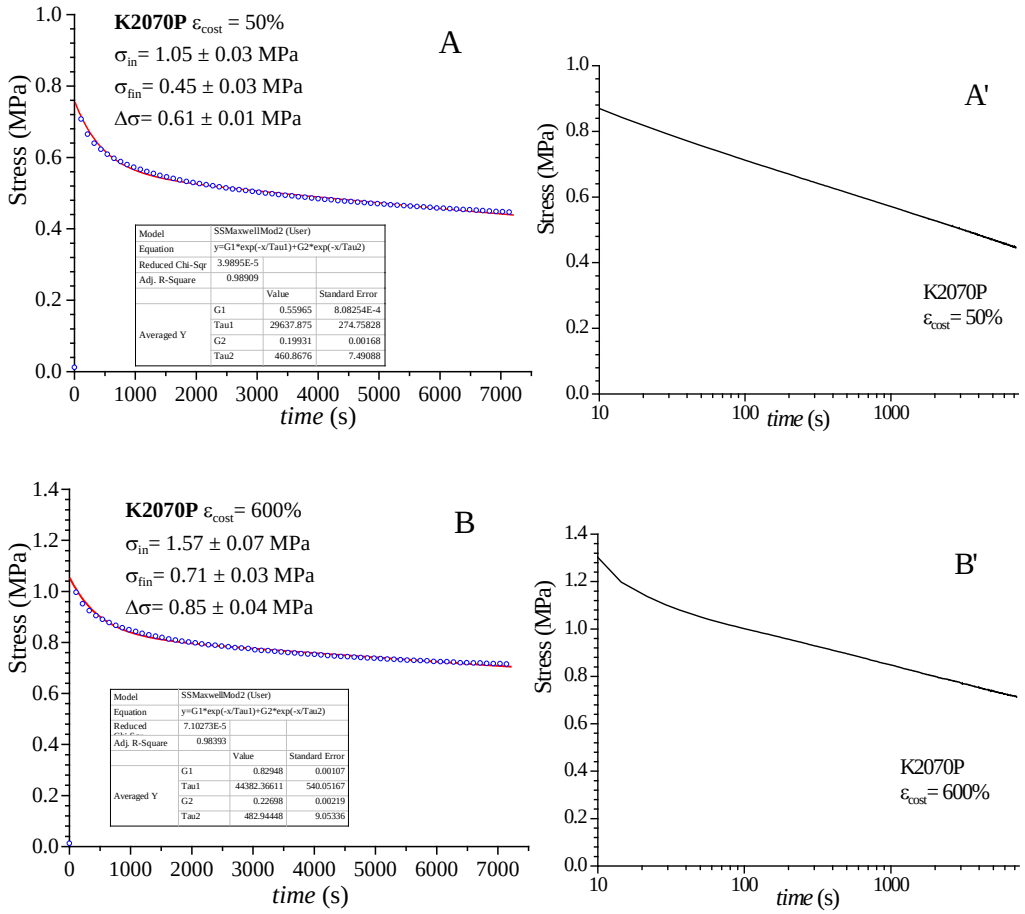

Figure 2.69. *Stress relaxation curves of sample K2070P (73 wt% of ethylene) obtained at ε_{cost}= 50% (A,A') and 600% (B,B') as a function of time in linear (A,B) and in logarithmic (A',B') scales. The fitting curve according with the equation 4 is also reported (blue curve in A,B).*

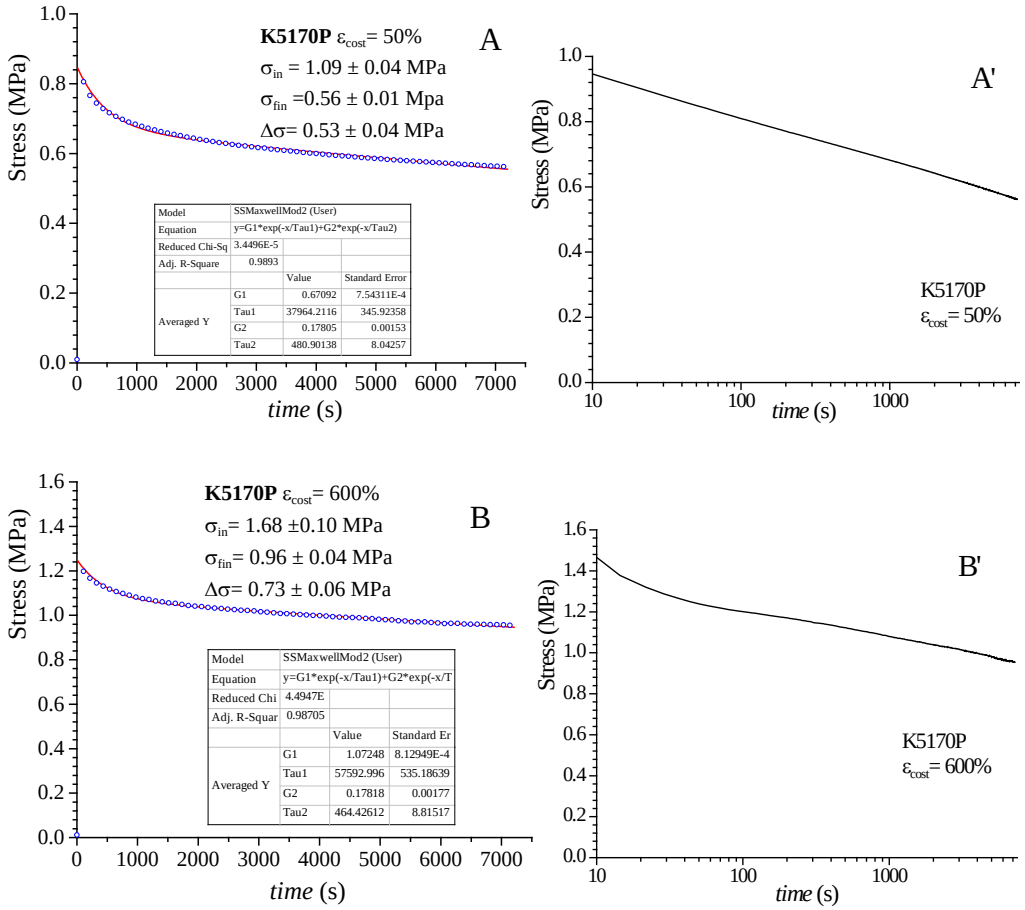

Model	SSMaxwellMod2 (User)		
Equation	y=G1*exp(-x/Tau1)+G2*exp(-x/Tau2)		
Reduced Chi-Sq	3.4496E-5		
Adj. R-Square	0.9893		
		Value	Standard Error
Averaged Y	G1	0.67092	7.54311E-4
	Tau1	37964.2116	345.92358
	G2	0.17805	0.00153
	Tau2	480.90138	8.04257

Model	SSMaxwellMod2 (User)		
Equation	y=G1*exp(-x/Tau1)+G2*exp(-x/T		
Reduced Chi	4.4947E		
Adj. R-Squar	0.98705		
		Value	Standard Er
Averaged Y	G1	1.07248	8.12949E-4
	Tau1	57592.996	535.18639
	G2	0.17818	0.00177
	Tau2	464.42612	8.81517

***Figure 2.70**. Stress relaxation curves of sample K5170P (71 wt% of ethylene) obtained at ε_{cost}= 50% (A,A') and 600% (B,B') as a function of time in linear (A,B) and in logarithmic (A',B') scales. The fitting curve according with the equation 4 is also reported (blue curve in A,B).*

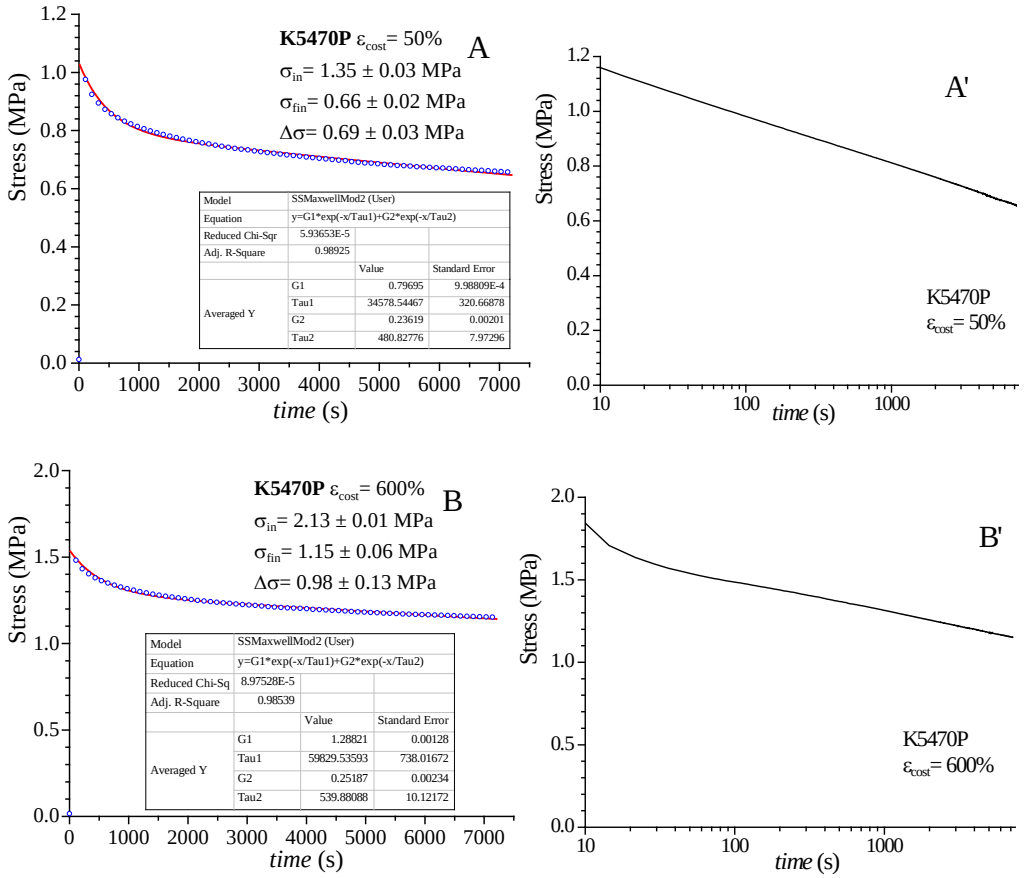

Figure 2.71. *Stress relaxation curves of sample K5470P (70 wt% of ethylene) obtained at ε_{cost}= 50% (A,A') and 600% (B,B') as a function of time in linear (A,B) and in logarithmic (A',B') scales. The fitting curve according with the equation 4 is also reported (blue curve in A,B).*

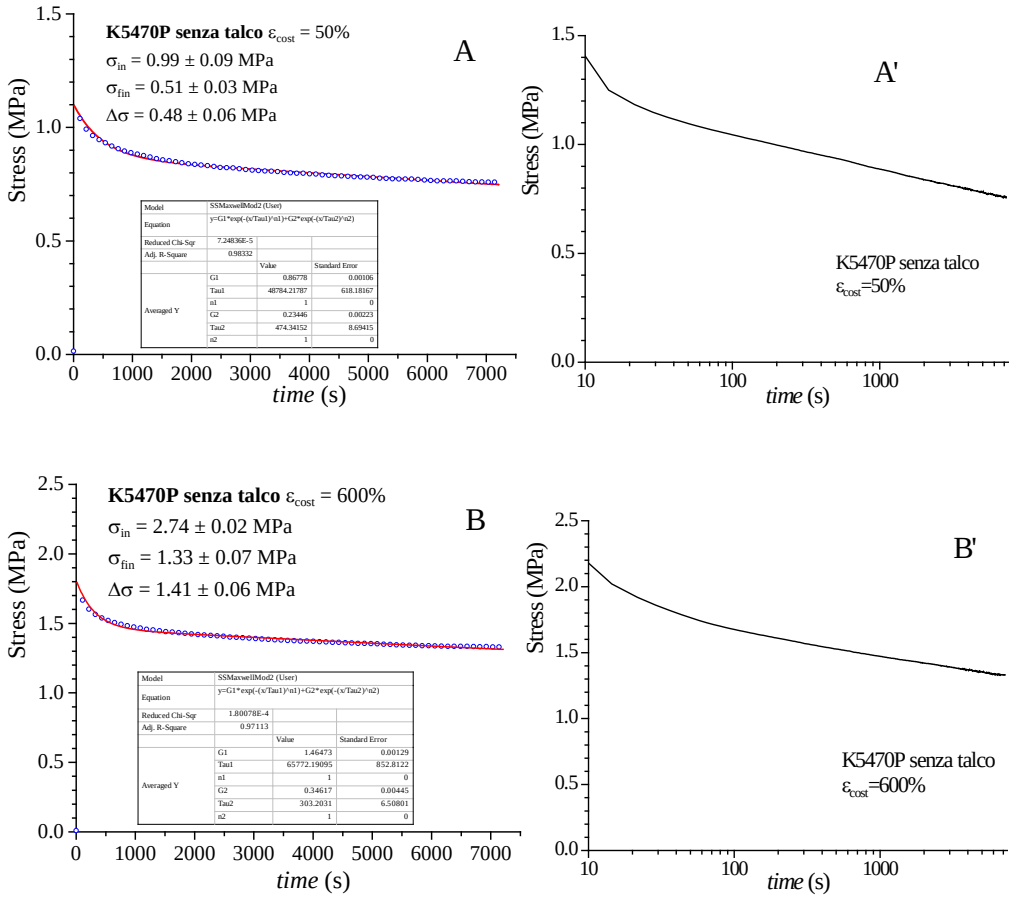

***Figure 2.72**. Stress relaxation curves of sample K5470NT (70 wt% of ethylene) obtained at ε_{cost}= 50% (A,A') and 600% (B,B') as a function of time in linear (A,B) and logarithmic (A',B') scales. The fitting curve according with the equation 4 is also reported (blue curve in A,B).*

Figures 2.73-2.76 report stress-relaxation curves of samples with ethylene concentration in the range 67-64 wt%. Also for these samples the drop of stress $\Delta\sigma/\sigma_{in}$ is higher in experiments performed at ε_{cost}= 50% than in experiments performed at ε_{cost}= 600%. In particular, the loss of stress at 50% deformation is very high for samples K6260Q with 67% of ethylene and K6160D with 64% of ethylene (95% and 85% respectively). These samples, however, show much lower loss of stress of nearly 60% at the higher deformation of 600%. The samples K8570C and K5470C show value of load drop similar to the samples of the first set with higher ethylene content even in measurements at ε_{cost}= 50%.

This different behavior depends on the occurrence of SIC and different amount of SIC. In samples K8570C and K5470C the amount of SIC is higher than in samples K6260Q and K6160D, therefore they show similar properties

of samples of the first set (78-70 wt% of ethylene). However, a deformation of 600% is enough to trigger SIC also in sample K6260Q and K6160D. The results is a lower drop of stress observed in experiments performed at ε_{cost}= 600% also in these two samples, as in the other samples of the first and second sets.

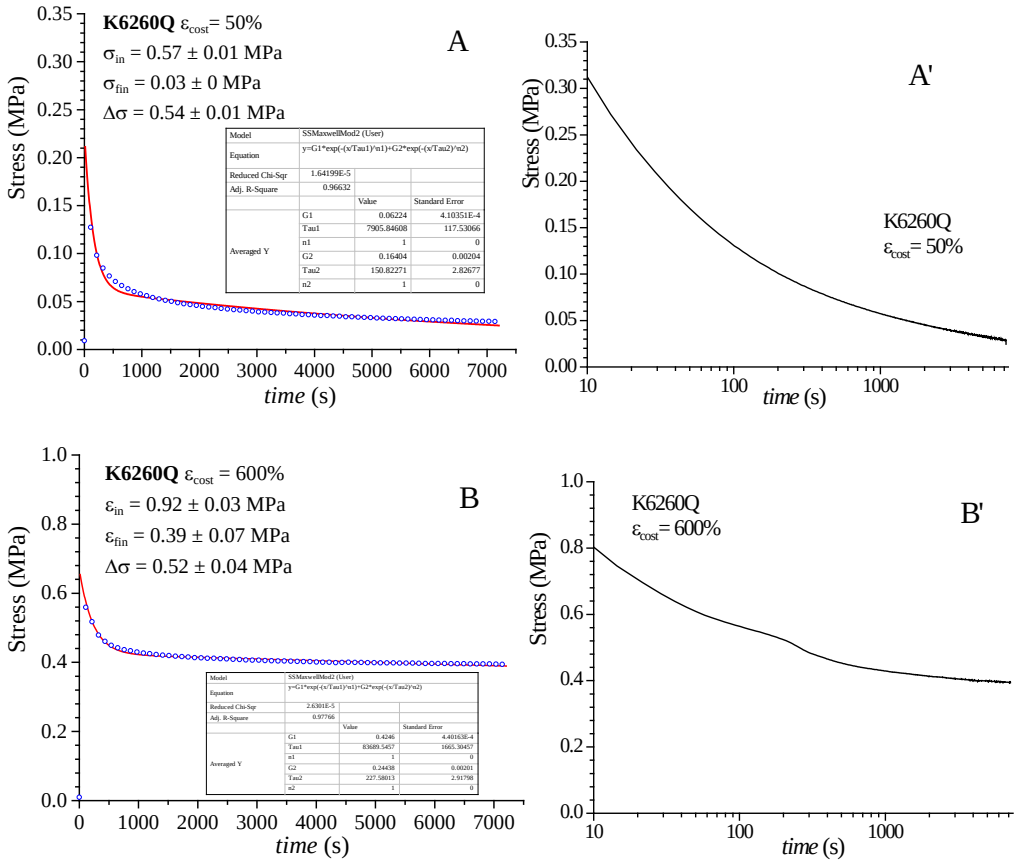

Figure 2.73*. Stress relaxation curves of sample K6260Q (67 wt% of ethylene) obtained at ε_{cost}= 50% (A,A') and 600% (B,B') as a function of time in linear (A,B) and in logarithmic (A',B') scales. The fitting curve according with the equation 4 is also reported (blue curve in A,B).*

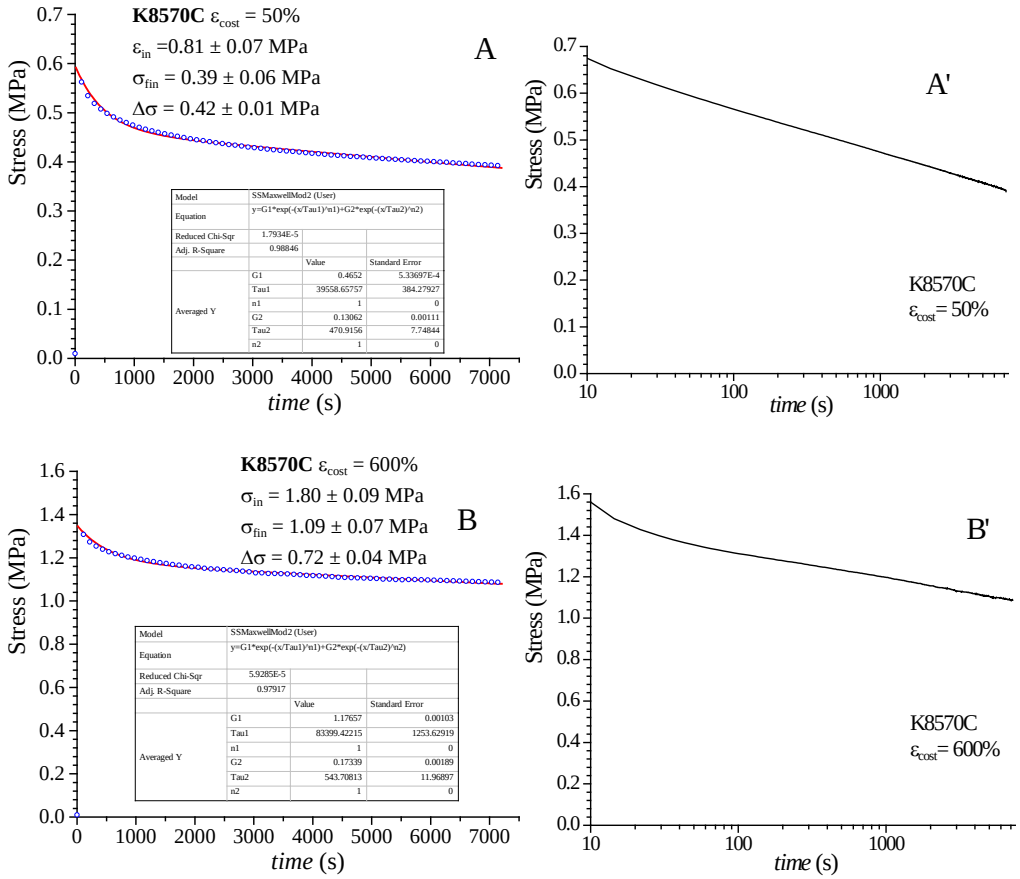

***Figure 2.74**. Stress relaxation curves of sample K8570C (66 wt% of ethylene) obtained at ε_{cost}= 50% (A,A') and 600% (B,B') as a function of time in linear (A,B) and in logarithmic (A',B') scales. The fitting curve according with the equation 4 is also reported (blue curve in A,B).*

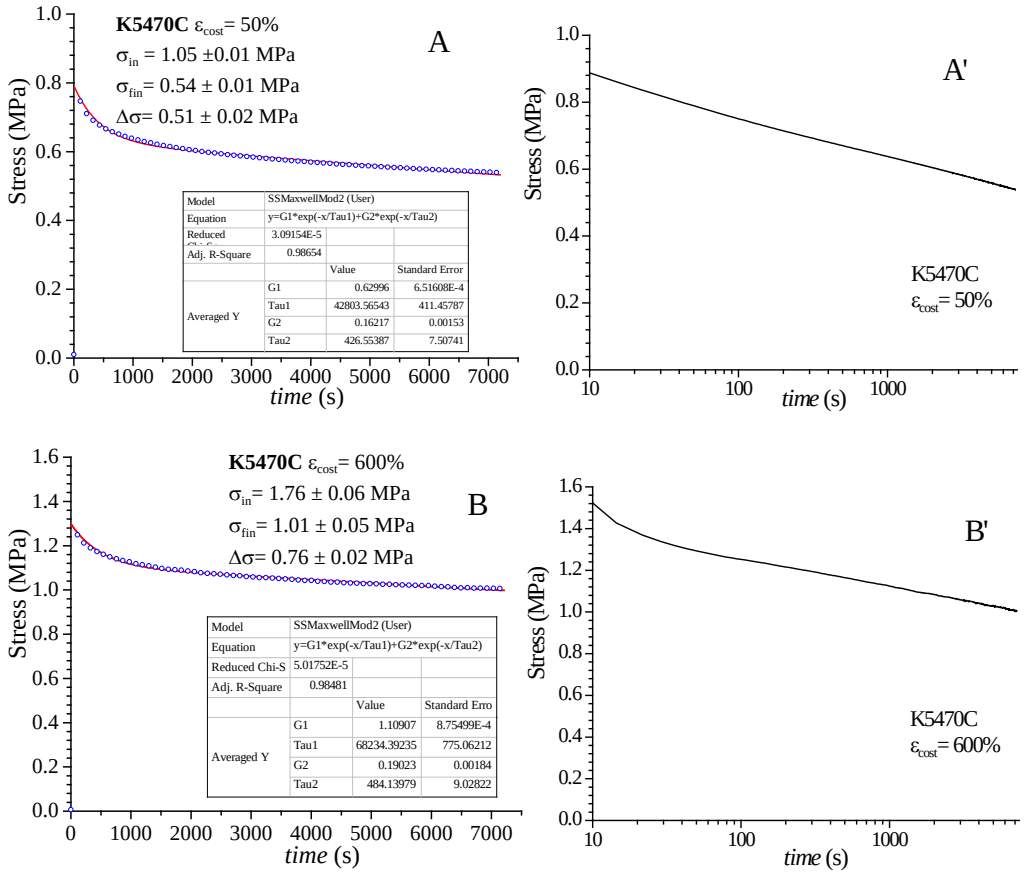

***Figure 2.75**. Stress relaxation curves of sample K5470C (66 wt% of ethylene) obtained at ε_{cost}= 50% (A,A') and 600% (B,B') as a function of time in linear (A,B) and in logarithmic (A',B') scales. The fitting curve according with the equation 4 is also reported (blue curve in A,B).*

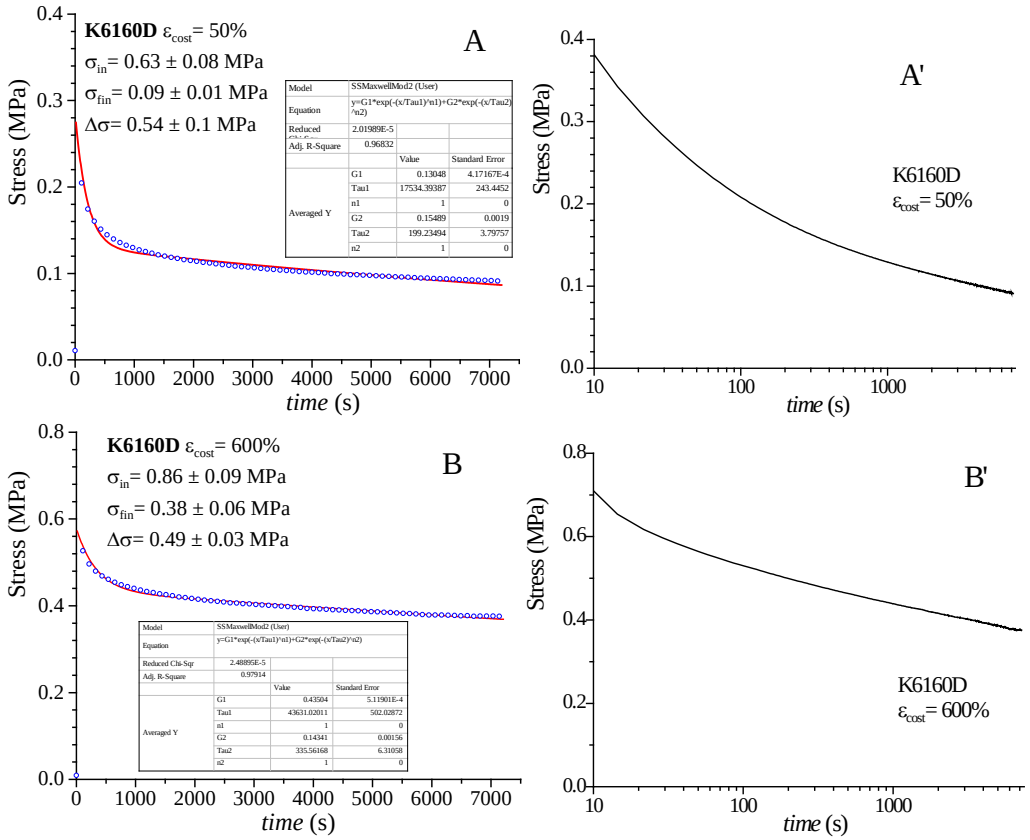

Figure 2.76. *Stress relaxation curves of sample K6160D (64 wt% of ethylene) obtained at ε_{cost}= 50% (A,A') and 600% (B,B') as a function of time in linear (A,B) and in logarithmic (A',B') scales. The fitting curve according with the equation 4 is also reported (blue curve in A,B).*

The stress-relaxation curves of samples with ethylene concentration in the range 52-44 wt% recorded only at ε_{cost}= 50% are reported in Figures 2.77-2.79. The measurements have been performed only at low deformation because at high deformation these samples show viscous flow. The loss of stress is very high and close to 100% in samples K4450 and K3050 while a lower value of 85% is observed in sample K9950C probably due to the higher molecular mass of this sample.

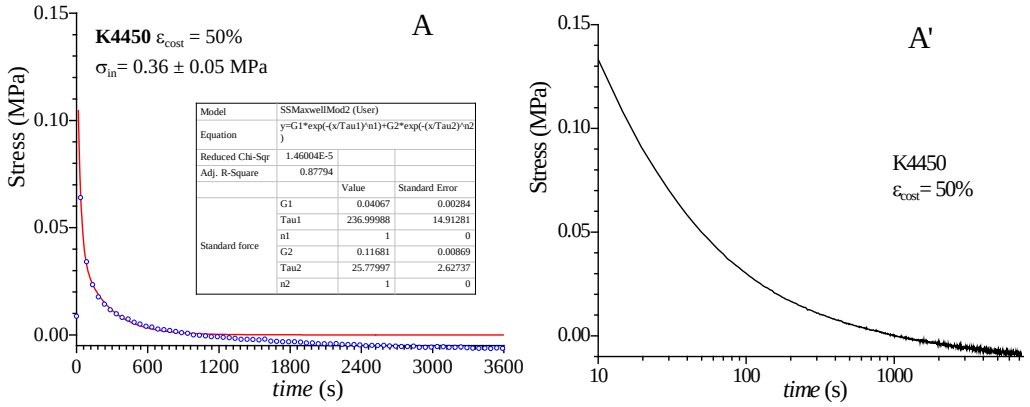

Figure 2.77. *Stress relaxation curves of sample K4450 (52 wt% of ethylene) obtained at ε_{cost}= 50% (A,A') as a function of time in linear (A) and in logarithmic (A') scales. The fitting curve according with the equation 4 is also reported (blue curve in A).*

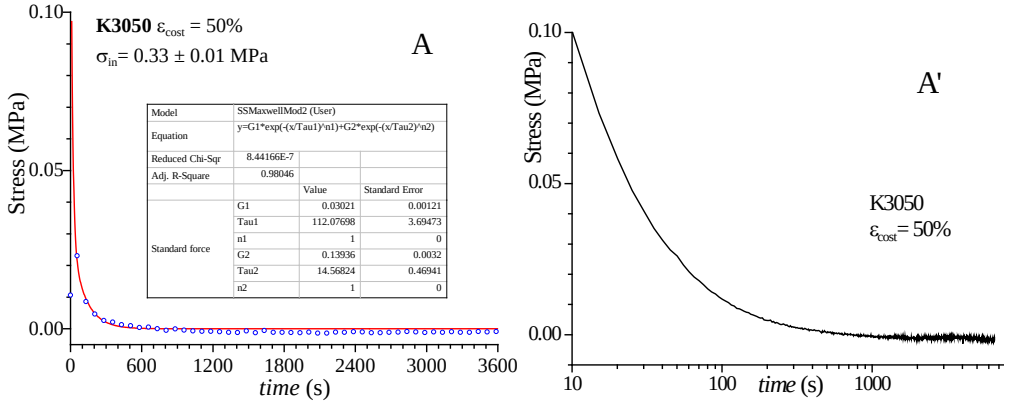

Figure 2.78. *Stress relaxation curves of sample K3050 (49 wt% of ethylene) obtained at ε_{cost}= 50% (A,A') as a function of time in linear (A) and in logarithmic (A') scales. The fitting curve according with the equation 4 is also reported (blue curve in A).*

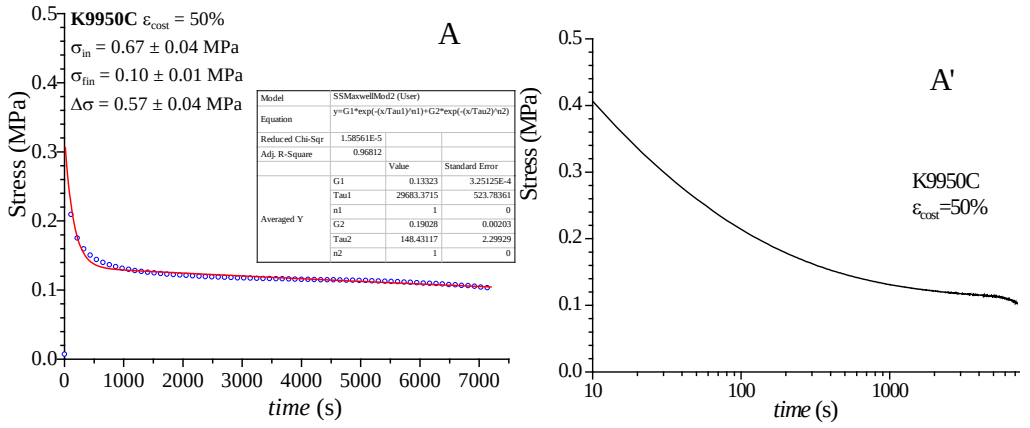

Figure 2.79. *Stress relaxation curves of sample K9950C (44 wt% of ethylene) obtained at ε_{cost}= 50% (A,A') as a function of time in linear (A) and in logarithmic (A') scales. The fitting curve according with the equation 4 is also reported (blue curve in A).*

It is worth noting that the experimental data are well fitted with equation (4) (blue curve). This means that the stress-relaxation of these samples can be easily interpreted with a model consisting of two Maxwell models connected in series. The stress decays over the time with two relaxation times τ_1 and τ_2 and, therefore, the whole relaxation is a results of the relaxation of two components that decay with different times and mechanisms. The values of the parameters evaluated from the stress-relaxation experiments of all samples at ε_{cost}= 50% and 600% (initial and final values of stress and the relative drop of the stress) are reported in Table 2.12 and in Figure 2.80. The values of parameters of equation 4 that fit the experimental data (relaxation times τ_1 and τ_2, initial stress σ_o and weights of the two relaxation mechanisms φ_1 and φ_2) are reported in Table 2.13 and Figure 2.81.

From this analysis it is possible to conclude that in semicrystalline samples of the first and second sets, with ethylene concentration in the range 78-64 wt%, at both deformations, the first component relaxes more slowly, in times of the order of magnitude of $\tau_1 \approx 10^4$ s (Figure 2.81B), with a weight of 80% of the total relaxation (Figure 2.81C), whereas the second component relaxes more rapidly, in time of the order of magnitude of $\tau_2 \approx 10^2$ s (Figure 2.81D), with a weight of 20% of the total relaxation (Figure 2.81C).

The sample K6260Q shows a different behavior because it shows very high load drop at deformation of 50% (Figures 2.73A and 2.80) and values of relaxation times τ_1 and τ_2 much smaller than those of the other samples (Figure 2.81B,D). Moreover, the slower component affects for about the 30% of the load drop in experiments at ε_{cost}= 50%, while values of the relaxation times similar to those of other samples are observed in measurements at ε_{cost}= 600% (Figure 2.81C). The values of τ_2 are similar for all samples of these sets at both deformations ε_{cost}= 50% and ε_{cost} = 600%, while the longer relaxation times τ_1 evaluated in experiments at ε_{cost} = 600% are twice of those evaluated in experiments at ε_{cost}= 50%.

In the amorphous samples belonging to the third set with ethylene concentration in the range 52-44 wt%, the drop of stress is close to 100% (ε_{cost}= 50%) except in the sample K9950C, and both the relaxation times τ_1 and τ_2 are two order of magnitude lower than those of samples with higher ethylene content (10^1 and 10^2 respectively).

***Table 2.12**.Values of initial stress (σ_{in}), final stress (σ_{fin}), relative drop of stress ($\Delta\sigma/\sigma_{in}$) evaluated form the experiments of stress-relaxation at constant deformations of ε_{cost}= 50% and 600% of EPM and EPDM samples.*

Sample	Ethylene content (wt%)	Diene content (wt%)	σ_{in} (MPa)		σ_{fin} (MPa)		$\Delta\sigma/\sigma_{in}$ (%)	
			ε_{cost}= 50%	ε_{cost}= 600%	ε_{cost}= 50%	ε_{cost}= 600%	ε_{cost}= 50%	ε_{cost}= 600%
EPM	78	0	2.23 ± 0.05	2.52 ± 0.12	1.04 ± 0.04	1.07 ± 0.12	54 ± 2	57 ± 2
K2070P	73	0	1.05 ± 0.03	1.57 ± 0.07	0.45 ± 0.03	0.71 ± 0.03	57 ± 1	54 ± 4
K5170P	71	1.5	1.09 ± 0.04	1.68 ± 0.1	0.56 ± 0.01	0.96 ± 0.04	49 ± 4	43 ± 6
K5470P	70	4.6	1.35 ± 0.03	2.13 ± 0.01	0.66 ± 0.02	1.15 ± 0.06	51 ± 3	46 ± 3
K5470NT	70	4.6	0.99 ± 0.09	2.74 ± 0.02	0.51 ± 0.03	1.33 ± 0.07	48 ± 6	51 ± 6
K6260Q	67	2.8	0.57 ± 0.01	0.92 ± 0.03	0.03	0.39 ± 0.07	95 ± 1	56 ± 4
K8570C	66	5.0	0.81 ± 0.07	1.80 ± 0.09	0.39 ± 0.06	1.09 ± 0.07	52 ± 1	40 ± 4
K5470C	66	4.6	1.05 ± 0.01	1.76 ± 0.06	0.54 ± 0.01	1.01 ± 0.05	48 ± 2	43 ± 2
K6160D	64	1.2	0.63 ± 0.08	0.86 ± 0.09	0.09 ± 0.01	0.38 ± 0.06	86 ± 1	57 ± 3
K4450	52	4.3	0.36 ± 0.05	/	0	/	100	/
K3050	49	0	0.33 ± 0.01	/	0	/	100	/
K9950C	44	9	0.67 ± 0.04	/	0.10 ± 0.01	/	85 ± 4	/

***Table 2.13**. Values of parameters of equation 4 based on the model composed of two Maxell models connected in series that fit the experimental stress-relaxation curves at ε_{cost}= 50% and 600% of EPM and EPDM samples: applied stress (σ_0), relaxation times (τ_1 and τ_2), and relative weight of the first relaxation mechanisms φ_1 ($\varphi_2 = 1 - \varphi_1$).*

Sample	Ethylene content (wt%)	Diene content (wt%)	**$\sigma_0 = \sigma_1 + \sigma_2$ (MPa)**		**τ_1 (s)**		**φ_1**		**τ_2 (s)**	
			ε_{cost}=50%	ε_{cost}=600%	ε_{cost}=50%	ε_{cost}=600%	ε_{cost}=50%	ε_{cost}=600%	ε_{cost}=50%	ε_{cost}=600%
EPM	78	0	1.63	1.57	34828	43927	0.77	0.78	536	525
K2070P	73	0	0.76	1.04	29637	44382	0.74	0.79	460	483
K5170P	71	1.5	0.85	1.25	37964	57593	0.79	0.86	480	464
K5470P	70	4.6	1.02	1.53	34578	59829	0.77	0.84	480	540
K5470NT	70	4.6	1.09	1.80	48784	65772	0.79	0.81	474	303
K6260Q	67	2.8	0.22	0.66	7906	83689	0.27	0.64	150	227
K8570C	66	5.0	0.59	1.34	39558	83399	0.78	0.87	471	543
K5470C	66	4.6	0.79	1.29	42803	68234	0.80	0.85	427	484
K6160D	64	1.2	0.28	0.57	17534	43631	0.46	0.75	199	335
K4450	52	4.3	0.14	/	236	/	0.21	/	25	/
K3050	49	0	0.14	/	112	/	0.21	/	14	/
K9950C	44	9	0.32	/	29683	/	0.40	/	148	/

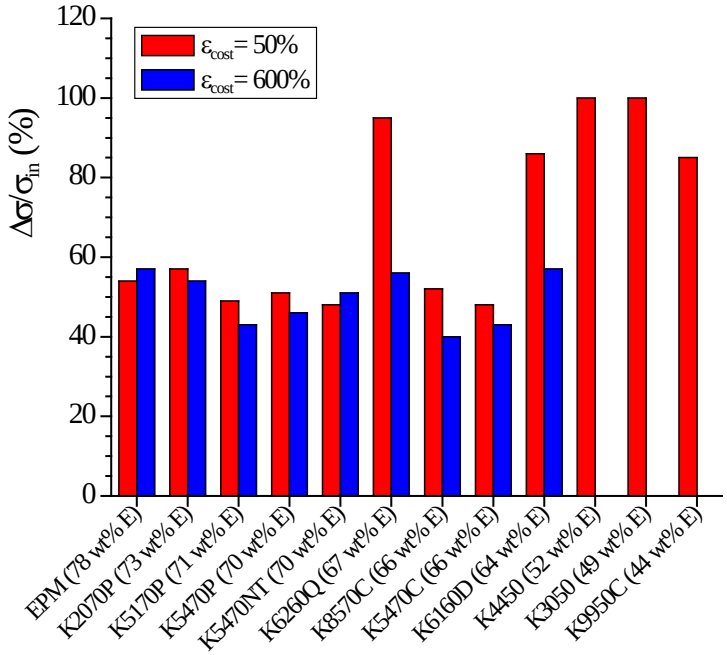

Figure 2.80. *Values of the relative drop of stress ($\Delta\sigma/\sigma_{in}$) evaluated from stress-relaxation curves at constant deformatuions ε_{cost}= 50% (red) and 600% (blue) for all samples of EPM copolymers and EPDM terpolymers.*

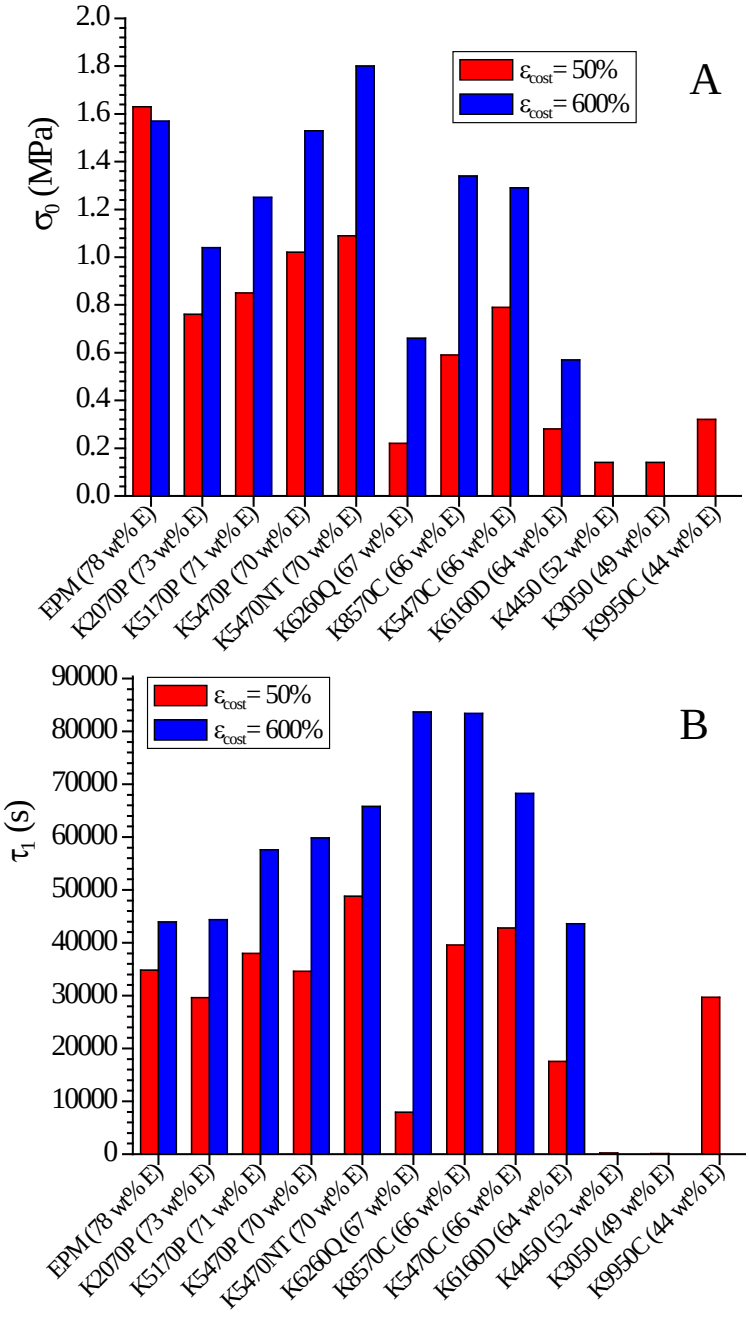
A
ε_{cost} = 50%
ε_{cost} = 600%
σ_0 (MPa)
2.0
1.8
1.6
1.4
1.2
1.0
0.8
0.6
0.4
0.2
0.0
EPM (78 wt% E)
K2070P (73 wt% E)
K5170P (71 wt% E)
K5470P (70 wt% E)
K5470NT (70 wt% E)
K6260Q (67 wt% E)
K8570C (66 wt% E)
K5470C (66 wt% E)
K6160D (64 wt% E)
K4450 (52 wt% E)
K3050 (49 wt% E)
K9950C (44 wt% E)
B
ε_{cost} = 50%
ε_{cost} = 600%
τ_1 (s)
90000
80000
70000
60000
50000
40000
30000
20000
10000
0
EPM (78 wt% E)
K2070P (73 wt% E)
K5170P (71 wt% E)
K5470P (70 wt% E)
K5470NT (70 wt% E)
K6260Q (67 wt% E)
K8570C (66 wt% E)
K5470C (66 wt% E)
K6160D (64 wt% E)
K4450 (52 wt% E)
K3050 (49 wt% E)
K9950C (44 wt% E)

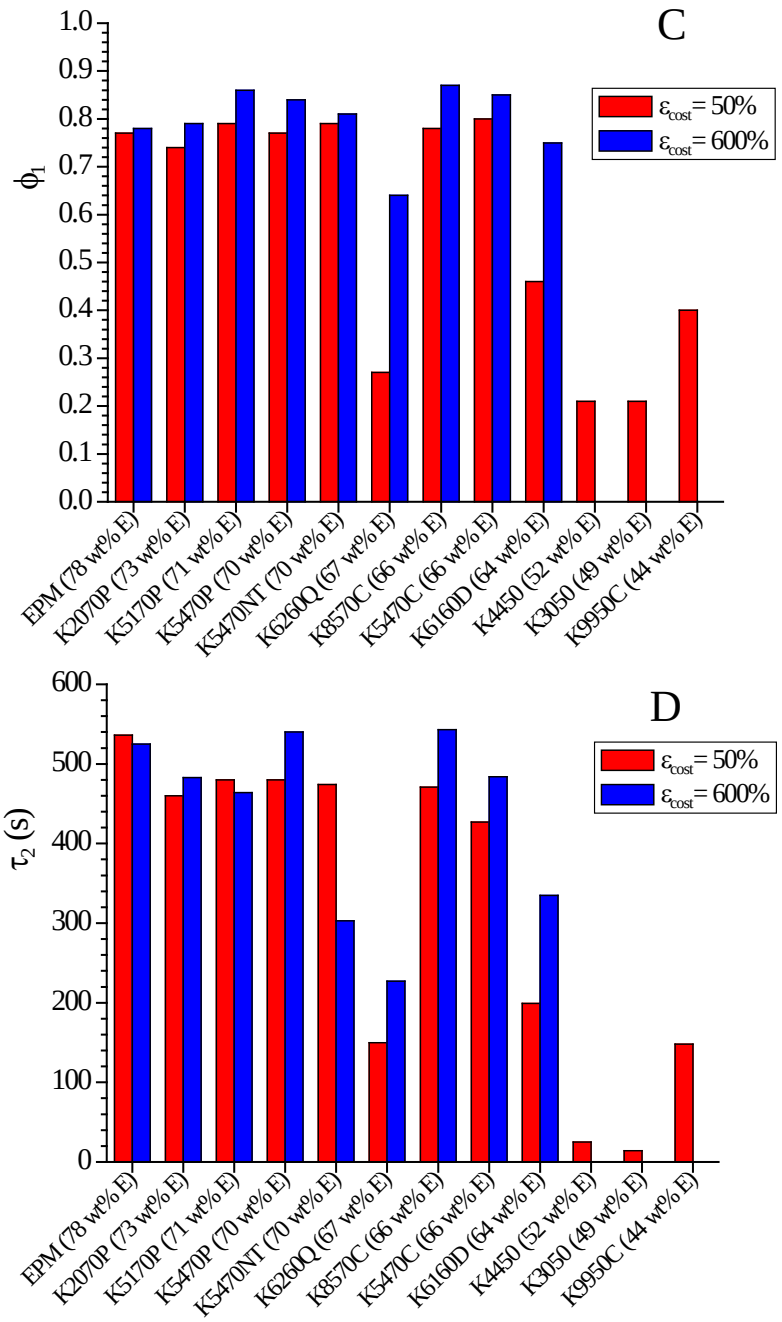

Figure 2.81. *Values of applied stress σ_0 (A), relaxation time τ_1* (B)*, relative weight of the first relaxation mechanisms φ_1 ($\varphi_2 = 1 - \varphi_1$) (C), relaxation time τ_2* (D)*, calculated from the fitting of stress-relaxation curves at ε_{cost}= 50% (red) and 600% (blue) for all samples of EPM copolymers and EPDM terpolymers.*

2.6.8 Relationships between SIC and mechanical properties

In this section a more detailed correlation between mechanical properties and SIC already introduced in sections 2.6.5 and 2.6.6 will be presented.

It is well-known that SIC influences mechanical properties of materials such as tensile strength, ductility, ability to relax when stress is applied and then removed (elastic recovery) or in experiments of stress-relaxation or creep. In many natural and synthetic elastomers, crystallinity may develop upon stretching providing higher tensile strength/strain hardening without using fillers or vulcanization/curing processes. At the same time they improve the entanglement effect acting as physical knots in the elastomeric network preventing viscous flow of the chains during stretching. This generally results in improvement of ductility and elastic recovery. In the case of EPM and EPDM samples, all differences in the mechanical behavior observed for samples of the three sets analyzed in this work are due to the occurrence of SIC and its entity.

Figure 2.82 shows a comparison between stress-strain curves of the crystalline sample EPM (78 wt% of ethylene) and one of the three copolymers belonging to the first group (K5470NT, 70 wt% of ethylene) and the corresponding X-ray diffraction patterns recorded during deformation. As discussed in section 2.6.6 the sample EPM is already crystalline in the undeformed state and stretching produce only orientation of these crystals of pseudohexagonal form of PE. The sample K5470NT, instead, is initially amorphous or shows faint crystallinity, but further crystallization occurs during stretching via SIC. The two samples show great differences in modulus and stress at yield, the crystalline sample EPM having higher modulus and yield stress, but they display similar stress at break and ductility thanks to occurrence of SIC in the sample K5470NT. As a matter of fact, the sample K5470NT shows stress at break even slightly higher than the crystalline sample EPM, even though it is initially nearly amorphous.

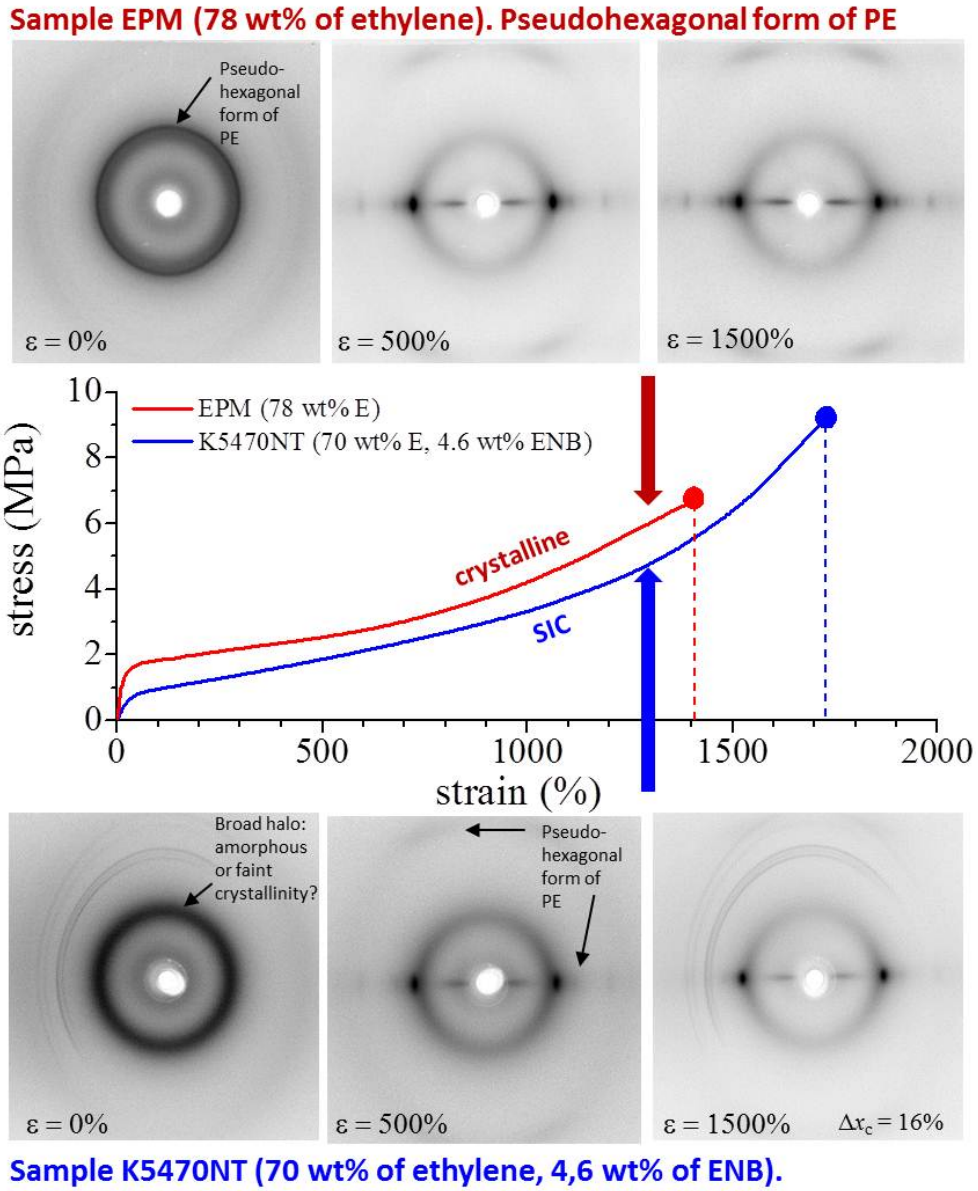

Figure 2.82 *Comparison of stress-strain curves and corresponding X-ray diffraction patterns recorded during stretching of the copolymer EPM (78 wt% of ethylene, red curve) and the terpolymer K5470NT (70 wt% of ethylene, blue curve).*

Figure 2.83 shows a comparison between stress-strain curves and corresponding X-ray diffraction patterns recorded during deformation of samples K5470NT (with 70 wt% of ethylene) and K6160D (with 64 wt% of ethylene). Both samples initially appear amorphous or contain the discussed cryptocrystallinity. Crystallization occurs upon stretching but the entity of SIC is higher in the sample K5470NT (belonging to the first set of samples) than in

sample K6160D (belonging to the second set of samples), as demonstrated by X-ray diffraction patterns and the corresponding values of the crystallinity increment Δx_c shown in the section 2.6.6. The difference in the amount of SIC has been explained in the section 2.6.6 in terms of difference of ethylene content and, hence, difference in the lengths of ethylene sequences, between samples belonging to the first set (having ethylene content in the range 78-70 wt%) and samples belonging to the second set (with 67-64 wt% of ethylene). The two samples show big differences in ductility and tensile strength due to different amounts of SIC. Without (or with small) SIC the mechanical properties do not improve during deformation.

SIC in elastomers may be a reversible phenomenon. Also for the samples of EPDM, when the tension is removed after deformation at a maximum strain, a partial melting of crystals formed upon stretching and a partial loss of crystal orientation have been observed, correspondingly to the elastic recovery (see section 2.2.6). Nevertheless, a residual crystallinity remains in stress-relaxed fibers. The residual crystallinity, as evaluated in section 2.6.6, is related to ethylene concentration (Figure 2.67A,B). Since crystals act as physical knots in the elastomeric network, the residual crystallinity also influence the elastic recovery and the mechanical properties of stress-relaxed fibers. In the section 2.6.5 it has been demonstrated that the tension set $t_s(\varepsilon)$ decreases and the percentage of the deformation ε which is recovered after removing the tension $R(\varepsilon)$ from deformation ε increases with decreasing ethylene concentration (Table 2.9 and Figure 2.51E). The amount of elastic recovery is related to the presence of initial crystallinity and of residual crystallinity after relaxation. In sample EPM with 78 wt% of ethylene the residual crystallinity, similar to the initial crystallinity, is very high, so that the tension set is high and $R(\varepsilon)$ is low. A fast decrease of the tension set is observed already for small decrease of ethylene concentration and all samples with ethylene content in the range 73-64% show similar low values of tension set and high values of elastic recovery (Table 2.9 and Figure 2.51E). Therefore, in this range of ethylene concentration, between the two vertical dashed lines in Figure 2.51E, the presence of initial crystallinity the occurrence of strain-hardening and the low values of tension set give the best elastic properties associated with remarkable strength.

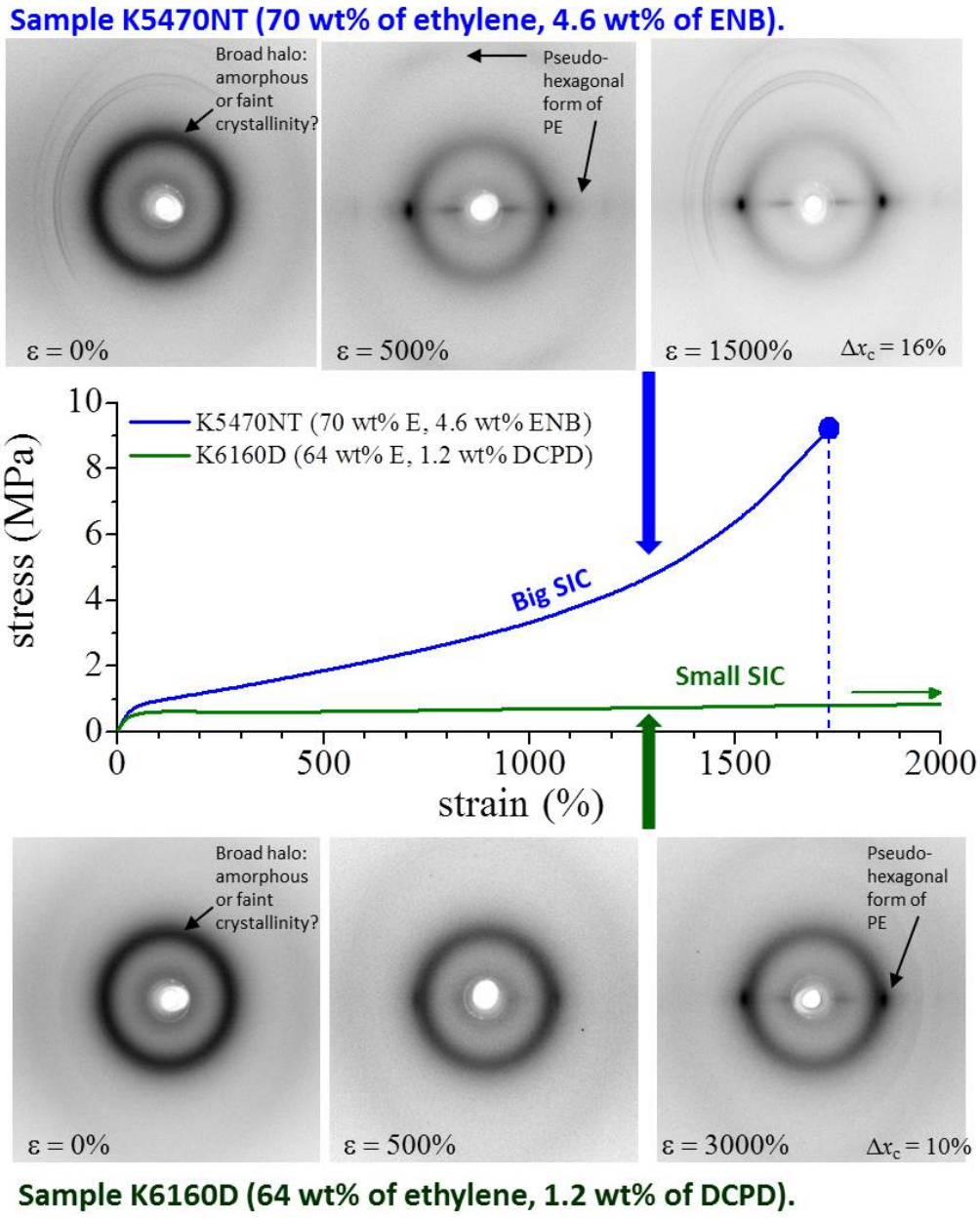

Figure 2.83 *Comparison of stress-strain curves and corresponding X-ray diffraction patterns recorded during stretching of the terpolymer K5470NT (70 wt% of ethylene, blue curve) and the terpolymer K6160D (64 wt% of ethylene, green curve).*

A comparison between stress-strain hysteresis cycles of samples EPM (78 wt% of ethylene) and K5470NT (70 wt% of ethylene) is shown in Figure 2.84. Although the undeformed films of these samples show similar values of stress and strain at break (Figure 2.49A,E), but different values of yield stress due to the different initial crystallinity, the mechanical behavior of stress-relaxed fibers is different. The sample K5470NT, and all samples with 73-70 wt % of ethylene, appears amorphous or very low crystalline in the undeformed state but crystallizes upon stretching. After releasing the tension a partial melting of crystals formed upon stretching occurs and the residual crystallinity after relaxation is lower than that in the sample EPM. This transformation is reversible. The continuous crystallization and melting phenomena occurring during stretching and relaxation allow development of good elastic properties associated with a remarkable strength. The mechanical strength of the sample K5470NT is lower than that of the sample EPM that, however, shows less elasticity.

A comparison of first and successive hysteresis cycles of stress-relaxed fibers of sample K5470NT (70 wt% of ethylene) and K6160D (64 wt% of ethylene) is shown in Figure 2.85. The residual crystallinity evaluated from X-ray diffraction patterns is lower in the sample K6160D (and in all samples of the second set, except samples K5470C and K8570C). Therefore, as discussed in section 2.6.5, stress-relaxed fibers of samples K6260Q and K6160D with 67 and 64 wt% of ethylene, respectively, show higher elastic recovery than samples with ethylene content in the range 73-70 wt%.

In section 2.6.7 the influence of SIC on stress-relaxation experiments has also been discussed. The main effect of SIC has been observed in the drop of stress occurring at different values of the constant deformation ε_{cost}. The drop of stress is unexpectedly lower in experiments performed at ε_{cost}= 600% than in experiments performed at ε_{cost}= 50% (Figure 2.69-2-72). This is due to the occurrence of stress induced crystallization (SIC) at the high deformation of 600%. Crystals formed upon stretching at high deformation act as physical knots in the elastomeric network preventing the viscous flow and limiting the drop of stress in the stress-relaxation.

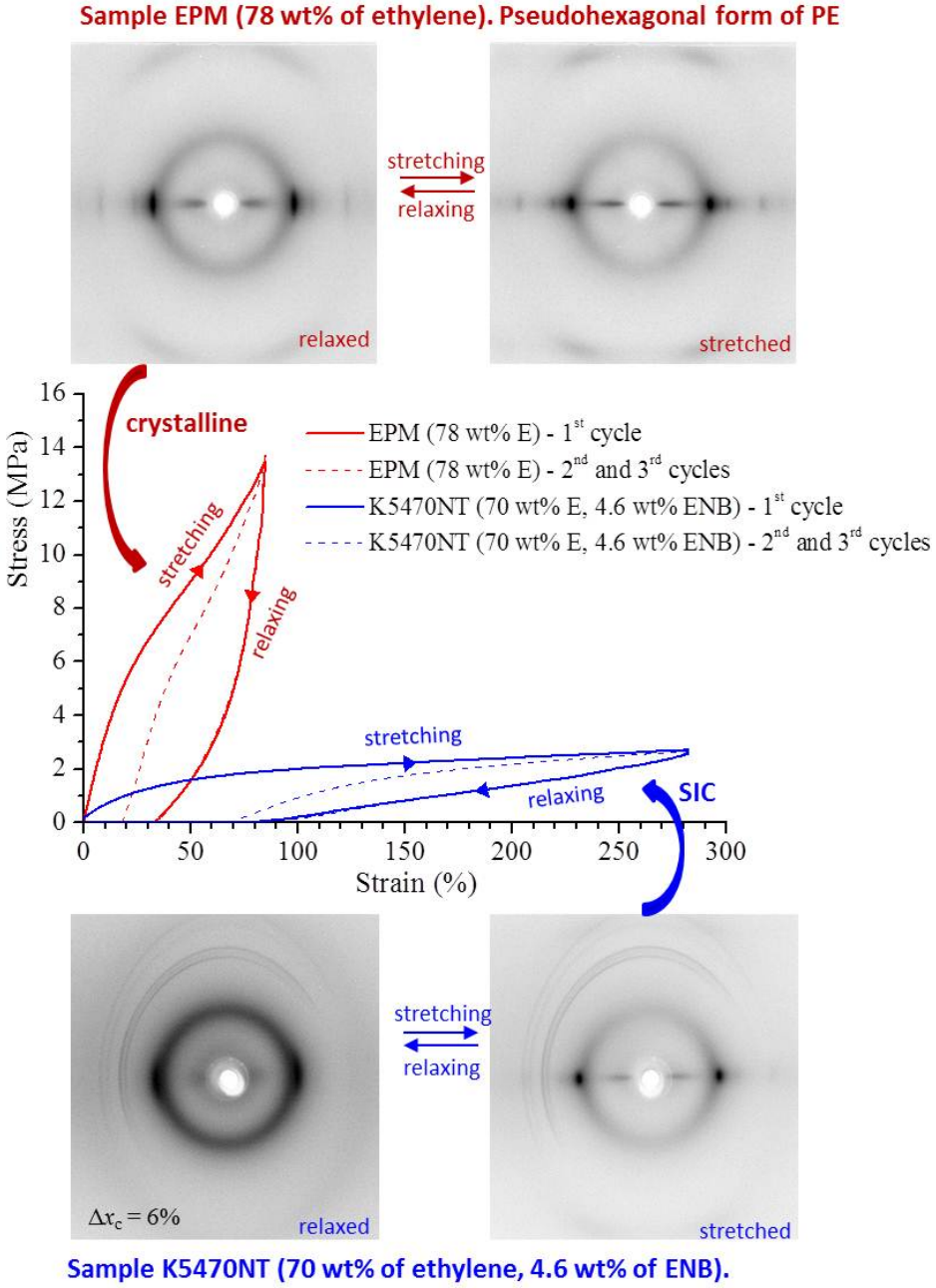

Figure 2.84. *Comparison of stress-strain hysteresis cycles of stress-relaxed fibers and corresponding X-ray diffraction patterns recorded during stretching and relaxation of the copolymer EPM (78 wt% of ethylene, red curve) and the terpolymer K5470NT (70 wt% of ethylene, blue curve).*

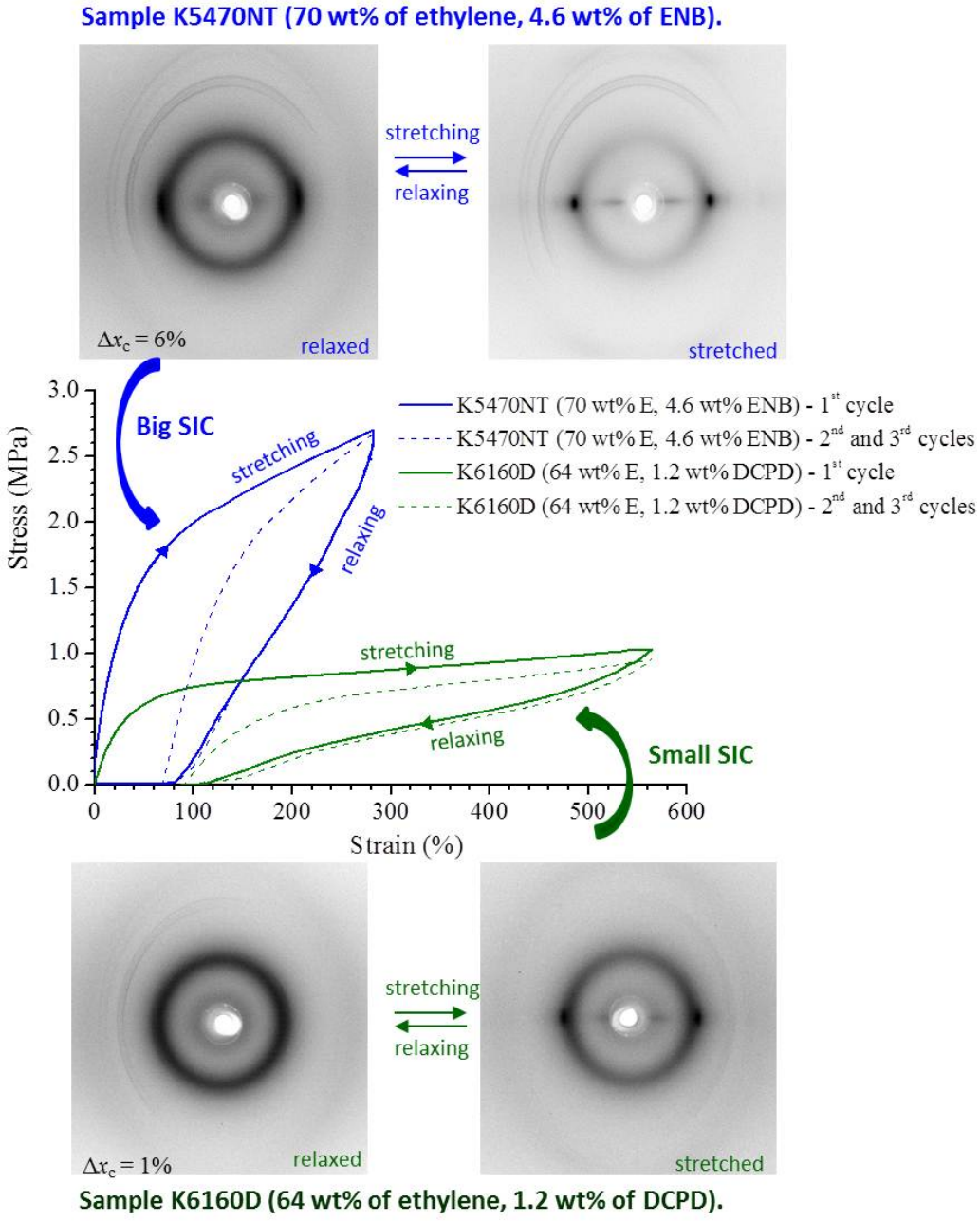

Figure 2.85 *Comparison of stress-strain hysteresis cycles of stress-relaxed fibers and corresponding X-ray diffraction patterns recored during stretching and relaxation of samples K5470NT (70 wt% of ethylene, blue curve) and K6160D (64 wt% of ethylene, green curve).*

2.7 Conclusions

In this chapter the relationships among composition, initial crystallinity, stress induced crystallization, residual crystallinity after relaxation and physical properties of EPM copolymers and EPDM terpolymers have been analyzed.

EPDM terpolymers with high ethylene contents (higher than 78-80 wt%) are generally crystalline, with crystallinity arising from crystallization of ethylene sequences in the polymorphic forms of polyethylene (PE). EPDM samples with ethylene concentration in the range 60-70 wt% appear instead amorphous in the undeformed state, if analyzed by classic wide-angle X-ray diffraction (WAXS). However, the possible presence of crystallinity in the underformed state in these copolymers, even when not visible through WAXS (***faint or crypto crystallinity***), has been analyzed in detail with different techniques of structural analysis in different length scales. In particular, analysis by small-angle X-ray diffraction scattering (SAXS) has surprisingly revealed the presence of a correlation peaks in samples with low ethylene concentration (67-64 wt%) that appear amorphous from the WAXS profiles. For these samples the presence of crystallinity has also been revealed by the presence of endothermic and exothermic peaks in the DSC heating and cooling curves. Therefore, SAXS and DSC data indicate the presence of a ***cryptocrystallinity*** in the undeformed state of these samples, surprisingly not detected by WAXS but revealed by SAXS. This result also indicate that, depending on the catalyst used for the synthesis, these samples are characterized by ethylene sequences long enough to crystallize even in the presence of a so high concentration of propylene units.

Crystallization further occurs during deformation and the Stress-Induced Crystallization (SIC) in EPM copolymers and EPDM terpolymers has been studied and correlated with the ethylene concentrations and the presence of initial crystallinity in the undeformed state. We found that initial crystallinity, SIC and residual crystallinity after elastic recovery are influenced by the ethylene concentration and distribution of comonomers along the chains and, in particular, by the length of ethylene sequences, which, in turn, is defined by the used catalyst. Hence, different microstructures induced by different catalysts produce different degrees of crystallinity and SIC, and consequent different mechanical properties and elastic behavior.

This study is an exemplary case of how the properties of targeted materials can be retro-designed by tailoring the microstructure by controlling the polymerization through the rational choice of catalysts and condition of polymerization.

References

1) a) Ethylene-Propylene Rubbers & Elastomers (EPR/EPDM), in https://iisrp.com/, *International Institute of Synthetic Rubber Producers*. b) Handbook of Elastomers, Second Edition, **2001**. A. K. Bhowmick, H. L. Stephens, Eds., CRC Press. c) E. K. Easterbrook, R. D. Allen, *Ethylene-Propylene Rubber*, in Rubber Technology, M. Morton Ed., Springer **1999**. d) J. W. M. Noordermeer, *Ethylene–Propylene Elastomers*, Encyclopedia of Polymer Science and Technology, Wiley, **2002**. e) Advances in Elastomers Vol. I: Blends and Interpenetrating Networks, Springer, Editors: P. M. Visakh, S. Thomas, A. K. Chandra, A. P. Mathew, **2013**. f) Advances in Elastomers, Vol.II: Composites and Nanocomposites, Springer, Editors: P. M. Visakh, S. Thomas, A. K. Chandra, A. P. Mathew, **2013**. d) Handbook of Specialty Elastomers - CRC Press Book, Robert C. Klingender Editor. **2008.**

2) G. Natta, G. Mazzanti, G. Boschi, *Italian Patent* **1955**, 554, 803

3) M. Galimberti in Proceeding of "Elastomers 2001" First European school of European Polymer Federation. Gargnano (BS) (I), June 2001.

4) R. J. Wehrle, Master Thesis, B.S. Northern Kentucky University, **2012**.

5) C. M. Blow, C. Hepburn, *Rubber technology and manufacture*. Butterworth Scientific, London (1982).

6) F. R. Eirich, *Science and technology of rubber*. Academic Press, New York, **1978**.

7) M. S. Khan, D. Lehmann, G. Heinrich *Express Polymer Letters* **2008**, *2*, 284.

8) D. Pantea, H. Darmstadt, S. Kaliaguine, C. Roy, *Applied Surface Science* **2003**, *217*, 181.

9) D. Pantea, H. Darmstadt., S. Kaliaguine., C. Roy *Journal of Analytical and Applied Pyrolysis*, **2003**, *67*, 55.

10) J. Donnet, A. Vidal, *Advances in Polymer Science* **1986**, 103–127, Eds.: A. Abe, A. C. Albertsson, R. Duncan, K. Dusek., W. H. de Jeu, H. H. Kausch., S. Kobayashi, K. S. Lee, L. Leibler, T. E. Long., I. Manners, M. Mölle, O. Nuyken, E. M. Terentjev, B. Voit, G. Wegner, U. Wiesner, Springer Berlin, Heidelberg.

11) D. C. Edwards, *Journal of Materials Science*, **1990**, *25*, 4175.

12) V. M. Litvinov, P. A. M. Steeman, *Macromolecules*, **1999**, *32*, 8476.

13) G. Heinrich, T. A. Vilgis, *Macromolecules* **1993**, *26*, 1109.

14) F. W. Barlow, Rubber compounding: Principles, materials, and techniques. Marcel Dekker, New York, 1988.

15) S. Wolff, M. J. Wang, *Rubber Chemistry and Technology* **1991**, *64*, 714.

16) S. Wolff, M. J. Wang, *Rubber Chemistry and Technology*, **1992**, *65*, 329.

17) S. Wolff, *Rubber Chemistry and Technology*, **1996**, *69*, 325.

18) J. Fröhlich, W. Niedermeier, H. D. Luginsland, *Composites Part A: Applied Science and Manufacturing*, **2005**, *36*, 449.

19) Z.H. Li. J. Zhang, S. J. Chen, *eXPRESS Polymer Letters*, **2008**, 2, 695.

20) a) G. Natta, G. Mazzanti, A. Valvassori, G. Sartori, *Chim. Ind.(Milan)* **1958**, *40*, 717. b) G. Natta, G. Mazzanti, A. Valvassori, G. Sartori, *Chim.Ind.(Milan)* **1958**, *40*, 896.

21) M. Kakugo, Y. Naito, K. Mizunuma, T. Miyatake, *Macromolecules* **1982**, *15*, 1150.

22) S. Cesca, *Macromol Rev* **1975**, *10*, 1.

23) C. J. Carman, C. E. Wilkes, *Rubber Chem Techonol* **1971**, *44*, 781.

24) a) G. Natta, I. Pasquon, A. Zambelli, *J. Am. Chem. Soc.* **1962**, *84*, 1488. b) A. Zambelli, G. Natta, I. Pasquon, *J. Polym. Sci. Part C* **1963**, *4*, 411.

25) Y. Doi, S. Suzuki, K. Soga, *Makromol Chem Rapid Commun* **1985**, *6(10)*, 639.

26) a) A. Zambelli, G. Natta, I. Pasquon, R. Signorini, *J. Polym. Sci.* **1967**, *C16*, 2485. b) A. Zambelli, I. Pasquon, R. Signorini, G. Natta G. *Makromol Chem* **1968**, *112*, 160.

27) G. Natta, A. Zambelli, G. Lanzi, I. Pasquon, E. R. Mognaschi, A. L. Segre, P. Centola, *Makromol Chem* **1965**, *81*, 161.

28) Y. Ma, D. Reardon, S. Gambarotta, G. Yap, H. Zahalka, L. C. Hyder, *Organometallics* **1999**, *18*, 2773.

29) H. N. Cheng, *Macromolecules* **1984**, *17*, 1950.

30) H. Sinn, W. Kaminsky, H. J. Vollmer, R. Woldt, *Angew. Chem. Int Ed Engl* **1980**, *92*, 396.

31) J. A. Ewen, *J Am Chem Soc* **1984**, 106, 6355.

32) W. Kaminsky, K. Kulper, H. H. Brintzinger, F. R. W. Wild, *Angew Chem Int Ed Engl* **1985**, *24*, 507.

33) H. H. Brintzinger, D. Fischer, R. Mülhaupt, B. Rieger, R. M. Waymouth, *Angew Chem, Int Ed Engl* **1995**, *34*, 1143.

34) L. Resconi, L. Cavallo, A. Fait, F. Piemontesi, *Chem Rev* **2000**, *100*, 1253.

35) V. Busico, R. Cipullo, *Prog. Polym. Sci*. **2001**, *26*, 443.

36) P. Corradini, L. Cavallo, G. Guerra G in Metallocene based polyolefins, J. Schevis, W. Kaminsky Editors, vol.2 Chichester, Wiley, 2000 p 3-36.

37) a) J. C. Stevens, F. J. Timmers, D. R. Wilson, G. F. Schmidt, P. N. Nickias, R. K. Rosen, G. W. Knight, S. Y. Lais (Dow Chemical Company) *Eur. Pat Appl* 0 416 815, 1990. b) J. C. Stevens *Stud Surf Sci Catal* **1994**, *89*, 277.

38) J. Okuda In Metalorganic catalysts for synthesis and polymerization, W. Kaminsky editor, Berlin: Springer, 1999. p. 200.

39) W. J. Whang, S. Zhu, *Macromolecules* **2000,** *33*, 1157.

40) J. C. Randall, *Macromolecules* **1978**, *11*, 33.

41) I. W. Bassi, P. Corradini, G. Fagherazzi, A. Valvassori, *Eur. Polym. J.* **1970**, *6*, 709.

42) F. P. Baldwin, G. Ver Strate, *Rubber Chem. Tecnol.* **1972**, *45*, 709.

43) E. R. Walter, E. P. Reding, *J. Polym. Sci.* **1956**, *21*, 561.

44) E. A. Cole, D. R. Holmes, *J. Polym. Sci.* **1956**, *46*, 245.

45) P. R. Swann, *J. Polym. Sci*. **1962**, *56*, 409.

46) B. Wunderlich, D. Poland, *J. Polym. Sci*. **1963**, *1*, 357.

47) C. H. Baker, L. Mandelkern, *Polymer* **1965**, *7*, 71.

48) G. Crespi, A. Valvassori, V. Zamboni, V. Flisi, *Chim. Ind. (Milan)* **1973**, *55*, 130.

49) J. Preedy, *Polym. J*. **1973**, *5*, 13.

50) G. Ver Strate, Z. W. Wilchinsky, *J. Polym. Sci*. Part A2 **1971**, *9*, 127.

51) B. J. R. Scholtens, E. Riande, J. E. Mark, *J. Polym. Sci. Polym. Phys. Edn*. **1984**, *22*, 1223.

52) L. Mandelkern, *Crystallization of Polymers,* McGraw-Hill, New York pp.166-214 (1964).

53) R. M. Eichorn, *J. Polym. Sci.* **1958**, *31*, 197.

54) C. W. Bunn, *Trans. Faraday Soc*. **1939**, *35*, 482.

55) O. Ruiz de Ballesteros, F. Auriemma, G. Guerra, P. Corradini, *Macromolecules* **1996**, *29*, 7141.

56) T. Seto, T. Hara, K. Tanaka, *J. Appl. Phys*. **1968**, *37*, 31.

57) A. Muller, K. Lonsdale, *Acta Crystallogr*. **1968**, *1*, 129.

58) C. De Rosa, F. Auriemma. *Crystals and Crystallinity in Polymers,* Wiley, 2014.

59) F. Auriemma, P. Corradini, C. De Rosa, *Adv. Polym. Sci.* **2005**, *181*, 1.

60) G. Guerra, O. Ruiz de Ballesteros, V. Venditto, M. Galimberti, F. Sartori, R. Pucciariello, *J. Polym. Sci., Part B: Polym. Phys.* **1999**, *37*, 1095.

61) M. Galimberti, E. Martini, F. Piemontesi, F. Sartori, L. Resconi, E. Albizzati, *Macromol. Symp*. **1995**, *89*, 259.

62) M. Galimberti, L. Resconi, E. Martini, F. Guglielmi, E. Albizzati, (Spherilene srl (Italy)). Eur. Pat. EP-B **1993**, *586*, 658.

63) L. R. G. Treloar, *The Physics of rubber elasticity* Clarendon Press, Oxford (1975).

64) G. Guerra, M. Ilavský, J. Biroš, K. Dušek, *Colloid Polym Sci.* **1981**, *259*, 1190.

65) https://www.mt.com/it/it/home.html

66) R. P. Quirk, M. A. A. Alsamarrie, *Physical constants of polyethylene*. In: Polymer Handbook, Eds J. Brandrup, E. H. Immergut, 3rd Ed. New York: Wiley; 1989. p. V/19.

67) R. J. Roe, *Methods of X-ray and Neutron Scattering in Polymer Science*; Oxford University Press: New York, 2000.

68) D. Debye, A. M. Bueche, *J. Appl. Phys.* **1949**, *20*, 518.

69) (a) F. J. Balta-Calleja, C. G. Vonk, *X Ray Scattering of Synthetic Polymers*. Elsevier: Amsterdam, 1989. (b) I. G. Voigt-Martin, R. Alamo, L. Mandelkern, L. *J. Poyml. Sci., Part B: Polym. Phys.* **1986**, *24*, 1283. R. Alamo, R. H. Glaser, L. Mandelkern, *J. Polym. Sci., Part B: Polym. Phys.* **1988**, *26*, 2169. R. Alamo, L. Mandelkern, *Macromolecules* **1989**, *22*, 1273. R. Alamo, R. B. D. Viers, L. Mandelkern, *Macromolecules* **1993**, *26*, 5740. J. R. Isasi, J. A. Haigh, J. T. Graham, L. Mandelkern, R. Alamo, *Polymer* **2000**, *41*, 8813.

70) B. Poon, M. Rogunova, A. Hiltner, E. Baer, S. P. Chum, A. Galeski, E. Piorkowska, *Macromolecules* **2005**, *38*, 1232.

71) G. Strobl, *The Physics of Polymers*; Springer: Berlin, 1996.

72) J. R. Katz, *Naturwiss*. **1925**, *13*, 410.

73) B. Huneau, *Rubber Chemistry And Technology*, **2011**, *84*, 425.

74) N. Bekkedahl, L. A. Wood, *Ind. Eng. Chem.* **1941**, *33*, 381.

75) L. A. Wood and N. Bekkedahl, *J. Appl. Phys.* **1946**, *17*, 362.

76) A. N. Gent, *Trans. Faraday Soc.* **1954**, *50*, 521.

77) J.-B. Le Cam, *Rubber Chem. Technol.* **2010**, *83*, 247.

78) E. H. Andrews, *Pure Appl. Chem.* **1972**, *31*, 91.

79) D. Luch, G. S. Y. Yeh, *J. Appl. Phys.* **1972**, 43, 4326.

80) D. Goritz, R. Grassler, *Rubber Chem. Technol.* **1987**, *60*, 217

81) M. Tosaka, S. Kohjiya, Y. Ikeda, S. Toki, and B. S. Hsiao, *Polym. J.* **2010**, *42*, 474.

82) Y. Tanaka, *Rubber Chem. Technol.* **2001**, 74, 355.

83) J. Rault, J. Marchal, P. Judeinstein, P. A. Albouy, *Macromolecules* **2006,** *39*, 8356.

84) A. M. Healey, P. J. Hendra, Y. D. West, *Polymer* **1996**, *37*, 4009.

85) S. Toki, I. Sics, S. F. Ran, L. Z. Liu, B. S. Hsiao, S. Murakami, M. Tosaka, S. Kohjiya, S. Poompradub, Y. Ikeda, and A. H. Tsou, *Rubber Chem. Technol.* **2004**, *77*, 317.